Automated Reduction of Data from Images and Holograms

*Proceedings of a workshop held at
Ames Research Center
Moffett Field, California
January 10-11, 1985*

NASA

Automated Reduction of Data from Images and Holograms

Edited by
G. Lee, J. D. Trolinger,
and Y. H. Yu
NASA Ames Research Center
Moffett Field, California

Proceedings of a workshop held at
Ames Research Center
Moffett Field, California
January 10-11, 1985

ERRATA

NASA Conference Publication 2477

AUTOMATED REDUCTION OF DATA FROM IMAGES AND HOLOGRAMS

Edited by: G. Lee, J. D. Trolinger, and Y. H. Yu
August 1987

Table of Contents, page vii: Mel Roquermore, U.S. Air Force Wright
Aeronautical Laboratories should be:

Mel Roquemore, U.S. Air Force Wright Aeronautical Laboratories

Table of Contents, page viii: J. Power and D. Netzer, Naval Postgraduate
School should be:

J. Powers and D. Netzer, Naval Postgraduate School

Table of Contents, page x: Cecil Hess and J. D. Trolinger, Spectron
Development Laboratories should be:

Cecil F. Hess and J. D. Trolinger, Spectron Development Laboratories

Pages 129 and 130 have been reversed.

Pages 218 and 219 have been reversed.

FOREWORD

This workshop had its origin with the meeting of a small
group of scientists from the U. S. Army Aeromechanics
Laboratory, NASA Ames Research Center, U. S. Air Force
Weapons Laboratory, Rocketdyne, and Spectron Development
Laboratories, at Kirkland Air Force Base, N. M., to swap
ideas on automated data reduction of holographic
interferometry data. The various groups were in the process
of solving virtually the same, extremely complex problem for
different applications. This is the same problem that has
escaped a truly practical solution for nearly twenty years.
Everyone left the meeting with more knowledge than he had
brought and most expressed conviction that the meeting should
be repeated and expanded to include other groups working on
the same or similar problems.

Planning of this workshop was done by George Lee, Yung
Yu and myself during several subsequent meetings and phone
conversations, and we received advice from a number of
individuals.

The basic philosophy and goals for the workshop were
agreed upon at the outset, but these continuously evolved
with time and discussions with attendees. Our intention was
to make this a workshop and not a seminar. The group we
assembled was unique. Everyone had an interest in automated
data reduction and was an expert in some aspect of the
problem.

We decided that every attendee should be a potential
contributor to the overall solution of the problem of data
reduction in holography and related areas. We contacted as
many people as we know working in this area and ask them for
additional candidates. I believe we reached, in this way, a
majority of the experts in the United States and a
significant representation from Europe and Asia. Most
likely, we overlooked some important people and can only
apologize for that shortcoming.

Initially, we had expected to persuade 25 or 30 people
to participate. The response to the workshop was
overwhelming and the number of people who expressed interest,

though satisfying, created the difficult problem of maintaining the desired workshop atmosphere for so many people. This makes it all the more important to establish clear goals and procedures.

This was not intended to be a meeting for simply giving a paper or listening to others give papers. We provided a formal meeting structure from which everyone was encouraged to work informally. One objective of the workshop was to bring together experts who has a common technical problem, questions to ask, ideas to air, observations to make, and to provide the atmosphere for brainstorming. Of equal importance was to allow the attendees to meet each other and to gain different prospectives on the needs and approaches being taken to solve the problem of automated data reduction. I believe that this workshop increased communication between workers, created a new synergism, and provided new incentives that will be felt by this field for years to come. The ultimate goal for the workshop was to speed up the solution of the problem of automated data reduction. I believe we accomplished that goal.

The first few lectures were selected to provide a cursory review, a foundation, and a common language for the rest of the workshop. It was assumed that attendees all know how holography and holographic interferometry was done. There was no need to go into great detail describing holographic setups.

We focused on data extraction from holograms, data handling, and interpretation.

A large part of the first day was devoted simply to having every attendee briefly describe his organization's need and plan to solve some part of this problem. We encouraged the informal interchange of ideas between all attendees during all parts of the workshop and requested that useful findings be described to the whole group at an appropriate time. Working groups interested in specific problem areas were formed on both days to further enhance this type of communication.

I would like to thank NASA Research Center for providing support and a place to assemble. Drs. Lyn Caveny and Julian Tishkoff of the Air Force Office of Scientific Research and Dr. Robert Singleton of the U. S. Army Research Office, provided advice as well as financial support.

J. D. Trolinger, General Chairman of Workshop

ABSTRACT

Proceedings of a Workshop on Automated Reduction

of Data from Images and Holograms

Editors: G. Lee, J. Trolinger and Y. Yu

Laser techniques are widely used for the diagnostics of aerodynamic flow and particle fields. The storage capability of holograms has made this an even more powerful technique. Unfortuately, the techniques to store optical data in holograms has far outpaced the ability to extract the data from the holograms. This data reduction bottleneck has for years obstructed the used of holography to its fullest potential. In several notable instances this shortcoming has led to the abandonment of the technique as a routine procedure.

In recent years several events have fostered a reversal in this trend. Holographic techniques have provided badly needed data which could not otherwise be obtained. Ever increasing, affordable computer power has offered a potential, practical solution to the extremely difficult problem of image processing and autometed data reduction.

Over 60 researchers in the fields of holography, particle sizing and image processing convened at NASA-Ames Research Center for a two day workshop to discuss the above topics. The research programs of ten government laboratories, several universities, industry and foreign countries were presented. A number of papers on holographic interferometry with applications to fluid mechanics were given. Several papers on combustion and particle sizing, speckle velocimetry and speckle interferometry were given. Finally, a session on image processing and automated fringe data reduction techniques and the type of facilities for fringe reduction was held.

TABLE OF CONTENTS

PRECEDING PAGE BLANK NOT FILMED

PAGE VI INTENTIONALLY BLANK

WORKSHOP OBJECTIVES

ACCELERATE SOLVING THE HOLOGRAPHY DATA REDUCTION PROBLEM

HOW?

- GET THE PEOPLE WORKING IN THE FIELD TOGETHER.

- REVIEW WHAT IS AVAILABLE.

- REVIEW PROBLEMS, POTENTIAL SOLUTIONS, PLANS, APPLICATIONS.

- AIR IDEAS, ASK QUESTIONS, BRAINSTORM.

- CREATE SYNERGISM THAT WILL LAST BEYOND THE WORKSHOP.

WORKSHOP GUIDELINES

- THE TALKS ARE TO SERVE ONLY AS A FRAMEWORK FOR THE WORKSHOP.
  - IMPROMPTU "IN THE HALLWAY" DISCUSSIONS ARE ENCOURAGED.
  - MEET AS MANY OF THE ATTENDEES AS POSSIBLE ... GET INVOLVED.
  - EXCHANGE IDEAS AND PAPERS AND ARRANGE SUBSEQUENT MEETINGS.
  - ENJOY BEING WITH YOUR PEERS.

- KEEP TALKS BRIEF, INTENSIVE, FOCUSED ON DATA REDUCTION.
  - ALL ATTENDEES ARE EXPERTS IN HOLOGRAPHY.
  - DO NOT EXPLAIN HOW HOLOGRAMS ARE MADE OR HOW THEY WORK.
  - DO NOT SPEND (MUCH) TIME TOUTING THE ADVANTAGES OR BENEFITS OF HOLOGRAPHY ("YOU WOULD BE PREACHING TO THE CHOIR").

- INNOVATE AND BE SPONTANEOUS.

- GO AWAY WITH SOMETHING YOU CAN USE ... LEAVE SOMETHING SOMEONE ELSE CAN USE.

85-68085/21

ONGOING PROGRAMS IN HOLOGRAPHY

85-68085/21

GENERAL AREA	PROGRAMS	
HOLOGRAPHY TOMOGRAPHY	(1)	DEVELOP AND APPLY NEW CODE FOR 3-D DENSITY MEASUREMENT
AERO-OPTICS HOLOGRAPHY	(2)	AIRBORNE HOLOGRAPHY OF FLOW OVER WINDOWS
	(3)	WIND TUNNEL STUDY OF FLOW OVER CAVITIES
	(4)	WIND TUNNEL STUDY OF HYPERSONIC FLOW OVER WINDOWS
FLUID MECHANICS HOLOGRAPHY	(5)	DEVELOP THERMOPLASTIC DEVICE AND APPLICATION
	(6)	FLOW DIAGNOSTICS IN A ROTARY ENGINE
	(7)	FLOW DIAGNOSTICS OF ZERO-G CRYSTALINE GROWTH
PARTICLE FIELD HOLOGRAPHY	(8)	PARTICLE BREAKUP IN ACCELERATING FLOWS
	(9)	PARTICLE HYPERVELOCITY IMPACT
	(10)	AUTOMATED DATA REDUCTION
NONDESTRUCTIVE TESTING	(11)	MANUFACTURING APPLICATION
	(12)	CIRCUIT BOARD INSPECTION
COMMERCIAL HARDWARE	(13)	HOLOCAMERA - MODEL HC5000
	(14)	RECONSTRUCTION SYSTEM
	(15)	HOLOGRAPHIC OPTICAL ELEMENTS

S1-35
103442
S1

INFORMATION RETRIEVAL FROM HOLOGRAPHIC INTERFEROGRAMS - FUNDAMENTALS AND PROBLEMS*

Charles M. Vest

The University of Michigan

ABSTRACT

Holographic interferograms can contain large amounts of information about flow and temperature fields. Their information content can be especially high because they can be viewed from many different directions. This multidirectionality, and fringe localization, add to the information contained in the fringe pattern if diffuse illumination is used. Additional information, and increased accuracy, can be obtained through the use of dual reference wave holography to add reference fringes or to effect discrete phase shift- or hetrodyne interferometry.

Automated analysis of fringes is possible if interferograms are of simple structure and good quality. However, in practice a large number practical problems can arise, so that a difficult image processing task results.

INTRODUCTION

Realization of the potential of holographic interferometry as a scientific and engineering tool requires quantitative interpretation of holographic interferograms. The usefulness of the technique increases appreciably if data aquisition is rapid and processing of information contained in interferograms can be highly automated. This is particularly true in fields like fluid mechanics and combustion diagnostics where the fields to be measured may be quite complicated and changing rapidly with time. In this paper we consider the information contained in holographic interferograms of transparent media, discuss the basic concepts of quantitative interpretation of holographic interferograms, and pose the problems which must be addressed by those in involved in the development of automated systems for analysis of interference fringe patterns.

The process of applying holographic interferometry to fluid mechanics or combustion diagnostics, or for that matter any other scientific or industrial problem area, consists of the following ten steps:

1. Problem definition and goals
2. Apparatus and setup
3. Establishment of flow
4. Recording the hologram
5. Developing the hologram
6. Reconstruction
7. Viewing and storing
8. Analysis of fringes
9. Physical interpretation
10. Use of information

Holographic interferometry is defined as the interferometric comparison of two or more waves, at least one of which is holographically reconstructed. The composite of these two or more waves is referred to as a <u>holographic interferogram</u>. The term <u>interferogram</u> with no modifying adjective denotes a pattern of interference fringes recorded on photographic film or formed on a two-dimensional viewing screen, video device or the retina of the eye. It is assumed that the reader is familiar with the basic technology of holography.

This process in fact contains at least two feedback loops because physical interpretation generally feeds back to refinement of the apparatus and setup, and the use of information obtained from the holographic analysis usually feeds back to refinement of problem definition and goals.

In this paper we emphasize, in broad terms, the analysis of fringes and physical interpretation. However, the designer of an automated system for analysis of holographic interferograms must consider all eight of the above steps.

FORMATION OF HOLOGRAPHIC INTERFEROGRAMS

In order to extract quantitative information from an interferogram, one must understand the process by which the interferogram was initially formed. This process is summarized in figure 1. A wave of coherent light enters, and propagates through, a test object which is the region of gas or liquid in which the phenomenon of interest occurs. The wavefronts of this coherent light are distorted, and possibly attenuated, by their interaction with the test object. The deformed wavefronts strike a holographic recording device where they are mixed with a reference wave in order to record a hologram. Most commonly this process is repeated twice, once with flow occurring and once with no flow, in order to form a two-exposure holographic interferogram. By illuminating such a two-exposure hologram the deformed an undeformed waves are simultaneously reconstructed. They enter some type of viewing or recording device to form an interferogram. This interferogram is the irradiance pattern of

the sum of the two coherent waves.

The basic information contained in a holographic interferogram is the distribution of relative phase of two waves encoded in a fringe pattern. However, there is additional information which may be of importance in quantitative evaluation. In many cases the fringes will be localized in space, and the apparent location of fringe localization provides some information about the field. Variation of background irradiance in the interferogram provides information about attenuation of the waves by the test object, and this attenuation constitutes spectroscopic data, i.e. it is related to the local absorbtivity of the fluid at the given wavelength of light. Knowledge of the precise direction of viewing of the interferogram is important information for quantitative evaluation.

To investigate evaluation of interferograms it generally is convenient to think in terms of ray optics, rather than wave fronts. Figure 2 is a general schematic diagram of the formation of an interferogram. This figure reminds us of three important facts about the formation of interferograms. First, rays are bent (refracted) as they pass through the active test object. Second, interference occurs only on the surface of the detector (film, viewing screen, video camera, retina, etc.). Third, knowledge of the imaging system such as its direction of view, location of image plane, and numerical aperture is required for proper interpretation.

In figure 2 we show two rays. The first (DFP') passed through the test section when no flow was occuring and its refractive index was a uniform value n_0 . The second ray (ACP') is bent by refraction as it passes through the nonuniform refractive index field $n(r,\phi)$ due to the flow of interest. These two rays meet and interfere on a detector surface at point P'. The imaging system is focused on the object plane indicated in the figure so that the interferogram appears to be an image of fringes in the plane containing point P within the test object. The optical path difference which can be determined from the fringe pattern is given by equation (1):

$$\Delta\widetilde{\Phi}(\rho,\theta) = \int_A^B n(r,\phi)ds + n_0(\overline{BC} - \overline{DE} - \overline{EF})\tag{1}$$

This expression for the optical pathlength difference can be thought of as a "pathlength transform" which must be inverted to determine the refractive index given measured values of the optical pathlength.

Fortunately in many cases refraction is sufficiently small that both rays contributing to the interference pattern at point

P'are very nearly straight lines passing in the same direction through the neighborhood of point P. We refer to this as the _refractionless limit_, a situation which usually can be assumed in aerodynamics if shocks are not present. In this case the path integral of equation (1) simplifies to the following line integral:

$$\overline{\Delta\Phi}(\rho,\theta) = \int_{E}^{F} [n(r,\phi) - n_o]dz. \tag{2}$$

To evaluate an interferogram we must carry out the following steps:

1. Measure the location of the fringes and convert them to a phase distribution.

2. Invert an equation such as (1) or (2) above to convert the phase distribution to a refractive index distribution within the fluid.

3. Convert the distribution of refractive index to a distribution of some fluid property (for example mass density).

4. Possibly convert the distribution of this fluid property to a derived property (such as velocity of a compressible flow).

Consider the simplest case of a boundary layer like flow over a flat surface. The refraction effects are negligible, the flow and refractive index fields have essentially no variation in the z direction, and the holographic object wave is a plane wave such that all optical rays are essentially straight lines parallel to the surface. In this case, which is shown schematically in figure 3, fringes are nonlocalized, i.e. they can be observed in any plane normal to the z axis. The fringe pattern is shown schematically in this figure. Fringe numbers are assigned as indicated and as shown in equations (3) and (4), the determination of the refractive index distribution is quite simple.

$$\overline{\Delta\Phi}(y) = \int_{0}^{L} [n(y) - n_o]dz$$

$$= [n(y) - n_o]L = N\lambda \tag{3}$$

$$n(y) - n_o = N\lambda/L \tag{4}$$

Now suppose that a diffusing screen, for example a plate of ground or opalized glass is placed behind the test section as shown in figure 4. Three things will be different in this

interferogram than in that considered above. First, the fringe pattern will be viewable from a variety of directions by the unaided eye or a camera. Second, the fringes will appear to be localized in space, as indicated in the figure. This means that the eye or other viewing instrument must be focused on the region of apparent localization of the fringes. For information about the phenonmenon of fringe localization, see reference 1. Third, the interferogram will now contain laser speckle. That is, the fringes will be a modulated speckle pattern.

To first approximation, the fringes will be localized in the region given by equation (5):

$$z_l = \frac{\int_{-\infty}^{\infty} \frac{\partial}{\partial y}[n(y) - n_o]zdz}{\int_{-\infty}^{\infty} \frac{\partial}{\partial y}[n(y) - n_o]dz} \tag{5}$$

This means that the fringes appear to the observer to be at the centroid of the normal transverse gradient of the field. An in-depth analysis of this type of fringe localization is given in reference 2. In the case of reasonably simple two- or three-dimensional fields, this localization gives the observer some qualitative understanding of the structure of the distribution. Decker (ref. 3) has shown that fringe localization in rapid-pulsed interferograms of complicated compressible flows leads to a very useful flow visualization technique.

An important technique for increasing the information content of an interferogram is to use two reference waves when forming the hologram as shown in figure 5. Reference wave R1 is used to record the first holographic exposure (no flow). Reference wave R2 is used to make the second holographic recording (with flow). After the hologram is developed if reconstruction waves identical to R1 and R2 are used, the interferogram will appear precisely as in figure 3(b). However, if we tilt the reconstruction wave R2 slightly relative to R1 we may form a pattern such as that in figure 5(b). Knowing the amount and direction of tilt, we will know the sign of the gradient of refractive index change (ref 9). This sign cannot be determined from the interferogram in figure 3(b) unless we understand the physics of the flow.

The use of dual reference beams also enables one to apply discrete phase shift interferometry (or quasiheterodyne interferometry). In this case the reconstruction waves are identical to R1 and R2 so that the interferogram appears as in figure 3(b). The irradiance at any point (x,y) can be written as

$$I_l(x,y) = I_o[1 + \cos(\overline{\Delta\phi})] \tag{6}$$

Now suppose that we sequentially introduce a phase shift first of +120° and then of -120° into one of the reconstuction waves, say R1. This has the effect of laterally shifting the position of each fringe by a known amount, or, equivalently the irradiance at the same point (x,y) is given by equations (7) and (8), respectively.

$$I_2(x,y) = I_0[1 - \cos(\overline{\Delta\phi}) - \sqrt{3} \cos(\overline{\Delta\phi})] \tag{7}$$

$$I_3(x,y) = I_0[1 - \cos(\overline{\Delta\phi}) + \sqrt{3} \cos(\overline{\Delta\phi})] \tag{8}$$

By combining equations (6) - (8) it follows that:

$$(1/\sqrt{3}) \tan(\overline{\Delta\phi}) = (I_3 - I_2)/(2I_1 - I_2 - I_3) \tag{9}$$

Thus, given these three irradiance values at a point one can calculate the corresponding phase difference. This technique has several advantages. First, it is naturally adapted to the use of solid-state array video cameras and digital data processing. Second, problems of sign ambiguity can be overcome. Third, the distribution of phase or optical pathlength can be calculated with great accuracy, regardless of variations of background irradiance. Useful papers on the topic include those of Dandliker, et. al (ref 4.) and Hariharan, et. al. (ref. 5).

A third two-reference wave technique based on analog rather than digital electronic processing is heterodyne holographic interferometry. Two separate holographic exposures are recorded as above. The resulting hologram is illuminated with reconstruction waves idential to R1 and R2. However, one of these recostruction waves is shifted in temporal frequency by an amount Ω. The resultant time-varying irradiance at a point (x,y) is given by equation (10).

$$I(x,y,t) = I_0[1 + \cos(\Omega t + \overline{\Delta\phi})] \tag{10}$$

From equation (10) it can be seen that the desired optical pathlength difference appears as a phase of a sinusoidal irradiance which can be detected by a sensor such as a photomultiplier tube or a photodiode because the frequency is sufficiently low (typically 100k Hz). The resultant signal can be fed into an electronic processor such as a phase meter or lock-in amplifier to determine the phase at any point. This technique is capable of high sensitivity up to the order of $\lambda/1000$, and the relative sign of the shift in phase, or equivalently optical pathlength, can be determined across the entire field. Figure 6 is a diagram of a heterodyne system used for interferometric measurements of temperature distributions in gasses (ref. 6). A detailed discussion of the theory and technology of heterodyne holographic interferometry is given in the review article by Dandliker (ref. 7).

MULTIDIRECTIONAL INTERFEROMETRY

It was noted above that if the test section is back illuminated with a diffusing screen a holographic interferogram can be viewed from many different directions. This multidirectional property is unique to holographic interferometry and is its richest source of information content. Other ways of creating multidirectional interferograms are indicated in figure 7. These include the use of phase gratings to break an incoming plane wave into a number of plane waves traveling in various directions through the test section, the use of multiple collimated beams, and the use of a fixed object wave through which the object itself rotates. Regardless of which technique is used to record the multidirectional interferograms, one obtains measurements of line integrals of the refractive index distribution corresponding to each direction of view. This is indicated in figure 8. With reference to this figure, the optical pathlength difference along a typical line through the test object can be written as:

$$\Delta \bar{\phi}(p,\theta) = \iint f(r,\phi)\delta[p - r \sin(\phi - \theta)]dxdy$$

$$= \lambda N(p,\theta) \tag{11}$$

Where $f(r,\phi) = n(r,\phi) - n_0$, δ is the Dirac delta function, λ is the wavelength of light and $N(p,\theta)$ is the fringe order number at point P. The set of all line integrals (eq. (11)) through a plane in the test region is know as the Radon transform (ref. 8). Reconstrution of the desired distribution $f(r,\phi)$ is accomplished by computing the inverse Radon transform:

$$f(r,\phi) = \frac{1}{2\pi^2} \int_{-\frac{\pi}{2}}^{\frac{\pi}{2}} d\theta \int_{-\infty}^{\infty} \frac{(\partial N/\partial p)dp}{r \sin(\phi - \theta) - p} \tag{12}$$

Computation of such reconstruction from projections is known as computed tomography. Because of the applicability of this computational technique to many scientific and engineering fields, predominantly x-ray and nuclear medicine, a very large literature exists, and is reviewed in reference 8. Examples of the combination of multidirectional holographic interferometry and computed tomography to fluid mechanics and heat transfer are given in references 9 and 10, respectively. An application to helicoptor rotor aerodynamics, in which data are gathered using a configuration like figure 7(d) is given by Kittleson (ref. 11). A proposed extension of this technique to cases in which refraction causes appreciable bending of the probing optical rays is given in reference 12.

RELATION OF REFRACTIVE INDEX TO OTHER PHYSICAL PROPERTIES

Once an interferogram has been analyzed to determine a spatial distribution of refractive index, this must in turn be related to the physical property of interest. Although this is a very important step in information retrieval from interferograms, we will not review this topic in detail here. The reader may refer to reference 1 for further information. However, we note that in aerodynamics the desired relation is quite simple, namely the Gladstone-Dale relation

$$n - 1 = K\rho \tag{13}$$

Where K is the Gladstone-Dale constant of the gas and ρ is its density. In some cases another derived property can in turn be computed from knowledge of the distribution density. For example, if a compressible gas flow can be considered essentially isentropic the velocity can be computed using equation (14).

$$\frac{v}{c_t} = \left[\frac{2}{\gamma - 1} \left(1 - \left(\frac{\rho}{\rho_t}\right)^{\gamma - 1} \right) \right]^{\frac{1}{2}} \tag{14}$$

Where c_t and ρ_t are the speed of sound and density at stagnation conditions, respectively, and γ is the ratio of specific heats of the gas. In reference 13 distributions of Mach number in a transonic flow, determined in this manner, are presented.

ANALYSIS OF FRINGE PATTERNS

Having described the general information content of holographic interferograms, we now turn to the problems associated with direct analysis of fringe patterns to determine the distribution of fringe order across an interferogram. Ideally this shold be a reasonably straightforward task. Consider the interferogram in figure 9. The broad region around the periphery of the pattern serves as a reference region in which no change has occured, so it is assigned the fringe order number N = 0. The center of the first dark fringe is assigned the value N = 0.5, the center of the next bright fringe is N = 1.0, etc. It should be a reasonably simple matter to digitally preform the assignment of fringe order number in this manner, and automation should be possible. However, there are a few difficulties. First, unless the operator understands the physics of the problem there is no way of knowing whether the fringe order numbers are positive or negative. Second, if the fringes are rather broad there may be some difficulty identifying their precise centers, and knowing values just at the fringe centers may not give a high enough density of data to analyze the physical properties of interest. Also, the fringes may be so

8

finely spaced that resolving them is difficult. Nonetheless,
with an ideal interferogram as in figure 9 a high degree of
automation should be possible. Unfortunately, in many
experiments in fluid mechanics and combustion the interferograms
may be far less than ideal. Figure 10 represents an
interferogram exhibiting many of the problems that can occur in
practice. Among difficulties that make analysis difficult,
especially automated analysis, are the following:

   1. Discontinuous fringes
   2. Extraneous fringes
   3. Broad, "cloud-like" fringes
   4. No fringe closure
   5. Very closely spaced fringes
   6. No region of known reference value
   7. Inadvertent wedge fringes
   8. Unknown sign of fringe order
   9. Nonuniform background irradiance
   10. Caustics due to refraction and diffraction
   11. Data blocked by opaque objects
   12. Diffraction by solid boundaries
   13. Laser speckle

   Some of these difficulties can be eliminated, or alieviated
by the use of the various two-reference-wave techniques
discussed above. Most, however are present regardless of how the
interferogram is recorded. Some of these factors lead inevitably
to errors in results, and some generally will require human
interpretation based on experience and/or knowledge of the
physics of the problem. Most are quite likely to cause serious
difficulties if one attempts to fully automate the readout
process.

   With the warning of these difficulties in mind, we now
consider the basic tasks which must be undertaken by readout
systems which are automated to some extent. It is convenient to
divide the problem into two categories: _Local analysis_ (i.e.
along single line scans), and _global analysis_ (i.e. over a two
dimensional interferogram). The local problem can be approached
by reasonably classical data analysis techniques. The global
problem is basically one of digital image processing.

   Line scan data are usually obtained by one of three means:
scanning with a photodetector or microdensitometer, scanning
with a video camera, or recording the output of a solid-state
photodetector array. In any of these cases the data to be
computationally analyzed consist of a vector of irradiance
values. Because of problems such as nonuniform background
irradiance, laser speckle, and variable fringe spacing, a simple
approach of finding the maxima and minima in this spector of
irradiance values generally is quite insufficient. One approach,

which is particularly suited to widely spaced fringes, is to
interpolate, generally through the use of curve fitting. A
variety of spline functions and polynomials have been used for
this purpose by various workers. An effective but
computationally-intensive approach is nonlinear regression
analysis to fit digitized irradiance data to the following
function which represents the general form of a fringe pattern:

$$I(x) = b(x) + a(x) \cos[\overline{\Delta\phi}(x)] \tag{15}$$

In equation (15) b(x), a(x), $\overline{\Delta\phi}$(x) represent the background
irradiance, the fringe amplitude, and the unknown optical
pathlength difference, respectively. Each of these can be
represented by a polynomial or other functional representation
including unknown constants. By nonlinear regression analysis
the unknown constants can be determined to fit the data optimally
with respect to some criterion. Figure 11 shows raw data
containing a lot of noise (laser speckle) and a curve of the form
of equation (15) fitted to it by regression analysis (ref. 14).

Because of the basically periodic nature of interference
fringes the Fourier transform can be used to analyze data
accumulated by a line scan. The spatial-frequency spectrum of
the irradiance data is computed using a fast Fourier transform
algorithm. Some filtering, for example by the use of a Hanning
window, and separation from carrier frequencies are generally
required. The appropriately filtered spectrum can then be
inverted by an FFT routine to determine the distribution of phase
(optical pathlength difference). A discussion of this approach
and examples of its use with real interferograms is presented in
reference 15.

Two basic issues immediately confront the designer of a
system for global (two-dimensional) analysis of interferograms.
The first is the basic strategy, i.e. to consider the
interferogram to be a collection of individual line scans, or to
connect and track each fringe. The second is to determine the
extent of automation, i.e. what, if any, degree of interaction
with a knowledgeable operator is permissable. An example of a
highly interactive approach is that given by Funnell (ref. 16),
and an example of a quite highly automated system is that of
Becker, et al (ref. 17). Systems of intermediate degrees of
automation are described in detail in the paper by Cline, et. al.
(ref. 18) the thesis of Choudry (ref. 19).

Generally the tasks to be performed by an automated fringe
read out system constitutes some subset of the following:

1.   Pre-processing
        Digitization
        Filtering

Contrast enhancement
Smoothing
Boundary specification

2. Fringe Tracking and Interpretation
    Segmentation
    Fringe edge detection
    Detection of obstacles
    Detection of fringe intersections
    Fringe numbering
    Noise reduction
    Polynomial fitting
    Operator interaction

3. Data Display
    Isometric representation
    Wire frame
    Contour plot
    Shaded surfaces

Details of systems developed by various workers are presented
elsewhere in these proceedings.

It should be noted that there are some applications in which
a high degree of automation is possible because the required
information is modest. For example in applications to
nondestructive testing the presence of a flaw may be made known
simply by a locally high density of fringes. A fully automated
system for this case is described in reference 20.

CLOSING

It is clear that a large amount of information about an
experiment in fluid mechanics or combustion diagnostics can be
encoded in a holographic interferogram. The concepts and basic
means for interpreting fringe order data are well known, although
in practice serious computational problems may be encountered.
Perhaps the most pressing problems in the field is that addressed
in this workshop, namely the automated analysis of interferograms
to provide fringe order data. In many applications this presents
a formidible image processing problem. Furthermore, in most
applications significant interaction with a knowledgeable
operator is likely to be required. As a closing comment I would
like to note that the problem of automated fringe analysis may be
ripe for application of concepts of artficial intelligence,
particularly expert systems.

REFERENCES

1. Vest, C. M.: Holographic Interferometry. John Wiley & Sons, Inc., 1979.

2. Schumann, W.: Fringe Localization in Holographic Interferometry in the Case of a Transparent Object with a Nonuniformly Varying Indes of Refraction. Opt. Lett., vol. 7, Dec. 1982, pp. 119-121.

3. Decker, A. J.: Holographic Flow Visualization of Time-Varying Shock Waves. Appl. Opt., vol. 20, 15 Dec., 1981, pp. 3120-3127.

4. Dandliker, R.; Thalmann, R.; and Willemin, J.-F.: Fringe Interpolation by Two-Reference-Beam Holographic Interferometry: Reducing Sensitivity to Hologram Misalignment. Opt. Commun., vol. 42, 1 Aug., 1982, pp. 301-306.

5. Hariharan, P.; Oreb, B. F., and Brown, N.: A Digital Phase-Measurement System for Real-Time Holographic Interferometry. Opt. Commun., vol. 41, 15 May, 1982, pp. 393-396.

6. Farrell, P. V.; Springer, G. S.; and Vest, C. M.: Heterodyne Holographic Interferometry: Concentration and Temperature Measurements in Gas Mixtures. Appl. Opt., vol. 21, 1 May, 1982, pp. 1624-1627.

7. Dandliker, R.: Heterodyne Holographic Interferometry, in Wolf, E. (Ed.), Progress in Optics Vol. XVII. North - Holland, 1980, pp. 1-84.

8. Deans, S. R.: The Radon Transform and Some of Its Applications. John Wiley & Sons, Inc., 1983.

9. Zien, T.-F.; Ragsdale, W. C.; and Srring, W. C.: Quantitative Determination of Three-Dimensional Density Field by Holographic Interferometry. AIAA J., vol. 13, 1975, pp. 841-842.

10. Sweeney, D. W.; and Vest, C. M.: Measurement of Three-Dimensional Temperature Fields Above Heated Surfaces by Holographic Interferometry. Int. J. Heat Mass Transfer, vol. 17, December, 1974, pp. 1443-1454.

11. Kittleson, J.: A Holographic Interferometry Technique for Measuring Transonic Flow Near a Rotor Blade. NASA TN84405, 1983.

12. Cha, S.; and Vest, C. M.: Tomographic Reconstruction of Strongly Refracting Fields and its Application to Interferometric Measurement of Boundary Layers. Appl. Opt., vol. 20, 15 Aug. 1981, pp. 2787-2794.

13. Johnson, D. A.; and Bachalo, W. D.: Transonic Flow About a Two-Dimensional Airfoil - Inviscid and Turbulent Flow Properties. Paper 78-117, AIAA 11th Fluid and Plasma Dynamics Conference, Seattle, WA, July 1978.

14. Schemm, J. B., and Vest, C. M.: Fringe Pattern Recognition and Interpolation Using Nonlinear Regression Analysis. Appl. Opt., vol. 22, 15 Sept., 1983, pp. 2850-2853.

15. Fakeda, M.; Hideki, I.; and Kobayoski, S.: Fourier-Transform Method of Fringe Pattern Analysis for Computer-BAsed Topography and Interferometry. J. Opt. Soc. Am., vol. 27, 1 January, 1982, pp. 156-160.

16. Funnell, W. R.: Image Processing Applied to the Interactive Analysis of Interferometric Fringes. Appl. Opt., vol. 20, 15 Sept., 1981, pp. 3245-3250.

17. Becker, F.; Meier, G. E.; and Wegner, H.: Automatic Evaluation of Interferograms. Proc. SPIE, vol. 359, 1982, pp. 386-393.

18. Cline, H. E.; Holik, A. S.; and Lorensen, W. E.: Computer-Aided Surface Reconstruction of Interference Contour. Appl. Opt., vol. 21, 15 Dec., 1982, pp. 4481-4488.

19. Choudry, A.: Automated Digital Processing of Interferograms. Doctoral Dissertation, Technische Hogeschool, Delft, 1982.

20. Tichenor, D. A.; and Madsen, V. P.: Computer Analysis of Holographic Interferograms for Nondestructive Testing. Opt. Engin. vol. 18, 1979, pp. 469-472.
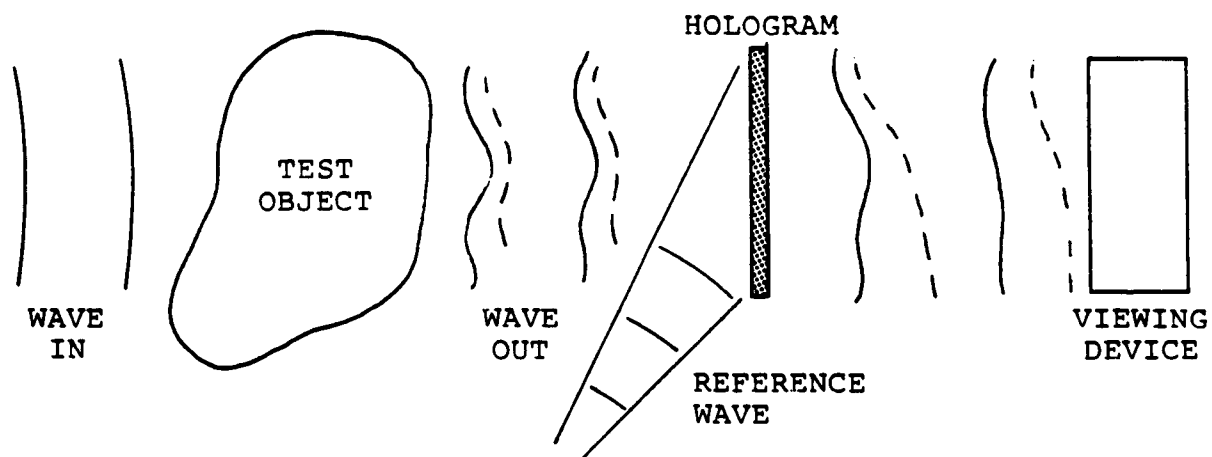
Figure 1. Holographic interferometry of transparent media.
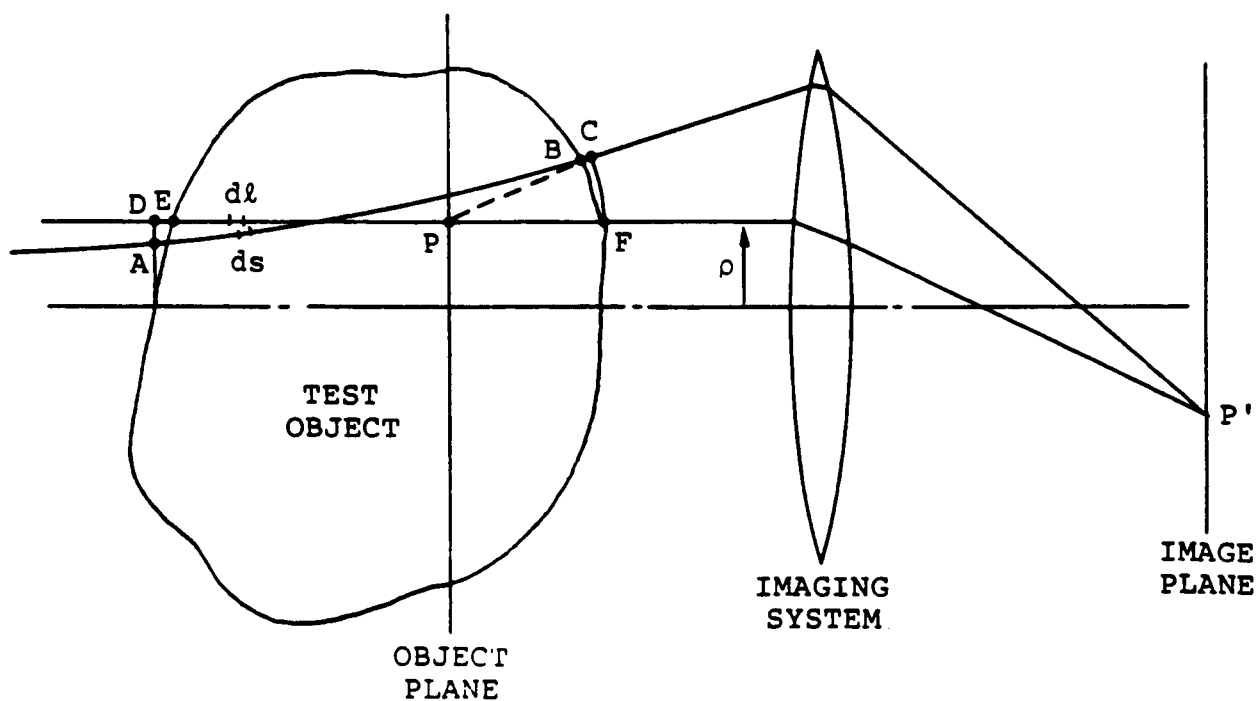
Figure 2. Ray optics of interferorgram formation.

14

RAYS

N = 0
N = 0.5
N = 1.0
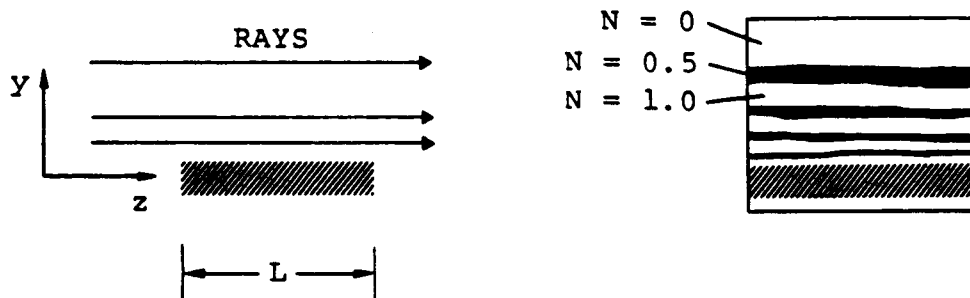
(a)   (b)

Figure 3. Formation of an interferogram with a plane object wave. The fringes are not localized.

LOCALIZED
FRINGES

DIFFUSING
SCREEN
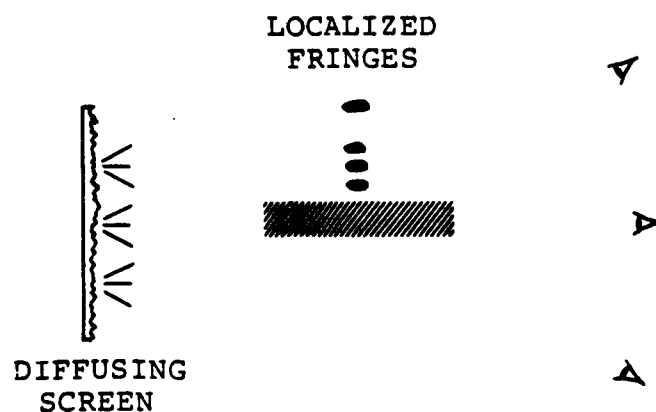
Figure 4. Formation of a holographic interferogram with diffuse illumination. The fringes appear to be localized, and they can be viewed from many different directions.

RAYS

HOLOGRAM

R1

R2
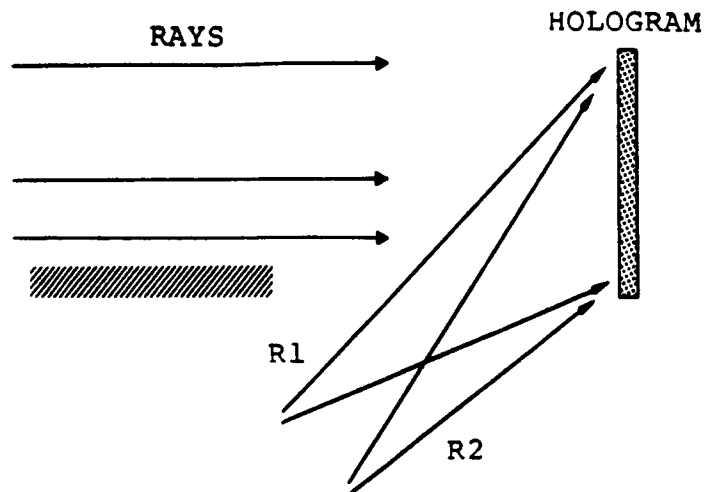
(a)
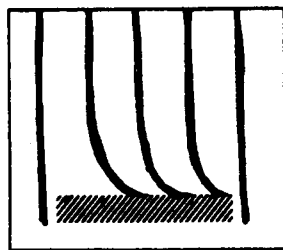
(b)

Figure 5. Two-reference wave holographic interferometry. (a) Separate waves are used to record each exposure; both are used for reconstruction. (b) Reference fringes can be introduced by tilting one reconstruction wave.
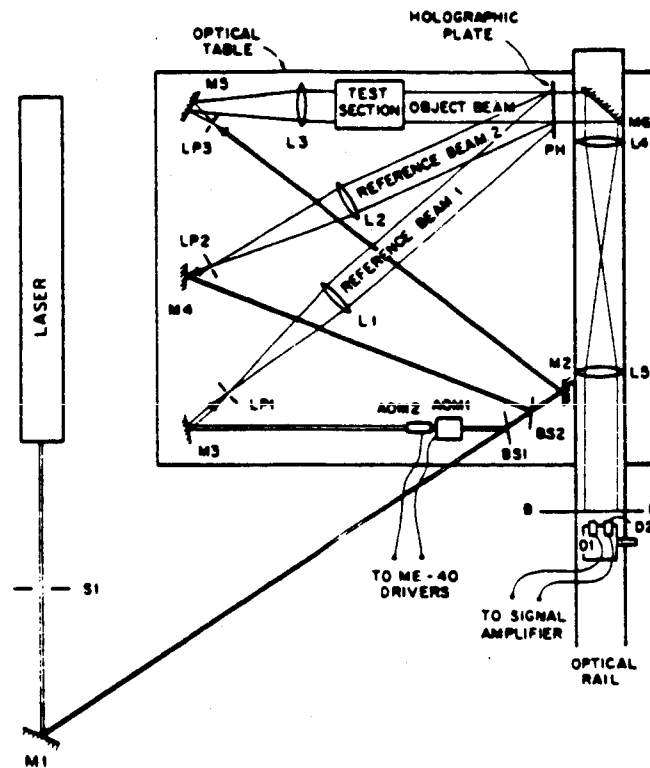
Figure 6. Heterodyne holographic inteferometer.
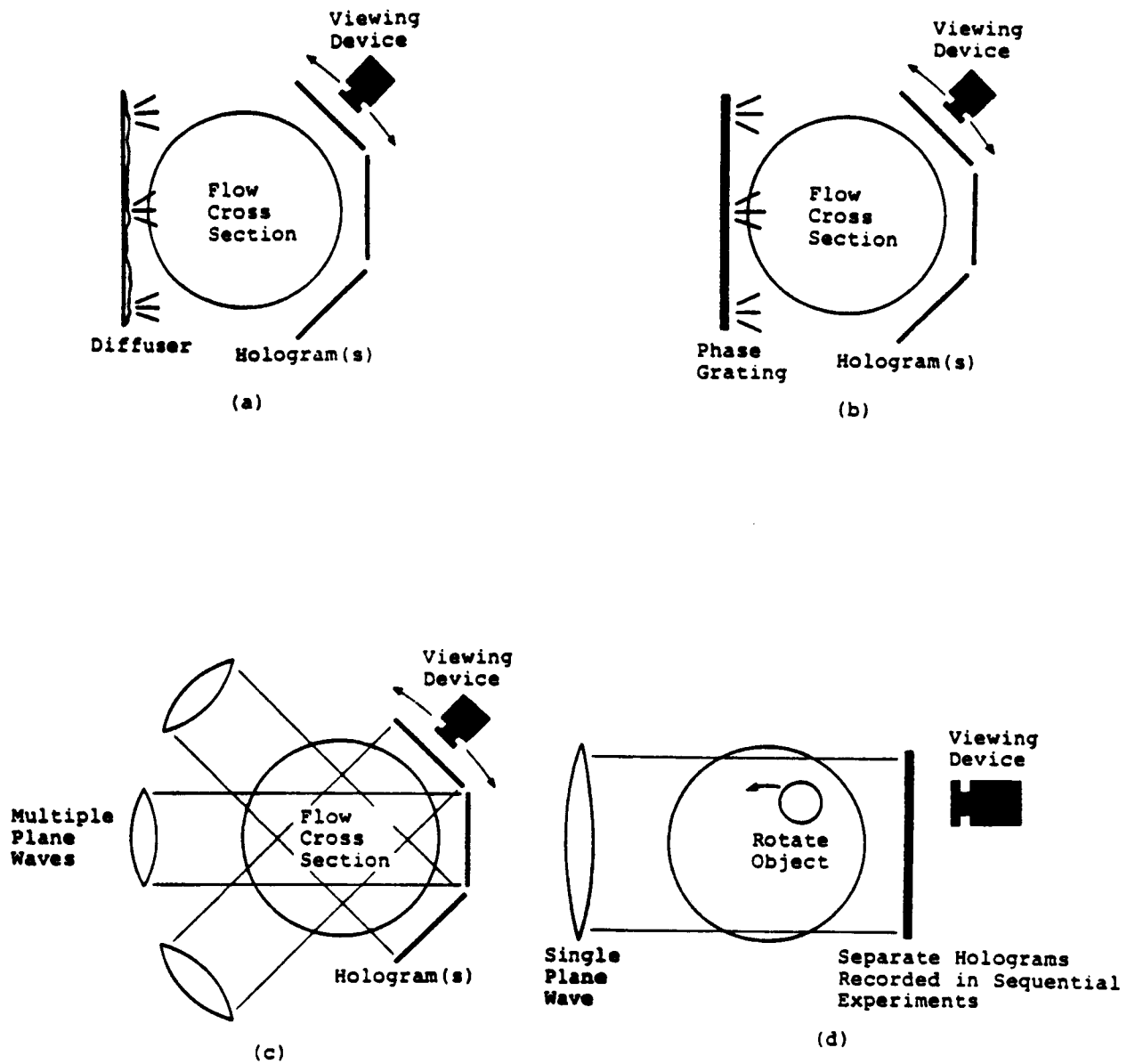
Figure 7. Techniques for recording multidirectional holographic intrferograms.
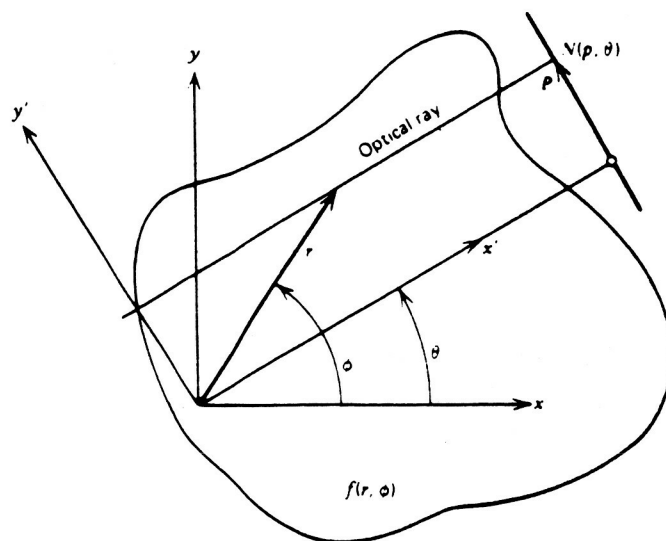
Figure 8. Nomenclature for multidirectional interferometry.
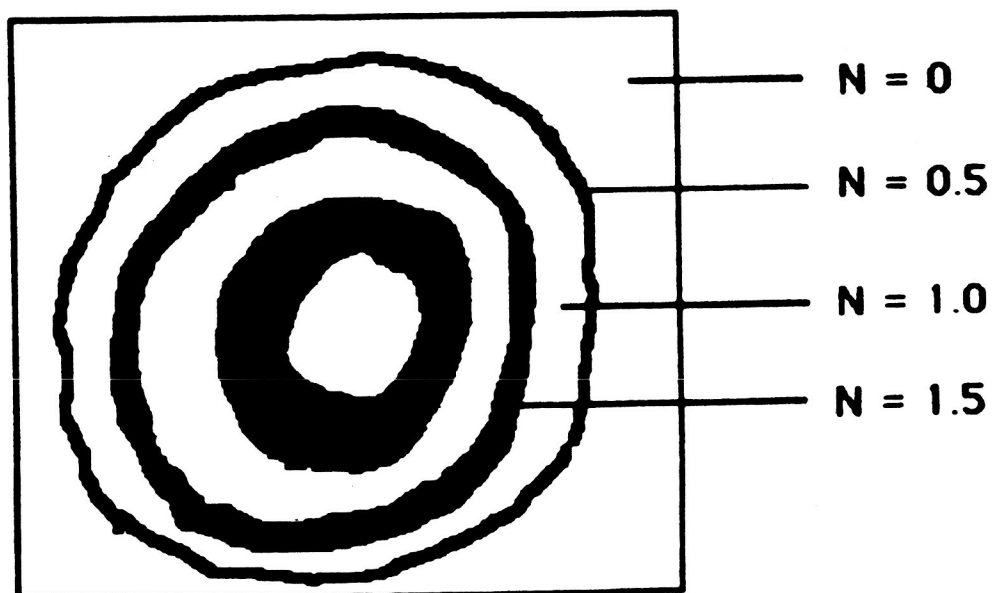
Figure 9. Ideal interferogram.

Figure 10. Interferogram exhibiting laser speckle and other problems encountered in practice.
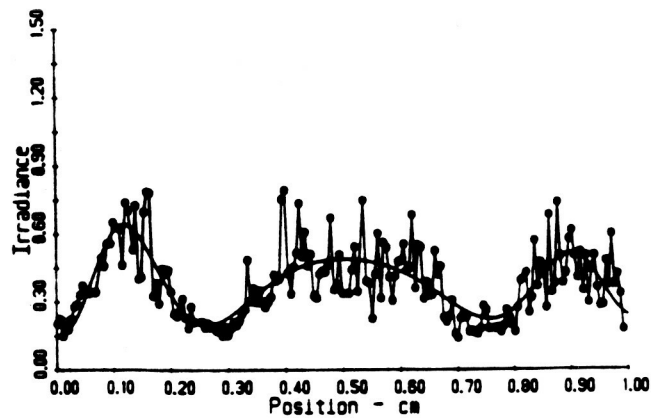
Figure 11. Irradiance distribution from real interferogram containing speckle noise. The solid curve was determined from these data by nonlinear regression analysis.

SUMMARY OF PROGRAMS IN FLUID MECHANICS

Five Minute Informal Presentations of Plans, Applications and Problems.

HOLOGRAPHIC INTERFEROMETRY

for

AERODYNAMICS

GEORGE LEE

NASA — AMES RESEARCH CENTER

23

APPLICATIONS

- ## 2-DIMENSIONAL AIRFOILS
  - LIFT
  - CODE VERIFICATION

- ## 3-DIMENSIONAL SHAPES
  - DENSITY FIELDS

24

DATA REDUCTION SCHEMES

- MANUEL

- GRAPHIC TABLET

- SEMI-AUTOMATED DIGITIZING

FUTURE PLANS

— DEVELOP AN AUTOMATED INTERFEROMETRY SYSTEM for TWO–DIMENSIONAL AIRFOILS

HOLOGRAPHIC INTERFEROMETRY AT NASA LANGLEY

Alpheus Burner

NASA Langley Research Center

NASA Langley Research Center

Applications:

* Holographic interferometry at the Hypersonic CF4 Tunnel

* In-line holography for turbulence studies (Weinstein)

* Particle image velocimetry at the Low Speed Calibration Tunnel (Childers)

* Model deformation measurements at the National Transonic Facility

Contract:

* General purpose fringe analysis system (KMS Fusion)

FUTURE WORK

* Reduce and/or evacuate optical paths

* Heterodyne interferometry during reconstruction

* Compare measured and predicted fringeshifts
  tunnel calibration
  verification of flow fields

31

FLUID CRYSTAL EXPERIMENT IN SPACE

R. C. RUFF

NASA Marshall Space Flight Center

PRECEDING PAGE BLANK NOT FILMED

MAHSHALL SPACE FLIGHT CENTER

WORKSHOP ON DATA REDUCTION AND
INTERPRETATION OF IMAGES AND
INTERFERROGRAMS

NAME:

R. C. RUFF

DATE:

JANUARY 10, 1985

- MSFC HAS DEVELOPED THE FLUID EXPERIMENT SYSTEM (FES) WHICH WILL FLY ON SPACELAB-3

- THE FES IS A FACILITY WHICH USES HOLOGRAPHY TO RECORD EXPERIMENTAL PHENOMENA OCCURRING IN A TEST VOLUME

- ON SPACELAB-3 THE FES WILL PROCESS THREE SOLUTION CRYSTAL GROWTH RUNS

- THE FES 70 MM FLEXIBLE FILM FOR HOLOGRAPHIC RECORDING

- MSFC HAS DEVELOPED A RECONSTRUCTION SYSTEM TO PRODUCE MICROSCOPIC, SHADOWGRAPH, INTERFERROMETRIC, AND SCHLIEREN IMAGES OF THE FLIGHT HOLOGRAMS

- MSFC NOW IN FINAL PLANNING STAGES FOR REDUCING SCIENCE DATA FROM RECONSTRUCTED IMAGES
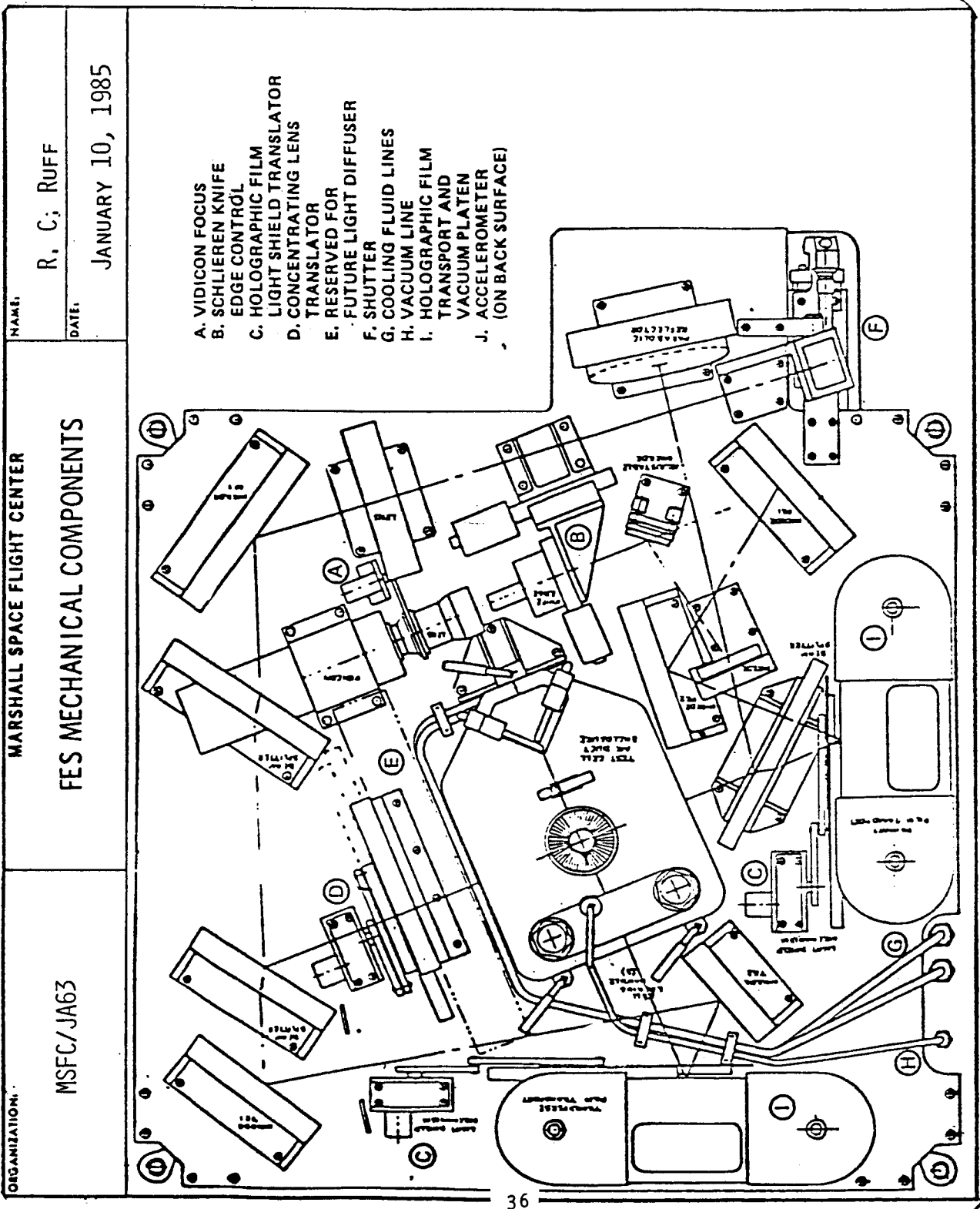
MARSHALL SPACE FLIGHT CENTER

FES MECHANICAL COMPONENTS

NAME: R. C. Ruff

DATE: JANUARY 10, 1985

ORGANIZATION: MSFC/JA63

A. VIDICON FOCUS
B. SCHLIEREN KNIFE
   EDGE CONTROL
C. HOLOGRAPHIC FILM
   LIGHT SHIELD TRANSLATOR
D. CONCENTRATING LENS
   TRANSLATOR
E. RESERVED FOR
   FUTURE LIGHT DIFFUSER
F. SHUTTER
G. COOLING FLUID LINES
H. VACUUM LINE
I. HOLOGRAPHIC FILM
   TRANSPORT AND
   VACUUM PLATEN
J. ACCELEROMETER
   (ON BACK SURFACE)

MARSHALL SPACE FLIGHT CENTER

FES
HOLOGRAPHIC COMPONENTS

NAME: R. C. RUFF
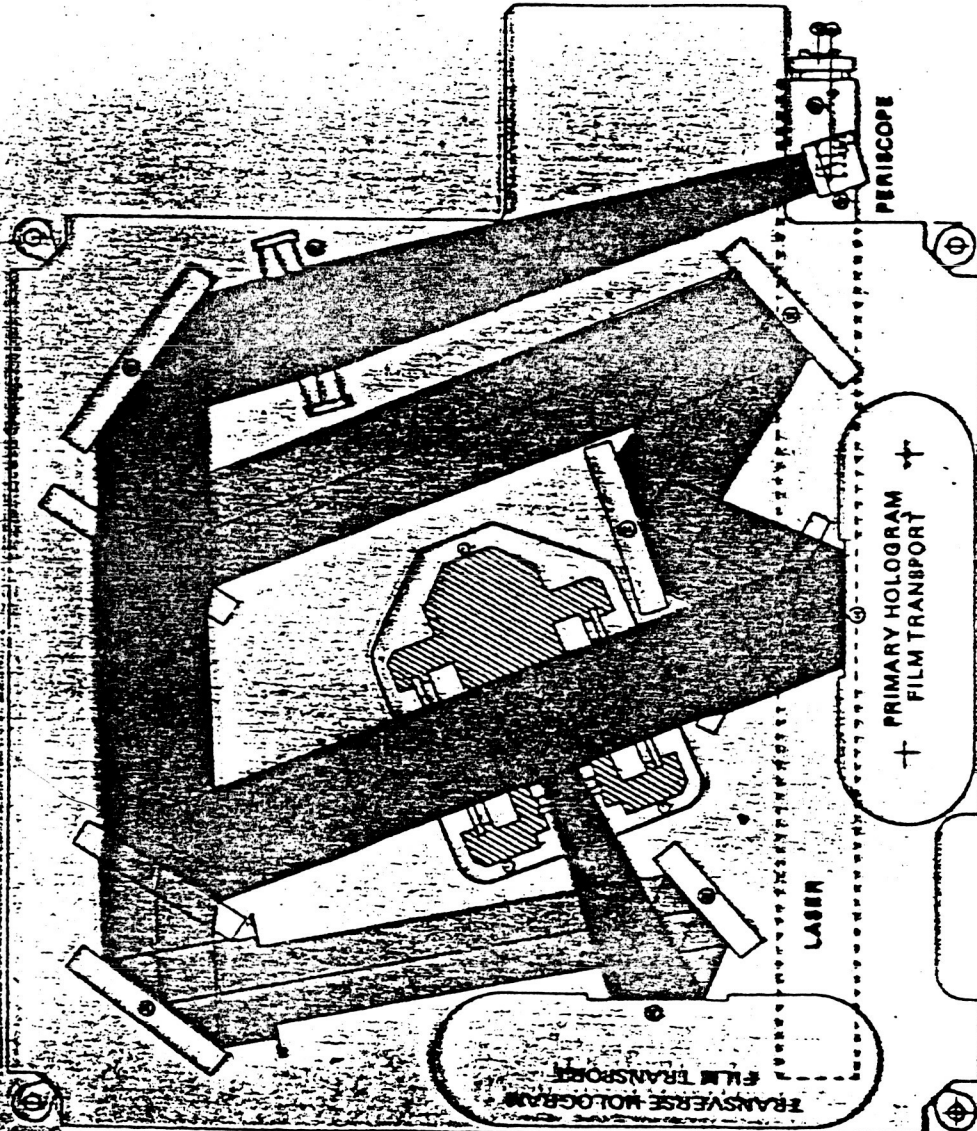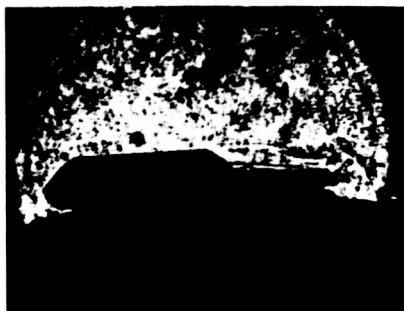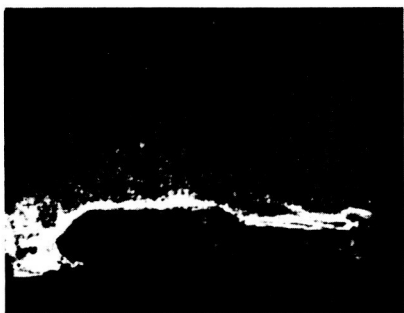
JANUARY 10, 1985

ORGANIZATION: MSFC/JA63

229-80

PERISCOPE

PRIMARY HOLOGRAM
FILM TRANSPORT

LASER

TRANSVERSE HOLOGRAM
FILM TRANSPORT

TAKEN FROM FES HOLOGRAM NO. CG 79
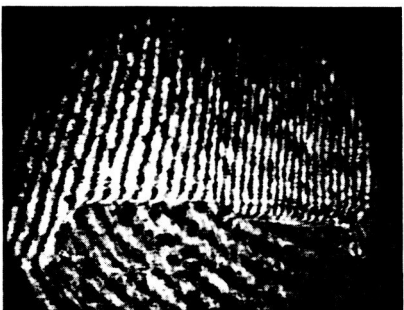
TAKEN FROM FES HOLOGRAM NO. CG 50

INTERFEROMETRY

INTERFEROMETRY
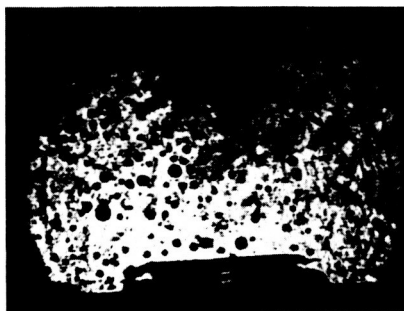
SCHLIEREN

SCHLIEREN

SHADOWGRAPH

SHADOWGRAPH
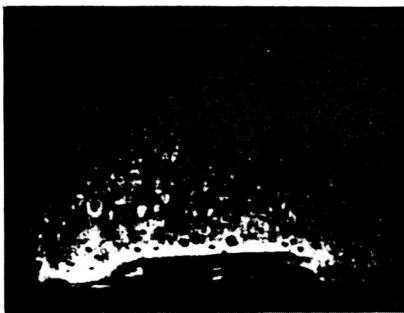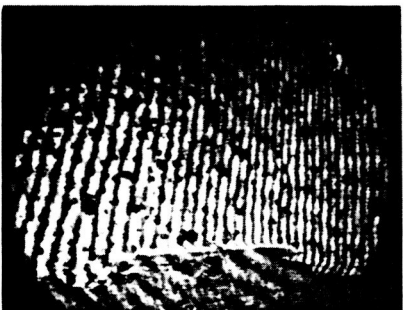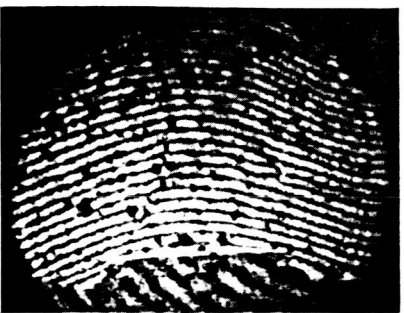
TRIGLYCINE SULFATE (TGS) CRYSTAL GROWING IN THE FLUID EXPERIMENT SYSTEM (FES)

CONCENTRATION PROFILE EXPECTED DURING
INITIAL DISSOLUTION PHASE OF EXPERIMENT IN ORBIT

TIME = 16.0492 min.

TEMP. = 46.0 °C.

C_o = 1.2088 x 10^{-3} (mole/cc)

C_i = 1.22895 x 10^{-3} (mole/cc)

ΔC = 1 x 10^{-6}

CRYSTAL

GLUE

STING TIP

INSULATOR

STING

0.75 (CM)

CYLINDRICAL SYMMETRY

CENTER
LINE

4.5

5.0

5.5

(CM)

39

ORGANIZATION:

MSFC / JA63

CHART NO.:

MARSHALL SPACE FLIGHT CENTER

WORKSHOP ON DATA REDUCTION AND
INTERPRETATION OF IMAGES AND
INTERFERROGRAMS

NAME:

R. C. Ruff

DATE:

JANUARY 10, 1985

EXPLANATION OF DESIRED DATA

- FINAL DATA
  - CRYSTAL GROWTH RATE
  - THERMAL DIFFUSION COEFFICIENT
  - SOLUTE DIFFUSION COEFFICIENT
  - RELATION BETWEEN CRYSTAL GROWTH RATE AND INTERFACE CONDITIONS

- REQUIRED INTERMEDIATE DATA
  - SEPARATE TEMPERATURE AND CONCENTRATION MAPS
    DERIVED FROM INDEX OF REFRACTION MAP
  - INFORMATION TO HELP IN SEPARATION
    - THREE TEMPERATURE MEASUREMENT POINTS IN CELL
    - THERMAL DIFFUSION MUCH FASTER THAN SOLUTE DIFFUSION
  - REAL IMAGE MICROSCOPIC DIMENSION MEASUREMENTS FOR
    CRYSTAL GROWTH RATE

ORGANIZATION:

MSFC / JA63

CHART NO.:

MARSHALL SPACE FLIGHT CENTER

WORKSHOP ON DATA REDUCTION AND
INTERPRETATION OF IMAGES AND
INTERFERROGRAMS

NAME:

R. C. Ruff

DATE:

JANUARY 10, 1985

PRELIMINARY PLANS FOR DATA ANALYSIS

- USE HOLOGRAPHIC GROUND SYSTEM (HGS) PHASE 1 TO RECONSTRUCT
  THE FOLLOWING IMAGES FROM FLIGHT HOLOGRAMS
  - REAL IMAGE MICROSCOPY
  - SHADOWGRAPH
  - INTERFERROMETRIC
  - SCHLIEREN

- IMAGE ANALYSIS (HGS PHASE 2)
  - FULL FUNDING FOR PHASE 2 IS ON HOLD UNTIL FLIGHT
    RESULTS JUSTIFY EXPENDITURE
  - PRELIMINARY CONCEPT FOR PHASE 2
    - ADD AUTOMATION TO PHASE 1 HARDWARE TO
      SPEED UP PRODUCTION OF IMAGES
    - IMAGE DIGITIZATION
    - DEVELOPMENT OF TECHNIQUES TO GO FROM IMAGES TO
      INDEX OF REFRACTION MAPS TO TEMPERATURE AND
      CONCENTRATION MAPS - ASSUMING DIFFUSION LIMITED
      CONDITIONS
    - DEVELOP SOFTWARE AND HARDWARE TO AUTOMATE THE
      PREVIOUS STEP
    - ANALYZE THE FLIGHT HOLOGRAMS

41

INTERFEROMETRY AT NASA LEWIS

Arthur J. Decker

NASA Lewis Research Center

INSTRUMENTATION & CONTROL TECHNOLOGY OFFICE

<u>WORKSHOP ON AUTOMATED REDUCTION OF DATA</u>

<u>FROM IMAGES AND HOLOGRAMS</u>

JANUARY 10 - 11, 1985 AT AMES RESEARCH CENTER

SOME SYSTEMS AND TECHNIQUES OF IMPORTANCE AT LeRC

ARTHUR J. DECKER

MAIL STOP 77-1

NASA LEWIS RESEARCH CENTER

21000 BROOKPARK ROAD

CLEVELAND, OHIO 44135

(216) 433-4000, EXT. 353

NASA LeRC

INSTRUMENTATION & CONTROL TECHNOLOGY OFFICE

	METHODS OR APPLICATION	READOUT
HOLOGRAPHY:		
ARTHUR DECKER	RAPID-DOUBLE-EXPOSURE. DIFFUSE - ILLUMINATION INTERFEROMETRY	STEREOSCOPIC IDENTIFICATION OF FLOW FEATURE
ARTHUR DECKER	DOUBLE EXPOSURE (INFINITE OR FINITE FRINGE)	ELECTRONIC HETERODYNE
ARTHUR DECKER	TIME - AVERAGE (WITH FLASHLAMP PUMPED DYE LASER AND BEAM MODULATION)	?
ARTHUR DECKER ROBERT ANDERSON	SINGLE EXPOSURE	DEFLECTOMETRY SPATIAL SPECTRUM ANALYSIS IMAGE ANALYSIS

INSTRUMENTATION & CONTROL TECHNOLOGY OFFICE

METHOD	READOUT

DEFLECTOMETRY:
WALTON HOWES   RAINBOW SCHLIEREN   DIRECT MEASUREMENT OF A PHOTOGRAPH

JOSEPH STRICKER   MOIRE FRINGE   ELECTRONIC HETERODYNE

SPECKLE TECHNIQUES:
JOHN BARRANGER
FRANK POLLACK   DOUBLE EXPOSURE PHOTOGRAPHY   ELECTRONIC HETERODYNE   SPECKLE PATTERN CORRELATION

INTERFEROMETRY:
WALTON HOWES   LOCAL REFERENCE BEAM USING 4-WAVE MIXING FOR GENERATION OF ABERRATION FREE REFERENCE WAVE

HOLOGRAPHIC OPTICAL ELEMENTS:
HAROLD SHOCK   CANCELLATION OF ABBERATIONS IN SAPPHIRE CYLINDER   TO BE USED WITH IMAGING SYSTEM AND COPPER VAPOR LASER FOR SPECKLE PHOTOGRAPHY

INSTRUMENTATION & CONTROL TECHNOLOGY OFFICE

<u>PROPULSION FLOWS (MOST CHALLENGING APPLICATION)</u>

O   REQUIREMENT FOR HIGH HOLOGRAM RECORDING RATE

O   LIMITED ACCESS

O   BOUNDARY LAYERS

S2-35

3 P

/03443

Transonic Rotor Flow-Measurement Technique Using Holographic Interferometry

John K. Kittleson* and Yung H. Yu*

U.S. Army Research and Technology Laboratories - AVSCOM

NASA Ames Research Center, Moffett Field, California

Abstract

Holographic interferometry is used to record interferograms of the flow near a hovering transonic rotor blade. A pulsed ruby laser recorded 40 interferograms with a 2-ft-diam view field near the model rotor-blade tip operating at a tip Mach number of 0.90. This paper presents the experimental procedure and example interferograms recorded in the rotor's tip-path-plane. In addition, a method currently being pursued to obtain quantitative flow information using computer-assisted tomography (CAT) with the holographic interferogram data, is outlined.

*Research Engineers.
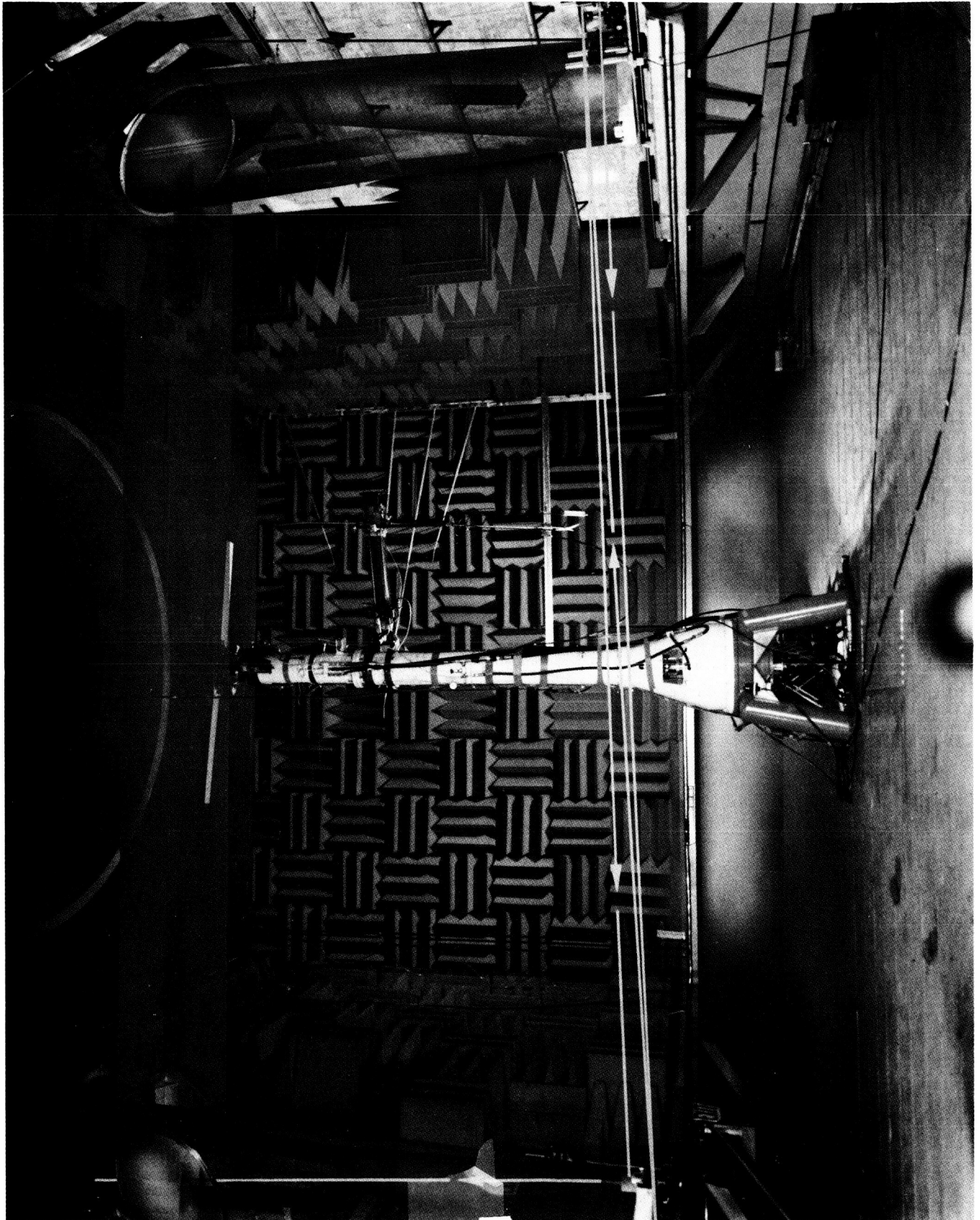
INTERFEROGRAMS AT VARIOUS AZIMUTHAL ANGLES

$\theta = 20°$
(a)

$\theta = 30°$
(b)

$\theta = 34°$
(c)

$\theta = 90°$
(d)

$\theta = 166°$
(e)

$\theta = 180°$
(f)

$\theta = 186°$
(g)

FILM

θ
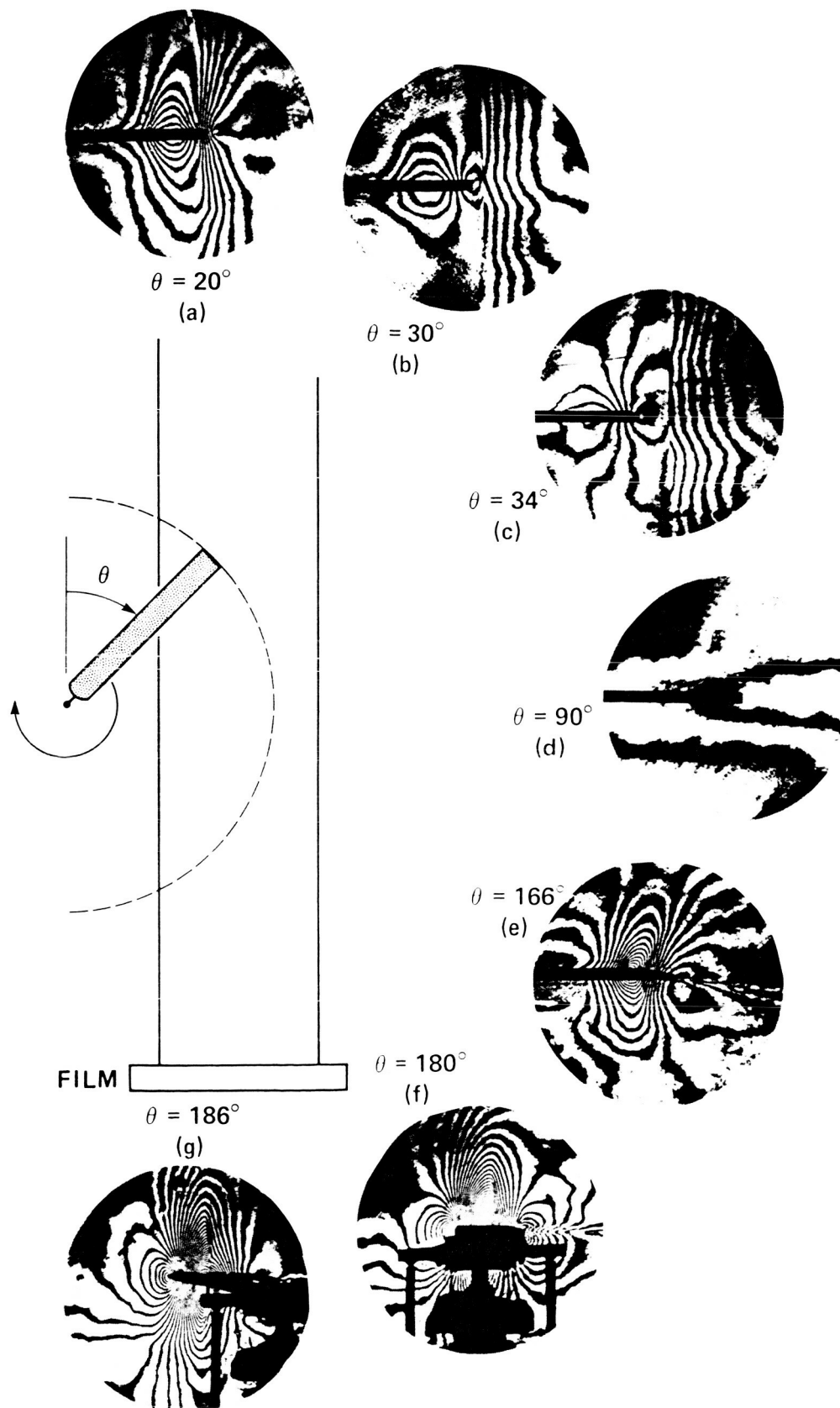
Flow Over Cavities

Bill Walker
U. S. Army Missle Command

The aerodynamics-optics problem over cavities is being studied by double pulse holographic interferometry. Air flow over a double cavity of rectangular shape and the effects of the shear layer on laser beams traversing through the cavities was investigated. The degradation of the flow in second cavity due to the first cavity strongly influenced the beam traversing the second cavity.

PRECEDING PAGE BLANK NOT FILMED

PAGE *52* INTENTIONALLY BLANK

HOLOGRAPHIC APPLICATIONS AT ARNOLD ENGINEERING DEVELOPMENT CENTER

Marshall Kingery

AEDC

ARNOLD ENGINEERING DEVELOPMENT CENTER

HOLOGRAPHY APPLICATION AT AEDC

- PROPULSION TESTING
  - ICING
  - FOREIGN PARTICLES
  - FUEL ATOMIZATION

- REENTRY SIMULATION
  - PARTICLE EROSION
  - RAIN
  - ICE

- AERODYNAMIC TESTING
  - FLOW VISUALIZATION

- STRESS ANALYSIS

PRECEDING PAGE BLANK NOT FILMED

TYPES OF HOLOGRAPHY

- PARTICLE FIELD
  - ICING WATER DROPLETS
  - FUEL ATOMIZATION
  - RAIN EROSION SIMULATION
  - SOLID PARTICLE EROSION
  - FLOW QUALITY

- INTERFEROMETRIC HOLOGRAPHY
  - AERODYNAMIC FLOW VISUALIZATION
  - STRESS ANALYSIS
  - MODEL GEOMETRY

AEDC MISSION

- **AERODYNAMIC SIMULATION**
  - SUBSONIC
  - TRANSONIC
  - SUPERSONIC
  - HYPERSONIC

- **PROPULSION TESTING**
  - AIRBREATHING ENGIINES
  - ROCKET
    - LIQUID FUEL
    - SOLID FUEL

- **REENTRY SIMULATION**
  - GUN RANGES/ TRACKS
  - ARC HEATERS
  - DUST EROSION/ ABLATION

- **SPACE SIMULATION**

HOLOGRAPHIC APPLICATIONS TO FLUID MECHANICS

Gary Lynch

U.S. Air Force Weapons Laboratory

U.S.A.F. WEAPONS LABORATORY

HOLOGRAPHIC APPLICATIONS TO FLUID MECHANICS

Maj. Gary Lynch

● DETERMINE OPTICAL ABERRATIONS CAUSED BY AERODYNAMIC FLOW FIELD

  ●● OPTICAL MEASUREMENT

     DOUBLE PULSE HOLOGRAPHY

  ●● AERODYNAMIC MEASUREMENT

     HOT FILM AND MEAN FLOW PROBES

● DATA REDUCTION METHODOLOGY

  ●● OPTICAL - FRF

  ●● AERODYNAMIC - IN HOUSE

● RESULTS

  ●● BOTH MEASUREMENTS SUCCESSFUL

  ●● COMPARISON YIELDS SAME RESULT

EXPERIMENTAL DESIGN PROBLEMS

● PATH LENGTH MATCHING

● VERTICAL – HORIZONTAL FRINGES (RELATIVE TO FLOW)

● DOUBLE PULSE SPACING (20 μSEC – 2 MSEC)

● RECONSTRUCTED INTERFEROGRAM QUALITY

● GREASE ON MIRROR

● A/C ELECTRICAL NOISE

   ● ● PHASE LOCK OF TILT MIRRORS

   ● ● PULSE SPACING

● REALIGNMENT IN FLIGHT REQUIRED

● TEMPERATURE CONTROL (AIR-WATER)

● TILT ARBITRARY

64

ADDITIONAL APPLICATIONS

- BMD AOA WIND TUNNEL TEST (MID 85)

  - LASER - HOLOCAMERA SYSTEM

    - FRF

- COMPLETION OF LARGE SCALE AERODYNAMIC EXPERIMENT

- IN-HOUSE

S3-35

NES ON-7

103444

Holographic Inteferometry at Wright Aeronautical Laboratories

Mel Roquemore
U. S. Air Force Wright Aeronautical Laboratories

Described the optical diagnostics requirements and plans for the Aero Propulsion Laboratories at the U. S. Air Force Wright Aeronautical Laboratories. This laboratory is performing work in combustion as related to aero propulsion systems. They would like to use holography and other types of optical instrumentation for combustion diagnostics and flow visualization. A movie of a laser light sheet flow visualization of a combustor in operation was shown. This movie showed extremely clear examples of vortical and unsteady flows, and it would be of interest to use image analysis to quantify such data.

S4-35
ABS. ONLY

103445
18

STATUS OF HOLOGRAPHIC INTERFEROMETRY

AT WRIGHT PATTERSON AIR FORCE BASE

by

Dr. George Seibert - AFWAL

At Wright Patterson Air Force Base, holographic interferometry has been used for nearly firteen years in a variety of supersonic and hypersonic wind tunnels. Specifically, holographic interferometry has been used to study boundary layers, shock boundary layer interaction, and general flow diagnostics. Although a considerable amount of quantitative work is done, the difficulty of reducing data severly restricts this. In the future, it is of interest to use holographic interferometry in conjuction with laser Doppler velocimetry to do more complete diagnostics. Also, there is an interest to do particle field diagnostics in the combustion research facility. Finally, there are efforts in non-destructive testing where automated fringe readout and analysis would be extremely helpful.

PAGE 68 INTENTIONALLY BLANK

S5-35
103446

Welding Arc and Plasma Studies Using Real Time, Multipass Holographic Interferometry

Vance Deason
EG&G Idaho, Inc.
Idaho National Engineering Lab.

Flow visualization of the plasma process in a welding arc is
being studied with a multipass Argon-ion interferometer.
High speed movies at 10,000 frames per second are taken. The
multipass interferometer and several interferomgrams of the
plasma near the electrode of the welding arc are given in the
following photographs. Digitization of the fringes is
currently done by hand.
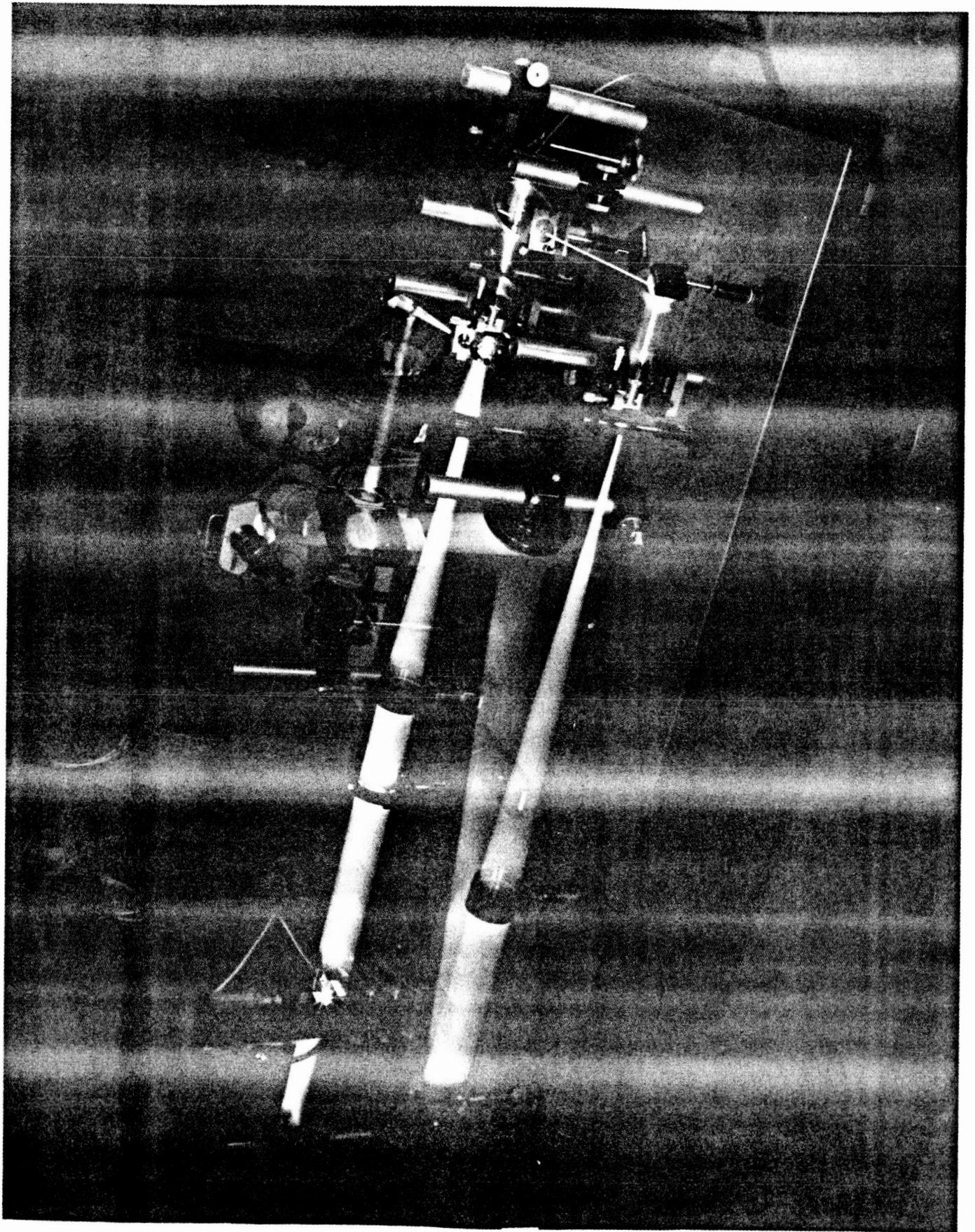
74
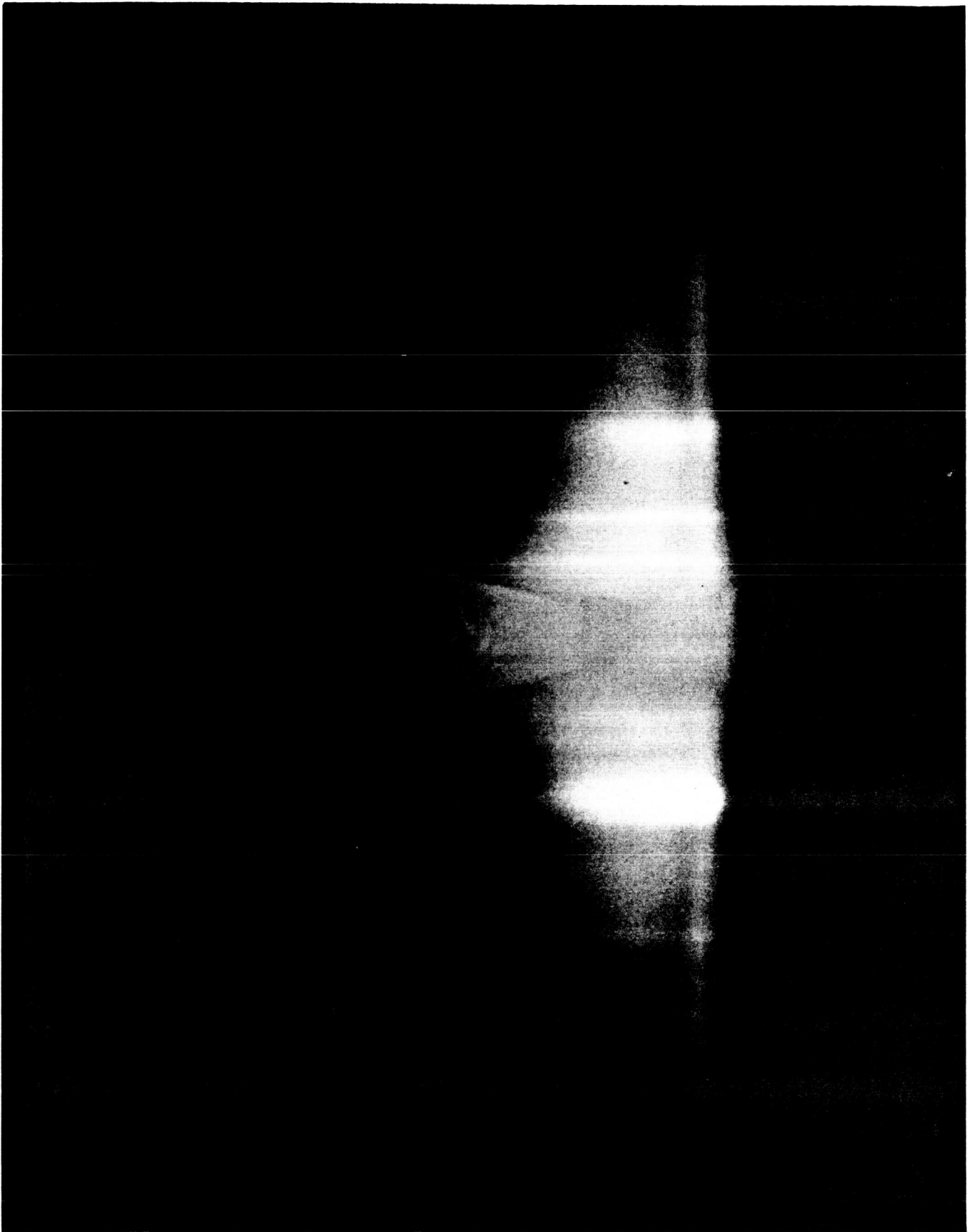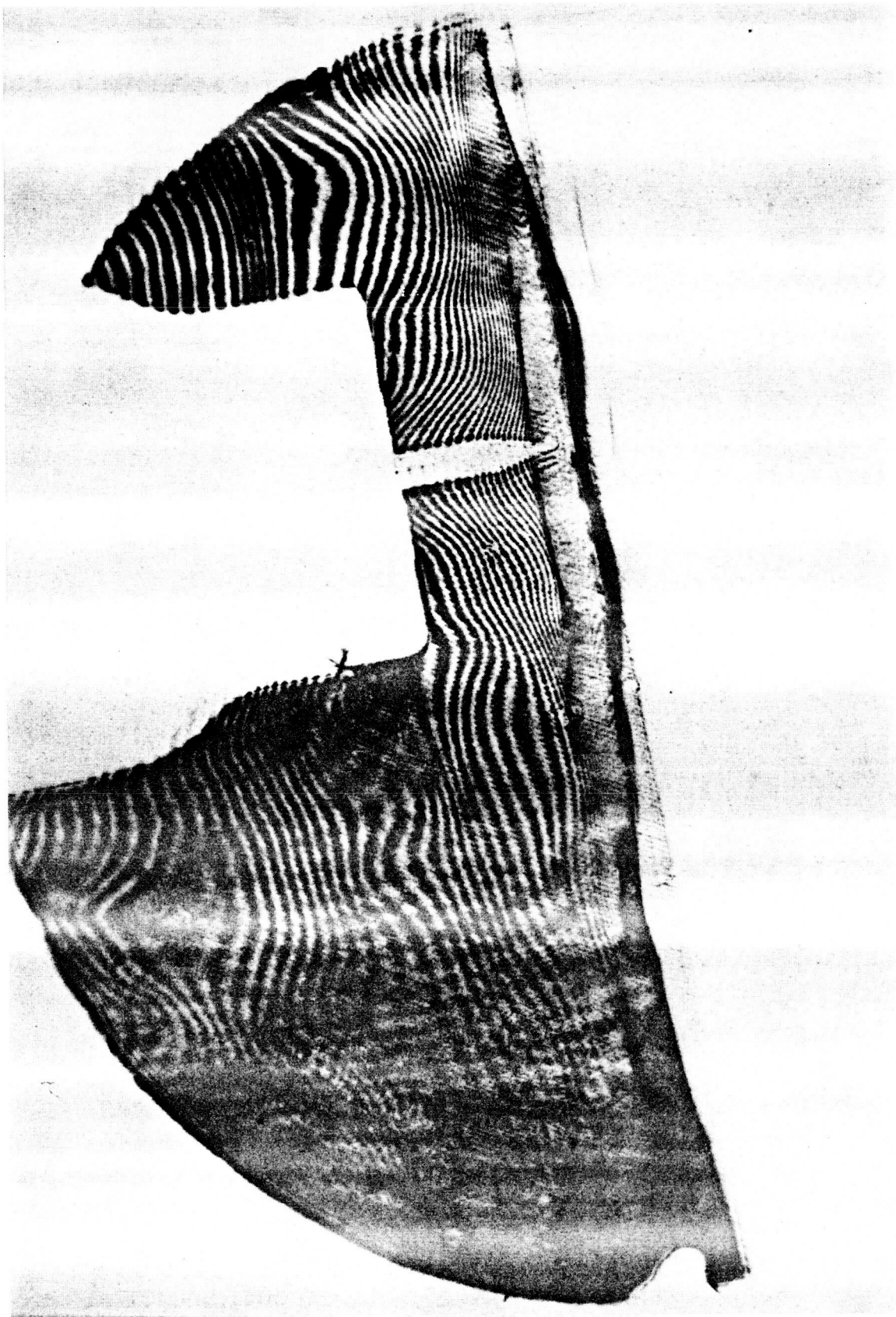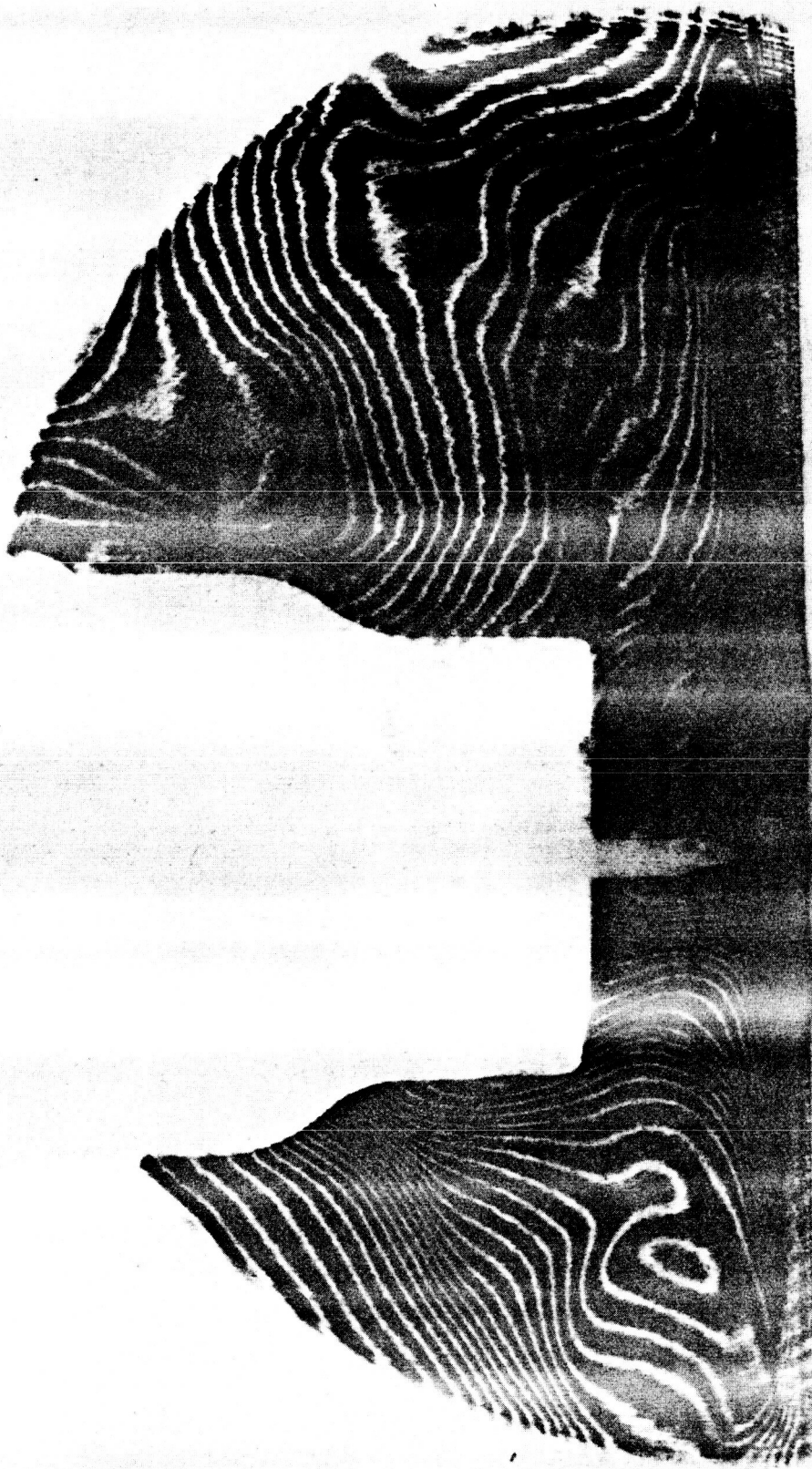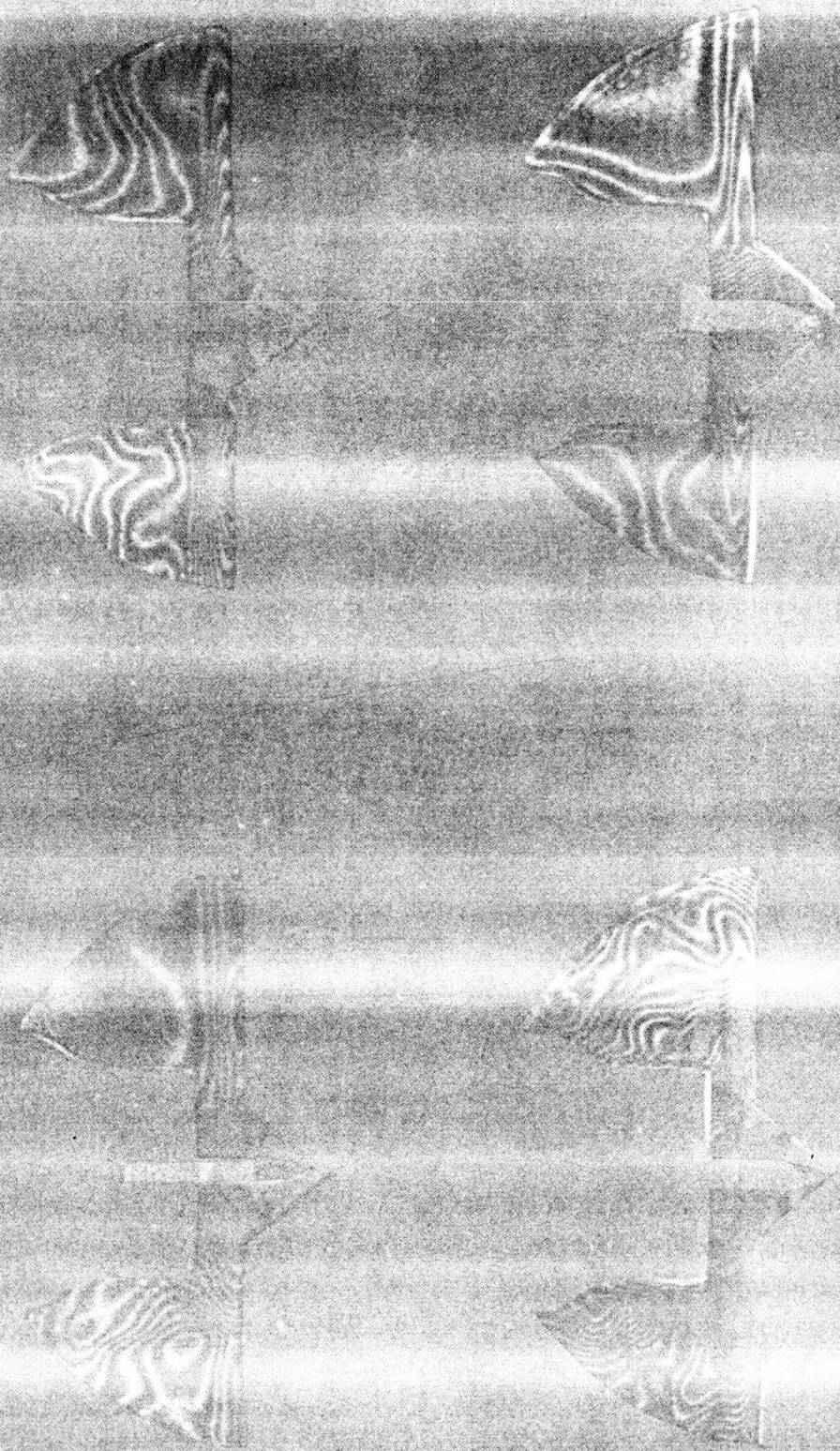
Holographic, Particle Imaging and Data Reduction at Spectron Development Laboratories

J. D. Trolinger
Spectron Development Laboratories

Spectron has been deeply involved in the development and use of a wide variety of particle and flow diagnostic, electro optical instruments for the past twelve years. Holography and imaging systems have played an important role in this work, but the extraction of data from images and holograms have always presented a limit in their use. We have been working on systems and techniques to speed up and automate the extraction of data from holographic and conventional interferograms, particle images and holograms, and other types of optical flow visualization techniques. We have developed an IBM/AI based image analyzer that is capable of automatically analyzing many useful image types including interferograms. A key feature of this system is the low total cost of the required hardware. In the particle field work we have also adapted a commercial diffraction field analyzer to the image reconstructed from a hologram. This could expand the use of holography in particle diagnostics greatly.

HOLOGRAPHY IN THE UNITED KINGDOM

Peter Bryanston-Cross, Cambridge, England

People in the UK Working in Holography

Cambridge TopExpress	P.Bryanston-Cross	(Transonic Flows)
Cambridge PA Technology	P.Story	(Holographic Optical Components)
Rolls Royce Derby	R. Parker	(Gas Turbine Engines)
Rolls Royce Derby	I. Davidson	(Gas Turbine Engines)
CEGB Southampton	J. Webster	(Nuclear Fuel Rods)
University College London	D.Preater	(Rotating Surfaces)
University College London	M.Collins	(Low Speed Heat Transfer)
Loughborough University	N.Philips	(Holographic Research)
Richmond Holographic	P.Miller	(Pictorial Holography)
Applied Holographic	H.Shearer	(Pictorial Holography)
Nottingham Univerity	D.Lempart	(Mass Transfer Analogy)
Oxford University	Solymar	(Holographic Optical Elements)

Holographic Data Reduction.

There are several current problems in holographic data reduction.

1. The quantity, unless the holographic image can be reduced to a single gray level low resolution picture, the amount of data tends to prevent the use of sophisticated computer data reduction techniques. The size of the number field and the time taken to process the data can prevent all but the simplest operations.

2. In many fluid dynamic cases the physics of the fluid has to solved simultaneously with the collection of data. There is little point in accumulating data mountains without being able to interpret them.

3. Often because of the expense of the experiments they can only be held together for a short period. The more complicated the measurement system the higher the risk of a negative result.

4. The experiment must be interpreted; the concept of optical phase changes and refractive index bending, is not within the common experience of many Engineers. This lack of knowledge can produce ambiguity and error.

5. Particular holographic features, such as found in three dimensional flow fields are difficult to digitize, there being an optical trade off between resolution and speckle noise. It is noted that the three dimensional refractive index field solvers tend to require large angles of view which is often incompatable with actual experiment. If also the refractive index field is a well behaved continiuum then a reconstruction depth of field of the similar size is needed, otherwise the fringe data can be incoherently washed out.

6. In the case of the British CEGB the standard of each o components had to be raised until they could reach their 'real image 10micron measurement point'. This is the accuracy they required to measure the distortion in a nuclear fuel rod. This has ment using very large diffraction limited lens's and specially made holographic plates. They are now learning how to image, a projected holographic real image, into a TV camera and eventually digitally store selected test points on the rod into a computer.

7. Rolls-Royce UK currently manually spend about half an hour digitizing each hologram of a three dimensional flow fields. They complete large scale holographic tests every two months, during which they will make approximately 200 holograms. After each test many hours are spent logging the data into their computers.

8. High power pulse lasers are expensive and can only be
transported with some care. Failure in their operation can
produce ambiguities in the holograms which either degrade the
result or prevent logical analysis.

Holographic analysis is now being used in many laboratories. In
conclusion, though the technique of ruby pulse holography is
difficult and expensive. It is the only diagnostic method
currently available which produces a whole field
visualization quickly, in three dimensions, of a transonic
flow. It also has micron resolution of surfaces upto 10m in
size.

Current Research in Cambridge.

The current direction of research has been to develop the high resolution image plane interferometry a stage further. It is now possible to set the aerofoil section dicussed previously at different angles of incidence to the airflow. A dedicated framestore and image procesing system has been constructed so that it also possible to log photograhic interferometric reconstucted images directly into the memory of a 16 bit microcomputer. It is intended that by making one 'no flow hologram', developing it and then replacing it back in its original position; it will be possible to store the diference between the flow condition and the no flow condition directly into the computer without an intermediate photographic stage. The memory and speed of the mirco (1Mbyte and 10Mhz) not only allows the storage of the interferometric data but also has memory to run a two dimenion version of Dentons Time Marching method. The intention is to compare the theoretical solution with the measured flow within the micro.

A second experiment in the aeronautics laboratory is currently using holography among several optical techniques to visualise the shock boundary layer interaction under a vibrating (100 Hz) normal shock.

Non holographic image processing is being researched for three dimensional vortical structures in water. A system has also been devloped using Moire grids to visualise a mercury suface as it deformed by the action of a powerful magnetic field.

TopExpress in Cambride is currently active in particle tracking in water, and in the interpretation of saterlite data. It is intended that the laser holographic turbocharger test be developed to a second stage where, holography could be used to monitor the change in shock structure with performance change.'

DATA REDUCTION OF IMAGES IN FLUID DYNAMICS AT DFVLR

J. Kompenhans
DFVLR
Institut für Experimentelle Strömungsmechanik
Bunsenstrasse 10
D-3400 Göttingen
W.-Germany

I. Flow visualization methods such as:

- Schlieren
- shadowgraph
- interferometry
- holography
- surface flow methods
- tracers
- liquid crystals etc.

are widely used in DFVLR windtunnels and laboratories.

Pictures of Schlieren and liquid crystal flow visualization experiments have already been processed by means of digital computers.

II. In the last two years some new projects were started to get more quantitative data out of flow visualization pictures:

- improvement of standard flow visualization methods
- test of new techniques
- improvement of equipment (optics, lasers, tracers etc.)
- installation of an user-friendly image processing system
- first tests of data reduction with our image processing system

III. In the moment there is need for automated data reduction for the following projects:

SPECKLE VELOCIMETRY   (J. Kompenhans)

SPECKLE VELOCIMETRY IN TURBULENT FLOW
- cooperation with University of Oldenburg (Prof. Hinsch) and University of Göttingen (Priv. Doz. Dr. Ebeling)
- Measurements with the ruby laser system of the University of Oldenburg were carried out in the DFVLR Low Turbulence Windtunnel
- Specklegrams were taken at different turbulence levels
- Fringe visibility shall give information on structure of turbulence
- Semi-automatic data reduction was tested

DFVLR SYSTEM for speckle velocimetry
- Feasibility study was carried out for double pulse
  Nd:YAG laser system
- DFVLR laser system will be available in a few months

PROBLEM
- automated data reduction of specklegrams

HYDROGEN BUBBLE FLOW VISUALIZATION in a water towing tank   (Dr. Bippes)

- 3D flow visualization by means of holography

PROBLEM
- automated detection of bubble location

SHOCK CONFIGURATION in supersonic corner flow   (Niehuis)

- tomographic methods for Schlieren flow visualization

PROBLEM
- algorithm for tomography

IV. Projects which will start in near future:

LAMINAR-TURBULENT TRANSITION, HEAT TRANSFER BY MEANS OF LIQUID CRYSTALS
                        (Schöler, Dr. Bütefisch)

    PROBLEM
    - automated detection of the colour of the crystals at different
      angles of incident light

HOLOGRAPHIC INTERFEROMETRY   (Basler)

    PROBLEM
    - automated detection of interference patterns

PULSED LASER VELOCIMETRY
FOR STUDY OF TURBULENT
FLOW STRUCTURE

Ronald J. Adrian
University of Illinois at Urbana-Champaign
Department of Theoretical and Applied Mechanics

PULSED LASER SYSTEM I

Hardware Recording System

Non-holographic

Photographic recording of individual 20 μm particle images

Double-pulsed ruby laser sheet @ 1J

100 mm x 125 mm recorded field

12,500 point grid of 1mm diameter interrogation spots

Automatic Interrogation System

0.1% f.s. resolution of 2-D vector components

Spatial correlation analysis to determine the mean displacements of the particles in each interrogation spot in real time

3.5 hours to interrogate 12,500 two-dimensional vectors using an LSI 11/23 with a SKymnk array processor

PLV THEORETICAL ANALYSIS

Theory of interrogation by 2-D spatial correlation

Signal interpretation

Particle scattering and imaging properties for air and water

PLANS

Use PLV I hardware to measure turbulent convection in water

New methods of interrogation for low image density gaseous flow

Measurement of velocity polarity

Theoretical analysis of signal interrogation methods

- Variance of displacement estimators

- Spatial and temperal resolution and interpretation of results

- Effects of particle concentration, particle image non-uniformity

- Effects of 1-D compression on accuracy

- Biasing effects and methods of compensation

- Design criteria

Turbulent Pipe Flow
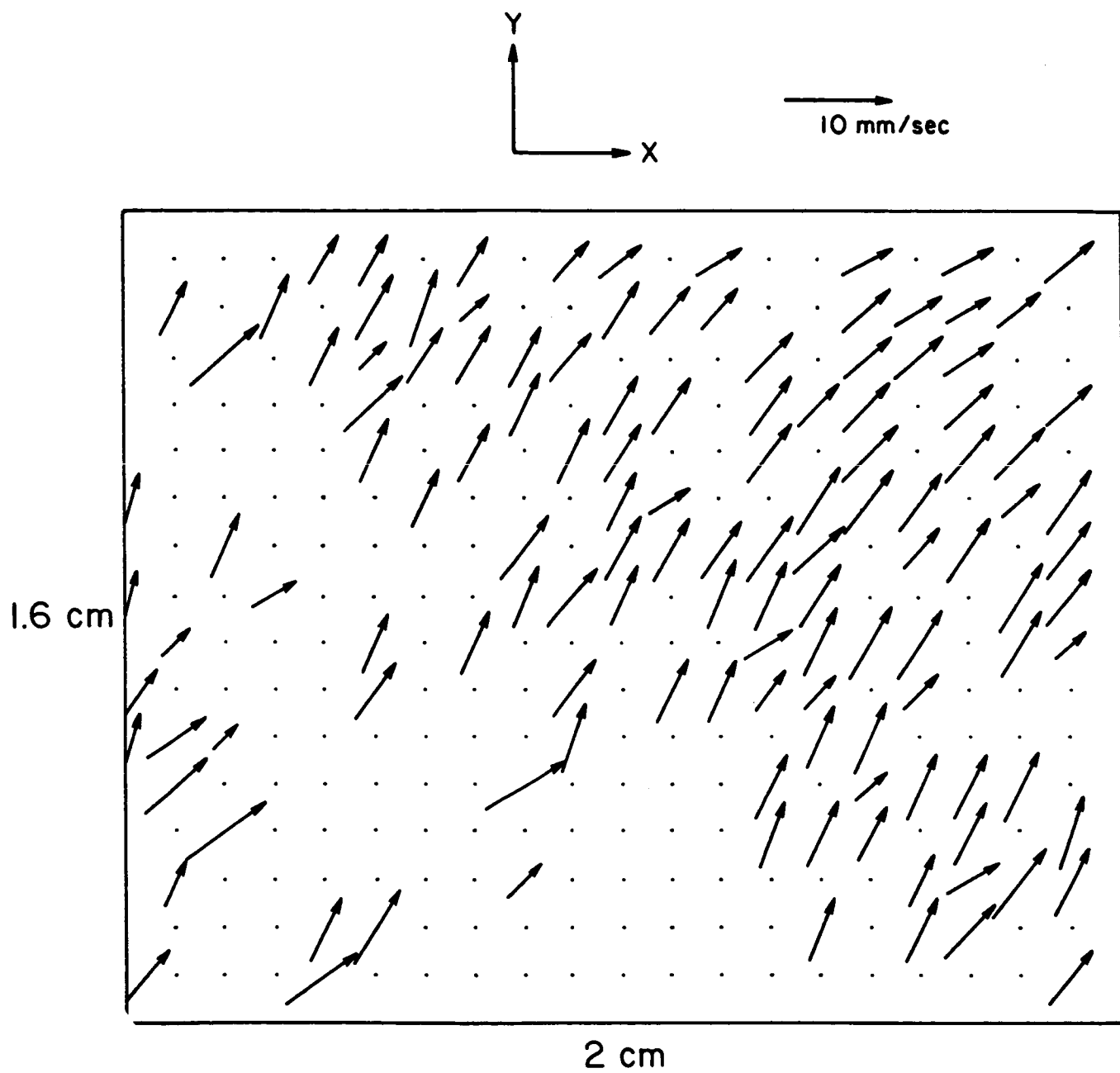
PULSED LASER VELOCIMETRY
APPLICATIONS

BUOYANCY DRIVEN FLOWS

technique using thymol blue. The heating rate is higher in
the photograph at the right. *Sparrow, Husar & Goldstein*
1970
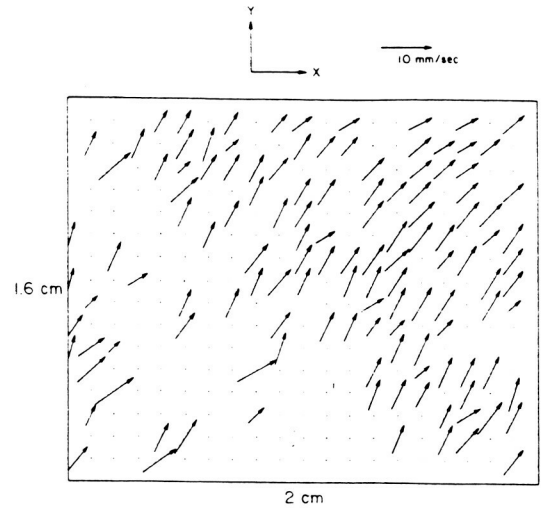
TURBULENT PIPE FLOW
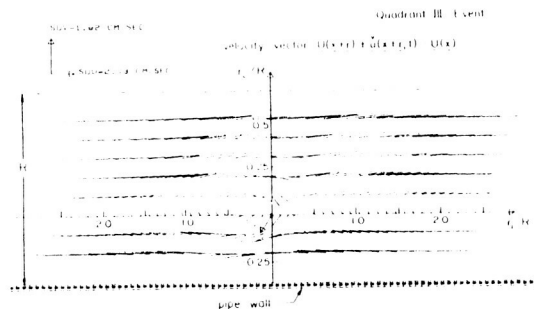
Figure 5.0-15: Conditional flow orbits of the velocity vector $\tilde{u}(x,r) + \tilde{u}(x,r,t) - U(x)$, the given velocity in quadrant III.

SHEAR LAYER INTERACTIONS & REATTACHMENT
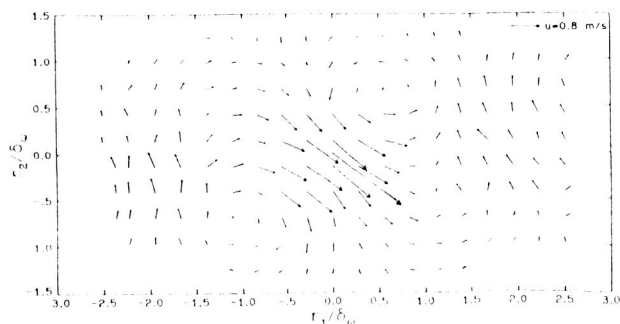
Fig. 4-8 Measured conditional fluctuating velocity vector field; $\lambda = 71.4$ mm, under condition IV. The solid-head arrow denotes the conditioned velocity vector.

S7-35
ABS. ONLY
103448
II

Status of Holographic Interferometry
at University of Michigan

Charles Vest
University of Michigan

Reflection holograms were taken of a jet of air injected
traverse to a subsonic stream. The technique of reflection
holograms allowed maximum viewing angle and minimum distance
to the jet.

Holographic interferometry is being used to measure the
temperature distribution in a growing crystal. Computations
of the temperatures are being made.

A phase shift interferometer was used to study flows with
very weak changes in refractive index, of the order of 1
shift.

Tomographic techniques are being developed for strong
refractive cases.

Flow Visualization of Acoustic Levitation Experiment

Ed Baroth
Jet Propulsion Laboratory

Jet Propulsion Laboratory is currently involved in acoustic levitation experiment for space application. Holographic interferometry is being used to study the heat transfer rates on a heated rod enclosed in a 6-inch cubic chamber. Acoustic waves at levels up to 150 db increased the heating rates to the rod by factors of three to four. High speed real time holographic interferometry was used to measure the boundary layer on the heated rod. Data reduction and digitization of the interferograms are being implemented.

PAGE 92 INTENTIONALLY BLANK
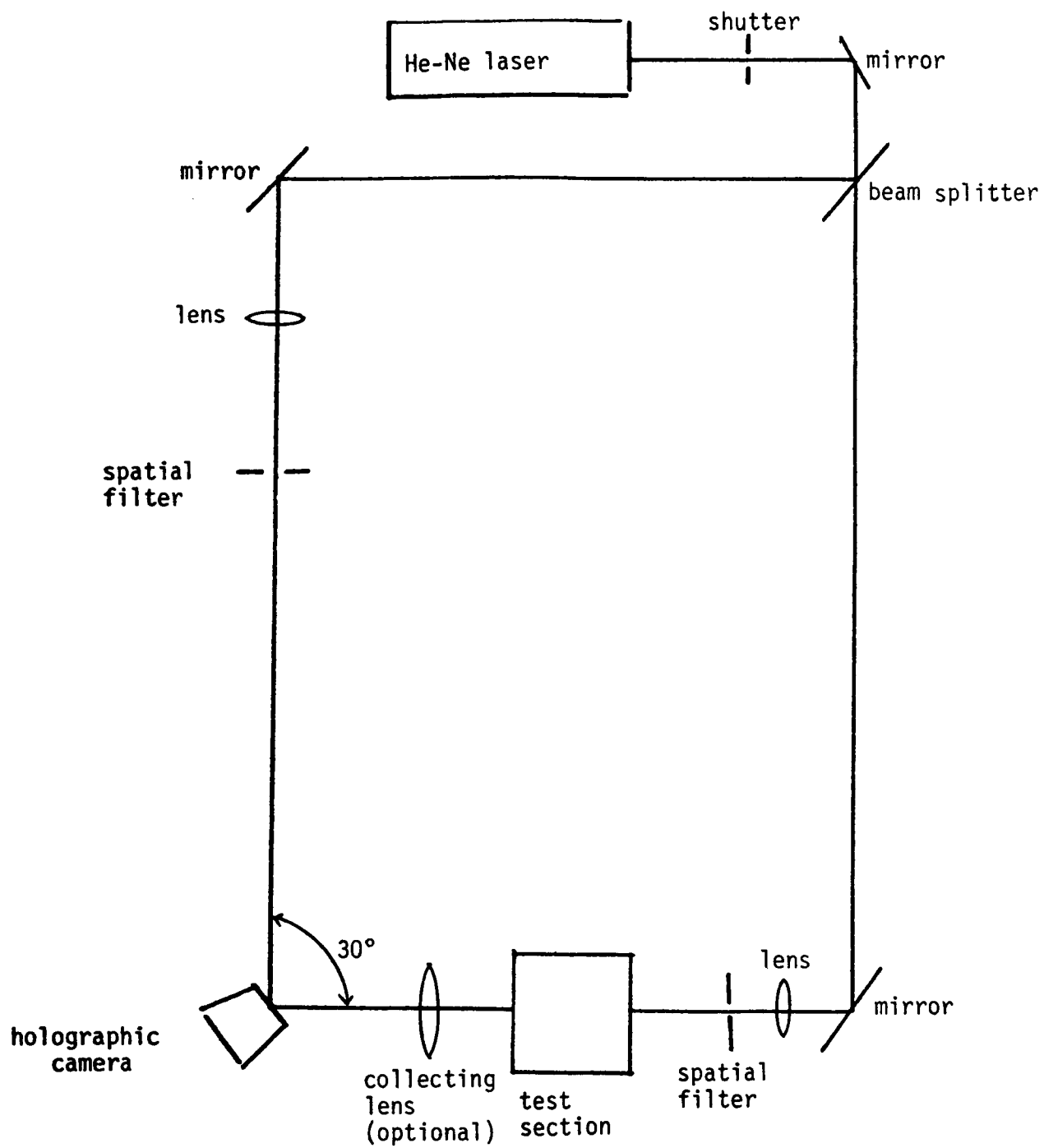
He-Ne laser

shutter

mirror

mirror

beam splitter

lens

spatial
filter

30°

lens

holographic
camera

collecting
lens
(optional)

test
section

spatial
filter

mirror

HOLOGRAPHIC INTERFEROMETER

C-2

134dB
c

150dB
f
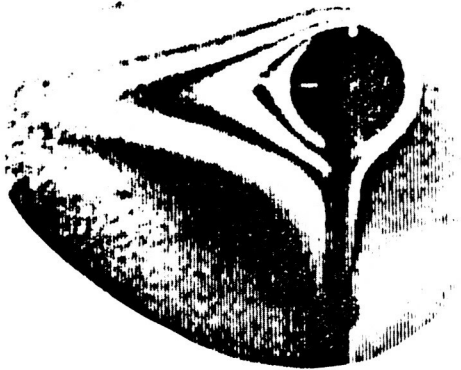
130dB
b

143dB
e

FREE CONVECTION
a

140dB
d

98

c

f

b

e

a

d

99
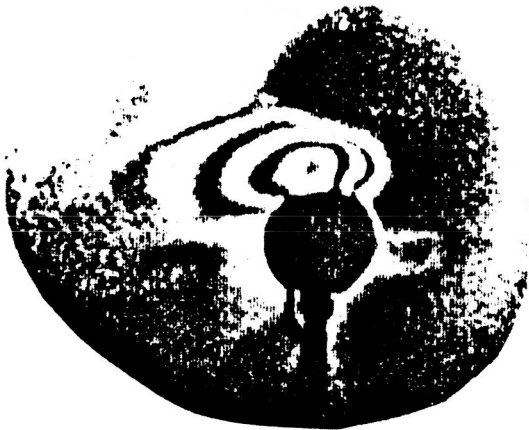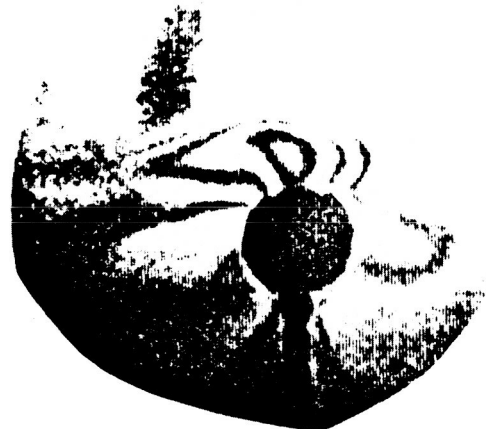
ARI-RR-449

TOWARD AUTOMATED ANALYSIS OF PARTICLE HOLOGRAMS

Prepared by

H.J. Caulfield
Aerodyne Research, Inc.
45 Manning Road
Billerica, MA 01821

January 1985

PRECEDING PAGE BLANK NOT FILMED

PAGE _100_ INTENTIONALLY BLANK

TOWARD AUTOMATED ANALYSIS OF PARTICLE HOLOGRAMS

H.J. Caulfield, Aerodyne Research, Inc., 45 Manning Road, Billerica MA 01821

ABSTRACT

A preliminary study of approaches for extracting and analyzing data from particle holograms concludes that

o   For "thin" spherical particles out-of-focus methods are optimum,

o   For "thin" nonspherical particles out-of-focus methods are useful but must be supplemented by in-focus methods, and

o   A complex method of projection and back projection can remove the unwanted out-of-focus data for "deep" particles.

I. INTRODUCTION

Particle holograms are capable of instantaneous recording of a large three-dimensional (3D) field particles. Given a particle hologram, we might have two tasks:

1.   Find all of the particles and

2.   Characterize them.

The verbs "find" and "characterize" must be defined more carefully for each particular situation. In most cases this analysis is carried out using a human observer to

1.   Locate the plane of best focus for each particle,

2.   Record the in focus image,

3.   Characterize that image.

There are two major difficulties with this human-operator-based analysis: one obvious and one slightly more subtle. The obvious difficulty is that human-based analysis is notoriously slow, nonrepeatable, and (hence) costly and inaccurate. It is this analysis bottleneck which keeps particle holography equipment on the shelf while far less powerful technologies perform a few of the tasks holography could perform. The less obvious difficulty is that human-based analysis may be inherently less accurate than analysis based on a computer oriented algorithm.

This paper explores past and current approaches to computer analysis of fields produced by particle holograms based on "multiplane" algorithms. Multiplane algorithms are based on data obtained in several depth planes (rather than simply the "focal" plane).

II. PHILOSOPHICAL BACKGROUND

A human observer looking at a point of laser light will see that point clearly. A recording surface moving through the field produced by such a point will produce a point image in focus and a diffraction pattern out of focus. This assymetry between the human (who sees only what is in focus) and the camera (which sees the out of focus data as well) leads to different data analysis schemes. In principle, all of the information in the particle wavefront is contained in every plane (including, of course, the hologram plane). Nonholographic cameras do not record the whole information, however, so observations in different planes give different information.

To these fundamental observations we must add some practical ones. Particle hologram wavefronts are noisy and complicated. Other particles are present. Refractive artifacts occur. These complications mean that otherwise-equivalent observations are not really equivalent. More observations can mean reduced influence of these "noise" effects.

III. ANALYSIS OF SPHERICAL PARTICLES

Spherical particles are guaranteed in some cases, e.g. bubbles. For known spheres only two questions can be asked:

1. Where are they?

and

2. What are their diameters?

The old (human-oriented) approach is to move to the focal plane and there measure the lateral (x-y) position of the particle's center and measure its diameter. The depth (z) dimension is that of the camera in the focal position.

In the newer (computer oriented) approach, all of these quantities are measured in out of focus planes. We will review this past work briefly here.

The first work in this field was by Vikram and Billet.[1] They showed that diameter determination was far more accurate out of focus than in focus simply because the pattern is, in effect, magnified. Two derivative observations can be made immediately:

1. Localized film or detector noise is less of a problem out of focus than in focus and

2. The centroid of the sphere (x-y location) can be located more accurately out of focus than in focus.

The second work in this area was by Stanton, et.al.[2] They showed that

1. The depth of the particle could be found more accurately by out of focus measurements than by in focus measurements and

2. This obviates the need for searching all depth planes.

The explanation of the increased accuracy in depth (z) location is a fairly universal one worthy of a little more explanation. If we plot "spot" size, s, versus z (z $\equiv$ 0 in focus), we obtain a curve with a minimum at z = 0. We can seek to find z = 0 by the z finding minimum s. Or we can measure s at two z $\neq$ 0 positions on the same side of z = 0 and extrapolate to s = 0. The z sensitivity

$$\alpha = \left| ds/dz \right|$$

is a maximum away from z = 0 and minimum at z = 0. Indeed maximum α occurs at maximum numerical aperture and way from z = 0.

IV. SHALLOW OBJECTS

A shallow object is one with unresolvable depth information. All that counts is its two-dimensional cross section normal in x-y. The questions which can be asked include

1. What is the x-y-z centroid location?

2. What is the shape? (Not a well defined question) and

3. What is the orientation?

Whether these questions can be answered out of focus depends on what we mean by "shape" and "orientation." Suppose we mean by "shape" the best fit enclosing rectangle and by "orientation," the direction of the rectangle's predominant direction. Then clearly these are accessible out of focus. On the other hand many details of shape *are* simply not detectable out of focus, e.g. a particle shaped like a "6" and a particle shaped like a "9".

When details of particle shape are of interest, we must go to a focal plane. This does not mean, however, we should ignore the out of focus information. Extrapolation from out of focus data is still probably the best way to obtain focus. Furthermore, the out of focus data can be used, at the price of considerable computational complexity, to improve our knowledge of the in focus image. The idea, of course, is to use some generalized Gerchberg[3] algorithm to iterate back and forth between the in-focus image and the out-of-focus diffraction pattern using

o   Known Fraunhofer diffraction laws,

o   Measured data in both domains, and

o   Imposed constraints in both domains (e.g. nonnegativity in the image plane).

Such techniques are exceedingly powerful[4] and would, no doubt, be useful here as well.

V. DEEP OBJECTS

The hardest problems for any automatic, semiautomatic, or even human analysis is the deep object. Such an object is deeper than the depth of focus of its hologram. It is never all in focus in any plane. Of such objects we ask the usual questions (shape, size, 3D orientation, 3D location), but finding the answers is quite difficult.

The first problem which must be solved is that of separating in-focus images from out of focus artifacts. In any depth plane there are probably some of both. We suggest here an automated approach not as a final solution but as a starting place for more sophisticated analyses.

We might begin by projection of the 3D scene into 2D. To do this we sort all x-y pixels by some focus criterion. That is at each x_i, y_i we examine each discrete depth. We might estimate focus by brightness. Let the intensity at x_i, y_i in the kth/ depth slice be $I_{ij}k$. We define

$$P_{ijk} = \max \begin{cases} I_{ijk} \\ P_{ij(k-1)} \end{cases}$$

That is, P_{ijk}, is the largest of the I_{ijk}'s seen so far. By the time we have sorted through all N depth slices, P_{ijN} is a "projection" of the 3D image into 2D (i,j). All in focus pixels regardless of their depth are collected in one plane.

The next step would be to reproject P_{ijN} back into 3D. The 3D reprojection of P_{ijN} is

$$R_{ijk} = \begin{cases} I_{ijk} & \text{if } I_{ijk} = P_{ijN} \\ 0 & \text{otherwise} \end{cases}.$$

108

Thus R_{ijk} should have no out of focus parts. The subsequent analysis must group non-zero R_{ijk} components into likely particles, characterize them, etc.

VI. PROSPECTS

The sole objective of this paper is to point out numerous opportunities to explore automated computer analysis of 3D particle fields obtained by holography. For shallow spheres the analysis is easy and only implementation is needed. For other shallow objects some analogous work can be borrowed from the spherical case but much new work is required. For deep objects, no work has been done. The critical observation, however, is that full automation appears to be within our grasp.

REFERENCES

1. C.S. Vikram and M.L. Billet, Appl. Phys. B.33, 149 (1984).

2. A.C. Stanton, H.J. Caulfield, and G.W. Stewart, Opt. Eng. 23, 577 (1984).

3. R.W. Gerchberg, Optica Acta 21, 709 (1974).

4. J.R. Fienup, Opt. Eng. 18, pp. 529-534 (1979).

SUMMARY OF PROGRAMS IN COMBUSTION/PARTICLE SIZING

Five Minute Informal Presentations of Plans Applications and Problems.

R. FIELD

U.S. ARMY ARMAMENT R&D CENTER (ARDC)

PICATINNY ARSENAL, DOVER, NJ

GUN PROPELLANT IGNITION AND COMBUSTION STUDIES USING HOLOGRAPHIC METHODS

OBJECTIVES: FUNDAMENTAL INFORMATION ON THE PHYSICAL NATURE OF THE COMBUSTION PROCESSES OF CONDENSED PHASE ENERGETIC MATERIALS, ESPECIALLY IGNITION AND FLAMESPREADING

APPLICATIONS:

- PARTICLE FIELD HOLOGRAPHY

  COMBUSTION BEHAVIOR OF BLACK POWDER AND OTHER IGNITER MATERIALS
  - PARTICLE FORMATION AND DISPERSION
  - PARTICLE SIZING AND VELOCITIES

  •• PROBLEMS - MANUAL DATA REDUCTION
                  - RESOLUTION IS VARIABLE FUNCTION OF THE COMBUSTION PROCESS, E.G., NOISE DUE TO SMOKE SCATTERING AND THERMAL CELLS

- FLOW VISUALIZATION

  FLAME STRUCTURES

  FULL FIELD VISUALIZATION OF TRANSIENT PROCESSES, I.E., IGNITION AND FLAMESPREADING

  •• PROBLEMS - COMPLEXITY OF REACTIVE FLOWS IS NOT EXTERNALLY CONTROLLABLE; EXTRACTION OF QUANTITATIVE DATA IS UNCERTAIN

S₁₀-35
NBS SN4
103451
18

Temperature and Concentration Measurements in Combustion

Takashi Kashiwagi
National Bureau of Standards

A high speed two wavelength holographic interferometer is being used to simultaneously measure temperature and concentration distributions for ignition and flame spread. Lines from a c w CO_2 laser was used and the holograms recorded on movie at 500 frames per second, individual frames were digitized with a mirco-densitometer. The detection on the fringe center was a major problem.

PRECEDING PAGE BLANK NOT FILMED

PAGE 114 INTENTIONALLY BLANK

PARTICLE DATA REDUCTION IN JAPAN

Mitsushige NAKAYAMA

Department of Mechanical Engineering,

Gunma University

1-5-1 Tenjin-cho, Kiryu, JAPAN 376

1. INTRODUCTION

The author is engaged in research of the characterization of atomized particles generated by various atomizer (Refs. 1.2) and the mechanisms of their evaporation and combustion processes (Refs. 3, 4, 5, 6, 7)

In the course of his research, he has felt the needs for visualizing the internal structures of flames including evaporation and combustion processes as well as for a better way of understanding spray particle generation mechanisms and internal structures, and for the information of the system user, he is using a particle sizer based on a Fraunhofer diffraction for detecting particle size and in-line Fraunhofer holograms for observation of local spray particles. Recently, he has developed a novel visualizing technique based on Computed Technology for these fields (Refs. 6, 8).

For measuring spray, various technique are available including such methods as liquid immersion, freezing, trace, molton-wax, and microscopic. And ideal conditions of measurement include (Ref. 9);

1. Should not disturb the fuel spray pattern or atomization.

2. Should provide a rapid means of sampling.

3. Should provide a rapid means of counting the samples obtained.

4. Should be enough to provide meanigful data in the less than 10um.

5. Should permit the variation of liquid and ambient gas properties.

6. Should permit one to obtain drop size distribution in space.

7. Should permit one to obtain the drop size distribution produced by the nozzle in a given time.

Many novel laser diagnostics such methods as LDV, Scattering, Diffraction, Holography, etc. are satisfying above items. Pulse laser holography which meets all the requirements listed above excluding 3, is expected to be an effective means for spray measurements. However, past works suggest that in the case of high space particle density, such as of a diesel spray, measurement is only possible in the extra-low density field of peripheral regions and that much time and labor are required for reduction of particle diameter from the hologram. This will account for it being less frequently used when compared with its application field, such as in vibration or material research.

Of various combuston system, combustion spray is widely used in diesel engine, gas turbine and boilers. For analysis of combustion mechanism using intermittent sprays, such as in a diesel engine, obtaining detailed information on sprays is of vital importance.

2. HOLOGRAPHIC RESEARCH OF PARTICLE/COMBUSTION IN JAPAN

Generally, works on holography cover two fields, its recording and reconstruction, which is also in Japan. And regarding the subject of this work shop, namely, works on holography of spray particles, these can be classified into those from the point of optical or

instrumental engineering and those of combustion engineering. Of course, the former places emphasis on research and development of systems and the latter on analysis usig such systems.

As for recent moves in Japan, the Ministory of Education adopted "DYNAMIC MODELING AND LASER DIAGNOSIS OF COMBUSTION" as a theme of special 3-years research project starting in April 1983 and associated works are under way with a fund of approximately 2 million dollars. About 60 researchers representing combustion engineering, chemical analysis, numerical calculation, instrumentation engineering other field are participating in the project. Among them, there are ten researchers dedicated to particle study and five dealing with holography, but a few researchers are engaged in data reduction.

Works under way at various universities in the following.
KYUSHU UNIVERSITY (Professor T. Murakami, et al.)

With development of optic instrumentation and its application, the activities of the group are well known. They have published many papers as follows:

(1) Establishment of recording and reconstruction techniques of fuel injection spray by diesel nozzles in normal and elevated ambient pressure using in-line holography with a pulse laser (Refs. 10, 11). Fig.1 shows an original in-line hologram of diesel injection and reconstruction region is presented.

(2) Holographic measurements of size and velocity of particles by means of two pulsed dye lasers of different wavelength (Ref.12).

(3) Development of dierect analysis method of particle size and position from hologram using an image analyser (Ref.12). The radial distribution of holographic intensity $I(r)$ on the plane at distance Z from the particle of diameter d is given by using the Fresnel approximation. The typical patterns of log $I(R)$ are shown in Fig.2.

119

The reduced fringe diameters, $\tilde{D}max=Dmax/d$ and $\tilde{D}min=Dmin/d$ are uniquely related the far feild nuber N in Fig.3. They proposed that they can be determine the N value with observed ratio $\tilde{H}$ ($=\tilde{H}obs$), then get Dmax or Dmin for corresponding to N. Consequently, the diameter d and the distance Z are obtained by using the observed Dmax or Dmin as $d=Dmax/\tilde{D}min$ or $=Dmin/\tilde{D}min$, and as $z=d^2 N/\lambda$, respectively. An examle of particle data and a digital intensity distribution are shown in Fig.4, and on upper left corner on CRT the data of particle position and size are pictured.

TOKAI UNIVERSITY (Professor T. Uemura, Y. Yamamoto and H. Yokota)

Holographic research is being conducted fron the view point of optical and instrumentation engineering. They have made positive progress in the fields of in-line and off-axis holography with unique works on high speed photography and holography. Holograms of non-burning and burning fuels injected under atomospheric condition have been taken (Ref.13) and combustion state has been observed with aceton in place of fuel, fed to a model 4-cycle SI engine having transparent cylinders (Ref.14). Also information has been furnished on change of spray particle size by back pressure recorded as fuel was injected fron diesel nozzle into a high pressure vessel (Ref.15).

HIROSHIMA UNIVERSITY (Professor H. Hiroyasu, et al.)

Modeling and simulation for diesel spray combustion, diesel engine performances etc., activities of this university are well known. As for research into holography which was only recently started, they are using double pulse lasers and the off-axis method to measure diesel injection sprays injected in to high temperature (up to 733K), and high pressure atomosphere (up to 3.0Mpa). Fig.5 shows the example

result of reconstructed image of the diesel spray injected into elevated pressure and temperatures. At around 773K, droplets can not be found and the puffing of liquid vapor was observed.

GUNMA UNIVERSITY (Professor M. Nakayama, et al.)

Researches on spray particle generation mechanism and internal structure of spray using various nozzles as well as researches on internal strucure in the evaporation and combustion processes are under way. The subjects covered include diesel combustion, gas turbine combustion and pulverized coal combustion. In the course of these studies, visualization technique of spray, solid particle or their combustion flames was found and hence,

[1] Observation of local spray particles by in-line Fraunhofer holograms.

[2] Measurements of particle size by a Fraunhofer diffraction principle (Refs. 4, 5, 7).

[3] Measurements of evaporating constant rate utilizing time and positional change rate of diffraction energy (Refs. 5, 7).

[4] Detection of transmitted light intensity distribution for computed tomography by means of computer Television Camera system (Refs 6, 9).

[5] Development and prototype fabrication of automatic data reduction systen for hologram.

are also under way. Their researches will be shown later section.

3. PROBLEMS ASSOCIATED WITH HOLOGRAPHY

3.1 Non-burning Atomosphere   Research results of the author and co-workers or other researchers in Japan indicate that there will not be significant problems so long as the space density is relatively low such as in the case of swirl chamber atomizer for boiler or gas

turbine combustor application. If the space density is high as with spray particles from diesel nozzles, however, it appears that the particle information available from an in-line hologram system is limitted to local very low density peripheral regions of spray.

3.2 Combustion field of Particles   On open flames there will be no significant problems such as small spray combustion, but there will be difficult on closed combustion such as diesel spray. It is owing to the limitation of window size and optical set up.

Deterioration of reproduced image quality due to fluctuation or sub-micron vapor is unavoidable regardless of normal or high temperature/pressure atomosphere.

3.3 Data Reduction   One of reasons which have prevented the extension of holography is owing to work time, that is, the reconstruction process takes appreciable time even enough a TV system used.

The author et al. adopts the image hologram method produce holograms, and is now developing and fabricating prototype of automated data reduction system. It will be completed in September, 1985.

4. IMAGE ANALYSIS OF INTERMITTENT SPRAY

Holograms of diesel injection sprays by in-line Fraunhofer holography cannot be an adequate method for high density spray. However, in view of the importance of establishing the limit of effective density, application of Computed Tomography using transmitted light intensity distribution to acquire particle information is now under study (Refs. 7, 8). It appears that there is correlation between hologram images and CT images. Fig.6 shows density distribution of a spray at an arbitrary spray section reconstructed by

the CT method of diesel fuel injection into space at normal
pressure.The figure shows the density information on section 20, 30,
40 and 50 mm away from nozzle tip derived from shadow photos of spray
1.1 ms after start of injection. Fig.7 presents the data of spray
particle density change with time at 30mmm position from nozzle tip.
Comparison of Figs. 6 and 7 indicates that, with diesel spray, later
sprayed particles catch up with and overtake preceding particles,
which suggest that care should be taken in holography.

The regions available where particle information reproducible by
hologram are those peripheral regions in Figs. 6 and 7.

Fig.8 shows reconstructed spray concentration of diesel injection
which has been recorded in-line hologram. The information of particle
size and their distribution has not be analysed in this time. We are
undergoing to analyse these problem by using onion peeling model for
axi-symmetric spray.

5. SUMMARY

The author introduced about the works of particle field data
reduction in Japan. Many excelent works were done, but we can not get
the information of particle characterization in high density particle
fields. I think, in near futute, it will be able to get reasonable
data of high density particle field such as diesel injection spray.

6. REFERENCES

1. NAKAYAMA M. and OHONO T., "Experimental Investigation of Atomizing Characteristics of Grooved Swirl Nozzle", Proc. of Ist Int. Conf. on Liquid Atomization and Spray Systems(ICLAS)., Tokyo, (1978) 44.

2. NAKAYAMA M. and TAKAHASHI Y., "Experimental and Theoretical Invesigation of Longitudinal Vibrations on Liquid Jets and Sheets", Proc. of 2nd ICLAS., Madison, Wisconsin, USA (1982) 1.

3. NAKAYAMA M. and SUZUKI T., " Studies on Luminous and Non-Luminous Flames with Spray Combustor(2nd Rport; Case of Swirl Combustor). Bull. of JSME. 26-216 (1983) 1036.

4. NAKAYAMA M. and ARAI T., "An Investigation into Laser Diagnostic Technique of Liquid Droplets(Part 1; Measurements in High Temperature Stream)", Bull of JSME. 27-224 (1984) 235.

5. NAKAYAMA M. and ARAI T., "An Investigation into Laser Diagnostic Technique of Liquid Droplets(Part 2; Measurements of Evaporation Rate Constant in Hot Spray)", Bull of JSME. 27-224 (1984) 241.

6. NAKAYAMA M. and ARAKI T., "Visualization of Spray Structure by Means of Computed Tomography", Int. Symp. on Diagnostics and Modeling of Combustion in Reciprocating Engines. Sept. 4-6, 1985, Tokyo. (Will be appeared).

7. NAKAYAMA M. and ARAI T., "Spray Droplets Evaporation Rate Constant Measurements by Laser Diffraction Technique", Proc. of 20th Intn. Symp. on Combustion. Ann Arbor Michigan USA, (1984-8).

8. NAKAYAMA M. and ARAKI T., "Study of Spray Droplets Evaporation Process in Hot Spray by Computed Tomography Technique", 3rd ICLAS, London (July 7-9, 1985) (will be appeared).

9. DECORSO S. M., "Effect of Ambient and Fuel Pressure on Spray Drop Size", Trans. ASME. Jan. (1960) 10.

10. ISHIKAWA. M. and MURAKAMI T., "Characteristics of Intermittent Sprays generated by an Orifice Atomizer", 2nd ICLAS., Madison, Wisconsin, (1982) 75.

11. OGATA S., ISHIKAWA T. and MURAKAMI T., "Velocity Measurements of Electrostatically Sprayed Droplets by Means of Two Laser Pulses of Different Wavelength", J. Electros., 9 (1981) 223.

12. MURAKAMI T. and ISHIKAWA M., "A Direct Analysis Method of In-line Hologram for Measuring the Particle Size and Location", Proc. 13th Congr. Intn. Comm. Optics. Saporro, Japan (1984) 98.

13. UYEMURA T., YAMAMOTO T., YOKOYAMA N., DOI A. and HISAOKA M., "Application of High Speed Holography to Measurement of Particle Size in Flame", SPIE 348 High Speed Photography. San Dirego, (1982) 662.

14. UYEMURA T., FU I., YAMAMOTO T., YOKOYAMA N. and HISAOKA M., "Observation of Firing in Four-cycle Internal Combustion Engine by High Speed Photography and Holography", ibid., 670.

15. MORIYAMA T., KOMACHI Y., KAJIYAMA K., MORO N., KANO S. and YOKOTA H., "Measurement of Fuel Spray Behavior under High Ambient Pressure using Pulsed Laser Holography", Proc. Faculty of Engng. Tokai University, 2 (1980) 179.

16. NISHIDA K., HIROYASU H. and MURAKAMI N., "Observation of Fuel Spray and its Vapor using Pulsed Laser Holography", (in Japanese) Paper of Japan Soc. Aero. & Spac. Sci. (1984) 41.

Fig. 1   In-line hologram of diesel injection spray (after Murakami)

Original Hologram
and
Its Enlarged Holograms
for Measuring the
Droplet Size.

Reconstructed Region

Core Part of Spray

Original In-line Hologram

Reconstructed Region

1mm
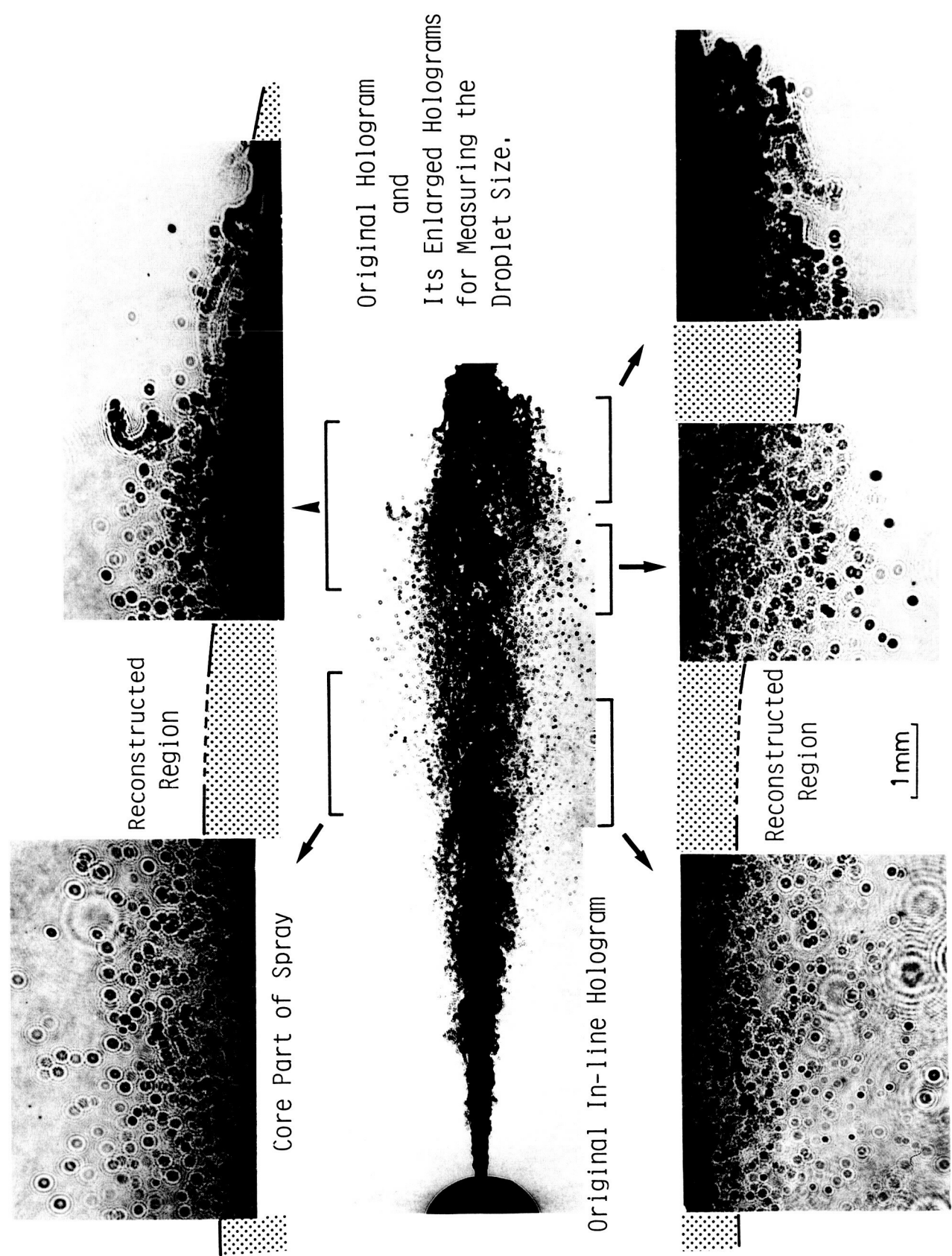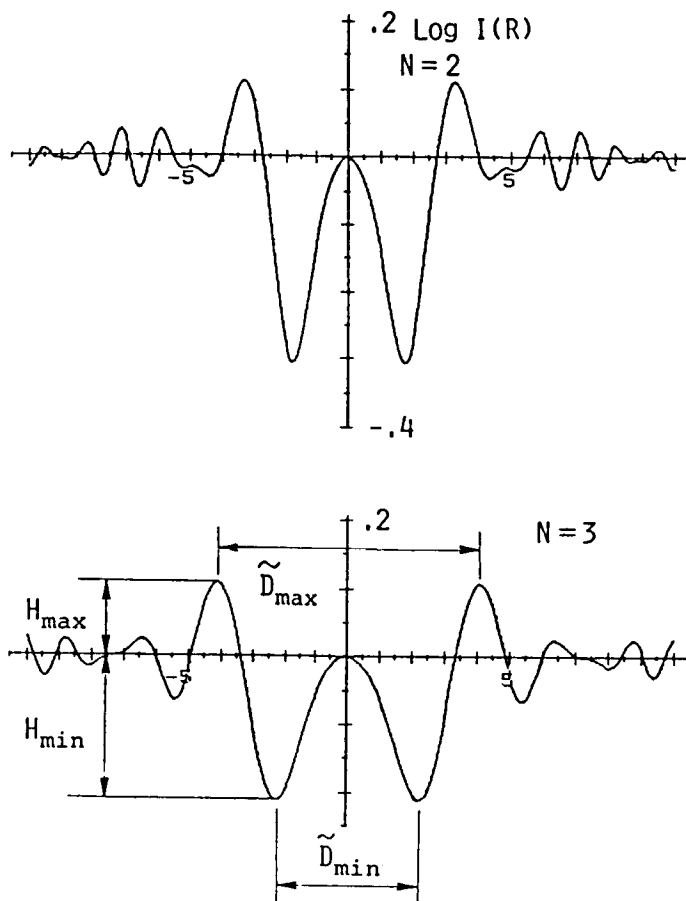
Fig.2 Calculated intensity distribution Log(R) (After Murakami)
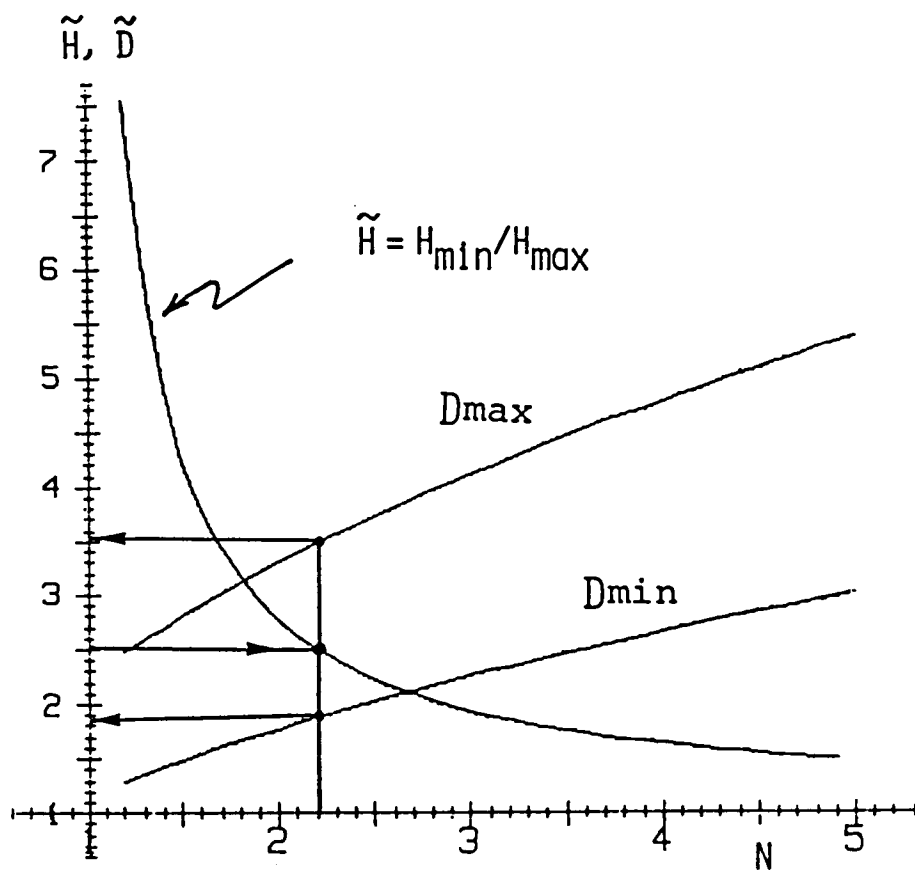
Fig.3 Charactristic diagram of parameter H, Dmax, Dmin vs far field
number N (After Murakami)

t =1.0ms Ta=293K   473K   673K   773K

t =1.8ms Ta=293K   473K   673K   773K
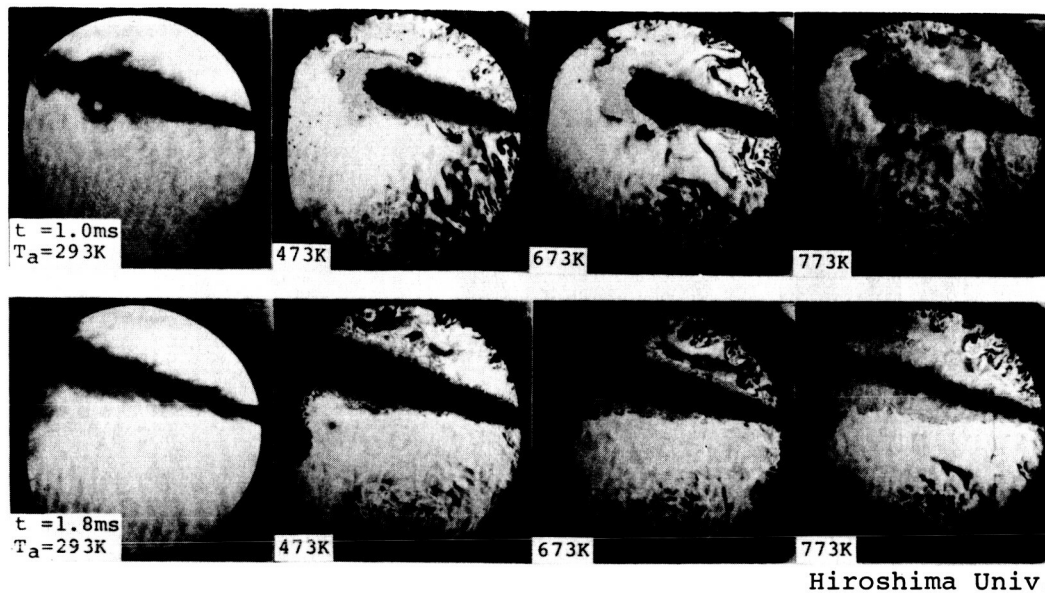
Hiroshima Univ.

Double-pulsed Interferograms of a Diesel Spray

Pulse Interval : 0.2 ms
Atmospheric Density : 13.5 kg/m³

t =1.8ms Ta=293K   473K   673K   773K

Ta=773K
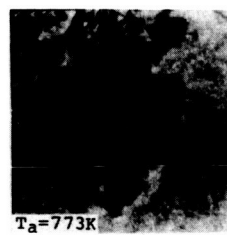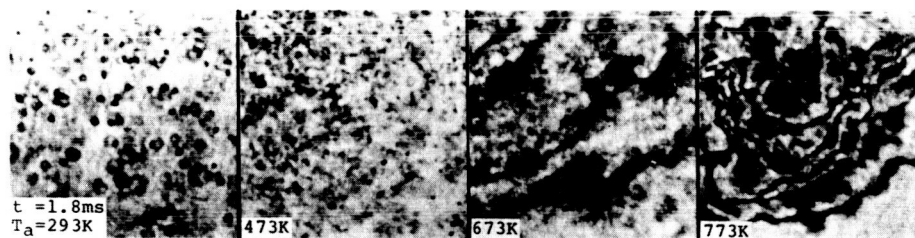
Hiroshima Univ.

0   1.0mm

Puffing

Enlarged Reconstructions from Double-pulsed Holograms

of a Diesel Spray

Pulse Interval : 0.2 ms
Atmospheric Density : 13.5 kg/m³

Fig.5 Off-axis hologram of diesel injection spray under
the condition of high temperature/pressure atomosphere (After
Hiroyasu)
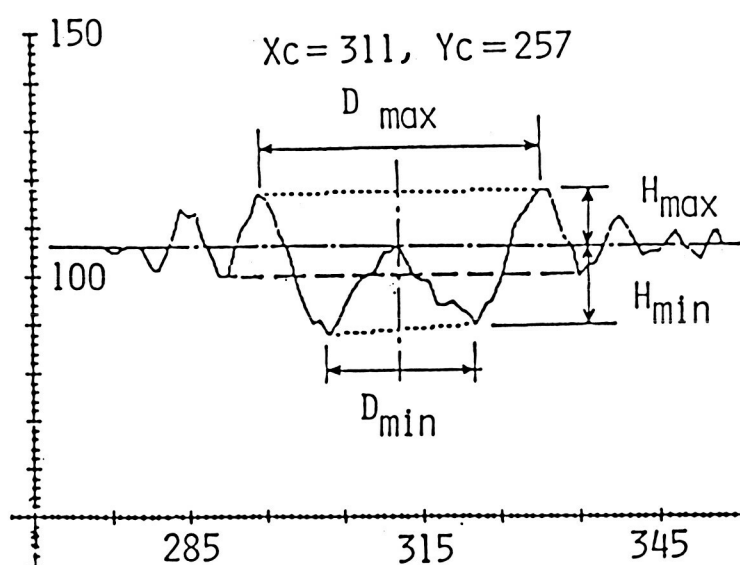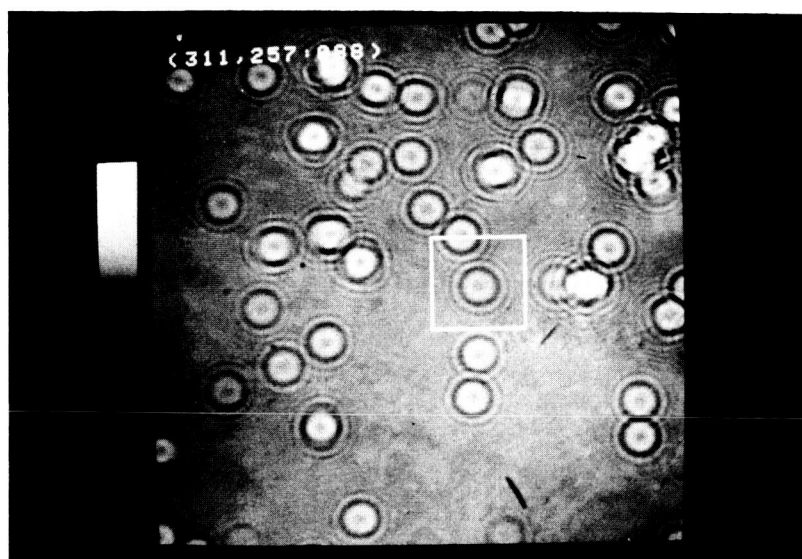
Fig.4 Example of a digital intensity distribution (After Murakami)

(a)

z=20mm

z=30mm

z=40mm

z=50mm

(b)

Fig.6 Spray density distribution by Computed Tomography
Diesel nozzle: Throttle type. Pi: 12Mpa.
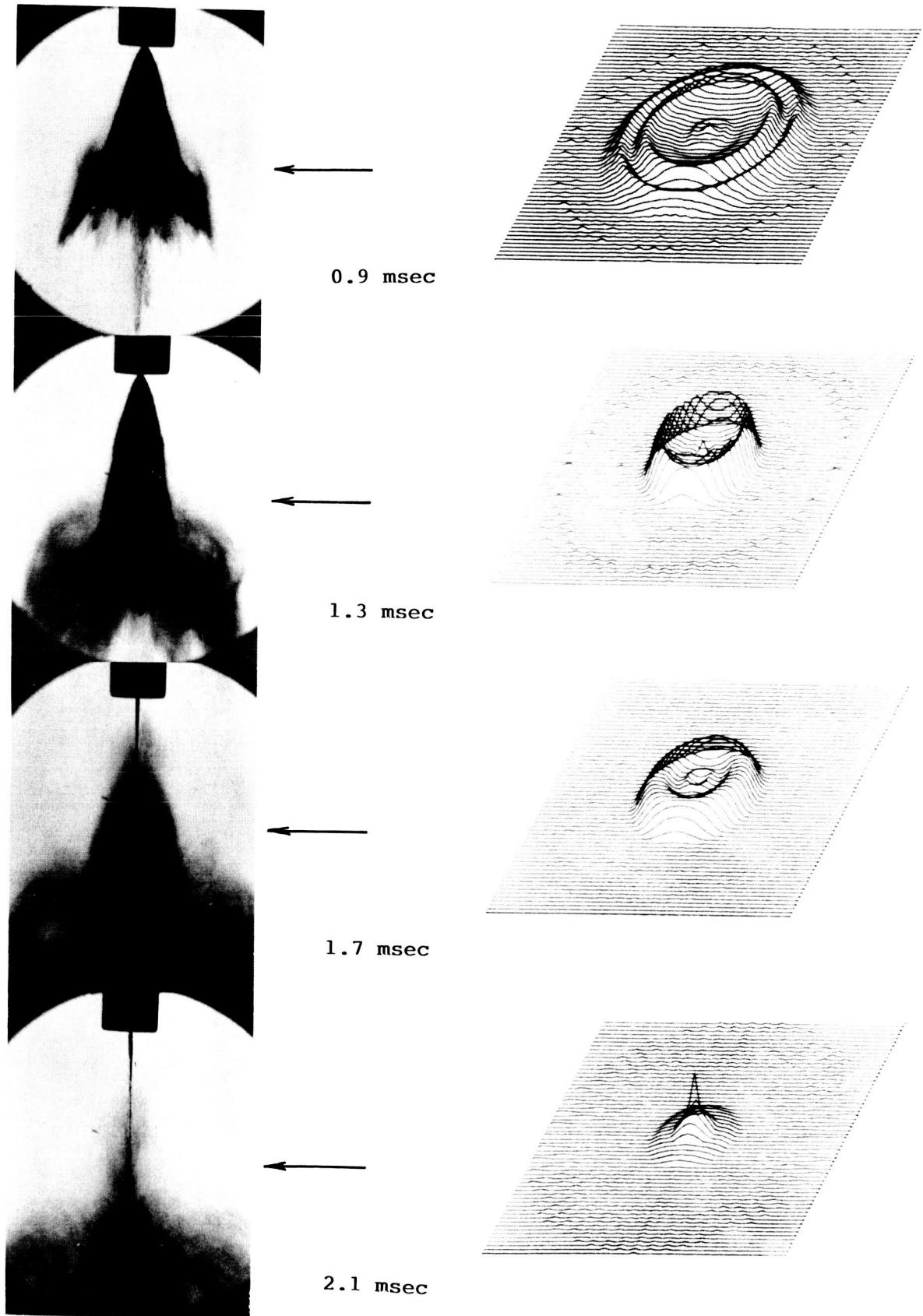
131

0.9 msec

1.3 msec

1.7 msec

2.1 msec

Fig.7 Time dependence of spray density distribution by
Computed Tomography
Diesel nozzle: Throttle type. Pi: 12Mpa.

132
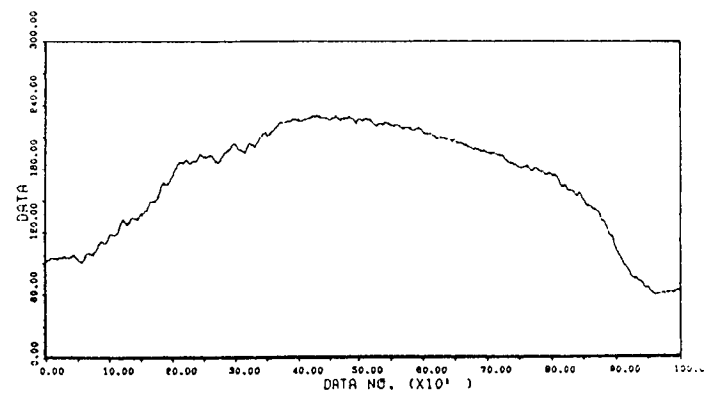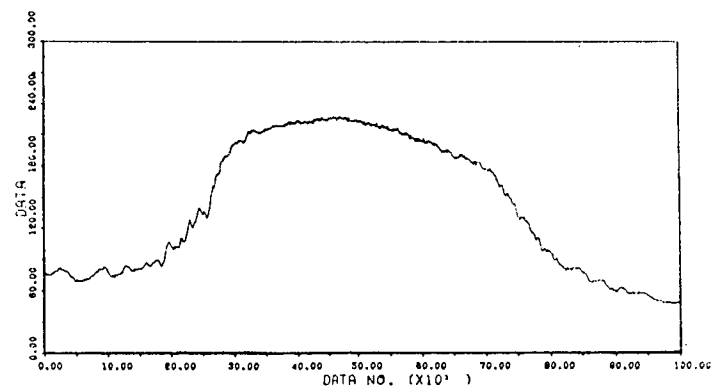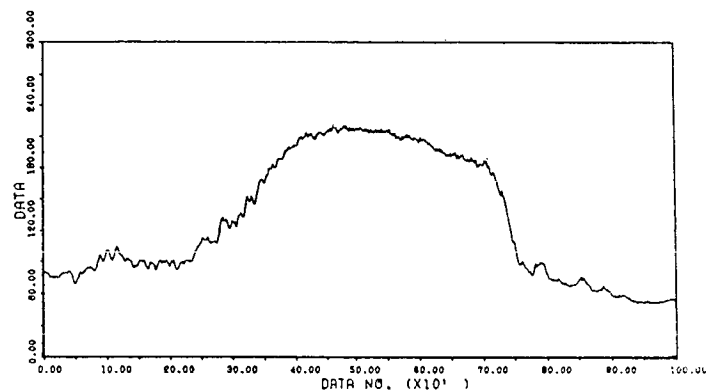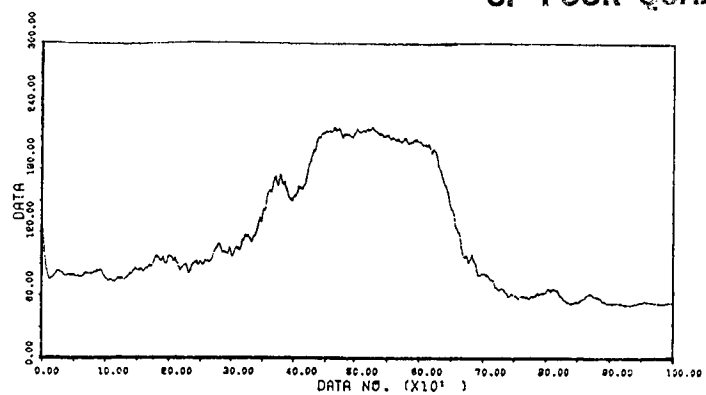
Fig.8 Spray concentration by Computed Tomography
from in-line hologram

133

COMBUSTION/PARTICLE SIZING EXPERIMENTS
AT THE NAVAL POSTGRADUATE SCHOOL
COMBUSTION RESEARCH LABORATORY *

John Powers and David Netzer

Naval Postgraduate School
Monterey, California 93943

Particle behavior in combustion processes is an active research area at the Naval Postgraduate School (NPS). Currently, four research efforts are being conducted at the Combustion Research Laboratory.

There is a long standing need to better understand the soot production and consumption processes in gas turbine combustors, both from a concern for improved engine life and to minimize exhaust particulates. Soot emissions are strongly effected by fuel composition and additives. NPS efforts are directed at these two effects. Soot particles in gas turbine engines are generally quite small, typically between 0.01 and 1.0 micron. This size range is beyond present holographic capabilities and, therefore, light transmission measurements at three wavelengths and light scattering measurements at large angles (10-50°) are being used to determine mean particle sizes within a small gas turbine combustor. Probe sampling is also being employed for comparison with the optical measurements.

A more recent need for particle sizing/behavior measurements is in the combustor of a solid fuel ramjet which uses a metallized fuel. In this combustor, metallic agglomerates are formed on the surface. The agglomerates are then either swept along the surface or are ejected from the surface and follow a trajectory up through a developing turbulent boudary layer. Eventually the particles pass through a turbulent diffusion flame which is located within the boundary layer. Upon reaching the flame (or oxygen above the flame) the particles ignite and continue to burn as they pass down the port of the motor. Predictions of the fuel regression rate and the combustion efficiency are both dependent upon a good understanding of the behavior of the particles throughout their lifetimes. Currently, high speed motion pictures are being used to study these rather large (20-500 microns) burning particles. Holographic studies are planned within the current year.

135

In solid propellant rocket motors, metals (typically aluminum) are used to improve specific impulse and/or to provide damping for combustion pressure oscillations. The size of the particles vary from approximately 0.5 to 200 microns, depending upon the combustion region being studied and the propellant properties and motor operating environment. The smaller (less than 2 microns) sizes are generally not of primary interest. Although they produce primary exhaust smoke, they do not contribute significantly to two-phase flow losses in the exhaust nozzle or to losses in combustion efficiency. It is important to know the size distributions of the particles (and how the sizes change with location) if accurate predictions of combustion efficiency, particle damping, and two-phase flow losses are to be made. The particles within the motor generally are not moving too rapidly and are of large enouph size to permit holographic investigations. However, the high number density of burning particles generally requires the use of diffuse illumination in the scene beam and speciallized apparatus to permit penetration of the combustion zone. Both two-dimensional and three-dimensional motors are currently used together with a pulse ruby laser/holocamera. Within the exhaust nozzle velocities become quite high and particle size can rapidly decrease due to high shear stresses. In this region particle sizing experiments are being conducted using diode arrays to measure the light intensity as a function of scattering angle.

Being able to obtain good quality holograms within the solid propellant rocket motor environment is one task. However, once this is attained, a need exists for obtaining the particle size distributions from the holograms in a reasonable period of time. Automatic or semi-automatic data retrieval methods are mandatory, but complicated by the presence of speckle and nonuniform light intensity in the reconstructed holograms. NPS efforts in this area are currently based on the use of a Quantimet 720 Image Analyzer.

EXAMPLES OF APPLICATION USING IMAGE PROCESSING
AT GENERAL MOTORS RESEARCH LABORATORIES

Gary Bertollini

General Motors Research Laboratories

Examples of Applications using Image Processing at General Motors Research Laboratories

I) Quality Control Measurements (30%)

- Weld Quality
- Panel Surface Quality
- Material Quantity Ratio

II) Image Enhancement (10%)

- Photograph Enhancement

III) Research Experiment Quantification (60%)

- Flame Propagation
- Particle sizing & velocity
- Polymer Fiber Orientation
- Crystal Growth Rate
- Flow Studies
- Biomedical Cell Distribution
- Paint & Fuel Spray Diagnostics

GMR IMAGE PROCESSING FACILITY

Coherent Source Experiments

| Optical Table etc. |——————| Camera |

Non-Coherent & Photographic Sources

| Light Table |——————| Camera |

Video RS-170

Video Sources

| VHS, Tape, Disk, High Speed Video Recorder |

Magnetic Video Disk Recorder

Time Base & Video Level Corrector

Signal Monitor

Image Processor VCO3

4 Image Planes
19" Color Monitor
Term 1
Term 2
Digitizer Tablet
16 MB Disk
Printer
High Resolution Copier

Network Link - - - - - - - -

Image Processor VDP

8 Image Planes
19" Color Monitor
Term 1

Track Ball
50 MB Disk
200 MB Disk

Digital

Corporate Computers

Fuel Spray Droplet Size Analyzer Using Image Processing Techniques

○ Direct imaging method using laser to freeze droplet motion .

○ Allows automatic size distribution analysis in difficult spray locations & optically harsh environments. (ex. nozzle tip, in running engine)

○ Discussion will include:
- Hardware
- Shading removal algorithm
- Droplet segmentation
- Preliminary experimental results

PARTICLE IMAGING VELOCIMETRY

M. C. Whiffen

Lockheed-Georgia

PARTICLE IMAGING VELOCIMETRY

(PARTICLE STREAK VELOCIMETRY)

ALSO KNOWN AS;

LASER SPECKLE VELOCIMETRY

PULSE LASER VELOCIMETRY
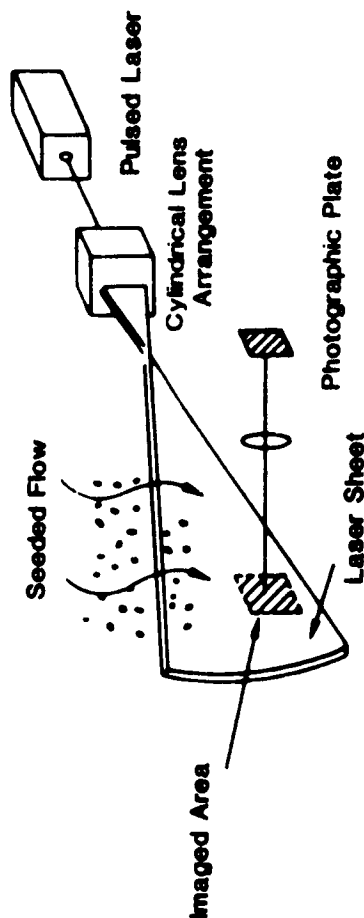
MAJOR PROBLEMS

LIGHT ENERGY DENSITY/FILM CHARACTERISTICS

PARTICLE SIZE/DENSITY

ACCESS TO EXPERIMENT

DATA REDUCTION

Pulsed Laser

Cylindrical Lens Arrangement

Seeded Flow

Imaged Area

Laser Sheet

Photographic Plate

flow

particle images

particle streak images
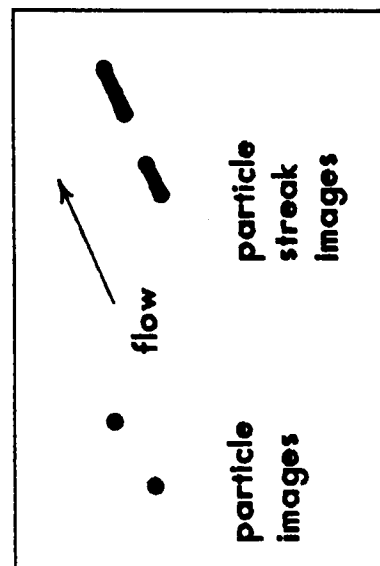
3D PARTICLE IMAGING VELOCIMETRY

OBJECTIVE IS TO EXTEND DOUBLE PULSE PARTICLE HOLOGRAPHY
TO ACCOMODATE MICRON SIZE PARTICLES AND TO AUTOMATE
DATA REDUCTION TECHNIQUE.

POOR ACCESS TO EXPERIMENT LIMITS
APPLICATIONS.

LIMITED TO GABOR GEOMETRY
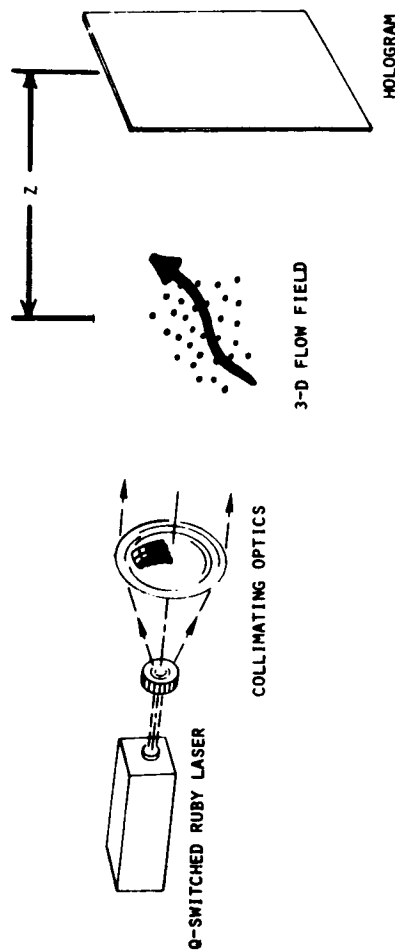
MAJOR PROBLEMS

PARTICLE SIZE/HOLOGRAM DISTANCE (Z)
- Experimentally determined

RECORDING MEDIUM SNR, GAMMA
- Dichromated Gelatin

DATA REDUCTION
- Use "out of focus" wavefront
  to determine depth.

Q-SWITCHED RUBY LASER

COLLIMATING OPTICS

3-D FLOW FIELD

Z

HOLOGRAM

PAPERS IN INTERFEROMETRY, DATA REDUCTION, VELOCIMETRY AND PARTICLE SIZING

RECONSTRUCTION OF A THREE-DIMENSIONAL, TRANSONIC ROTOR FLOW FIELD FROM HOLOGRAPHIC INTERFEROGRAM DATA

John K. Kittleson* and Yung H. Yu*
Aeromechanics Laboratory, U.S. Army Research and Technology Laboratories—AVSCOM
NASA Ames Research Center, Moffett Field, California

Abstract

Holographic interferometry and computer-assisted tomography (CAT) are used to determine the transonic velocity field of a model rotor blade in hover. A pulsed ruby laser recorded 40 interferograms with a 2-ft-diam view field near the model rotor-blade tip operating at a tip Mach number of 0.90. After digitizing the interferograms and extracting fringe-order functions, the data are transferred to a CAT code. The CAT code then calculates the perturbation velocity in several planes above the blade surface. The values from the holography-CAT method compare favorably with previously obtained numerical computations in most locations near the blade tip. The results demonstrate the technique's potential for three-dimensional transonic rotor flow studies.

Nomenclature

a_0 = speed of sound, ft/sec

A = wave amplitude

C = blade chord, ft

$f(x')$ = filter function

I = irradiance

k = Gladstone-Dale constant, ft^3/slug

L = path length, ft

n = refractive index

n_0 = ambient refractive index

N = fringe-order number

R = spanwise coordinate, ft

R_0 = blade span, ft

t = hologram amplitude transmittance

U_c = reconstruction wave complex amplitude

U_i = transmitted wave complex amplitude

U_r = reference wave complex amplitude

U_{01} = ambient object wave complex amplitude

U_{02} = test object wave complex amplitude

V = perturbation velocity, ft/sec

---

*Research Engineer. Member AIAA.

This paper is declared a work of the U.S. Government and therefore is in the public domain.

x' = projection coordinate, ft

X = chordwise coordinate, ft

Y = height above blade centerline, ft

β = film proportionality constant

γ = ratio of specific heats

$\Delta\phi$ = optical path-length difference (OPD)

θ = field projection angle, deg

λ = laser wavelength, ft

ρ = air density, slug/ft^2

ρ_0 = ambient air density, slugs/ft^3

Ω = blade rotational speed, rpm

Introduction

On many helicopters, the rotor blade's advancing tip encounters transonic flow during forward flight. At these high Mach numbers, the rotor blade's performance suffers from compressibility effects that often cause shock waves to form near the blade tip; the shocks can extend to the acoustic far-field. Through theoretical and computational investigations, researchers attempt to understand the local shock generation of high-tip-speed rotors and its propagation to the far-field. However, because of the problem's complexity and the difficulty of obtaining detailed experimental information about the flow, accurate means for confirming transonic rotor-blade designs have been notably lacking.

Shock waves cause a number of aerodynamic, dynamic, and acoustic problems on high-speed helicopter rotor blades. First, the shock rapidly increases the aerodynamic drag through energy dissipation, flow separation, and wave effects. Second, local shocks cause sudden large changes in pitching moment which can excite various blade torsional modes. As the blade rotates in forward flight, its Mach number and angle of attack vary. The shock appears on the advancing side of the rotor disk and often results in large chordwise movements; these movements can be in opposite directions on the upper and lower surfaces as the Mach number and angle of attack change during each revolution. The changing shock positions on the upper and lower surfaces cause an unsteady loading, which produces fluctuating pitching moments. These moments can cause unexpected blade motions, oscillating loads on pitch links, and vibrations throughout the entire aircraft. Third, shock waves on an advancing-blade surface can "delocalize" (Ref. 1) and extend directly to the far-field. Large amounts of acoustic energy radiate in front of the helicopter near the tip-path plane. This helicopter impulsive noise is

annoying in general and too easily detected in military applications.

In an attempt to describe the transonic rotor flow field and to resolve the problems associated with it, promising theoretical models[2] and numerical codes[3,4] have been developed. The numerical codes compare favorably with blade-pressure measurements,[5] but are not yet verified at points away from the blade's surface.

Previous attempts to measure the flow field have been severely limited. Pressure-instrumented airfoils are expensive and difficult to fabricate—especially in scale models. In addition, pressures can be measured only at the blade surface. Hot-wire anemometry requires that a probe be positioned within the field, therefore disturbing the flow. Laser velocimetry requires flow-seeding and, when shock waves are present, it is uncertain whether the seeds follow the flow faithfully. Both hot-wire anemometry and laser velocimetry can take only point-by-point measurements, requiring large amounts of running time to survey the rotor's three-dimensional field, a distinct disadvantage for rotor testing. Schlieren and shadowgraph photography provide only a qualitative two-dimensional representation of a three-dimensional flow. And Mach-Zehnder interferometry provides quantitative information, but is extremely difficult to use in a large-scale experiment. Clearly, another experimental technique which overcomes these limitations must be employed.

Holographic interferometry is an effective diagnostic technique for making transonic flow measurements.[6] Previous investigations[7,8] in which two-dimensional flows over airfoils were studied show that accurate quantitative information is obtainable using holographic interferometry. However, the transonic flow around a helicopter rotor blade is three-dimensional and requires a tomographic technique to compute the correct flow information from several interferograms. To date, most applications of this technique have been limited to axisymmetric flow or to simple three-dimensional flow with a small model under ideal laboratory conditions.[9,10]

This paper discusses the procedures necessary to obtain quantitative measurements of a transonic, three-dimensional flow field near a rotor-blade tip, using holographic interferometric data and CAT. Though most helicopter rotor problems caused by shock waves occur during forward flight, this experiment investigates the steady problem (hover), which simulates many physical phenomena of forward flight.[11] The method for recording interferograms and example interferograms is included, and the steps that must be followed in extracting quantitative information from the interferograms are outlined. The technique's potential for measuring three-dimensional transonic rotor flows is demonstrated, and the results it yields are compared with those from previously performed numerical computations.

Background Concepts

For the experiment to be successful, it is necessary to 1) record high-quality interferograms near a rotor-blade tip from multiple viewing angles, and 2) implement a suitable CAT code with the interferogram data. Familiarity with holography,

holographic interferometry, and computer-assisted tomography principles provides the necessary insight for understanding this technique.

Holography

Holography is a two-step imaging process in which diffracted light waves are recorded and reconstructed.[12,13] The first step is recording, or storing, the hologram. This is accomplished by dividing a single coherent laser beam into two beams and exposing a photographic film to the two light waves, as shown in Fig. 1a. The object wave, which is the wave containing the flow information, passes through the measured field (the air near the blade tip in this experiment). The second wave, the reference wave, passes around the field. By adding the coherent reference wave to the object wave, the photographic film records a high-frequency interference pattern. Once the film is developed, it is known as a hologram, which is a complicated diffraction grating.

The second step in holography is reconstruction, or playing back the hologram. This is accomplished in two ways. First, a reconstruction wave identical to the reference wave illuminates the hologram (Fig. 1b). The hologram diffracts the reconstruction wave and produces a replica of the original object wave, forming the original object's virtual image. In the second method of reconstruction, a reconstruction wave conjugate to the reference wave illuminates the hologram (Fig. 1c). The hologram diffracts the conjugate wave forming the original object's real image. The real image may be photographed without the use of a lens by placing a sheet of photographic film in the real image space.

Several important characteristics of holography are applicable to the experiment at hand. There are very few geometrical constraints in a holographic optical system; thus, holography can be applied in a large-scale, nonlaboratory environment. Note that recording and reconstruction of the hologram can be done in different locations if the reference wave is reproducible. This allows the reconstruction to be done in a laboratory, far from the harsh environment in which the hologram was previously recorded. The reference wave serves only as a method of recording and reconstructing the object wave. Thus, a hologram does not produce quantitative information about the field of interest. To obtain quantitative information (in the form of interference fringes) an interferogram must be recorded.

Holographic Interferometry

Holographic interferometry is the interferometric comparison of two object waves recorded holographically (see the Appendix for further detail). In this experiment, the two object waves are recorded sequentially in time with double-exposure holographic interferometry. The interferogram is recorded by first exposing a photographic film to a reference wave and an "undisturbed" object wave. Later in time, the same photographic film is exposed to a reference wave and to a second "disturbed" object wave.

When the holographic interferogram is reconstructed, the virtual or real image shows the object (the transparent field) with an

150

interference fringe pattern. The fringe pattern represents the difference between the "undisturbed" and "disturbed" flow states. The irradiance of the reconstructed wave is proportional to

$$I = |U_{01} + U_{02}|^2$$

which can be written as[12,13]

$$I = 2A^2[1 + \cos(\Delta\phi)] \qquad (1)$$

Equation (1) represents the interferogram with a fringe pattern of dark and bright fringes of constant optical path-length difference (OPD) $\Delta\phi$, where $\Delta\phi$ is given by

$$\Delta\phi = \int [n(x,y,z) - n_0]ds = N\lambda \qquad (2)$$

To determine the flow-field properties, the line integral of Eq. (2) must be inverted and solved for $n(x,y,z)$, the refractive index at a specific point in the field.

In a two-dimensional flow (i.e., the flow over a fixed airfoil in a wind tunnel), the evaluation of Eq. (2) is simplified. Since the refractive index is constant across the width of the test section L, Eq. (2) becomes

$$n(x,y) = n_0 + N\lambda/L \qquad (3)$$

In a two-dimensional flow, the fringes on an interferogram are contours of constant refractive index and the refractive index at any point in the field can be determined from a single interferogram. However, since the transonic flow near a rotor-blade tip is three-dimensional, Eq. (3) cannot be used. To invert Eq. (2) and solve for the refractive index at a specific point in the field, computer-assisted tomography (CAT) must be employed.

Computer-Assisted Tomography

Tomography is a mathematical technique for reconstructing a three-dimensional field from its two-dimensional projections (see Refs. 14 and 15 for a wide variety of applications). A projection of a three-dimensional field is the fringe pattern recorded on an interferogram. All methods require multidirectional projection data of the field. Tomographic codes develop in two directions: 1) iterative algebraic reconstruction techniques,[16] and 2) Fourier transform techniques. A version of the latter method, termed filtered back-projection,[17,18] appears most suitable for this application.

Most Fourier transform techniques employ back-projection. Projection data from the field are recorded in one plane at several azimuthal angles around the field. For example, one projection of a uniform absorbing disk is shown in Fig. 2a (taken from Ref. 19). Beyond the disk boundary (no path length through the disk), the light ray's OPD is unchanged, producing no interference fringes. Near the disk boundary (short path length through the disk), the light ray's OPD is changed slightly, producing a few interference fringes. And near the disk center (long path length through the absorbing disk), the light ray's OPD is changed substantially, producing several interference fringes. Similar projections

(fringe number vs position) at different azimuthal angles are also recorded. Each projection is then back-projected, or smeared back along the direction in which it was recorded (Fig. 2b). Values are added point by point to form a reconstruction of the field. Unfortunately, simple back-projection produces an undesirable spoke pattern which severely degrades the quality of the reconstructed field.

To eliminate the spoke pattern, the back-projections are filtered. A one-dimensional convolution (indicated by an asterisk) is performed between each projection and an appropriate filter function (see Ref. 20 for a discussion of filter functions) before back-projection, as shown in Fig. 3a (taken from Ref. 19). Each filtered projection is then back-projected over the reconstruction space (see Fig. 3b). The negative side-lobes introduced by the filter eliminate the spoke pattern during the point-by-point addition process. With many projections, this technique yields an accurate reconstruction of the original field.

Procedure

Several steps must be performed to quantitatively reconstruct the three-dimensional transonic field near a model helicopter blade tip. First, several holographic interferograms must be recorded along planes perpendicular to the rotor tip-path plane at various azimuthal angles (Fig. 4). Data must then be extracted from the interferograms. This can be done 1) manually, 2) by using a graphic tracing tablet,[21] or 3) by using a system that digitizes the interferograms and extracts fringe-order numbers. The digital interferogram evaluation technique was used; it will be presented in detail by Becker and Yu (Ref. 22). Finally, the data are transferred as input to a tomography code, which computes the refractive index at specific points in a horizontal plane above the blade surface. This procedure is repeated in several planes to yield a reconstruction of the entire three-dimensional field.

Recording Holographic Interferograms

The holographic system for recording interferograms near a model rotor blade was assembled in the Aeromechanics Laboratory Anechoic Hover Chamber. Figure 5 shows a schematic of the optical system and Fig. 6 shows the Anechoic Hover Chamber. A ruby laser with a 20-nsec pulse width, a 694.3-nm wavelength, and a power of 1 J "freezes" the rotating blade at any desired azimuthal angle. A beam-splitter divides the laser beam into two separate beams at the laser outlet. A microscope objective lens expands the object beam to fill a 24-in.-diam spherical mirror. Since the foci of both the objective lens and the spherical mirror coincide, a collimated plane wave forms as the beam passes through the rotor area. The object beam then strikes a second 24-in.-diam spherical mirror, emerges as a converging wave, and illuminates a 4-in. by 5-in. photographic plate. The reference beam is lengthened by causing it to strike several plane mirrors. This beam must be lengthened so that the difference in the path lengths of the object and reference beams is less than the coherence length of the laser (one of the very few, and

151

easily met, geometrical constraints in a holographic system). The reference beam is expanded by an objective lens, then collimated with a 5-in.-diam lens; finally, it is directed toward the film so that it overlaps the object beam.

The entire procedure is conducted from outside the hover chamber, once the optical system is aligned. Firing the laser, changing the photographic film plates, and controlling the test conditions are all done by remote control. Recall that to record an interferogram, two exposures at different times (different flow states) must be made on a single film plate. The film records the first exposure while the rotor blade remains stationary. In this case, the air has no velocity and therefore has a uniform refractive-index distribution. The film records the second exposure while the blade rotates at the desired speed. The nonhomogeneous refractive-index distribution in this case introduces phase changes in the second object wave, producing interference fringes on the film plate. This double-exposure recording procedure repeats at various angles around the flow by synchronizing the laser pulse with the desired blade position. Because of the long optical pathlengths (90 ft), the recording system is very sensitive to vibrations of the optical components. At several azimuthal angles, it was necessary to record multiple interferograms to obtain one high-quality interferogram. The photographic plates are then removed from the recording system in the hover chamber, developed, and reconstructed in a laboratory for further processing.

Holographic interferograms record the flow near a hovering 1/7-scale (geometric) model UH-1H rotor with untwisted NACA 0012 airfoil sections. The blade runs at a tip Mach number of 0.90 so that the flow is transonic and a shock wave is present.[1] This model normally uses two blades; however, in views along the span, the optical beam would pass through the refractive-index field of both blades. Because the refractive-index fields of the two blades are inseparable at these angles, a single-bladed rotor with a counterbalance is used instead (Fig. 7).

Holographic interferograms near a transonic rotor blade are recorded at 40 different viewing angles. The blade rotates in a clockwise direction and can be captured at any desired viewing angle with the pulsed laser. The tomography code requires flow data from certain viewing angles within a 180° range. Numerical simulation results[2,3] using numerical computations of the flow[3] suggest recording interferograms from $\theta = 8°$ to $\theta = 40°$ and from $\theta = 140°$ to $\theta = 186°$ in 2° increments, as defined in Fig. 8. The missing views, $\theta = 42°$ to $\theta = 138°$, were presumed to have very few interference fringes and were not utilized.

Illustrated in Fig. 8 are examples of holographic interferograms recorded near the model blade tip. The fringe pattern's appearance depends on the viewing direction. Interferograms recorded along the chord (near $\theta = 90°$) display very few interference fringes, since the optical rays pass through the field's thinnest (weakest) region. No observable details are present in these views. However, in views along the span , (near $\theta = 0°$ or $\theta = 180°$), numerous fringes are visible, because the optical rays pass through the

longest (strongest) region within the field. The leading-edge stagnation point, shock structures, boundary-layer separation, and wake system are clearly visible. In particular, a lambda shock ($\theta = 180°$) and the radiated shock ($\theta = 186°$) appear above the blade. Several interferograms are described in detail in Ref. 24.

Data Extraction

There is an important step that must be taken between recording the interferograms and making the tomographic reconstruction: evaluating the interferograms. During this evaluation, integrated quantitative information is extracted from the interferogram fringe pattern. Previously, most interferograms were evaluated manually, which is a time-consuming and inaccurate procedure. To overcome these limitations, a scheme for digital interferogram evaluation was implemented that digitizes, enhances, and records fringe coordinates and numbers from the interferograms (see Ref. 22 for a discussion of this system).

An image-processing system (De Anza IP-6400) connected to a VAX 11/780 host computer digitizes the 40 interferograms. A one-dimensional fringe evaluation is then performed by assigning fringe-order numbers to each interferogram. To make a correct assignation of fringe-order numbers, some information about the flow is required. Positive values are assigned to high-density regions and negative values to low-density regions. The zero fringe-order number is assigned to the regions where the field is undisturbed. Each interferogram is then scanned at a desired height above the blade, as shown in Fig. 9a. For each projection angle, fringe numbers and locations are recorded (Fig. 9b) and stored. The fringe-order functions serve as input data for the CAT code to reconstruct the field in one horizontal plane above the blade surface.

CAT Reconstruction

Fringe-order functions are transferred to the filtered back-projection CAT code which computes the refractive-index field at specific points in a chosen horizontal plane above the blade surface. The code assumes refractionless light rays; therefore, each horizontal plane can be treated independently, even though data for each plane is taken from one set of interferograms. The perturbation velocity is computed by first converting refractive index to density, using the Gladston-Dale relation:

$$\rho = (n - 1)/k$$

Density is then converted to perturbation velocity from a form of Bernoulli's equation for steady (with respect to the rotation blade), compressible, isentropic flow:

$$V = -\Omega R + \left\{ (\Omega R)^2 - \frac{2a_0^2}{\gamma - 1} \left[\left(\frac{\rho}{\rho_0} \right)^{\gamma - 1} - 1 \right] \right\}^{1/2} \tag{4}$$

The procedure is repeated in several planes above the blade to reconstruct the entire three-dimensional field near the model blade tip.

Reconstruction Results

The holography-CAT reconstruction of the blade-tip velocity field is compared with numerical computations. The computations used here are conservative, mixed-difference solutions of the transonic small-disturbance equation. Results from both sources are presented in four horizontal planes, as identified in Fig. 10a. Three plot types are used to visualize the flow field. First, velocity contours are given in plan view (see Fig. 10b), where the blade's leading and trailing edges are at $X/C = 0.0$ and $X/C = 1.0$, respectively. The blade tip is located at $R/R_0 = 1.0$, the rotation center is at $R/R_0 = 0.0$, and the blade rotates in a clockwise direction. Second, perspective views are displayed in which velocity values are plotted along the vertical axis. The data and geometry are identical to the contour plots, though the data are viewed from near the rotor hub. Third, velocity distributions are shown at six radial locations (see Fig. 10b) for each plane.

Figure 11 compares the velocity contours derived from the holographic-CAT method and the numerical computations near the blade surface ($Y/C = 0.08$). Both methods display low-velocity regions near the leading and trailing edges, and also display a high-velocity region over the blade surface containing a shock at approximately $X/C = 0.60$ near the blade tip. The general contour shapes show a strong resemblance except near the blade tip (roughly the last 5% of blade span). The maximum velocity region appears at the shock foot in the computational analysis, but it appears closer to the leading edge and farther from the shock foot in the holography-CAT results.

Figure 12 shows velocity values for the same plane in perspective view. Again, the general flow shapes appear very similar. The major difference between the two results is the roughness (minor "ridges") in the reconstructed flow. This may be due to reconstruction artifacts caused by noncontinuous data (interferograms recorded in 2° azimuthal increments) or by noise (erroneous fringes) in the interferogram data caused by optical component motion. Figure 13 compares velocity distributions at six radial locations. The roughness of the reconstructed flow can be seen throughout the figures. Also, the holography-CAT method determines the shock location to be slightly more downstream (3%) than does the numerical code solution. The major differences can be observed in Fig. 13d, where the discrepancies at the leading edge and over the blade surface are clearly visible. The leading edge ($X/C = 0.0$) difference may result from a breakdown of the small crossflow assumption [Eq. (4)] near the blade tip. The difference over the blade surface ($X/C = 0.2$ to $X/C = 0.6$) may be attributed to the existence of a lambda shock, in the interferogram data (i.e., Fig. 9a), which cannot be predicted by the nonviscous numerical potential code. A lambda shock was also observed in Schlieren photographs from a previous wind-tunnel test (Fig. 14, taken from Ref. 25) using the same airfoil and tip Mach number.

Figure 15 compares the velocity contours from both the holography-CAT method and numerical code at $Y/C = 0.22$ (near the upper region of the lambda shock). The general velocity contours show an excellent agreement in both shape and magnitude

throughout the plane. The maximum velocity region on the blade surface (near $X/C = 0.50$, $R/R_0 = 0.96$) match much closer in this plane than in the plane near the blade surface (Fig. 11). The perspective view of Fig. 16 also shows an excellent agreement in shape and magnitude. Again, the most noticeable difference is the extra ridges in the reconstructed flow at the same locations and orientations as seen in the previous plane (Fig. 12a). The velocity distributions in this plane (Fig. 17) compare favorably, especially inboard of the blade tip (see Figs. 17a-17c), as well as at the blade tip (Fig. 17d). The lambda shock's effect near the tip is apparently weaker in this plane; thus, the velocity distribution magnitudes and shapes are much closer than those in Fig. 13.

Figure 18 compares velocity contours at $Y/C = 0.49$ above the blade. The velocity contour shapes and magnitudes are similar in all regions except that the holography-CAT method shows the maximum velocity point to be slightly (1% span) outboard of the numerical result. The extra ridges seen in the perspective view (Fig. 19) are in approximately the same location and orientation as those in the previous plane; however, the magnitude of the ridges has decreased. Figure 20 shows velocity distributions for this plane. There is good agreement at all locations except beyond the blade tip (Fig. 20e) where the holography-CAT method shows slightly larger velocity magnitudes.

Finally, Fig. 21 shows velocity contours for $Y/C = 1.17$. The velocity contours match throughout, though there are no distinguishing features in the flow at this height above the blade surface. In this plane, the extra ridges are almost unobservable in the perspective view (Fig. 22). The velocity distributions of Fig. 23 also show a strong similarity between the two methods at all radial locations, for both results show that this plane is at the perturbed flow's upper extent.

Overall, the agreement between the holography-CAT results and the numerical solution is extremely encouraging. However, comparisons with other experimental data sources are required before a final decision can be made about the holography-CAT results. Several discrepancies must be resolved. First, data from pressure-instrumented blades will aid in confirming the shock location and whether a lambda shock does exist in the flow. Second, the extra ridges appearing in the reconstructed results must be eliminated or reduced; the ridges may be caused by poor data recorded in the interferograms. To improve the quality of the interferograms, a modified optical system (for both hover and forward flight testing) is necessary. In addition, neither the holography-CAT reconstruction nor the numerical code solutions compute the expected shock strength beyond the blade tip. Acoustic measurements indicate a much stronger radiated shock than is indicated by these two results.

Concluding Remarks

The holographic interferometry computer-assisted tomography technique proved to be a highly effective way of measuring the three-dimensional, transonic flow field near a model

rotor-blade tip. Results from this method compare favorably with those of numerical computations, except very near the tip region. That discrepancy may be due to the existence of a lambda shock recorded by the interferograms (and in previous Schlieren photographs) which is not predicted by the nonviscous potential code. In other regions, the velocity distributions along the chord are similar in both shape and magnitude. However, the results from the technique must be further verified against other experimental data.

Since this is the first successful implementation of the holographic interferometry, computer-assisted tomography method in rotor flow studies, many improvements are indicated. For example, the optical system must be improved so that better quality interferograms can be recorded, and an automatic fringe-reading technique must be completed so that the time required to evaluate interferograms can be shortened. Upon verification of these results and after the system is improved, measurements of other model rotor-blade flow fields, including those of forward flight, will be performed.

Appendix: Holographic Interferometry

Double-exposure holographic interferometry is the interferometric comparison of two object waves that are recorded holographically sequentially in time. The interferogram is recorded by first exposing a photographic film to a reference wave and an "undisturbed" object wave, as shown in Fig. 24a. Later in time, the same photographic plate is exposed to a reference beam and a second "disturbed" object wave, as shown in Fig. 24b. The irradiance at the film plane is

$$I = |U_r + U_{01}| + |U_r + U_{02}|$$

$$= 2I_r + I_{01} + I_{02} + U_r^*(U_{01} + U_{02}) + U_r(U_{01} + U_{02})^*$$

$$\text{(A1)}$$

The last two terms of Eq. (A1) represent the interference pattern recorded on the film, which contains both amplitude and phase information about the two reference and the two object waves. The amplitude transmittance of the developed film, called a holographic interferogram, is

$$t = (2I_r + I_{01} + I_{02}) + U_r^*(U_{01} + U_{02})$$

$$+ U_r(U_{01} + U_{02})^*$$

When the reconstruction wave illuminates the interferogram, as shown in Fig. 24c, the transmitted light is

$$U_i = U_c t$$

$$= U_c(2I_r + I_{01} + I_{02}) + U_r^* U_c(U_{01} + U_{02})$$

$$+ U_r U_c(U_{01} + U_{02})^* \qquad \text{(A2)}$$

The second term in Eq. (A2) is the "composite" virtual image reconstruction of the two object waves $(U_{01} + U_{02})$. By illuminating the interferogram with a conjugate reconstruction wave

(Fig. 24d), the transmitted light is

$$U_i = U_c^* t$$

$$= U_c^*(2I_r + I_{01} + I_{02}) + U_r^* U_c^*(U_{01} + U_{02})$$

$$+ U_r U_c^*(U_{01} + U_{02})^* \qquad \text{(A3)}$$

The third term in Eq. (A3) is the composite real image reconstruction of the two object waves $(U_{01} + U_{02})$, which is the image that is photographed and presented in this paper.

The primary reason for using holographic interferometry is that it possesses a property called cancellation of path-length errors. In a holographic interferometer, the interfering waves divide temporally. That is, the two interfering (object) waves are recorded at two different times but travel the same path through the optical system (recall that the reference wave serves only to store and play back the interferogram). Since there is no difference between the two path lengths of the interfering object waves in the optical system, only changes in the path lengths caused by the different states of the test field are displayed as fringes in the interferogram. This leaves a useful interferogram, even though low-quality optics are used. Therefore, holographic interferometry can be used in a large-scale experiment in which relatively low-quality optics are used and still yield high-quality interferograms.

References

[1] Schmitz, F. H. and Yu, Y. H., "Transonic Rotor Noise—Theoretical and Experimental Comparisons," Vertica, Vol. 5, 1981, pp. 55-74.

[2] Isom, M. P., "Unsteady Subsonic and Transonic Potential Flow Over Helicopter Rotor Blades," NASA CR-2463, 1974.

[3] Caradonna, F. X., "The Transonic Flow on a Helicopter Rotor," Ph.D. dissertation, Stanford U., Stanford, Calif., Mar. 1978.

[4] Arieli, R. and Tauber, M., "Computation of Subsonic and Transonic Flow about Lifting Rotor Blades," AIAA Paper 79-1667, 1979.

[5]Tung, C., Caradonna, F. X., and Boxwell, D. A., "The Prediction of Transonic Flows on Advancing Rotors," Proceedings of the 40th Annual National Forum of the American Helicopter Society, Arlington, Va., May 1984.

[6]Trolinger, J. D., "Laser Instrumentation for Flow Field Diagnostics," AGARDograph 186, 1974.

[7]Johnson, D. A. and Bachalo, W. D., "Transonic Flow About a Two-Dimensional Airfoil—Inviscid and Turbulent Flow Properties," AIAA Paper 78-1117, 1978.

[8]Bachalo, W. D., "Measurements of Supercritical Airfoil Flow Fields Using Interferometry," Douglas Aircraft Company, McDonnell Douglas Corporation, Mar. 1982.

[9]Matulka, R. D. and Collins, D. J., "Determination of Three-Dimensional Density Fields from Holographic Interferometry," Journal of Applied Physics, Vol. 42, 1971, pp. 1109-1119.

[10]Sweeney, D. W. and Vest, C. M., "Reconstruction of Three-Dimensional Refractive Index Fields from Multidirectional Interferometric Data," Applied Optics, Vol. 12, 1973, pp. 2649-2664.

[11]Boxwell, D. A., Yu, Y. H., and Schmitz, F. H., "Hovering Impulsive Noise: Some Measured and Calculated Results," Vertica, Vol. 3, 1979, pp. 35-45.

[12]Vest, C. M., Holographic Interferometry, Wiley-Interscience, 1979.

[13]Collier, R. J., Burckhardt, C. B., and Lin, L. H., Optical Holography, Academic Press, 1971.

[14]Marr, E. B., ed., Proceedings of the International Workshop on Techniques of Three-Dimensional Reconstruction, BNL 20425, Brookhaven National Laboratory, Upton, N.Y., 1976.

[15]Technical Digest of the 1975 Optical Society of American Technical Meeting, Stanford University, OSA, Washington, D.C., 1975.

[16]Gordon, R. and Herman, G. T., International Review of Cytology, Vol. 38, 1974.

[17]Shepp, L. A. and Logan, B. F., "The Fourier Reconstruction of a Head Section," IEEE Transactions on Nuclear Science, Vol. NS-21, 1974, pp. 21-42.

[18]Ramachandran, G. N. and Lakshminarayanan, A. V., "Three-Dimensional Reconstruction from Radiographic and Electron Micrographic Applications of Convolutions Instead of Fourier Transforms," Proceedings of the National Academy of Sciences of the United States of America, Vol. 68, 1971, pp. 2236-2240.

[19]Swindell, W. and Barrett, H. H., "Computerized Tomography: Taking Sectional X-rays," Physics Today, Dec. 1977, pp. 32-41.

[20]Herman, G. T., "Image Reconstruction from Projections, Implementation and Applications," Topics in Applied Physics, Vol. 32, Springer, Berlin, 1979.

[21]Modarress, D., Tan, H., and Trolinger, J., "Tomographic Reconstruction of Three-Dimensional Flow over Airfoils," Paper No. 85-0479 to be presented at AIAA 23rd Aerospace Sciences Conference, Reno, Nev., Jan. 14-17, 1985.

[22]Becker, F. and Yu, Y. H., "Application of Digital Interferogram Evaluation Technique to the Measurement of Three-Dimensional Flow Fields," Paper No. 85-0037 to be presented at AIAA 23rd Aerospace Sciences Conference, Reno, Nev., Jan. 14-17, 1985.

[23]Snyder, R. and Hesselink, L., "Optical Tomography for Flow Visualization of the Density Field Around a Revolving Helicopter Rotor Blade," Applied Optics, Vol. 23, 1984, pp. 3650-3656.

[24]Kittleson, J. K., "A Holographic Interferometry Technique for Measuring Transonic Flow near a Rotor Blade," Proceedings of the Ninth European Rotorcraft Forum, B, Stresa, Italy, Sept. 1983.

[25]Schmitz, F. H., Boxwell, D. A., and Vause, C. R., "High-Speed Helicopter Impulsive Noise," Journal of the American Helicopter Society, Oct. 1977.
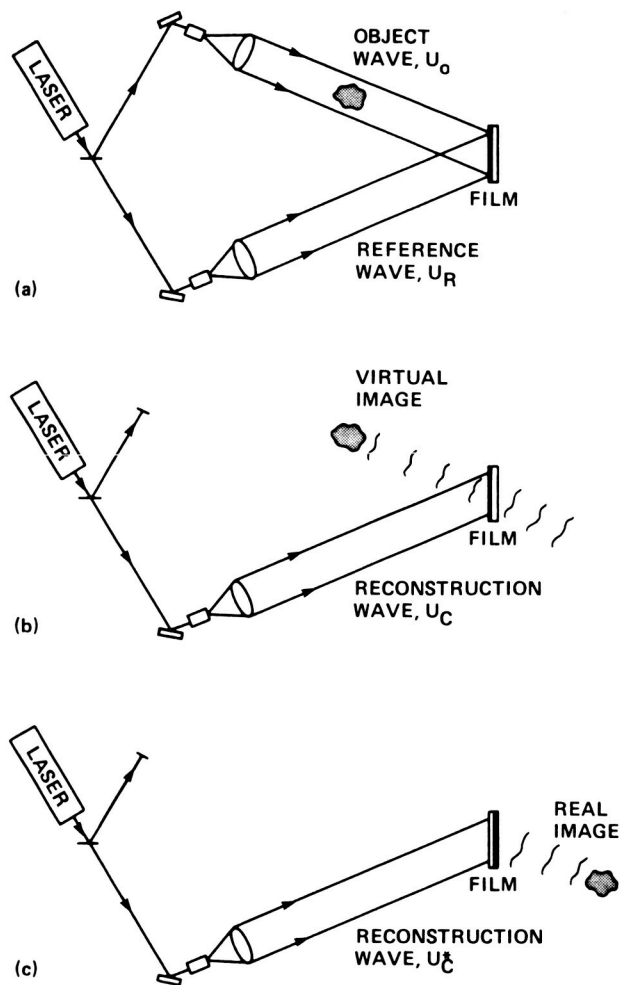
Fig. 1 Optical holography recording and reconstruction.   a) Recording the hologram; b) reconstruction of the true, virtual image; c) reconstruction of the conjugate, real image.
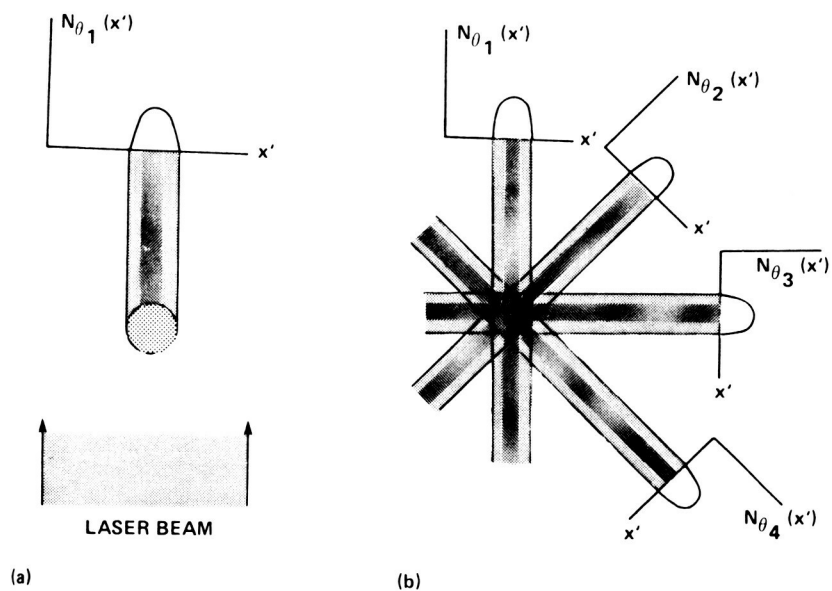
Fig. 2 Back-projection.   a) One projection of an absorbing disk; b) back-projecting consists of smearing each projection back along the direction in which the original projection was made. (From Ref. 19.)

156
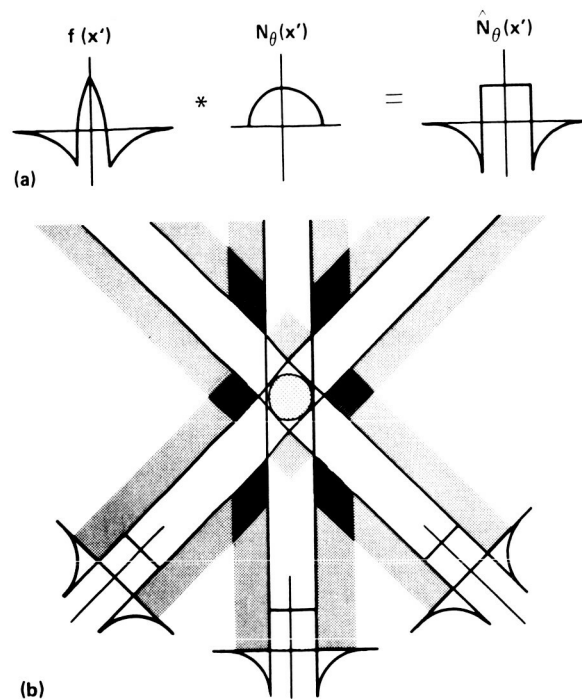
Fig. 3 Filtered back projection. a) The projection data are convolved (filtered) with a suitable processing function before back-projection; b) three back-projections of an absorbing disk. (From Ref. 19).

$$\Delta\phi = \int (n - n_o)\,ds = N\lambda$$
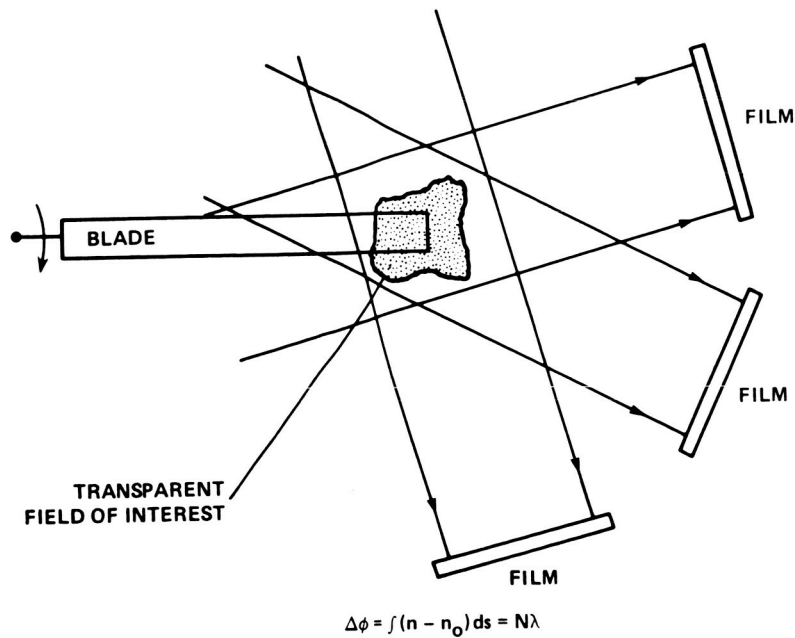
Fig. 4 Recording interferograms at various angles around the field of interest for tomographic reconstruction.

157
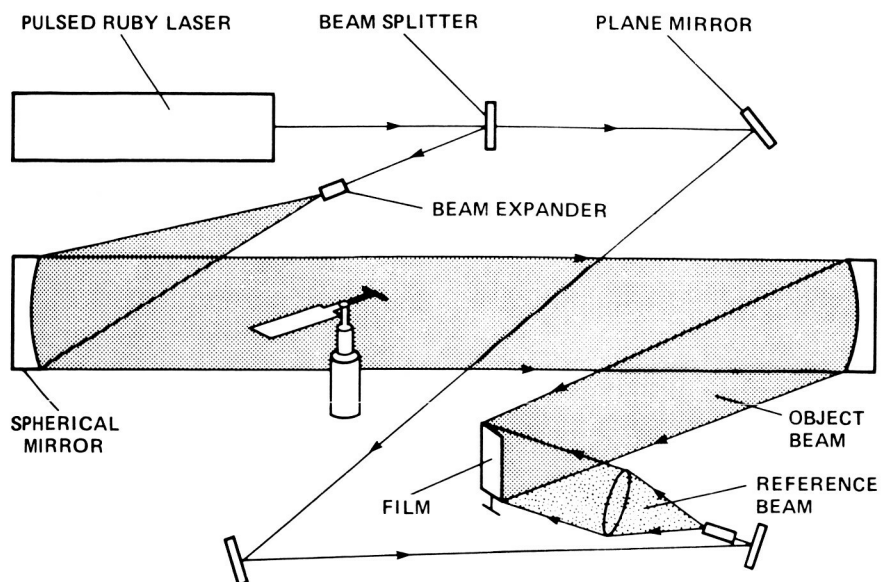
Fig. 5 Schematic drawing of the holographic recording system.
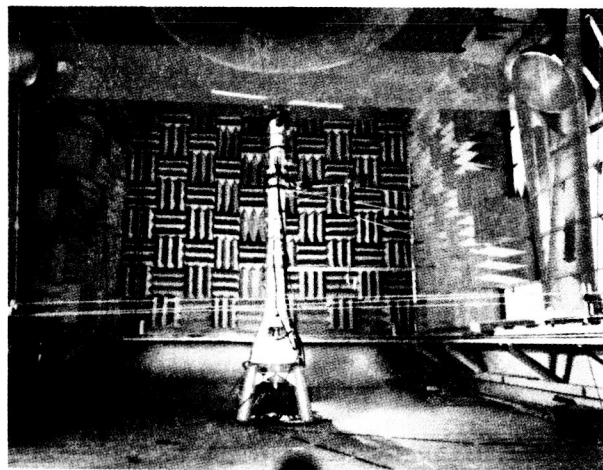
Fig. 6 **Holographic setup at Anechoic Hover Chamber.**
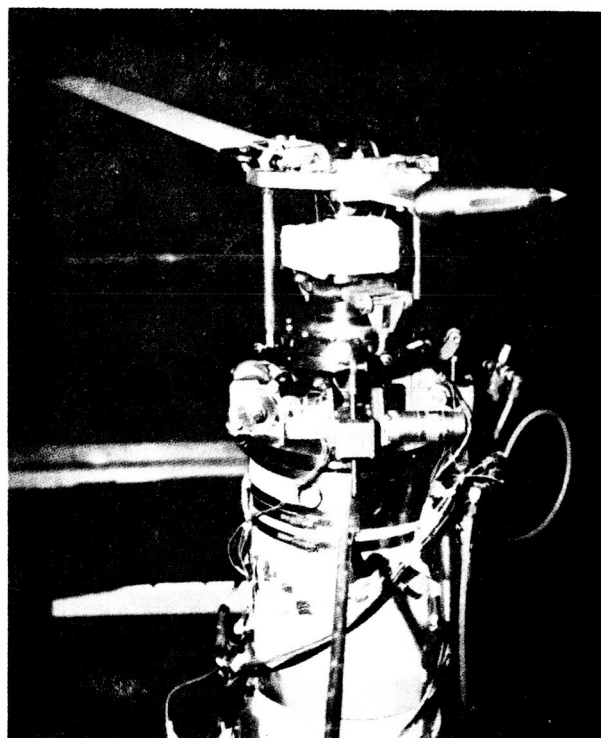
Fig. 7 One-blade rotor with a counterweight balance.

$\theta = 20°$
(a)

$\theta = 30°$
(b)

$\theta = 34°$
(c)

$\theta = 0°$

$\theta = 180°$

$\theta = 90°$
(d)

$\theta = 166°$
(e)

$\theta = 180°$
(f)

FILM

$\theta = 186°$
(g)
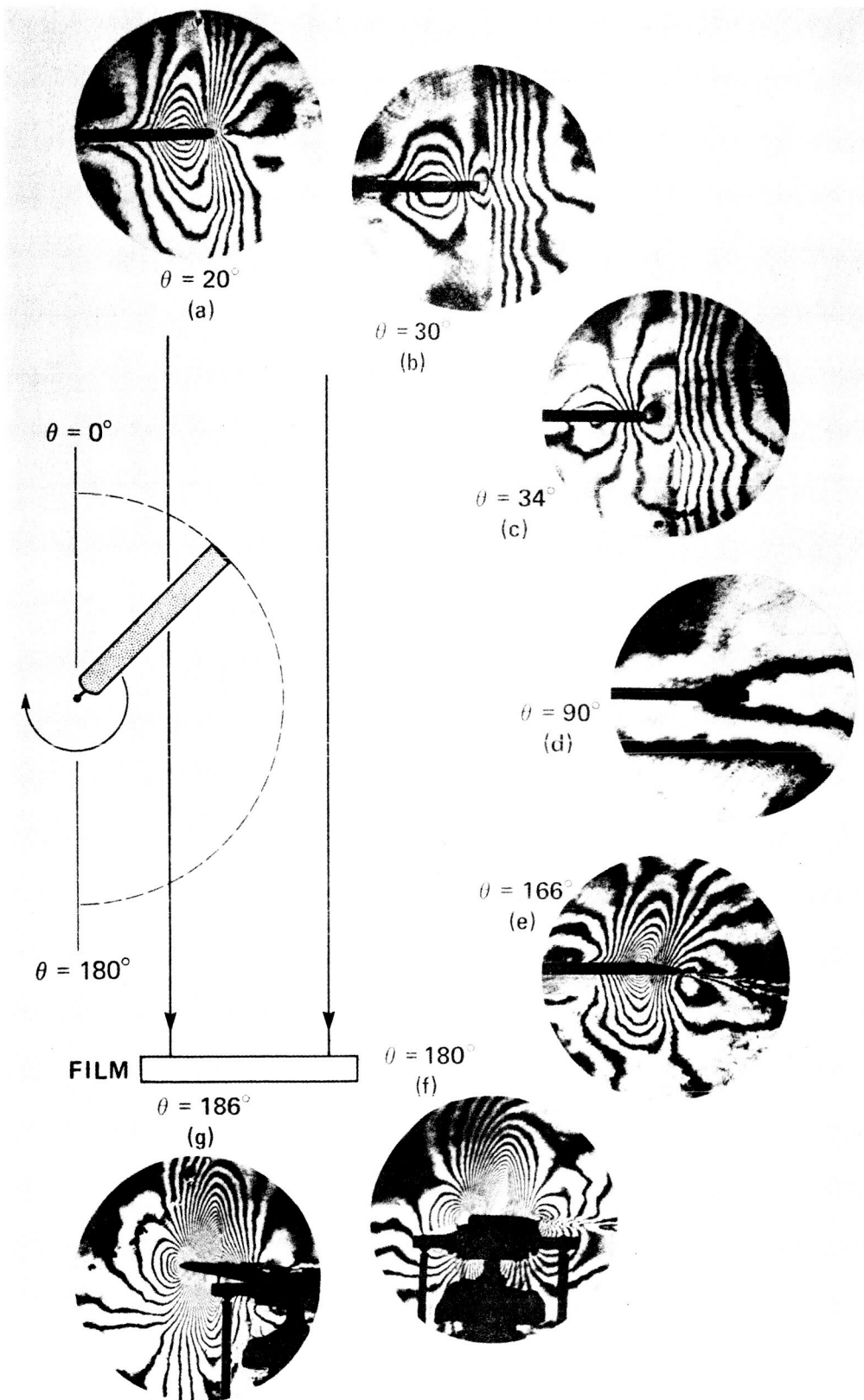
Fig. 8   Example interferograms recorded at various azimuthal angles.

159

(a)

(b)
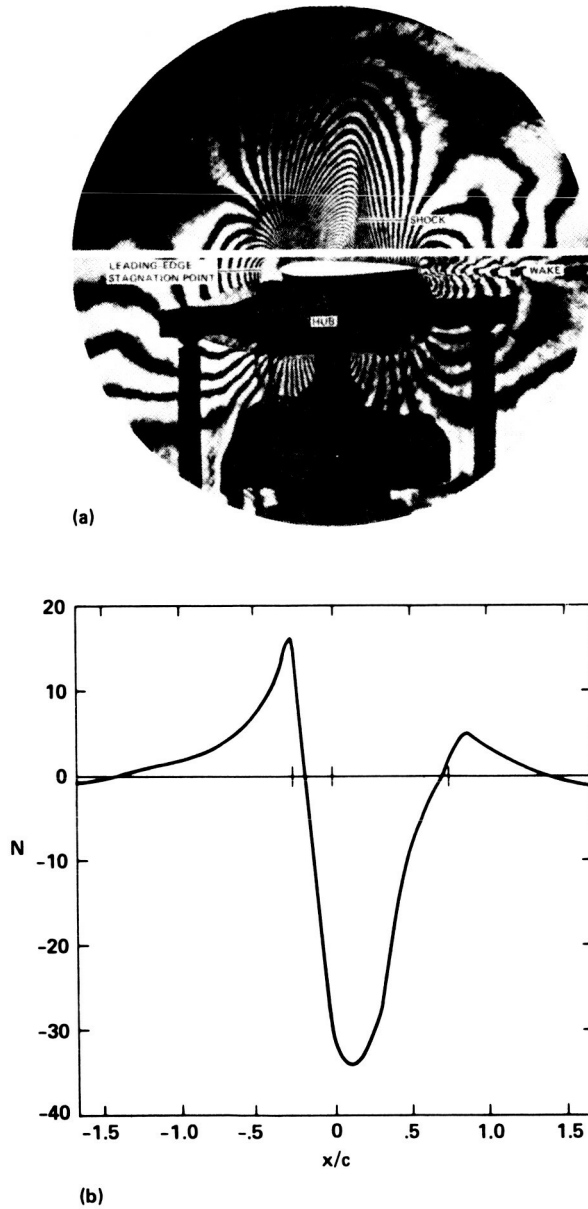
Fig. 9 Data extraction. a) One-dimensional interferogram evaluation is performed by scanning each interferogram at a chosen height above the blade surface; b) fringe-order numbers and coordinates are recorded as input to the CAT code.
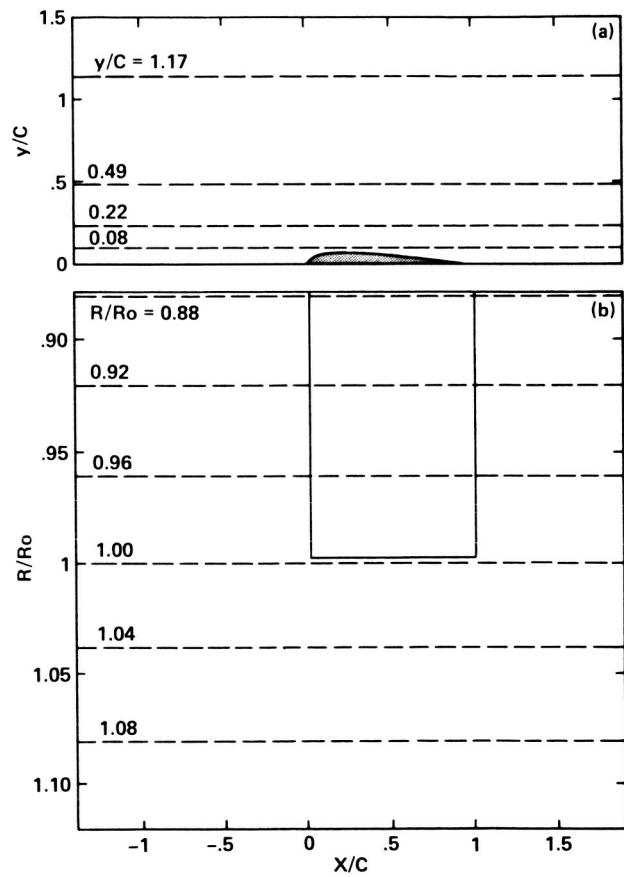
Fig. 10 Reconstructed flow-field geometry. a) Location of four horizontal planes for velocity contour maps and perspective views; b) location of six radial stations for velocity distribution plots.
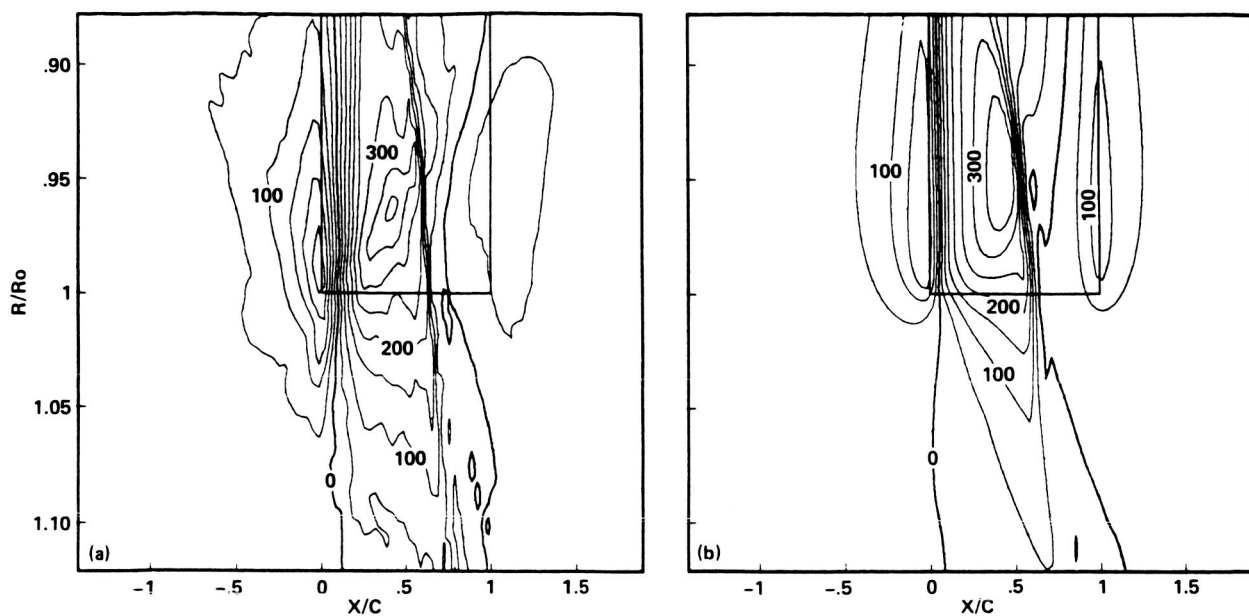
Fig. 11 Perturbation velocity contours in plan view for Y/C = 0.08 above blade centerline: contour interval = 50 ft/sec. a) Holography-CAT reconstruction; b) numerical code.

(a)   (b)
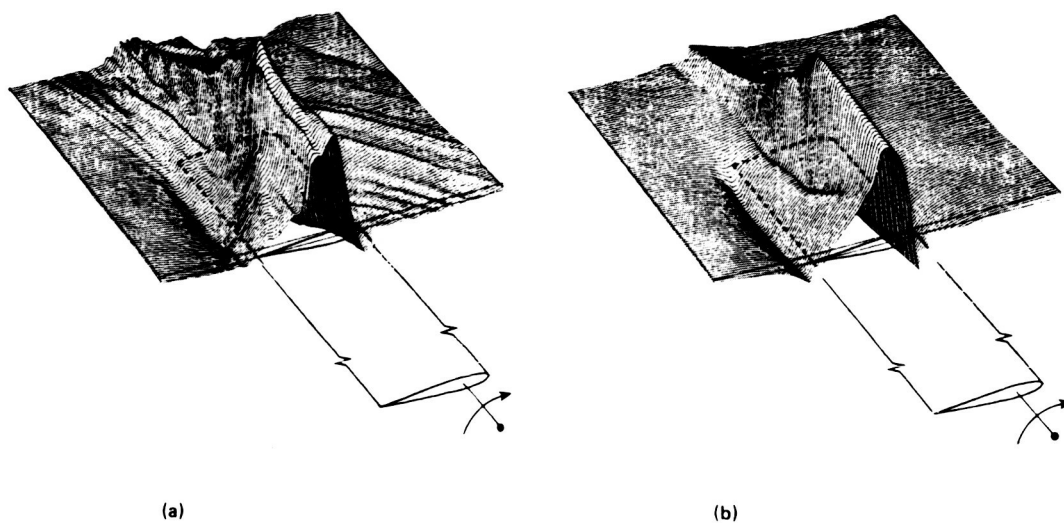
Fig. 12 Perturbation velocity values for Y/C = 0.08 above blade centerline. a) Holography-CAT reconstruction; b) numerical solution.
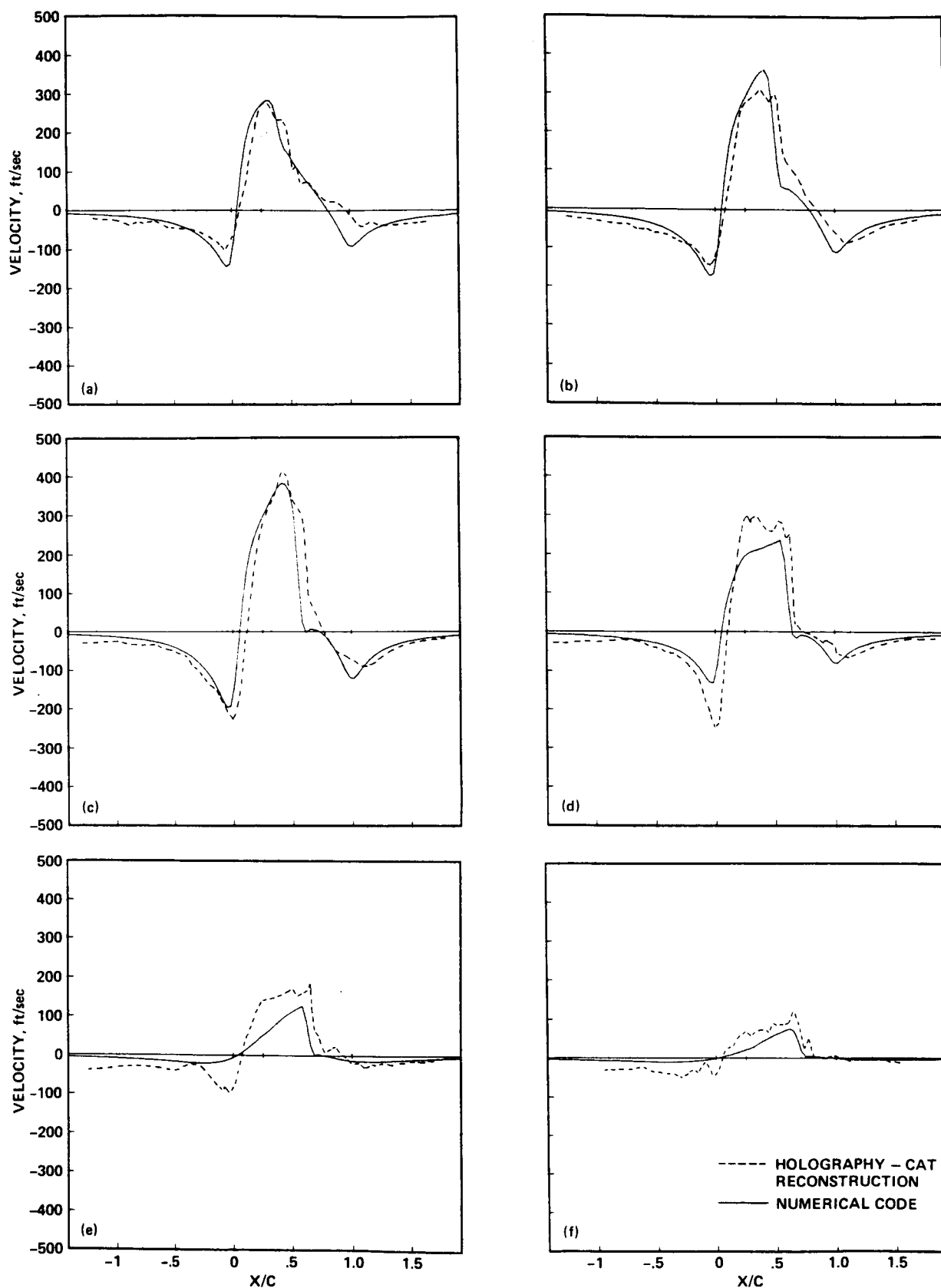
Fig. 13   Perturbation velocity distributions at six radial locations for   Y/C = 0.08   above blade centerline.   a) R/R_0 = 0.88; b) R/R_0 = 0.92; c) R/R_0 = 0.96; d) R/R_0 = 1.00; e) R/R_0 = 1.04; f) R/R_0 = 1.08.
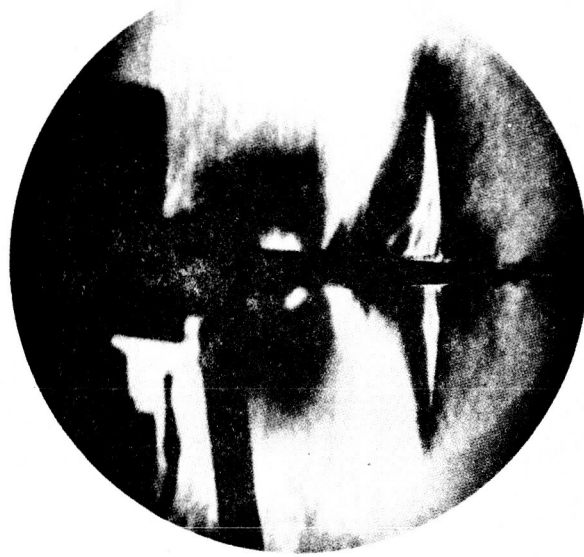
Fig. 14 Schlieren photographs illustrating lambda shock on a NACA 0012 airfoil operating at a tip Mach number of 0.90 in forward flight. (From Ref. 25.)
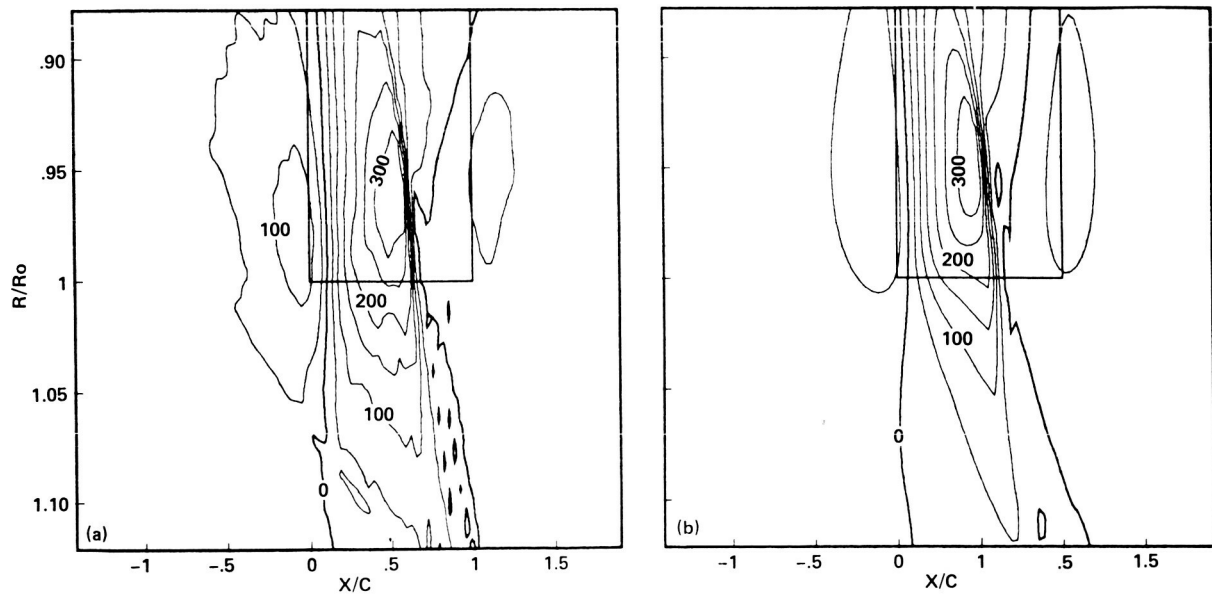
Fig. 15 Perturbation velocity contours in plan view for Y/C = 0.22 above blade centerline: contour interval = 50 ft/sec. a) Holography-CAT reconstruction; b) numerical code.

163
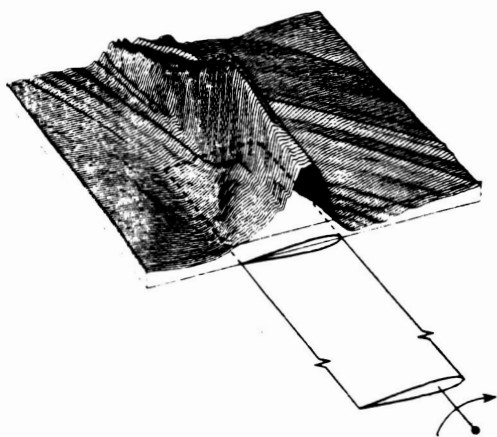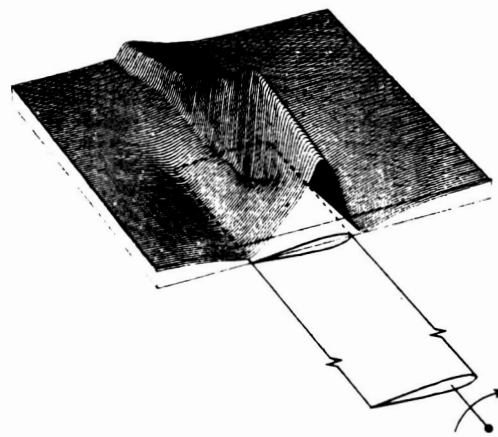
(a)   (b)

Fig. 16   Perturbation velocity values for   Y/C = 0.22   above blade centerline.   a) Holography-CAT
reconstruction; b) numerical solution.
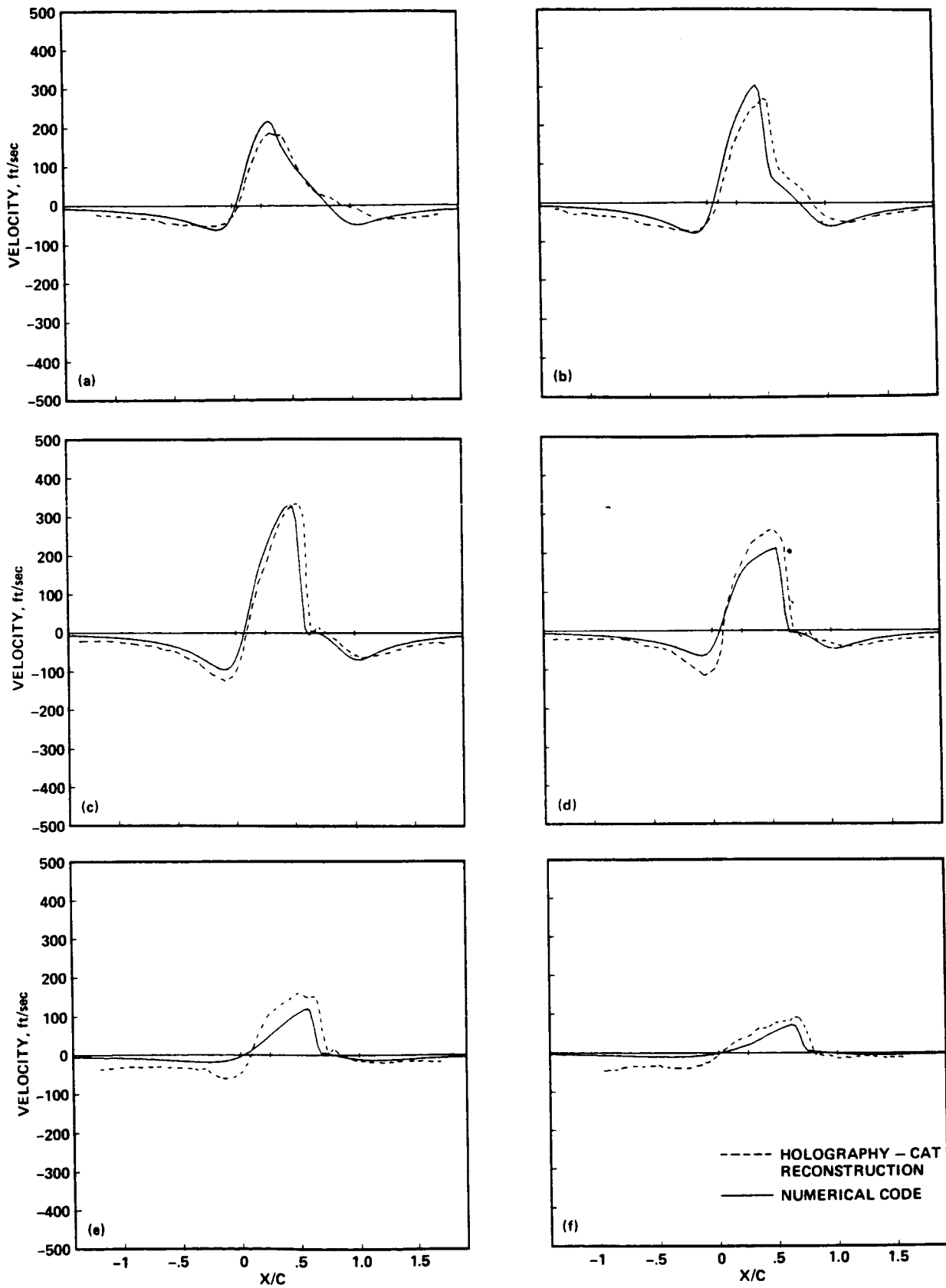
Fig. 17 Perturbation velocity distributions at six radial locations for Y/C = 0.22 above blade center-line.   a) R/R_0 = 0.88; b) R/R_0 = 0.92; c) R/R_0 = 0.96; d) R/R_0 = 1.00; e) R/R_0 = 1.04; f) R/R_0 = 1.08.
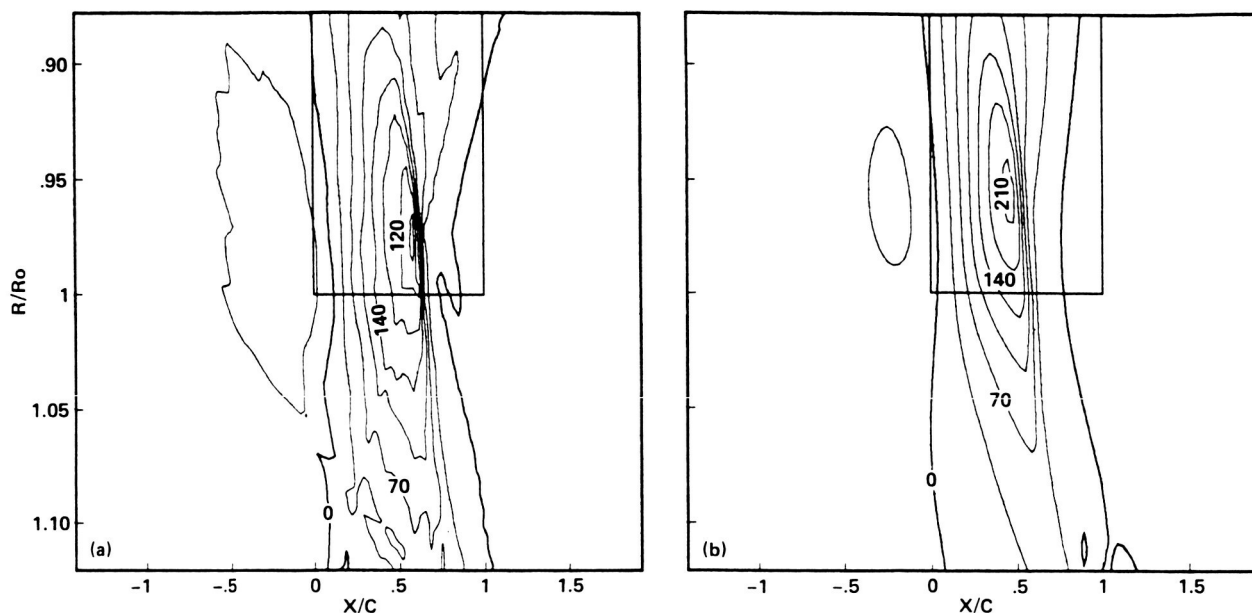
Fig. 18 Perturbation velocity contours in plan view for Y/C = 0.49 above blade centerline: contour interval = 35 ft/sec. a) Holography CAT-reconstruction; b) numerical code.
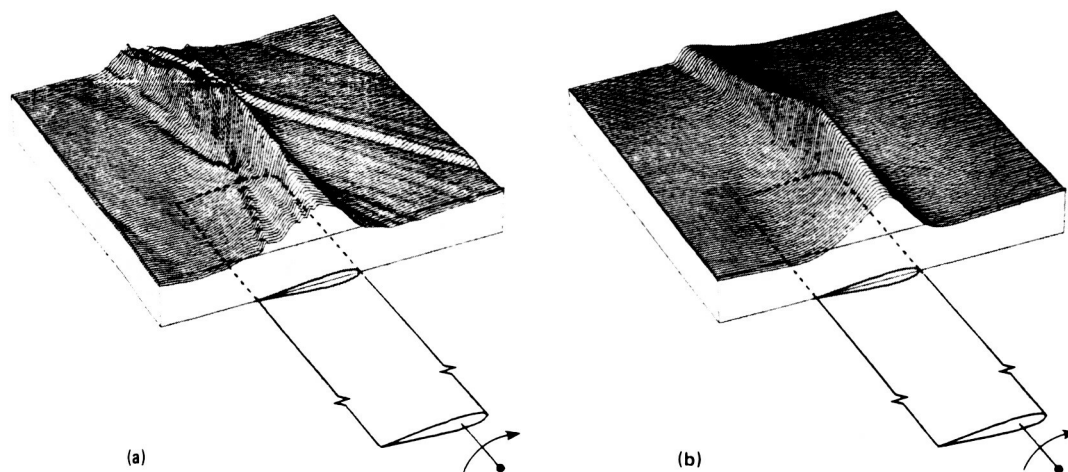
Fig. 19 Perturbation velocity values for Y/C = 0.49 above blade centerline. a) Holography-CAT reconstruction; b) numerical solution.
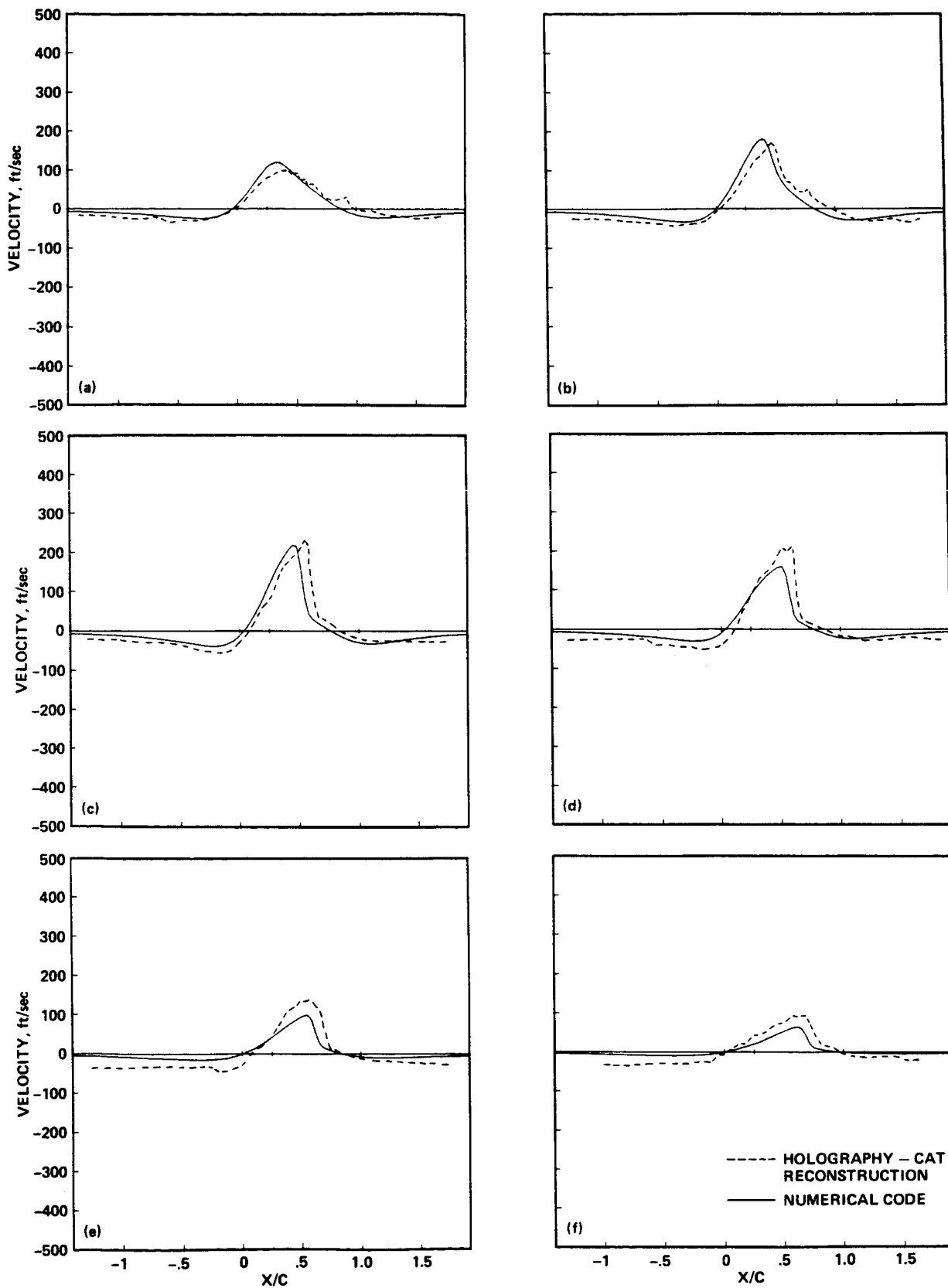
Fig. 20 Perturbation velocity distributions at six radial locations for Y/C = 0.49   above blade center-line. a) R/R_0 = 0.88; b) R/R_0 = 0.92; c) R/R_0 = 0.96; d) R/R_0 = 1.00; e) R/R_0 = 1.04; f) R/R_0 = 1.08.
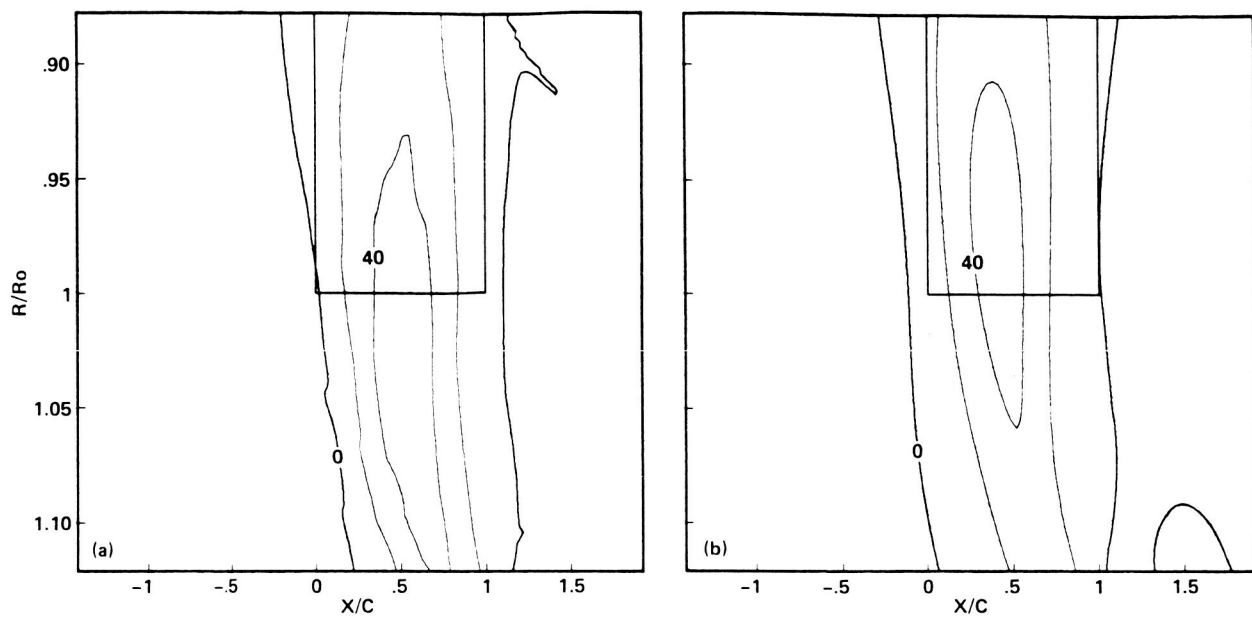
Fig. 21   Perturbation velocity contours in plan view for   Y/C = 1.17   above blade centerline: contour interval = 20 ft/sec.   a) Holograph-CAT reconstruction; b) numerical code.
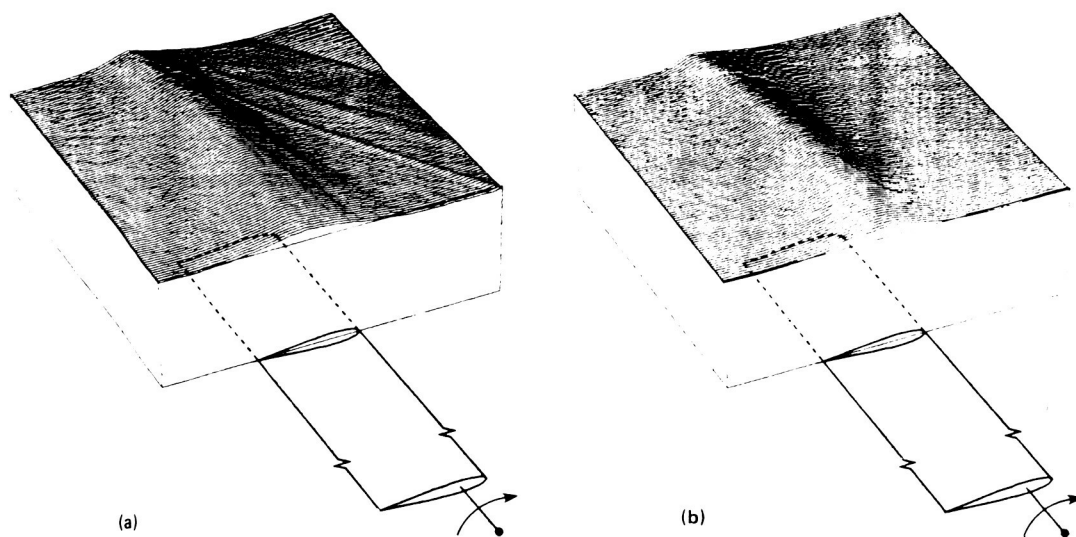
Fig. 22   Perturbation velocity values for   Y/C = 1.17   above blade centerline.   a) Holography-CAT reconstruction; b) numerical solution.
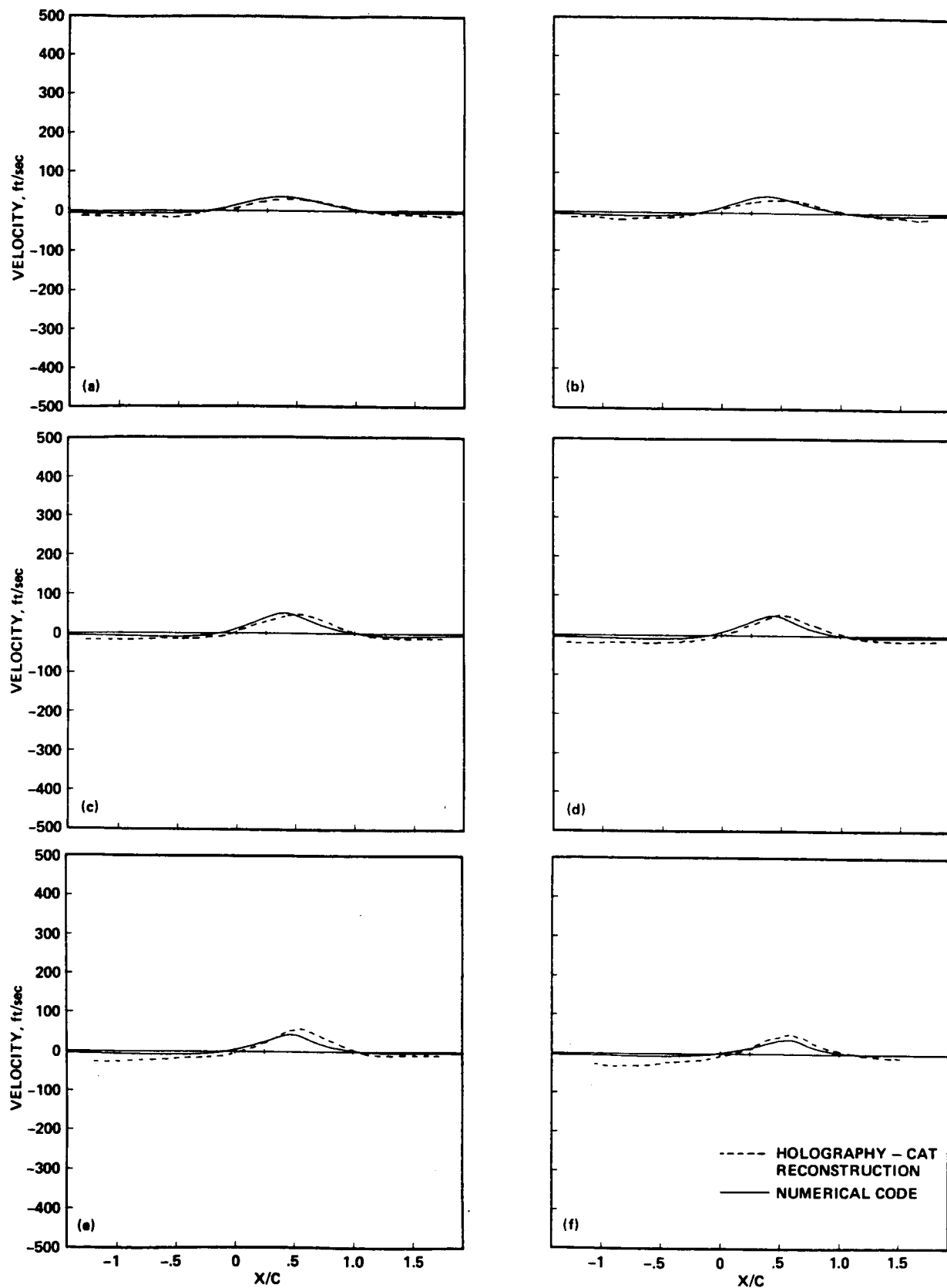
Fig. 23 Perturbation velocity distributions at six radial locations for Y/C = 1.17 above blade center-line. a) R/R_0 = 0.88; b) R/R_0 = 0.92; c) R/R_0 = 0.96; d) R/R_0 = 1.00; e) R/R_0 = 1.04; f) R/R_0 = 1.08.
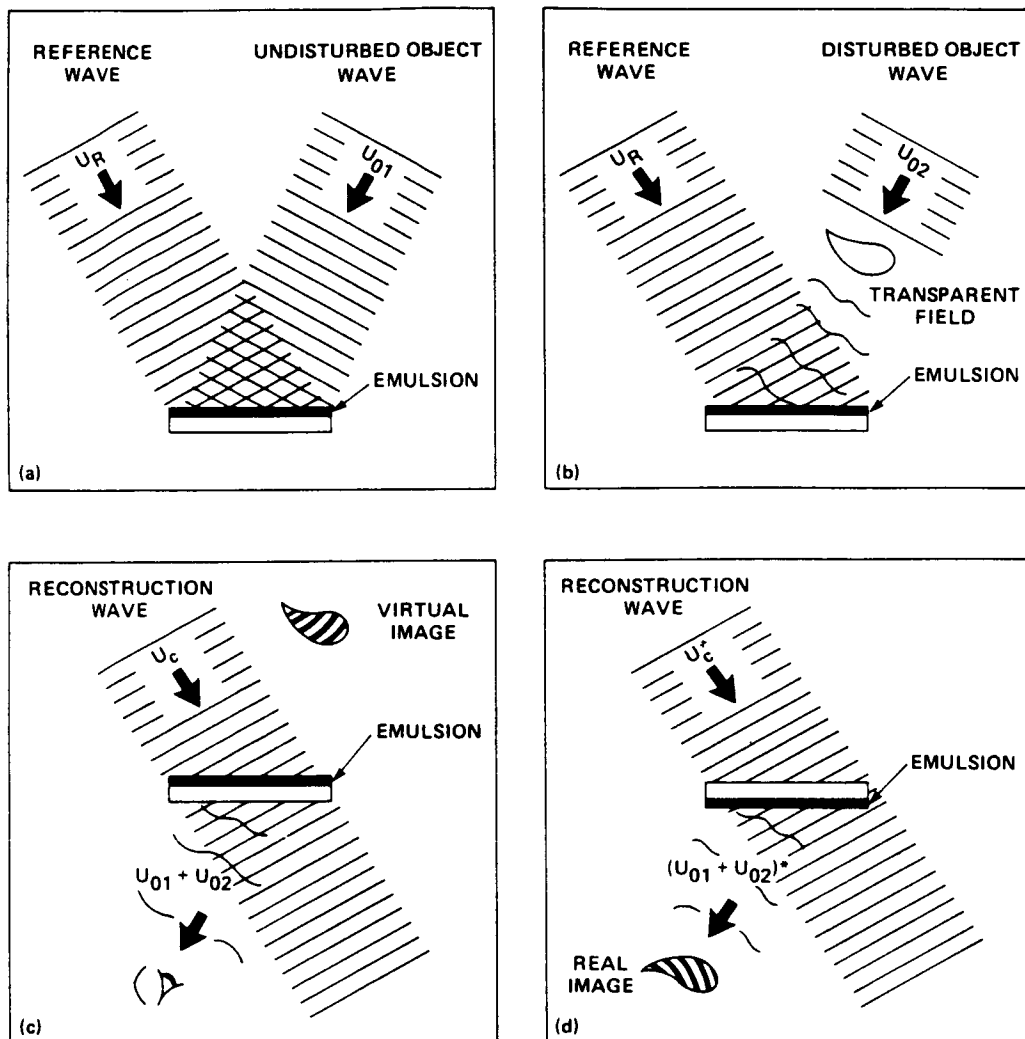
Fig. 24 Double-exposure holographic interferometry. a) First-exposure recording; b) second-exposure recording; c) reconstruction of the virtual image; d) reconstruction of the real image.

HIGH SPEED OPTICAL TOMOGRAPHY FOR FLOW VISUALIZATION

Ray Snyder and Lambertus Hesselink

*Department of Aeronautics/Astronautics
and Electrical Engineering
377 Durand
Stanford University
Stanford California 94305-2186*

ABSTRACT

A novel optical architecture (based on holographic optical elements) for making high speed tomographic measurements is presented. The system is designed for making density or species concentration measurements in a non-steady fluid or combusting flow. Performance evaluations of the optical system are discussed and a test phase object has been successfully reconstructed using this optical arrangement.

INTRODUCTION

Optical computer assisted tomographic (OCAT) reconstruction of a three-dimensional unsteady object requires simultaneous acquisition of many line-of-sight measurements (projections). A projection represents an integrated measurement of absorption or index-of-refraction along a ray path. To acquire one projection a source, often a laser, is used in conjunction with beam steering and recording elements; all necessary projections can be obtained by either rotating the object, by rotating the data acquisition apparatus or alternatively by replicating the system required for making one projection. These approaches have been investigated by us and others for the purpose of making, for instance, measurements of the flow around a revolving helicopter rotorblade[1] or time averaged measurements of complicated turbulent flows[2]. Byer and coworkers have proposed OCAT for monitoring

of atmospheric pollutants; they have devised a data acquisition system which, at least in principle, could provide time-resolved measurements (at a rate of approximately 1 millisecond per cross section), but at present has only been used to make measurements of static objects in their configuration. A rotating mirror is located at the center of a ring of detectors and isotropic scatterers. This system measures absorption in a plane only (but could possibly be extended to make volumetric measurements) and the signal-to-noise ratio is severely limited by speckle noise when using a laser light source[3]. Sweeney and Vest[4] used holographic interferometry for making temperature measurements above a heated plate, but their system was not designed for making time-dependent measurements either.

In this paper we discuss a novel optical data acquisition system which is simple in its layout, involves only two rotating parts and incorporates holographic optical elements (HOE) for beam steering and beam shaping. The system proposed and investigated here is capable of recording high resolution images (10,000 - 100,000 pixels per cross section) at a rate of 500-1000 cross sections per second. The performance of the HOEs is investigated in terms of efficiency, resolving power and signal-to-noise ratio. To investigate the validity and usefulness of the concept, a test phase object consisting of a glass rod placed in a container filled with index-matching fluid is reconstructed from a series of interferograms which have been made with the new optical system.

OPTICAL DATA ACQUISITION ARCHITECTURE

To reconstruct a complex three-dimensional object from its projections it is usually necessary to obtain projections spaced at regular angular intervals over a 180° arc. Sometimes it is possible to reconstruct an object from a limited number of projections[1], but this is only useful for a restricted class of problems. Therefore we will concentrate on optical data acquisition systems which allow full viewing of the object over a 180° arc.

Schematically, the experimental configuration is indicated in figure 1. An argon

pumped dye laser beam is incident on a beam splitter. The object wave is expanded, collimated and directed by a combination of a spatial filter and a holographic optical element (HOE1). The expanded beam probes the test object and either the absorption coefficient or the optical pathlength is measured along the raypaths. The transmitted object beam is then imaged by element HOE2 onto the image plane (camera). At this location the intensity of the transmitted beam is measured or phase information is recorded by heterodyne detection with a reference wave. Multiple views are obtained by using two synchronized spinning mirrors, M1 and M2. For the test configuration described here only two HOEs are used and the mirrors M1 and M2 are stationary; to obtain multiple views for this test case the glass rod, which is immersed in an index matching fluid, is rotated about the cylinder axis. The objective of this experiment is to test the usefulness of the HOEs for optical tomographic data acquisition and to investigate the pertinent properties of the elements, such as diffraction efficiency, aberration tolerances and ease of fabrication.

As an example we discuss the design requirements for the different components, assuming that 100 projections are taken per millisecond and each projection contains 100 rays or bins. The object cross-section is 25 square centimeters and the probe beam diameter is 5 centimeters so that the area of overlap of all projections covers the complete cross-section of the flowfield. These requirements imply that the mirrors should be spinning at a rate of 30,000 rpm (assuming two mirror faces per scanner in order to minimize the offset from the spinning axis) and a 100 element linear detector array should be read out at a rate of 10 Megabytes per second assuming 8 bits of accuracy. If film is used as a recording medium the framing speed should be 100,000 frames per second. These specifications can be achieved with presently available commercial instrumentation. However, if the time requirement is relaxed to obtaining 100 projections every 2 milliseconds (500 Hz) the implementation of the data acquisition system becomes substantially simpler; we have adopted the latter requirements during the initial phase of the work, but intend to find ways to improve the time resolution at a later stage after we have obtained experience

with a less demanding system.

METHOD

Although higher efficiency HOEs could be obtained in dichromated gelatin emulsions, we have selected conventional silver halide film (Agfa 8E75HD-NAH holographic plates) for its ease of use. The holograms are developed in the catechol developer described by Cooke and Ward[5]; no fixer is used. The developed plates are bleached in GP432[6] for increased efficiency.

The holograms are constructed in a geometry identical to that for which they are to be used; a converging beam is interfered with a collimated beam at an angle of 33° from opposing, representative of the geometry for an average element in a multi-projection system. Since the beams enter the plate from opposite sides, a reflection hologram is formed. The converging beam is focused to a spot 47 centimeters from the plate, so that the created holograms have a focal length of 47 centimeters. The collimated beam to converging beam intensity ratio is 2. The resulting HOEs are reflecting, focusing lenses at the construction wavelength of 589 μm in and near the construction geometry. 10% diffraction efficiency (diffracted intensity in desired component / incident intensity) is easily obtained for an aperture greater than 3 centimeters in diameter. Substantially higher efficiency (approximately 24%) has been achieved with this process in other configurations in our laboratory.

Two HOEs are used in the experiment as shown in figure 1. To evaluate the spatial resolving power of the HOEs, a standard Air Force test target is placed at the object position and imaged onto the image plane by the second HOE at 2.4× magnification. The result is shown in figure 2; resolution better than 10 lines per millimeter is obtained. Illumination falls off in the corners of the image due to nonuniformity of the illuminating beam but it is uniform in the central region and no distortions are apparent. The potential

for achieving resolution greater than 200 pixels per projection is clearly evident.

To obtain interferograms, a reference beam was split off from the laser before the spatial filter shown in figure 1 and independently filtered, directed and focused using conventional optics. The reference beam and the object beam are recombined at the image plane. The fringes resulting are viewed in the image plane corresponding to the object. The resulting fringe patterns show a high signal-to-noise ratio.

For the tomographic experiment, a 2.2 millimeter cylindrical pyrex rod is used as the object. The rod, with a nominal index of 1.474, is immersed in index matching fluid with an index of 1.47. The magnification in the image plane is 3.5×; the imaging greatly reduces the distortion caused by raybending as the rays passing through the object encounter index of refraction gradients[7]. A sample interferogram is shown in figure 3. Ten interferograms are recorded, each corresponding to one angular position of the rod. The rod was rotated 36° between images so that an arc of 360° is viewed.

The images are digitized with a PDS model 1010A scanner with a pixel size of 50 μm square to form a 512×512 array. The data base is reduced by extracting a 128 pixel high by 360 pixel wide window from each image as shown in figure 3. Since the rod is very nearly vertical and the properties of the rod depend only slightly on its axial coordinate as demonstrated in figure 3, the fringes are periodic along the z coordinate. It is seen that any pixel in the windowed data is reproduced periodically along a vertical axis. The period is one seventh of the window height. A one-dimensional Fourier transform of a column of data yields a spectrum from which the phase offset of the fringes can be determined across the width of the window. Figure 4 shows the averaged magnitudes for the whole window of the vertical frequency components of one view. Note that aside from the large D.C. component, seven cycles per window is the major energy containing component, the one corresponding to the fundamental spacing of the fringes; lower energy harmonics are also present. If the phase of the seventh component is extracted for each column and

plotted versus the width of the window, the result is as shown in figure 5. This phase plot corresponds to the relative spatial offset of the fringes in the interferogram.

The phase information is unraveled by addition and subtraction of integer multiples of π at discontinuities in figure 5. The correct multiple was selected manually by comparing figures 3 and 5; the correct phase plot is expected to be identical in form to the trace of a single fringe in figure 3. The background phase variation is eliminated by fitting a third order polynomial to the background phase at either side of the rod in each interferogram, and then subtracting the function from the whole field. The result is as shown in figure 6, which constitutes the reduced optical pathlength measurements of one projection.

The ten single projections are averaged with their complementary projections, 180° away, to yield five projections spaced at 36° to cover a 180° arc of view. These five projections are aligned to the same origin, or axis of rotation, by placing the axis at the centroid [where values less than $-\frac{\pi}{2}$ are weighted uniformly and values greater than $-\frac{\pi}{2}$ receive no weight] of the image and filling in at the sides with zeros. By linear interpolation the five projections are extended to one hundred projections at 1.8° spacing as shown in figure 7. Convolution backprojection[8] with a Shepp-Logan filter[9] is used for reconstruction. When median filtering with a 3×3 window is performed (to remove spikes caused by reconstruction of sharp gradients) the results are as shown in figures 8 and 9 on a 128×128 grid. Figure 10 shows a cross section through the center of the reconstruction*. After the tomographic measurements had been completed, the rod was cut and polished so the cross section could be examined. A photograph of the index of refraction field through a 6 millimeter thick section of the rod is shown in figure 11. Note the spiral pattern which is revealed by incandescent light. The hole in the center is evident and the index of refraction is clearly non-uniform in the cross section, consistent with the tomographic results.

---

* Note that the dip in the middle of the graph indicates a hole in the center of the rod which was filled with fluid. The index in the hole is slightly lower than the index of the external fluid; this is probably becaused some cleaning solvent, which could not be removed, is mixed in with the index matching fluid. It is also possible that the dip is too low because of the reconstruction scheme used, but this could not be verified.

CONCLUSIONS

Although HOEs have been used to visualize the flow inside a circular cylinder[10], this paper discusses the first application of HOEs for interferometry and tomography of fluid flows. The results indicate that very good data can be obtained with the optical system described here; the signal-to-noise ratio is high and the resolution of the reconstruction can be at least 200×200 pixels. A comparison between the tomographic results shown in figure 9 and the photograph of the cross section in figure 11 shows that the tomographic reconstruction reveals much of the structure of the index-of-refraction present in the rod. In particular the hole and very small index-of-refraction variations are recovered as is the spiral structure of the rod.

Presently an effort is underway in our laboratory to implement the full optical tomographic system; this apparatus will be used to investigate a time-varying, three-dimensional, combusting flow.

ACKNOWLEDGEMENTS

REFERENCES

[1] R. Snyder and L. Hesselink, "Optical Tomography for Flow Visualization of the Density Field Around a Revolving Helicopter Rotor Blade," *Applied Optics*, Vol 23, Sept. 1984.

[2] R. J. Santoro, H. G. Semerjian, P. J. Emmerman and R. Goulard, *AIAA*, Vol 80, 1541, 1980.

[3] K. Bennet and R. L. Byer, "Optical Tomography: Experimental Verification of Noise Theory," *Optics Letters* Vol. 9, 1984.

[4] D. W. Sweeney and C. M. Vest, *International Journal of Heat and Mass Transfer*, Vol 17, 1443, 1974.

[5] D. J. Cooke and A. A. Ward, "Reflection-hologram processing for high efficiency in silver-halide emulsions," *Applied Optics*, Vol 23, No. 6, 934-941, March 1984.

[6] Agfa-Gevaert, Holography Newsletter 1, Oct. 1979.

[7] C. M. Vest, "Interferometry of strongly refracting phase objects," *Applied Optics*, Vol. 14, No 7, 1601-1606, July 1975.

[8] G. N. Ramachandran and A. V. Lakshminarayanan, *Proc. Natl. Acad. Sci. U.S.*, Vol. 68, No. 9, 2236-2240, 1971.

[9] L. A. Shepp and B. F. Logan, *IEEE Trans. NS*, Vol. 21, 21-43, 1974.

[10] L. Hesselink, M. Richmand and W. C. Reynolds, "Holographic Optical Element for Flow Visualization Inside a Circular Cylinder," submitted to Appled Optics.

FIGURE 1: Schematic of the experimental configuration. For the tests described, only the beam path shown is employed. The coordinates shown are fixed to the rod. The rod is rotated to obtain projections at angles measured relative to the beam as shown.

FIGURE 2: Image of Air Force test pattern. Smallest visible pattern corresponds to a resolution of at least 10 lines per millimeter in the object.

FIGURE 3: Interferogram for 144° projection. The region outlined by the box is the data window for the projections. Note the periodic structure parallel to the axis of the rod.

FIGURE 4: Spectral energy density averaged over the whole data window of one projection (144°). The seventh component is clearly prominent, with some energy in the 15th component second harmonic).

FIGURE 5: Phase offset of the fringes versus the horizontal component in one projection (144°). Discontinuities occur as the phase exceeds $\frac{\pi}{2}$ or $-\frac{\pi}{2}$.

FIGURE 6: Unraveled phase offset for one projection (144°). The phase wraparound has been removed to make the projection continuous.

FIGURE 7: Interpolated projections. The complete reduced data base is shown inverted for easier viewing.

FIGURE 8: Reconstruction of the index of refraction in the rod.

FIGURE 9: Reconstruction of the index of refraction in the rod. Lighter values correspond to a higher index of refraction. Note the asymmetry and the hole in the center.

FIGURE 10: Cross section through center of the reconstruction. Radial structure is shown as well as hole in the center of the rod.

FIGURE 11: Transmittance photograph of a 6 millimeter long slice of the rod. Note the correspondence with the results of the reconstruction in figure 9. The edge of the rod was chipped as it was being cut.
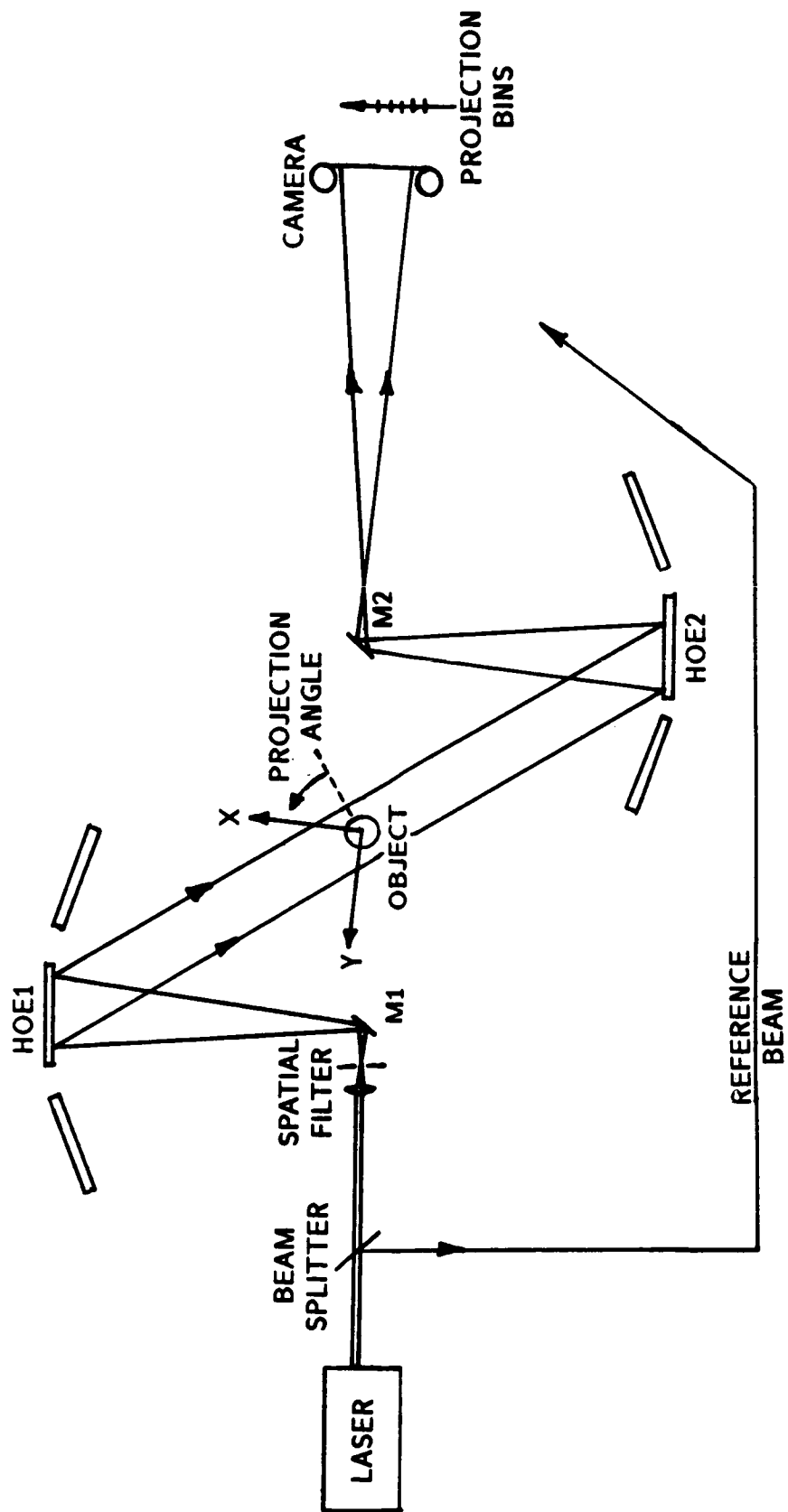
Fig. 1
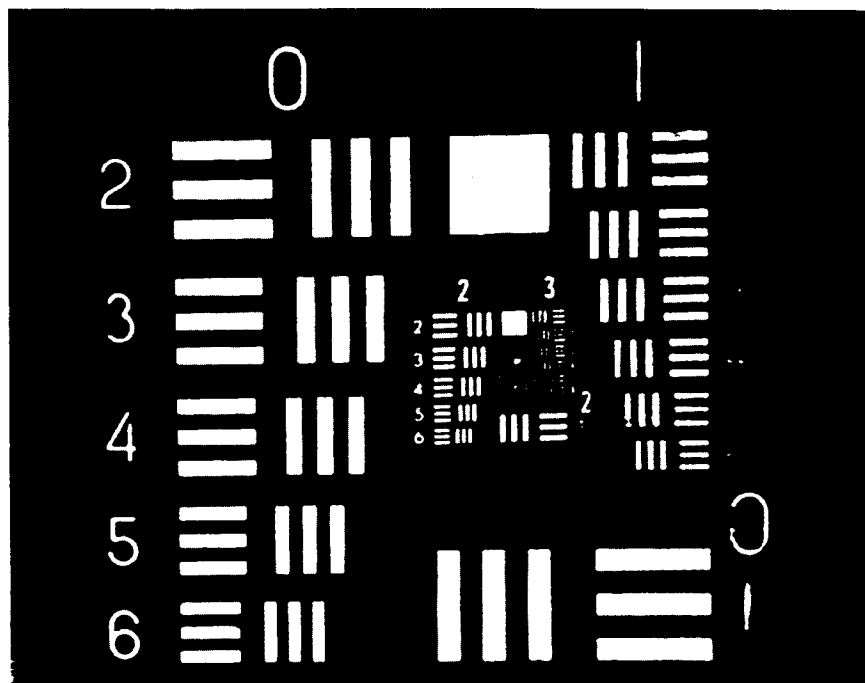
Fig. 2
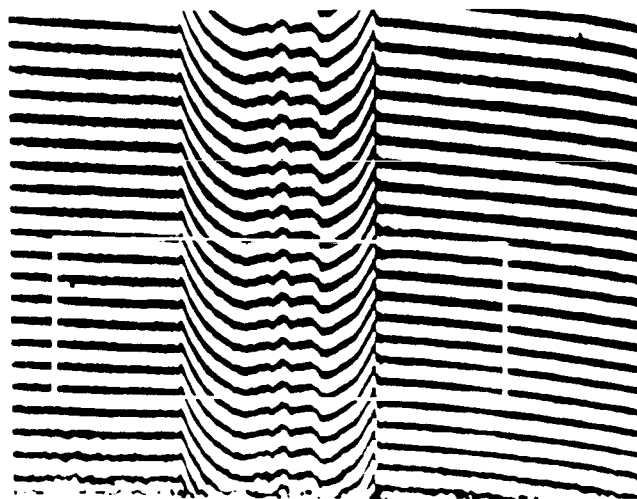
Fig. 3
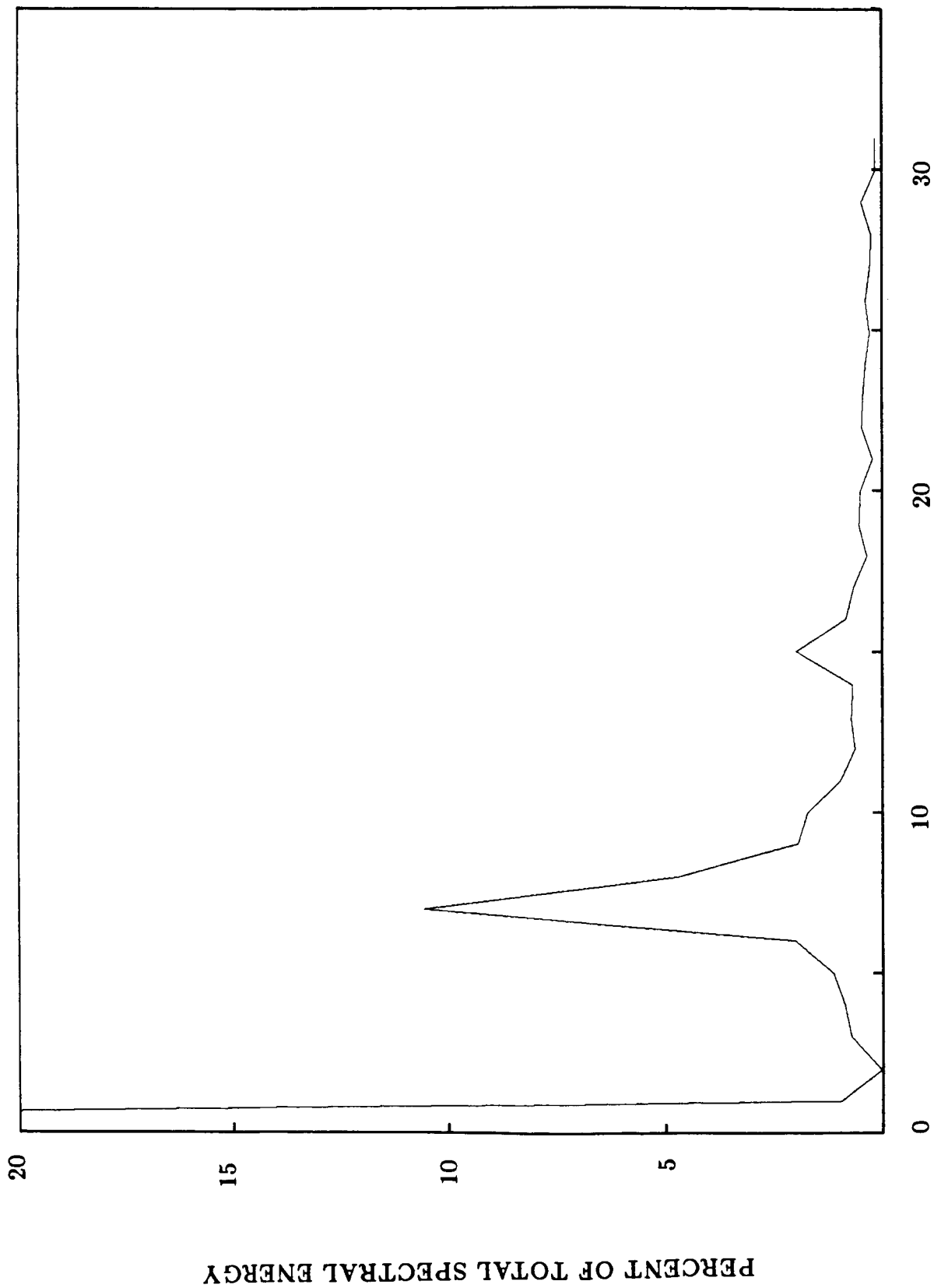
FREQUENCY COMPONENT (CYCLES IN WINDOW)
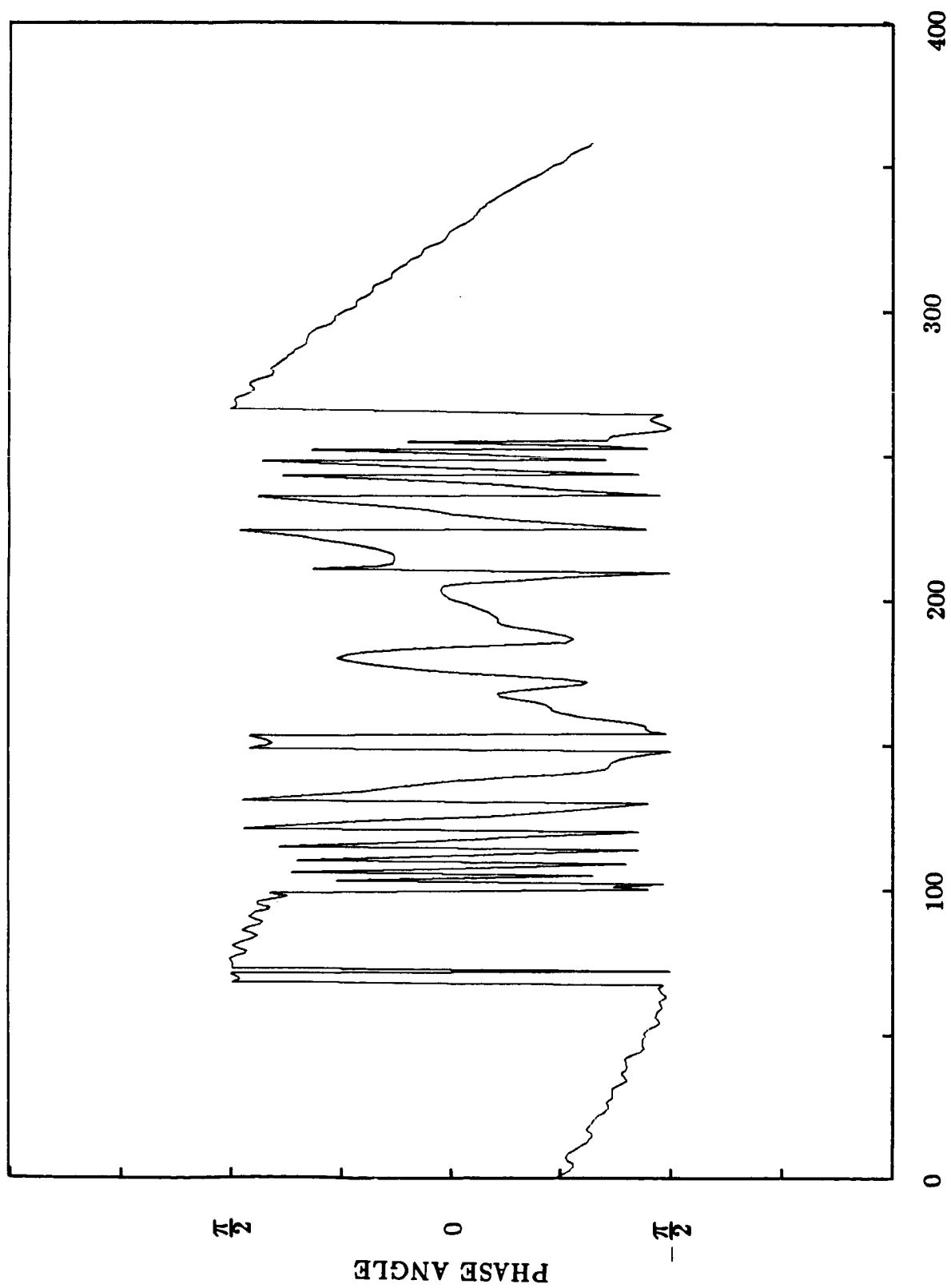
Fig. 4

PERCENT OF TOTAL SPECTRAL ENERGY

184

PROJECTION BIN

Fig. 5
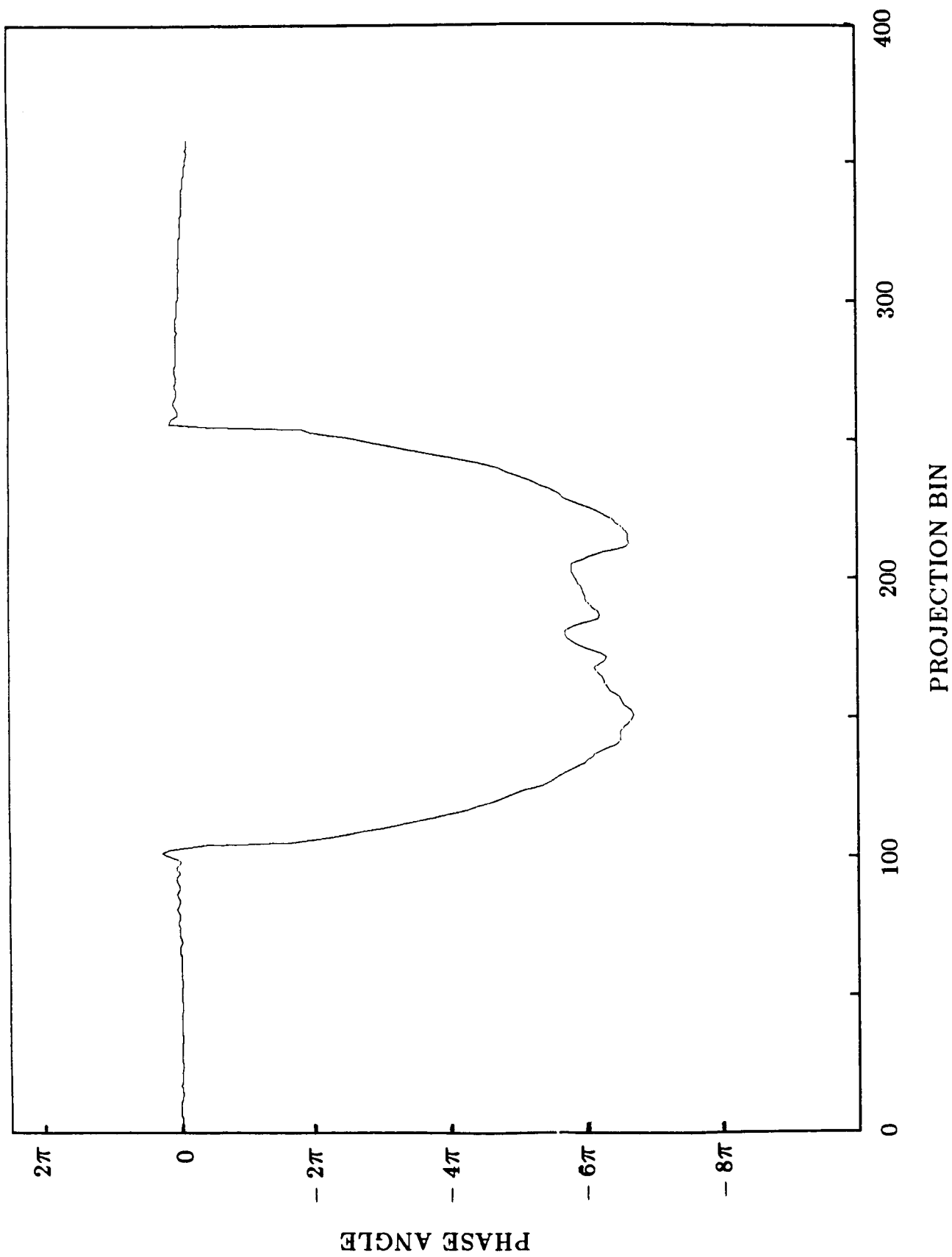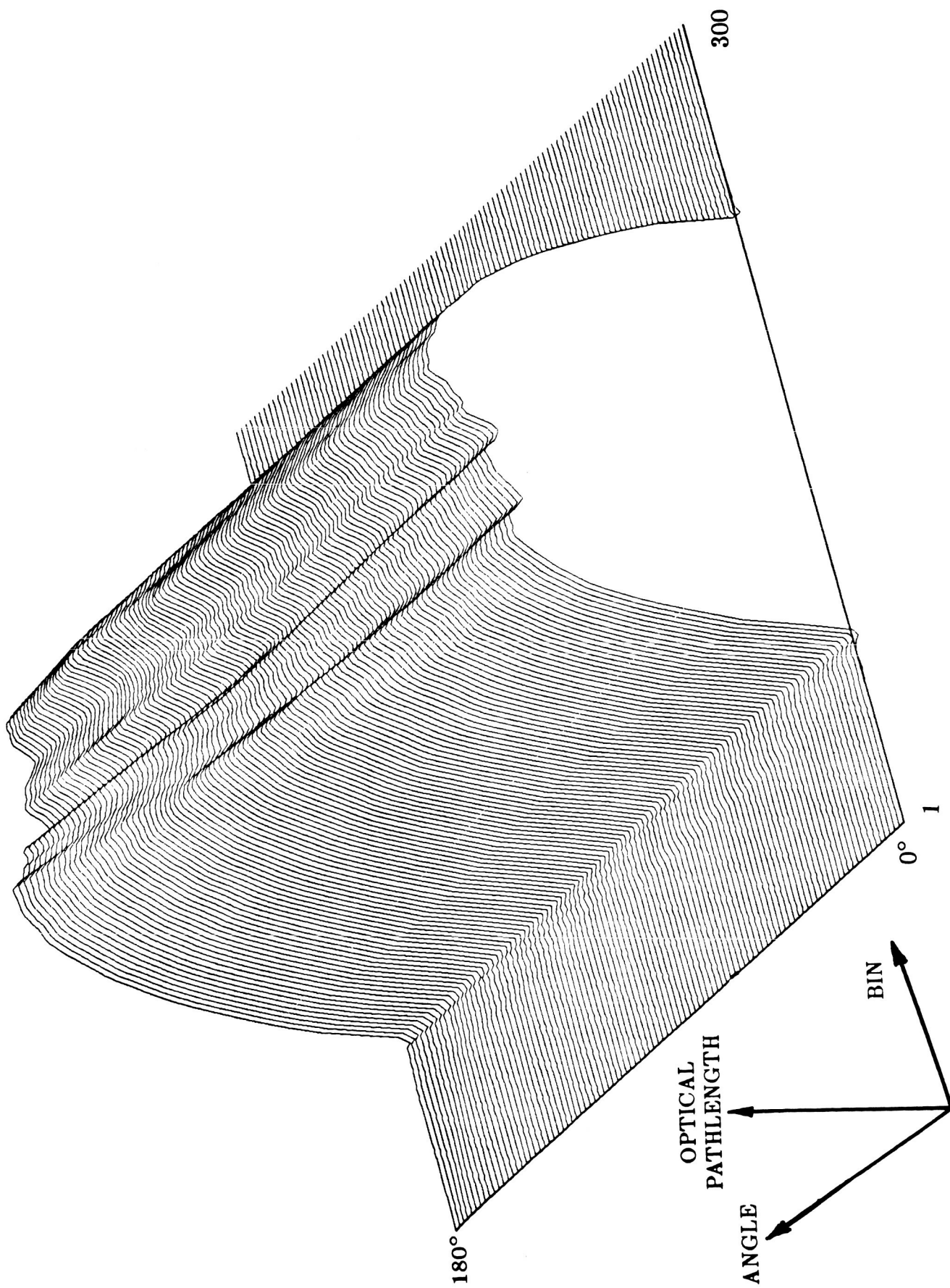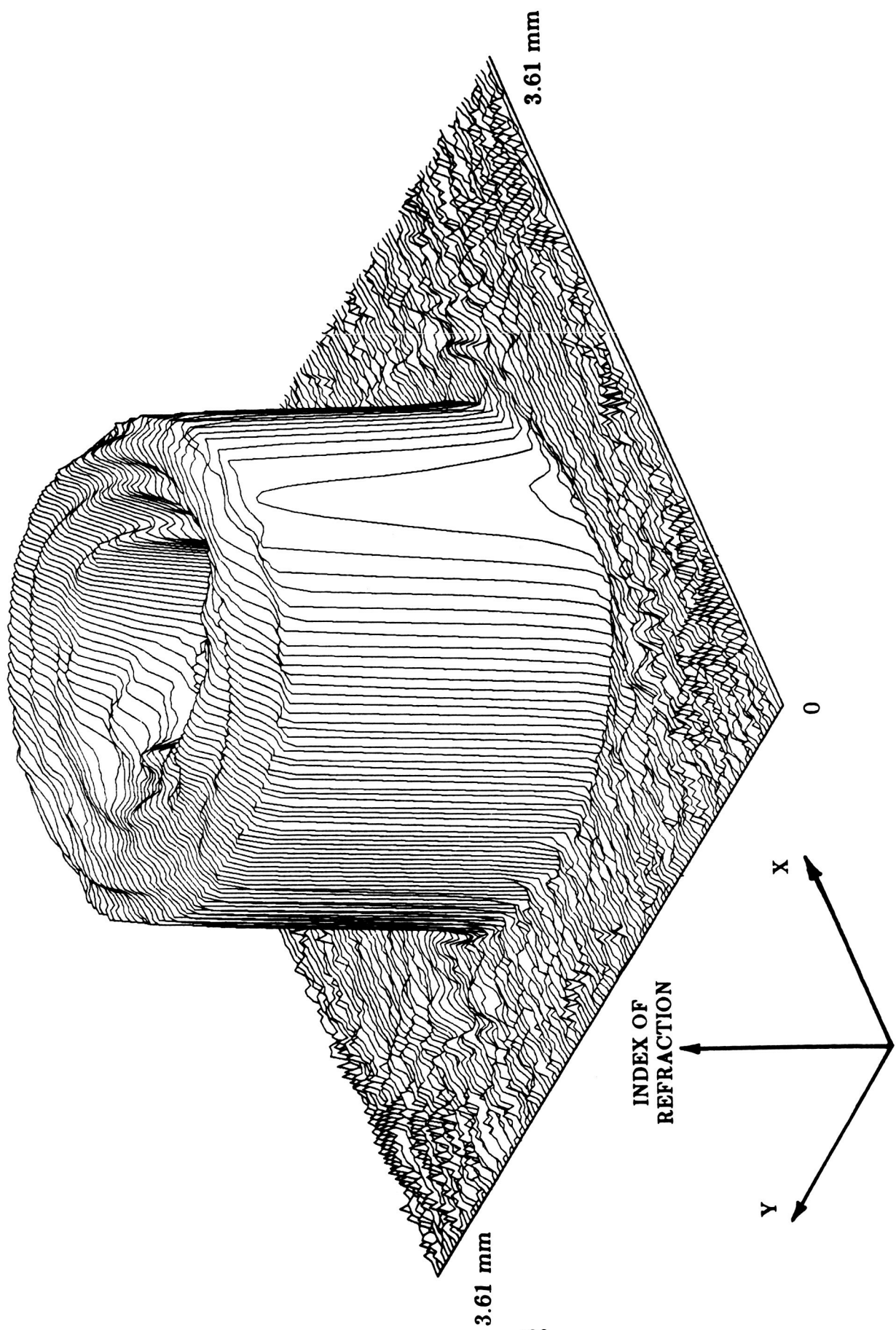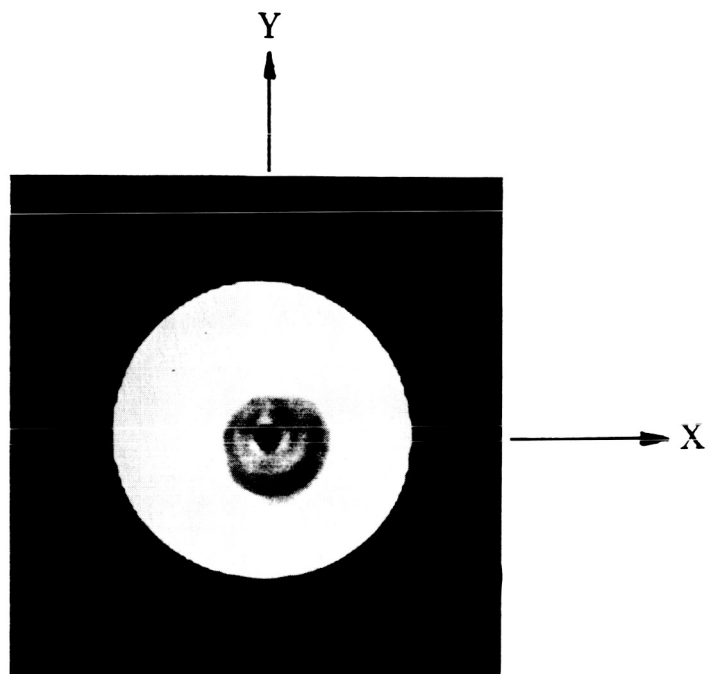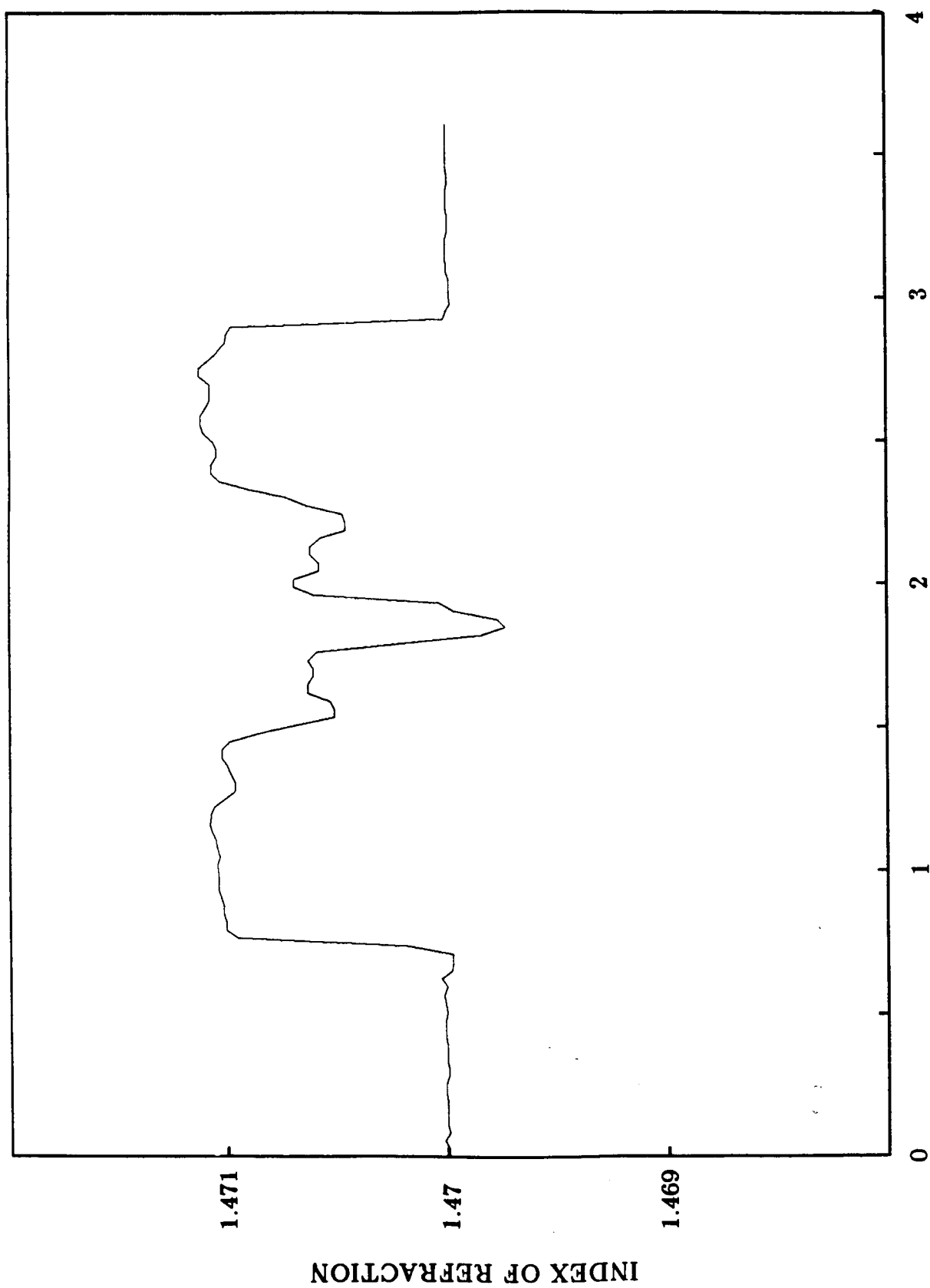
185

PHASE ANGLE

PROJECTION BIN

Fig. 6

186

300

1

0°

180°

BIN

OPTICAL
PATHLENGTH

ANGLE

Fig. 7

3.61 mm

3.61 mm

0

INDEX OF
REFRACTION

X

Y

Fig. 8

188

Fig. 9

189

X (MILLIMETERS)

Fig. 10

INDEX OF REFRACTION

Fig. 11

191
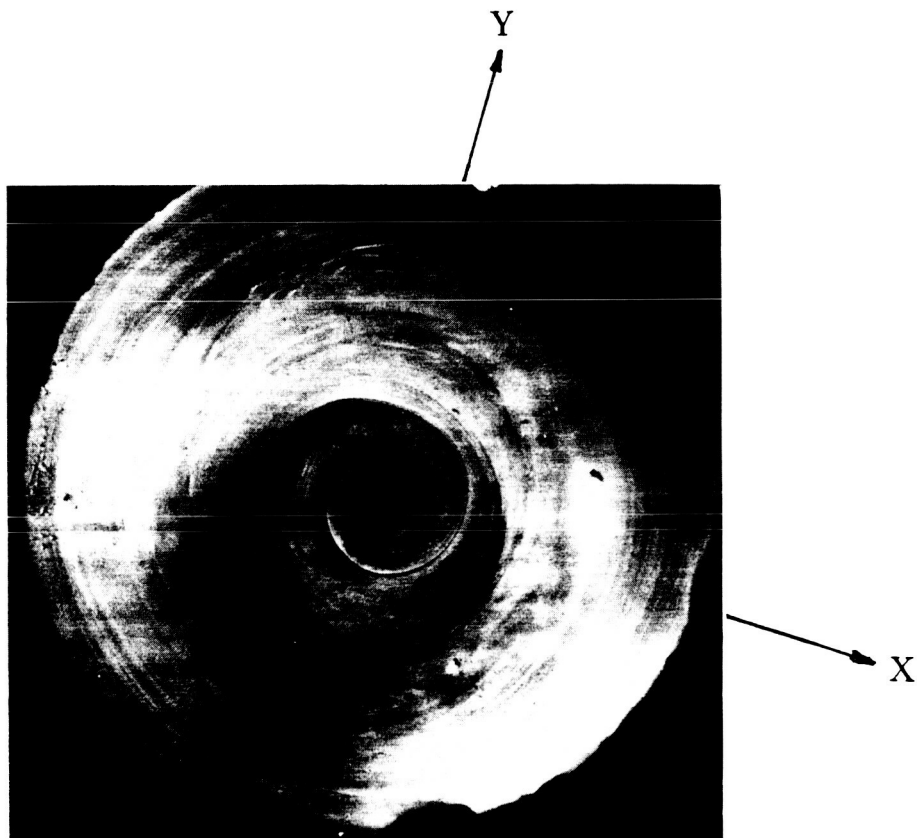
OPTICAL INTERFEROMETRY IN FLUID DYNAMICS RESEARCH

by

W. D. Bachalo

and

M. J. Houser

Aerometrics, Inc.

P.O. Box 308

Mountain View, CA 94042

Abstract

Optical interferometry techniques have been applied to the investigation of transonic airfoil flow fields in large scale wind tunnels. Holographic interferometry techniques were used in the study of two-dimensional symmetric NACA 64A010 and supercritical DSMA671 airfoil performance in the NASA Ames 2-by-2-foot Transonic Wind Tunnel. Quantitative data obtained from the interferograms were compared to the surface pressure data. The excellent agreement obtained verified the accuracy of the flow visualization and demonstrated the potential for acquiring quantitative scalar results with interferometry. Measurements of the inviscid flow speed and the boundary layer and wake velocity profiles were extracted from the interferograms and compared to laser Doppler velocimeter measurements. These results were also in good agreement indicating that the flow was sufficiently two-dimensional to obtain reliable (visual), quantitative data from the spatially integrated results provided by the interferometer.

A method for acquiring real-time interferometric data in large scale facilities was developed. This method based on the point diffraction interferometer was successfully tested in the Ames 2-by-2-foot Transonic Wind Tunnel.

PRECEDING PAGE BLANK NOT FILMED

The holographic and real-time interferometry methods were applied to the investigations of circulation control airfoils utilizing the Coanda effect. These results revealed the details of the jet interaction with the trailing edge boundary layer and the other parameters affecting the lift augmentation.

C -3

OPTICAL INTERFEROMETRY IN FLUID DYNAMICS RESEARCH

1.0 Introduction

Optical interferometry has been used as a diagnostic tool in fluid dynamics research for approximately a century beginning with the work of Ernst Mach (1838-1916). More recently, the method has also been used effectively in heat transfer, combustion, and plasma dynamics research. However, the scale of the flow fields that could be addressed with interferometry was severely limited by the coherence of the light source and extreme sensitivity to vibration. These problems were partially alleviated by the development of the laser.

The introduction of holography by Horman [1] and the initial applications to aerodynamic measurements by Heflinger, Wuerker and Brooks [2, 3] represented a notable advance in terms of where the method could be applied. Holographic light wave reconstruction and pulsed lasers provided the means through which the limitations associated with vibration and optical quality were essentially eliminated.

Trolinger [4] applied the method to the visualization of small scale supersonic and hypersonic flow fields. These results suggested the possibility of utilizing the method in large scale

transonic flow field investigations. A holographic interferometer was developed and installed on the NASA Ames 2-by-2-foot transonic wind tunnel for this purpose by the author in 1974. Extensive testing and evaluations of the results were undertaken over the subsequent years. During that time, the method was proven capable of acquiring detailed flow visualization and accurate quantitative data in the NASA Ames 2-by-2-foot, 6-by-6-foot, and 11-foot transonic wind tunnels [5, 6, 7, 8, 9].

Transonic flows proved to be especially suitable to the application of interferometry since compression of the fluid occurs continuously throughout the field, whereas in supersonic flows, the density changes occur primarily through shocks. In addition, the shocks that are present in the transonic flow fields are weak so the entire flow can be assumed to be isentropic. Thus, in the two-dimensional flows studied, the interference fringes were at the same time a mapping of the isopycnics, constant static pressure, flow speed, and Mach contours. These data could readily be reduced with the use of other wind tunnel flow conditions to obtain the quantitative results.

The strong coupling between the inviscid and viscous phenomena in transonic flows predicates the simultaneous observation of the global features of the flow fields and the local viscous-inviscid interactions. Conditions such as the shock boundary layer interaction, turbulence-induced compression waves,

and pressure gradients generated by the model profiles influence the character of the entire flow field. Holographic interferometry furnished the means for obtaining detailed visualization of these flow chracteristics and for producing scalar quantitative data in both the inviscid and viscous regions. By using very short duration exposures, the time-varying phenomena in the flow could be recorded and analyzed. These details are often lost in time-averaged surface pressure and probe measurements.

Several two-dimensional transonic flow fields were investigated using interferometry techniques. The emphasis on helicopter rotor flows led to the investigation of symmetric airfoil flows [5, 6]. These flows posed a significant challenge to the computational fluid dynamicist, and as such, required the acquisition of detailed experimental data. The holographic interferometer and two-component frequency shifted laser Doppler velocimeter (LDV) were combined in an effort to attain these goals. Because of the range of parametric conditions investigated, the interferometry data proved effective in directing the LDV measurements to the regions where flow angle and the turbulence quantities were needed. The detailed flow visualization provided by the interferometer made a significant contribution toward the understanding of the complex fluid dynamics which characterize these flows.

Supercritical airfoils were also studied under a cooperative program with the Douglas Aircraft Corporation and the Ames Research Center [7]. The series of tests were part of an overall program with the goal of completely documenting these flow fields and providing further insights for the improved design of this class of airfoil. Flow fields produced by supercritical airfoils operating at their design Mach number and lift coefficient are characterized by regions of strong viscous-inviscid interactions. These airfoils are also characterized by large aft loading. As such, the iterative procedures used for calculating conventional airfoil flows failed because the initial inviscid calculations were often so different from the actual flow field that convergence to a physically realistic solution did not occur. Simiempirical methods were required for the treatment of the trailing edge region.

The investigations covered under the research program were intended to provide data for comparison with the results of numerical computations. Based on the data obtained in the first phase of the program, modifications were made to the airfoils used in subsequent tests. Laser Doppler velocimeter, surface and pitot pressure data were combined with data from the holographic interferometer to provide an unusually complete description of the flow fields.

Research on advanced rotorcraft utilizing Coanda blowing for circulation control was also supported using holographic interferometry and a new method for real-time interferometry [10]. These investigations were conducted over a period of three years on a number of airfoil configurations operating at transonic speeds. Circulation control airfoils utilizing the Coanda effect introduce an added complexity to the transonic flow fields which increases the difficulty in understanding and predicting these flows. The Coanda effect occurs when a high-velocity jet emits tangentially from a surface slot and remains attached to the surface because of the reduced pressure produced beneath the jet. External fluid is entrained by the jet assisting the flow in remaining attached well-around the typically blunt trailing edge of the airfoil.

Interferometry and other techniques were applied to generate a complete visualization of the flow which helped resolve some of the questions regarding the flow behavior particularly in the neighborhood of the training edge. A range of operating conditions were investigated including the stall condition and jet detachment. Because the understanding of the circulation control airfoil flows at transonic speeds was rather primitive at the initiation of the program, these investigations were needed for elucidating some of the complex phenomena.

In this report, the development efforts that were required in bringing the interferometric techniques to fruition as diagnostics for large scale transonic wind tunnel testing will be reviewed. Comparative measurements are presented to demonstrate the reliability of the flow visualization and quantitative data. Application of a new method for obtaining real-time interferometry data in large scale facilities is also described. The method which is currently under development by Aerometrics has been demonstrated in the Ames 2-by-2-foot Transonic Wind Tunnel.

2.0 Interferometry Techniques

Holographic Interferometer

As a flow diagnostic, the holographic interferometry technique does not differ, in principle, from the Mach-Zehnder method. In comparison, the holographic method creates interference between two reconstructed light waves which have followed similar paths at different times whereas the Mach-Zehnder interferes two light waves from dissimilar paths at the same time. This distinction is important because component imperfections in the optical path tend to cancel when holographic recordings are reconstructed and interfered.

Although there are several ways in which holography can be used as an intermediary for interferometry including double exposure, real-time, and dual plate methods, the latter technique was found to be most useful in aerodynamic applications. With this method, an exposure is made on a holographic (photographic) plate while there is no flow in the wind tunnel. This hologram is later used to reconstruct the reference light wave. Subsequent plates are exposed at the flow conditions under investigation. After processing, the plates are positioned in the reconstruction plate holder, illuminated by a duplicate of the reference beam, and aligned for the infinite fringe mode. One reference plate can be used consecutively with plates taken at the test conditions. Vibrations in the system are insignificant because the exposure duration is extremely short (20 nanoseconds). Random displacements between images on the plates are accounted for in the reconstruction process.

One major difficulty arises when utilizing the dual plate technique. If the density of the flow is disturbed over the entire field of view, as is often the case, it is difficult to ascertain when the interferometer is aligned to the infinite fringe condition. That is, to the case wherein fringes only occur as a result of changes in the flow density. Fortunately, a knowledge of the transonic flow characteristics and other alignment criteria have led to accurate reconstructions that produced results in good agreement with other measurements.

The first conversion of the wind tunnel schlieren system to holography utilized a pulsed ruby laser with a helium neon laser for alignment. Ruby lasers produce sufficiently high energy (50 millijoules) pulses of short duration (20 nanoseconds) to "freeze" the flow being recorded. These lasers also have a coherence length on the order of one meter which simplified the alignment requirements. Holograms produced with the ruby laser had good diffraction efficiency but the alignment of the system tended to be very time consuming. This was due primarily to the relatively long time periods (30-60 seconds) required between laser firing and the need to align with a separate CW laser. Optical path lengths on the order of 30 meters and the makeshift optical system supports exacerbated the problem.

Based on the feasibility investigations using the ruby laser and a makeshift optics system, a permanent instrument was designed and installed in the Ames 2-by-2-foot facility. A Quanta Ray DCR-1 Nd:YAG laser was used as the light source. The Nd:YAG laser is capable of producing pulse repetition rates between 1/sec and 22/sec at up to 80 mJ of energy in the frequency doubled green line (0.532 m). The Quanta Ray DCR-1 laser produces a beam that has a so-called "donut" intensity distribution due to the laser cavity's unstable resonator configuration. Thus, a means was required to transform this intensity profile into a filled-in beam with a quasi-gaussian shape.

The optical system consisting of a transmitter and receiver stage is shown in Figure 1. In order to transform the beam intensity profile, a combination of a lens and spatial filter with a 150 micrometer aperture was used. The beam was then split into two paths with a beamsplitter. The object or information beam was reflected from the beamsplitter and expanded to overfill the schlieren mirror. With the foci of the expansion lens and schlieren mirror coinciding, a collimated beam was formed and transmitted through the wind tunnel test section. The object beam which was 46 cm in diameter was received by a second spherical schlieren mirror and refocused to the receiver stage. An additional lens was used to collimate the beam at an appropriate size for recording at the holographic plate holder.

Laser light transmitted through the beamsplitter was passed under the wind tunnel via a trench. Because of the long optical paths, a beam collimating system was provided to control the beam divergence. Optical path length matching was achieved with mirrors used to fold the beam within the trench. The reference beam was expanded and collimated to 90 mm in diameter at the receiver and directed onto the holographic plate.

The angle of intersection of the object and reference beams at the holographic plate was kept small enough to produce interference fringes that were within the spatial frequency resolution of the film. Beam intersection angle determines the

spatial carrier frequency which has variations due to the flow
field superimposed on it. Thus, an adequate margin on the
frequency is required to ensure adequate diffraction efficiency of
the holograms.

Point Diffraction Interferometer

A relatively new interferometry concept was investigated for
feasibility in compressible flow applications. The method was
attractive in that it presented the possibility of providing real-
time interferometric results.

The point diffraction interferometer (PDI) as described by
Smartt [11] is like some other forms of radial shear
interferometers insofar as it has the unique configuration wherein
the light is divided into two components to produce the test and
reference waves, _after_ passing through the test field. However,
the PDI is the only known concept capable of producing the
quantitative information on the light wave distortion directly.

With the PDI, the spherical reference wave is generated by
diffraction at a point discontinuity located in the path of the
beam. The discontinuity can be either a circular aperture or an
opaque disk. Figure 2 illustrates the principle of operation.
The aperture (or opaque disk) is located at the image of the
wavefront to be analyzed. In the embodiment proposed by Smartt,
an aperture in an absorbing film or an otherwise nondiffracting

substrate was used. Light incident upon the film and aperture is transmitted with a reduction in amplitude while the aperture produces a spherical diffracted wave. If the aperture is sufficiently small, a spherical diffracted wave is produced which will then interfere with the entire transmitted test wave.

Movement of the aperture along the optical axis away from the focal plane will produce circular fringes. Lateral movement of the aperture can be used to produce linear fringes for finite fringe operation. Deliberate displacement of the aperture will reduce the intensity of the diffracted wave which, in turn, reduces the visibility of the resulting fringes.

The important parameters effecting the visibility of the resulting fringes are the aperture size and the relative film and aperture transmittances. The cone angle defined by the first minimum in the diffraction pattern should be greater than that of the receiver system. These requirements can be satisfied with the proper selection of the aperture size. However, in the special case of fluid dynamics applications, where the wave distortions are expected to be large, the fulfillment of these requirements will become more difficult.

Another requirement that is specific to fluid dynamics applications is the need for very short duration exposures to freeze the motions in the flow field. Short exposures, in turn, demand the use of high power continuous wave (CW) or pulse

lasers. The use of substrates with apertures or disks cannot withstand such high energy levels. Our preliminary tests demonstrated that, even at very low energy levels, the pulsed laser burned holes in the substrates rendering the device inoperable.

Because of the large range of wave distortions present in fluid dynamics applications, a greater range of amplitudes in the diffracted and transmitted waves will occur. The distribution of energy incident upon the aperture will be significantly reduced when the focused beam is spread as a result of the flow field turbulence and refractive gradients in the inviscid flow. With relatively weak disturbances to the wavefronts, a greater amount of energy will be focused onto the aperture resulting in a greater amplitude in the diffracted wave. The resulting changes in the amplitudes of the focused beam will produce large variations in the relative intensities of the object and reference waves which will reduce the visibility of the interference fringe pattern, possibly to an extent where the pattern may be imperceptible. Some of these difficulties can be corrected by changes in the size of the aperture and the relative absorption of the substrate. However, if the aperture is too large, the diffracted cone of light will be too narrow and some of the distorted wave could appear on the diffracted wave. By increasing the absorption of

the substrate the possibility of burning it out is increased and there may be insufficient energy for the high speed recordings.

Clearly, the advantages of the technique which include relative simplicity of operation, insensitivity to vibration, and the opportunity for real-time recording suggested that attempts to modify the concept were worthy of attention. The aforementioned limitations to the application of the method in fluid dynamics research could be solved by redesigning the optical configuration.

A great deal of flexibility in the operation of the method was achieved with the optical configuration shown in Figure 3. A similar concept was also considered by Howes [13]. The layout of the system was the same as for a schlieren system up to the receiver section. Either a CW or pulse laser could be used as the light source. Because the path lengths can be carefully matched, in principle, a white light source could also be used. The light beam must be spatially filtered and expanded to fill the lenses or mirrors of the transmitter system to form a collimated beam. The field to be tested is located in the beam path, as with a conventional schlieren system. The receiver mirror serves to focus the light after passing through the test section. At the receiver, the beam was split into two optical paths with a beamsplitter. The transmitted beam was spatially filtered to remove the high spatial frequencies which were produced by the refractive field in the test section. This diffracted beam forms

the reference wave. The reflected beam retains the wave distortion information produced by the refractive field. It was then recombined with the reference wave. This section of the system was aligned in the same manner as a common Mach-Zehnder interferometer. However, optical components on the receiver section were made very compact and were rigidly mounted such that vibration was no more serious than for a schlieren system.

Inasmuch as this configuration complicates the technique, it also offered the needed flexibility for the application of the method in fluid dynamics investigations. First of all, the use of two separate optical paths allowed the reduction of energy incident upon the aperture. The apertures could now consist of pinholes that would withstand the high energy levels and which were commerically available. Because of the losses involved in the filtering process, a variable beamsplitter was used instead of an absorbing substrate to maximize the use of the available light. Additional attenuation may be introduced to maximize the visibility of the interference fringe pattern and, hence, the signal-to-noise ratio. Both the transmitted and reflected images produced by the beamsplitter may be exploited. One image can be used for real-time viewing while the other is being recorded.

The description of the amplitude and angular distribution of light scattered by a circular aperture used in the interferometer can be approximated by the Fraunhofer diffraction theory as

$$I_{sca}(\Theta, d) = I_0 \left(\frac{\pi d^2}{4\lambda} \right)^2 \left[\frac{J_1 \left(\frac{\pi d}{\lambda} \sin \Theta \right)}{\left(\frac{\pi d}{\lambda} \sin \Theta \right)} \right]^2$$

where Θ is the scattering angle measured from the incident beam, I_O is the incident beam intensity at the aperture, d is the aperture damager, λ is the laser wavelength, and J_1 is the first order Bessel's function of the first kind. Using this expression, the diffraction pattern can be matched to the numerical aperture of the collimating lens of Figure 3. Estimates of the relative intensities of the reference and object wave were also made.

The method was tested in the laboratory by introducing phase shifts in the beam, optically filtering it and then interfering the filtered wave with a test wave that was spherical or planar as appropriate. With this procedure, the filtering was evaluated under controlled levels of distortion on the incident waves. The relative transmission efficiency was measured. Several combinations of transform lenses and apertures were considered in the analysis. The controlling parameter was the intensity incident upon the pinhole. A short focal length lens would increase the intensity but would accelerate the burnout of the pinhole. On the other hand, a long focal length lens and larger pinhole would require a much longer focal length lens to collimate

the filtered reference beam at a diameter large enough to overlap the object or data beam.

These considerations also affected the selection of the recording media. In the early stages of the investigation, polaroid, 4" X 5" sheet, 16mm movie, and 35mm film was used. Estimates of the film resolution were made based upon the previous work with holographic interferometry. For example, the fringe spacing in the boundary layer of a supercritical airfoil was approximately 0.5mm. If the entire field of view was recorded (450mm), the approximate resolution for 4" X 5" film would be 10 lines per mm. On 35mm film, this represents a spatial resolution of approximately 30 lines per mm. Using 16 mm movie film, the resolution must be approximately 60 lines per mm. This is at the resolution limit of conventional films. High speed film generally has large grain size and lower resolution.

Thus, it was important to maximize the intensity on the pinhole in order to relax the requirements on the recording media. In an effort to mitigate this requirement, it was instructive to recognize that the scattered intensity (intensity of the reference) beam increases as the square of the aperture diameter. It is also known from diffraction theory that the angular distribution of the scattered light decreases as 1/d (eg. $\omega \approx \frac{1.22 \pi R}{d}$). If the aperture diameter and distance to the point of observation was increased by a factor of two, the area of

the reference beam would remain essentially the same. However, the intensity was increased by a factor of 4. The aperture size is limited by the relative distortion on the incident beam. If the aperture is too large relative to the focused incident beam, the diffracted wave will carry a distorted component of the incident wave.

Further parametric studies of the optical filtering are being carried out in the continuation of the research program. Optimization of the filtering aperture requires considerations that include pinhole survival, spatial filtering, reference beam intensity, and susceptibility to misalignment.

Data Reduction

Obtaining quantitative results from the interferograms is straightfoward for two-dimensional flows. The pathlength through the wind tunnel in the present case was 61 cm so the density changes at the test flow Mach numbers was sufficient to produce an optimum number of interference fringes in the infinite fringe mode. Using the infinite fringe mode has the advantage that the fringes produce a direct mapping of the constant density contours.

Evaluation of the density change per fringe can be determined using the following relationships. In an inhomogeneous density test field the phase shift of the light wave is

$$\left(\frac{\Delta\phi}{2\pi}\right) = \frac{1}{\lambda} \int_{\zeta}^{\zeta_1} [n(x,y) - n_o]dz$$

where   is the laser wavelength and n is the index of refraction. When the interferometer is aligned in the infinite fringe mode, the equation of the fringes is

$$\int_{\zeta}^{\zeta_1} [n(x,y) - n_o]dz = N\lambda$$

where N is an integer. Applying the Gladstone-Dale Constant relating phase variation to density, the integrated relationship is

$$\rho(x,y) = \rho_o + \frac{N\lambda}{KL}$$

The constant values used in the tests to be described were:

$$L = 609.6 \text{ mm}$$

$$= 0.532 \ \mu m$$

$$K = 0.226 \ (gm/cm^3)^{-1}$$

$$\frac{\lambda}{KL} = \frac{0.532 \times 10^{-3} \text{ mm}}{0.226 \ (gm/cm^3)^{-1} \ 609.6 \text{ mm}}$$

Combining the constants and adjusting for the wall boundary layers result in:

$$\rho_1 - \rho_0 = 2.46 \times 10^{-4} \frac{\text{lbm/ft}^3}{\text{fringe}}$$

It remained to identify a particular fringe to be used as the reference with its corresponding density. This was done in several ways. If there was a region of undisturbed flow in the field of view, the wind-tunnel conditions could be used. Unfortunately, this was not generally the case. Instead, a surface pressure measurement was converted to density by using the total temperature, T_0, and the total pressure, P_0. Another independent reference could be obtained from the inviscid flow velocity measured with the laser velocimeter, for example.

Flow Fields Investigated

The experiments which produced the examples in this paper were conducted in the Ames 2-by-2-foot Transonic Wind Tunnel. This tunnel is a closed-return, variable density flow facility with 21% open porous-slotted upper and lower walls for transonic testing. The airfoils tested were a NACA 64A010, a Douglas Aircraft Corporation DSMA671 supercritical airfoil and several circulation control airfoils utilizing the Coanda effect. Wind tunnel test conditions ranged from a free-stream Mach number of

0.3 to 0.9 and chord Reynolds number of 10^6 to 2 x 10^6.
Transition strips were used on the upper and lower surfaces of the
airfoils to ensure fully developed turbulent flows.

3.0 Results and Discussions

Interferometry data were obtained over a range of conditions
and the quantitive results compared to measurements obtained by
other means. Because of the possible uncertainties in the
alignment of the reconstructed light waves, a series of tests were
deemed necessary to determine how accurately the waves could be
aligned to the infinite fringe mode.

Evaluation of the optical system was conducted using pairs of
holograms exposed with no flow in the wind tunnel. Reconstruction
of the two light waves and alignment of the waves to the infinite
fringe mode ideally should result in no fringes over the field of
view. Typically, one or two fringes would occur after careful
alignment. This was considered to be an acceptable level of error
considering the number of fringes present under the test
conditions.

Interferograms could not be trusted even for flow
visualization in the initial phase of the instrumentation
development. With the light wave over the entire field of view
disturbed due to the flow, Figure 4, the alignment of the

interferometer was uncertain. Thus, the interferometric results were reduced to basic flow parameters and compared to measurements with other means. The most readily available and reliable data is the surface pressure distribution.

With the assumption of isentropic flow, the densities measured from the interferograms were reduced to surface pressure coefficient by the relationship

$$C_p = \frac{2}{\gamma M_\infty^2}\left[\left(\frac{P}{P_t}\right)\left(\frac{P_t}{P_\infty}\right) - 1\right]$$

and

$$\frac{P}{P_t} = \left(\frac{\rho}{\rho_t}\right)^\gamma$$

where M_∞ is the freestream Mach number, $\gamma = 1.4$, and P_t and ρ_t are the pressure and density at the stagnation conditions. The density of one of the fringes was identified using a pressure measurement at one point in the flow. Fringes were then simply counted from the reference to obtain the density at each point in the flow field.

Agreement between the measured surface pressure and the interferometric data, Figure 5 was generally very good which confirmed the interferometric results. It should be recognized

corrected downstream total pressure offered only a slight improvement in the pressure distribution.

Experiments were also conducted on supercritical airfoils for the Douglas Aircraft Corporation [7], Figure 8. Supercritical airfoils characteristically have flat upper surfaces to maintain shock-free flow or to hold the shock well aft on the airfoil. The trailing edge had a lower surface concavity which produced a relatively large aft loading. Comparisons to the 64A010 airfoil showed that the closed fringe contours in the primary inviscid flow were symmetrically located above and below the trailing edge. By contrast, the closed contours were displaced streamwise in the interferograms corresponding to the supercritical airfoils, indicating local maxima of pressure both in the lower-surface concavity and downstream of the trailing edge on the upper surface of the near wake.

The interferogram data provided static pressure distributions at the outer edges of the boundary layer and near wake, Figure 9, which are difficult to measure by other techniques. Significant static pressure gradients normal to the streamlines could be present in the near wake flows produced by supercritical airfoils. Pressure variations also occurred across the lower-surface boundary layer in the lower surface concavity. These data were used to correct the boundary layer and wake profile measurements using pitot and static pressure probe measurements.

that the surface pressure data represents time-averaged results obtained at points on the midspan of the airfoil. The interferometric results were spatially averaged over the span of the airfoil but recorded at an instant in time. Thus, the good agreement in the results also confirmed the relative two-dimensionality of the flow. A small difference in the data have occurred in the neighborhood of the shock. This was due to the interaction of the shock with the sidewall boundary layers. The interaction typically causes the shock to move forward at the sidewalls.

At an airfoil angle of attack of 3.5° wherein the shock was relatively strong, there was a concern with the loss of total pressure across the shock producing errors in the data. However, the good agreement with the pressure data verified that the total pressure loss across the shock and, hence, the change in entropy, was insignificant. With an increased angle of attack to 6.2°, Figure 6, massive shock-induced separation occurred. There was uncertainty as to whether the interferometric data obtained at the outer edge of the separated boundary layer would provide an accurate representation of the surface pressure in such cases. However, the results shown in Figure 7 demonstrated the very good agreement achieved even with a strong shock and severe flow separation. An estimation of the shock strength was made to obtain an estimation of the loss in total pressure. Using the

Once the relative accuracy of the interferometry data was confirmed, the Mach contours determined from

$$\frac{\rho}{\rho_t} = \left(1 + \frac{\gamma-1}{2} M^2\right)^{-\frac{1}{\gamma-1}}$$

were traced from the interferograms. The Mach contours provide a quantitative mapping of the global features of the flow and are valuable for comparisons to numerical predictions of the inviscid flow field.

The flow speed was determined from the density distribution using the assumption of isentropic flow of a perfect gas and the relationship

$$\frac{V}{c_t} = \left[\frac{2}{\gamma-1}\left(1 - \left(\frac{\rho}{\rho_t}\right)^{\gamma-1}\right)\right]^{\frac{1}{2}}$$

where c_t is the speed of sound at the stagnation or total conditions. Figure 10 shows the flow speed data compared to laser Doppler velocimeter measurements. The results were in very good agreement indicating that flow speed measurements could be easily obtained for the inviscid flow. This represents an efficient

means for mapping the flow speed when coupled with the laser Doppler velocimeter to obtain flow angle information where this parameter cannot be inferred from the model geometry.

Viscous flow information may also be obtained from the interferograms. One of the advantages of the interferometry method when applied to aerodynamics investigations is the ability to visualize the boundary layer and wake flows. This information can be used to direct the laser Doppler velocimeter or other probe methods to regions of interest in the flow. In addition to the flow visualization, flow speed within the viscous layer may also be obtained. Assuming constant pressure across the layer, Crocco's relationship given by

$$\frac{T}{T_e} = 1 + r \frac{\gamma-1}{2} M_e^2 \left[1 - \left(\frac{U}{U_e}\right)^2 \right] + \frac{T_w - T_{ad}}{T_e} \left(1 - \frac{U}{U_e} \right)$$

and the perfect gas law. T_e, T_{ad}, and T_w are the edge, adiabatic, and wall temperatures, and r is the turbulent recovery factor which is set equal to 0.88.

Comparisons were made to boundary layer and wake profiles measured with pitot probes and the laser Doppler velocimeter. Representative results obtained on the supercritical airfoil, Figure 8, are presented in Figure 11. Overall, the measurements

were in good agreement. However, the differences in the minimum flow speed regions may have been due to slight three-dimensionality in the wake and to the reduced sensitivity of the interferometer in this region. At low flow speeds, the density change is very small with variation in velocity.

A program of testing was performed to evaluate circulation control airfoils utilizing the Coanda effect. Circulation control airfoils produce a rather complex flow field that is associated with the high speed jet interacting with the turbulent boundary layer. Although the entire flow field was of interest, attention was focused on the jet flow entrainment mechanisms at the trailing edge. This region of flow does not lend itself to measurements by probes or the laser Doppler velocimeter because of the small scales involved and the proximity to a reflecting surface.

Holographic interferometry data were obtained over a wide range of parameters including Mach numbers, Reynolds numbers, angles of attack, and Coanda blowing pressures [13]. Because of the very large lift coefficients produced and the interaction of the Coanda jet with the sidewall boundary layers, there was justifiable concern with three-dimensionality in the flow. As in the previously described investigations, comparisons of the interferometric data to surface pressure measurements were used to evaluate the results. The results were found to be in very good agreement except over the Coanda jet. In this region, there was a

substantial normal pressure gradient between the inner and outer parts of the jet. Thus, the differences were expected and acutally provided a means for determining the normal pressure gradient.

In the absence of blowing, the boundary layers separated from the airfoils at approximately the tangency points where the change in body curvature began for the blunt trailing edge. With Coanda blowing the flow remained attached much further around the trailing edge. This movement of the rear stagnation point produced increased circulation. Circulation typically increases with increased blowing until stall occurs. One type of stall that occurred was a result of jet detachment which was documented in this work.

The degree of jet mixing that takes place determines the ability of the jet to entrain the external flow. How effective this entrainment process is, depends upon the character of the incident turbulent boundary layer. Upstream shock strength, compression waves and the trailing edge pressure gradient produced by the airfoil geometry will thus influence the efficiency of the Coanda jet. These pheomena were effectively visualized using the interferometry techniques and quantitative results were correlated with the airfoil performance. Only the preliminary results of these investigations can be presented since the remaining data

have been classified because of their importance to the DARPA X-Wing Program.

Figure 12 is a typical example of the flow fields studied. The airfoils are typically elliptic in shape with or without camber. With blowing, the flows revealed a very high streamwise pressure gradient at the trailing edge as indicated by the close spacing of the fringes in that area. The local pressure maxima represented by the center of the concentric fringe patterns moved upstream to the trailing edge of the airfoil as the blowing was increased. The rear stagnation point became localized and was observed to move around the trailing edge.

Interferometry provided a very efficient means for visualizing the details of the flow at the trailing edge of the airfoil. Figures 13 a and b show typical results for the unblown (13a) and the blown (13b) cases. The fringes running essentially parallel to the flow represent the boundary layer and the small notch on the upper surface is the blowing slot (h=250 micro-meters). Without blowing, the boundary layers separated from the airfoil and produced a large wake. When blowing was introduced, the boundary layer became entrained by the jet. The jet is clearly visible around the trailing edge. The ability to visualize these features of the flow and obtain incident boundary layer data is valuable to the aerodynamicists and the

computational fluid dynamacists attempting to predict these flow fields.

The real-time point diffraction interferometry method was also used in this series of tests. However, before implementing the method in the wind tunnel, several laboratory tests were conducted to ensure that the results produced were reliable. Comparisons of interferograms obtained using holography were made for simple free convection flows (Figure 14). The results were essentially identical. One significant advantage of the real-time interferometer was the speed with which the results could be obtained. Using Polaroid film, the real-time interferogram was available in a matter of seconds whereas the holographic interferometer required approximately 20 minutes.

A makeshift optical system for the PDI method was installed on the Ames 2-by-2-foot transonic tunnel. Both the Nd:YAG laser and an 18-watt Argon-ion CW laser were alternately used as the light source. A high speed movie camera was used to record the interferometric data. No special vibration isolation equipment was required even in the wind tunnel environment.

Real-time viewing of the interferometry results proved to be an excellent means for visualizing the flow field phenomena. Dynamic events such as the vortex shedding and the turbulent interactions of the Coanda jet and the boundary layer are often lost when recorded on single exposures. Relative motion between

225

the various parts of the flow provided the added dimension needed
to better understand the flow behavior. Although not recognized
in the still images, large scale aperiodic shedding of vorticity
was clearly visible at certain flow conditions. Recordings of
these flow phenomena were made on movie film at 400 frames per
second. This framing rate and shutter speed were adequate in
preventing the blurring of the fringe patterns as a result of flow
field unsteadiness.

Unfortunately, these results have been classified as
proprietary by NASA and, thus, were not available for this report.

4.0 Summary and Conclusions

Although holographic interferometry was previously used for
flow field visualization and to obtain some quantitative results
in small wind tunnels (13 cm X 13 cm), it had not been utilized
in full scale facilities. The program of research on transonic
flow fields conducted at the NASA Ames Research Center was
successful in demonstrating the potential of the interferometry
techniques. Because the interferometry data from the two-
dimensional flows was easy to interpret and reduce to quantitative
results, the reliability and accuracy of the method were easily
confirmed by comparison to measurements by other means. The
method provided detailed flow visualization of the entire flow

226

field and produced accurate results for both the inviscid and viscous flow.

A new interferometry method was developed and applied to flow field investigations. The method promises to provide a valuable alternative to holographic interferometry for practical aerodynamics research. Real-time interferometric results made available with the method enhanced the level of detail available to the experimental fluid dynamicist.

Future development efforts are planned for improving the point diffraction interferometer (PDI) system. The availability of real-time interferometry and the very high data recording rates that can be achieved places added importance on data reduction techniques. Aerometrics personnel are currently investigating methods for reducing the interferometry results from the PDI on-line. Methods have been considered that can produce the quantitative results in essentially real time.

5.0 Acknowledgements

6.0 References

1. M. H. Horman, "An Application of Wavefront Reconstruction to Interferometry," Appl. Opt. 4, 333-336 (1965).

2. R. E. Brooks, L. O. Heflinger, and R. F. Wuerker, "Interferometry With a Holographically Reconstructed Comparison Beam," Appl. Phys. Letters, 7, 248-249 (1965).

3. L. O. Heflinger, R. F. Wuerker, and R. E. Brooks, "Holographic Interferometry," J. Appl. Phys., 37, 642-649 (1966).

4. J. D. Trolinger, "Laser Instrumentation for Flow Field Diagnostics," AGARD-AG-186, 1974.

5. W. D. Bachalo, and D. A. Johnson, "Laser Velocimetry and Holographic Interferometry Measurements in Transonic FLows," Laser Velocimetry and Particle Sizing," Hemisphere Publishing Corp., 1979, edited by H. Doyle Thompson and Warren H. Stevenson.

6. D. A. Johnson, and W. D. Bachalo, "Transonic Flow Past a Symmetrical Airfoil-Inviscid and Turbulent Flow Properties," AIAA Journal, 78-117R, Vol. 18, No. 1, January 1980, p. 16.

7. F. W. Spaid, and W. D. Bachalo, "Experiments on the Flow About a Supercritical Airfoil Including Holographic Interferometry," Journal of Aircraft, Vol. 18, No. 4, April 1981.

8. W. D. Bachalo, "An Experimental Investigation of Supercritical and Circulation Control Airfoils at Transonic Speeds Using Holographic Interferometry," AIAA Paper No. 83-1793, Danvers, Massachuetts, July 1983.

9. W. D. Bachalo, "An Experimental Investigation of Circulation Control Flow Fields Using Holographic Interferometry," NASA Contract Report CR 166482, 1982.

10. W. D. Bachalo and M. J. Houser, "A Real-Time Interformeter Technique for Compressible Flow Research," Paper No. 84-1600, AIAA 17th Fluid Dynamics, Plasma Dynamics and Laser Conference, Snowmass, Colorado, June 1984.

11. R. N. Smartt, "Special Applications of the Point-Diffraction Interferometer," SPIE, Vol. 192, Interferometry, 1979.

12. Walton L. Howes, "Large-aperture Interferometer with Local Reference Beam," Applied Optics, Vol. 23, No. 10, May 1984, p. 1467.

13. W. D. Bachalo, "Investigations of Circulation Control Airfoil Flow Fields at Transonic Speeds," NASA Contract Report 1983.

LIST OF FIGURES

231

Figure 11. Trailing-edge Boundary Layer and Wake Profiles.

Figure 12. Interferogram of the Circulation Control Airfoil Flow.

Figure 13. Enlargements of the Trailing-edge Flow Fields.

13a. Coanda Jet Off.

13b. Coanda Jet On.

Figure 14. Comparisons of Holographic and Point Diffraction
Interferometry
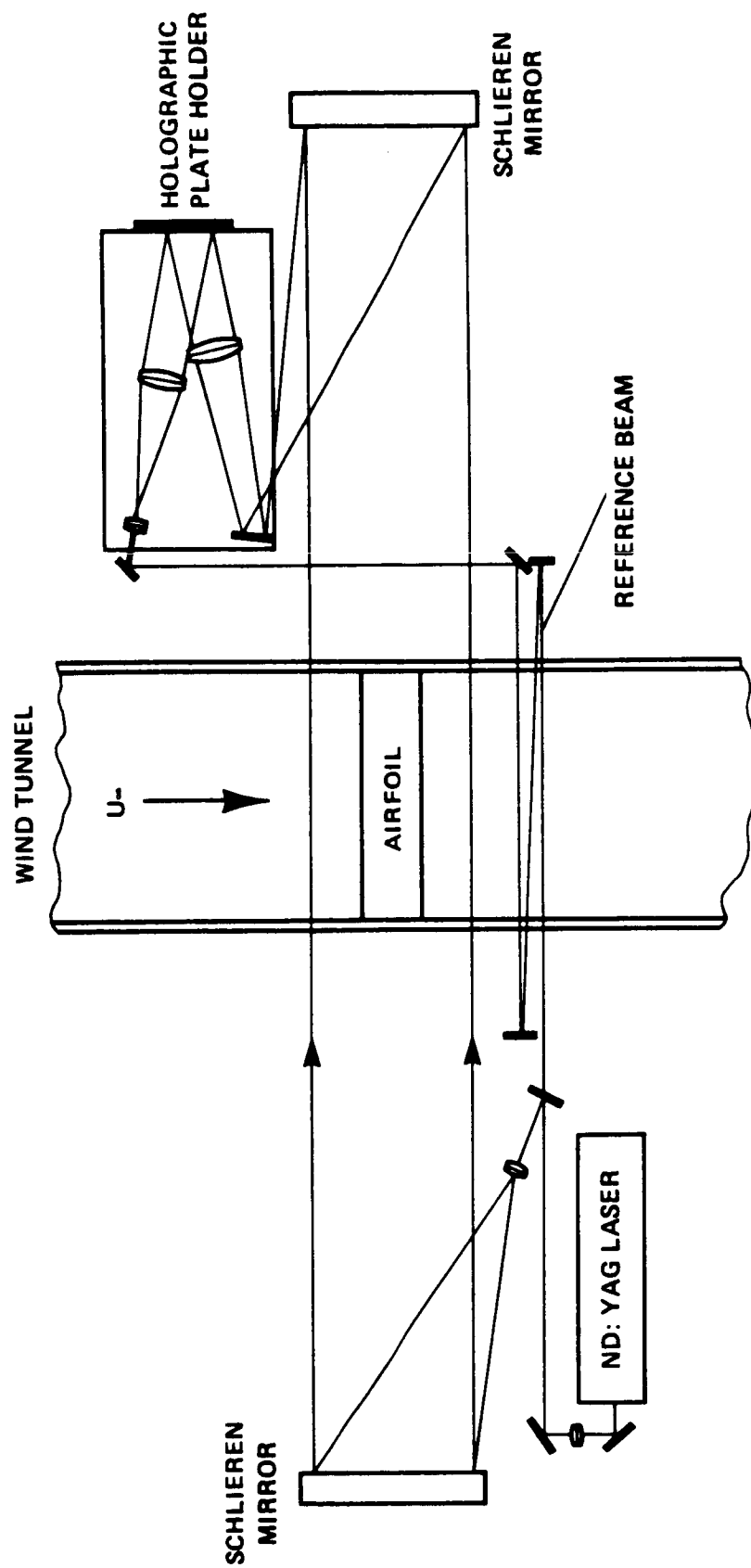
Figure 1. Schematic of the Ames Holographic Interferometer.

233

DIFFRACTED SPHERICAL
REFERENCE WAVEFRONT

TEST
WAVEFRONT

PDI
PLATE

TEST
WAVEFRONT

TEST SYSTEM
FOCAL PLANE

MICA

ABSORBING
THIN FILM

CIRCULAR
APERTURE
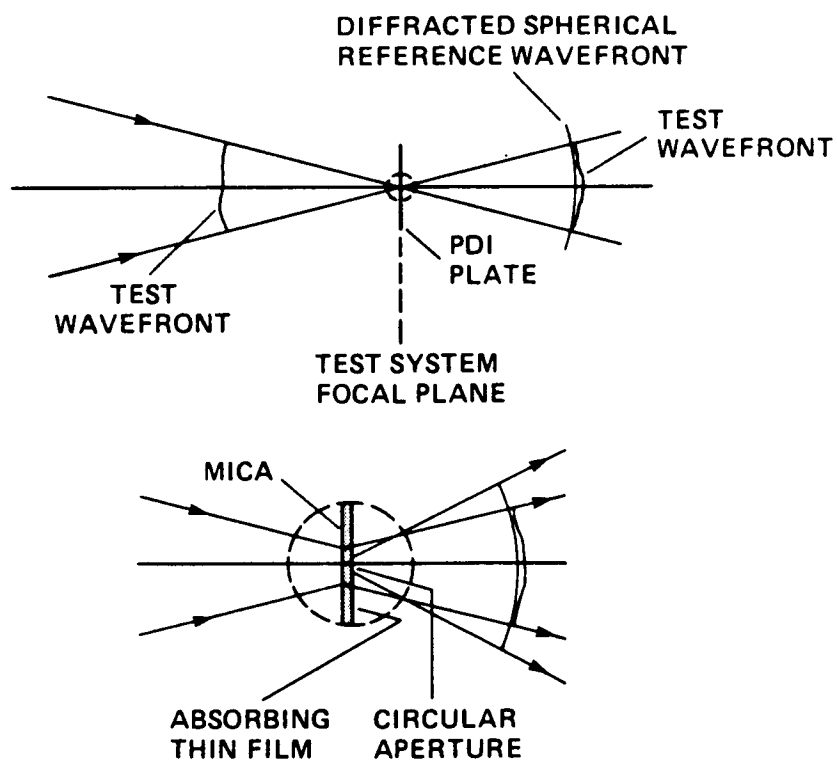
Figure 2.   Schematic of the Smartt Point Diffraction Interferometer.
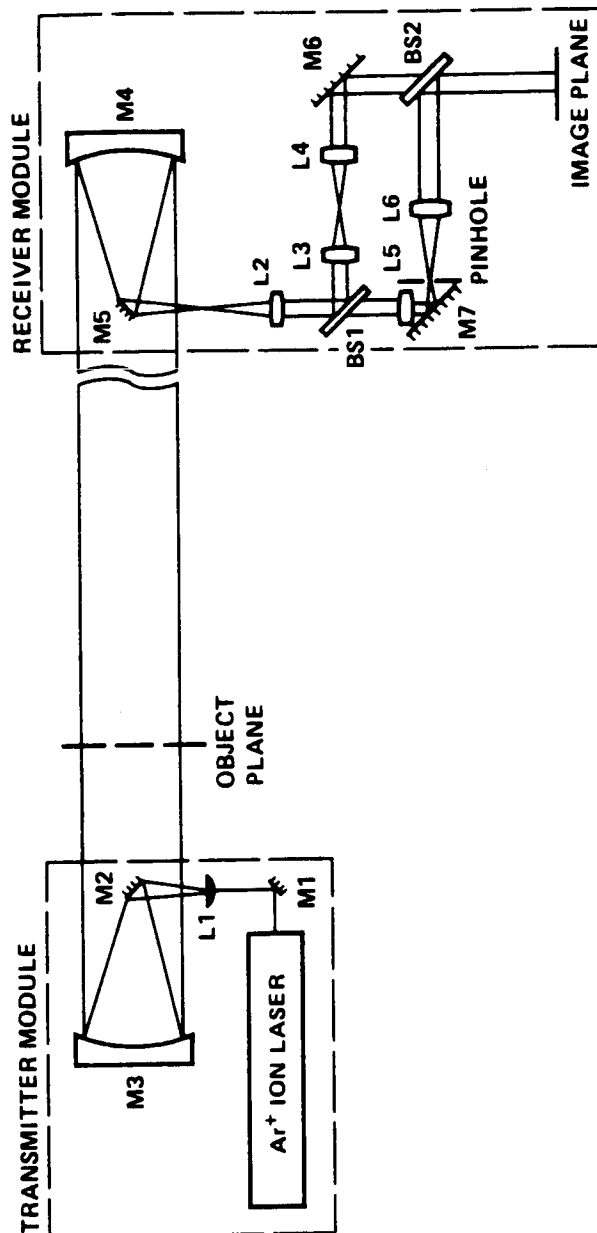
Figure 3. Schematic of the Improved Point Diffraction Interferometer.
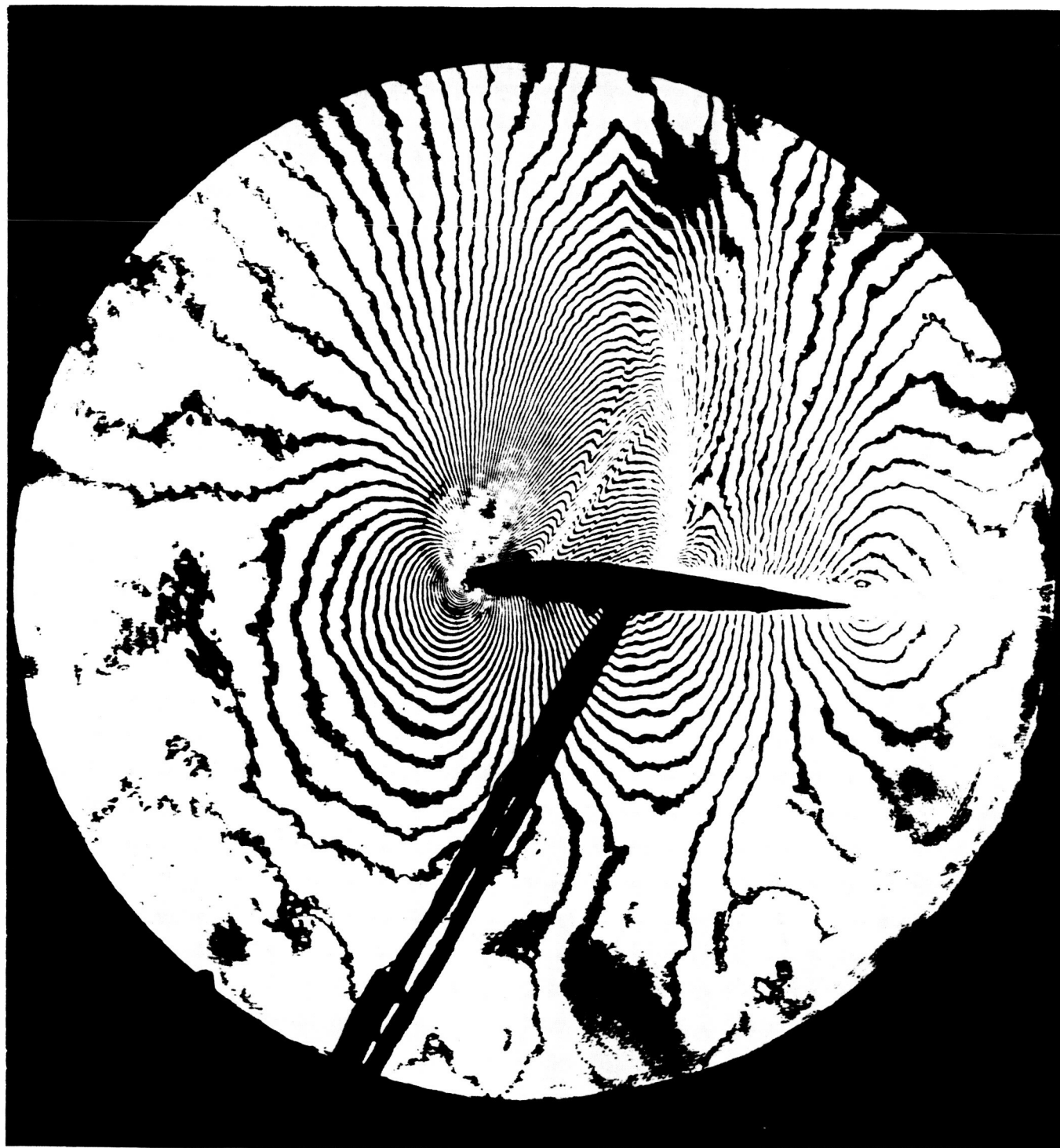
Figure 4.   Infinite – Fringe Interferogram of NACA 64A010 at M_∞ = 0.8, α = 3.5°.
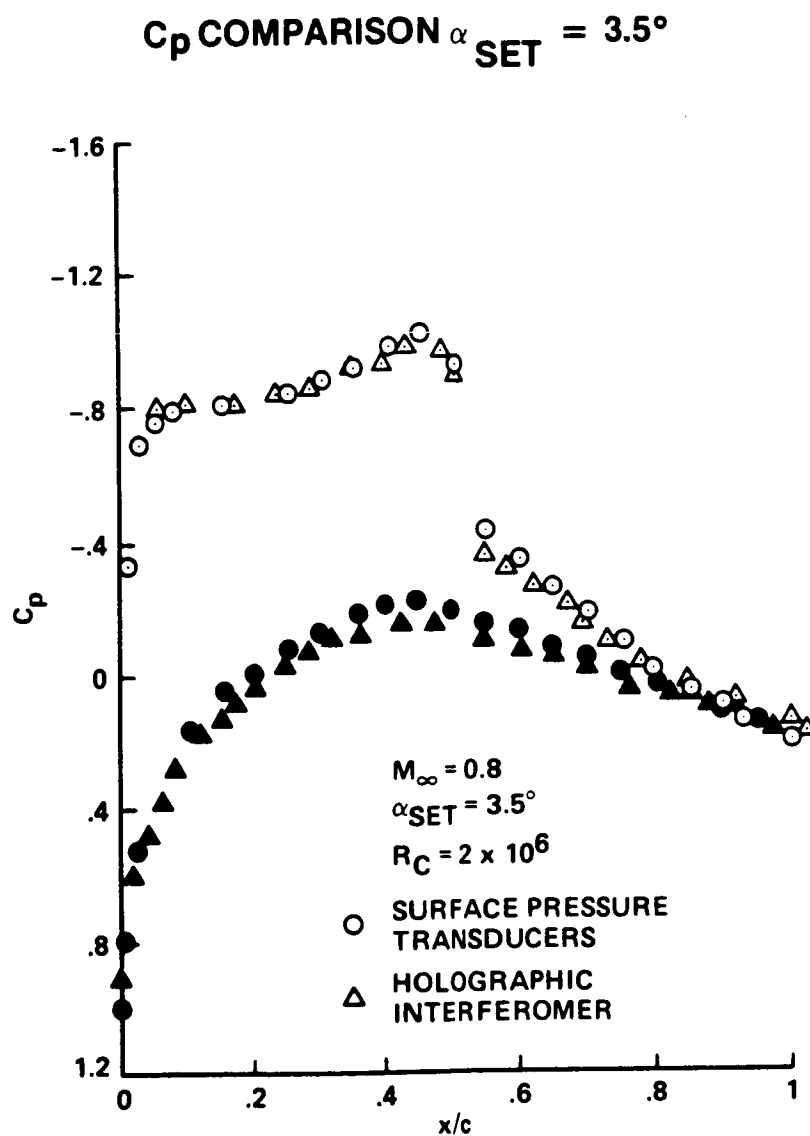
Figure 5.   Comparison of Boundary-layer Edge pressures with Surface Pressure.

237
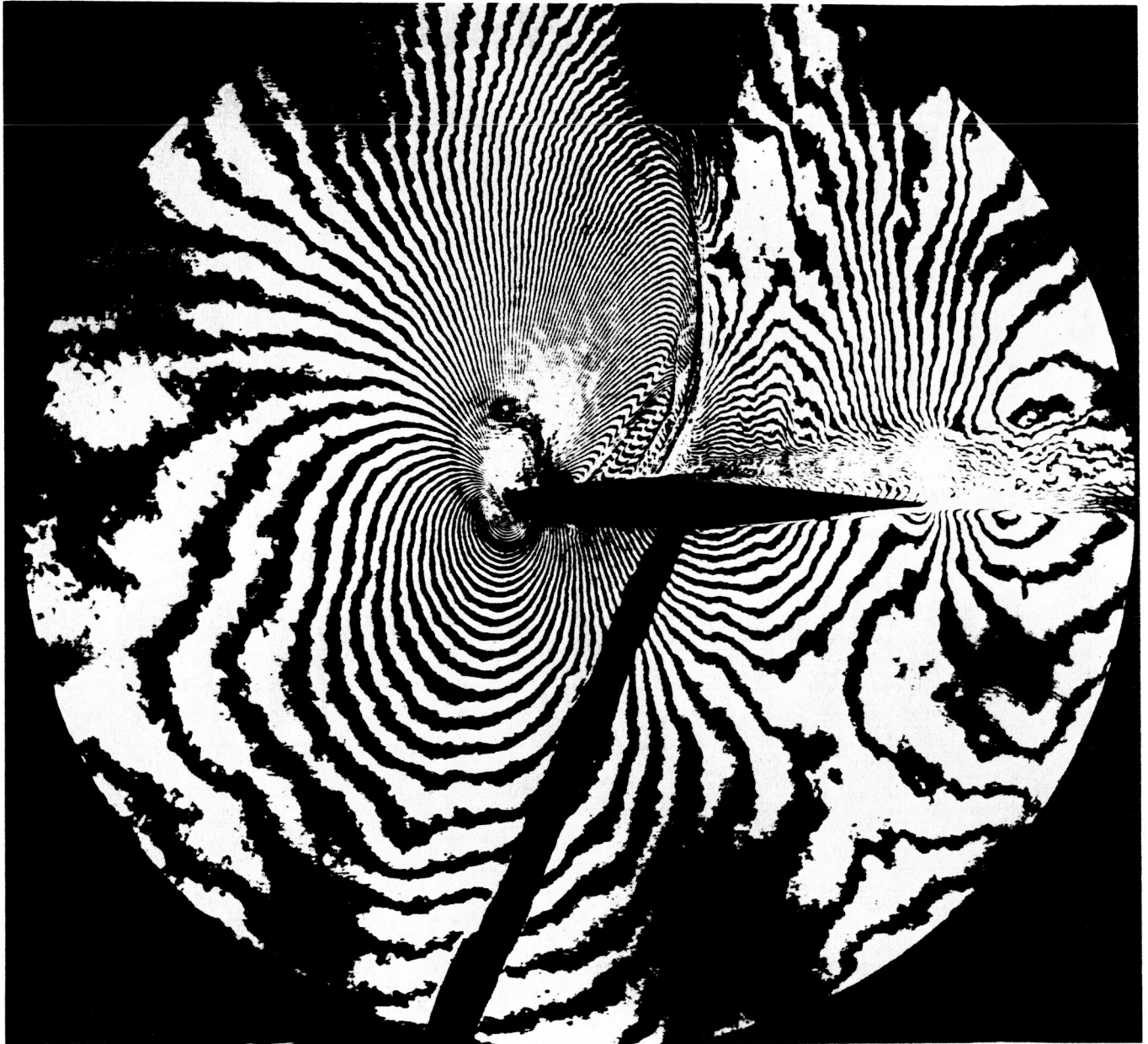
Figure 6. Infinite – Fringe Interferogram of NACA 64A010 at $M_{\infty} = 0.8$, $\alpha = 6.2°$

238

Cp COMPARISON α_{SET} = 6.2°

M_∞ = 0.8
α_{SET} = 6.2°
R_{e_c} = 2 x10⁶

NACA 64A010

○ SURFACE PRESSURE
    TRANSDUCER

△ HOLOGRAPHIC
    INTERFEROMETER

□ P_t LOSS CORRECTION
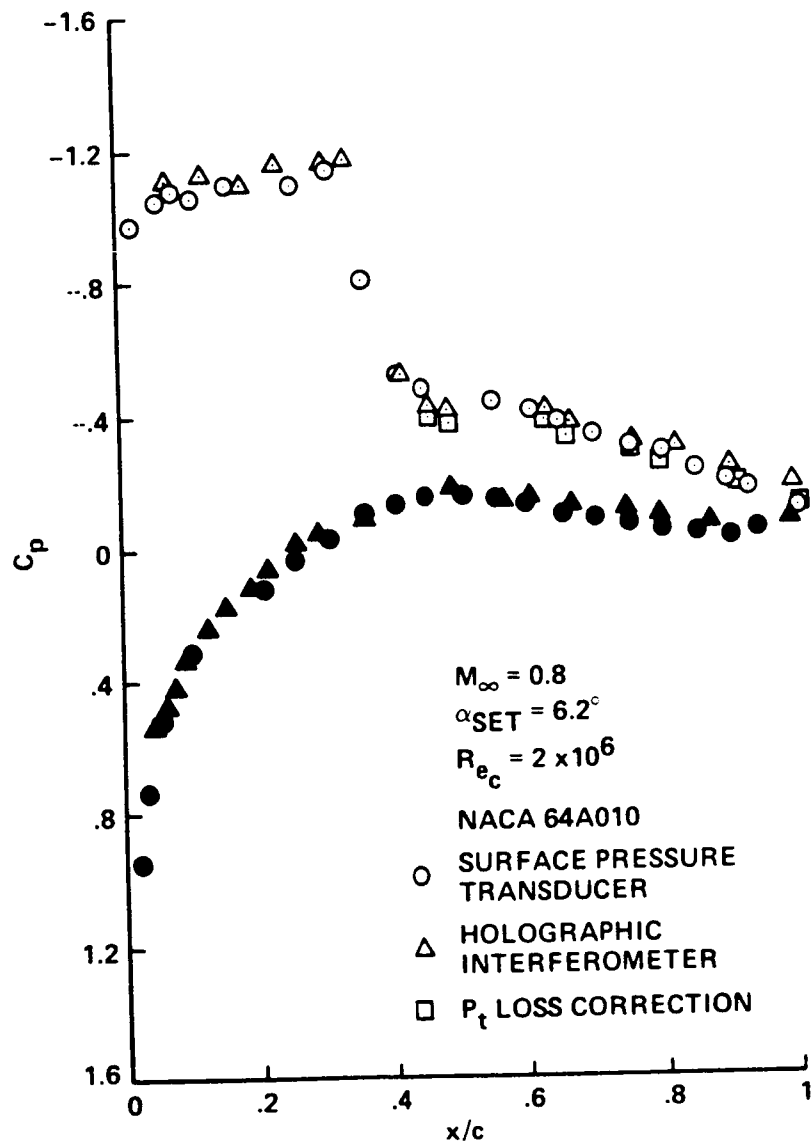
Figure 7.   Comparisons of Measured Surface Pressure Coefficients.

239
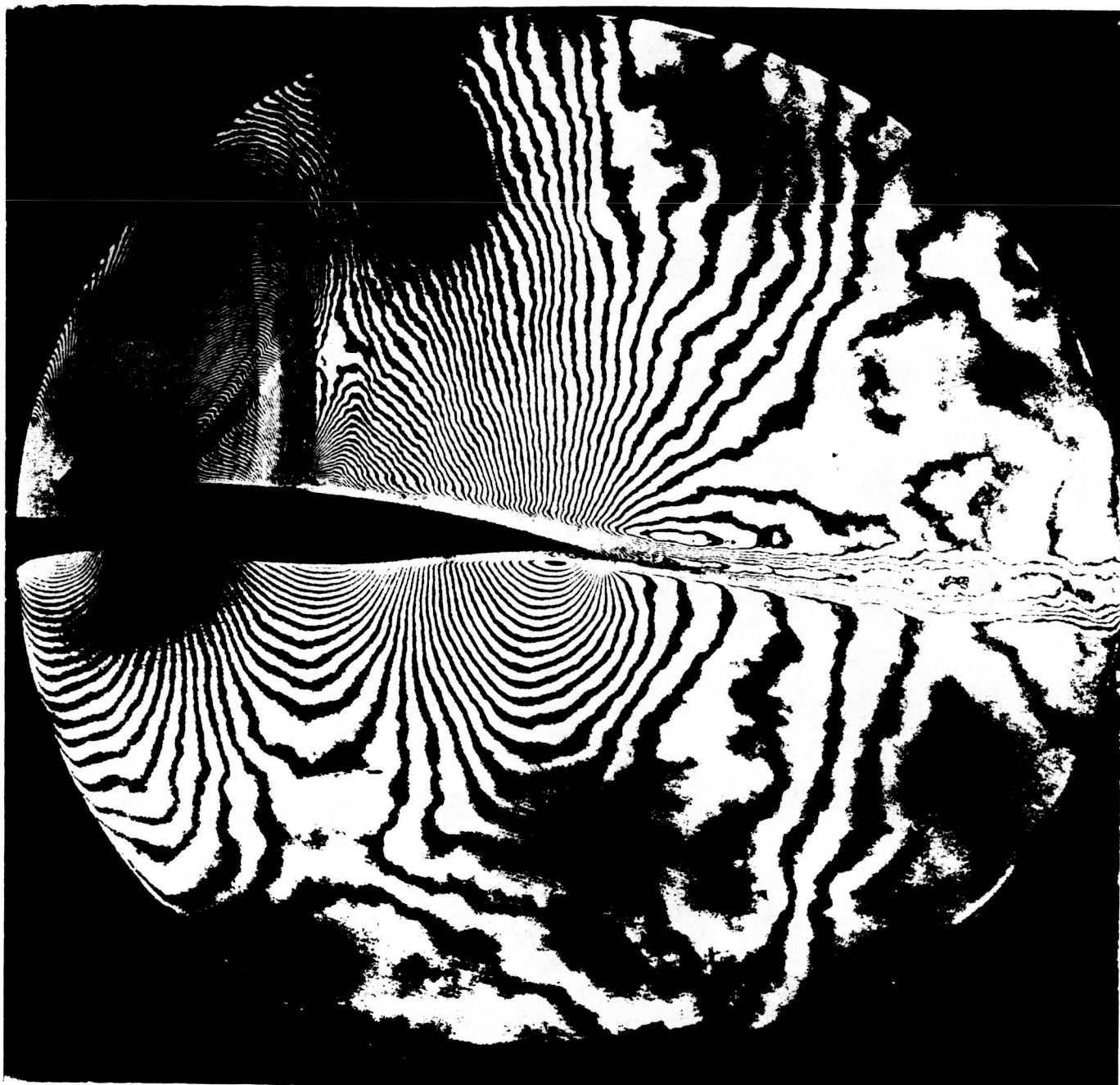
Figure 8.   Interferograms of DSMA 671 Supercritical Airfoil Flow Fields,

$M_\infty = 0.5$, $= 6.1^\circ$.
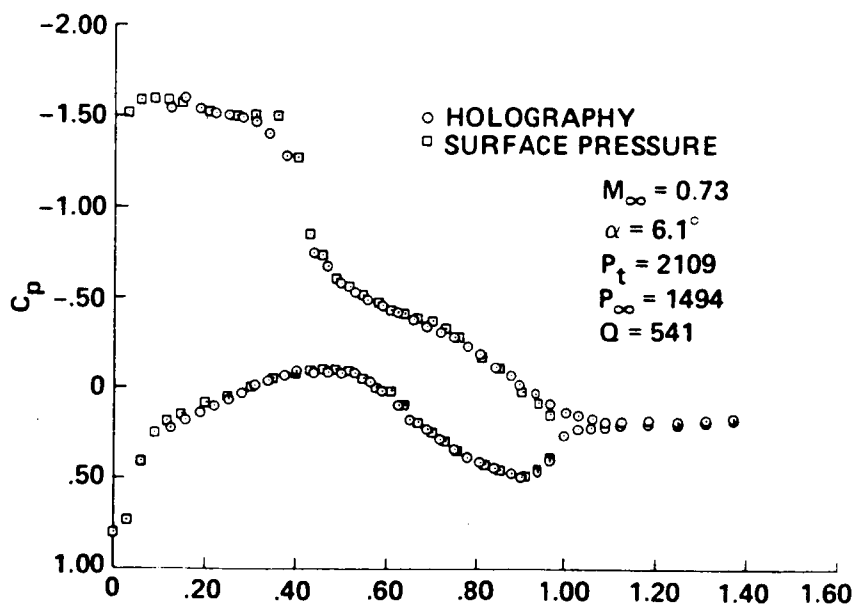
Figure 9.   Comparisons of Data from Static Pressure Orifices and Pressures
            Determined from the Interferograms.
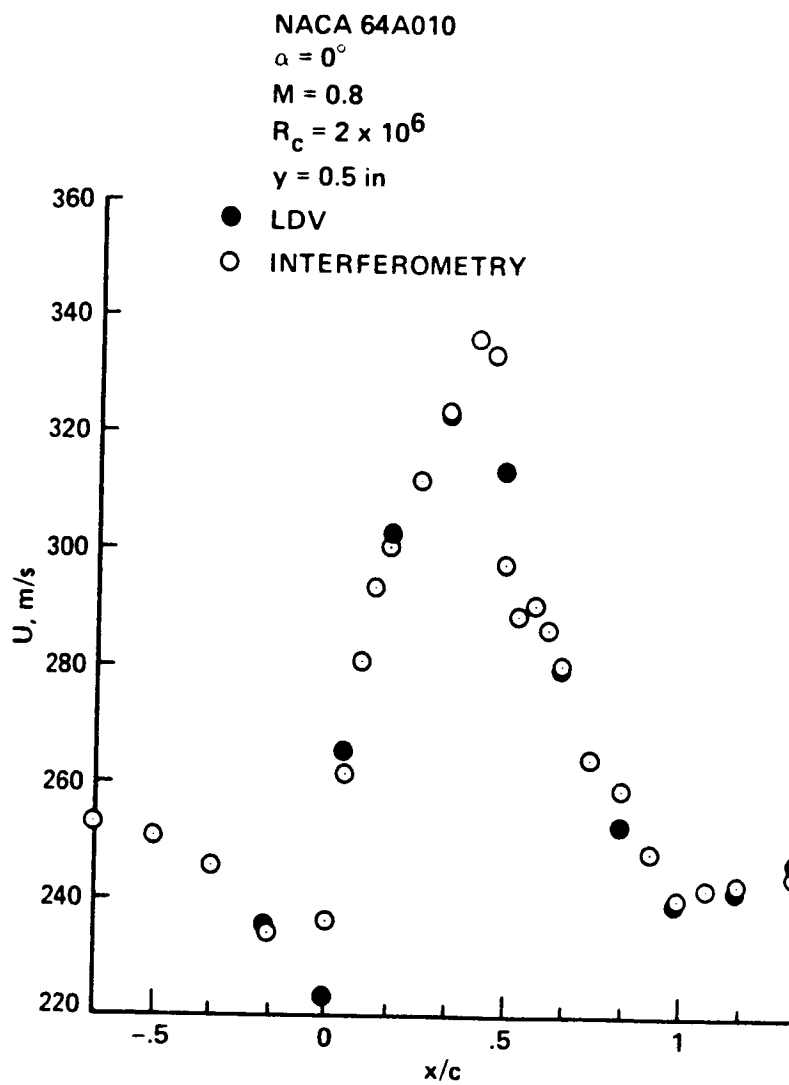
Figure 10. Flow Speed Distribution Measured with the Interferometer and the Laser Doppler Velocimeter.
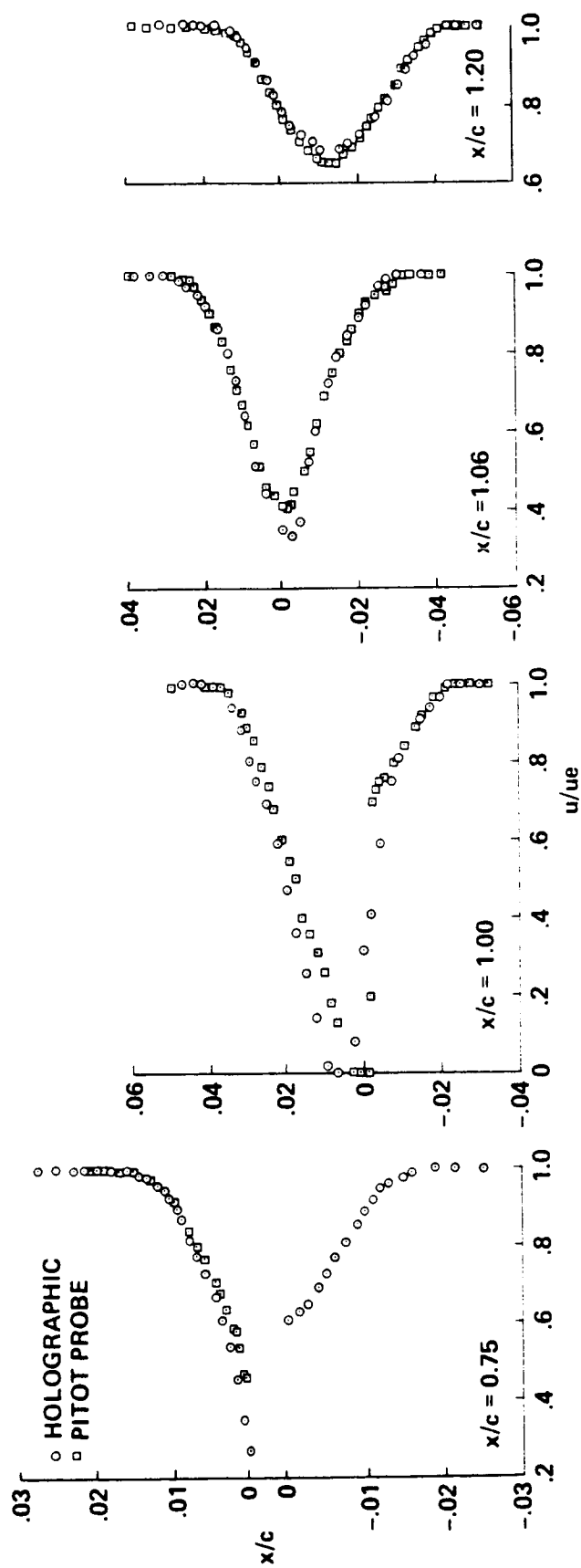
Figure 11. Trailing-edge Boundary Layer and Wake Profiles.

Figure 12. Interferogram of the Circulation Control Airfoil Flow.
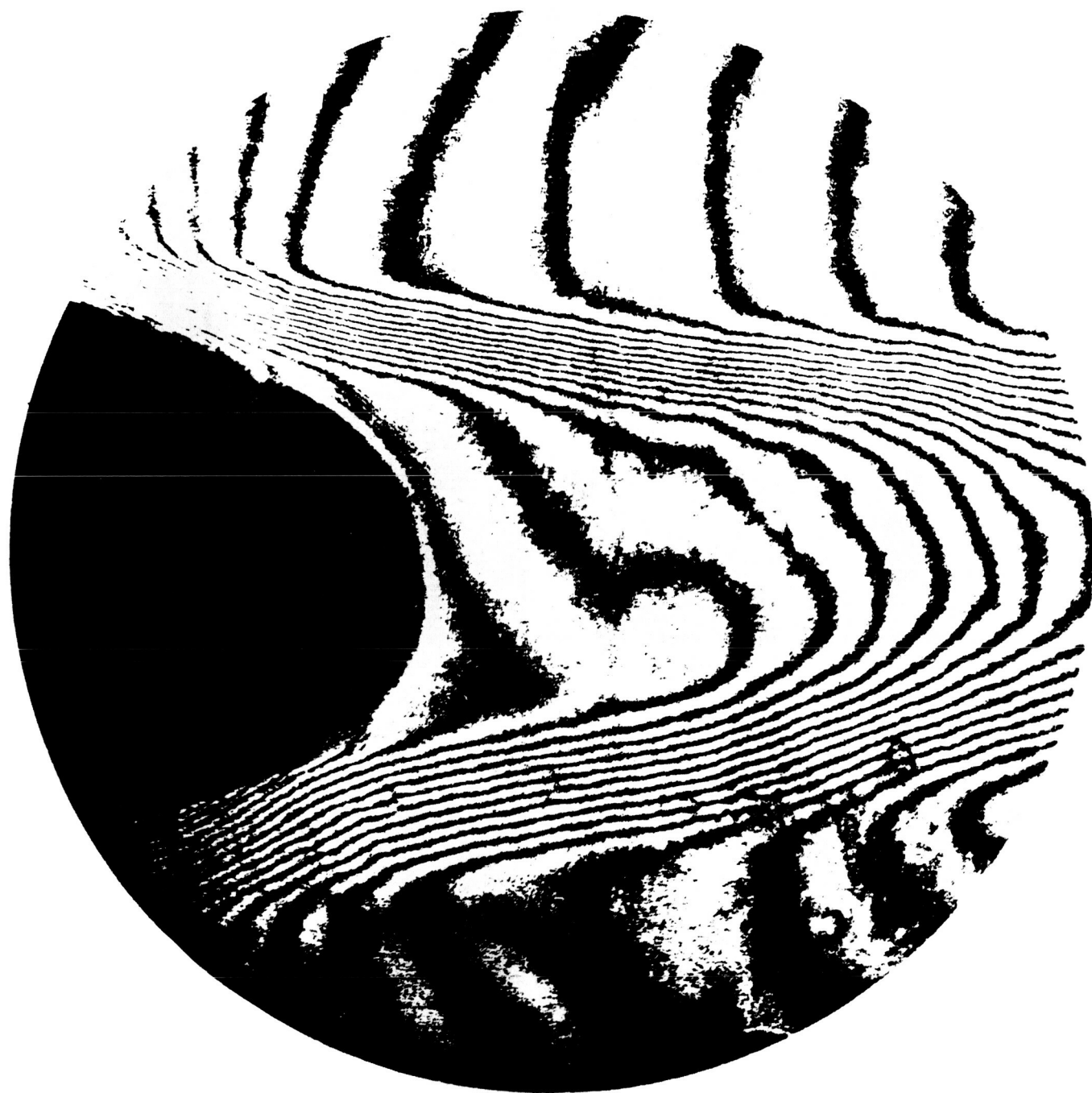
13a. Coanda Jet Off.

Figure 13. Enlargements of the Trailing-edge Flow Fields.

245

13b. Coanda Jet On.
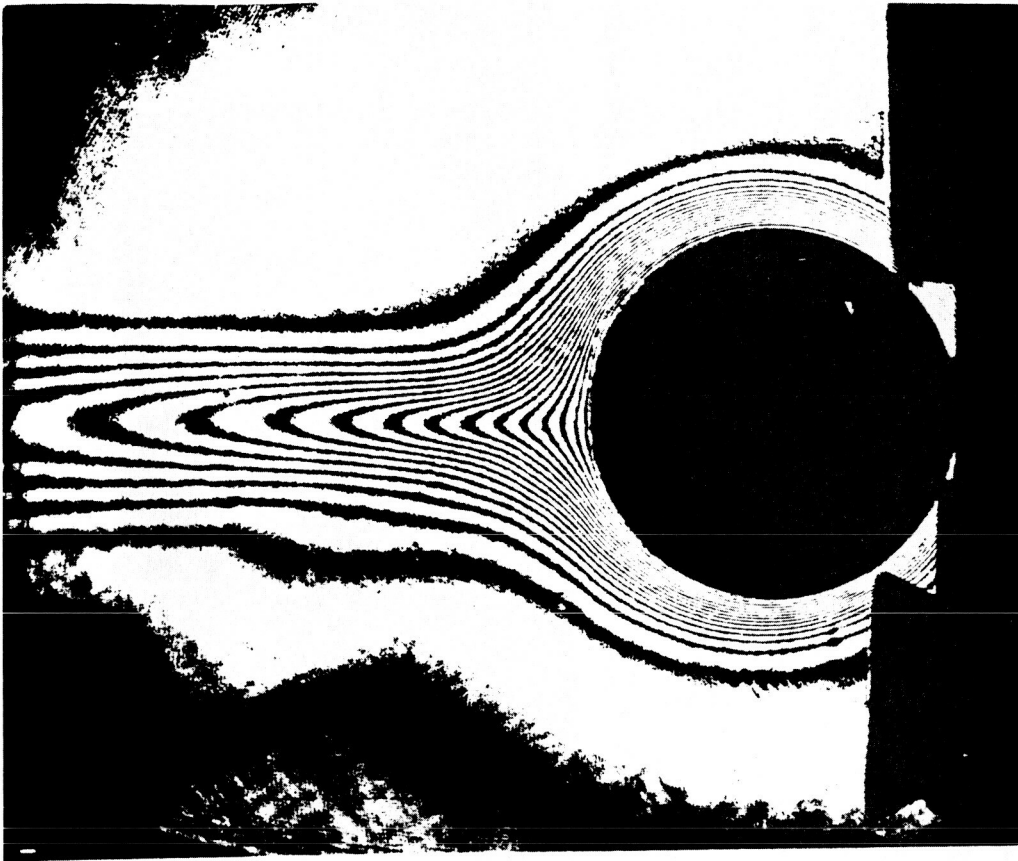
Holographic
Interferometry
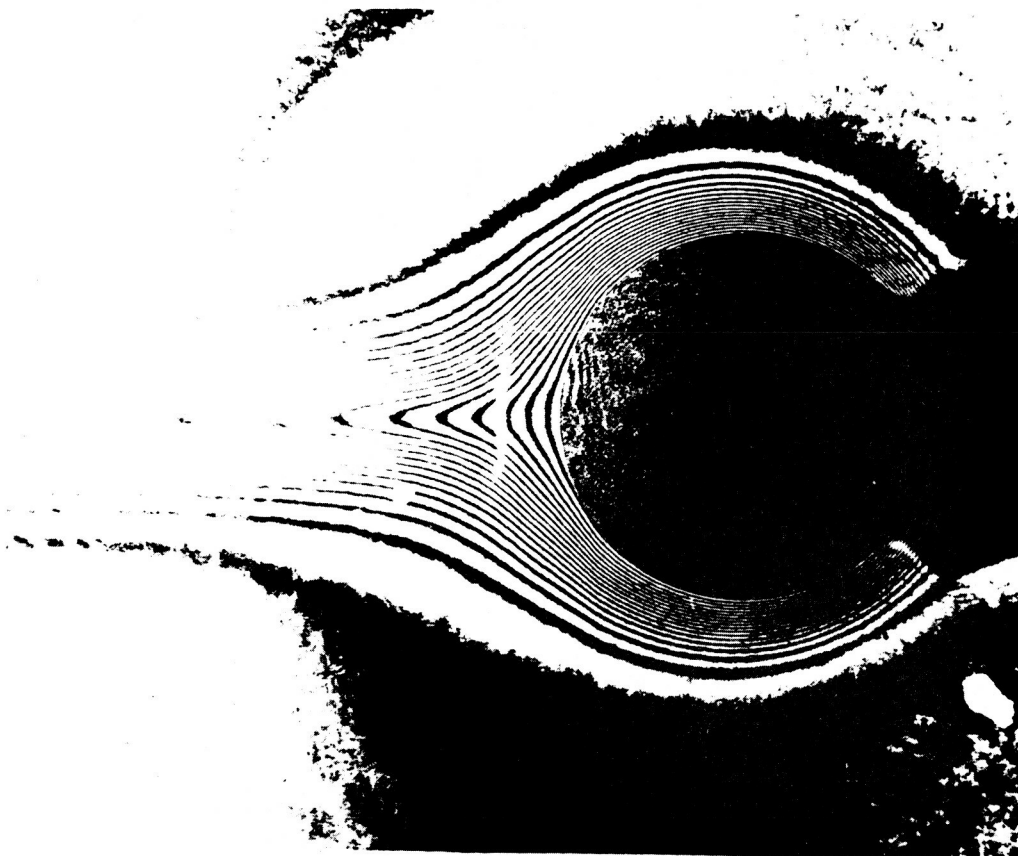
Point Diffraction
Interferometry

Figure 14. Comparisons of Holographic and Point Diffraction Interferometry.

OMIT TO P.61

ROCKWELL INTERNATIONAL-ROCKETDYNE DIVISION

HETERODYNE HOLOGRAPHIC INTERFEROMETRY

PRESENTED BY

DAVID SWAIN AND RICH TANSEY

10 JANUARY 1985

PRECEDING PAGE BLANK NOT FILMED

HOLOGRAM DATA REDUCTION
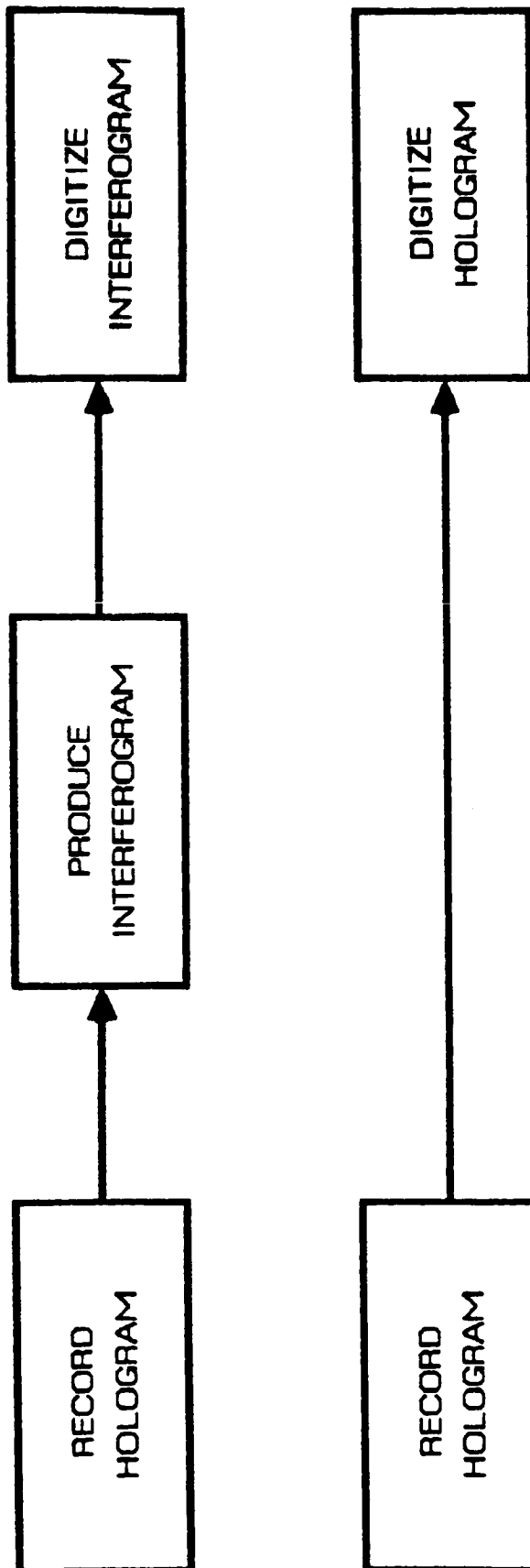
HOLOGRAM TERMINOLOGY

RECORD

DOUBLE PULSE HOLOGRAM

TW1 & TW2

Ref. Beam 1

Ref. Beam 2

Hologram

$\emptyset$

$\emptyset \approx 200\mu R$ (variable)

TWO SINGLE PULSE HOLOGRAMS

TW1 & TW2

Ref. Beam 1

Ref. Beam 2

Hologram

$\emptyset$

$\emptyset \approx 2500\mu R$ (repeatable)

PLAYBACK

Ref Beam 2

Reference Beam

Hologram

(TW1 + TW2)

Reference Beam 1 (ω_1)

Hologram

Reference Beam 2 (ω_2)

TW1 OR TW2

OR

Reference Beam 1 (ω_1)

Reference Beam 2 (ω_2)

Hologram

$\emptyset$

(TW1 + TW2)
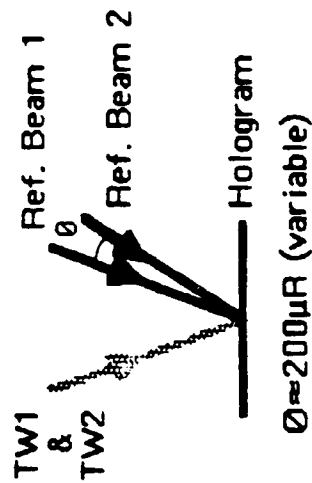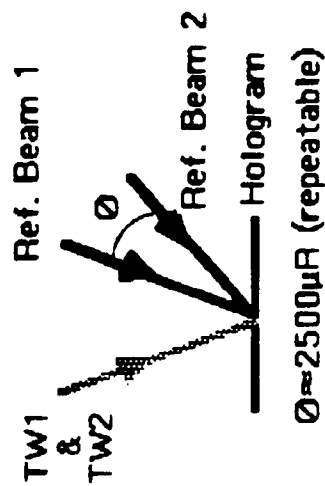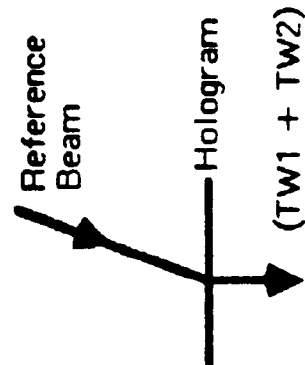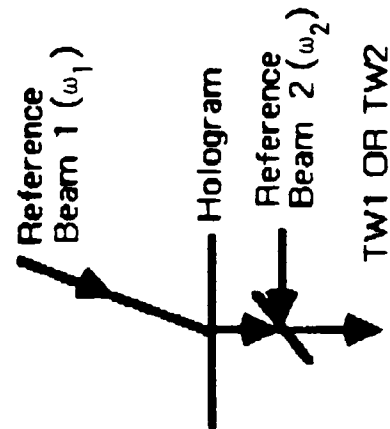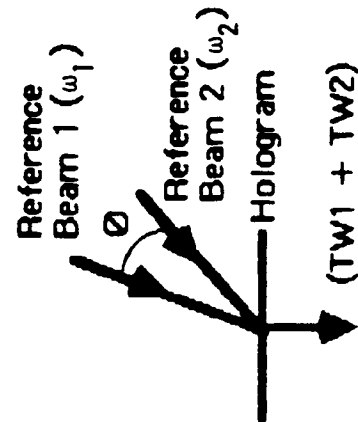
Directly digitize phase of $(\omega_1 - \omega_2)$

SYSTEM COMPARISON BETWEEN CURRENT AND PROPOSED
OPD AQUISITION AND REDUCTION SYSTEM

CURRENT SYSTEM

- MEASURES ΔOPD (X, Y, t+ Δt)

- REQUIRES TILT BETWEEN TWO HOLOGRAMS

- OPD DATA ONLY TAKEN ALONG TILT
  FRINGES (Variable sampling effects)

- SLOW DATA REDUCTION

- HOLOGRAM RECONSTRUCTION REQUIRED
  TO PRODUCE INTERFEROGRAM

PROPOSED MODIFIED SYSTEM

- MEASURES OPD (X, Y, T_n)

- NO TILT FRINGES REQUIRED

- OPD DATA CAN BE MEASURED AT ANY
  LOCATION (X, Y) IN HOLOGRAM

- RAPID DATA REDUCTION USING
  HETERODYNE DETECTION

- NO INTERFEROGRAM REQUIRED

- CAN PRODUCE CONVENTIONAL INTERFEROGRAM
  AND DIGITIZE USING CURRENT SYSTEM

- DEMONSTRATED TECHNOLOGY (1980)

COMPARISON BETWEEN EXISTING AND PROPOSED SYSTEM

254
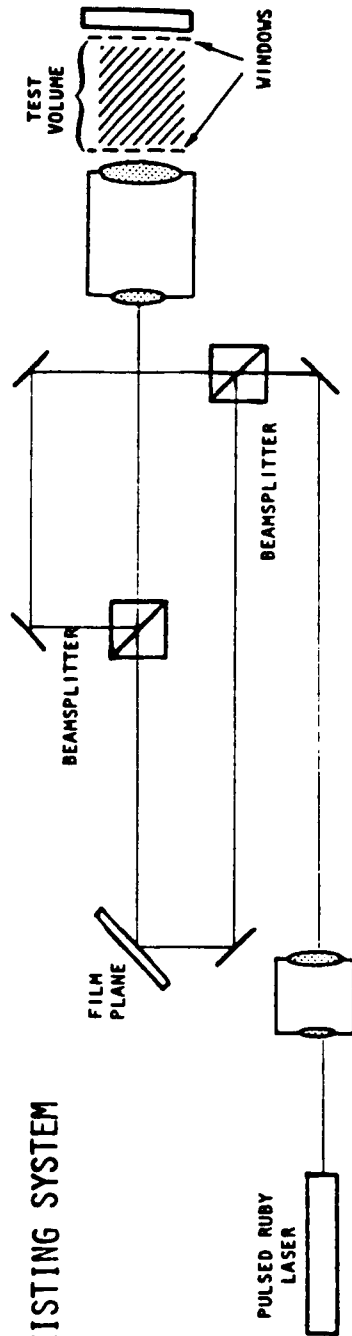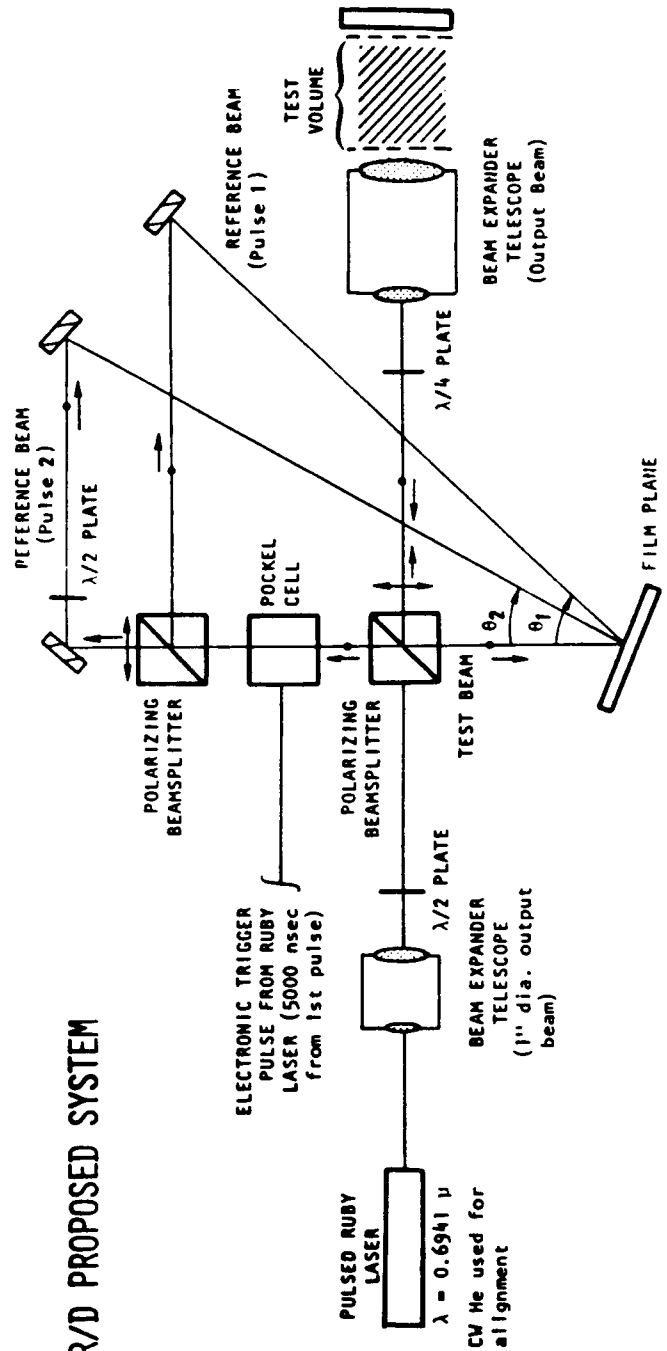
HOLOGRAM PLAYBACK

H12506-0884

255
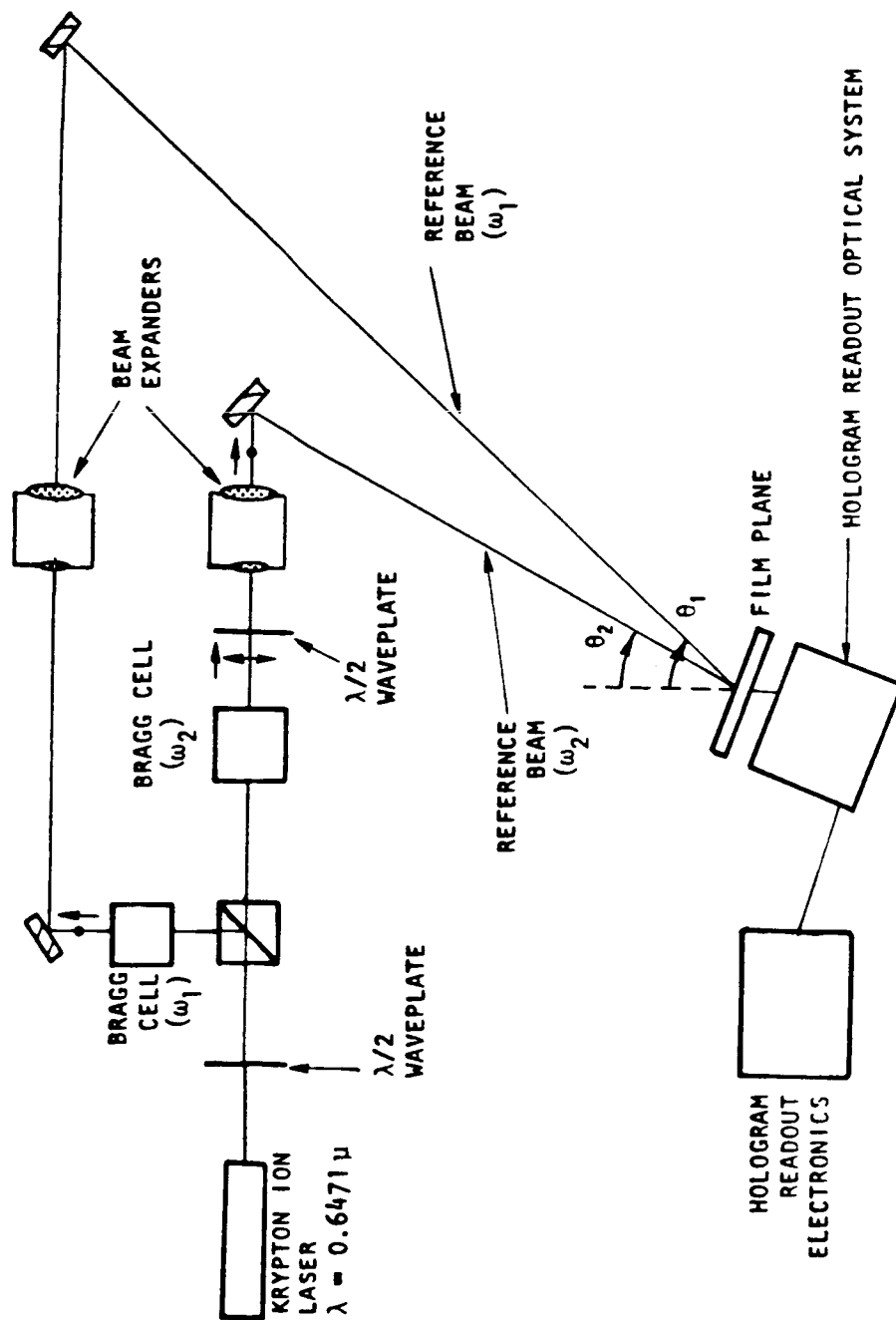
HOLOGRAM READOUT SYSTEM

H12508-0884

REFERENCE BEAM (ω_2)

REFERENCE BEAM (ω_1)

θ_2

θ_1

HOLOGRAM

RASTER SCAN
OPD PATTERN
W/FIBER

TEST FIBER

SCANNER MIRROR

SCANNER MIRROR

REFERENCE FIBER

OUTPUT INPUT

OUTPUT INPUT

SCANNER DRIVERS

DIA CARDS

6940 MULTIPROGRAMMER

MULTIPROGRAMMER INTERFACE

HPIB

OP10 PD30
TEST

REF

G
P
I
B

HP9836
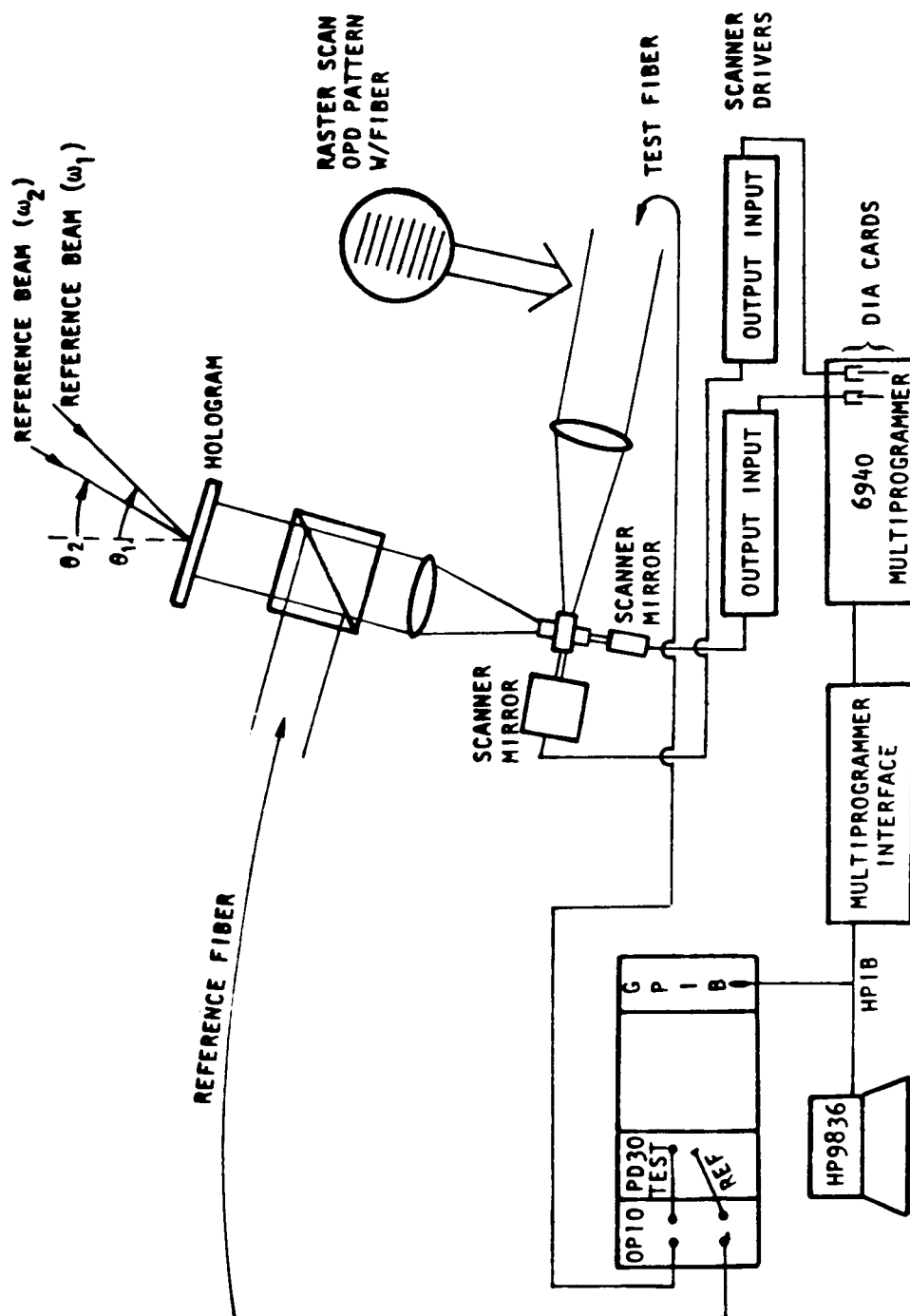
PLAYBACK SYSTEM IS IN USE AT ROCKETDYNE

- DIGITAL HETERODYNE INTERFEROMETER USED ON FLOW FIELD EXPERIMENTS WITH REPRODUCABILITY OF $<\lambda/300$ RMS

- FILM LIMITATION ON OPD TO ABOUT $\lambda/50$ RMS

- DEMONSTRATED TECHNOLOGY ON LASER NOZZLES (1980)

DOUBLE REFERENCE BEAM HOLOGRAPHIC INTERFEROMETER

258
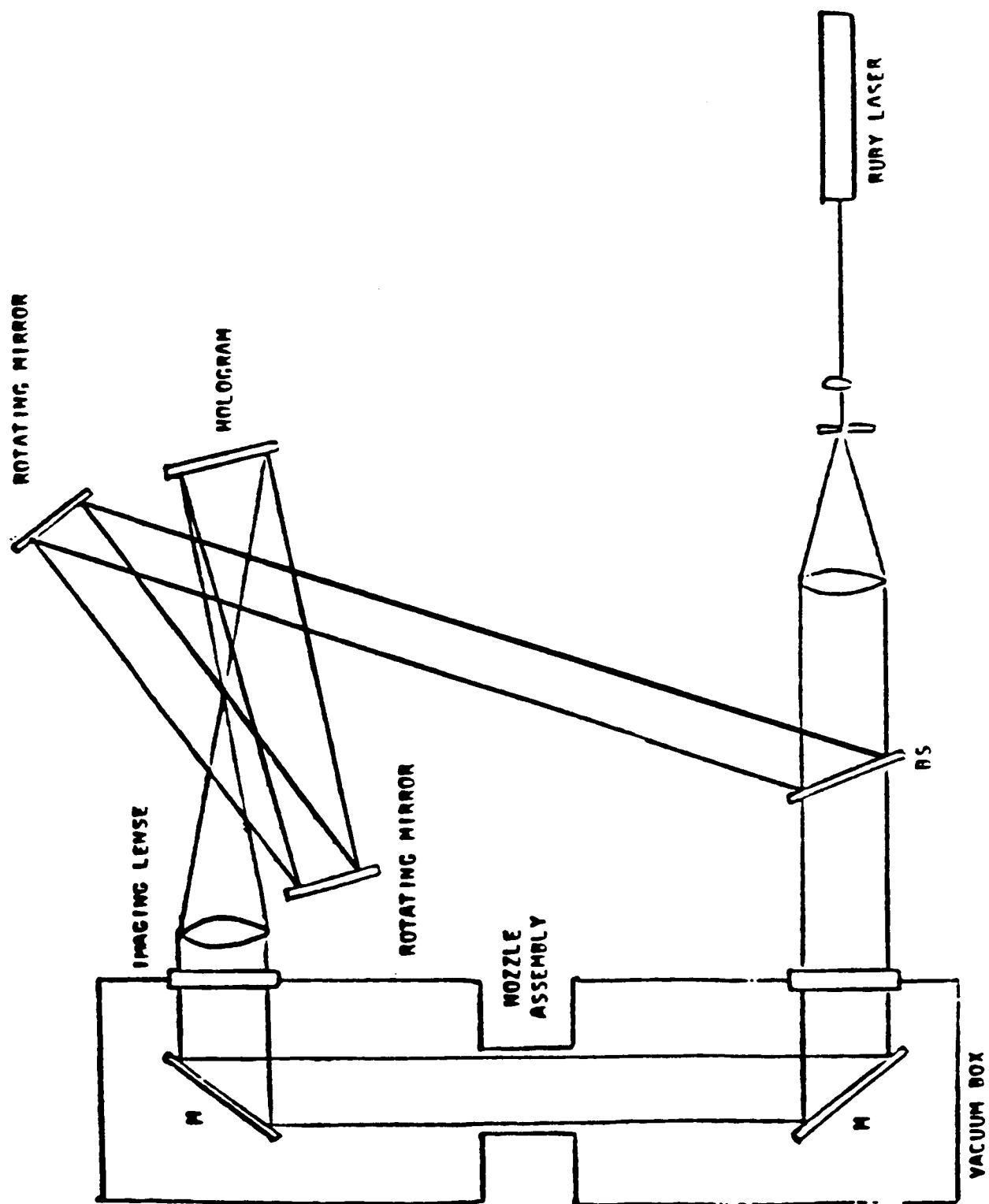
LASER NOZZLE OPD MAP

Date 2/21/80

RMS OPD .024 um
Max OPD .162 um
Min OPD .004 um
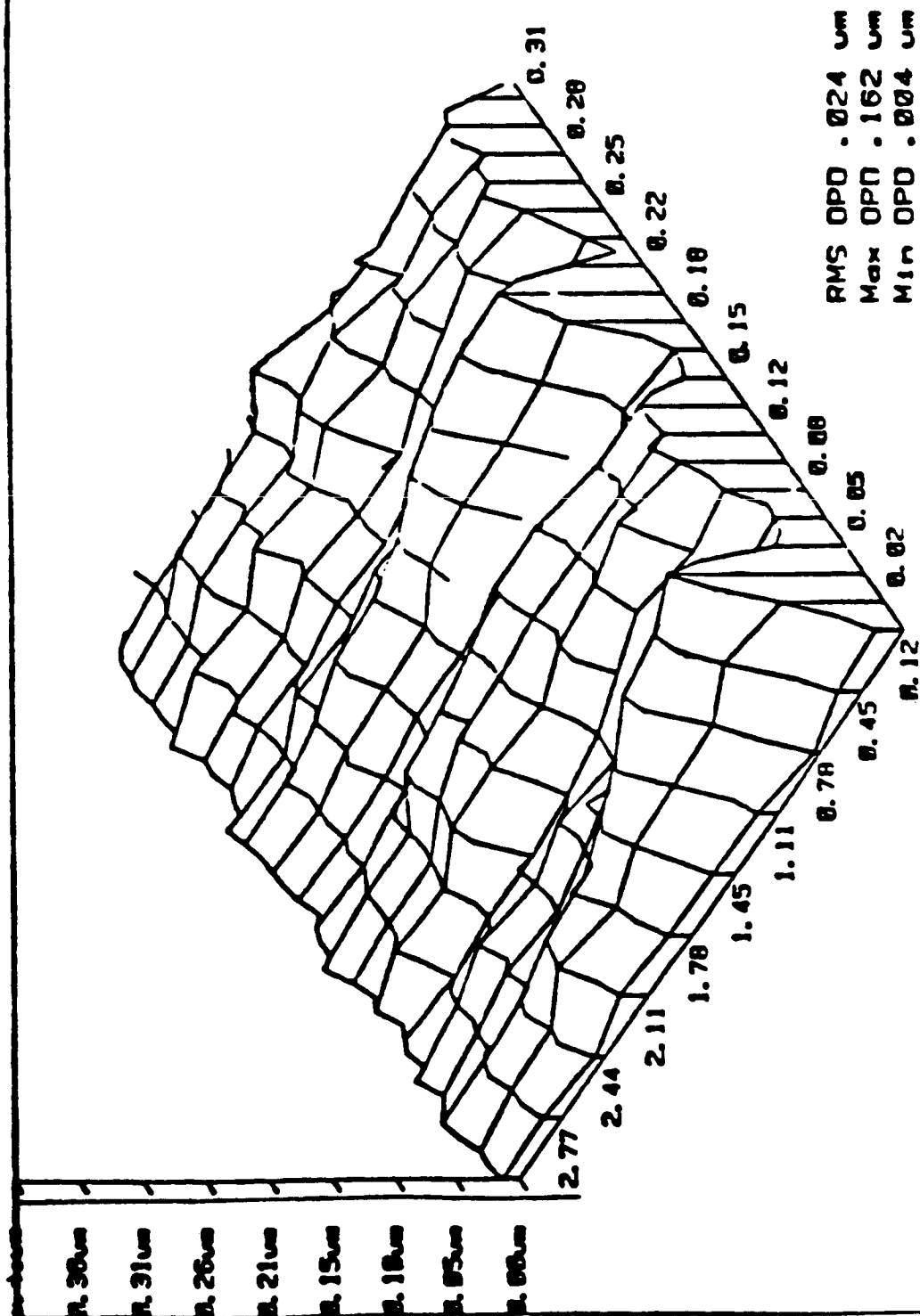
SUMMARY/CONCLUSIONS

- PROPOSED SYSTEM WILL ALLOW FEEDBACK TO TEST PROGRAM

- IMPROVED DATA QUALITY

- MODIFICATIONS TO RECORDING SYSTEM AND TO EXISTING PROGRAM SYSTEM ARE MINOR

- FUTURE APPLICATIONS FOR REDUCING HOLOGRAMS

260

Transonic Flow Visualisation using Holographic Interferometry.

Peter J Bryanston-Cross

Paper presented for the Nasa workshop on 'Data Reduction and Interpretation of Images and Interferograms' Nasa Ames Jan 10th & 11th 1985.

Over the past ten years experiments have been conducted with the objective of extracting useful fluid dynamic information from holograms. The fluid being studied has been air and its compressibility, at transonic speeds, measured interferometrically.

The type of problems to which holography has been found applicable at transonic speeds are:-

1. Axial Gas Turbines.

1.1 First stage compressor shock system.

One of the major optical measurement success has been the use of holography to visualise the leading edge shock structure on transonic compressors. This work was started by several groups in the late sixties, [1]. Their attempts to develop the method were limited by the quality of the lasers used and the test facilities available. Since then Rolls-Royce UK have taken the method and applied it to commercial gas turbine compressor problems. It is currently used to test each new compressor [2].

A typical first stage transonic compressor fan can be as large as 2m in diameter, figure 1, with the shock structure existing over two thirds of the blade height. The holographic system uses a ruby pulse laser to visualise this leading edge shock structure in three dimensions. The virtue of this method is speed, taking no more than 4hrs of rig running to map all the blades for 4 characteristic points on a performance curve. Approximately 200 holograms are made during each test. These are examined to select particular blade passages for more detailed study with LDA. Normally, the detailed LDA measurements take up to 40hrs of further rig running. Current data reduction in this area is achieved by logging the holographic data manually into a computer and then using 3 dimensional plotting packages to illustrate the shock position.

A detailed description of the method has been made in [2]. However for this part of the paper a simplified account will be made.

The output beam from a pulse laser is divided into two parts. One forms the reference beam the other the object beam, figure 2. The method can be used because of the type of laser currently available. The coherence length of the ruby pulse laser is of the order of 1 metre, making it possible to form holograms without contour fringes of objects up to 3 metres across. As a result it is possible to expand a laser beam to reflect from the inside surface of a gas turbine of 4 square metres. This illuminated area forms the background against which the shock structure can then be viewed. The second feature of the laser is that it can produce two such pulses of the same frequency and spatial coherence length, ie 'clean' , non-contoured holograms 95% of the time.

The sample beam illuminates the inside of the casing of the engine directly ahead of the rotor. From a view point just over the rotor it is possible to see between the passing blades the upstream illuminated area.

The air just ahead of the shock has a density lower than that just after the shock. If two holographic exposures are made (approximately 2 microseconds apart) then two holograms are made on the same piece of film. The only difference between the holograms being the movement of the shock as it passes the viewing window, figure 3. It is this difference in shock position and its overlap between the two exposures in the hologram, which is visualised as an optical phase shift. Such a shift makes the position of the shock apparent as a dark or bright area in the reconstructed hologram as shown in figure 4.

1.2 Modal vibration of fans.

Holography has also found application in the modal vibrational analysis of the compressor fans. This is done regularly on static fans and in a few instances on fluttering rotating assemblies, as described in [3] and [4]. For vibrational holography the digitisation of the data is far simpler, in that, the blade represents a two dimensional surface. The movement of the surface due to vibration can be calculated from the analysis of two photographic reconstructions made from two holograms of the same object at different viewing angles. However the accuracy of this stereographic reconstruction method relies on the exact location of both the object and the reconstructed hologram. It is noted, that the errors which can be generated by changing the reconstruction wavelength and by rotating the angle of analysis are not negligible.

262

1.3 Turbine stages

Holography is also being applied with growing success to the turbine stages of the Axial gas turbine. Starting with two dimensional cascade work discussed in [5] and now developing into a diagnostic for rotating test rigs.

An interesting situation has arisen with the development of complicated numerical prediction codes, in that, there are few well documented test cases against which they can be critically tested. Interferometric data has sufficient resolution to test the codes at the points where they are most sensitive. Currently this is the leading edge, where a comparison with an inviscid code has been made, figure 5 [6], and trailing edge of the blade, figure 6 [7]. This academic research has led to improvements in the numerical modelling of these regions and has contributed to the understanding of the turbulence modelling, essential in the development of full Navier Stokes solvers. An illustration of this is shown in figure 7 where the sidewall boundary layer separation has been predicted and compared with interferometric data. The simplest method of evaluating and interpreting data in these cases has been to scale the output contour plots of the numerically generated data to match in size the photographic reconstructions made from two dimensional interferograms [8]. The contour's heights, which then match the optically generated isodensity fringe spacings, give a sharp test of the ability of the code to model the flow.

One experimental series completed at the Whittle laboratory CUED, was designed to explore the possibility of being able to form holograms with interferometic tolerances without the need of a rigid framework. In effect the cascade walls formed the optical framework, with the pulse laser situated outside of the 2m diameter test facility. To achieve this result a drop in optical resolution has been tolerated; however it has been possible to make the following measurements. The Isodensity data shows in detail the leading edge stagnation position, the shock boundary layer interaction region, the trailing edge vortex structure and on the surface of the blade a projection of the flow distribution, figure 8. For these cases the data reduction has been achieved by hand in two stages. Firstly the data has been photographed and then the photographs digitised. The objective of this work is directed towards producing a holographic diagnostic which could be attached to a rotating test facility. Such a device could then be used to examine the stator rotor interaction and related rotor passing effects.

All the experiments have been completed with the use of a high power solid state laser. High resolution 3,000 lines per millimetre holographic film and plates have been used as the data storage material.

2. Steam Turbines.

There has been less holographic interest in steam turbines, partly due to lower funding and the lack of available test facilities. Industrial steam turbine sets also tend to be less accessible than the large aero gas turbines, which have had the external fittings pared down to meet the weight and pod mounting needs of a flying engine. One of the main difficulties is that the gas density passing through the last stage of the turbine set is sub atmospheric which makes holographic density change measurements rather insensitive. The speed of air passing through atmospherically pressured Reynolds number scaled linear and annular model steam turbine cascades is similar enough for holography to be applied to without difficulty.

The problems being addressed in this area are similar to those of the gas turbine, with the emphasis more towards understanding the high exit Mach flows and their effect on the base flow. This has been shown in the two dimensional approach developed at EPFL (Ecole Polytecnique Federale de Lausanne) for visualising the trailing edge shock structure around the trailing edge of a 30 times scaled model of a steam turbine, figure 9, [9]. The boundary layers on the object can clearly be seen followed by an isentropic Prandtl-Meyer expansion where the flow accelerates from M=1.3 upto M=1.9 figure 10. The shear flow converging to form the confluence region can also be seen in greater detail in figure 11 where the interferometric reconstruction has been enlarged to show the separation of the boundary layer at the end of the trailing edge. By adding finite fringes to the interferogram it is possible to obtain the exact location of the sonic line in the boundary layer. Figures 12 and 13 show the same trailing edge but with the sidewall liners adjusted for a subsonic outlet. In the first case, figure 12, the exit velocity is Ma.=0.61 and a classical Karman vortex street has been observed. In the second case at just sonic outlet conditions the trailing edge flow is unstable being neither the previous subsonic flow nor the fully developed supersonic exit shown in figure 10. Figure 14, made using two holographic pulses 3 microseconds apart, shows the unsteady component of the fully developed flow of figure 10. For the first time and as a consequence of the scale of this trailing edge it is possible to observe the vortex structure present in the shear layer directly after the separation point. The size and strength of this vortex structure can be seen to increase at the end of the confluence region with the influence of the downstream compression shock.

The other problems of current interest being, the effect of off condition incidence, flow separation, shock position, flutter and the effect of inserting measurement probes into the blade passage. Figure 15 is a photographic reconstruction made from a three dimensional flow visualisation of the shock structure within an annular cascade also at EPFL.

3. Boundary Layer Flow

A recent data interpretation problem has been approached using a combination of optical techniques [10]. Using a short duration pulse separation from a ruby pulse laser, it has been possible to observe a discrete and regular structure in the boundary layer. This structure which can be observed over a range of Mach numbers from just sonic, figure 16 to a Mach number of 2.5, figure 17 gives the appearance when visualised using a two dimensional interferometric approach of dark striations occurring with a spatial periodicity of the boundary layer height along the boundary layer. The striations were then measured again using a technique defined as dynamic Schlieren, described in greater detail in [11] and [12]. From these measurements; the time of flight of the striation between two optical probes placed in the Schlieren system image plane, showed them to be moving with the expected boundary layer velocity figure 18. It was also possible to find from this system the autocorrelation function. This did not indicate a regular periodicity in the flow but a strongly turbulent decay similar to that seen in hot-wire data. The third optical measurement used a three dimensional scatter plate holographic set-up. It can be seen in the resulting holograms that the seemingly periodic structure in the boundary layer is being created by a discrete bursting process. This is not unlike the method which is described by Head 'the action of vortex bursting within the boundary layer' [13]. Further the disturbances which have the appearance of a small 'explosion' have a width and height of the boundary layer. Certainly in terms of a holographic density change this implies that a significant part of the density gradient within the boundary layer being disturbed over a time period of between 3 to 20 microsecs. This would be consistent with a turbulent bursting process. The problem has taken considerable time to understand, because there was a limit in the speed by which either temporal or spatial information can be stored. In this case the three separate measurements which give the temporal and spatial data occurring during the bursting process would have been difficult to make with one single data collection system.

Holographic interferometry is also being used to visualise the supersonic flow around a corner [14]. Here the objective is to compare the 'instantaneous' density profiles obtained using holography with temporally averaged pitot static measurements and theory. Figure 19 shows a supersonic boundary on the tunnel floor, whereas figure 20 is a reconstruction made from a flow around a two dimensional compressional corner.

4 Radial Turbomachinery

Until April 1984 no holographic flow visualisation experiments had been peformed on small (100mm diameter) radial turbochargers. A typical turbocharger is shown in figure 21 with an insert photograph showing the holographic view of the compressor. These machines, which are used to boost the compression power of large truck engines, rotate at up to 80,000 revs. They can reach transonic speeds at the blade tip, and generate loss through shock waves. Using a holographic system, developed from that used previously on large axial fans, it has been possible to produce visual evidence of this shock structure.

In a second experiment described in [15] made in April 1985 the holographic system was rearranged to view the exit passage from the rotor. Again a high aerodynamic loss area has been identified. Here a vortex structure was postulated to occur as a result of backflow into the rotor passage. Laser anemometry results were obtained showing a slip factor of 1.2. Holography has been used for the first time to visualise this disturbance as shown in figure 22.

Conclusion

An account has been made of some of the applications of holographic interferomtry to the visualisation of transonic flows.

In the case of the compressor shock visualisation, the method is used regulary and has moved from being a research department invention to a design test tool. The need to speed up the data extraction from the method is still a weakness; although it is still an order of magnitude faster at collecting data than the current alternative LDA.

With the implementation of automatic processing and simple digitisation systems, holographic vibrational analysis has also moved into routine NDT testing.

The code verification interferograms have been instructive, but the main turbomachinery interest is now in three dimensional flows. A major data interpretation effort will be required to compute tomographically the three dimensional flow around the leading or the trailing edges of a rotating blade row. Holography, however is the only current technique with adequate resolution to meet this problem.

The bolt on approach shows the potential application to current unsteady flows of interest. In particular that of the rotor passing and vortex interaction effects experienced by the new generation of unducted fans. It can also provide data on the stator rotor interaction without requiring the construction of specialised facilities.

The turbocharger tests present a new area for the application of holography. The tests made have been at a preliminary level. A more detailed study should help in reducing some of the high viscous losses experienced.

Figures

1. Axial gas turbine first stage compressor fan as used in a holography test. The arrow shown, points to the 19mm diameter negative lens through which the sample beam of the ruby pulse laser was expanded. The opposite side of the casing has been painted white to diffuse and reflect the laser light.

2. Diagram showing the method by which the holographic system was applied to the first stage compressor fan during a test.

3. Diagram showing the movement of the compressor blade fan assembly between two holographic pulses.

4. Photographic reconstruction showing the shock structure at the tip of the compressor fan as visualised using holography.

5. Comparison between an interferometric measurement made of the transonic flow around an isolated aerofoil and its numerical prediction using a time marching solution.

6. Comparison between the trailing edge flow in a linear cascade measured interferometrically, and a loss predicting Navier-Stokes solver computed solution.

7. Comparison of a transonic wedge profile with sidewall boundary layer separation and a viscous numerical solution.

8. Interferographic reconstructions made from the 'Whittle Lab bolt on interferometer'. Both the leading and trailing flows can be seen clearly, with the confluence region enlarged to show the formation of the trailing edge vortex structure.

9. Diagramatic layout of the EPFL image plane ruby pulse interferometric system as applied to a two dimensional Laval nozzle.

10. Supersonic trailing edge flow showing the Prandtl-Meyer expansion of the flow from a Mach number of Ma.= 1.3 to Ma.=1.9.

11. A photographic enlargement of figure 10, showing in detail the trailing edge separation point and the formation of the exit shear layer.

12. Laval nozzle now adjusted to operate in the subsonic region. Ma.=0.6

13. Laval nozzle adjusted to operate in an unstable region neither a typical Karman vortex street or as a fully formed supersonic exit.

14. Unsteady components of the stable exit flow shown in figure 10.

15. A photographic reconstruction made from a hologram showing the shock structure within the EPFL supersonic inlet annular cascade.

16. Two holographic pulses 30 microseconds apart show a 'regular' structure within a 10mm thick boundary layer at just sonic Mach numbers.

17. Two holographic exposures made 3 microseconds apart in a supersonic (Ma.=2.5) boundary layer.

18. Velocity measurements using Dynamic Schlieren.

19. Density gradient within a supersonic boundary layer, Ma.=2.5. The interferogram was formed by taking one exposure before the tunnel ran, the other during the run on the holographic plate.

20. Density gradient within a supersonic boundary layer at a compression corner, showing the penetration of the shock.

21. Photograph showing a typical turbocharger, the inset shows the view taken in the holographic visualisation of the leading edge shock structure. In this case part of the housing has been spark eroded away and a glass window fitted. A metal mirror has also been mounted onto the turbocharger to provide an optical viewpoint perpendicular to the flow direction.

22. Reconstruction made of the exit diffuser vortex.

References

[1] Wuerker R F, Kobayashi R J, Hejlinger L D and Ware T C 'Applications of Holography to flow Visualization within Rotating Compressor Blade Rows.' NASA CR 121264 1974

[2] Bryanston-Cross P J. 'Three dimensional Holographic Flow Visualisation'. Presented September 1981 at the Symposium on Measuring Techniques in Transonic and Supersonic Cascade Flow. Lyon.

[3] Hockney B S, Ford R A and Foord C A. 'Measurement of Fan Vibration using Double Pulse Holography.' Journal of Engineeering for Power Vol 100 pp 655-668 Oct 1978.

[4] Storey P A. 'Holographic Vibration Measurement of a Rotating Fluttering Fan.' AIAA Vol 22 no 2 pp 234-241 Jan 1984.

[5] Bryanston-Cross P J, Lang T, Oldfield M and Norton R. 'Interferometric Measurements in a Turbine Cascade using Image Plane Holography'. Journal of Engineering for Power Jan 1981.

[6] Bryanston-Cross P J and Denton J. 'Comparison of a Measured and Predicted Flow around the Leading Edge of an Aerofoil'. AIAA Vol 22 pp 1025-1026 1984

[7] Dawes W N and Bryanston-Cross P J. 'A Numerical and Experimental Study of the Loss Generation in a Transonic Rotor Blade'. to be published, International Journal of Heat and Fluid Flow.' Late 1985.

[8] Bryanston-Cross P J and Dawes W N. 'Comparison of Inviscid and Viscous Computations with an Interferometrically Measured Transonic Flow.' To be published AIAA July/August 1985

[9] Bryanston-Cross P J, Beretta-Piccoli F and Ott P. 'Implementation of the Ruby Pulse Laser Holography System at the LTT/EPFL.' Internal report LTT-TM-16-84. Ecole Polytechnique Federale de Lausanne Sept 1984.

[10] Bryanston-Cross P J, Edwards J and Squire L. 'Measurements in an Unsteady Two Dimensional Shock/Boundary Layer Interaction.' Presented at the IUTAM Unsteady Aerodynamics Conference, Jesus College Cambridge Sept 1984

[11]   Bestwick T.   'The Structure of Turbulence in
Supersonic Boundary Layers.' CUED final year project
report April 1984.

[12]   Bryanston-Cross P J, Camus J-J and Richards P.
'Dynamic Correlation of a Schlieren Image in a Transonic
Airflow.' Published in 'Photon Correlation Techniques in
Fluid   Mechanics', Springer-Verlag Series in Optical
Sciences Vol 38 pp 270-275 1983.

[13]   Head   and   Bandjopadhyay.   'New   Aspects   of
Turbulent Boundary Layer Structure.' JFM Vol 107 pp
297-338 1981.

[14]   Liu X. 'Holographic Interferometry, Measurements
of Shock/Boundary Layer Interaction at a Compression
Corner.' CUED internal first year PhD report April 1984.

[15]   Bryanston-Cross P J. 'A Holographic System for
Visualising   a   Vortex Structure in a Turbocharger'.
Presented at the meeting of Holographic Measurement,
Speckle and Allied Phenomena at the CEGB headquarters
London April 16th to 17th 1985.

Fig. 1

ILLUMINATING
BEAM

CAMERA

MIRROR

REFERENCE
BEAM

FROM
LASER

Fig. 2

272
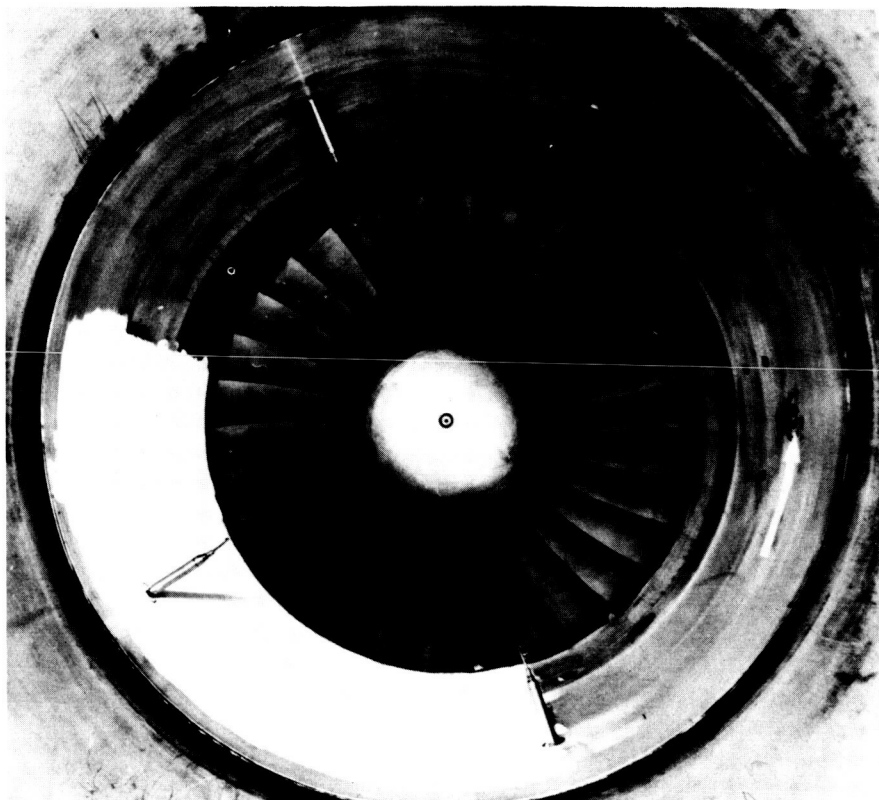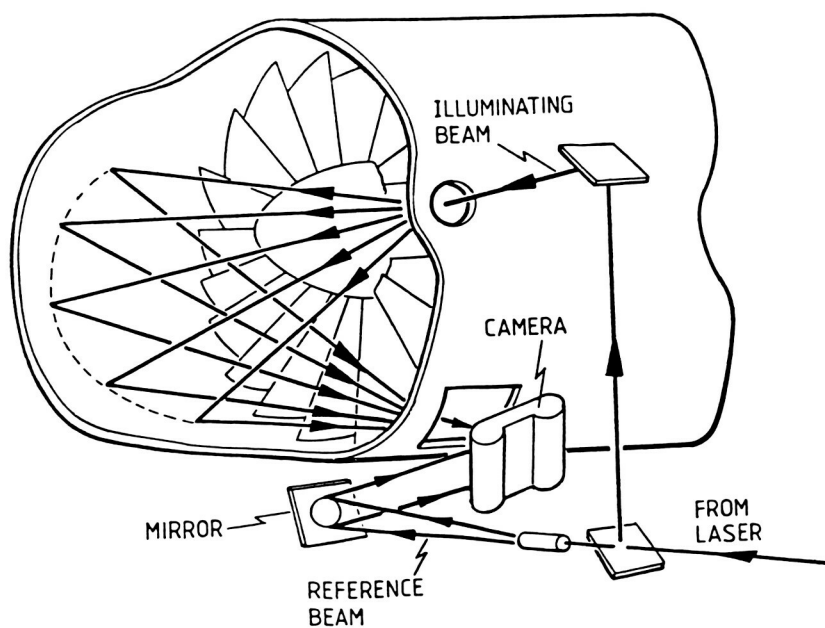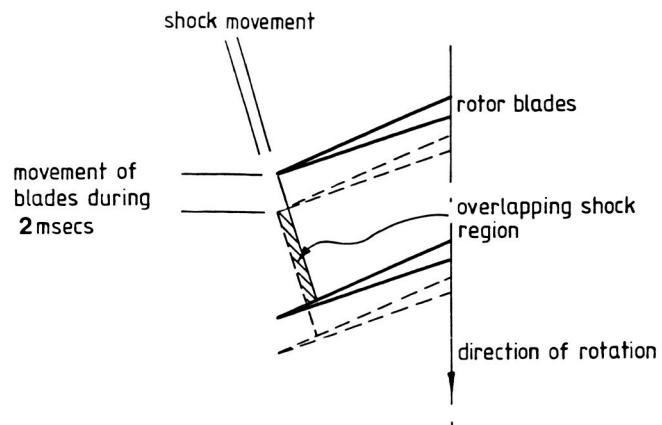
Movement of a normal shock between two pulses with a 2msecs separation.
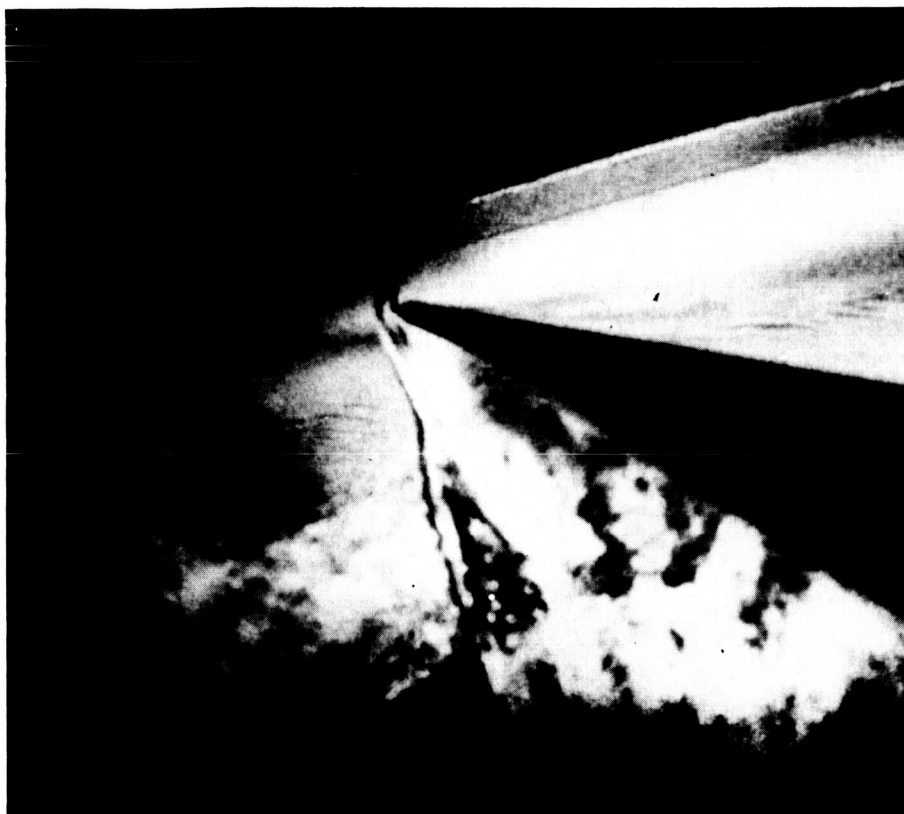
Fig. 3

Fig. 4
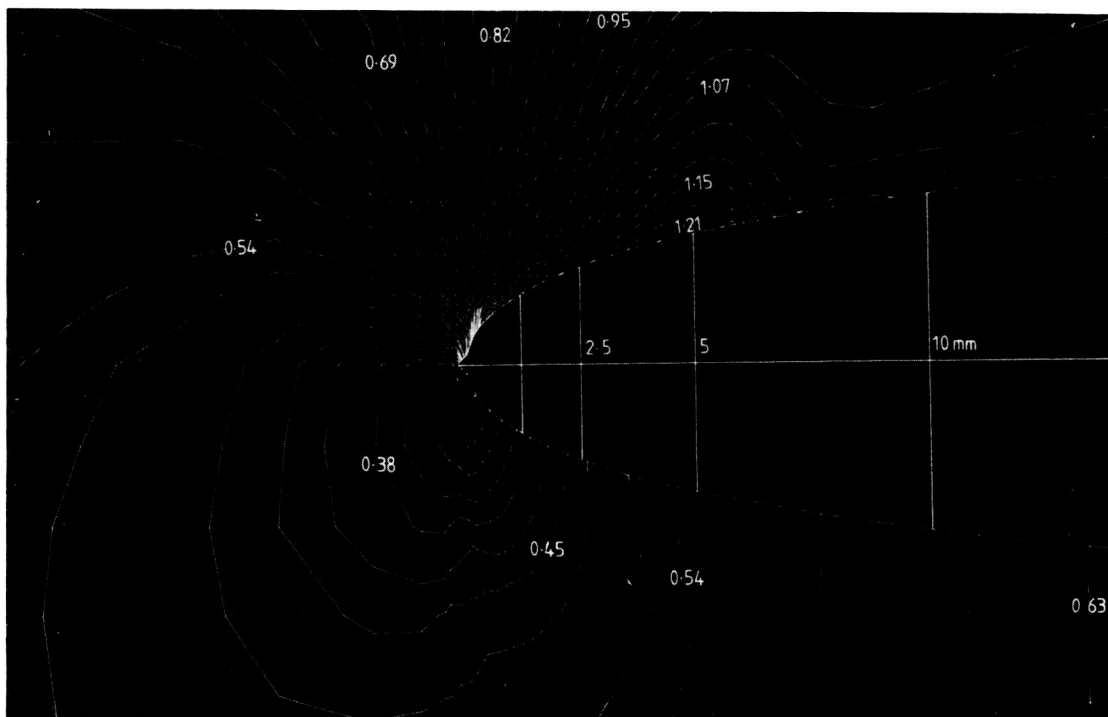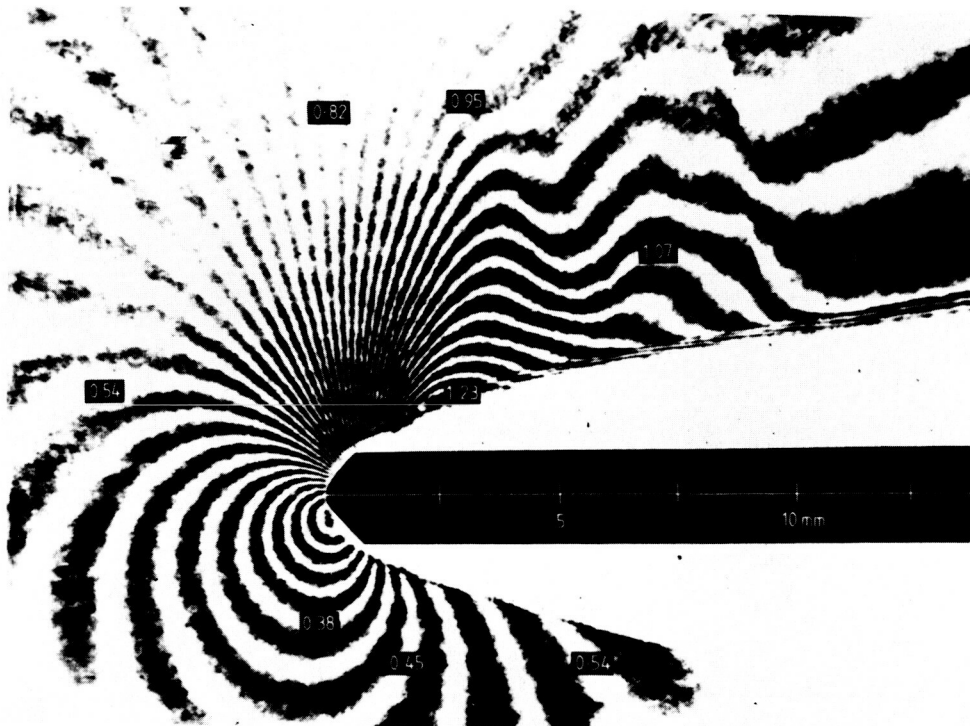
Fig. 5
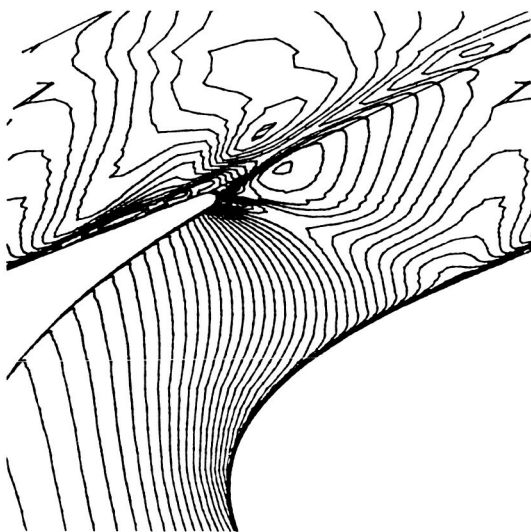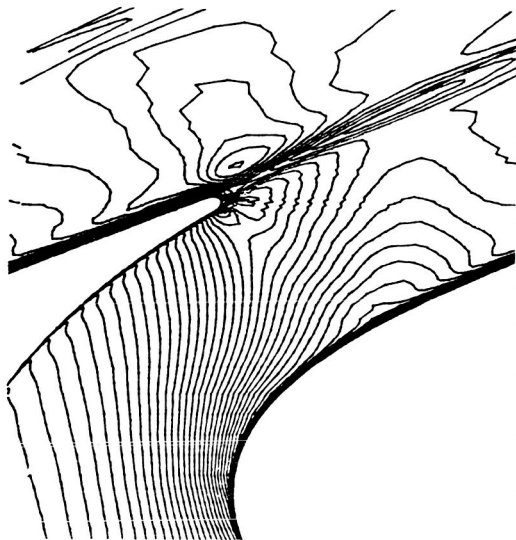
Fig. 6
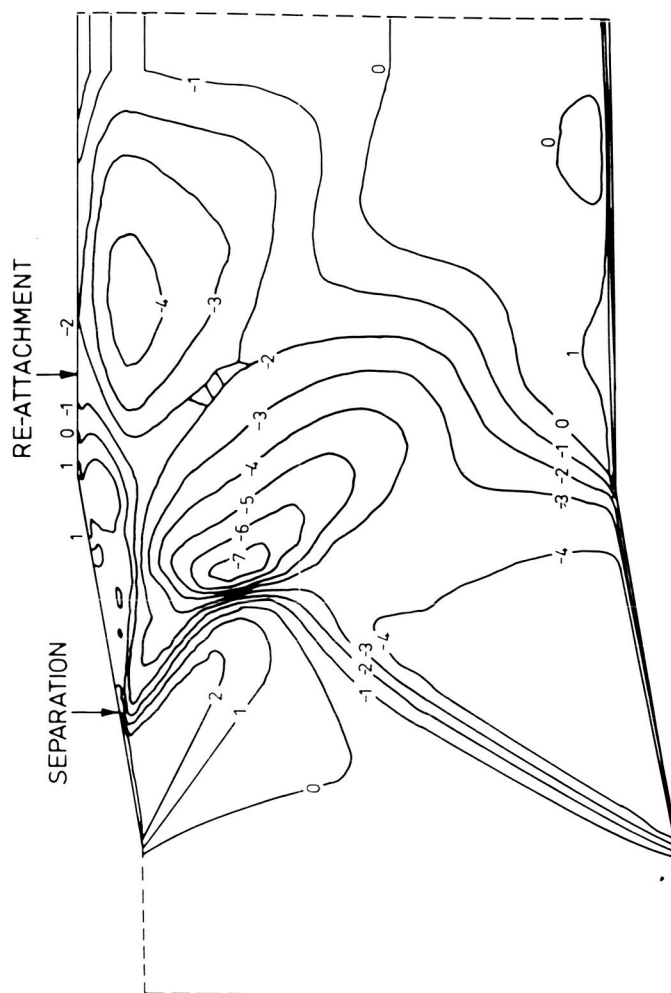
Fig. 7
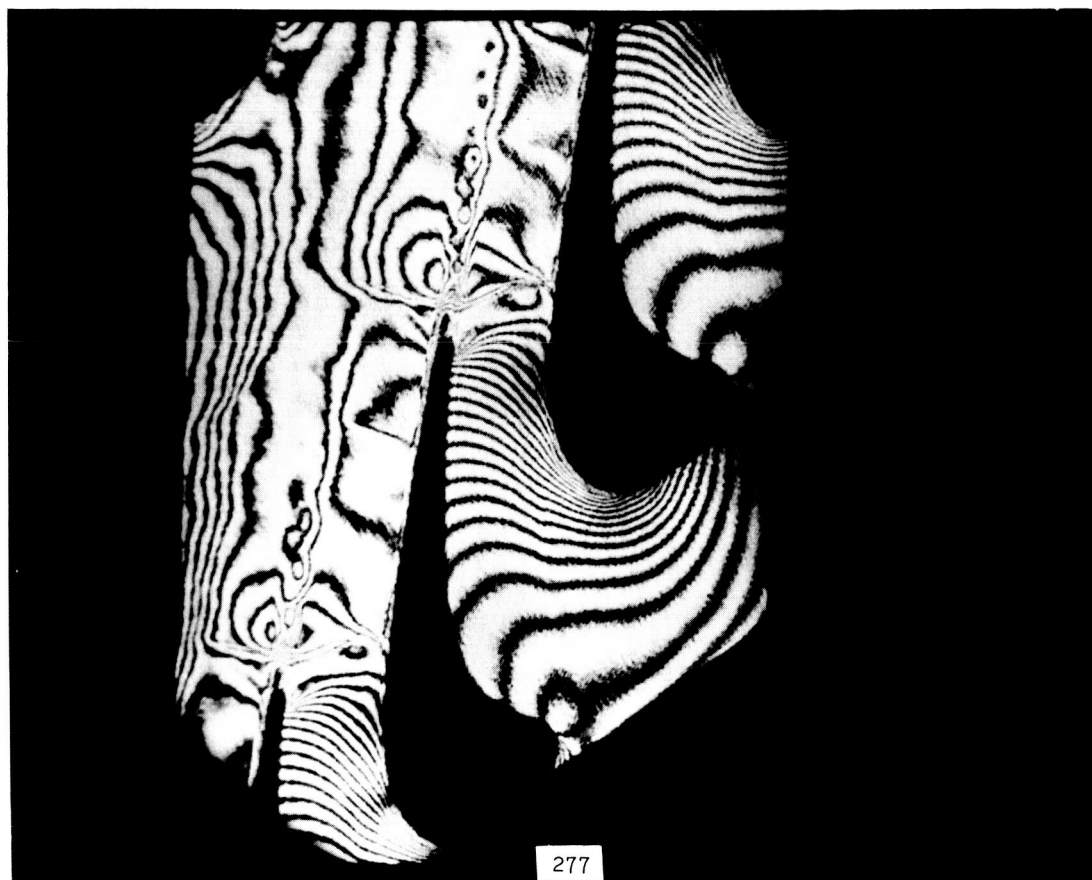
Fig. 8
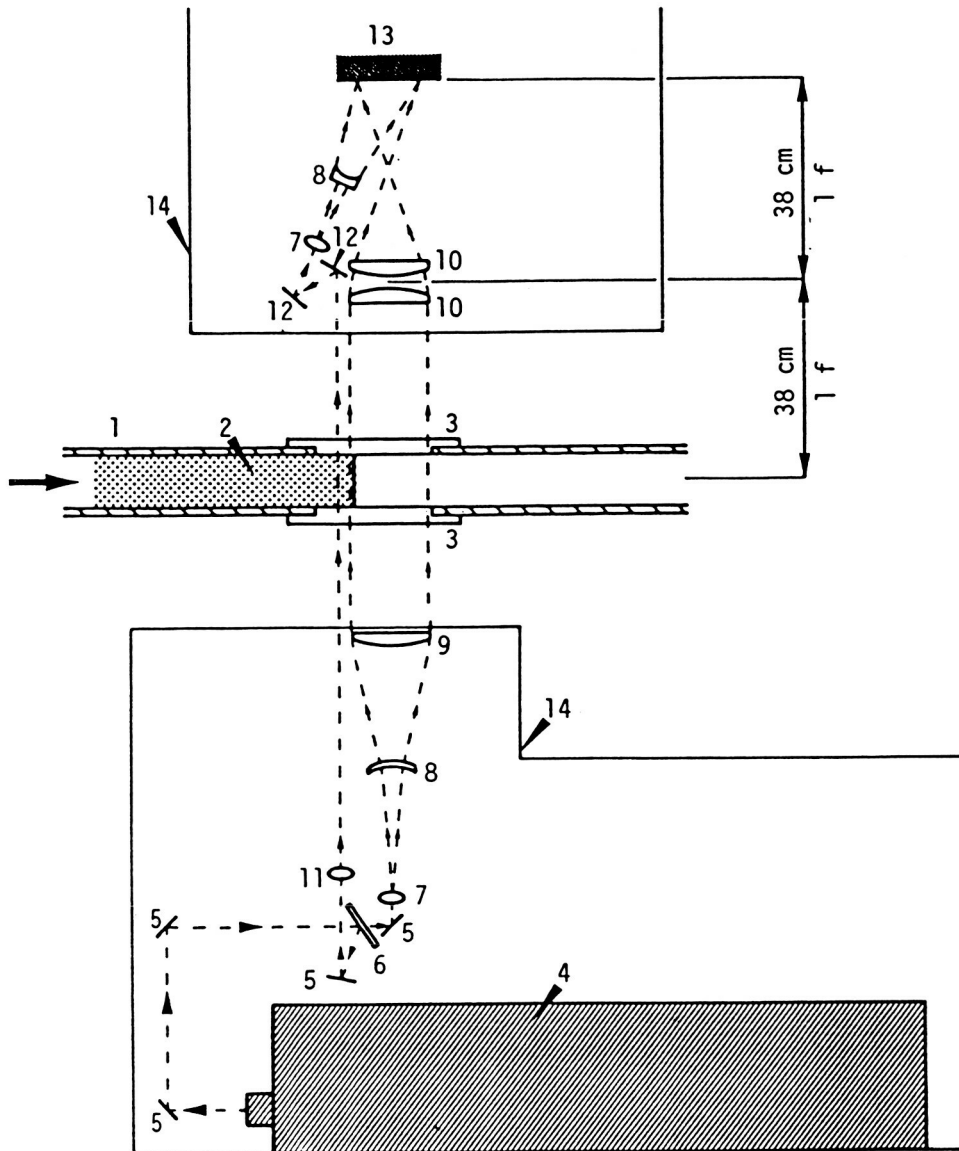
1	Sidewalls of the Laval Nozzle	8	Negative lenses
2	Trailing edge model	9	Large aperture collimating lens
3	Perspex vindows	10	Large aperture plano-convex lenses
4	Pulse Laser (J.K.)	11	Collimating lens
5	Dielectrically coated mirrors	12	Mirrors
6	50% beam splitter	13	Holographic plate
7	Microscope objective x5	14	EPFL optical table

2-D (two dimensional) Holographic System EPFL 1984

Fig. 9
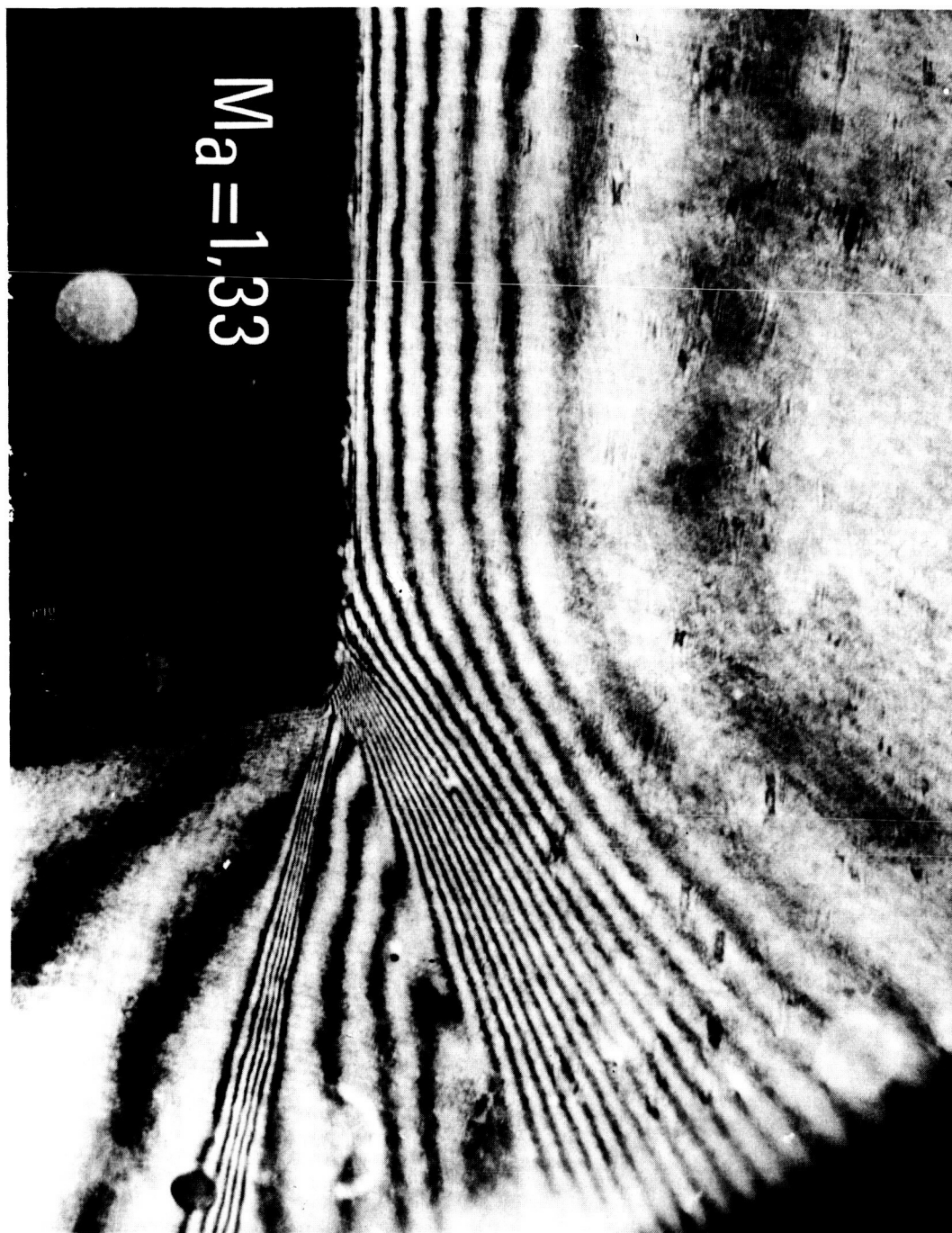
Fig. 10

Fig. 11

Fig. 12

Fig. 13

Fig. 14

Fig. 15

284

Fig. 16

Fig. 17.

286
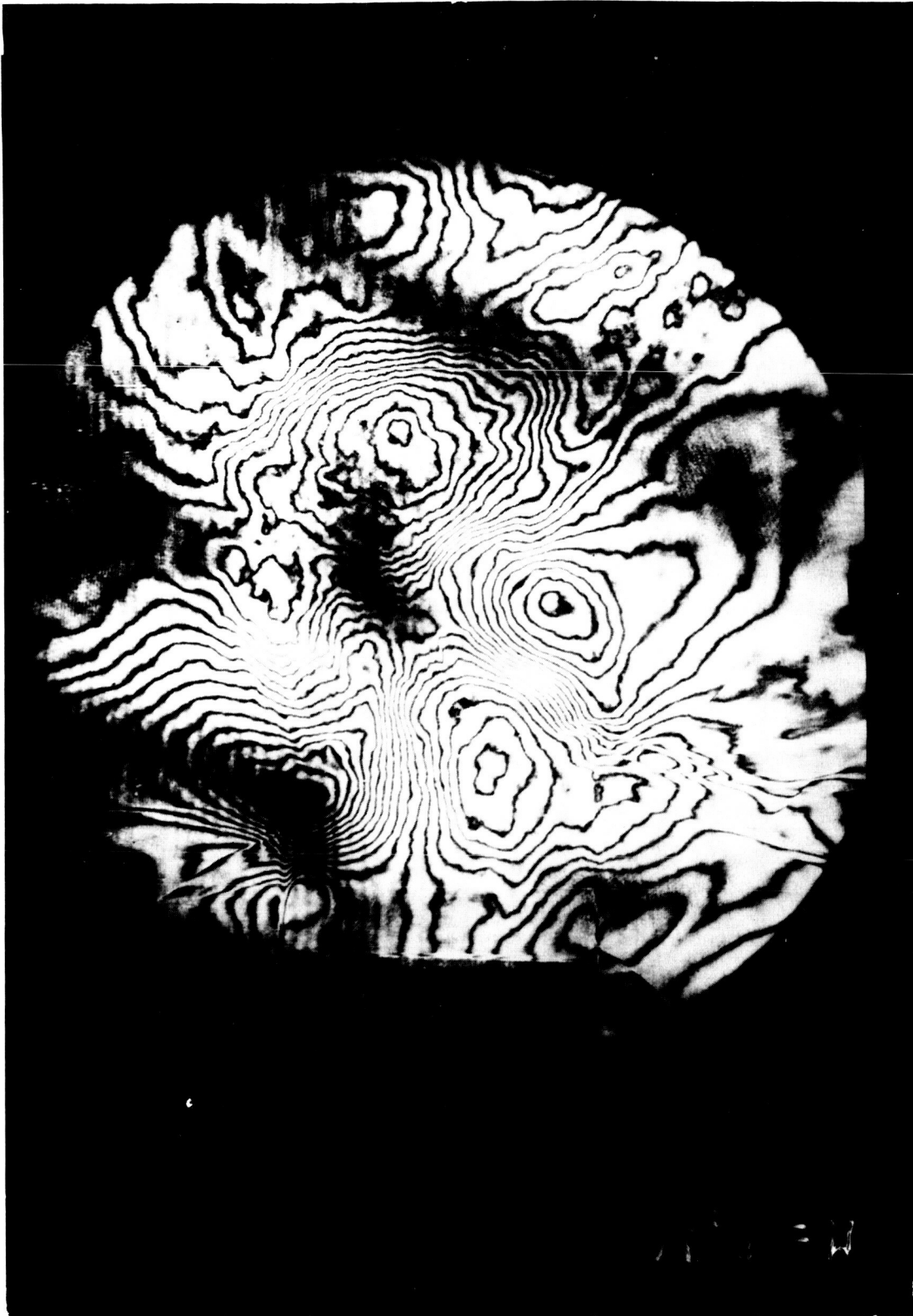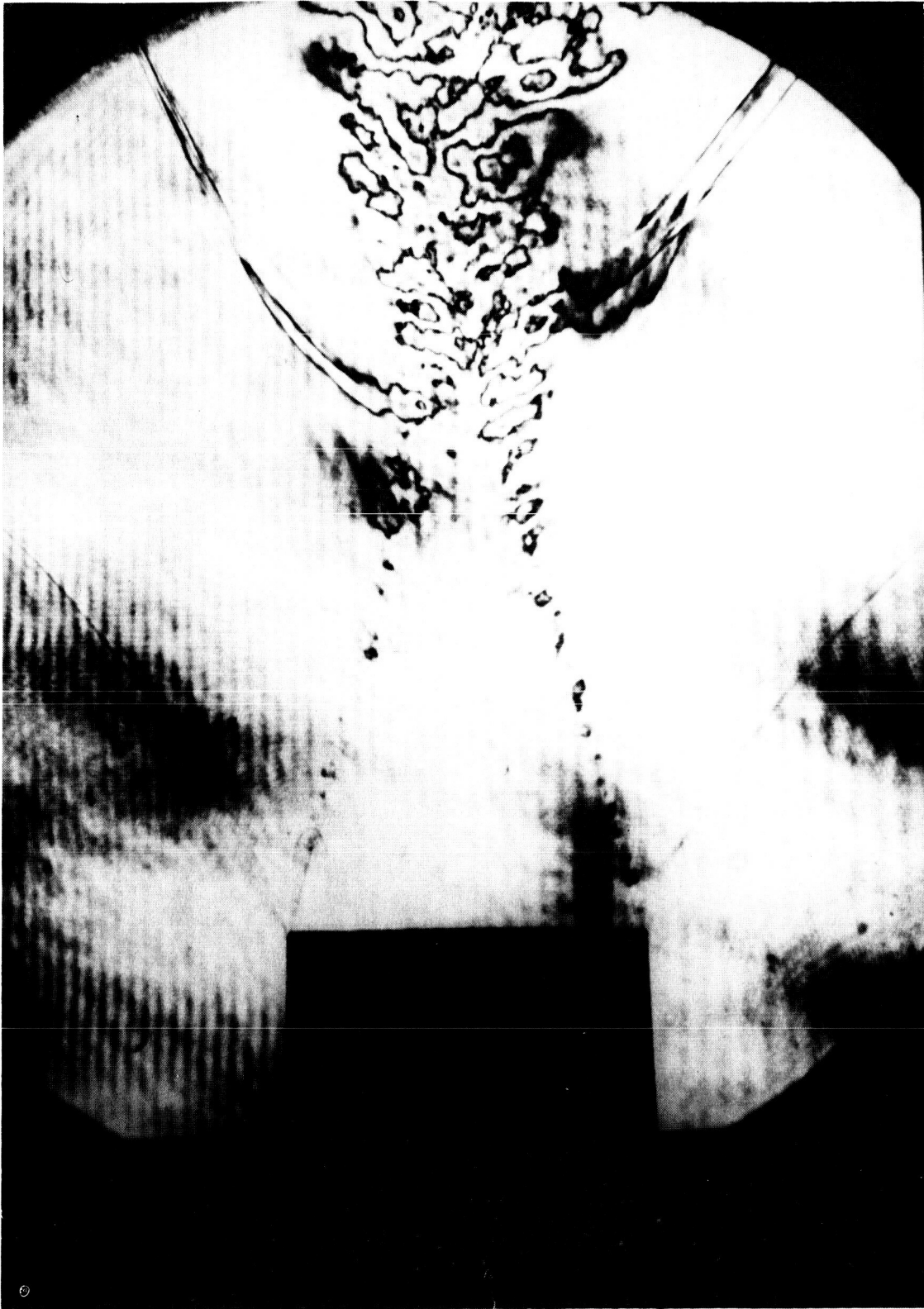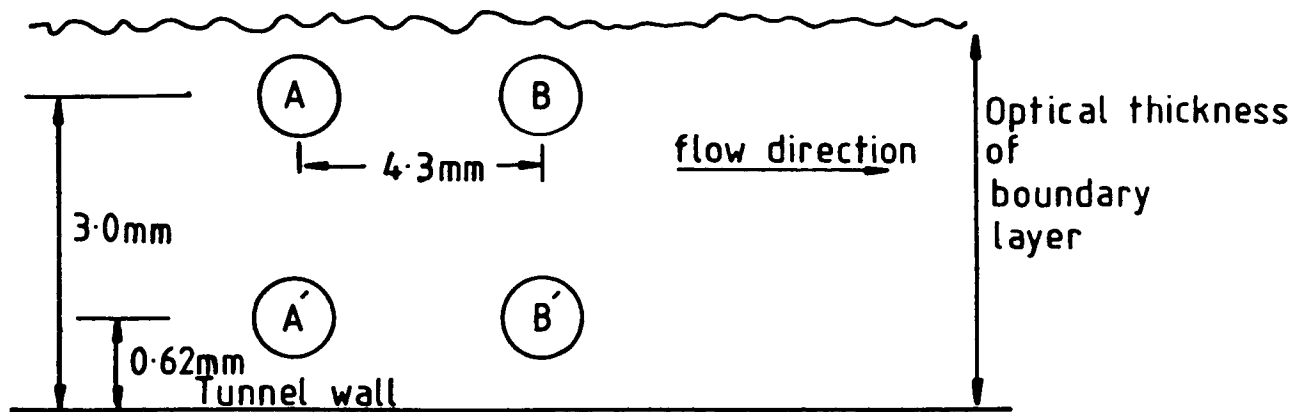
A×B cross-correlation 3·0 mm into boundary
             layer
A´×B´ cross-correlation 0·6 mm into boundary
             layer

Detector positions for cross-correlation of boundary layer structures

Fig. 18a

T = 20 μsecs.

NORMALIZED CONTENTS

CHANNEL

4   99
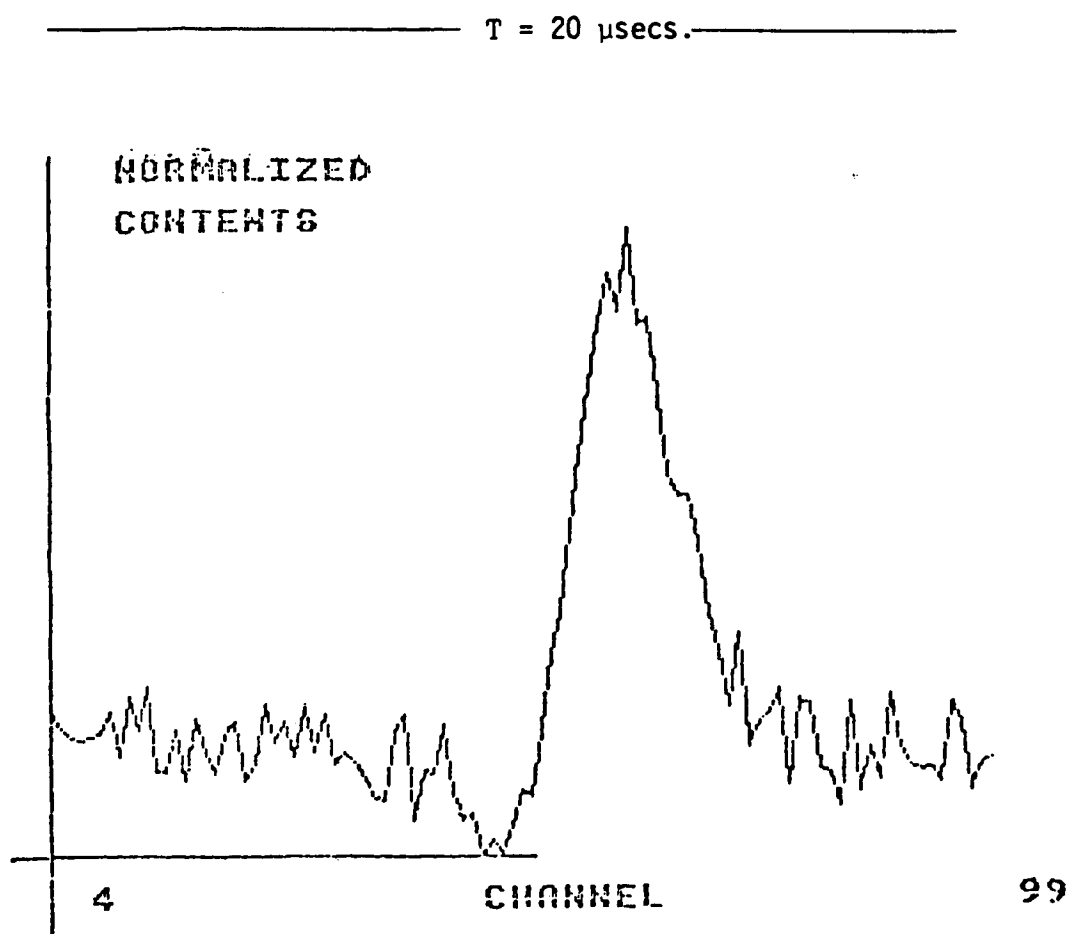
CROSS CORRELATION MEASUREMENTS TAKEN 3.0 mm INTO BOUNDARY LAYER

Fig. 18b

288

T = 10 μsecs.

NORMALIZED
CONTENTS

4   CHANNEL   99
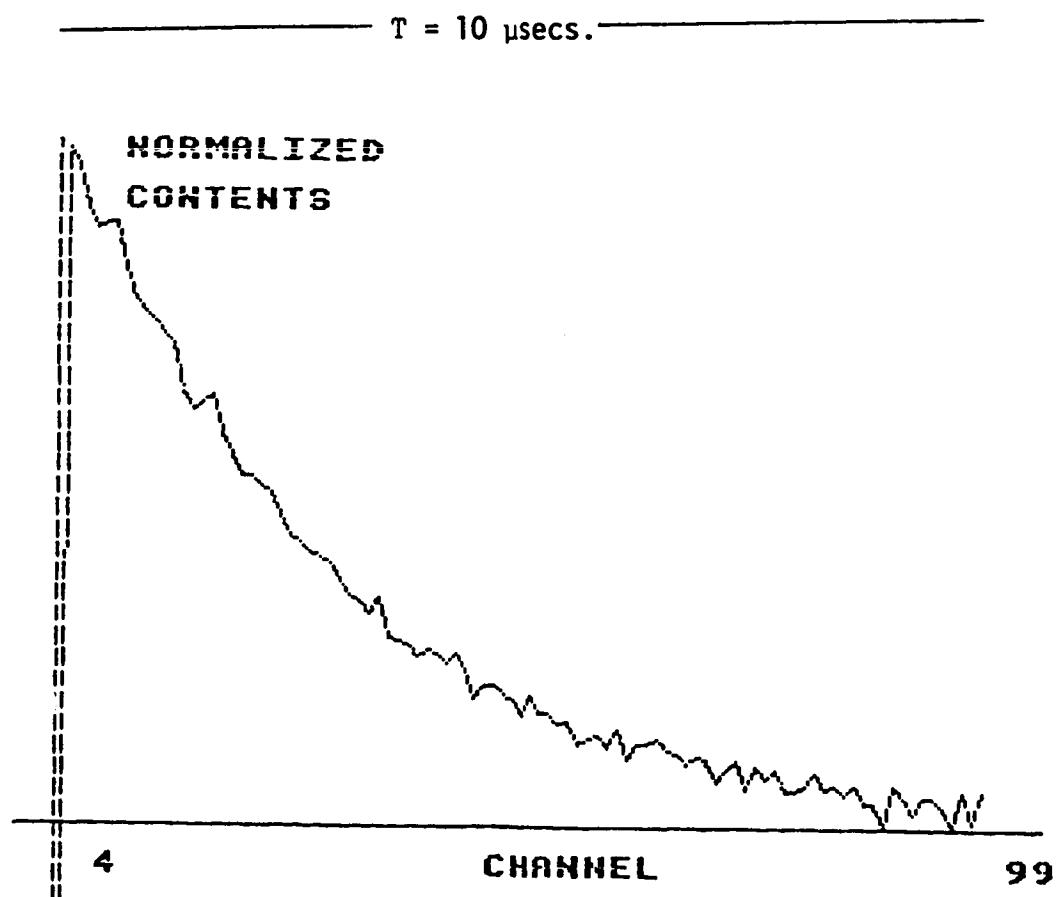
AUTOCORRELATION FUNCTION IN BOUNDARY LAYER DOWNSTREAM
OF STEADY SHOCK

Fig. 18c
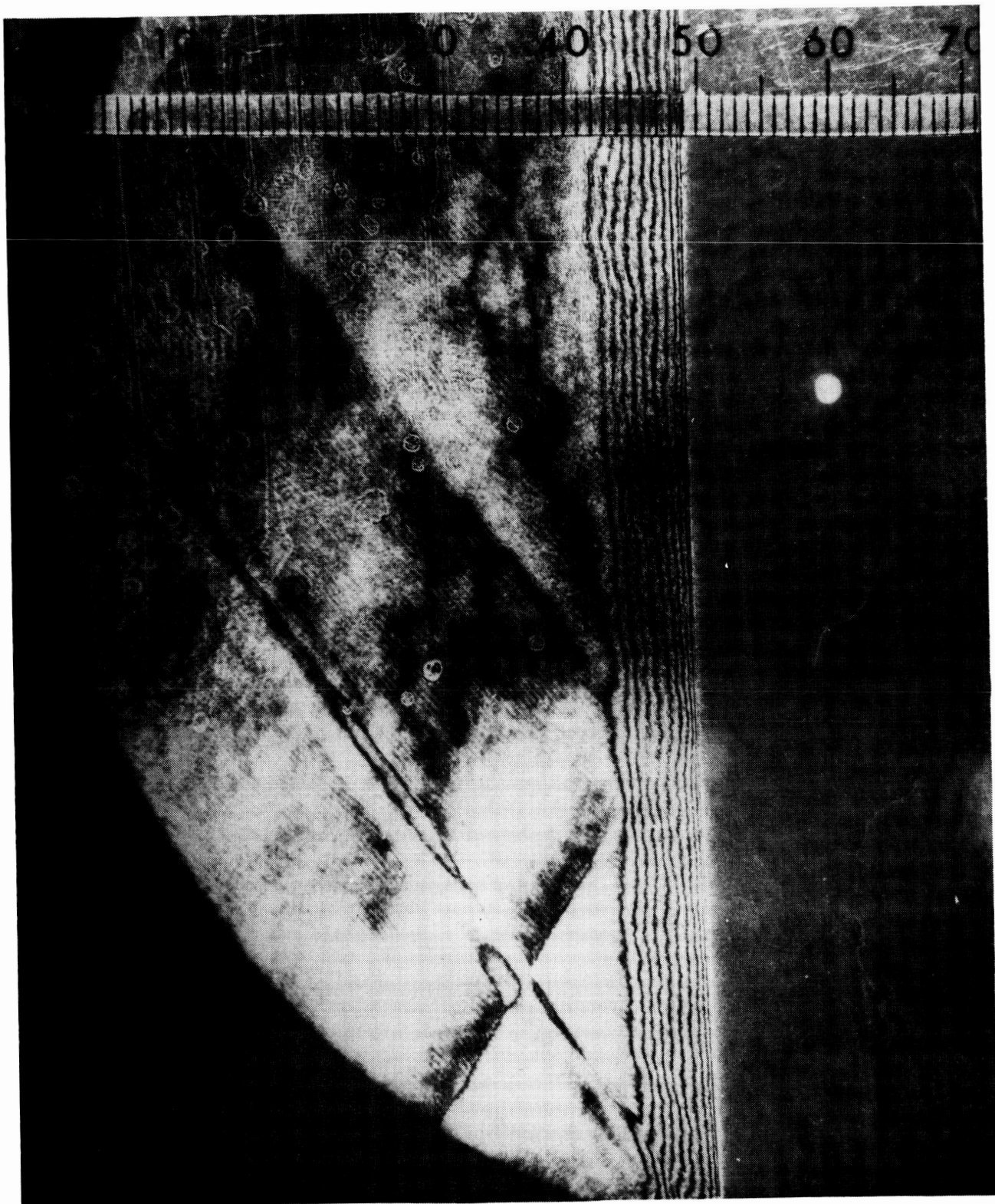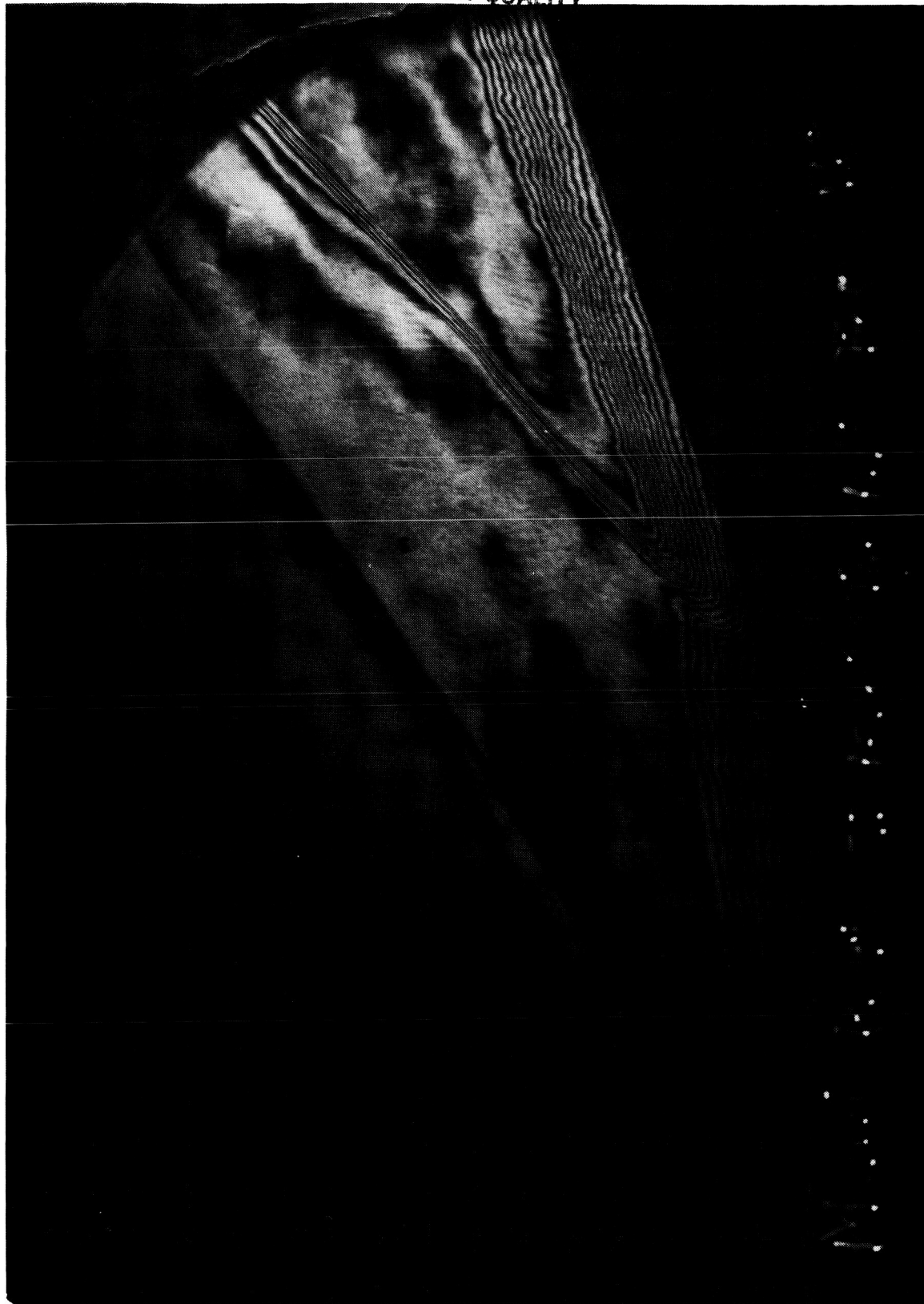
Fig. 19

Fig. 20
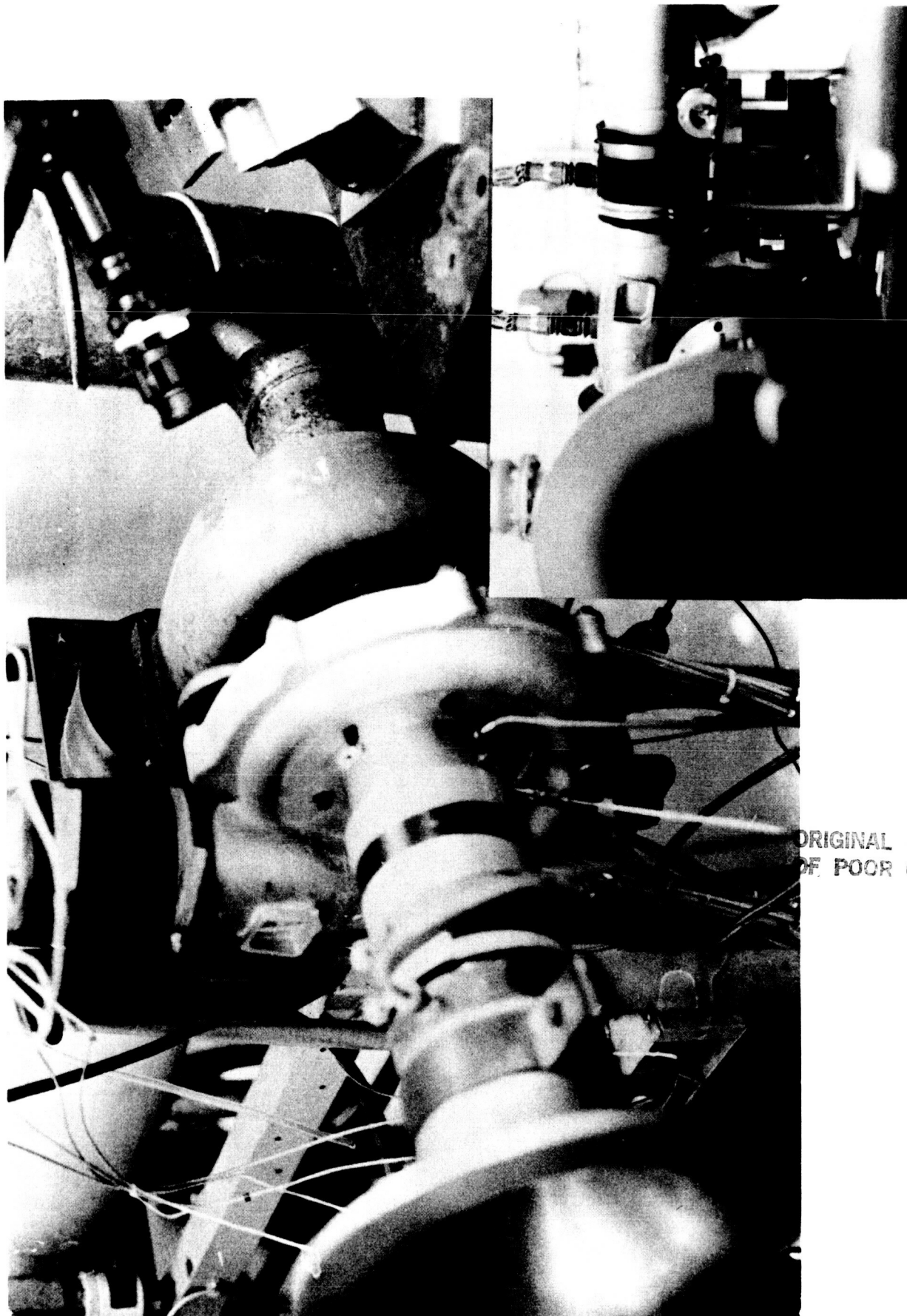
Fig. 21

Fig. 22   Photographic reconstruction, made from a white light copy hologram, showing the vortex structure in the diffuser

293

FLUID MECHANICS RESEARCH LABORATORY

FMRL TR-1

The Development of Laser Speckle or Particle Image
Displacement Velocimetry. Part I: The Role of
Photographic Parameters

by

L.M.M. Lourenco and A. Krothapalli

FAMU/FSU College of Engineering
Department of Mechanical Engineering
The Florida State University
Tallahassee, Florida 32306

May 1985

ACKNOWLEDGMENTS

Table of contents:

1. INTRODUCTION

One of the difficult problems in experimental fluid dynamics remains the determination of the vorticity field in fluid flows. The difficulty arises from the fact that vorticity is a quantity defined in terms of local velocity gradients and the available velocity measurement techniques e.g. Laser Doppler Velocimetry and Hot Wire Anemometry, are only sensitive to the local flow velocity. Current methods for vorticity measurements use multiple probes to independently measure one or more components of the velocity vector at two closely spaced spatial locations, from which a vorticity value is inferred by applying some kind of finite difference scheme (1,2). These methods suffer from some drawbacks. Firstly, when Hot-Wire probes are used, the local flow vorticity may be strongly influenced due to non-negligible blockage effects caused by the multiple probes. Secondly, the location of each individual measuring probe volume (LDV and HW alike) may not be spatially close enough to resolve and accurately measure the local velocity gradients. As a consequence the measured vorticity is only a "spatially filtered" estimate of the actual vorticity field. Another important aspect that needs to be considered is that these techniques can only provide "one point" information. In order to obtain whole field data, measurements must be carried out sequentially one point at a time. Although this sequential method can be easily implemented in applications involving steady flows, it is of rather difficult application in unsteady flow phenomena.

Recently, a novel velocity measurement technique, commonly known as Laser Speckle or Particle Image Displacement Velocimetry became available (3-7). This technique permits the simultaneous visualization of the two-dimensional streamline pattern in unsteady flows and the quantification of the velocity field.

The main advantage of this new technique is that the whole two-dimensional velocity field can be recorded with great accuracy and spatial resolution, from which the instantaneous vorticity field can be easily obtained. This constitutes a great asset for the study of a variety of flows that evolve stochastically in both space and time, and in the case of interest, to the study of unsteady vortical flows which occur in rotorcraft and in high angle of attack aerodynamics.

2. PRINCIPLE OF THE TECHNIQUE

The application of Laser Speckle or Particle Image Displacement Velocimetry to fluid flows followed the use of Laser Speckle methods in solid mechanics, in which object displacement and rotation were accurately measured (8).

When applied to the measurement of fluid flows the technique involves two equally important steps. In the first step a selected plane of the flow field is recorded. Similarly to Laser Doppler Velocimetry the flow is seeded with small tracer particles. A sheet of coherent light is used to provide a "surface" within the fluid. A pulsed laser such as a Ruby or a NdYag laser, or a CW laser with a shutter device is normally used as the light source. The laser sheet is formed, for example, by focusing the laser beam first with a long focal length spherical lens, to obtain minimum thickness, and then diverging the beam in one dimension with a cylindrical lens (Fig. 1). The light scattered by the seeding particles in the illuminated plane provides a moving pattern. When the seeding concentration is low, the pattern consists of resolved diffraction limited images of the particles. When their concentration increases, the images overlap and interfere to produce a random speckle pattern. A multiple exposure photograph records this moving pattern.

In a second step the local fluid velocity is derived from the ratio of the measured spacing between the images of the same tracer, or speckle grain, and the time between exposures. The recorded image formed by isolated Airy disks, in the cases of low seeding concentration, or speckle grains for high seeding concentration, is a complicated random pattern. In this image the local displacements can hardly be measured by visual or computer-aided inspection. Methods for the direct analysis of these images have been used but with limited success (9). The displacement measurements have an associated error which becomes important when the spacing between successive tracer images becomes small. This method also fails when the mean distance between tracers is of the same order of magnitude as the distance a tracer particle travels during the time between exposures. As a consequence the tracer concentration is usually kept small, resulting in velocity measurements with poor spatial density.

Alternative methods used in similar data analysis in solid mechanics are applicable and provide good results. Two methods are currently being

developed and investigated. These are the local coherent illumination to produce Young's fringes and local two-dimensional correlation of the image. In the first method, the diffraction produced by local coherent illumination of the multiple images in the photograph generates straight fringes in the Fourier plane of a lens. These fringes have an orientation which is perpendicular to the direction of the local displacement vector and a spacing which is inversely proportional to its magnitude (Fig. 2). The displacement vector is determined by the analysis of these fringe patterns. Amongst the various analysis methods being developed, Fourier and Autocorrelation techniques seem to be the most effective and accurate. In the two-dimensional correlation method a small area of the image being interrogated is digitized, in a NXN point format (where N is the number of pixel rows or columns), and a two-dimensional correlation is performed. This results in a digital autocorrelation function with a maxima at the coordinates corresponding to the average displacement of the tracers (Fig. 3). Basically this method is equivalent to the general Young's fringe method because the two-dimensional fourier transform of the fringe pattern is equal to the autocorrelation function. The major drawback of this method is that the computation of the autocorrelation function requires large data arrays and becomes extremely slow when N (number of pixel rows or columns) is large. A new processing method, proposed by Yao and Adrian (10), reduces the general NXN element of a two-dimensional problem to two N element one-dimensional problems, by compressing the information in two orthogonal directions using integration techniques. Although attractive, this procedure leads to some loss of information. Therefore, what has to be balanced is this loss versus the gain in computational speed. Future plans in this research include a critical evaluation of each of the above mentioned methods. However, we believe that the image analysis using the Young's fringe method is the most promising approach.

2.1 Image Analysis Using the Young's Fringe Method

Consider the function $D(x,y)$ describing the light intensity produced by the scatterers in the image plane of the photographic camera, where x,y are the plane coordinates. Considering that there is a in-plane displacement, dy, of the scatterers, the speckle or particle images will be translated by Mdy,

where M is the magnification of the camera lens. The resulting intensity distribution in the image plane becomes

$$D(x,y) + D(x,y+Mdy) = D(x,y) \circledast [\delta(x,y) + \delta(x,y+Mdy)] \tag{1}$$

where $\delta(x,y)$ is the Dirac delta function centered on x,y, and considering that a translation can be represented as a convolution with a delta function. The total intensity is recorded on a photographic plate. After development, the transmittance, Γ, of the negative is given by

$$\Gamma = a+b \, D(x,y) \circledast [\, \delta(x,y + Mdy)] \tag{2}$$

where a and b are characteristic constants of the photographic emulsion.

Two-dimensional Fourier transformation of the image is efficiently performed by optical processing of the photographic negative. This is achieved by locally analyzing the film negative with a probe laser beam. This process produces, as explained in the following, a straight fringe pattern whose orientation and magnitude are related to the direction and magnitude of the displacement. The resulting Fourier transform of the transmittance distribution, Γ, is

$$\tilde{\Gamma}(u,v) = a \, \delta(u,v) + b \, \tilde{D}(u,v) \, [1 + \exp(i2\pi vMdy/\lambda_a)] \tag{3}$$

where $\tilde{\Gamma}$ represents the Fourier transform of Γ, u and v are angular coordinates of a point in the Fourier plane of the lens, λ_a is the wavelength of the interrogating laser light beam.

The first term, a $\delta(u,v)$ on the r.h.s. of equation 3 represents the image of a point source, i.e. the interrogative beam, when diffraction effects are neglected. This image is seen as a small bright spot in the center of the Fourier plane (Fig. 2). The second term is composed of a diffraction pattern, characteristic of the speckle or particle images, modulated by
$[1+\exp(i2\pi vMdy/\lambda_a]$
The intensity distribution for the second term is obtained by multiplication with its complex conjugate, resulting in

$$|\tilde{D}(u,v)|^2 \, [\, 4 \cos^2(\pi vMdy/\lambda_a)] \tag{4}$$

301

The diffuse background, $|D(u,v)|^2$ is modulated by a set of Young's fringes whose spacing is given by

$$d_F = \frac{\lambda_a f_L}{M dy} \qquad (5)$$

where f_L is the focal length of the converging lens. Knowing M, f_L, λ_a and measuring d_F, the displacement dy is easily found from equation 5, with the direction of the motion perpendicular to the orientation of the fringes.

By scanning the multiple exposed photograph, one can resolve the two components of the displacement and derive the velocity vector at every point in the field. This is a unique capability of this technique.

2.1 Nature of the Present Research

The motivation for the present work is to determine and develop the necessary background for the use of Laser Speckle or Particle Image Displacement Velocimetry to study vortical unsteady flows.

In this phase of the work we report on the optimization of the photographic parameters involved in obtaining the multiple exposure photograph.

3. A GUIDELINE FOR THE CHOICE OF THE PHOTOGRAPHIC PARAMETERS INVOLVED IN A MEASUREMENT USING LASER SPECKLE (LSV) OR PARTICLE IMAGE DISPLACEMENT VELOCIMETRY (PIDV)

The parameters playing a role in velocity measurements using Laser Speckle or Particle Image Displacement Velocimetry are:

(i) Tracer: type, concentration and dimensions.

(ii) Exposure parameters: time between exposures, exposure time and number of exposures.

(iii) Film parameters: sensitivity, grain and resolution.

These parameters are interrelated and their choice depends upon several factors as follows: the flow field of interest, namely the velocity range and area of the flow to be recorded; the required spatial resolution and accuracy; available hardware such as type of laser, CW or pulsed, laser power and laser light wavelength, and on the camera used for the photography.

3.1 Tracer

Tracers to be used in a measurement involving LSV or PIDV have to be as small as possible to accurately follow the fluid motions, and good light scatterers. These requirements are usually met by tracers used in LDV applications. In liquid flows we recommend the use of pliolite particles, which are practically neutrally buoyant in water, latex and titanium dioxide. In air flows, oil smoke or fog produces a relatively uniform seeding.

As previously mentioned, the light scattered by the seeding particles can create, depending on the seeding concentration, two entirely different patterns. This originates two modes of operation of the technique. For low seeding concentrations, the pattern consists of resolved diffraction limited images of the particles. When this concentration increases, the images overlap and interfere in the image plane to produce a random speckle pattern. In either case, the pattern is recorded in a multiple exposed photograph from which the velocity data is obtained. However, in the Particle Image mode of operation, due to light seeding, regions of the flow field may be left unseeded, or with poor seeding, resulting in signal drop-out. On the other hand, in the Laser Speckle mode of operation, the drop-out problem is minimized but other more restrictive complications may occur, as described

below. These problems preclude the use of the Laser Speckle mode of operation in the majority of flow fields of interest.

The Laser Speckle mode of operation relies on the recording of identical laterally shifted speckle patterns. Slight out-of-plane motion of the scatterers, due to flow three-dimensionality, between the exposures results in speckle patterns that are not entirely similar. As a consequence, their correlation decreases and local coherent illumination does not produce Young's fringes, or produces fringes with poor contrast and signal to noise ratio (SNR). This poses a severe limitation in the use of the Laser Speckle Displacements for the measurement of velocity in turbulent flows, or flows with an important velocity component in the direction perpendicular to the measuring plane. The fringe quality becomes less dependent on the out-of-plane motion when individual particle images are imaged and recorded, i.e. in the Particle Image mode of operation. In this case the tolerance to out-of-plane motion is roughly equivalent to the width of the illumination sheet and focusing depth of field of the recording optics. In addition, the high concentrations required by the Speckle mode of operation cause multiple scattering effects which result in the spreading of the thin laser illuminating sheet. Furthermore, the high concentration of tracers may strongly influence the flow field.

In conclusion, for a successful measurement using this technique, there are practical bounds to seeding concentration (Fig. 4). The upper boundary for the seeding concentration being set by a value above which a speckle pattern is formed due to the interference of light scattered by the individual particles. If C_p is the particle concentration and ΔZ the width of the laser sheet, we obtain for the maximum concentration

$$\sqrt{\frac{1}{\Delta Z C_p}} \gg dp \tag{6}$$

where dp is the particle diameter. Considering typical values for $dp = 0.01\text{mm}$ and $\Delta Z = 0.5\text{mm}$ we obtain $C_p \ll 5.10^{12} \text{ m}^{-3}$.

The lower end for the seeding concentration can be determined by considering that, in order to have a valid measurement, a minimum number of particle image pairs must be present in the area scanned by interrogation beam. The case of having a single particle image pair in the interrogation area is an ideal one, because it yields fringes with optimum SNR (Fig. 2).

However, this situation can only be achieved by lightly seeding the flow, thus giving rise to the so-called drop-out problem. An interesting case occurs when only two particle pairs are present in the interrogation area. The corresponding diffraction pattern includes multiple equally intense fringe patterns due to cross interference of non-corresponding image pairs. In this case, the local displacement cannot be resolved (Fig. 5). Finally, as the number of particle image pairs in the interrogation area increases, the cross interference fringes become weaker in comparison with the "main fringe pattern" which reflects the local displacement (Fig. 6). The cross-interference fringes are sometimes designated as a "background speckle noise." Our experience shows that, for reasonable fringe quality, at least four particle image pairs need to be present in the interrogation area. This number can be somewhat relaxed if more than two exposures were used for the photography. Considering that these particles exist in the volume defined by the width, ΔZ, of the laser sheet, scanned by the beam whose diameter is D, we obtain for the average concentration:

$$C_p = \frac{16}{\Delta Z \ \pi \ D^2} \simeq 10^{-11} \ m^{-3}$$

(7)

3.2 Exposure Parameters

The exposure parameters are chosen in accordance with the maximum expected velocity in the field and the required spatial resolution. The spatial resolution, which is equal to the cross sectional area of the interrogating laser beam, is dictated by the scales involved in the fluid motion and should be less than the smallest scale.

The time between exposures, T, is determined by the maximum permissible displacement of a particle such that a correlation is obtained when locally analyzing the film negative with the probe laser beam. A necessary condition to obtain Young's fringes requires that the distance between adjacent particle images be less than a fraction of the analyzing beam diameter. In practice the maximum permissible displacement that can be detected corresponds to the case when the fringe spacing, d_F, is larger than the diffraction limited spot size, d_s, of the interrogating optics. In analytical terms:

$$d_F = \frac{\lambda_a f_L}{M v_{max} T} \ > \ d_s = \frac{4 \lambda_a f_L}{\pi \ D}$$

(8)

where M is the magnification factor, D and λ_a are respectively the

305

interrogation beam diameter and laser light wavelength. We obtain for the
time between exposures

$$T = \frac{0.5 \, D}{M v_{max}} = \frac{1}{F}$$ (9)

v_{max} is the maximum expected velocity in the field, and F the frequency
corresponding to the inverse of the period T. For practical purposes we use
the constant 0.5 instead of 0.8 as it would be given by equation 9.

The exposure time, t, is a free parameter when a CW laser source is used
together with a shutter. In previous applications (3-7) the exposure time has
been kept as small as possible for minimum particle image size. In a later
study, Lourenco (11) demonstrated that the duration of the exposure time can
be of the same order of magnitude as the time between exposures.

For very short exposures the recorded particle images are identical to
the diffraction limited particle images as the particles appear to be
stationary during the exposure. For longer exposures the recorded images
become streaks whose length is directly proportional to the exposure time.
Coherent illumination of these images generates Young's fringes superposed on
a diffraction pattern which depends on the streak length. In the limiting
case of a very short exposure, the diffraction pattern is symmetric and has a
circular shape (Fig. 2). When the exposure time is increased, small streaks
are generated, and the diffracted light in the spectrum is concentrated in a
band whose width is inversely proportional to the streak length (Fig. 7).

Because of the finite width of the diffraction pattern, the number of
fringes, n_F, in the pattern becomes a function of the ratio between the streak
separation to the streak length, l_s. In analytical terms:

$$n_F = \frac{dy}{l_s} + 1$$ (10)

For an accurate measurement of the fringe spacing, it is necessary to have a
reasonable number of bright fringes. Usually five bright fringes give good
results.

Another parameter determining the degree of accuracy with which the
fringe spacing can be determined is the contrast and sharpness of the Young's
fringes. If the number of exposures, N, is larger than two and the particles

are displaced by the same amount after each exposure, the sharpness of the interference fringes can be greatly improved.

For a multiple exposure, the function describing the light intensity of the point sources becomes

$$D(x,y) \ @ \ \sum_{n=0}^{N-1} \delta(x,y + nMdy) \qquad (11)$$

resulting in an amplitude distribution of the transmittance of the negative in the Fourier plane of a lens, as follows:

$$|\widetilde{D}(u,v)|^2 \ \left\{ N+2 \ \sum_{n=1}^{N-1} n \cos [(N-n) \ 2 \ \pi M \ dy/\lambda_a] \right\} \qquad (12)$$

For a number of exposures, N, equal to two a relation similar to equation 4 is obtained as expected.

Figure 8 displays the fringe width for multiple exposures, normalized with the corresponding width for a double exposure, versus the number of exposures. It is clearly seen that an optimum fringe width can be obtained with a limited number of exposures.

The sharpening of the fringes using a multiple exposure recording technique is of great advantage because it allows a very easy visual and qualitative "measurement" of the direction and spacing of the young's fringes. It also increases their signal to noise ratio. Note that this improvement in the signal to noise ratio is a result of the artificial increase in particle concentration due to the multiple exposure.

3.3 Choice of the Film and Laser Power Requirements

The technique relies on the ability to detect and record on photographic media the seeding particles images. The particle is a function of the scattering power of the particles within the fluid, the amount of light in the illuminating sheet, camera lens and film sensitivity at the wavelength of the illuminating laser light. Although the particle detection increases

proportionally with increasing power of the illuminating laser, it is of great importance to keep the laser power requirement to its minimum. An important reason for this limitation is economy as the main component in the cost of the apparatus is the laser source and its price increases very rapidly with the power delivered.

In this section, we suggest films to be used and the laser power required to expose these films.

To compensate for the limited illuminating laser power, the films used to record the particle images, are required to have good sensitivity, but without sacrificing film resolution. When good precision is necessary, films with a resolution of about 300 line-pairs/mm and sensitivity from 25 to 125 ASA (Afga Ortho 25, Kodak Technical Pan 2415) are suitable for the use either with pulsed Ruby lasers ($\lambda \sim 700$nm) or pulsed, frequency doubled, NdYag lasers and CW Argon-Ion lasers ($\lambda \sim 500$nm). When a NdYag or a CW Argon-Ion laser are used more sensitive films may be used. A particular film, Kodak Royal-X Pan, 1250 ASA, has excellent sensitivity in 400-600nm range, and retains fairly good resolution (100 line-pairs/mm).

Another parameter to be accounted for is the film grain. When illuminating the film negative to produce Young's fringes, the film's unexposed grains can introduce amplitude and/or phase changes into the wavefront of the analyzing laser beam and thus create additional noise. This noise has generally a frequency content which is in the same range as the Young's fringes. Therefore its elimination is difficult either from optical or digital filtering. Film grain cannot be totally eliminated and it will always be present in different degrees, especially in applications where fast film is used, to cope with low power density of the illuminating sheet. A method of solution as been proposed (6) by which this source of noise is considerably reduced. It consists of producing a positive copy by contact printing on a very high resolution fine grain film, for example holographic plates. The positive copy is analyzed in the same manner using the laser probe beam. Figures 9a) and 9b) display respectively the interference fringe patterns generated for the film negative and corresponding positive. A remarkable decrease in noise level is achieved. Another advantage of using this procedure is that the intensity of central zero order spot, due to the laser probe beam, is also decreased or eliminated.

Once the film is selected, the amount of laser power required for the

exposure can be computed. For a successful exposure of the photographic emulsion the energy scattered by a tracer particle and viewed through the camera lens has to be larger than the film sensitivity at the wavelength of the illuminating laser. It is customary to write this condition in the following analytical form:

$$\bar{E} = \int_{\Delta t} T dt > C E_O \tag{14}$$

where $\bar{E}$ is the mean exposure level for a single particle (J/m^2), T is the average intensity of the light scattered by a particle (W/m^2), $E_\emptyset$ is the film fog level and Δt is the exposure time. C is a constant between 1 and 10. The fog level is defined as the exposure level below which the transmissivity of the film is independent of the incident intensity (Fig. 10). The average intensity, T, of the light scattered by a single particle can be expressed in terms of (10)

$$T = \frac{4}{\pi k^2 d_i^2} I_O \int_\Omega \sigma^2 \, d\Omega \tag{15}$$

where I_O is the intensity of the illuminating sheet (W/m^2), k is the illuminating laser light wavenumber, $\sigma = \underline{g} \cdot \underline{g} *$ is the Mie parameter, the viewangle of the camera lens and d_i is the dimension of the diffraction limited particle image composed of two terms (10), neglecting aberrations and grain noise, as follows

$$d_i = \sqrt{d_p^2 + d_e^2} \tag{16}$$

The first one being the particle diameter and the second one the edge spread caused by the limited response of the recording optics

$$d_e = 2.44 \ \lambda(1+M)F\# \tag{17}$$

with F# the camera objective F number.

When a pulsed laser is used the laser power required is simply determined from equation 14, considering that the particle is stationary during the exposure

$$I_o > \frac{CE_o(\pi K^2 d_i^2)}{4 \int \sigma^2 \, d\Omega} \tag{18}$$

Considering that for a pulsed laser the pulse duration (= exposure time) is a fixed parameter, it is customary to express equation 18 in terms of energy per pulse, ε_o

$$\varepsilon_o > \frac{CE_o(\pi K^2 d_i^2)}{4 \int \sigma^2 \, d\Omega} \tag{19}$$

The recommended value for the constant C is between 3 and 5 to compensate for film reciprocity effects caused by the very short exposure.

In applications involving the use of CW laser the exposure time is variable and considerably longer. In this case integration of equation 14 is somewhat more elaborate. For the sake of simplicity let us assume that the fluid motion, and hence the seeding particles displacement is unidimensional. Let r_o, r and u be respectively the initial position, current position and velocity of a tracer particle, in the film plane. The current particle position can be expressed as

$$r = r_o + u \, t \tag{20}$$

The exposure can be determined integrating equation 14 and considering two cases, $t < \frac{d_i}{u}$ and $t \geq \frac{d_i}{u}$

$$\overline{E} = \int_{\Delta t < \frac{d_i}{u}} T(r) \, dt = \begin{cases} T \dfrac{(r - r_o)}{u} & r_o < r \leq r_o + u. \Delta t \\[2mm] T \Delta t & r_o + u \Delta t < r \leq r_o + d_i \\[2mm] \dfrac{T}{u}(r_o - r + d_i + u \, \Delta t) & r_o + d_i < r \leq r_o + d_i + u. \Delta t \end{cases}$$

$$\tag{21}$$

$$\overline{E} = \int_{\Delta t \geq \frac{d_i}{u}} T(r) \, dt = \begin{cases} T \dfrac{r - r_o}{u} & r_o < r \leq r_o + d_i \\[2mm] T \dfrac{d_i}{u} & r_o + d < r \leq r_o + d_i + u. \Delta t \\[2mm] \dfrac{T}{u}(r_o - r + 2d_i + u \, \Delta t) & r_o + d + u. \Delta t < r \leq r_o + 2d_i + u. \Delta t \end{cases}$$

310

The maximum exposure is obtained for exposure times larger or equal to $\frac{d_i}{u}$
Thus, for the whole field, the optimum exposure, is equal to d_i/V_{max} which results in the maximum exposure, without a significant reduction on the dynamic range of the technique, as shown in the following section.

The CW laser power required is given by,

$$I_o \geq \frac{CE_o(\pi K^2 d_i^2)V_{max}}{4 \int \sigma^2 \, d\Omega \, d_i} \tag{22}$$

Equation 19 shows that CW laser power required for a measurement increases with the flow velocity. This limitation does not apply to the case of a pulsed laser where the pulse duration is independent of the flow velocity.

4. VELOCITY DYNAMIC RANGE

In the following we will analyze the technique's abilities of resolving large velocity gradients in flow fields, i.e. its dynamic range. The dynamic range is defined as the largest velocity difference that can be detected in the flow field.

The low end of the dynamic range is determined by considering that for a measurement the spacing between the successive particle diffraction limited images or streaks is well resolved, i.e. do not collapse on each other. In analytical form

$$l_s = d_i + V.t < V.T \tag{23}$$

Considering that the time between exposures, T, is a function of the maximum velocity V_{max}, substituting $t \simeq o$ for a pulsed laser and, $t = \frac{di}{V_{max}}$ for a CW laser, yields the following expressions for the minimum velocity,

$$V_{min} = \frac{2\ M\ V_{max} d_i}{D} \qquad \text{pulsed laser} \tag{24}$$

$$V_{min} = \frac{2\ M\ V_{max}\ d_i}{D - 2\ M\ d_i} \qquad \text{CW laser} \tag{25}$$

The velocity difference $\Delta V = \frac{V_{max} - V_{min}}{V_{min}}$ is the velocity dynamic range and we obtain,

$$\Delta V = \frac{D}{2\ M\ d_i} - 1 \qquad \text{pulsed laser} \tag{26}$$

$$\Delta V = \frac{D - 2\ M\ d_i}{2\ M\ d_i} - 1 \qquad \text{CW laser} \tag{27}$$

The dynamic range increases with shorter pulse durations and is maximum in applications involving the use of a pulsed laser. Considering typical values for $d_i = .03mm$, $D = 0.5mm$ and $M = 1$, we obtain for the dynamic range,

$$\Delta V \simeq 7.5 \qquad \text{pulsed laser} \tag{28}$$

$$\Delta V \simeq 6.5 \qquad \text{CW laser} \tag{29}$$

5. ACCURACY OF THE TECHNIQUE

The overall accuracy of the technique depends on the accuracies which can be achieved in the photographic procedure and processing techniques. In this report we only discuss the accuracy of the photographic recording. The sources of error are the lens aberrations and the limited film resolution, causing the position of the particles to be recorded with an inherent error, and the spurious contributions on the in-plane displacement recording by the out-of-plane motion.

In section 3.1 it was pointed out that out-of-plane motion was a severe limitation on the use of speckle in Fluid Dynamics applications. The reason for this limitation was that slight out-of-plane motion by the scatterers, between the multiple exposure, results in non-identical shifted patterns poorly correlated. To cope with this problem one operates in the Particle Imaging mode, where the particles are directly imaged and recorded. However, as shown in the following, out-of-plane motion may also contribute to considerable errors in the velocity measurement.

Let us consider the imaging system of figure 11 and the particle in position P_o within the laser sheet. Between exposures the particle moves to a position M_o, due to three-dimensional fluid motion. The components of the displacement vector are dx, dy, dz, with dx and dy, the in-plane and dz the out-of-plane components of the displacement. In the image plane the photographic plate records the position of the particle at P_L and M_L. The coordinates of these points are given by:

$$\left.\begin{array}{l} -Mx \\ -My \\ d_o + d_L \end{array}\right\} P_L \qquad\qquad \left.\begin{array}{l} -M(x+dx)\,(1+ dz/d_L) \\ -M(y+dy)\,(1+ dz/d_L) \\ d_o + d_L \end{array}\right\} M_L \qquad (30)$$

where second order terms have been neglected for simplicity.

The displacement $P_L M_L$, measured by means of Young's fringes is given by

$$dx_m = Mdx \left(1 + \frac{xdz}{dxd_L}\right) \qquad\qquad dy_m = Mdy \left(1 + \frac{ydz}{dyd_L}\right) \qquad\qquad (31)$$

and the measured displacement components referred to the object plane are

313

$$dx_o = dx + \frac{xdz}{d_L} \qquad\qquad dy_o = dy + \frac{ydz}{d_L}$$

The contribution of the out-of-plane displacement to the measured displacement is given by two parasite terms (xdz/d_L) and (ydz/d_L). The error produced by the out-of-plane motion while negligible in the neighborhood of the optical axis, increases linearly, and may become important, with the distance from the optical axis. The influence of the out-of-plane motion becomes particularly important when imaging the flow with short focal and wide angle objectives.

A relation can easily be found for the theoretical error in a measurement due to out-of-plane motion:

$$E_x = \frac{dz}{dx} \tan \psi x$$

(33)

$$E_y = \frac{dz}{dy} \tan \psi y$$

where ψ_x and ψ_y are respectively semi-field angle components along the x and y axis respectively. Hence the error depends only on the ratio of the out-of-plane to in-plane component of displacement and the tangent of the semi-field angle. Figure 12 shows the theoretical relative error for various ratios of dz/dx and tan ψx.

6. VALIDATION OF THE TECHNIQUE

6.1 Experimental Configuration

In order to evaluate the present capabilities of the technique a bench-top experiment was performed. In view of the application of the technique to vortical flows, two flows that include important vortical motions were generated and recorded. Both flows were created by towing models in the reduced scale Fluid Mechanics Research Laboratory towing tank facility (Fig. 13). The first one consisted of the Karman vortex street generated by a cylinder with 10 mm in diameter, and the second one by the flow over a 60mm chord airfoil (NACA 0012), at a 30 degree incidence. Both models were towed with a velocity of 23.5 mm/sec. The fluid used in these experiments was water seeded with small, .004 mm in diameter, particles (TSI model 10087). The corresponding Reynolds numbers were 230 for the cylinder and 1400 for the airfoil. These flows are excellent test cases because they include large scale vortical motions and extreme velocity gradients. These extreme ngradients serve as a test to the technique's capabilities of providing information over a large velocity range.

A view of the laser sheet arrangement is also shown in figure 13. The laser beam from a 5 Watt Argon-Ion laser (Spectra-Physics series 2000) is steered and focused to a diameter of .3mm using an inverse telescope lens arrangement. A cylindrical lens, with a focal length of -6.35 mm, is used to diverge the focused beam in one dimension, creating a light sheet. The laser sheet is 70 mm wide and illuminates the mid-span section of the models.

For the multiple exposure, the CW laser beam is modulated using a Bragg cell. This shutter has been assembled using standard equipment. A schematic is shown on figure 14. The advantages in using this shutter arrangement are the possibility of an independent choice of the number of exposures, the time between exposures and the exposure time.

Due to conditioning optics and Bragg cell losses, the available laser power was reduced to 70% of the total power. In this experiment the laser delivered 8 Watts in the multiline mode. The power density, I_o, of the laser sheet was

$$I_o = \frac{I}{d_b \Delta Z} = .27 (W/mm^2) \tag{34}$$

with d_b ΔZ the laser sheet cross section, where d_b = .3 mm is the width of the focused laser beam, and ΔZ = 70 mm the laser sheet span.

The recording optics consisted of a 4x5" format camera with interchangeable objective lens. In this experiment we used a 135 mm lens. The lens aperture was set at F# 5.6 and the magnification factor was 0.47. The camera was positioned in the laboratory reference frame. Therefore, the flow field was recorded in the reference frame moving with the mean flow. The film used was a KODAK technical pan 2415 with a sensitivity of 125 ASA. This film has a resolving power of 320 line-pairs/mm and extremely fine grain. The large resolving power is required for increased recording accuracy. This corresponds to a inaccuracy of 0.002-0.003 mm in the recording of the position of the tracers which corresponds in the present case to an error of 1% or less in the high end of the velocity range.

6.2 Results and Discussion

6.2.1 Flow behind a circular cylinder

The technique was first tested in the measurement of the flow behind a cylinder. The frequency of exposures was optimized according to equation 9 and equal to 90 Hz. The exposure time was 1 msec, which corresponded roughly to d_i/V_{max}.

Figure 15 is a triple exposed photograph of the flow. Characteristic fringe patterns, resulting from coherent illumination of selected locations of the photograph are also displayed.

The velocity data was acquired in a regular mesh by digital processing of the Young's fringes, produced by point by point scanning of the photograph. The scanning step size and the dimension of the analyzing beam diameter were .5 mm, which corresponds to a spatial resolution of about 1 mm in the object plane. The fringe patterns were processed using the interactive one-dimensional averaging software described in references 4,6 at the von Karman Institute Digital Image Processing Facility.

Figure 16 shows the mapped two-dimensional velocity vector field superposed on the original photograph. As it can be observed, this data represents with great fidelity the flow field. However, in some regions velocity data drop-out occurs, due to the following reasons. Firstly, at the

locations near the instantaneous centers of rotation of the flow, the velocity of the particles is very close to zero and beyond the low end of the dynamic range of the technique. This could be avoided if the convective flow velocity was measured, for example, by having the camera traveling with the model. Secondly, some data drop-out occurs at random locations due to various reasons such as scratches in the film, fringes with bad SNR or lack of seeding. These regions of signal drop-out were "filled-in" using an interpolation algorithm. Because the two-dimensional velocity field is measured on a square mesh, the spatial derivatives of the velocity, and consequently the vorticity, can be estimated by a simple algorithm. Considering that the grid location of the measurement points are labeled with indices i and j, the vorticity component, $\Omega_{i,j}$, at location i, j is

$$\Omega_{i,j} = \frac{V_{i+1,j} - V_{i-1,j}}{2 \Delta x} - \frac{U_{i,j+1} - U_{i,j-1}}{2 \Delta y} \tag{35}$$

For the boundaries of the velocity field, an excentered scheme is used to evaluate the spatial derivatives. This results in a small inaccuracy on the evaluation of the vorticity at the boundary. Figure 17 shows the vorticity contours for the flow behind the cylinder. Improved visualization of the velocity and vorticity fields is obtained by color encoding the different levels of the vorticity component Ω as shown in figure 18.

6.2.2 Flow over the NACA 0012 Airfoil

For the flow over the airfoil the frequency of exposures was varied over a wide range from 60 Hz to 90 Hz. Preliminary analysis of the film negatives showed that best results were obtained with a frequency of 90 Hz. The exposure time was 1 msec and kept constant throughout the experiment. Photographs obtained with different number of exposures are shown in figure 19. The figure demonstrates that a significant increase in quality of the "flow visualization" is achieved with a larger number of exposures. Another equally important effect of the number of exposures is the improvement of fringe sharpness and SNR.

A complete analysis of the triple exposed photograph (Figure 19 b)) was also carried out and results are presented on figure 20.

7. CONCLUSIONS

Using the apparatus described in the previous sections a series of
Particle Displacement Images were successfully taken using different exposure
parameters. Local coherent illumination by the probe laser beam yielded
Young's fringes of good quality at almost every location of the flow field.
Using the von Karman Institute Image Processing facility, these fringes were
analyzed and the velocity and vorticity fields were derived. The present
study has lead to the following conclusions:

(i) Particle Image Displacement Velocimetry is indeed suitable for the study
     of flows with vortical motions.

(ii) In the present study, the flow velocities were limited to a small value
     (50mm/sec) because of laser power limitations. However this limitation
     does not apply if a pulsed laser delivering high energy pulses is used.
     Once a pulsed laser becomes available to us, tests in the FMRL wind
     tunnel will be conducted to prove the feasibility of the technique in
     higher velocity (up to 100m/sec) air flows.

(iii) A larger towing tank facility has just become available to the FMRL in
     which tests can be carried out in a wide range of towing velocities.
     This facility is provided with camera mounts that travel with the towed
     model. Therefore it is possible to capture the flow in two reference
     frames: the one traveling with the model and that of the laboratory.

(iv) The next step in the development of the technique will consist on the
     development of schemes to compensate for the error introduced by the
     out-of-plane motion and device methods for its correction.
     Simultaneously a method for the measurement of the magnitude of the
     out-of-plane motion will be developed.

(v) The FMRL capabilities in the area of digital processing of the Young's
     fringes is presently being developed. In a later stage Image
     Correlation techniques, will also be investigated, and a comparison of
     the performance of the two methods will be carried out.

References

1. Dimotakis P.E. "Laser measurements in turbulent flow"
   Bull. Amer. Phys. Soc., vol. 28, 1983
2. Wallace J.M. "Measurement of vorticity using hot-wire anemometry"
   Bull. Amer. Phys. Soc., vol. 28, 1983
3. Simpkins P.G., Dudderar T.D. "Laser speckle measurements of transient
   Bernard convection"
   J. Fluid Mech., vol. 86, 1978
4. Meynart R. "Instantaneous velocity field measurements in unsteady gas flow
   by speckle velocimetry"
   Applied Optics, vol. 22, 1983
5. Meynart R. "Speckle velocimetry study of a vortex pairing in a low Re
   unexcited jet"
   Physics of Fluids, vol. 26, 1983
6. Lourenco L.M.M., Meynart R. "Laser speckle velocimetry in fluid dynamics
   applications"
   in VKI lecture series 1984-03, Digital Image Processing in Fluid Dynamics,
   1984
7. Adrian R.J., Yao C.S. "Development of pulsed laser velocimetry (PLV) for
   the measurement of fluid flow"
   in Proceedings, Eighth Biennial Symposium on Turbulence, Rolla, Mo., 1984
8. Erf R.K. "Application of laser speckle to measurement"
   Laser Applications, vol. 4, Academic Press
9. Elkins R.E., Jackmann G.R., Johnson R.R., Lindgreen E.R., Yoo J.K.
   "Evaluation of stereoscopic trace particle records of turbulent flows"
   Rev. Sci. Instrum., vol. 48, 1977
10. Yao C.S., Adrian R.J. "Orthogonal compression and one-dimensional analysis
    technique for measurement of two-dimensional particle displacements in
    pulsed laser velocimetry"
    Applied Optics, vol. 23, 1984
11. Lourenco L.M.M. "Velocity measurement by optical and digital processing of
    time exposed particle images"
    Bull. Amer. Phys. Soc., vol. 29, 1984
12. Adrian R.J. "Scattering particle characteristics and their effect on
    pulsed laser measurements of fluid flow: speckle velocimetry vs. particle
    image velocimetry"
    Applied Optics, vol. 23, 1984
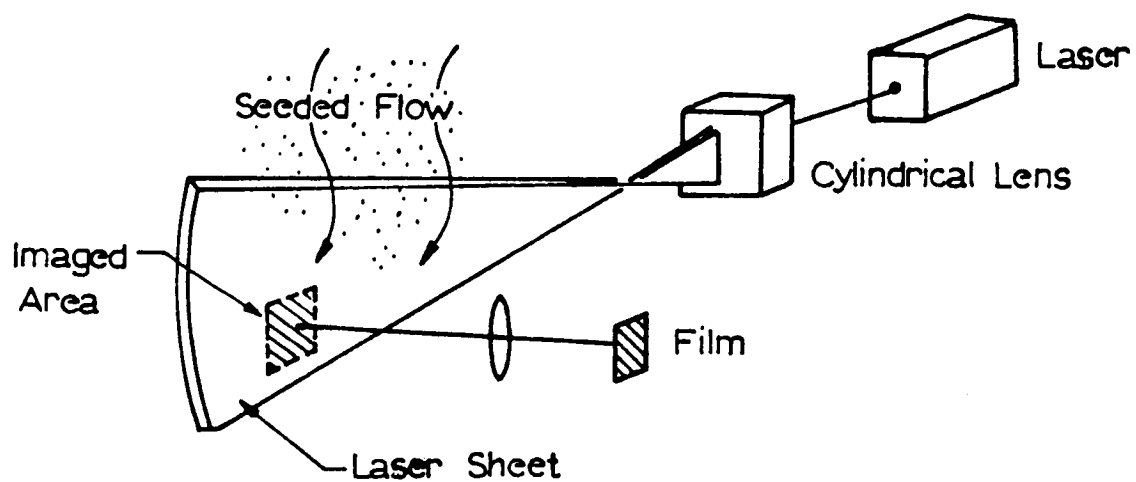
Figure 1. Schematic of an arrangement for photography
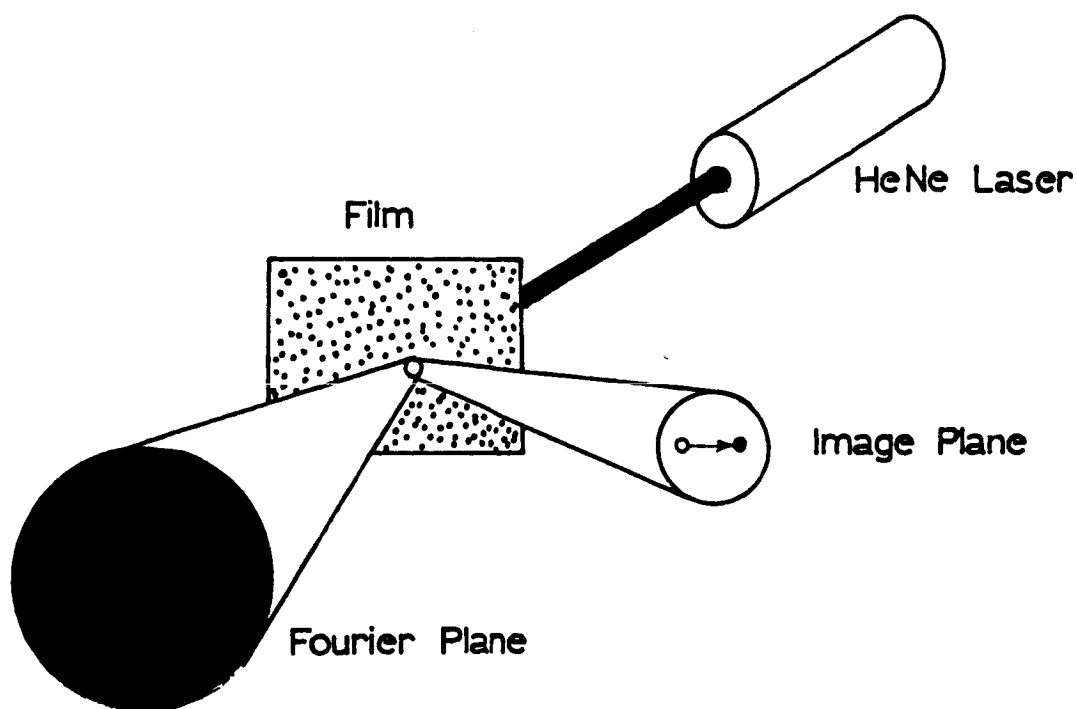
Figure 2. Young's fringe pattern generated by a particle pair.
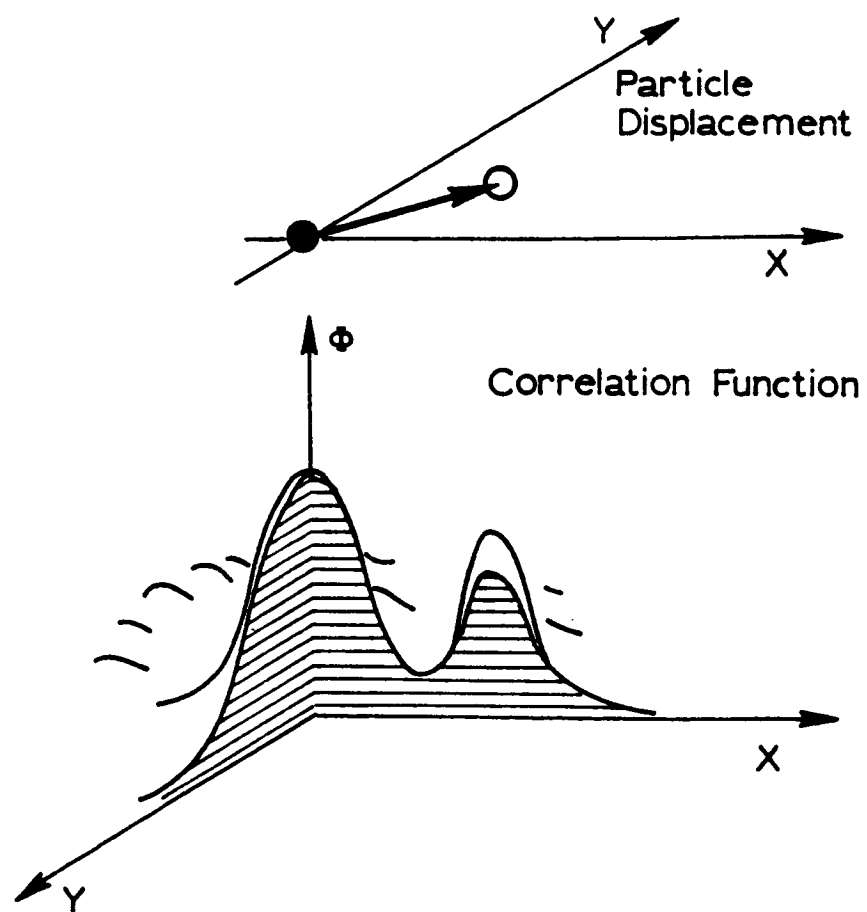
Figure 3. Schematic of the image correlation function
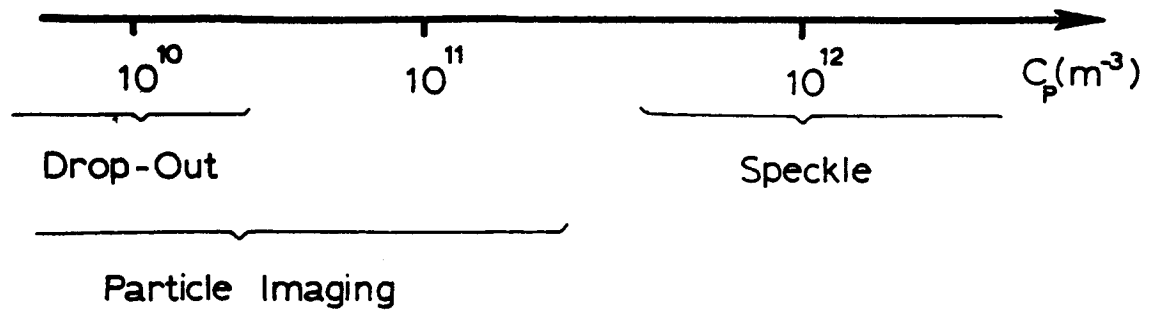
Figure 4. Mode of operation versus seeding concentration
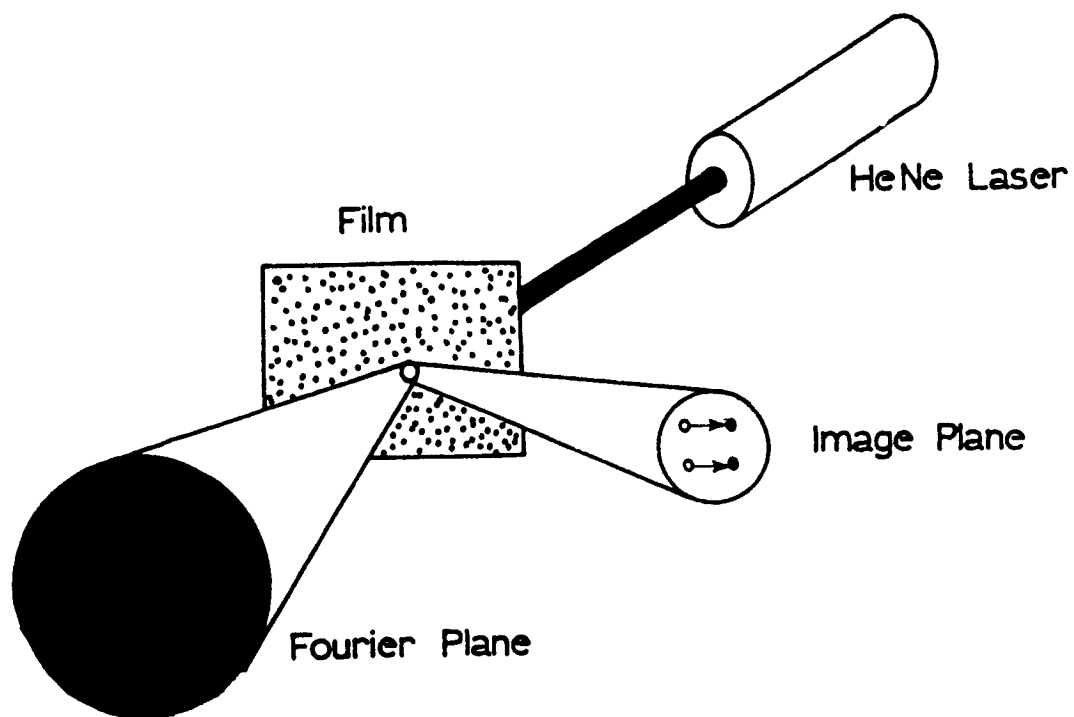
Figure 5. Cross-interference fringe pattern generated by two
particle pairs.
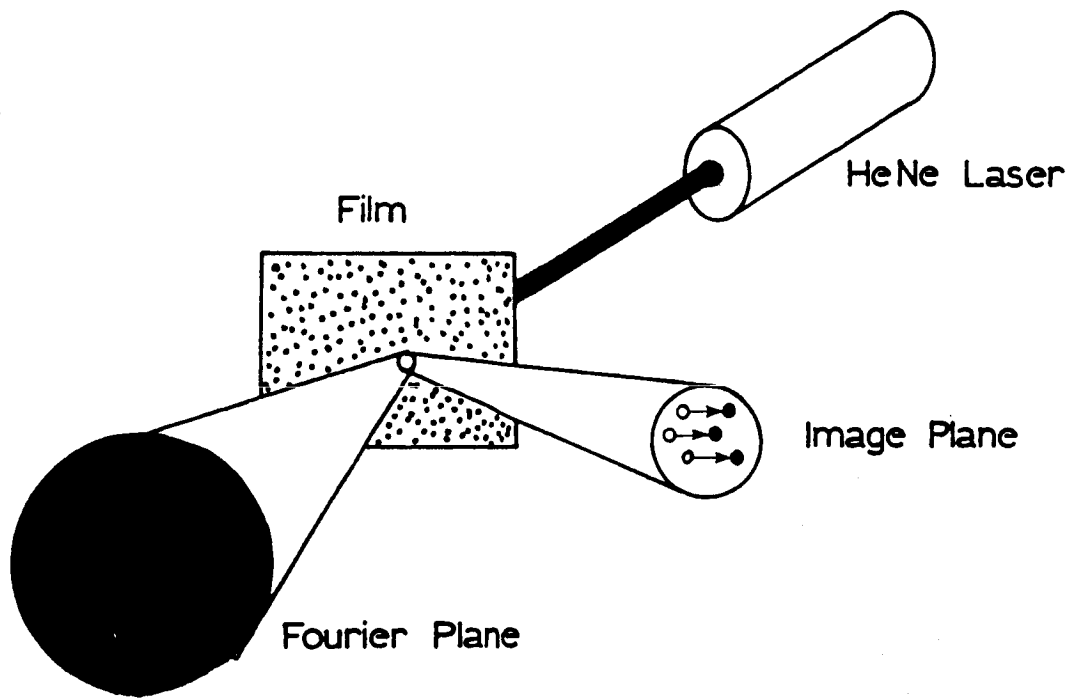
Figure 6. Fringe pattern generated by multiple image pairs.
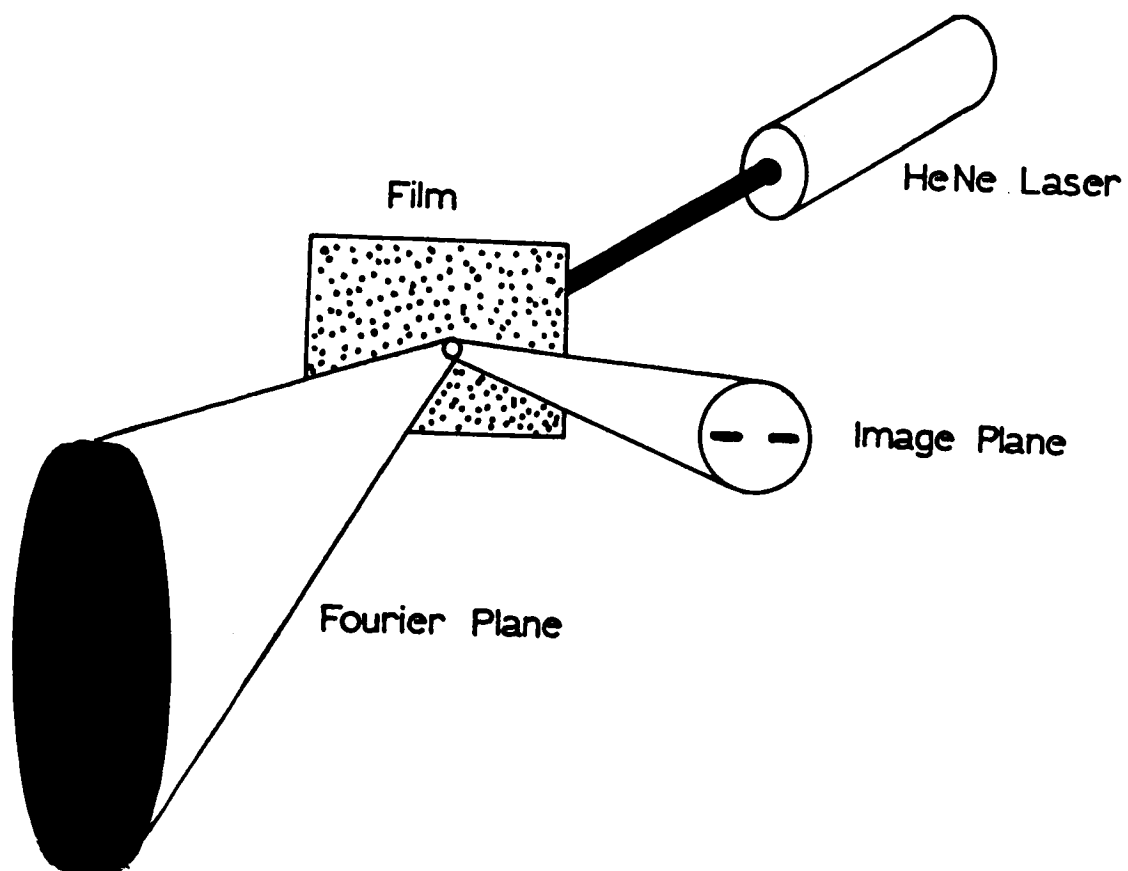
Figure 7. Fringe pattern generated by streak images.
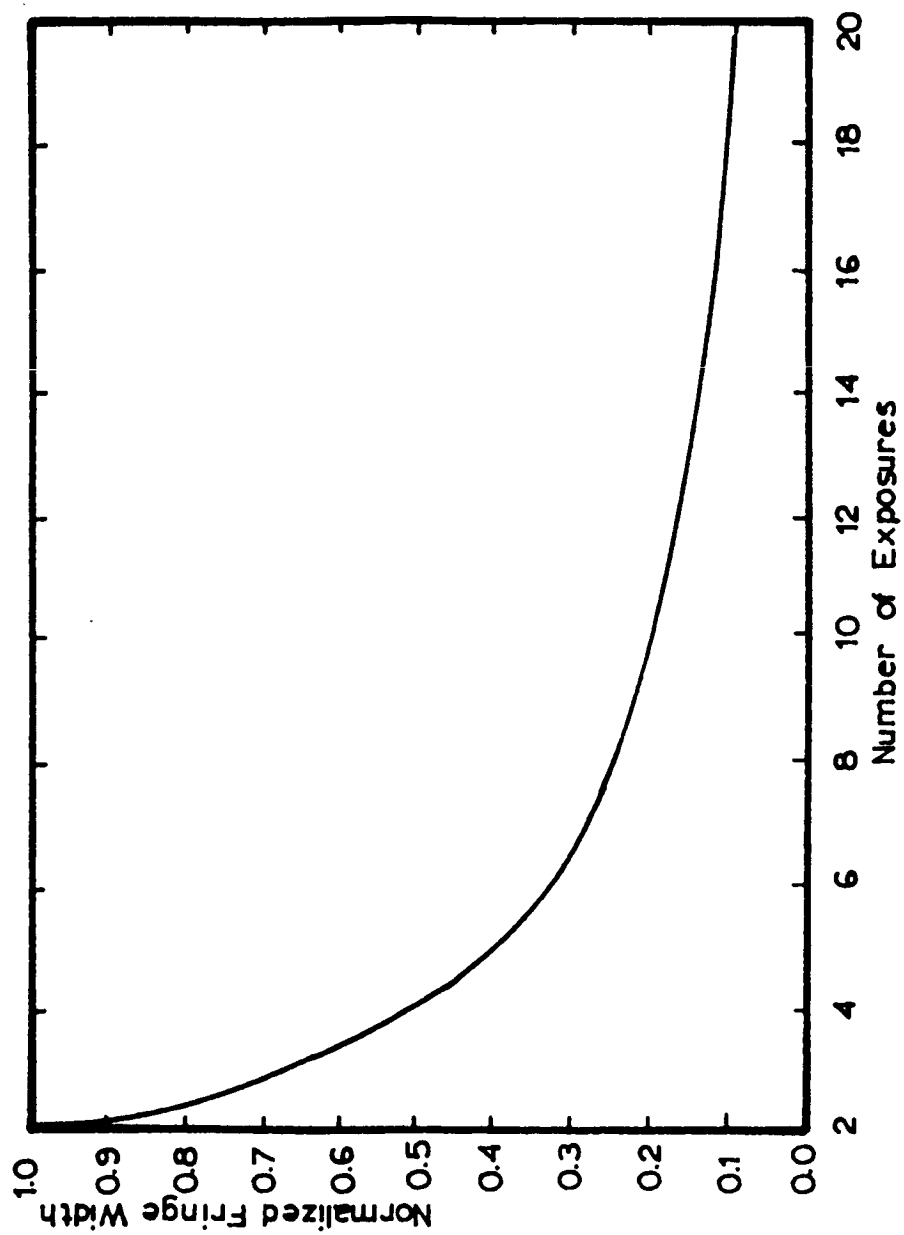
Figure 8. The variation of fringe width with number of exposures.

Young's Fringes
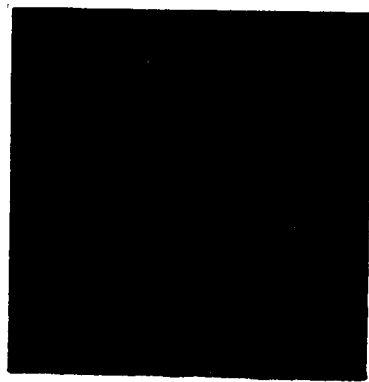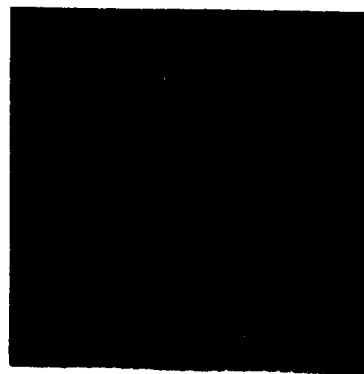
a) film negative   b) film positive

Figure 9. Young's fringe patterns obtained with film negative
and positive.
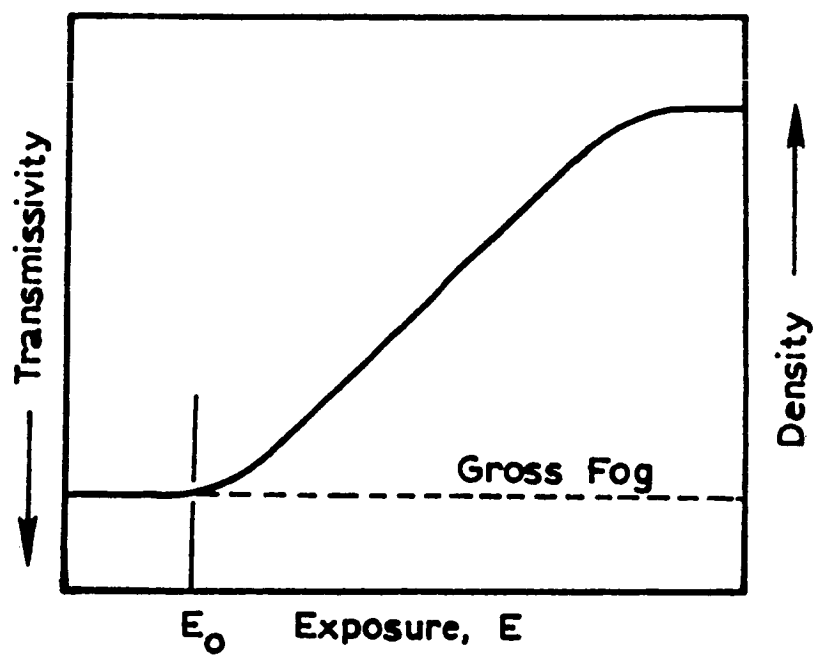
Figure 10. The density-exposure curve for a film
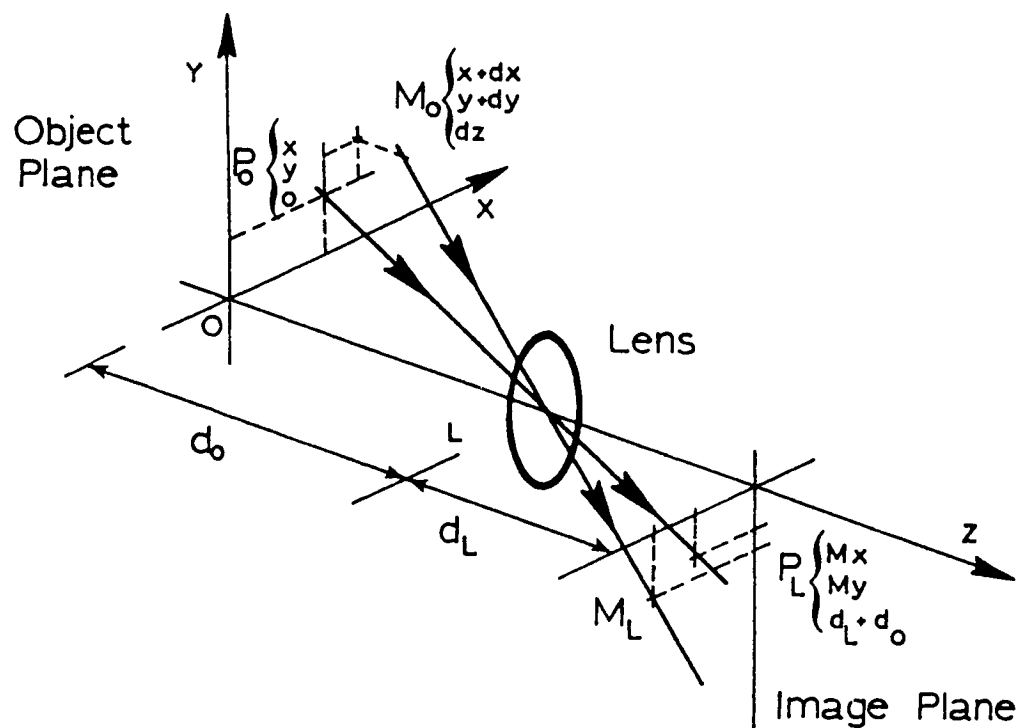
Figure 11. A schematic of the imaging system for the estimation of the out-of-plane motion.
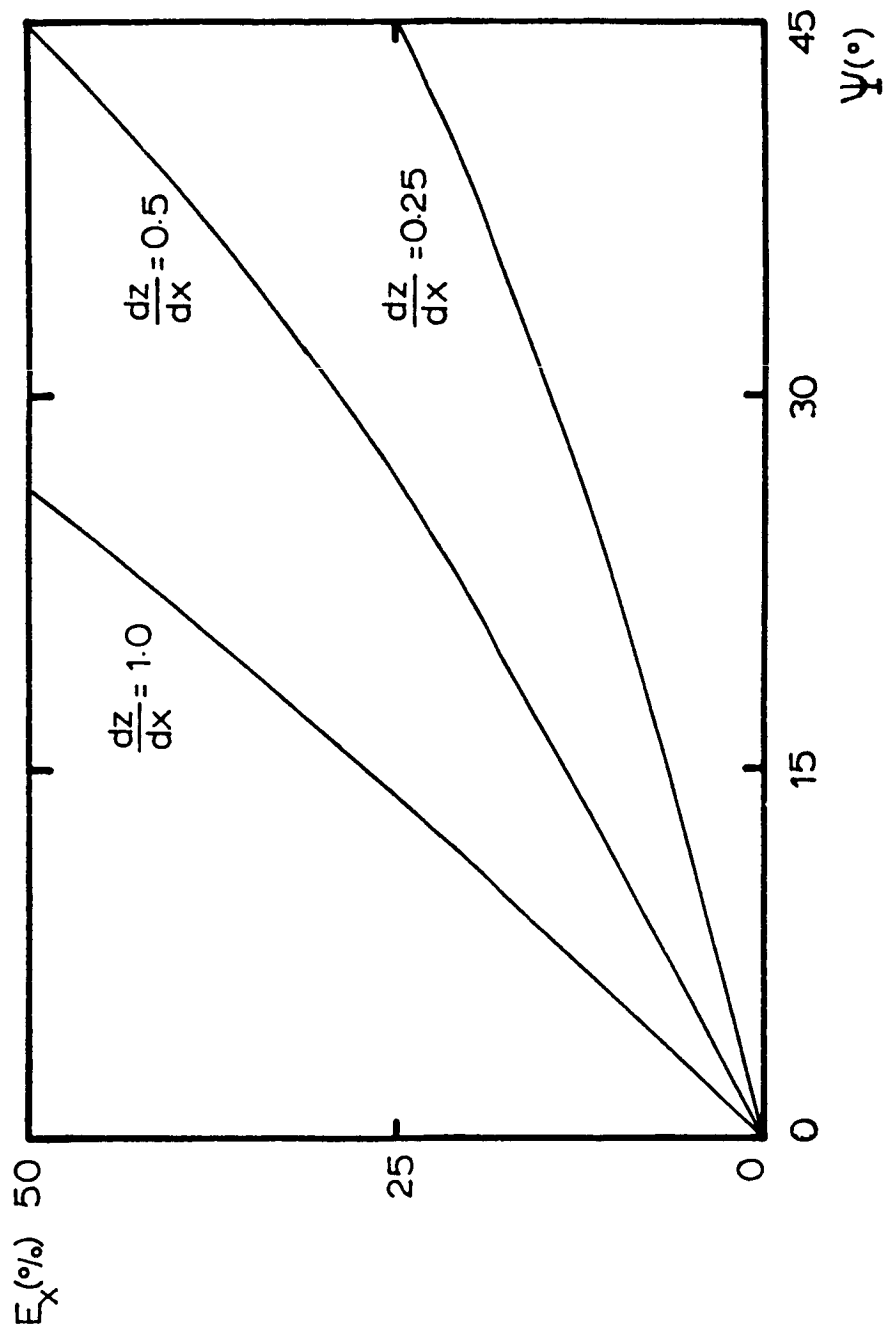
Figure 12. Theoretical relative error of in-plane component due to out-of-plane motion.

Figure 13. Photograph of the experimental facility.
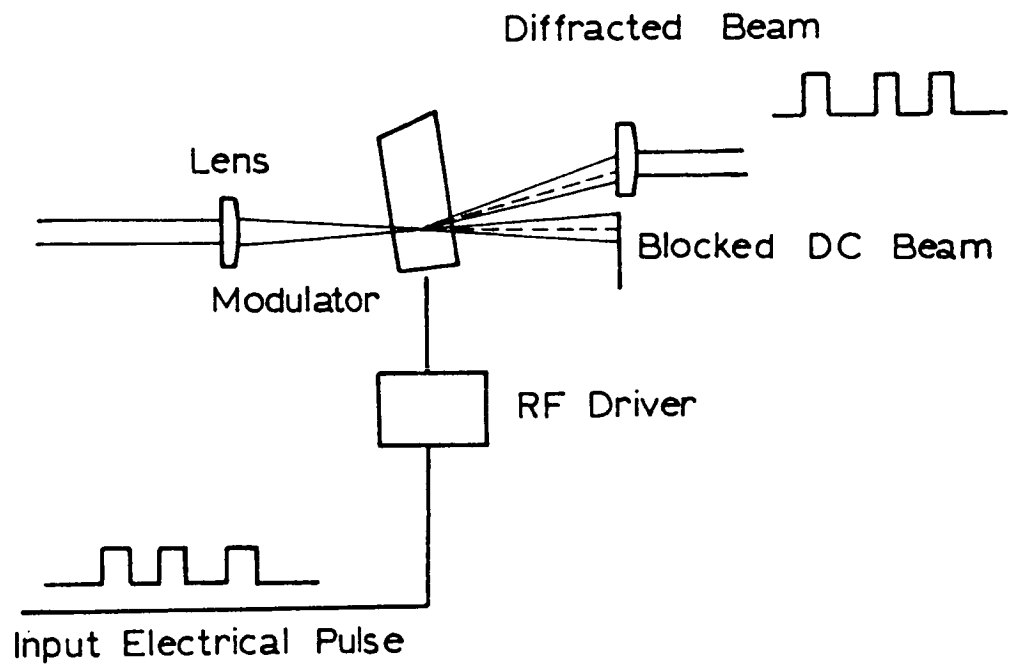
Figure 14. Schematic of the laser shutter
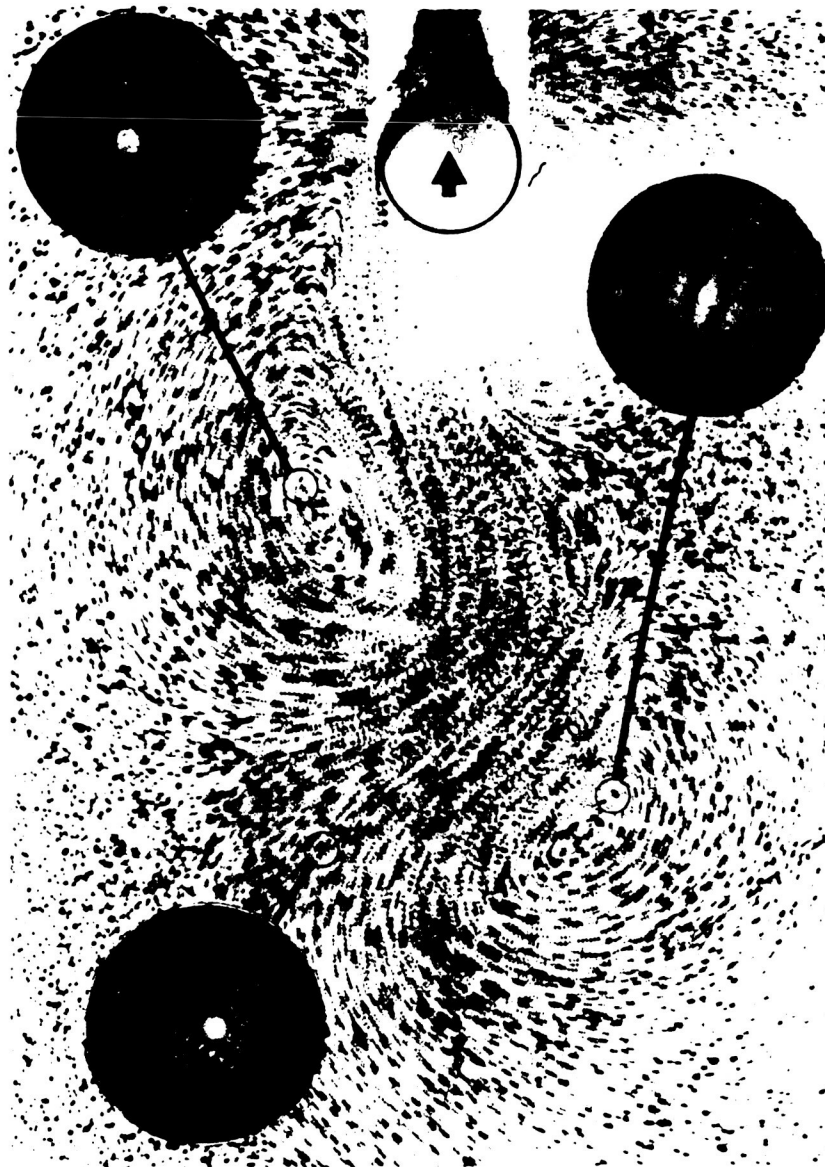
Figure 15. Triple exposed photograph of the vortex street.

334

5 cm/sec
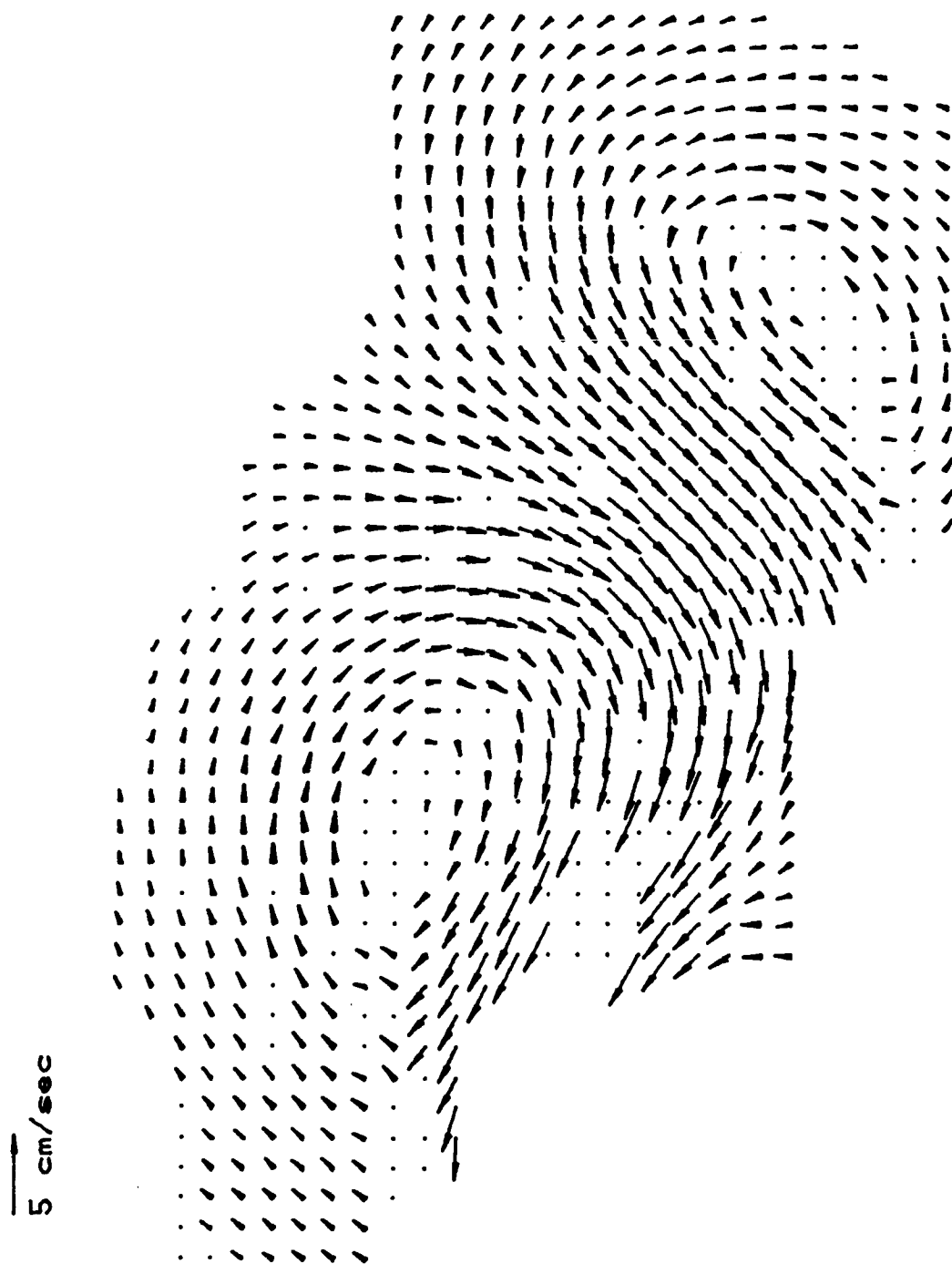
Figure 16. Velocity vector map of the vortex street
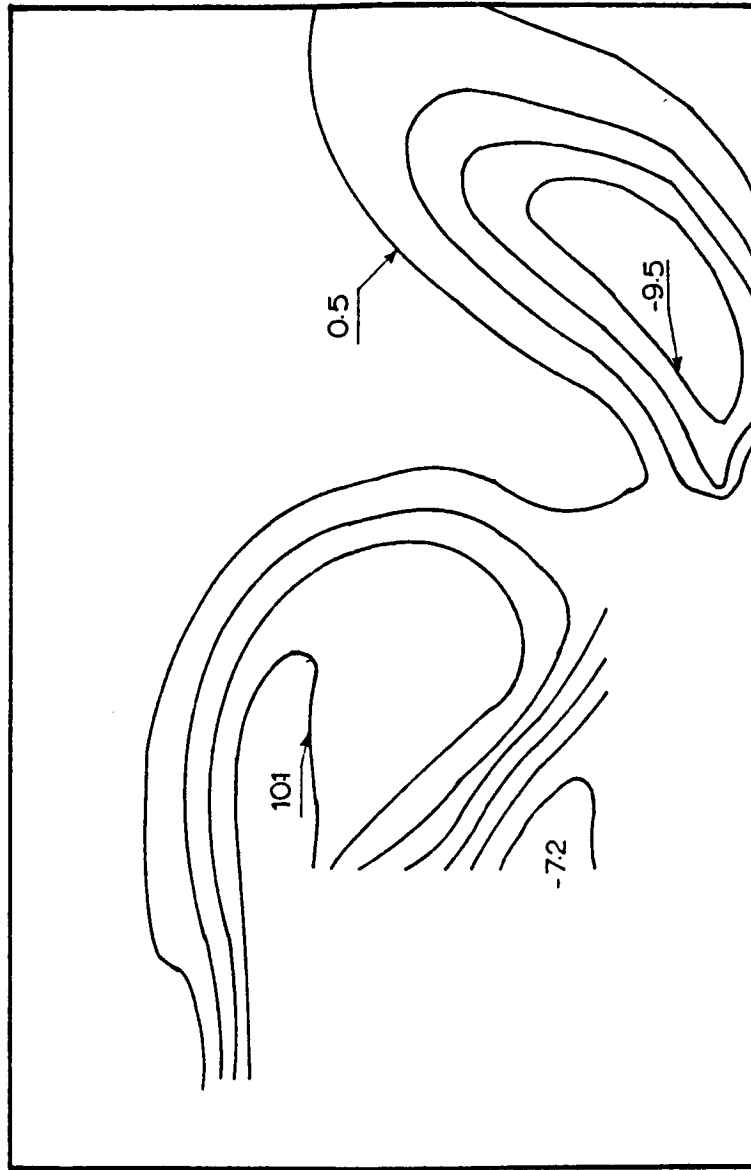
Figure 17. Constant vorticity contours of the vortex street.
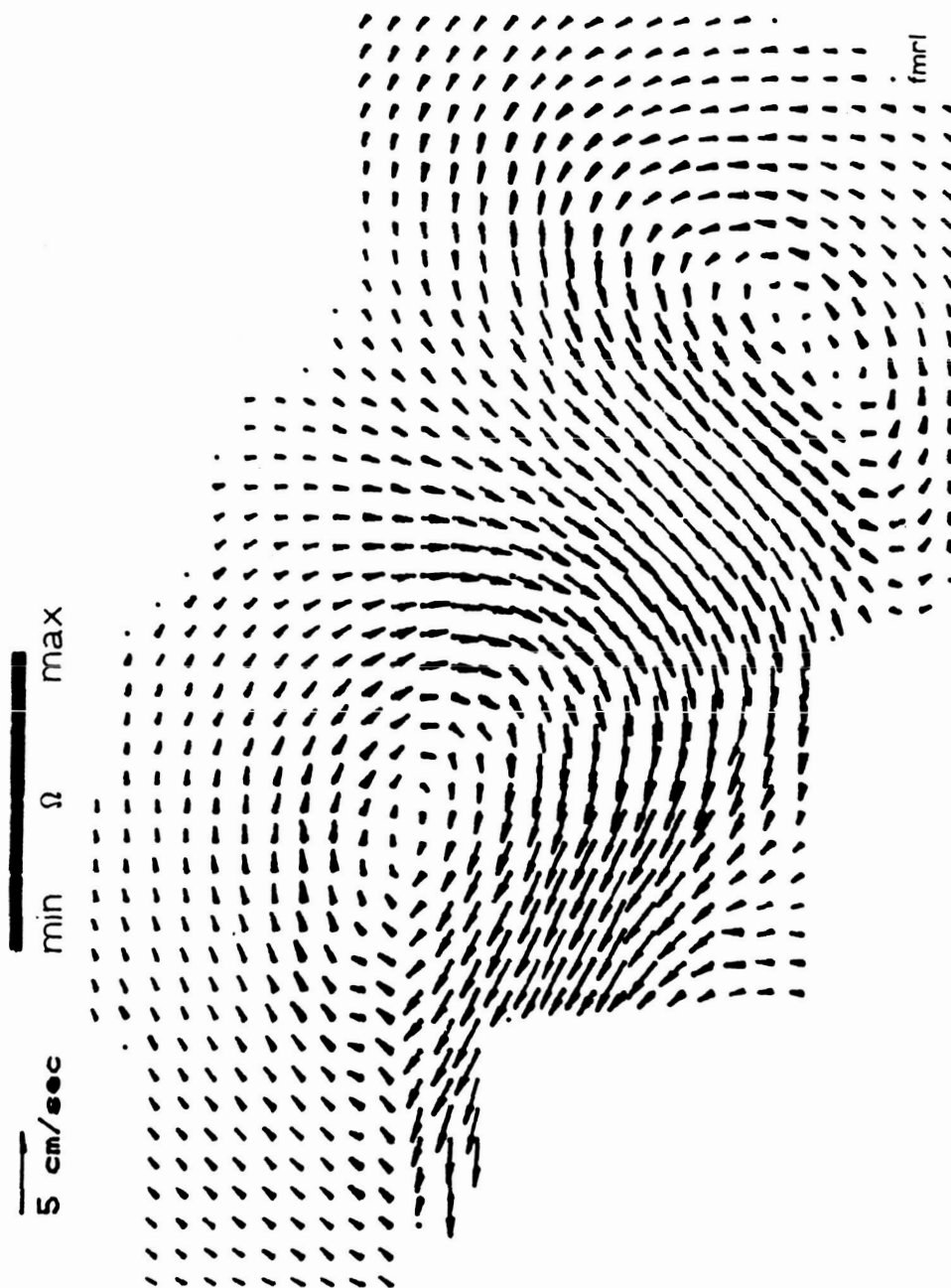
Figure 18. Velocity and vorticity fields of the Karman vortex street.
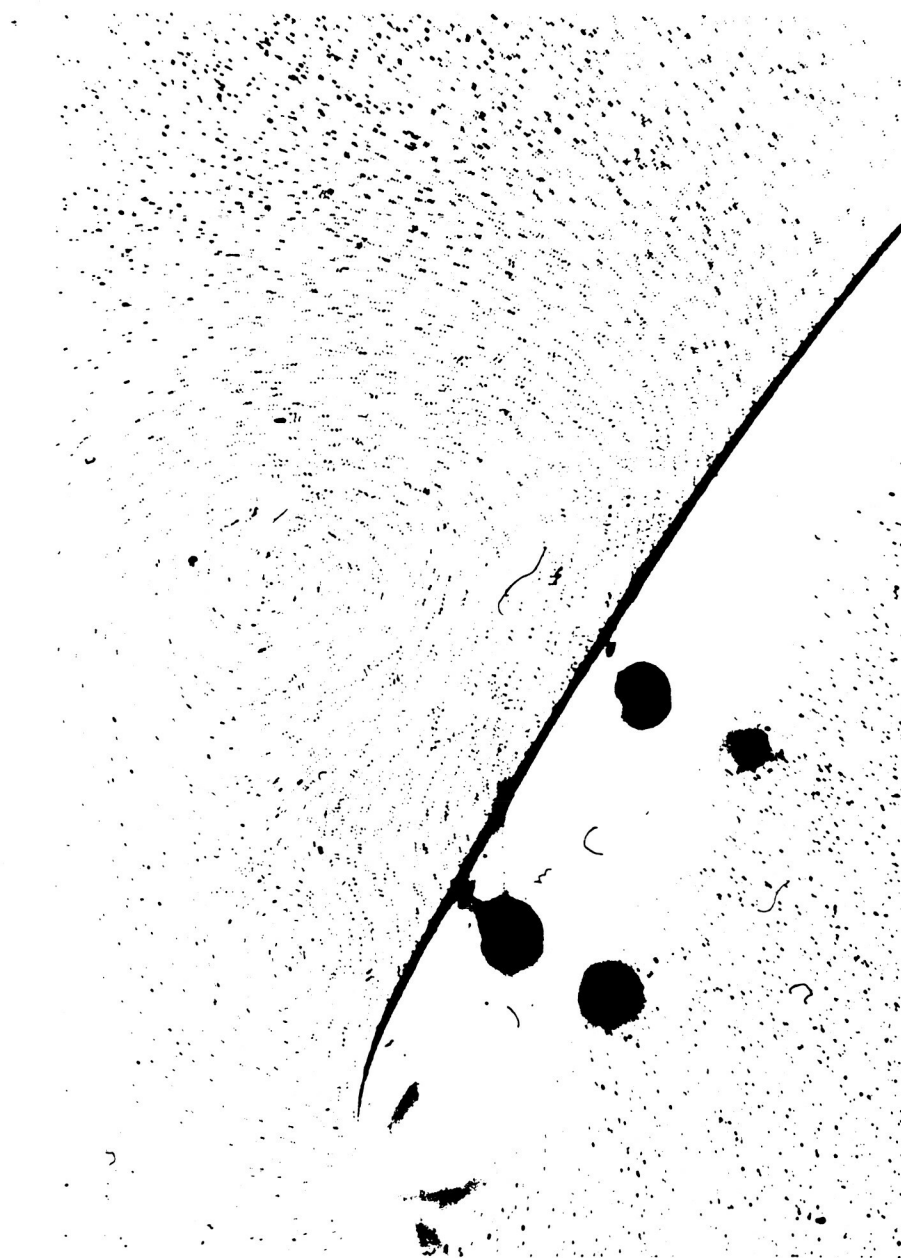
Figure 19a. For legend see figure 19c.

338
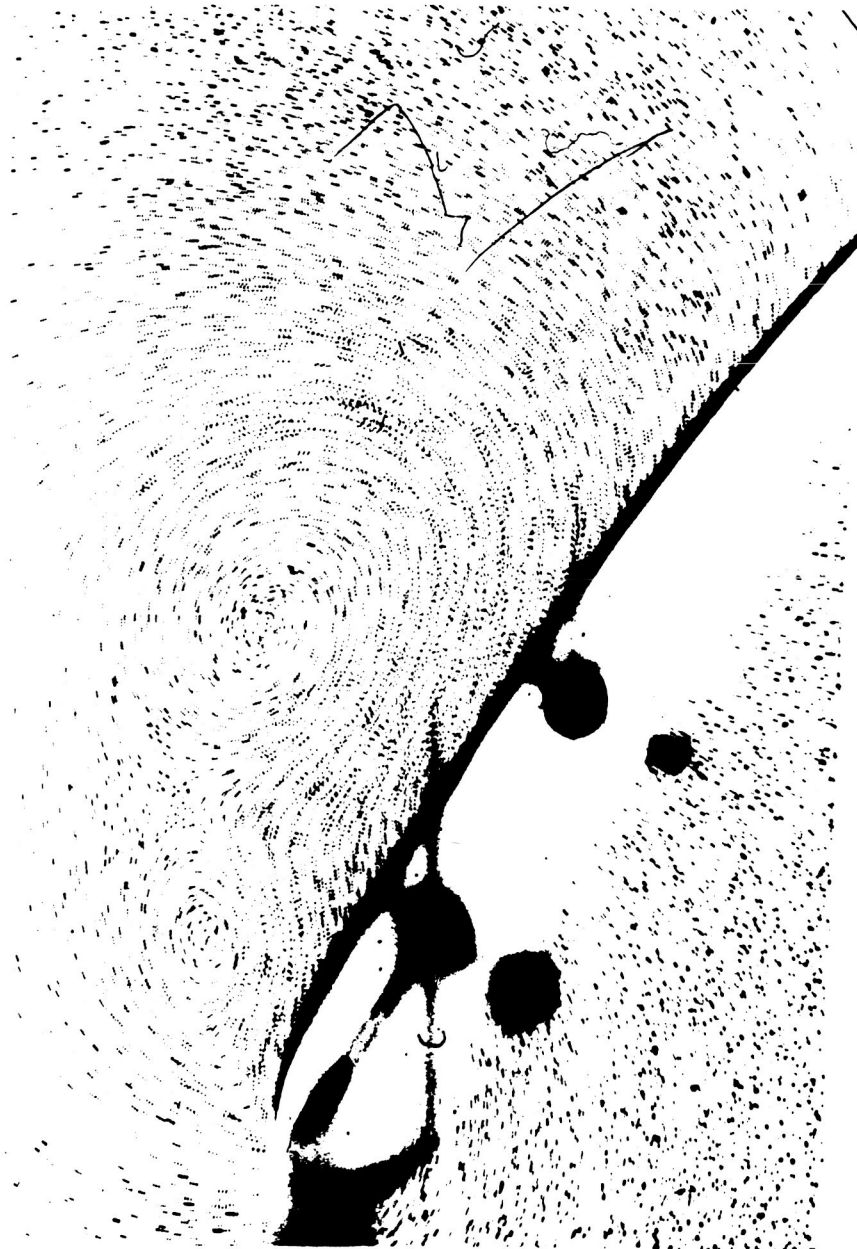
Figure 19b. For legend see figure 19c.
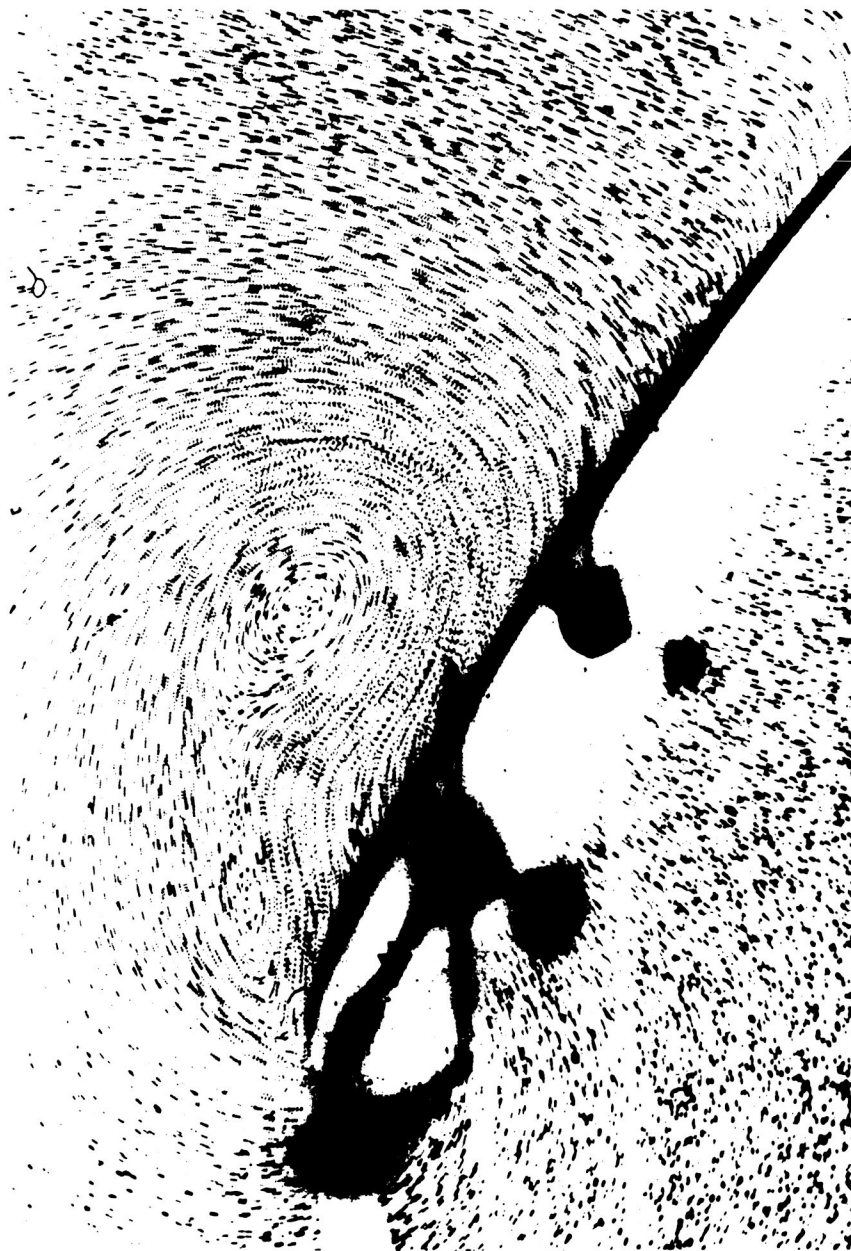
Figure 19c. Multiple exposure photographs of flow past an airfoil at 30 degrees angle of incidence; a) double exposure, b) triple exposure, c) Quadruple exposure.
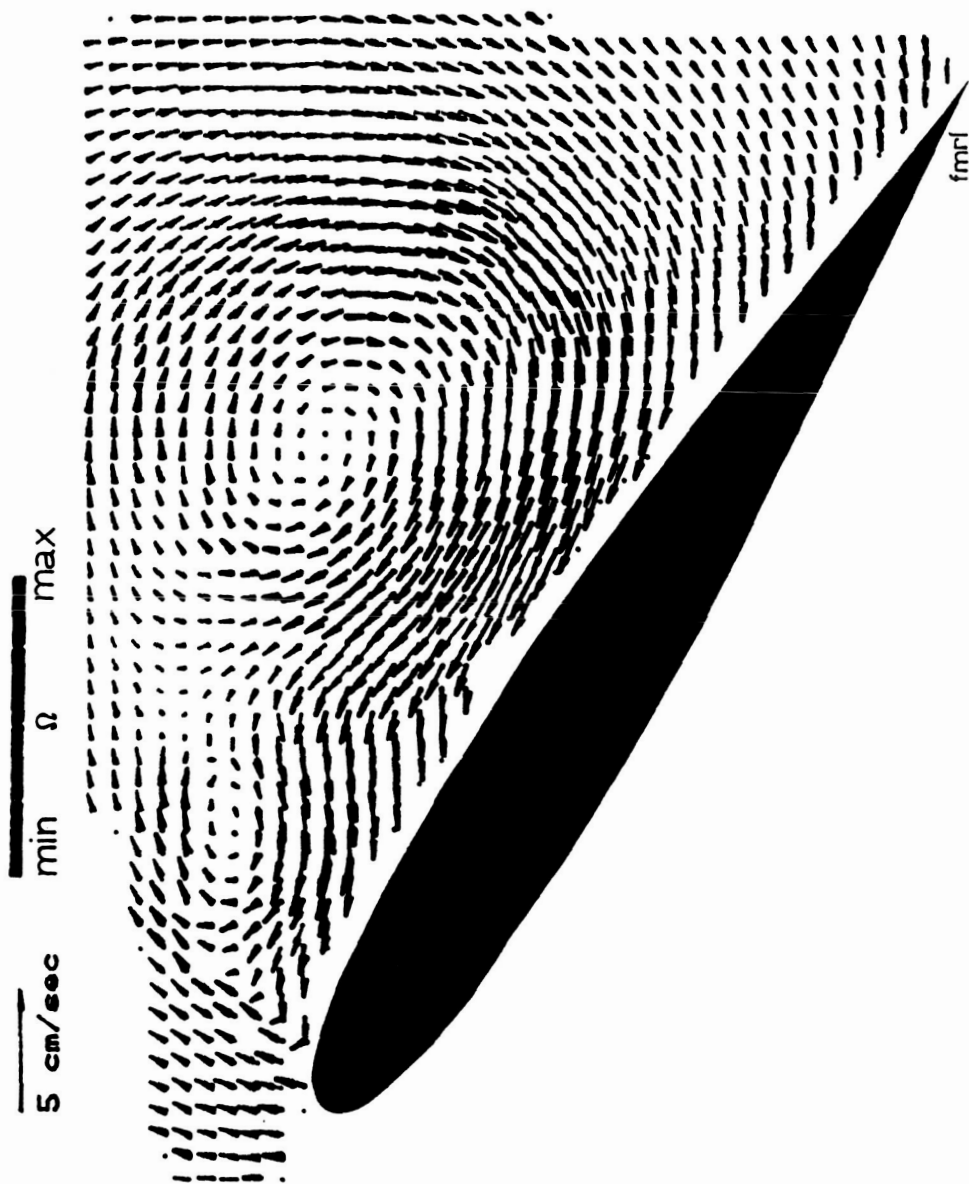
Figure 20. Velocity and vorticity fields of flow over a NACA 0012 airfoil.

341

S,8-35

103459

COMPUTATIONAL INTERFEROMETRIC DESCRIPTION

OF NESTED FLOW FIELDS

A. George Havener, Ph.D.
Assistant Professor, Mechanical Engineering
University of Dayton, Dayton, Ohio 45469

L. A. Obergefell
Staff Researcher
Systems Research Laboratories
Dayton, OH 45431

December, 1984

342 INTENTIONALLY BLANK

Abstract

Computer graphics and theoretical descriptions of density are used to obtain computer generated flow visualizations called computational interferograms. Computational interferograms are pictorially analogous to optical interferograms, and examples showing the fringe pattern for the flow about a sharp tip cone in a supersonic air stream are presented. To ascertain the effect of unsteady behavior, local density disturbances are added to the steady state flow field. This introduces irregularities to the computational interferogram like those seen in the optical interferograms. These theoretical disturbances can be varied in geometry, density description, translated with time, and strengthened or dissipated. The accuracy of computational interferometry relies on the accuracy of the theoretical density descriptions and therefore, it provides a way of verifying existing models of flow fields, especially those containing unsteady or turbulent behavior. In addition to being a unique method of flow visualization, computational interferometry can be used to develop and modify theories or numerical solutions to both simple and complex flow fields. The present research is a general description of this process.

Keywords

Introduction

This research describes an innovative process for depicting and understanding specific details of flow fields. The process is called

PRECEDING PAGE BLANK NOT FILMED

computational interferometry, and it combines the drawing features of computer graphics with the principles of interferometry to obtain computer drawn displays of numerical solutions to flow fields.

Computational interferometry is a unique approach to obtaining flow field visualizations and a relatively new approach to the general study of simple and complex flows. The main ideas of this process originally Reference 3. The present work refines the original process to handle asymmetric and nested flows. The motivation for this research stems from the fundamental difficulties associated with normal interferometric applications, especially to complex flows. Normal applications are troubled by adequate treatment of the derivative of the experimental data, coping with limited data, and are generally restricted in scope to 3-D axisymmetric flows. Conceptually, computational interferometry is not effected by these problems. The present research describes a general process for treatment of asymmetric flows, and special development is made for nested flow fields. The term "nested flow" as used here pertains to central fields that are embedded with one or more smaller fields. The smaller fields of this research are ficticious, but they are representative of local turbulent structures commonly found in real in many flows.

Theoretical Modeling

Interferometry is an optical process that can be used to measure variations in optical path length. Optical path length is proportional to the density integrated along the geometric path, and therefore, interferometry can be used to measure density variations in a defined volume. Basic techniques using interferometry are well documented (Ref.1,2).

The basic equation for the interferometry process is,

$$S_i = G \int f(x,y,z) \, dl_i \qquad (1)$$

where,

$S_i(x,y)$ is the fringe shift.
G is a constant that depends on the wavelength and a reference density.
l_i is the geometric length traveled by the light waves.
$f(x,y,z)$ is the density function.

The present study is for the axisymmetric flow about a sharp tip cone, and the curvature of the light waves through the flow field is assumed to be small compared to the distance traveled by the waves. Figure 1 shows the coordinates and line of sight for this case.

For axisymmetric fields that are assumed to be refractionless, $S(x,y) = S(y)$ and $f(x,y,z) = f(r^2)$ where $r^2 = y^2 + z^2$. Then for any plane normal to the x-axis $(x = x_c)$, Equation (1) becomes,

$$S(y) = G \int_{y^2}^{r^2} \frac{f(r^2)}{\sqrt{r^2 - y^2}} \, dr^2 \qquad (2)$$

Following the method of Bradley (Ref. 7), evaluation of Equation (2) is done using the transformations:

For which,

$$\eta = 1 - (r/R)^2 ; \qquad \xi = 1 - (y/R)^2 \qquad (3)$$

$$S(\xi) = GR \int_0^{\xi} \frac{f(\eta)}{\sqrt{\xi - \eta}} \, d\eta \qquad (4)$$

Equation (4) is seen to be Abels integral equation which can be evaluated when $f(\eta)$ is aptly defined. For example, if $f(\eta)$ is represented by a polynomial, all integrals are finite at both limits even though the integrand is singular at $\eta = \xi$.

For experimental applications, the unknown quantity is $f(\eta)$, the

density, which is sought from a knowledge of $S(\xi)$, the fringe shift. Mathematically, $f(\eta)$ is obtained by inverting Equation (4), a step that has two general difficulties. First, unless the flow field is two dimensional or 3-D axisymmetric the inversion can not be done because there is no general analytical solution to Equation (3) for asymmetric fields. Second, inversion of Equation (3) requires differentiation of $S(\xi)$. Since $S(\xi)$ is based on experimental measurements, differentiation can easily amplify scatter in the $S(\xi)$ data to a level where the final determination of $f(\eta)$ is worthless.

The Computational Interferometric Approach

Computational interferometry is a reverse of the experimental approach. Starting with a known $f(\eta)$, Equation (4) is used to calculate $S(\xi)$ for the entire field. Then, computer graphics are used to draw the $S(\xi)$ data, and the final result is a computer generated interferogram that is similar to the corresponding real interferogram. Note that since the computational interferogram results from direct application of Equation (4), no inversion is required, no differentiation of data is done, and the flow fields may be complex or asymmetric. Conceptually, only a proper description of $f(\eta)$ and Equation (4) are required. In the present application, the density throughout the inviscid flow is known from the Taylor-Maccoll solution for a cone (Ref. 8) whereas the density in the boundary layer is determined from a numerical solution for axisymmetric boundary layer flow (Ref. 5).

A fringe in an interferogram is a line of constant optical phase. The spacing between adjacent fringes defines one wave length changes in the optical path lengths through the field. When an interferometer is

adjusted to produce a finite fringe interferogram in which the reference fringes are oriented vertically, an optical reference field of known phase is established. Along any fringe, the phase is constant which means the optical path lengths are also constant. When local changes in the optical path lengths are introduced, the optical phase of the waves changes which results in a lateral bending of the fringes from their vertical orientations. The bending is necessary to maintain the continuity of the preestablished phase relationships, and the magnitude of the bends—the fringe shifts—is directly proportional to the local changes in the optical path lengths through the field.

Figure 2 illustrates the fringe shift principles for an interferogram of the cone case. Only two fringes and the upper plane are shown to simplify the diagram. As shown, the local coordinates of fringe 1 are (x,y) which are defined with respect to the body axis system located at the tip of the cone. The x_c plane is taken to coincide with the reference position of fringe 1. Due to increases in the optical path lengths through the inviscid field, fringe 1 is bent laterally to the right, the magnitude of this shift is, $S = \mathcal{L}/D$. Had the optical path lengths decreased, fringe 1 would have shifted to the left. Note that this happens for the boundary layer, because the optical path lengths through the boundary layer are less than those of the inviscid flow fields. The length, $\mathcal{L}$, is the actual distance that fringe 1 is shifted and D is the reference spacing between fringes 1 and 2. The distance D signifies that in the reference state, the optical path length for fringe 2 is one wave length longer than it is for fringe 1. The ratio of $\mathcal{L}/D$ is, therefore, a percentage change in the optical

path length relative to fringe 1 and the x_c plane. Therefore, the coordinates are seen to be,

$$X = X_c + \ell = X_c + SD \; ; \quad Y = X \tan\phi \qquad (5)$$

For the conical flow of the inviscid field, the fluid properties are only functions of the angle ϕ and the fluid properties are constant along rays for ϕ equal to a constant. Hence, fringe shifts can be written as,

$$\frac{S}{X} = \frac{S}{X_c} = \left(\frac{S}{X}\right)_{ref} \qquad (6)$$

and rearranging terms, the x, y coordinates are,

$$X = \frac{X_c}{1 - (S/X)_{ref} D} \qquad Y = \left(\frac{Y}{X}\right)_{ref} X \qquad (7)$$

The quantity $(S/x)_{ref}$ is obtained by numerically evaluating Equation (4) for a reference x_c plane and subsequently dividing each computed S by x_c. To obtain a polynomial function for the density discrete values of density are calculated from a numerical solution to the Taylor-Maccoll differential cone equation for covical flow. Then the radial distribution of density is obtained from a least squares curve fit of these computed Taylor-Maccoll values. The distribution of density in planes normal to the cone axis is required, because the evaluation of the integrals of Equation (4) is for vertical planes. Note that since Equation (4) is defined in terms of the transformed coordinates, the polynomial distribution for the density must be expressed in terms of η. Substituting the polynomial into Equation (4) and completing a term-by-term evaluation of the integrals,

$$S(\xi)= 2GR\sqrt{\xi}\;\sum_{i=0}^{m}(i)!\,b_i\,\xi^i\left(\sum_{j=0}^{i}\frac{(-1)^j}{(2j+1)(j)!\,(i-j)!}\right) \qquad (8)$$

Evaluation of the interferometric integral involves a double series; one series accounts for the polynomial distribution of the density while the other series is a consequence of the term-by-term evaluation of the integral. The accuracy of this fringe shift computation for the inviscid flow is discussed in Ref. 4 where the relative error is shown to be less than 0.15%.

With fringe shift data now available, the procedure for computing the coordinates of the fringes for the inviscid field is:

(1) Select D, the reference fringe spacing.

(2) Select x_c, the fringe starting position.

(3) Compute from $\phi = \tan(y/x_c)$ for each y coordinate where $(S/x)_{ref}$ is known.

(4) Compute (x,y) from Equation (7) for all values of $(S/x)_{ref}$.

(5) Index x_c by D; $x_c = x_c + D$.

(6) Repeat steps (2)-(5) until the field is defined completely.

For the boundary layer, the fluid properties are not constant along rays eminating from the cone tip, nor are they scalar multiples from one plane to the next. Consequently, a new radial distribution for the density is required for each new x plane being surveyed. This leads to an iteration process. The quantities required are the boundary layer thickness and the radial distribution for the density. Both of these are obtained from theory (Ref. 5). The iteration procedure involves picking x and y and using Equation (8) with additional terms for the boundary layer to compute S. This value is compared to S = ℓ/D, and x is iterated until the two S values agree.

Figure 3 is a computational interferogram that illustrates the

351

above procedures. The field is for supersonic flow over a sharp tip cone and includes treatment of the boundary layer. The straight fringes of the reference region are seen to shift abruptly to the right as they cross the shock wave. Then they make a smooth curve through the inviscid field to the boundary layer at which point they shift back to the left. The fringe reversal in the boundary layer is due to a shortening of the optical path lengths for this region.

Computational Interferometry for Nested Flow Fields

The fringes seen in interferograms of real flow fields are generally unlike the smooth, uniform fringes of the computational interferograms, because the real flow fields often contain time varying local disturbances that are omitted from the theoretical solutions. For example, real flow fields can contain turbulent eddies which are seen as irregularities in the interferograms. Figure 4 exhibits an irregularity which is circled for identity. This is an enlargement of a section of the flow field presented in Figure 6. The exact nature of the irregularity is unknown, and because only one view of this flow field is possible, an exact determination of the density associated with this irregularity can not be determined from this interferogram. Since this irregularity is in the midst of a presumeably stable field, the interferogram definitely shows the presence of a secondary flow. Using computational interferometry, a possible resolve of this irregularity-- the others as well--is obtained by inserting secondary flow fields in the theoretical description of the primary field, and then by computing and displaying the resultant alterations to the fringe pattern.

When secondary flows are placed in the primary flow, the composite field is no longer axisymmetric, and Equation (8) must be changed. The integration is still valid for y = constant, but $f(\eta)$ must be modified to account for the secondary fields.

An illustrative example of an embedded field is shown in Figure 5. The primary field is still the inviscid field, and it is centered on the y-z axes. The disturbance is arbitrarily located a distance h and k from the y-z axes respectively.

The principle of linear superposition is used to determine the fringe shift for the y_i ray passing through this composite field,

$$S(y_i) = S_i(y_i) + S_d(y_i) \qquad (9)$$

Here, $S_i(y_i)$ is the fringe shift for the inviscid field and $S_d(y_i)$ is the fringe shift for the embedded disturbance. $S_i(y_i)$ is expressed as the fringe shift of the disturbance free field minus the portion occupied by the disturbance,

$$S_i(y_i) = G \int_{y^2}^{R^2} \frac{\bar{f}(r^2)}{\sqrt{r^2 - y^2}} \, dr^2 - S_{id}(y_i) \qquad (10)$$

where $S_{id}(y_i)$ is the inviscid field contribution to the total fringe shift that is overlapped by the disturbance. $S_{id}(y_i)$ is determined using Equation (1) and integrating from z_1 to z_2.

$$S_{id}(y_i) = G \int_{z_1}^{z_2} f(y_i, z) \, dz \qquad (11)$$

Since the inviscid field is axisymmetric,

$$S_{id}(y_i) = \frac{G}{2} \int_{r_1^2}^{r_2^2} \frac{f_i(r^2)}{\sqrt{r^2 - y_i^2}} \, dr^2 \qquad (12)$$

From the circular geometry of the disturbance,

353

$$r_1^2 = z_1^2 + y_1^2 = \left[h - \sqrt{\gamma - (y-k)^2} \right]^2 + y_i^2$$

$$r_2^2 = z_2^2 + y_2^2 = \left[h + \sqrt{\gamma - (y-k)^2} \right]^2 + y_i^2$$

(13)

Using Bradley's transformations,

$$g_1(\xi) = 1 - \left(\frac{r}{R}\right)^2 \qquad g_2(\xi) = 1 - \left(\frac{r}{R}\right)^2$$

Equation (12) becomes,

$$S_{id} = GR \int_{g_1(\xi)}^{g_2(\xi)} \frac{f_i(\eta)}{\sqrt{\xi - \eta}} d\eta$$

(14)

Equation (14) is solved in the same manner as the axisymmetric case, and $f_i(\eta)$ is the same density function as that used in Equation (3).

For the disturbance $S_d(y_i)$ is,

$$S_d(y_i) = G \int_{Z_1}^{Z_2} f_d(z) dz$$

(15)

$f_d(z)$ is the density function for the disturbance at (x_c, y_i).

To avoid a discontinuity at the geometric boundaries of the disturbance, $f_d(z)$ is matched with $f_i(z)$ at z_1 and z_2, and a peak density is arbitrarily chosen for the center point. With these three points known, a quadratic distribution for the density as a function of z is calculated and used to evaluate Equation (15).

The computational interferogram for the nested fields is obtained in the same manner as the interferogram for the axisymmetric field, but when a light ray falls within the disturbance boundaries, a combined fringe shift is calculated using Equations (8), (14) and (15). This calculation is a trial and error process in which an interation for the x coordinate of the fringe is carried out for a constant y coordinate. The process involves selection of x, calculation of S(y) using Equations (5), (8) and (9), and a second calculation of S using S = $\mathcal{L}$/D. The two S values are compared, and the intersection process is repeated until

these S-values agree. Computational interferograms for multiple disturbances are obtained in a similar manner simply by summing the contribution of each disturbance.

Results

Figure 6 shows a comparison between the computational and optical interferograms for a flow field similar to that of Fig. 3. This flow field is for steady state, irrotational, adiabatic, inviscid flow with a boundary layer over a sharp tip cone in a supersonic air stream. The agreement between these two interferograms is good but there are some differences. The main difference between the two interferograms of Fig. 6 is the nonuniformities and subtle irregularities in the fringes of the optical interferogram. These irregularities are present because the optical interferogram is an instantaneous recording of an unsteady turbulent flow field and these irregularities are exhibiting the turbulence. For the present research, models for these disturbances are added to the computational interferogram by nesting ficticious density fields in the inviscid field. The disturbance fields selected here are arbitrary and are used only to study the disturbance effects on the fringe pattern and the general degradation of the fringe patterns in interferograms of stable, steady flows.

A computational interferogram for a section of the inviscid field is illustrated in Fig. 7. This section is a nested field because it contains a disturbance. The geometric description of this disturbance is a diamond that has circular cross sections. The density of every point on the boundary of the disturbance is matched with the corresponding inviscid field density at all respective boundary points.

Comparing Figures 4 and 7, the computational fringe distortions of Figure 7 are beginning to resemble the irregularities seen in real interferograms. This strongly suggests that more careful and realistic modeling of the disturbances would produce good agreement between the computational and optical interferograms.

A final result of the present research is presented in Fig. 8. Figure 8 is a computational interferogram for a flow field with two nested disturbances. The disturbances are equal in geometry and they have the same centerline density distributions. However, as seen in Fig. 8, these disturbances have distinctly different effects on the fringe pattern. The upper disturbance is the same as that of Fig. 7. It is located in the primary field along the y-axis (h = 0, Figure 5). The lower disturbance is located off both axes. This disturbance occupies a portion of the primary field where the density of the primary field is stronger than that of the position of the upper disturbance. Hence, there is a net reduction in the optical path lengths for this disturbance which causes the fringes to bend to the left. The results of Fig. 8 are significant, because they show clearly that not only are the geometric definitions and the continuity of density distributions important factors, but the location of the disturbances within the field are of equal concern.

Conclusions

Computational interferometry is an innovative technique that can be used to obtain flow visualizations of theoretical flow fields. These interferograms are in every way analogous to the optical interferograms

of real flow fields, because they describe the theoretical phase content of events in the same way as the real interferograms. Practical application of computational interferometry lies in its usefulness to exhibit the numerical solution of flow fields in a way that allows researchers the opportunity to see the event just as it would appear in reality. A significant extension of computational interferometry involves applications to the analysis of nested flow fields, transient events and unsteady behavior in a manner that permits direct comparision to real flows. While the disturbance models studied in this research are ficticious, the effects they produce on the central fringe pattern indicate that with proper fluid dynamic modeling, the interferometric structure of flow field disturbances can be drawn and studied in detail. This capability is not known to exist in any other flow visualization process.

The most serious limitation of computational interferometry appears to be the concern for uniqueness: Can more than one arrangement of disturbances produce identical interferograms? The scope of this research can not answer this important question, and it certainly seems that more than one arrangement of nested flows could produce identical interferograms. Remembering that these nested fields are not axisymmetric and that more than one view of an asymmetric field is required for a complete analysis, the answer of uniqueness lies in drawing multiple views of computational interferometry for the same event, and then comparing these interferograms to optical interferograms of the real event. Accomplishing the latter step is difficult, possibly even impossible for transiant events, because multiple views of real flow fields are very difficult to obtain.

357

Recommendations

The findings of this research definitely suggest additional study. First, development for real disturbances should be undertaken so that more meaningful comparisons to optical interferograms of real events can be done. Following this, the question of uniqueness should be resolved by conducting a comprehensive experimental and theoretical study of a reproduceable asymmetric nested flow field which leads itself to multiple viewing.

Acknowledgements

References

1. Vest, C.M., <u>Holographic Interferometry</u>, John Wiley and Sons, New York, 1979.

2. Havener, A.G., "Users Guide Pulse Laser Holography For Wind Tunnel Testing," Aerospace Research Laboratories, ARL TR-0123, AD/A017710, June, 1975.

3. Havener, A.G., Grove,J., Hankey,W., "The Application of Computer Graphics Techniques to the Interferometric Description of Supersonic Flow About a Sharp Tip Cone at Zero Angle of Attack," AFFDL TM 79-15-FXM, (FOR OFFICIAL USE ONLY), Wright Patterson Air Force Base, Ohio, Nov. 1978.

4. Havener, A.G., "On the Application of Holographic Interferometry to Axisymmetric Air Flows," Ph.D. Dissertation, University of Dayton, Dayton, Ohio, 1983.

5. Shang, J.S. and Hankey, W.L., Jr., "Numerical Solution for Supersonic Turbulent Flow Over A Compression Ramp," <u>AIAA Journal</u>, Volume 13, October 1975, pp. 1368-1374.

6. Hodge, J.K., et al. "Numerical Solution for Airfoils Near Stall In Optimized Boundary Fitted Curvilinear Coordinates." <u>AIAA Journal</u>, 1978.

7. Bradley, J.W., "Density Determination From Axisymmetric Interferograms," <u>AIAA Journal</u>, Volume 6, No. 6, June 1968, pp. 1190-1192.

8. Shapiro, A. H., <u>The Dynamics and Thermodynamics of Compressible Fluid Flow</u>, The Ronald Press Company, New York, 1954.

FIGURE LEGENDS

FIG. 1 Geometry and Coordinates for a Shart Tip Cone in Supersonic
        Flow

FIG. 2 Friner Shift Description for a Sharp Tip Cone

FIG. 3 Computation Interferogram for Inviscio Field and Boundary Layer

FIG. 4 Optical Interferogram of Fringer Irregularities

FIG. 5 Coordinates for Disturbance Location

FIG. 6 Direct Comparison Between Computational and Optical
        Interferograms

FIG. 7 Computational Interferogram of Disturbance with Density and
        Geometrical Continuity

FIG. 8 Multiple Disturbances in a Computational Interferogram
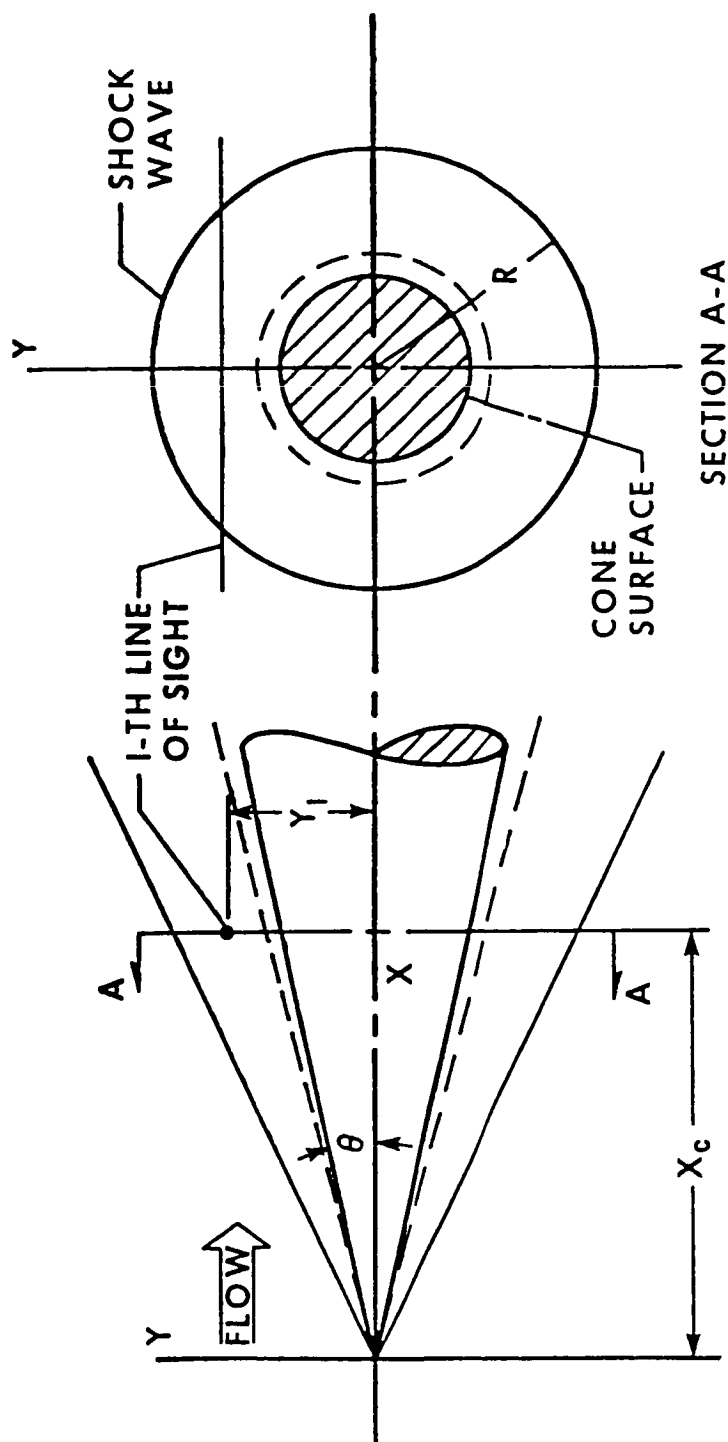
Fig. 1
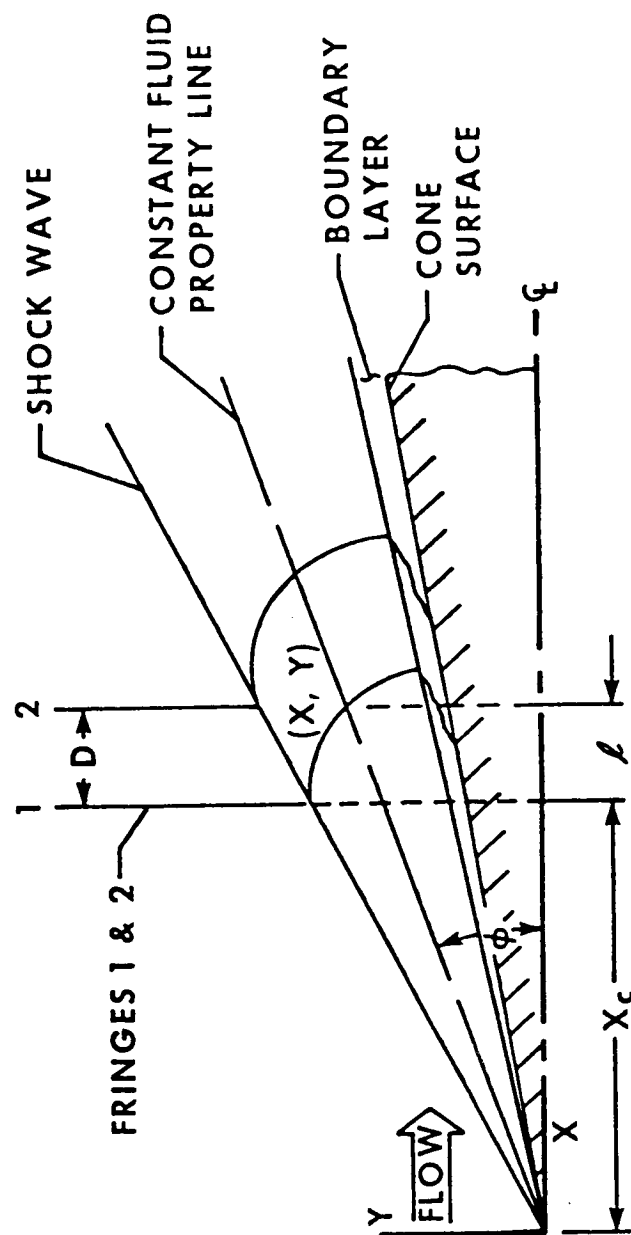
Fig. 2
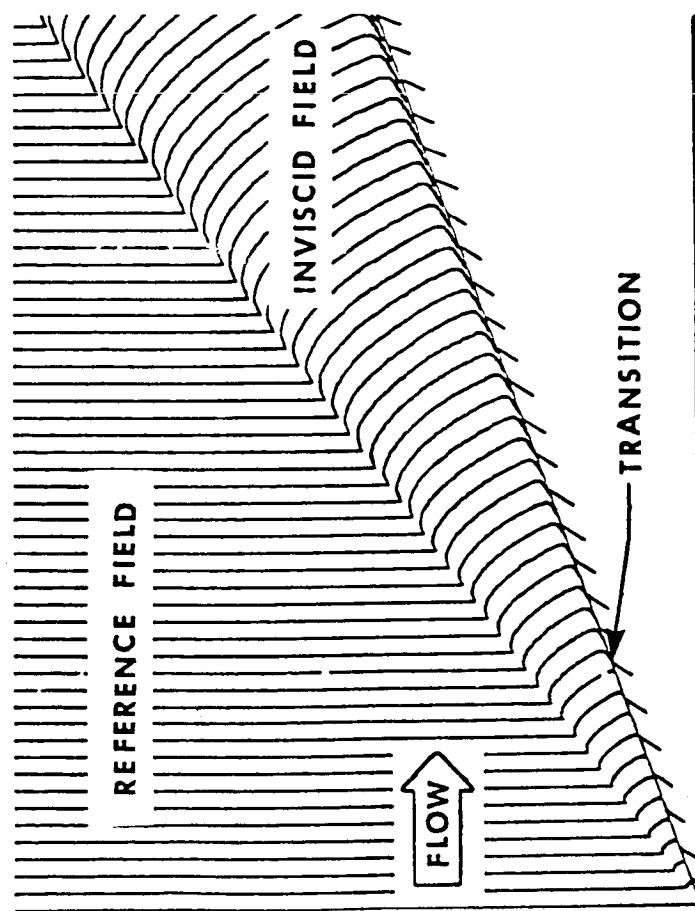
Fig. 3
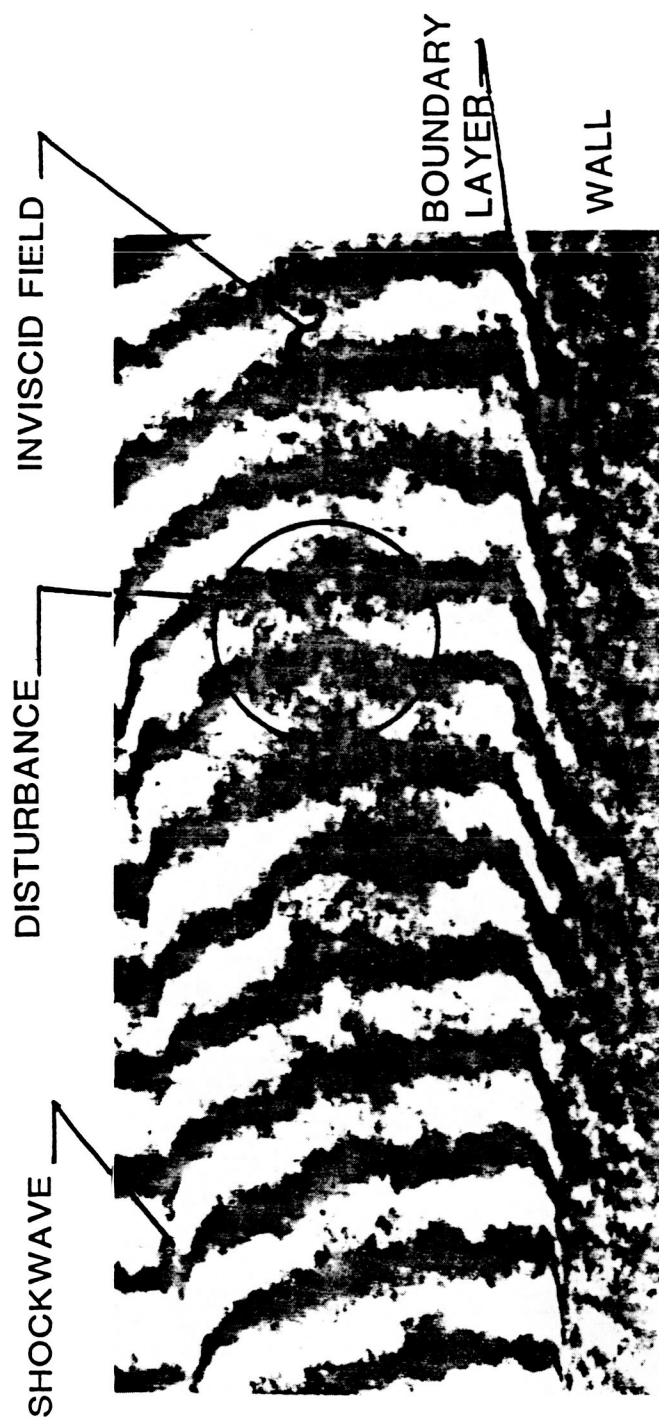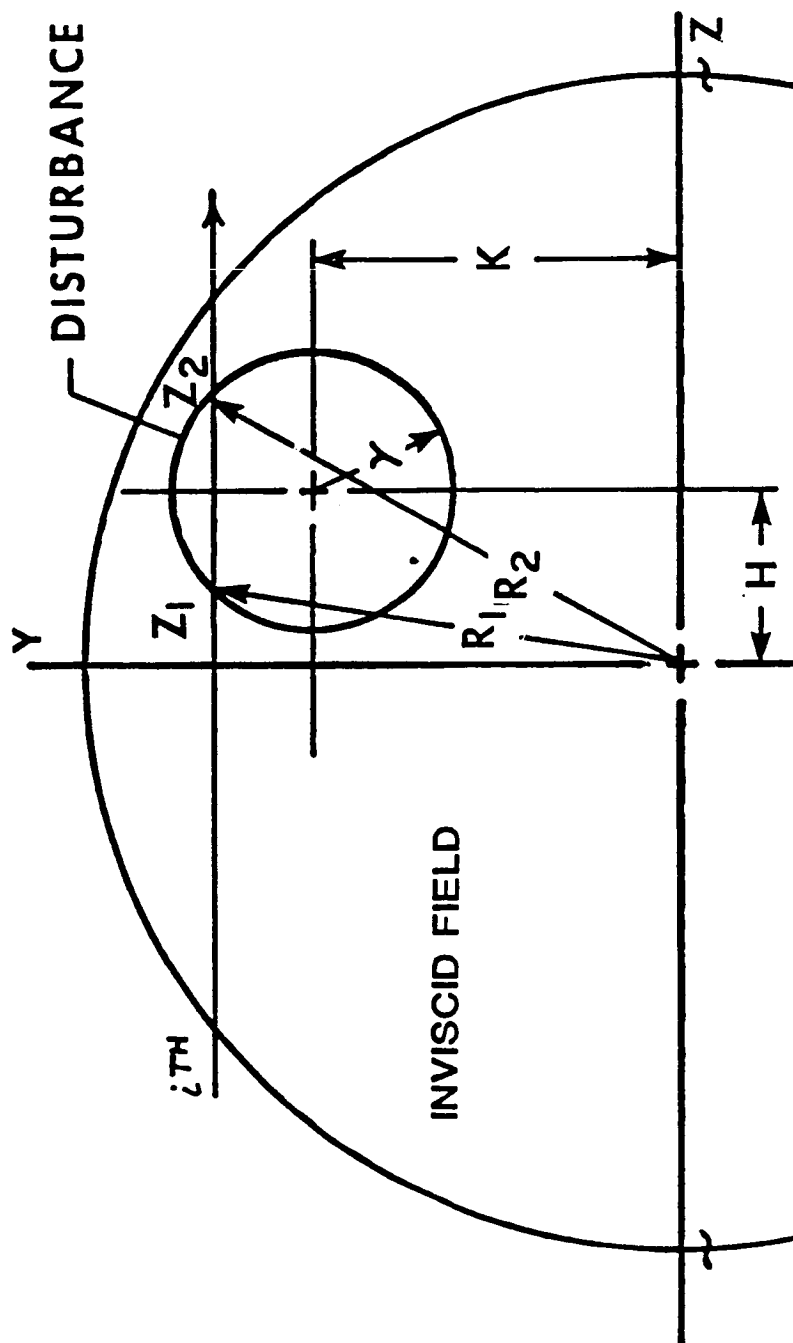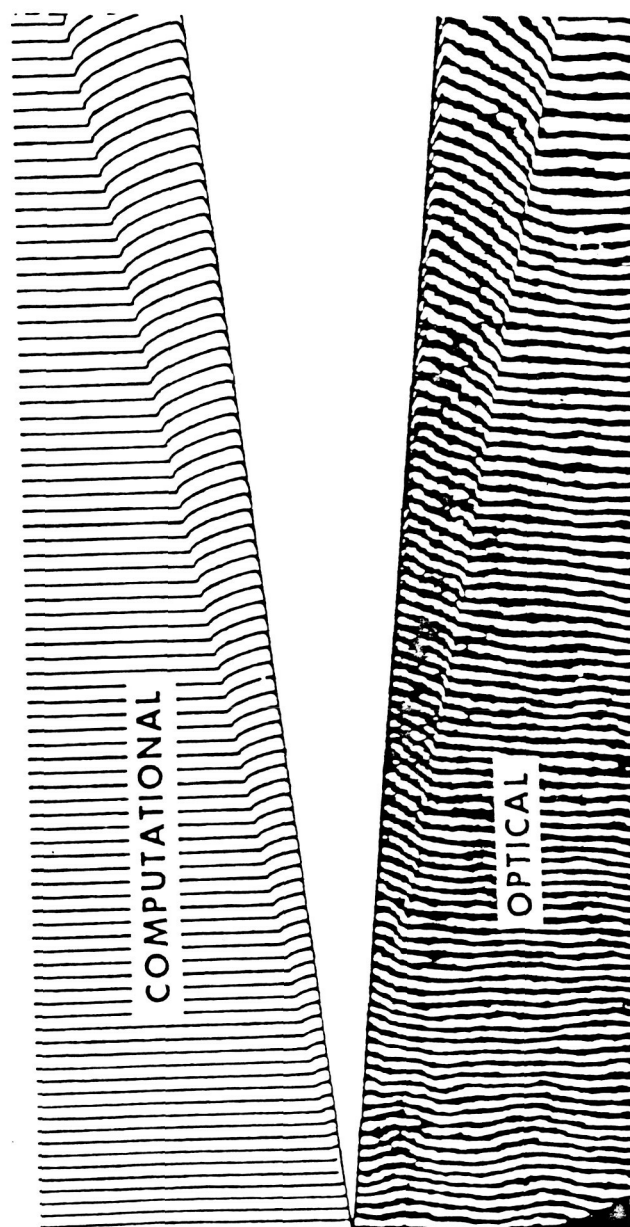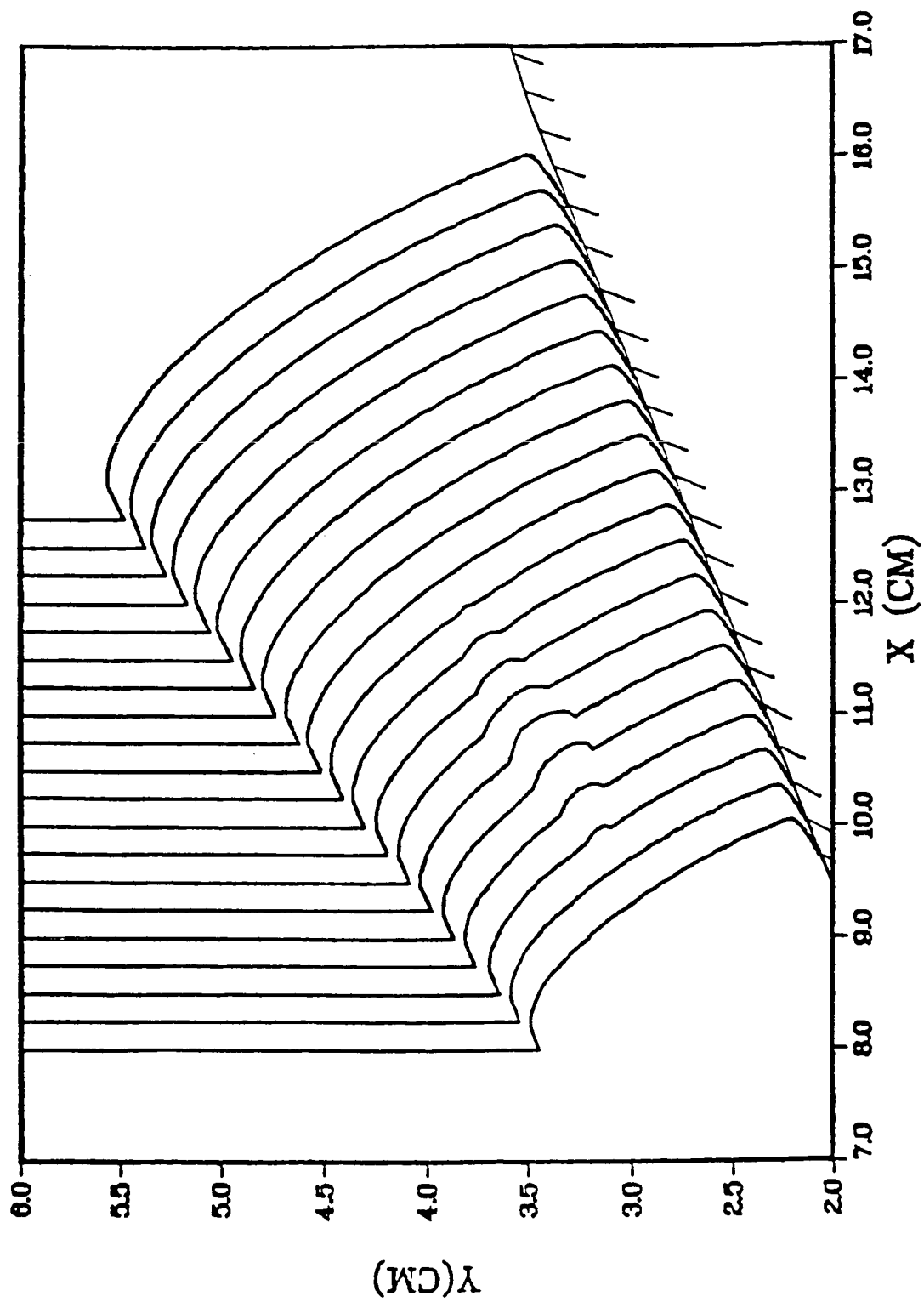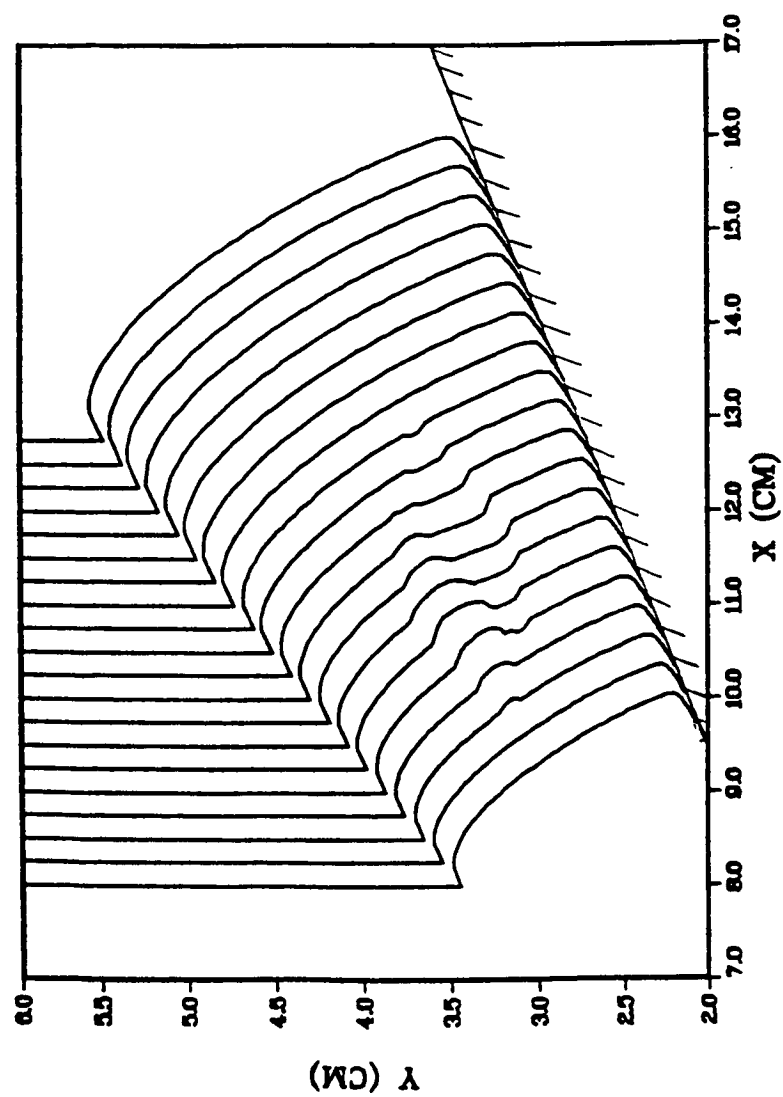
Fig. 4

DISTURBANCE

INVISCID FIELD

Fig. 5

365

COMPUTATIONAL

OPTICAL

Fig. 6

Fig. 7.

Fig.8

519-35

103460

Application of digital interferogram evaluation

techniques to the measurement of 3-D flow fields

Friedhelm Becker and Yung H. Yu

Aeromechanics Laboratory (AVSCOM)

NASA Ames Research Center

Moffett Field, California 94035, USA

Contents

1. Introduction

2. Experimental setup and holographic recording

3. Interferogram evaluation

3.1 Hardware components

3.2. Digitization and preprocessing

3.3. One dimensional evaluation

3.4. Two dimensional interactive processing

3.4.1 Segmentation, polygon representation

3.4.2 Numbering, Error correction

3.4.3 Interpolation

4. Reconstruction

5. Conclusions

6. Acknowledgments

7. References

Abstract

A system for digital interferogram evaluation has been implemented based on an image processing system connected to a host computer. The system supports one and two-dimensional interferogram evaluations. Interferograms are digitized, enhanced and segmented. The fringe coordinates are extracted and the fringes are represented as polygon data structures. Fringe numbering and fringe interpolation modules are implemented. The system supports editing and interactive features as well as graphic visualization. An application of the system to the evaluation of double exposure interferograms from the transonic flow field around a helicopter blade and the reconstruction of the 3-D flow field is given.

Keywords: automatic fringe analysis, interferometry, digital image processing, transonic flows, holographic techniques

1. Introduction

Holographic interferometric techniques have been widely used in recent years in the area of aerodynamics for flow visualization and quantitative measurement of flow properties, particularly for large field measurements in two- and three-dimensional transonic flows [1-4].

Interferometric techniques measure the optical pathlength differences (OPD) between the actual refractive index field $n(x,y,z)$ and a reference field n_0, in either the undisturbed flow or the test section without flow. The path length differences in the plane of observation, measured along the probing rays L in units of the wavelength λ, are registered as phase shifts $\Delta\psi$ of the fringes in an interferogram

$$OPD = \frac{\Delta\psi\lambda}{2\pi} = \int_L [n - n_0] \, ds = N\lambda \qquad (1)$$

where N is the fringe order number. The fringes in an interferogram represent contour lines of equal OPD.

In the two-dimensional case where a constant refractive index along the probing rays is assumed, the OPD is directly related to the refractive index and one interferogram is sufficient to obtain the flow field at any interesting location in the field of view.

In the general case, however, where the flow field is asymmetric, a set of interferograms has to be recorded at different viewing angles around the field to reconstruct the flow field. Such an interferogram is a projection of the index of the refractive index field as it represents line integrals of a scalar variable along rays. In general the line integral can be written:

$$N_\phi(\xi,z) = \frac{1}{\lambda} \int_{L_\phi(\xi,z)} [n(x,y,z) - n_o] \, ds \qquad (2)$$

where (ξ,z) denote the coordinates in the interferogram plane and $L_\phi(\xi,z)$ is a pathlength through the object.

The refractive index at any given point in the flow field may be obtained by applying computer assisted tomography (CAT) methods to invert the integral equation (2). In the refractionless limit, which is assumed here, the light rays passing through a horizontal plane (z=const) of the phase object form the fringe order function along a straight horizontal line in the interferogram plane. This assumption which is valid in the actual application, as shown by a numerical simulation [5], considerably simplifies the numerical reconstuction procedure, because it allows to reduce the 3-D reconstruction problem to a 2-D one by processing horizontal planes independently.

One important step between recording interferograms and applying tomographic reconstruction techniques, however, is the evaluation of

interferograms: reading fringe positions and fringe numbers. Up to now, most interferograms from aerodynamic tests have to be evaluated by either reading fringe numbers and its positions manually or by tracing the fringe lines by hand with the help of a tracking device (for instance a graphic tablet). Manual evaluation, however, is a very time consuming and inaccurate procedure. It is evident that in the current application, where large numbers of interferograms have to be evaluated at several horizontal planes, utilization of an automatic fringe reading procedure would enhance the evaluation considerably and would make the interferometric technique a much more powerful measurement tool.

There are some different approaches to automatize the interferogram analysis. One is direct phase measurement interferometry which uses phase shifting or heterodyne techniques to obtain a set of phase-shifted interferograms from which a relative phase at any given point in the plane of observation may be calculated [6-10]. A similar approach is point by point electronic phase measurement using heterodyne interferometry [11]. Both methods have been used for measuring deformations of opaque solid objects in nondestructive testing and for surface measurements in optical quality testing. Phase measurements on a point by point basis may be very precise, but are inherently slow and need a high acquisition time. The application of phase shifting techniques requires real time test environments, simultaneous recording of multiple phase shifted images, or multiple reference beam holography.

By introducing enough tilt into the interferometric system (finite fringe interferometry) it is possible to restrict the fringe field to a straight line type pattern. This may then be evaluated by using Fourier techniques [12], or spatial synchronous phase detection [13]. These techniques require high fringe densities and therefore a high resolution detection. Processing times are also very high.

Other approaches involve the use of image processing systems to enable a computer aided evaluation of the real fringe pattern. This systems usually digitize and digitally enhance the fringe pattern. Some perform one dimensional fringe analysis for nondestructive testing applications [14-16], locate fringe centers [17] or fringe sides [18-22] or trace the fringe extrema [23] in two dimenional analysis implementations. Interactive, computer-based systems allow the implementation of sophisticated algorithms for image enhancement, fringe segmentation, error correction and fringe numbering, which have to be applied for the evaluation of conventionally observed interferograms. Often the introduction of sufficient tilt (as e.g. in [19]) into the interferometric systems used in fluid mechanics is not feasible, so the fringe patterns are generally of higher complexity.

In this paper, digital interferogram analysis methods developed previously by one of the authors [20,21], implemented on an image processing system, will be described in more details and will be applied to the reconstruction of 3-D transonic flow fields around a rotor blade.

2. Experimental setup and holographic recording

The double exposure holographic interferograms of the flow near a hovering 1/7 geometrically scaled model UH-1H rotor were recently recorded. The one blade rotor system, 1.05 m of the span and 0.075 m chord length with NACA 0012 airfoil sections, was run at a tip Mach number of 0.9 in the anechoic hover chamber at Aeromechanics Lab. A pulsed ruby laser was used to record the double exposed holograms of the transonic flow field around the blade. The diameter of the object beam was 0.6 m, and the total path length was about 30 m.

The first exposure was recorded with the rotor stationary while the second exposure was recorded with the blade rotating by synchronizing the laser pulse with the desired blade position. A more detailed description of the holographic system and the rotor test is given in [3].

Fig. 1 shows a top view of the set-up with a few typical interferograms recorded at different azimuthal angles. Interferograms at 40 different views were recorded at 2 degree intervals. In Fig. 1, interferograms recorded at angles around 90 degrees have very few or no fringes, because the optical rays pass through a very thin portion of the refractive index field. Interferograms recorded around 180 degrees however contain many fringes as the optical rays pass through the longest portion of the refractive index field along the

377

blade. In some of these interferograms shock waves are present. Parts of the fringe pattern are blocked off by the shadow of the rotor system in several interferograms.

3. Interferogram evaluation

In order to reconstruct the 3-D flow field from these interferograms, using tomographic reconstruction techniques, the fringe number functions along cross-sections of a plane parallel to the rotor disk are required. Data from all the views are needed to reconstruct the index of refraction in a particular plane above the blade. Several planes have to be reconstructed in order to get a 3-D flow field representation. This procedure requires each interferogram be represented in a form which allows computing the fringe order function at any desired point.

Interferogram evaluation means to extract lines of equal phase $\Delta\psi$ (equal OPD) from the intensity $I(x,y)$ in the two-dimensional interferogram plane which may be written as

$$I(x,y) = I_0(x,y) + I_1(x,y) \cos(\Delta\psi). \tag{3}$$

The term I_0 describes the background illumination and the distortions, and I_1 is a modulation term. Both may vary over the field of view. The fringe's maxima, minima, or the fringe's sides are easily detectable

lines of equal phase. Each fringe has to be recognized (segmented) from its surrounding and those pixels which represent the constant phase line have to be picked up. In the simplest case where the fringe field is a sinusoidal pattern without any distortions (uniform background-illumination), the segmentation can be done by thresholding (level-clipping) using the mean gray value. This procedure would give the fringe-sides as constant phase lines.

Most of the holographic interferograms however have a nonuniform background illumination with varying contrast and several other distortions (speckle noise, electronic noise). The fringe segmentation in this case has to be somewhat more sophisticated to enable a trouble free postprocessing of the extracted data.

Another difficulty in evaluation of interferograms from transonic flows is the large variation in fringe density. In all of the near spanwise views, the fringes are very narrow above the blade, but are very wide in the rest of the field (see Fig. 1). Also the fringe frequency may change rather rapidly across the field, especially if a shock is present. In applying tomographic reconstruction techniques it is important to know the flow field over the entire field of view with high accuracy. This requirement, however, conflicts with the restricted resolution of the image processing system. A resolving power of more than 3000 pixels across the field of view would have been necessary to evaluate these interferograms. In order to achieve the same resolution with the available system blown-up parts of the

interferograms had to be processed individually and had to be merged subsequently.

The interferogram evaluation by computer aided methods can be subdivided into the following steps: digitization of the interferograms and image enhancement, fringe segmentation and fringe coordinate extraction, merging of fringe fields obtainded from several magnified views, fringe numbering and correction of fringe disconnections, coordinate transformations, interpolation and extrapolation of fringe number functions and finally, reconstruction of the flow field, conversion of fringe numbers into refractive index and interesting flow properties.

In the following, an interferogram evaluation system will be described, which supports all of the evaluation steps mentioned above. All the modules may be called interactively or in batch mode. An editing feature is also implemented, which allows supervision of the evaluation, correction of extraction errors, input of information by hand, modification of fringe numbers and excessive graphic visualization.

3.1 Hardware components

An image processing system (De Anza IP-6400) connected to a VAX 11/780 host computer features the main hardware to digitize the interferograms and to do some image enhancement processing as shown in Fig. 2.

The resolution of the system is 512 x 512 pixels with an 8 bit intensity range. Currently it is equipped with two of possible four memory planes as well as a graphic and an alpha numeric overlay.

A frame-grabbing unit is able to digitize a frame of a video-signal in real time (1/30 sec). A black and white video-camera (MTI series 68) with a resolution (bandwidth) of 18 MHz is connected to this input channel.

The system has an arithmetic-logic-unit (ALU), with which a real-time addition, subtraction or comparison of one or more image-planes may be made. The contents of each memory-plane may be routed through look-up-tables before input to the ALU, to the video-output-processor or to another plane. The actual contents of any or a combination of the image planes is output via a video-output-processor and can be shown on a color-display. Each channel has its own color-mapping tables.

A joystick control device is used for interactive input. It controls two cursors, which may be used in a number of different operating modes. A color print system (Dunn Instruments model 631) serves as a hardcopy device for the color monitor.

3.2. Digitization and preprocessing

During the recording of the holographic interferograms, two
fiducial points were marked in the image plane with a known position
relative to the rotor system. This allows a subsequent coordinate
transformation into a space fixed coordinate system.

Each interferogram was then digitized over an area of about 0.18 x
0.25 m^2 with several enlarged subsections, depending on the fringe
density in the interferograms. A scale, aligned to the fiducial
marks, was always digitized together with the interferogram to be
able to identify the position and the magnification of the enlarged
segments.

Before segmentation and fringe coordinate extraction are applied it
may be useful to do some image enhancement to reduce noise. Frame
averaging methods increase the signal-to-noise-ratio of the imaging
electronic components, thereby improving the picture quality. The
averaging is implemented in real time, over 30 frames in one
second. A spatial smoothing in a 3 x 3 kernel or in an N x M kernel
is useful to reduce high frequency noise introduced by the holographic
procedure like speckle noise. A histogram equalization may also be
done to improve the visibility of a fringe pattern on the display.
But our experience is that this technique has to be used with care
because it is a nonlinear transformation and it tends to amplify noise.

3.3. One dimensional evaluation

A one-dimensional interactive processing may be employed, if only one 2-D plane of the flow field is reconstructed, and hence only one cross section through each interferogram has to be known. In this case some of the overhead required for the full two dimensional evaluation of the fringe pattern may be avoided. But the procedure has to be interactive, because local information (i.e. knowledge of the fringe locations along one line) is not sufficient to number the fringes correctly or to detect lost fringes or other distortions. In an interactive procedure the information such as acceptance of the segmentation and assigning of fringe numbers has to be given by the user.

Several methods have been reported for pattern segmentation which involve gradient operators [24], adaptive thresholding [25], Fourier transforms [15] or piecewise approximation of elementary functions [26,27]. The gradient operators, often used in line detection algorithms, are easy to implement, but don't work well on sinusoidal patterns. They are also very noise sensitive. Adaptive thresholding methods are often used for document scanning and character recognition. They too fail on sinusoidal images. Fourier transform methods are difficult to adapt to fringe fields with varying fringe frequencies across the scan line. Also they require a certain number of fringes in the cross section and are mainly used for detecting phase shifts in patterns of parallel and equidistant fringes. The piecewise approximation of sinusoidal functions or polynomials has been used in a number of cases where precise phase measurements had to be

made in the presence of speckle noise with only a few fringes in the cross section. These methods generally require excessive computing time and the convergence and stability depends on a priori estimates of the fringe positions.

A floating threshold method [20] has been used here for segmentation. This is a two pass scheme. In the first pass the scan line is searched for extrema using a hysteresis detection scheme. A local extremum is only accepted, if it has a minimum gray value difference to the last accepted extremum of different type (after a minimum was accepted, it will be searched for a maximum and vice versa). With the minimum gray value difference, a noise rejection threshold is established. With the found extrema, a steplike threshold function is defined, which settles at the mean gray value between adjacent extrema. Comparison of this function with the original scan line then yields a binary fringe pattern. The transitions from black to white and white to black define the positions of the left and right fringe sides (see Fig. 3a). This method is fast and quite robust and works well even on fringe fields with abrupt changes in image brightness, fringe density, and contrast. The value of the acceptance threshold is not critical and may usually be varied in a wide range without affecting the segmentation. Also the recognized fringe positions do not depend on the actual value of the acceptance threshold. In images with a known modulation variation a spatially dependent acceptance threshold may be used [20].

An example of the segmentation applied to a typical interferogram

384

is shown in Fig. 3b. The actual intensity of a part of the scan line is plotted as a solid line and the extracted fringe-positions (left and right sides) are shown as dotted lines.

A program featuring the one-dimensional evaluation digitizes and preprocesses an interferogram and does a fringe segmentation along a line or a set of lines through the field of view. The result of the segmentation procedure (a binary fringe pattern) is written back to the image screen for monitoring reasons (see Fig. 3c,d). The user may interactively change the acceptance threshold or edit the segmented cross section in heavily distorted regions before he continues to the numbering section. The cursor can be moved to each part of the segmented line, and fringe numbers may be assigned interactively by various commands. The task of assigning fringe numbers is supported by color coding the black parts of the fringes which shows whether the fringe order function increases or decreses by one, or if a discontinuity is present between adjacent fringes. The resulting fringe order function may also be plotted onto a graphic terminal.

A postprocessing program merges all the data taken from different enlarged portions of an interferogram (as shown in Fig. 3c,d) and uses a spline-approximation to interpolate between the fringes. The left- and right-side coordinates, or the middle of the white or black parts of the fringes may be taken as nodes for the spline approximation. To allow discontinuities in the fringe-order function, a rational spline approximation is used. The type of approximation

here may be changed gradually from 1st order to 3rd order polynomials using a parameter derived from the slope of the OPD-function (see Fig. 3e).

3.4. Two dimensional interactive processing

Often the knowledge of only a cross section across the field of view is not sufficient to interpret a given flow problem, but the fringe patterns have to be evaluated over the whole field of view. To facilitate the two-dimensional interferogram evaluation, additional algorithms have been implemented to segment fringes, to extract each fringe's coordinates (trace the fringe sides), and represent the whole fringe field as a polygon data structure. Methods for numbering these line fields and detecting extraction errors have been developed. With a two-dimensional interpolation scheme fractional fringe order numbers may then be estimated at any given point in the field of view. The methods for two-dimensional evaluation will be discussed in the following paragraphs. Typical execution times of the most frequently used modules are given in Table 1.

3.4.1 Segmentation, polygon representation

The fringe segmentation in the two-dimensional case could be done using the same one-dimensional floating threshold method as described above in a sequential manner for each of the lines of an image. This

generally works well for fringe fields running more or less
perpendicular to the scan-line, however it may fail if the fringes
have significant components parallel to the scan-line and noise or
background modulations are present. An example is shown in Fig. 4,
where the floating threshold method with fixed acceptance treshold has
been applied to a digitized fringe field of low quality in Fig. 4a.
The resulting binary pattern are shown after the technique was applied
to lines (Fig. 4b) or to columns (Fig. 4c).

A truly 2-dimensional technique would be to subtract the
nonuniform background and subsequently apply a thresholding with the
mean gray value. In the case of dual reference beam holography the
background correction could be done by subtracting a 180° phase shifted
interferogram [14]. In our case the approximate background has to be
derived from the fringe field itself by a process called "very low
pass" filtering. This technique was also used in [17], each pixel was
replaced by the mean gray value in a relatively large window. To save
computing time the image area is divided into meshes of suitable size
(e.g. 64 x 64 pixels) and the mean gray values are estimated in these
meshes. A surface approximation is then constructed by bilinear
interpolation between the gray values in every four adjacent mesh
points. The discontinuities at the mesh boundaries due to the
bilinear interpolation do not affect the segmentation. This surface
is then subtracted from the original interferogram where an offset of
128 is added to all pixels to avoid negative intensities. An example

of the background subtraction is given in Fig. 4d. A thresholding at level 128 was performed after subtracting the approximated background illumination, from the original image in Fig. 4a. The background was constructed on a grid with meshsize 64 x 64. The method works better than the floating thresholding in most parts of the image, but doesn't work as well in the low contrast areas in the lower middle of the interferogram and in the region of the shock. In the interactive mode all the above mentioned methods may be combined so that each one works on the whole picture or in selected areas only. So it is possible to use the best suited method for each part of the image. Fig. 4e shows the resulting binary pattern after combining background subtraction with horizontal and vertical floating thresholding. After binarization, binary smoothing or shrinking-expanding operations can be applied to reduce pepper and salt noise and to fill in broken lines or truncate line artifacts as shown in Fig. 4f.

Coordinate extraction

After applying the segmentation procedures, the fringe field is transformed into a binary tone pattern. In some applications the binary fringe pattern are reduced to a line representation using skeletonization techniques [17-19], giving the middle of the black (or white) fringes as the fringe positions. In our implementation the coordinates of the fringes are determined at the transition from white to black (and vice versa) giving the fringe sides as the equal phase lines. A sequential tracking procedure similar to a technique used in [28] is

used to trace the fringe positions line by line from the top to the bottom of the picture to represent the fringe field as a polygon data structure.

To reduce the amount of data to store, a redundancy reduction algorithm [29] is activated whenever the temporary storage buffer of a certain polygon is filled. In this way the actual polygon is approximated by a subset of vertices of the original polygon within a certain given tolerance range.

If a fringe goes outside the field of view or a background object such as an airfoil resides inside the fringe field, the visible part of the fringe pattern can be handled by using the points on the boundary as edges of the fringes. Of course, the corresponding polygons may not be connected along the boundary of the background object because they may have different fringe orders. In order to establish the boundary test in a quick, easy and robust manner, it is not desirable to derive the boundary information from the fringe field itself. Therefore, the geometry of the test region (i.e. the coordinates of the boundary) is used to generate a binary valued mask which is compared pixel by pixel with the actual interferogram. The boundary of the test section may consist of a number of lines, and there may be several foreground areas or background areas imbedded in the field of view. The actual boundary may be generated from the known geometry of the set-up or may be manually entered and interactively drawn onto the screen.

Fig. 5 shows a typical example of the fringe coordinate extraction. An interferogram (Fig. 5a) is digitized over the whole field of view with low resolution. The white lines overlaying the display represent the extracted fringe sides, while the black line represents the border polygon which was input by hand before the coordinate extraction in order to mask off background objects and the part of the fringe field with high fringe density (in our implementation all the graphic is in color and therefore easier to distinguish from the displayed image).

The coordinates for each fringe polygon are stored in such an order that always the black part of the fringe is to the right of the polygon. This has some advantages when erroneous parts of the fringe field have to be corrected or fringe fields have to be combined. Lines may never be connected in a way that a "left" fringe side connects to a "right" one and vice versa and each line has to have a neighbor of different type.

The proposed segmentation with subsequent extraction of fringe sides has some advantages over tracking methods which follow the intensity minima or maxima along the fringes [23]. First it is more accurate because the fringe sides are better defined. In most practical cases the fringe pattern are sinusoidally modulated and the fringe sides are not affected as much by noise as are the fringe extrema due to the maximal slope at the sides. Another reason is that the method works well independently from the fringe density and the fringe contrast. Tracking methods tend to lose orientation in wide fringe areas and are unpredictable if the contrast is varying, because

390

they tend to run in the direction of maximal or minimal intensities. Also all points of the field of view have to be marked in order to avoid multiple tracking of the same fringe and to find all of the fringes. Because in the fringe side detection method two lines per fringe are read in one step, the accuracy is further increased over tracking methods. Another point is that the resulting line structures are of simpler type, because no line branchings occur. For this application tracking methods are much more unpredictable and slower, and too much intervening action would be necessary to use them successfully.

Enlarged subsections

As was discussed before, it may be necessary to digitize enlarged subsections to resolve regions with high fringe densities. The resulting fringe polygon field is then combined out of all the individual digitized and processed subsections, starting with the one with highest resolution. To handle the problem of partly overlapping polygon line fields, a boundary polygon is maintained for each subsection. This defines the definition area for each fringe polygon field. Upon combination of two overlapping fields, the border polygon of the one with higher resolution (priority) is used to intersect the lines of the other field. Both line fields are then connected at those intersection points. The new border polygon is the border of the combined areas.

Fig. 5b shows an enlarged digitized part of the interferogram as in Fig. 5a with the extracted fringe polygons overlaying. Fig. 5c shows a plot of the resulting polygon field which was combined from the lines in Fig. 5a and 5b and two other enlarged sections not shown.

3.4.2 Numbering, Error correction

If distortions are present in the interferogram, for instance, due to diffraction patterns, or there is insufficient contrast, or the fringe spacing exceeds the system resolution as in shock or boundary regions, disconnected fringes may occur and thus polygon segments representing fringes of different order may be connected. An example is given in Fig. 6, which is the extracted line field from Fig. 4f. In the lower middle portion of the interferogram there is a distortion of the fringe field due to a diffraction pattern, while in the lower right portion the lines are not resolved in the shock region.

In general, local information obtained from the close surrounding of these areas is insufficient to solve the problems, instead global knowledge about the entire fringe field is necessary. A complete correction of all the incorrectly linked polygon segments may be performed only during the fringe numbering. However, an error correcting scheme may be applied before starting the numbering

C-5

procedure. It uses the geometric parameters of the lines to detect suspicious lines. These are the shape features e.g. circularity (enclosed area divided by the perimeter squared), the distance of the polygon end points and the angles between polygon segments.

A fringe numbering scheme has to introduce the known numbering criteria into an algorithm. They are: (1) the fringe number difference of neighboring fringes must be zero or one, (2) fringes of different order do not intersect or touch each other, (3) fringes do not end inside the field of view unless they are circular fringes, and (4) the fringe number differences integrated along a closed line through the interferogram yield always zero. Furthermore the a priori known properties of the actual object have to be included. Different schemes have been developed to number various kinds of fringe fields [20,21].

One scheme suitable for the numbering of erroneously extracted line fields shall be described in some detail. The idea of the scheme is based on the fact that in general there are only a few locations which cover a small area, in which the fringe lines are falsely extracted, while the line field in most parts of the interferogram is represented correctly. The interferogram is divided into rectangular segments by a grid with suitably-sized meshes. The line segments inside the meshes are now numbered mesh by mesh, starting at the mesh with the maximal number of line segments and with a minimal number of inversion

points of fringe-counting (e.g. a mesh containing parallel lines). The algorithm now looks for the adjacent meshes in which the numbering can continue, i.e. which have at least two consecutive already numbered line segments at their common grid line. From these meshes, the one showing the best conditions is chosen. If the line numbering of the actual mesh is not in accordance with the numbering of the adjacent meshes, it is put back and handled later. In this way, the meshes containing disconnections are processed after all other meshes have been numbered. The numbering scheme now tries to number the line segments inside the erroneous meshes using the numbers already known in the neighboring meshes. If a line has to get different numbers, it is cut into two segments at the position where the angle between adjacent polygon segments is minimal. Another option is to cut at a position where a surface approximation onto the numbered polygon points exceeds a difference of more than a half order to a point of the actual line to be cut.

The procedure assigns relative fringe numbers. The absolute fringe order and direction of increase has to be specified at one location in the field to adjust the other numbers.

As an example of a relatively complex fringe pattern with respect to numbering, Fig. 7 shows the fringe lines of an interferogram of a membrane. The numbering grid is overlayed. The encircled numbers denote the order in which the meshes were processed by the algorithm. Note that the algorithm tends to number parts of the fringe field consisting of similar running lines in a monotonous manner. This is

the most basic rule used for fringe numbering, derived from the fact, that most physical object functions are monotonous and smooth in most areas of the field of view. If the fringe fields would not fulfil this basic requirement, a fringe numbering without further knowledge of the physical properties of the object would actually be impossible.

Fig. 8 shows the numbering grid used for numbering the line field in Fig. 6. The meshes containing the shock and the distorted area are detected by the algorithm because of their high number of inversion points. They are numbered after all other meshes have been processed. So the lines which could not be numbered uniquely will be cut somewhere in the mesh. The position where this is done, however, may not be the correct one. Often fringes of different order are connected through a shock without any indication of the existence of the shock (see e.g. Fig. 6). In this case, the area where the shock appears may be masked off by hand editing before starting the numbering (see Fig. 8).

In the edit mode, the fringe polygon fields may also be numbered manually by drawing a test line into the line field and numbering the intersected fringe lines by several commands using the cursor. Also all lines may be modified manually in the interactive edit mode before starting the numbering or the post processing.

3.4.3 Interpolation

After numbering the fringe lines, the OPD-function is defined at a set of contour lines, but most of the mathematical transformations to follow require interpolation of fractional fringe order numbers. Some methods for interpolation between random points on a surface have been discussed in [30] . An algorithm best suited in regard to computation time as well as numerical representation seems to be a local distance-weighted polynomial least squares approximation. At a given point (a,b) the coefficients of a two-dimensional polynomial of second order

$$P(x,y) = \sum_{k=0}^{2} \sum_{l=0}^{2-k} c_{kl} \ (x-a)^k \ (y-b)^l \tag{4}$$

are estimated to minimize the quadratic form

$$Q = \sum_{r=1}^{N} (P(x_r,y_r) - z_r)^2 \ w((x_r-a)^2 + (y_r-b)^2) = \text{Min.} \tag{5}$$

where $w(d^2) = \exp(-kd^2)$ is a weighting function, which gives more weight to the data points (x_r,y_r) having a shorter distance d to the point (a,b) than the more distant points. The additional advantage is that more distant points may be ignored in the computation. The solution of equation (5) is performed by solving a system of linear

equations (Gauss's method). The parameter k in the weighting function is chosen according to the local data point density. The whole fringe field may be represented with the polygon coefficients calculated on a regular grid. If a smooth approximation of the OPD-surface is desired a two-dimensional spline function may be defined at the meshes of a rectangular grid using only the zero and first order coefficients from the previously obtained polynomials.

An advantage of using a polynomial representation is the fact that an extrapolation of the fringe field is possible into regions blocked by background objects. As an example Fig. 9 shows an interpolated cross section through the numbered polygon field of Fig. 5c at z=c/3. Note, that the left side of the line is extrapolated over a region of the interferogram blocked off by the rotor system.

4. Reconstruction

A number of reconstruction algorithms such as Fourier transform methods, back-projection methods, and iterative methods are covered in the literature (see for instance [31]). Here a convolution backprojection algorithm with a filter function proposed in [32] was chosen, because it generally gives good results, is easy to implement, and is very efficient. The convoluted back-projection is given as

$$g_B(x,y) = \int_0^\pi \int_{-\infty}^\infty N_\phi(\xi) * F^{-1}\{|r|\} \, \delta(x\sin\phi + y\cos\phi - \xi) \, d\xi \, d\phi \qquad (6)$$

where $g_B(x,y)$ is the reconstructed field function in a horizontal plane (z=const), $N_\phi(\xi)$ are the cross sections through the fringe order function at angles ϕ to be convolved with the inverse Fourier transform of the abs-function. The integration of the convolved "projections" is done along the lines $L_\phi(\xi)$ which are expressed as

$$\delta(x\sin\phi + y\cos\phi - \xi) \qquad (7)$$

and over all the projections ϕ.

Fig. 10a shows a reconstruction of the flow field in a plane 8.28 percent chord above the blade obtained from the experimental data at 41 views for the angular interval from 8 to 40 and from 140 to 186 degrees in two degree intervals. The missing views are presumed to be zero (those interferograms have only a few or no fringes and were not evaluated). The resolution in the plane is 101 x 101 points, 101 rays were used in the projection data at each view (see Fig. 9). The time required for a reconstruction from 41 projections with 101 rays at a grid of 101 x 101 points is approximately 24 sec. CPU time on a VAX 11/780.

The reconstruction gives a map of the refractive index in the plane. Because the refractive index of gases is proportional to the density ρ (Gladstone-Dale relation)

$$\rho/\rho_0 = (n - 1) / (n_0 - 1) \qquad (8)$$

the density may directly be calculated. Other flow properties as pressure may be obtained by assuming isentropic flow. The perturbation velocity is derived by application of a form of the energy equation to the blade fixed flow problem.

The lines in Fig. 10a are contour lines of the perturbation velocity. This result may be compared to a cross section through a numerically obtained solution [33] which is shown in Fig. 10b. The basic features of the flow field, the shock position, and the amplitudes are very well confirmed. A slight difference appears in the velocity profiles across the chord in the tip region of the blade which can possibly be attributed to a lambda-shock, which can not be predicted by the nonviscous, potential numerical code.

A more detailed discussion of the reconstruction results and a comparison with hot wire and pressure measurements is given in [34].

5. Conclusions

The features of an image processor based system for interferogram analysis have been described. The system contains algorithms for all steps of digital interferogram processing from image processing techniques such as digitization, enhancement, segmentation to graphic data processing techniques such as fringe coordinate extraction, merging of line fields, error correction, fringe numbering, and approximation techniques for interpolation of 2-D fringe fields. All the modules may be called interactively and editing features are available to process interferograms even if they are of poor quality. The interactive modes are fully supported by graphic visualization. An application to the reconstruction of a 3-D flow field, which was recorded by holographic interferometry at several views around the field, was given. It showed that the evaluation of the interferograms could be considerably improved and accelerated by the digital techniques compared to manual evaluation. The full analysis of the flow field under investigation would hardly have been possible if the data had to be analysed manually.

However, in the described implementation some information has to be input manually even for interferograms of good quality. These are the geometric reference points, the decision whether blown up subsections should be digitized, choosing of an optimal enlargement factor, entering of background border polygons, and a reference number for the

fringe numbering. In order to use this system in a standard test facility the interactive action can be further reduced by using the same information for series of interferograms taken under similar conditions.

6. Acknowledgments

7. References

1.   Trolinger, J. D., ACARDograph 186, 1974

2.   D. A. Johnson, and W. D. Bachalo, AIAA Paper 78-1117, July 1978

3.   J. K. Kittleson, Ninth European Rotorcraft Forum,
      Paper No. 8, Sept. 13-15, 1983, Stresa, Italy

4.   G. Lee, NASA Technical Memorandum 84325, Jan. 1984

5.   R. Snyder and L. Hesselink, Appl. Opt. 23(20), 3650 (1984)

6.   J. H. Bruning, D.R. Herriott, J.E. Gallagher, D.P. Rosenfeld,
      A.D. White, and D.J. Brangaccio, Appl. Opt. 13(11), 2693 (1974)

7.   W. R. Fischer, H.-A. Crostack, and H.-D. Steffens,
      Laser 79 Opto-Electronics, Munich 2/6 July 1979, Conf. Proc.,
      IPC Science and Technology Press, London 1979, pp. 404-411

8.   T. Yatagal, and T. Kanou, Opt. Eng. 23(4), 357 (1984)

9.   R. Smythe, and R. Moore, Opt. Eng. 23(4), 361 (1984)

10.   ZYGO Automatic pattern processor, Technical description,
      Zygo Corp., (1981)

11. Dändliker, R., in "Progress in Optics", Vol. 17, Chap. 1
     E. Wolf, Ed., North-Holland, Amsterdam (1980)

12. M. Takeda, H. Ina, and S. Kobayashi, J. Opt. Soc. Am. 72, 156
     (1982)

13. K. H. Womack, Opt. Eng. 23(4), 391 (1984)

14. M. Schlüter, Optics and Laser Technology 12, 93 (1980)

15. D. W. Robinson, Appl. Opt. 22(14), 2169 (1983)

16. D. A. Tichenor, and V.P. Madsen, Opt. Eng. 18(5), 469 (1979)

17. S. Nakadate, N. Magome, T. Honda, and J. Tsujiuchi,
     Opt. Eng. 20(2), 246 (1981)

18. S. Nakadate, T. Yatagai, and H. Saito, Appl. Opt. 22(2), 237 (1983)

19. T. Yatagai, S. Inabu, H. Nakano, and M. Suzuki,
     Opt. Eng. 23(4), 401 (1984)

20. F. Becker, "Zur automatischen Auswertung von Interferogrammen",
     Mitteilungen des Max-Planck-Institutes, Göttingen, Nr. 74, (1982)

21. F. Becker, G. E. A. Meier, and H. Wegner, in "Applications of Digital Image Processing IV", Andrew G. Tescher, ed., Proc. SPIE 359, 386 (1982)

22. H. S. Cline, A. S. Holik, W. E. Lorensen, Appl. Opt. 21(24), 4481 (1982)

23. W. R. J. Funnel, Appl. Opt. 20(18), 3245 (1981)

24. A. Rosenfeld, and A. Kak, "Digital Picture Processing", Academic Press, New York (1976)

25. To Russel Hsing, Opt. Eng. 23(3), 288 (1984)

26. J. J. Snyder, Appl. Opt. 19, 1223, (1980)

27. J. B. Schemm, and C. M. Vest, Appl. Opt. 22(18), 2850 (1983)

28. A. K. Agrawala, and A.V. Kulkarni, Computer Graphics and Image Processing 6, 538 (1977)

29. U. Ramer, Computer Graphics and Image Processing 1, 244 (1972)

30. D. H. McLain, Computer Journal 17(4), 318 (1974)

31. G. T. Herman, (ed.), "Image Reconstruction from Projections, Implementation and Applications", Topics in Appl. Phys. 32, Springer, Berlin (1979)

32. L. A. Shepp, and B. F. Logan, IEEE Trans. NS-21(3), 21 (1974)

33. F. X. Caradonna, "The Transonic Flow on a Helicopter Rotor", Ph.D. Dissertation, Stanford Univ., Stanford, Calif., (3,1978)

34. J. K. Kittleson, and Y. H. Yu, AIAA Paper No. 85-0370, Jan. (1985)

Table 1. Execution times of some Hardware- and Software-modules

Function	approx. CPU time
Digitization, Look-Up-Table operations	1/30 sec
Averaging over N frames	N/30 sec
Convolutions[†] (k=kernel elements)	K/30 sec
Binary operations (smoothing, shrinking, expanding)	K/30 sec
Subtraction of approximated background	16 sec
Application of floating threshold method	14 sec
Extraction of fringe coordinates[*]	30 sec
Merging of line fields[*]	10 sec
Numbering, error correction[*]	10 sec
Interpolation[*] (comp. of coefficients per polynom)	0.05 sec

[†] For image processor equipped with three memory pages

[*] Times depend on the complexity of the image and the number of fringes. The times given are for a typical example like Fig. 5

Figures

Fig. 1 Top view of the holographic set-up with sample

       interferograms taken at different angles

Fig. 2 Sketch of the image processing hardware

Fig. 3 Example of one-dimenional processing

    3a Floating threshold fringe segmentation

    3b Demonstration of the threshold fringe segmentation on a

       scan line of an actual interferogram

    3c Digitized interferogram (182.5) with segmented cross-sections

       superimposed

    3d Evaluation of an enlarged section of the same interferogram

       as in Fig. 3c

    3e Fringe order function along cross section 3 of interferogram 182.5

       after combination of several enlarged subsections and rational

       spline interpolation

Fig. 4   Example of fringe segmentaion, binarization

4a Enlarged digitized subsection of interferogram (184.5) with

    superimposed grid of meshes of size 64 x 64

4b Floating threshold method applied to lines of Fig. 4a

4c Floating threshold method applied to columns of Fig. 4a

4d Thresholding after background subtraction, computed on the

    grid in Fig. 4a

4e Combination of methods b,c, and d

4f Result after binary smoothing and shrinking - expanding operations

    applied to Fig. 4c

Fig. 5   Example of fringe polygon extraction and merging of

         enlarged digitized subsections

5a Original digitized interferogram (8.5), extracted fringe

    polygons are overlayed in white, the border polygon is written

    in black

5b Enlarged digitized part of the same interferogram,

    extracted fringe polygons are overlayed

5c Plot of the resulting polygon field merged from 6a and 6b

    and two other enlarged sections not shown

Fig. 6   Extracted line field of Fig. 4t, showing disconnected

lines in an area disturbed by a diffraction pattern and in

a shock region

Fig. 7   Fringe numbering

Example of a complex fringe pattern with several minima

and maxima, encircled numbers give the order in which the

meshes were processed

Fig. 8   Numbered and error corrected line field of Fig. 5c with

numbering grid

Fig. 9   Interpolated fringe order function along a cross-section

at z=c/3 through the numbered line field of Fig. 5c, showing

extrapolation to the left. The symbols mark the

coordinates of the fringe polygons in the cross-section

Fig. 10   Reconstruction of the flow field in a horizontal plane

at z/c=0.0828 above the blade

The blade rotates clockwise, leading edge is at x/c=0.

(c is the chord length of the blade, Ro is the blade radius)

10a   Perturbation velocity contours in ft/s as reconstructed from

cross-sections through 41 interferograms, at 101 x 101 points

10b   Perturbation velocity contours at the same height above

the blade as given by a numerical solution of the flow

problem

$\theta = 20°$
(a)

$\theta = 30°$
(b)

$\theta = 34°$
(c)

$\theta = 90°$
(d)

$\theta = 166°$
(e)

$\theta = 180°$
(f)

$\theta = 186°$
(g)

FILM

GRAPHIC 4 BIT

VAX 11/780 VMS

GRAPHIC TERMINAL

PLOTTER

LOOK-UP TABLES

ARITHMETIC LOGIC UNIT

JOYSTICK-CONTROL

MEMORY 512 x 512 x 8

VIDEO-PROCESSOR

COLOR-CAMERA SYSTEM

B/W-VIDEO-CAMERA

COLOR-MONITOR
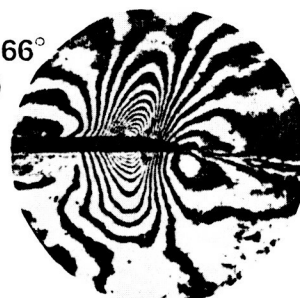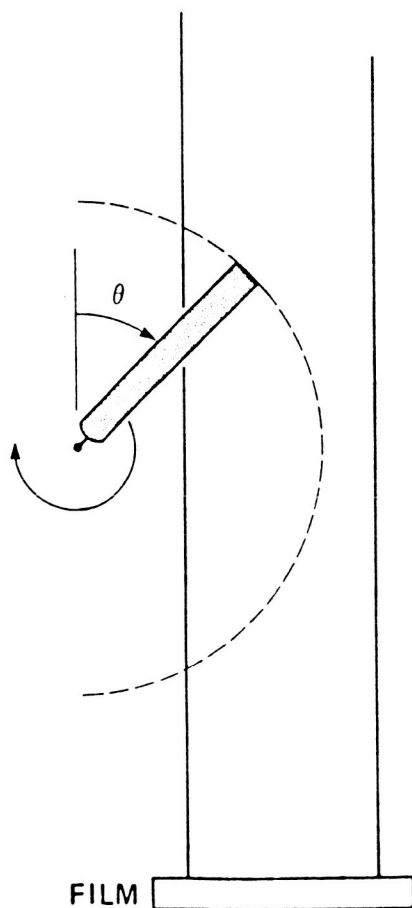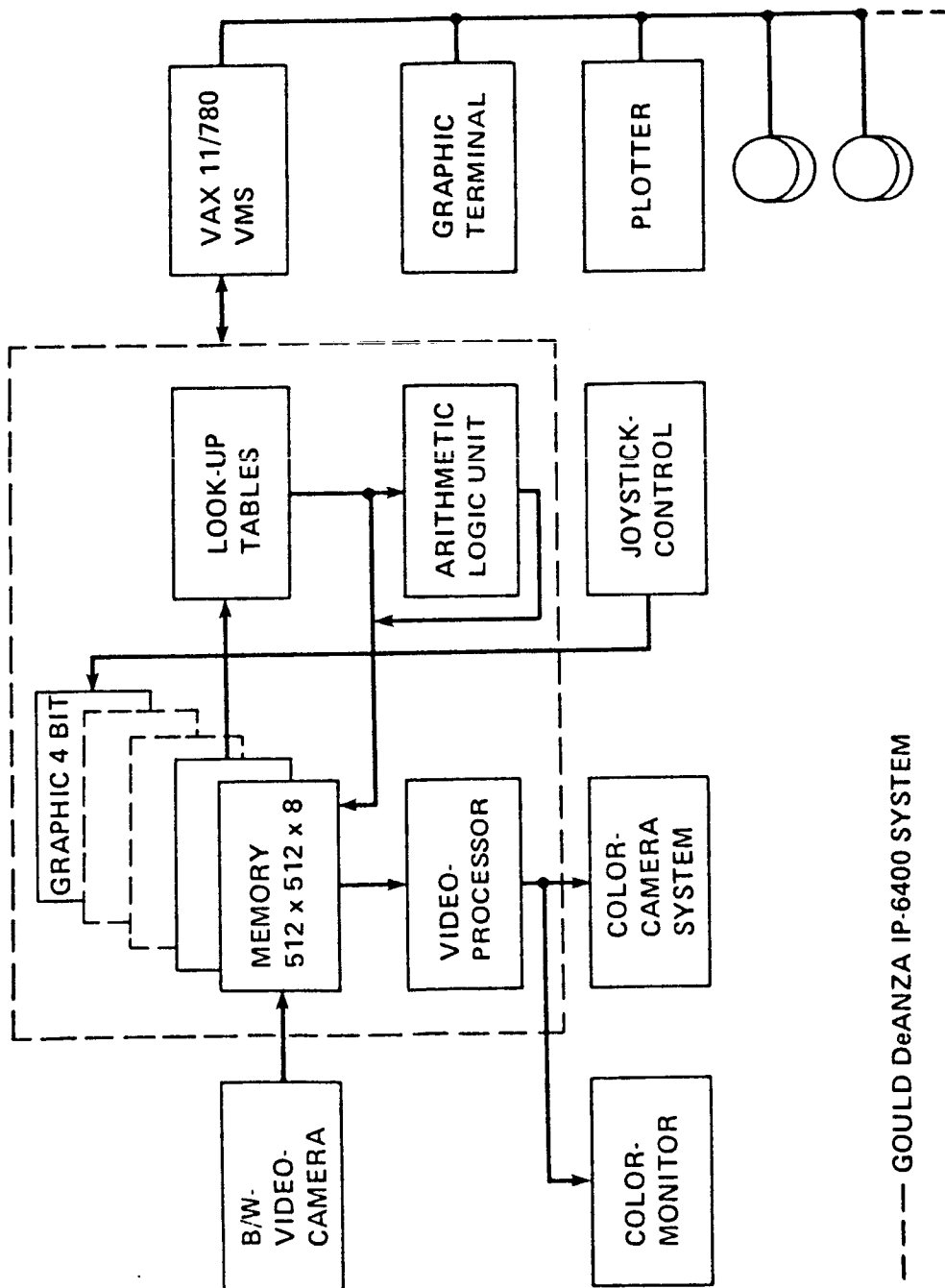
— — — GOULD DeANZA IP-6400 SYSTEM
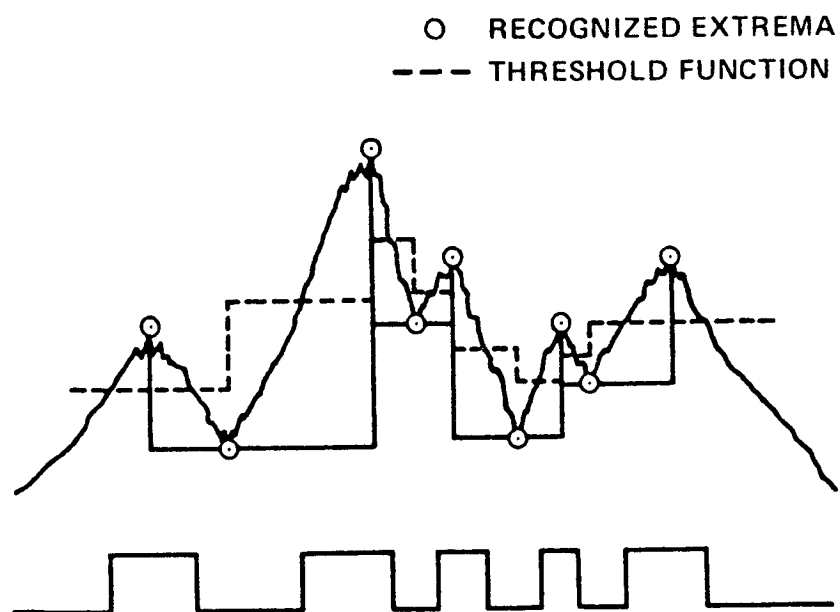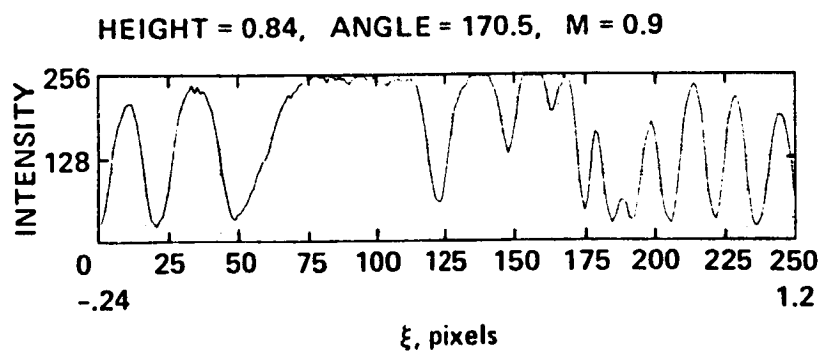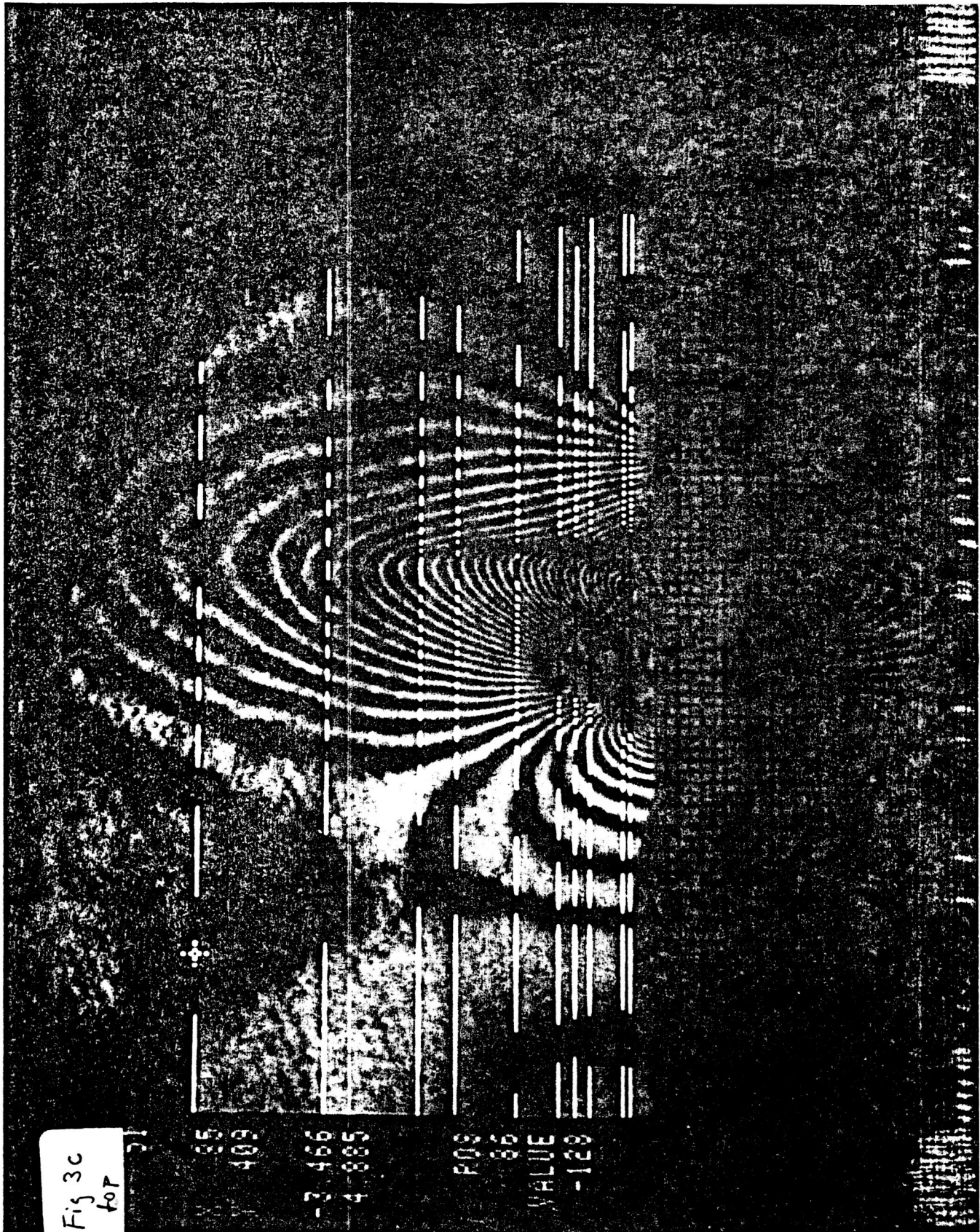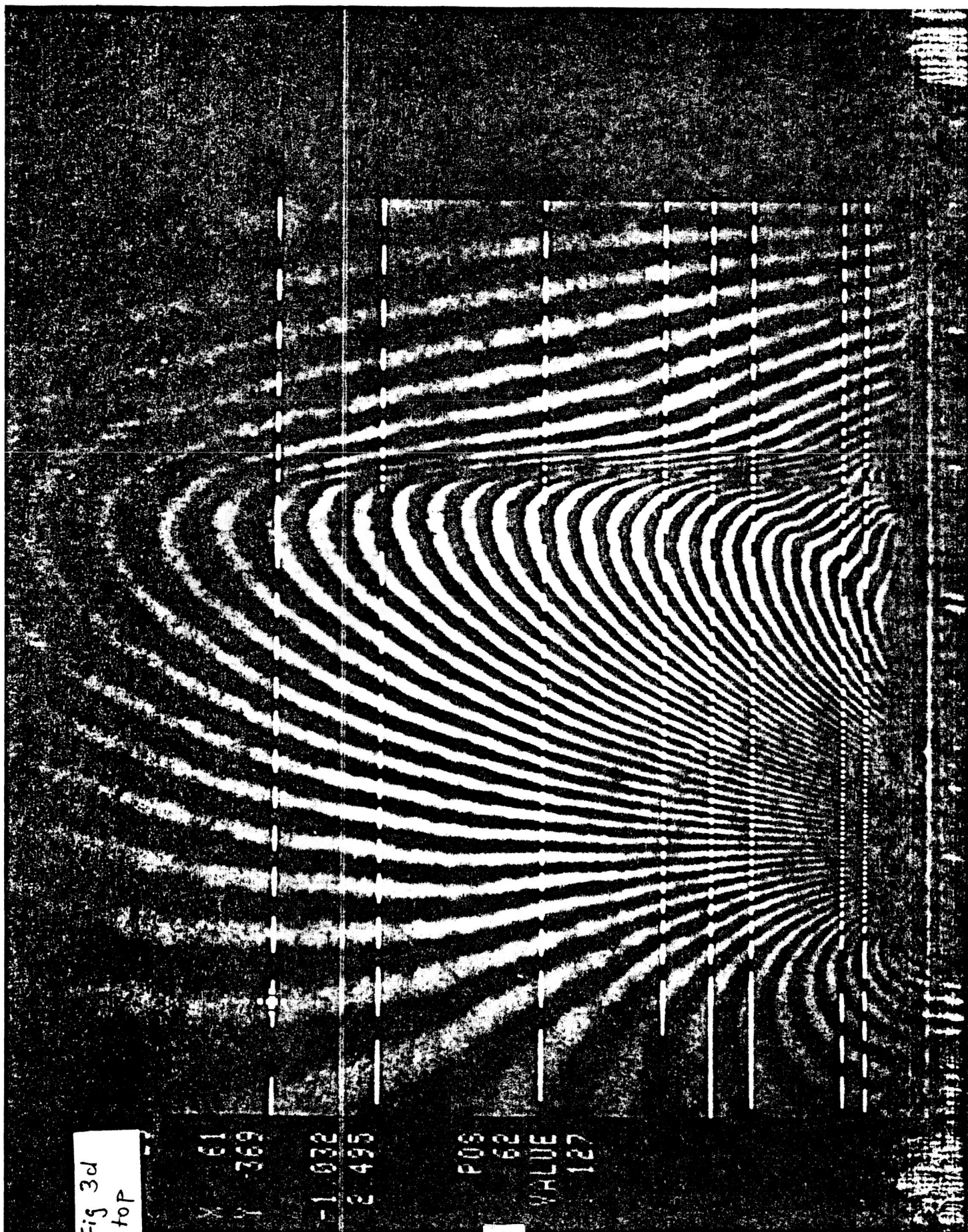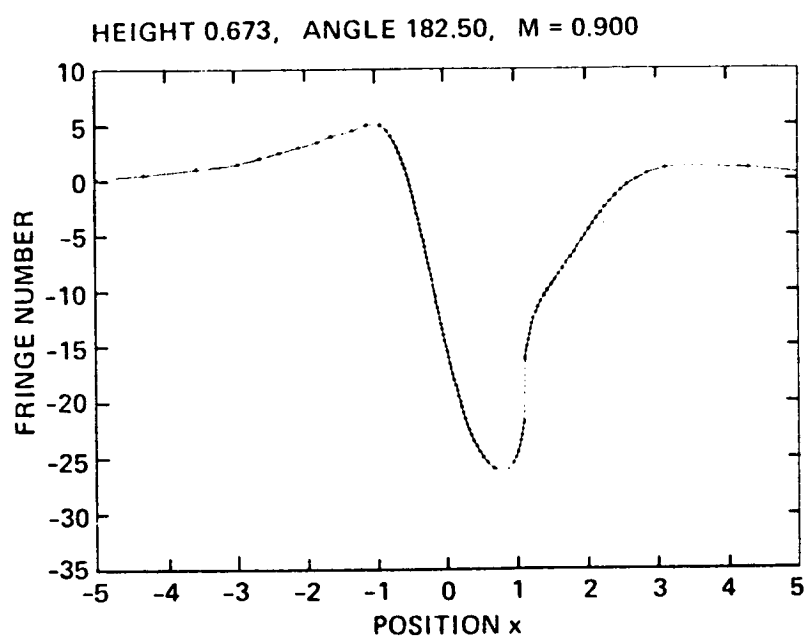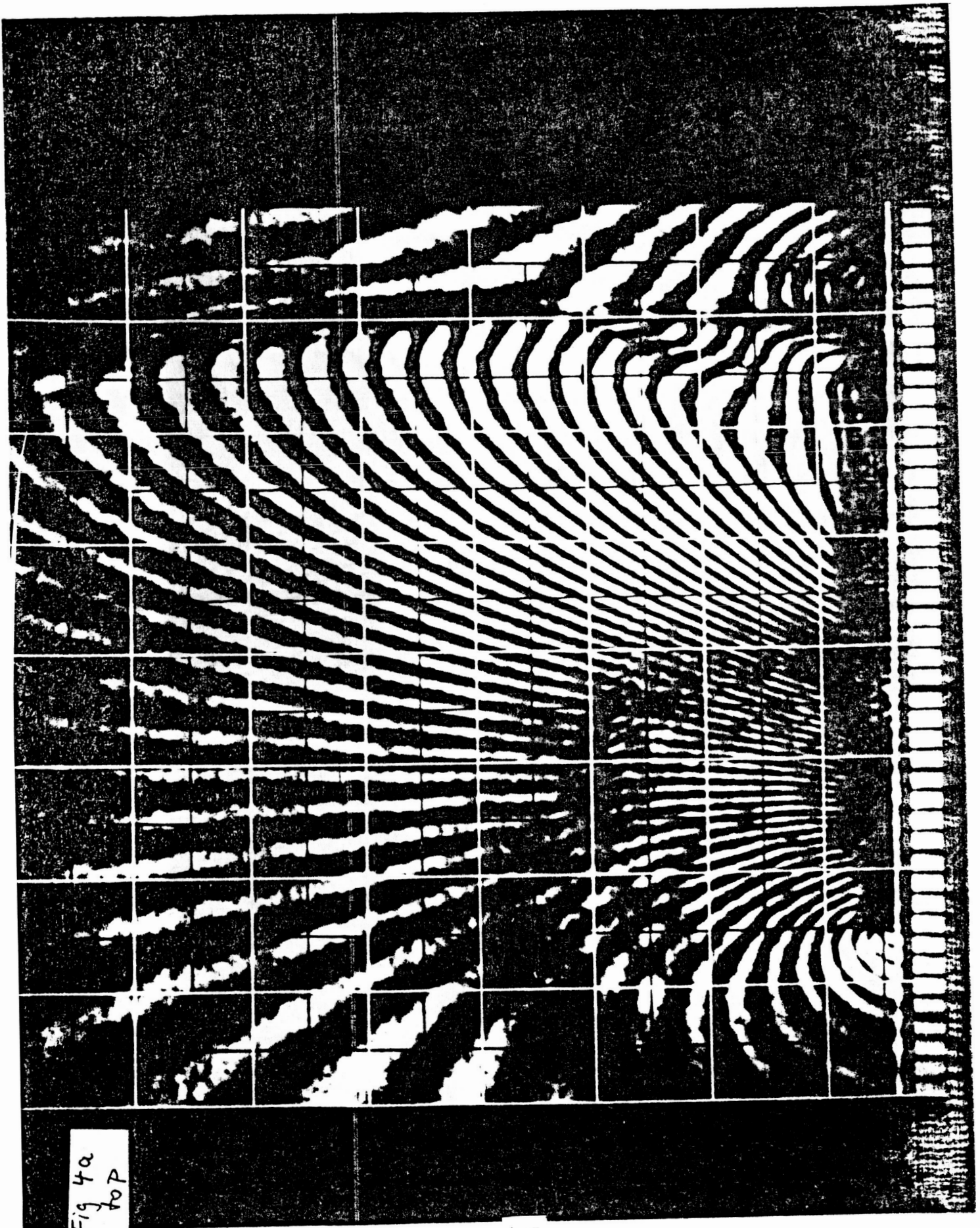
411

Fig 3a top

O   RECOGNIZED EXTREMA
— — — THRESHOLD FUNCTION

Fig 3b top

HEIGHT = 0.84,   ANGLE = 170.5,   M = 0.9

Fig 3c
top

Fig 3d top

Fig 3e   top

HEIGHT 0.673,   ANGLE 182.50,   M = 0.900

Fig 4a top

Fig 46 top

Fig 4c
top

Fig 4d
top
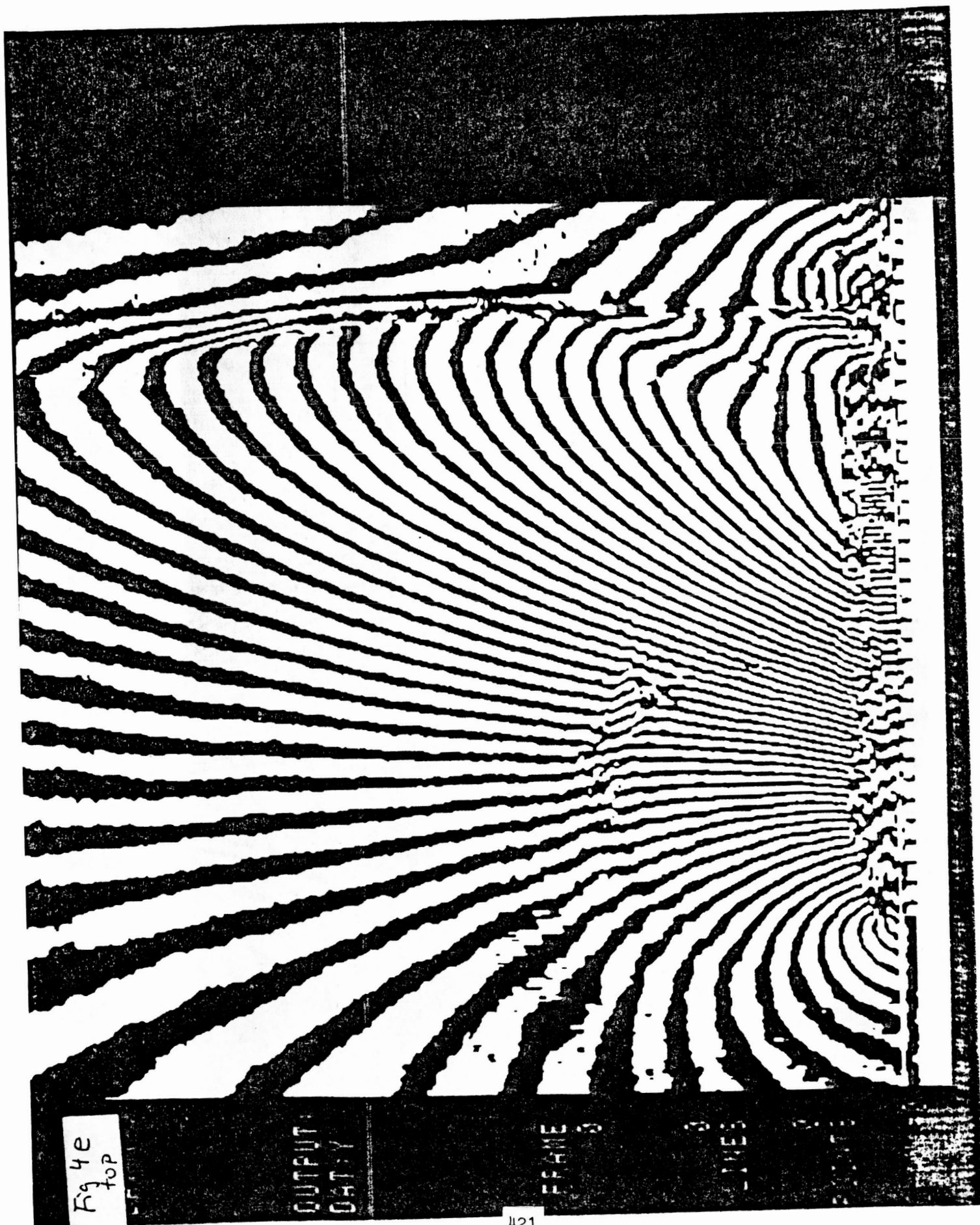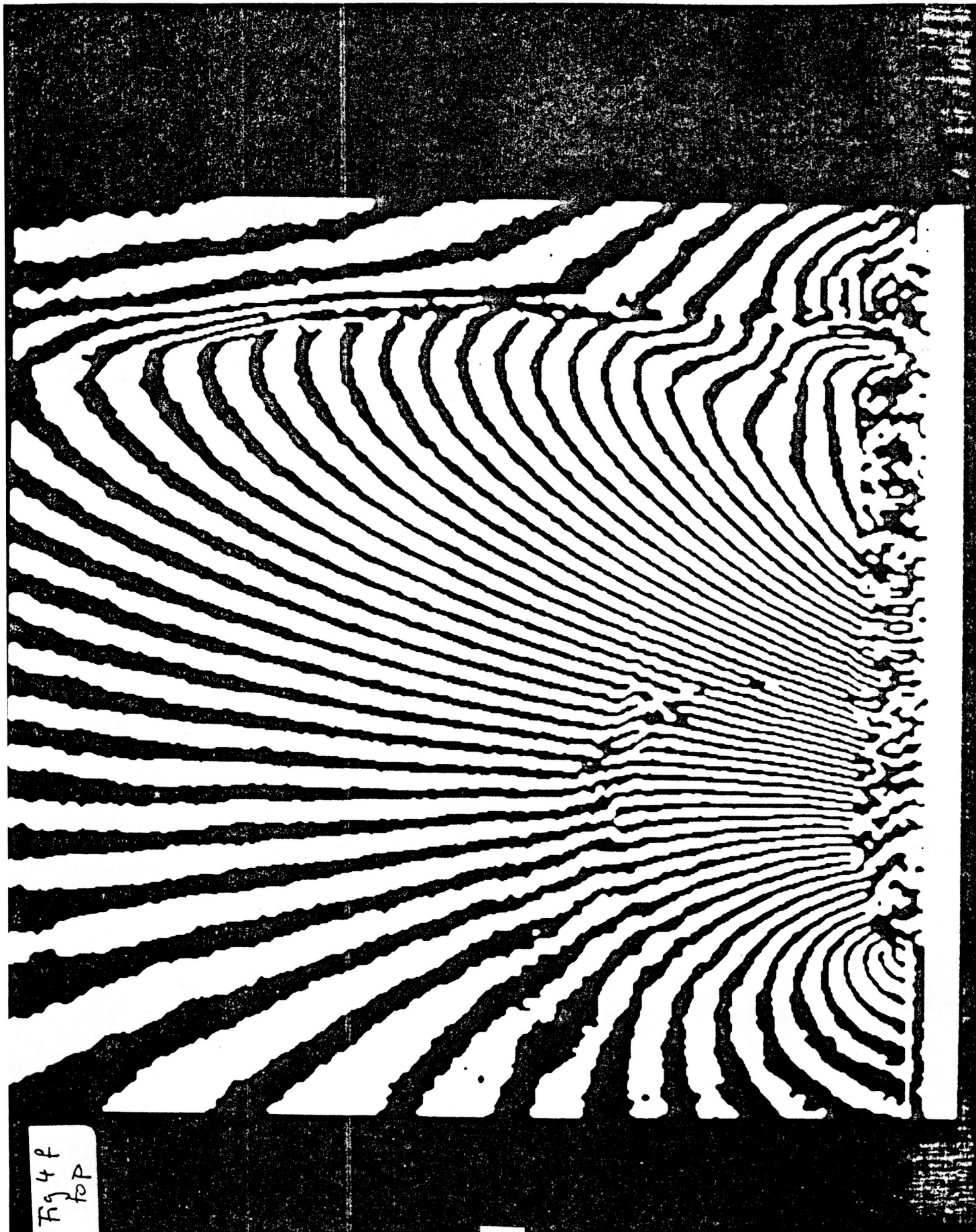
Fig 4e
top

Fig 4 f
top

422

Fig 5a
top

Fig 5b
top

424

Fig 5c   top

ANGLE = 8.5, M = 0.9

Fig 6   top

ANGLE = 184.5,   M = 0.9
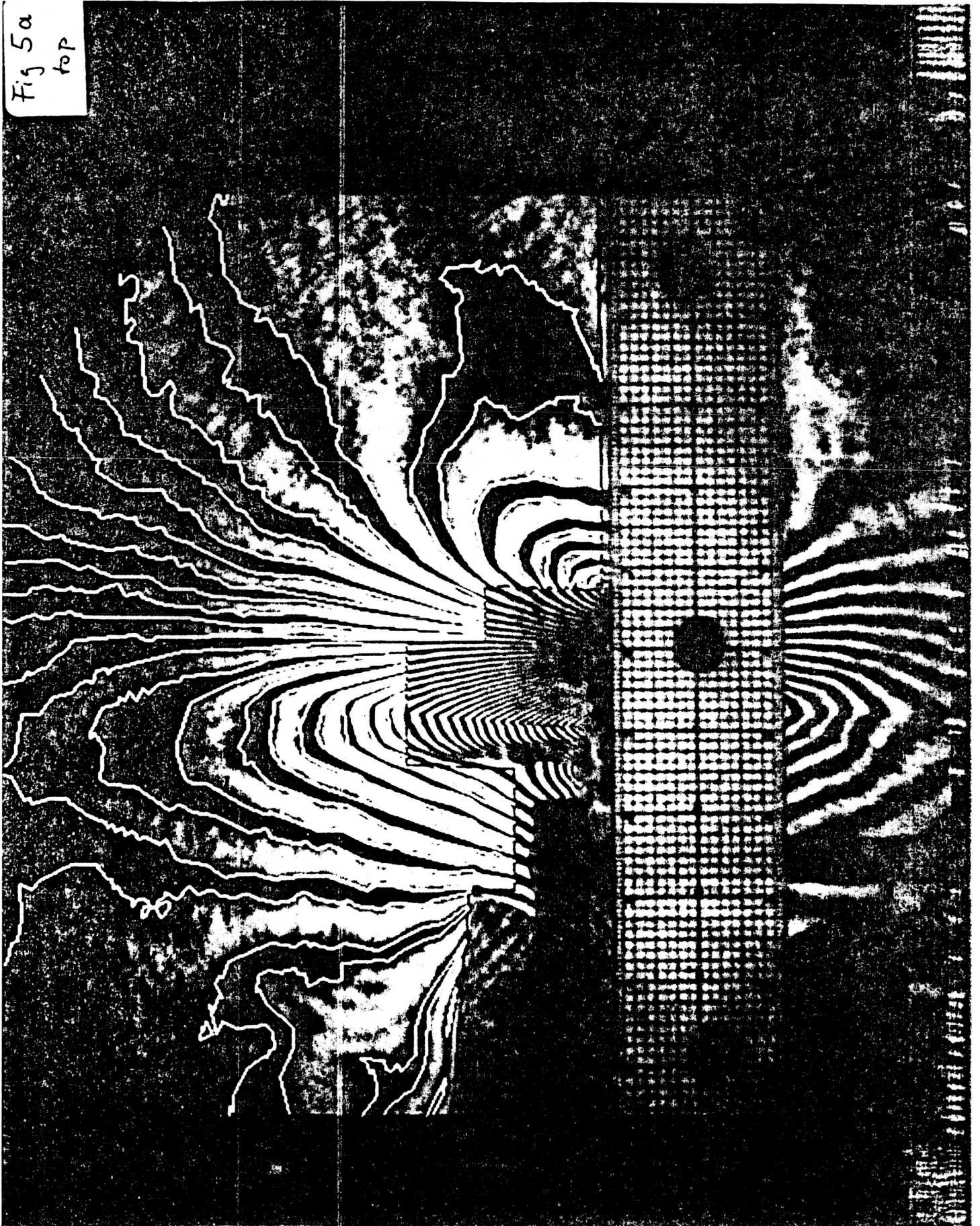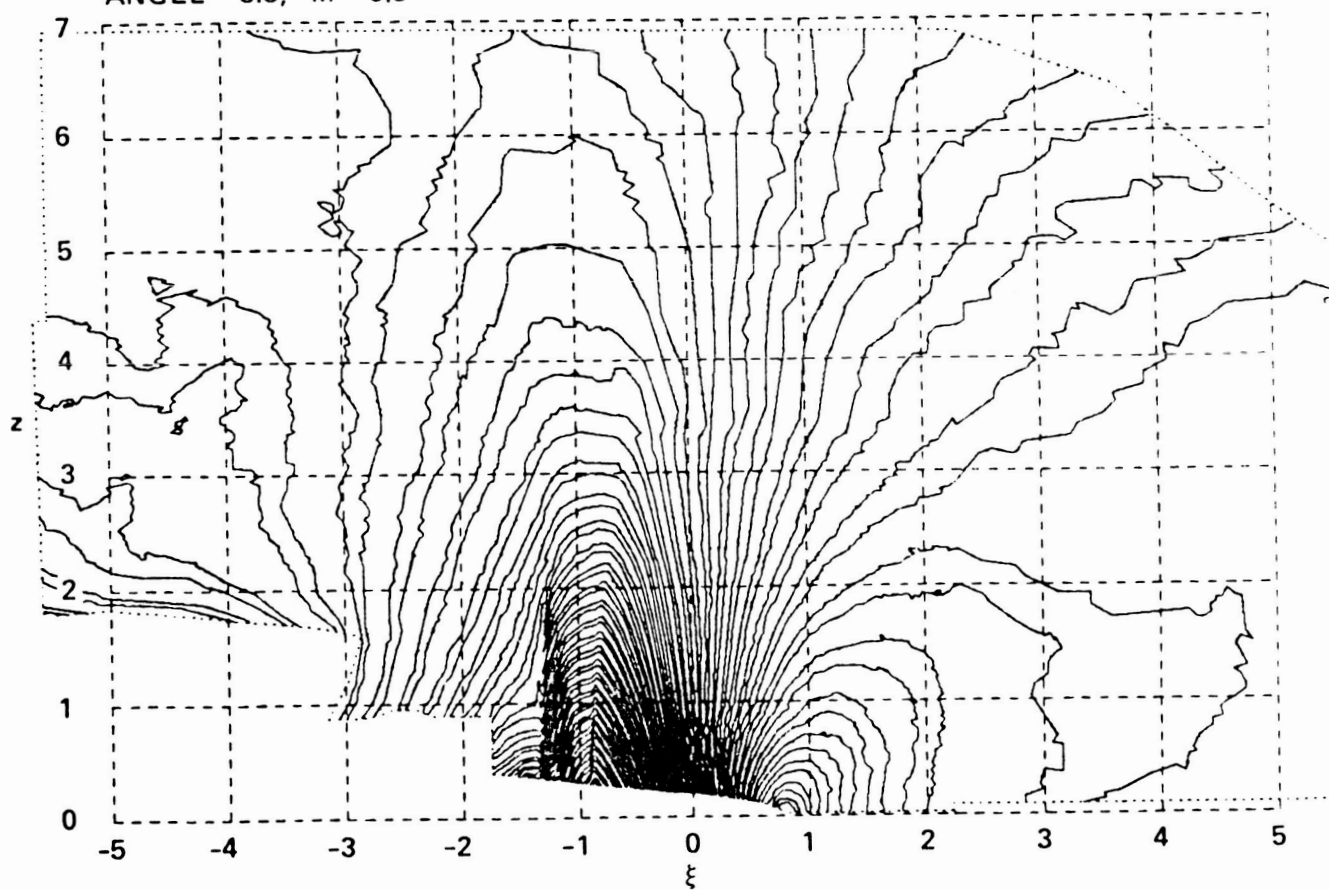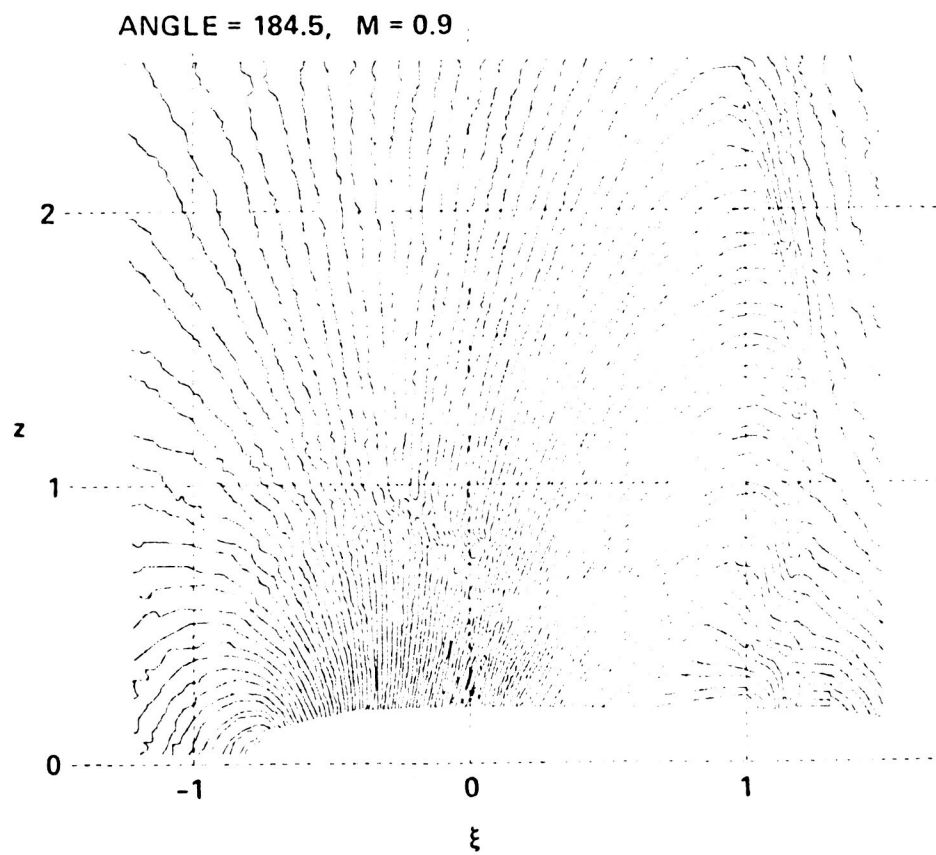
Fig 7   top
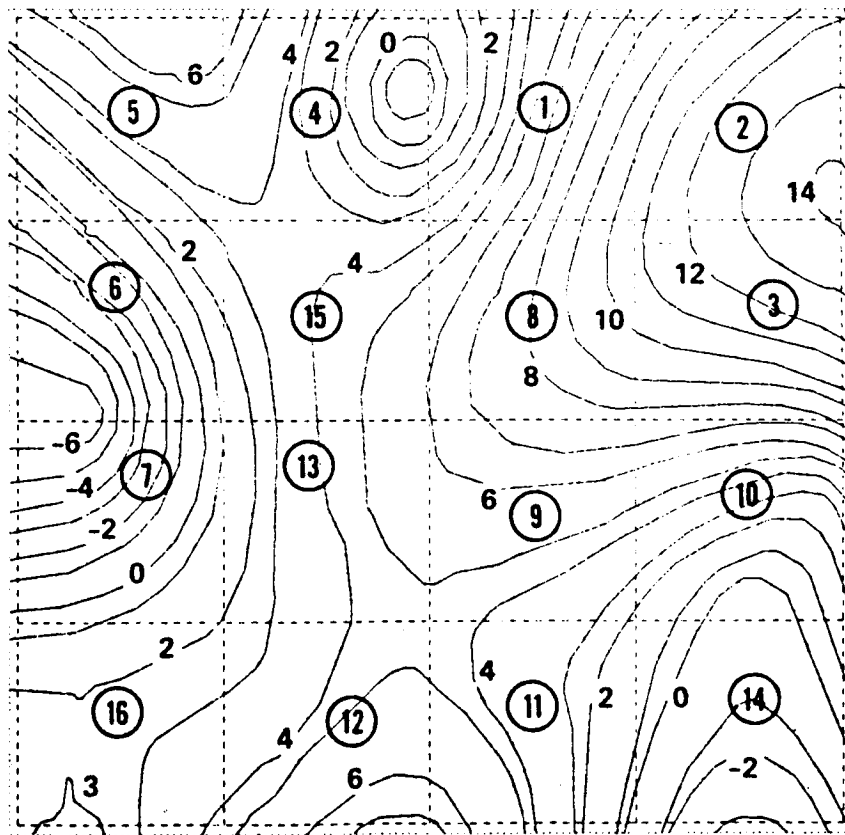
Fig 8   top
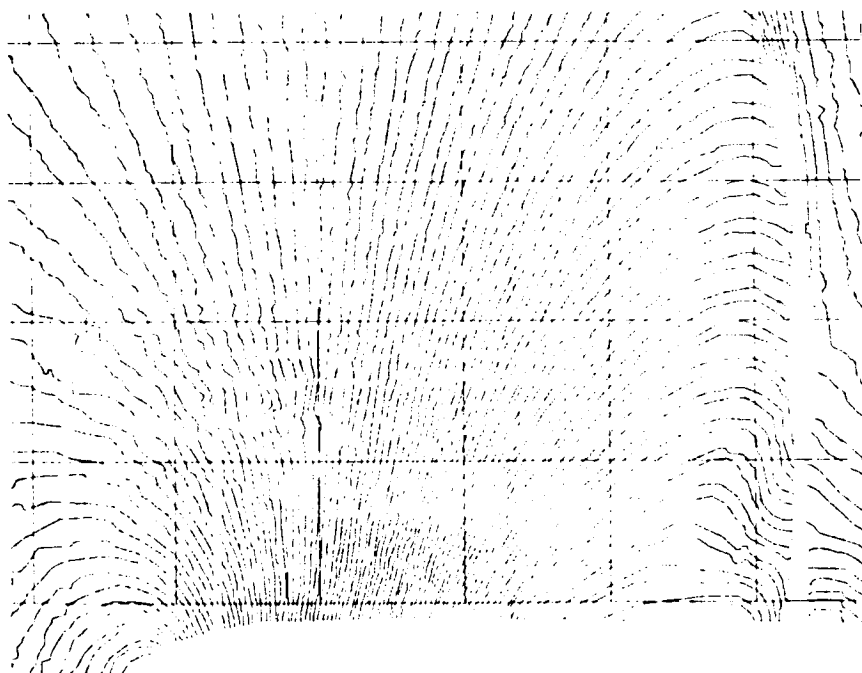
Fig 9 top

HEIGHT = 1.000, ANGLE = 8.50, M = 0.900
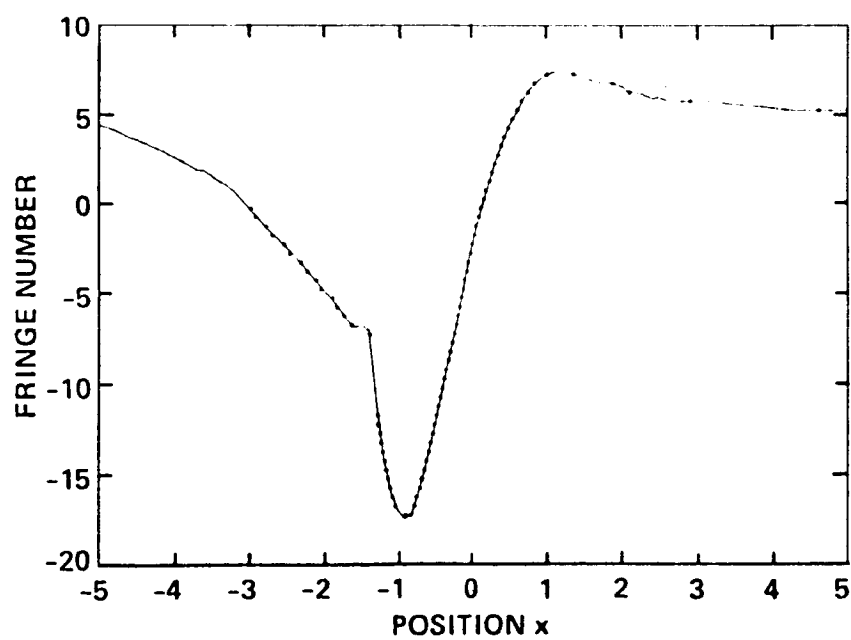
Fig 10a   top
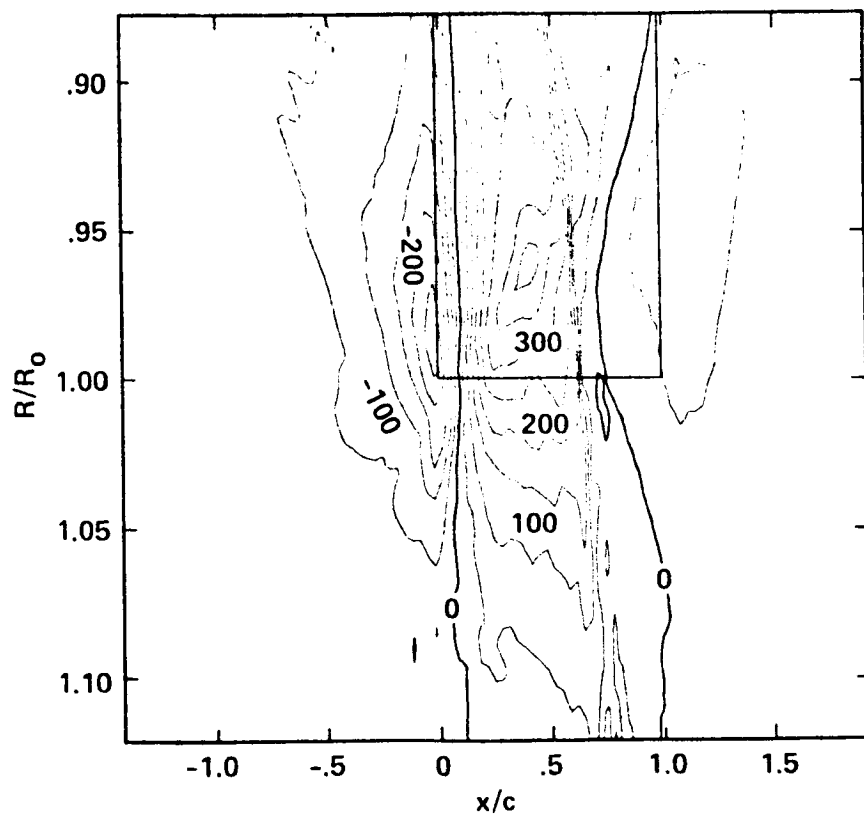
Fig 10 b top
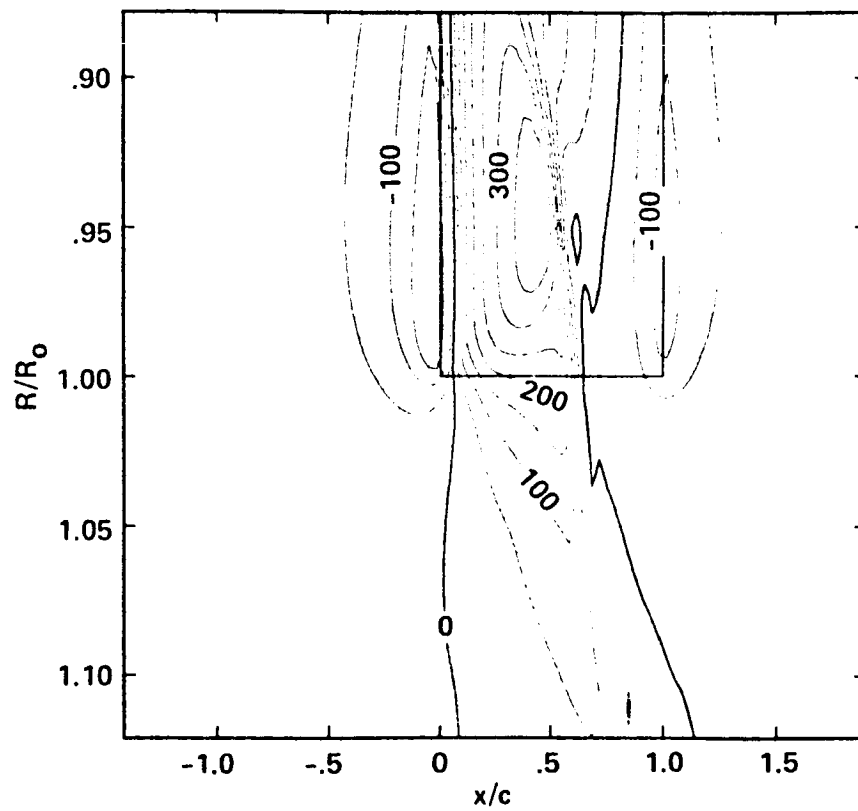
The Fringe Reading Facility at the
Max-Planck-Institut für Strömungsforschung

F.Becker,G.E.A.Meier,H.Wegner,R.Timm,R.Wenskus

Max-Planck-Institut für Strömungsforschung,Göttingen,W.Germany

1) Optical equipment

A Mach-Zehnder-interferometer is used for optical flow measurements in a transonic wind tunnel. The duct width is 100 mm. The light source is a spark chamber (Impulsphysik). High speed recordings can be made with a rotating drum camera at a frame rate of 10 kHz or with a rotating prism camera (Fastax) at frequencies up to 8 kHz. Periodic processes are frequently investigated by taking single pictures triggered by a controlling computer at a certain phase.

Holographic interferograms are reconstructed by illumination with a He-Ne-Laser and viewed by a video camera through wide angle optics. This setup has been used for investigating industrial double-exposure holograms of truck tires in order to develop methods of automatic recognition of certain manufacturing faults.

A Zeiss microscope used in conjunction with a Mirau interference device has been used for studying membrane oscillations.

2) Computer hardware (Fig.1)

Automatic input is achieved by a transient recorder (Biomation S8100) digitizing the output of a TV-camera and transferring the digitized data to a PDP11-34. Generally, a resolution of 512x512 pixels with 8 bit gray levels is used.
A graphic tablet and a graphic terminal are connected to the system to provide manual input.
Preprocessing of the images and fringe extraction are done with the PDP11-34.
Connections exist to a VAX11-750 which is used for more complex and time-consuming routines like fringe numbering or polynomial approximation and also to an array processor (Floating Point Systems AP120) used for FFT routines.
An image processing system (Imaging Technologies IP512) will partially replace the PDP11-34 and speed up image preprocessing.

The image processing routines mentioned above are described in refs. 1,2.

3) Current activities and plans

For some time the interest of our group has centered around sequences of interferograms showing the interaction of vortices with a profile and subsequent emission of sound generated by this process. Figure 2 shows two examples of this process; the experiment was performed with a NACA 0012 profile at Mach 0.8. These studies are of interest with respect to investigating the causes of helicopter rotor noise (ref. 3).

For better time resolution a higher photographic frequency will be needed. This problem may be solved by using a LED light source with a frequency up to 100 kHz as compared with the 8-10 kHz achieved with the spark lamp used until now.

Furthermore, evaluation is rendered somewhat difficult by the complicated structure of the interferograms, for example by the appearance of shock fronts. At present, routines for automatic recognition of vortices and shock fronts are being developed. Ultimately, the objective will be the extraction of quantitative data which relate to the emission of noise.

References:

1. Becker,F.; Meier,G.E.A.; Wegner,H.: Automatic Evaluation of Interferograms, SPIE Proceedings Vol.359 (1982)

2.Becker,F.: Zur automatischen Auswertung von Interferogrammen, Mitt. MPI für Strömungsforschung, Göttingen Nr.74 (1982)

3.Meier,G.E.A.; Timm,R.; Becker,F.: Initial Experiments on Profile Vortex Interaction, Berichte MPI für Strömungsforschung, Göttingen Nr.6 (1983)
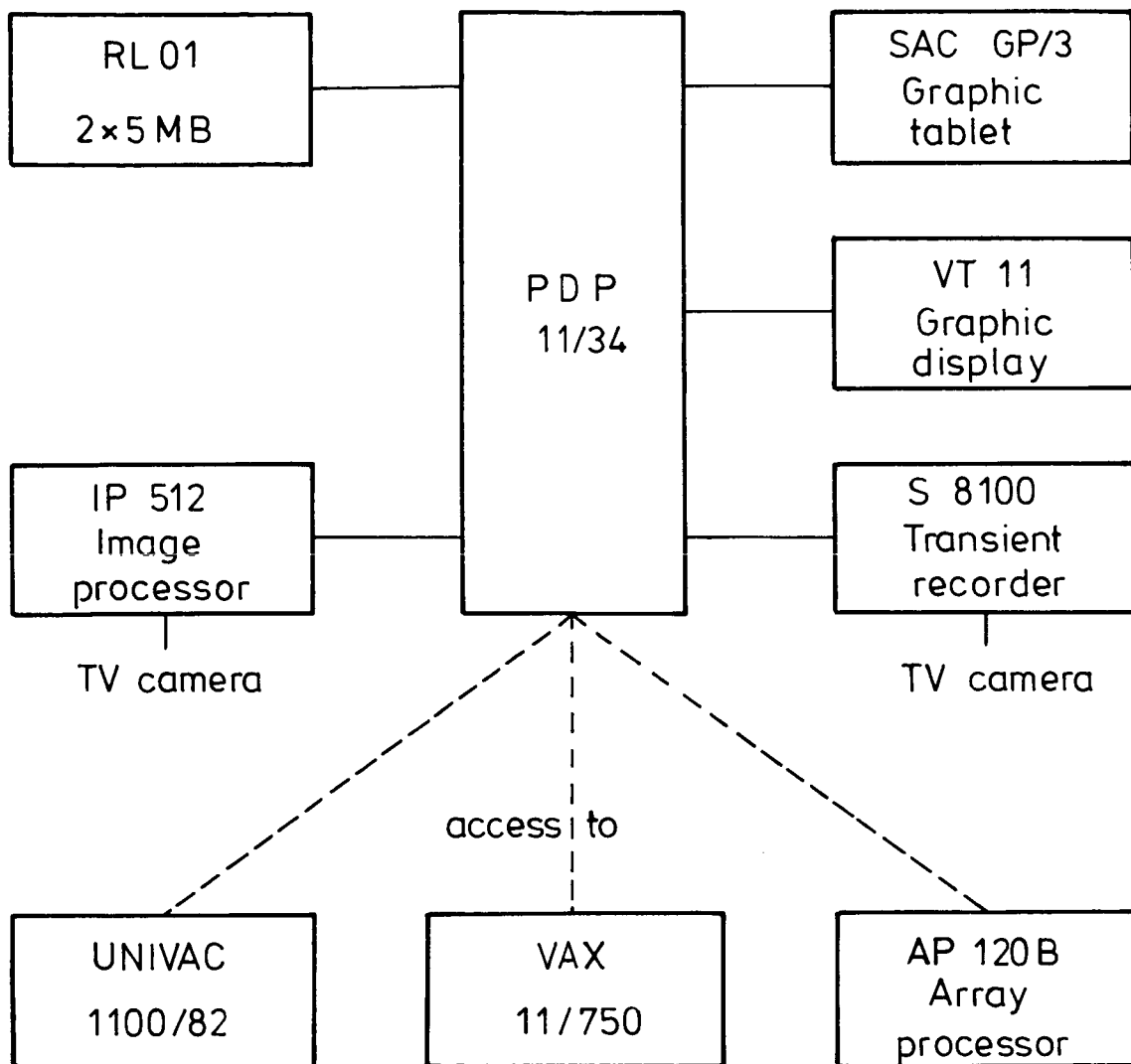
Figure 1
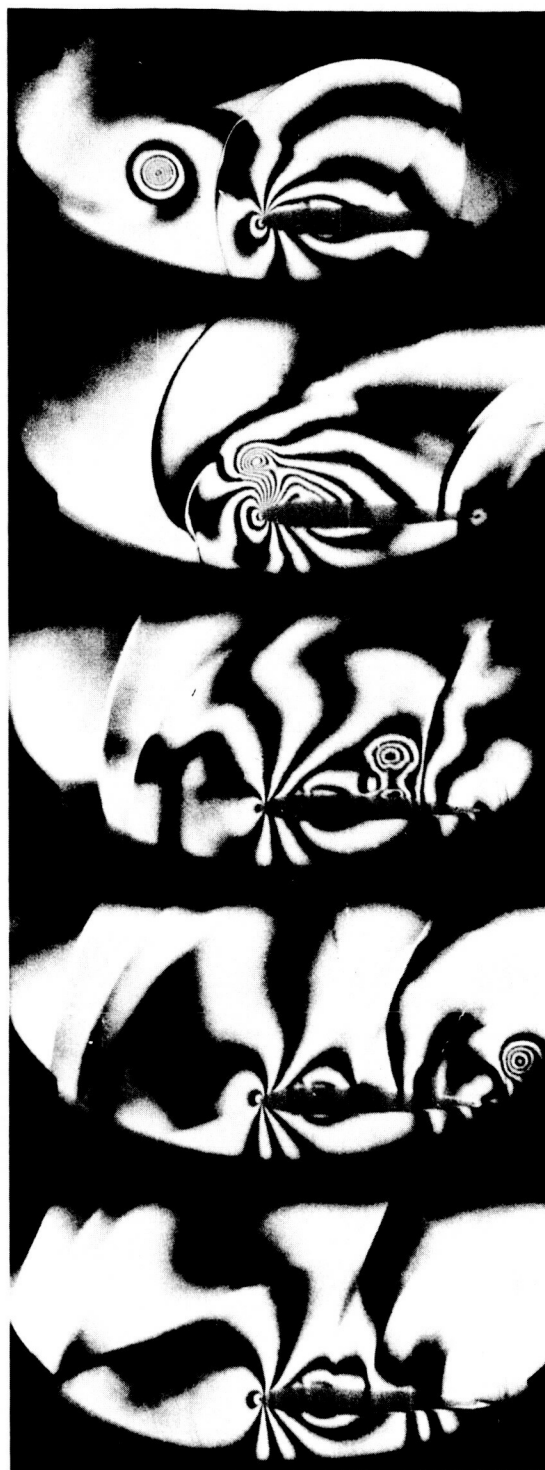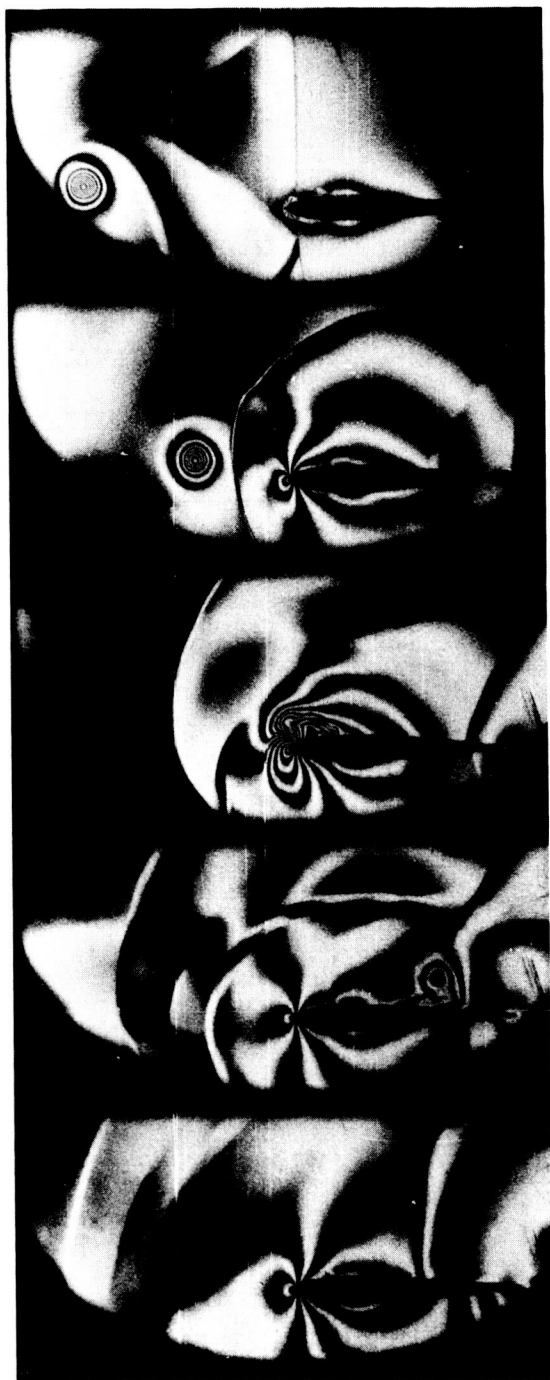
Figure 2

A NEW ART CODE FOR TOMOGRAPHIC INTERFEROMETRY

H. Tan and D. Modarress
Spectron Development Laboratories Inc.
3303 Harbor Blvd., Suite G-3
Costa Mesa, California 92626

ABSTRACT

A new ART code based on the iterative refinement method of least squares solution for tomographic reconstruction is presented. Accuracy and the convergence of the technique is evaluated through the application of numerically generated interferometric data. It was found that, in general, the accuracy of the results were superior to other reported techniques. The iterative method unconditionally converged to a solution for which the residual was minimum. The effects of increased input data error, limited total viewing angle, and reduced number of input data were studied. The inversion error was found to be only a function of the input data error. The convergence rate, on the other hand, was affected by all three parameters. Finally, the technique was applied to experimental data and results reported.

Key Words: Tomography, Interferometry, holography, image reconstruction

I. INTRODUCTION

During recent years, image reconstruction techniques have been successfully applied to several fields such as medicine, astronomy, electron microscopy, nuclear magnetic resonance, geophysics and optical interferometry. An extensive review can be found in Reference 1.

In 1964, prior to the development of optical holography the axially symmetric density field had been reconstructed by using the inversion of Abel's integral equation[2]. Under symmetry conditions the Radon transform reduces to the Abel equation. Since 1965, holographic interferometry has been applied to aerodynamics, heat transfer and combustion problems. These developments are discussed in detail by Vest[3].

There are several difficulties associated with the reconstruction of phase objects:

(a) No sharp boundaries can be defined for phase objects. The definition of the reconstruction region is based on a priori information about the flow field. In general, the contribution of the phase object outside the reconstruction zone is assumed to be negligible.

(b) Relatively large errors are present in the interferometry data. The optical path differences are recorded as interference fringes. The accuracy of the fringe data ordinarily may not be better than 1/2 of the fringe spacing. In

addition, for an unsymmetric density field, the number of
fringes for each projection varies for different view
angles resulting in a nonuniform data set. The ideal pro-
jection data is a set of non-overlapping, equally spaced,
parallel rays covering the whole reconstruction region.

(c)   Only the relative phase shift of the projection can be
        measured by the interferogram data. There is, therefore, a
        possibility of incorrect identification of fringe numbers.
        This results in a set of "slightly" inconsistent data.

The mathematical reconstruction method employed in such cases
should not be <u>overly sensitive</u> to the "noisy" or inconsistant data.
Although the Radon transformation

$$\ell(p,\theta) = \int\int_{-\infty}^{+\infty} n(x,y)\delta\big[p -x\cos(\theta)- y\sin(\theta)\big]dxdy \qquad (1)$$

provides a rigorous solution to the problem of reconstruction from
projections, the solution is uniquely determined only by an infinite set
of perfect projections. Here, ℓ is the optical path length, n is the
refractive index, δ is the Dirac delta function, θ is the projection
angle, p is the coordinate along the projection plane, and x and y are
the coordinates describing the reconstruction region. In practical
problems, the discrete nature of projection data and the unavoidable
measurement errors may result in the failure of reconstruction.

In this paper, the iterative refinement method of least squares solution for tomographic interferometry is discussed. A complete set of computer codes for density reconstruction from holographic interferograms was made. The effects of projection number, limited viewing angle and the measurement error on the reconstructed image are determined through numerical experimentation. The flow field around the tip region of a revolving helicopter rotor blade was reconstructed from 40 interferograms. The results of the reconstructed density field are presented.

II. ITERATIVE REFINEMENT METHOD OF LEAST SQUARE SOLUTION

In principle, the ART (algebraic reconstruction technique) algorithms are the schemes for solving a large system of linear equations. The reconstruction region is divided into a square grid (M = m x m cell) and the refractive index within each cell or pixel, n_{ij}, is assumed constant. The Radon transformation then reduces to a set of discrete linear equations

$$\sum_{i=1}^{m} \sum_{j=1}^{m} W_{ij}(p,\theta) \, n_{ij} = L(p,\theta) \tag{2}$$

where $W_{ij}(p,\theta)$ are weight factors determined from geometric relations. It should be noted that only those factors associated with pixels through which the projection ray passes are nonzero. For k different

DM-12/21

projection angles, each having n nonoverlapping and equally spaced parallel rays, the number of equations N, is given by $N = k \times n$.

Equation (2) can be written in the form

$$C \, X + L = 0 \qquad\qquad (3)$$

where, L and X are N and M dimensional vectors respectively, and C is the coefficient matrix with $N \times M$ elements. Equation (3) can be transformed into a symmetric, positive definite, NORMAL EQUATION given by

$$C^T L + C^T C X = 0 \qquad\qquad (4)$$

In practice, due to measurement errors and other inconsistencies, Equation (3) becomes

$$R = C \, X + L \qquad\qquad (5)$$

where R is the residual vector. An approximate solution is sought for which the Euclidean norm of the residual vector $\|R\|$ is minimum. The Euclidean norm is defined as $\|R\| = \sqrt{\sum_i R_i \cdot R_i^*}$. The solution of the normal equation gives the standard least square solution of (3).

Procedures for obtaining solutions to a large system of linear equations can be found in a number of different scientific areas. Iterative techniques have been widely used. It begins with an initial estimate and then it repeatedly modifies the estimate until some threshold condition is satisfied. There are different ways to modify the

estimate. The effectiveness of a method depends on the matrix character. Considering the features of matrix C (large and sparse) and relatively large measurement errors, the method of CONJUGATE GRADIANTS is found to be applicable for image reconstruction.[4]

The computer procedures of conjugate gradiant method are as follows:

Initial vector

$$k = 0: \quad X(0) = 0; \quad R(0) = L \tag{6}$$

For iterative number $k = 1, 2 ...$

$$r(k-1) = C^T R(k-1) \tag{7}$$

$$s(k) = - r(k-1) \text{ for } k = 1$$

$$s(k) = - r(k-1) + s(k-1)\|r(k-1)\|/\|r(k-2)\| \text{ for } k > 1 \tag{8}$$

$$q(k) = C\, s(k) \tag{9}$$

$$X(k) = X(k-1) + s(k)\|r(k-1)\|/\|q(k)\| \tag{10}$$

$$R(k) = R(k-1) + q(k)\|r(k-1)\|/\|q(k)\| \tag{11}$$

The matrix C has only five percent nonzero elements. It can be stored permanently or, in the case of limited storage capacity, may be computed according to a simple geometric relation for every ray. The vectors that must be stored are X, R, s, and q. Accordingly, a procedure written in PASCAL running under CPM-86 with MT+86 compiler has been written. This procedure runs on IBM PC microcomputer, and is limited to 20 x 20 mesh size.

DM-12/21

It can be proven[5] that: The norm of the residual vector R decreases with increasing iteration number. Thus, in principle, this code is a technique minimizing the residual R to the level determined by the inherent errors associated with the computer truncation and measurement data. Therefore, the final reconstruction accuracy is determined by data noise. Here the errors associated with the measurement of the optical path length (fringe lines) are the major attributor to the data noise.

To evaluate the characteristics of the developed tomography code, a numerically generated density field, Figure 1a, was used as the input for the numerical test. It represents the calculated air density distribution over the tip region of the rotor blade in a plane above the blade [6]. The distribution of the refractive index variance, $x = (n_o-n)$, is calculated and shown in Figure 1b. The data for the integral optical length difference as a function of ray parameters, θ and p, was generated from Equation (2). The errors associated with optical length measurement, encountered in real tomography, were artificially added to the fringe data file. Fringe round-off errors of ±0.5, ±0.05 and ±0.005 were used here. The reconstruction code was parametrically evaluated for different numbers of equations and total viewing angles. The numerical test matrix is shown in Table 1.

Figure 2 shows the reconstructed field for Case 1 after different iterations. The overall features are apparent after two iterations and further refinement of the solution is obtained with additional iterations. The total reconstructed error, R_r, is also noted on Figure 2. Here, the reconstruction error is defined as

DM-12/21

$$R_r = \sqrt{\sum_i \sum_j \left[x_{ij,in} - x_{ij,rec}\right]^2 / \sum_i \sum_j \left[x_{ij,in}\right]^2} \qquad (12)$$

where $x_{ij,in}$, and $x_{ij,rec}$ are input and reconstructed refractive index variances, respectively.

The dependence of the residual vector norm on the number of iterations for Cases 1 to 7 of Table 1 is shown on Figure 3. Figures 4, 5 and 6 demonstrate the effects of fringe number round-off error and view angle range on the reconstruction error. From these and other numerical experimentations, the following conclusion may be drawn:

- The convergence rate is increased as the projection ray number, N, is increased. The corresponding inversion error for a sufficient number of iterations is, in general, independent of N.

- The normal of the residual vector, R, in all cases, unconditionally converges to a limit which is a strong function of the input data error. The resulting error for the first few iterations is independent of the input data error. However, for more accurate input data, additional iterations result in more accurate results. This underlines the importance of the accuracy of the data set. It also proposes a guideline for determining the maximum number of iterations based on the rate of change of the residual.

DM-12/21

Finally, limited look angles, (>30°) do not have a significant effect on the convergence rate or the accuracy of the reconstructed data. Acceptable results were obtained for a total view angle of 30°. Care must be taken to ensure that sufficient information is recorded on the interferograms when the view angle limitations are imposed.

III. THE PROCEDURE FOR PROCESSING EXPERIMENTAL DATA

Figure 7 shows the holographic interferometry arrangement at the AVRADCOM Laboratory of NASA Ames for studying the flow around a revolving helicopter blade.[7] The coordinate system (x,y) is wing-fixed (x-spanwise, y-chordwise). The projection of point "A" on the wing defines the origin for coordinate p along any azimuthal angle. The photograph of a typical interferogram is shown in Figure 8.

Forty interferograms were digitized using a Tektronix 4112 display terminal and a graphic tablet. The data were reduced and a map of the optical path as a function of height above the blade was developed. Data at each elevation and for all viewing angles were grouped (Z-files), and constituted the input data for the reconstruction code.

The reconstructed density distribution, (ρ/ρ_o), produced by the tomographic reconstruction code is shown in Figures 9 & 10 for the heights z = 0.5, 1, 1.5 and 2 inches (chord C = 3 inches; the leading edge of the blade Y/C = -0.5; aspect ratio = 13.7). The optimum number of iterations was about 3 to 6 for the experimental data. The computation time on an IBM PC was approximately 3 minutes per iteration.

DM-12/21

IV. DISCUSSION

A new ART code based on the iterative refinement method of least square solution is developed for tomographic reconstruction of the three-dimensional density field. The features of the technique was investigated using numerically generated interferometry data. It is shown that, in general, the ART code used here, is capable of reconstructing phase objects using limited viewing angle or using data with relatively large errors.

In comparison to other reconstruction techniques, it is believed that it is possible to obtain more accurate results with the ART code.

For similar numerical tests, the reconstructed mean-square error for view angles of $\pm 90°$ and $\pm 40°$ were reported to be 6.7% and 11%, respectively, when the convolution back projections technique was used.[6] The corresponding values for R_r become 26% and 33%, respectively. Similar situations were examined in Cases 3 and 10 with R_r at only 3% and 10% for 20 iterations. On the other hand, the computation time for iterative techniques are generally higher than some other techniques.

An important feature of the technique is that with limited resolution (say, 20 x 20), it is possible to repeatedly use the same code and zoom into the regions surrounding important features of the flow, and hence, reconstruct the flow field in greater detail. For this, the input data for the subsequent analysis must be corrected.

Finally, a strong feature of the reconstruction code is its ability to accept data within limited view angles. The density field of the

numerically generated data was reconstructed for a total view angle of 30° and with a final error of 10%. This result is extremely important when the application of tomography to the flow field within a wind tunnel is considered.

ACKNOWLEDGEMENTS

REFERENCES

1. Deans, S. R., The Radon Transform and Some of its Applications, Chap.1, Wiley, New York (1983).

2. Barakat, R., J. Math and Phys., Cambridge Mass., 43,325 (1964).

3. Vest, C. M., Holographic Interferometry, Wiley, New York (1979).

4. Reid, J. K., Large Sparse Sets of Linear Equations, edited by J. K. Reid, Academic Press (1971).

5. Westlake, J. R., Handbook of Numerical Inversion and Solution of Linear Equations, Wiley, New York (1968).

6. Snyder, R. and Hesselink, L., Applied Optics, 23(20),3650 (1984).

7. Kittleson, J. K. and Yu, Y., AIAA 23rd Aerospace Sciences Meeting, Jan 14-17, Reno, Nevada (1985).

DM-12/21

TABLE 1.   THE NUMERICAL TEST MATRIX

CASE	FRINGE NUMBER ROUND OFF ERROR	VIEW ANGLE (degree)			NUMBER OF VIEWS	NUMBER OF POINTS PER VIEW
1	0.005	0	..	180	61	20
2	0.005	0	..	90	61	20
3	0.005	0	..	180	31	20
4	0.050	0	..	180	61	20
5	0.050	0	..	180	31	20
6	0.500	0	..	180	61	20
7	0.500	0	..	180	31	20
8	0.005	-75	..	75	31	20
9	0.005	-60	..	60	31	20
10	0.005	-45	..	45	31	20
11	0.005	-30	..	30	31	20
12	0.005	-15	..	15	31	20
13	0.050	-75	..	75	31	20
14	0.050	-60	..	60	31	20
15	0.050	-45	..	45	31	20
16	0.050	-30	..	30	31	20
17	0.050	-15	..	15	31	20

LIST OF FIGURES

Figure 1. Numerically generated density and refractive index distribution.

ITER   Rr

2   31%

8   11%

20   3%

40   0.6%

DM-12
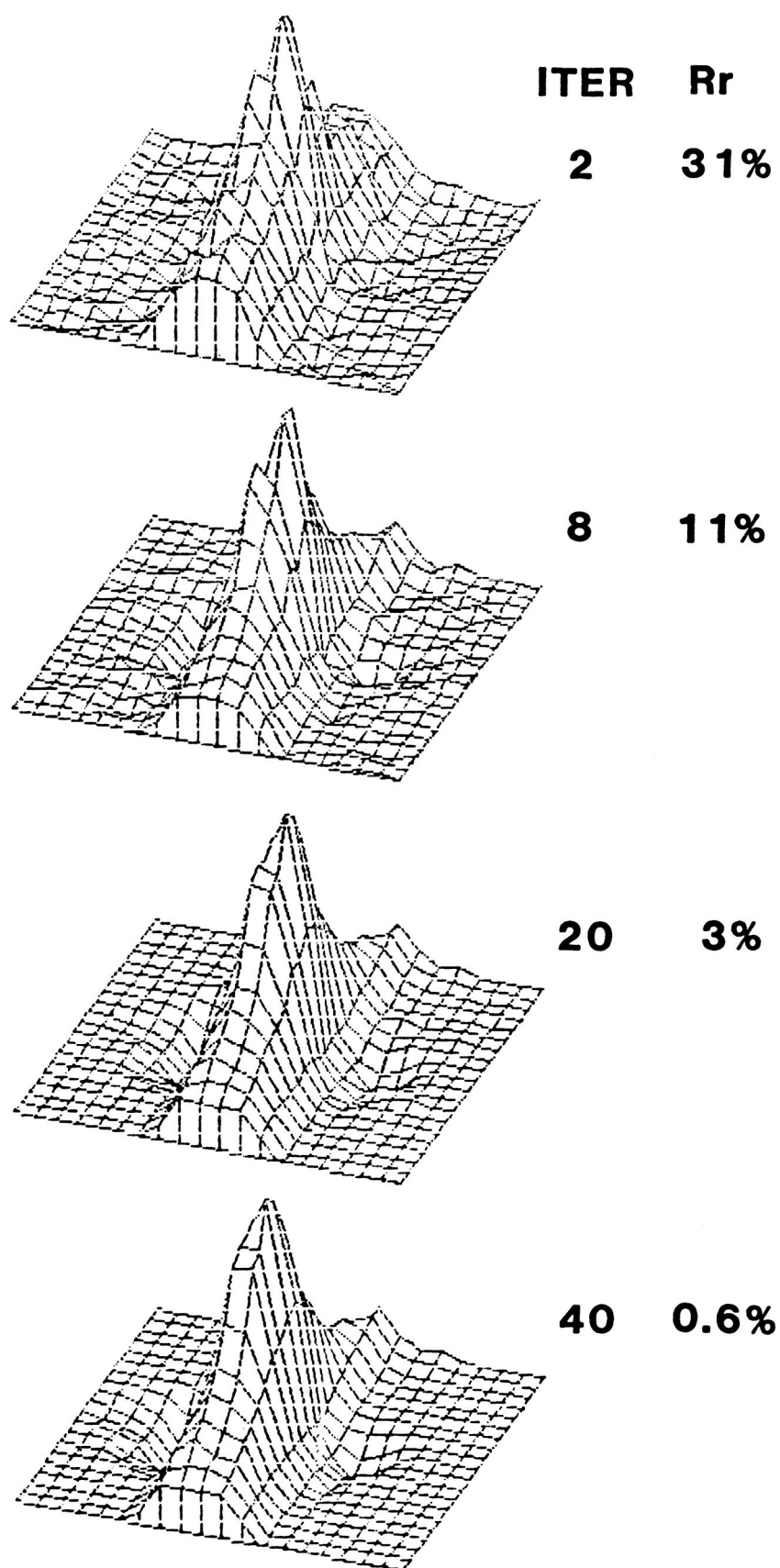
Figure 2.   Reconstructed field of refractive index variance (n_o-n) for Case 1.

451
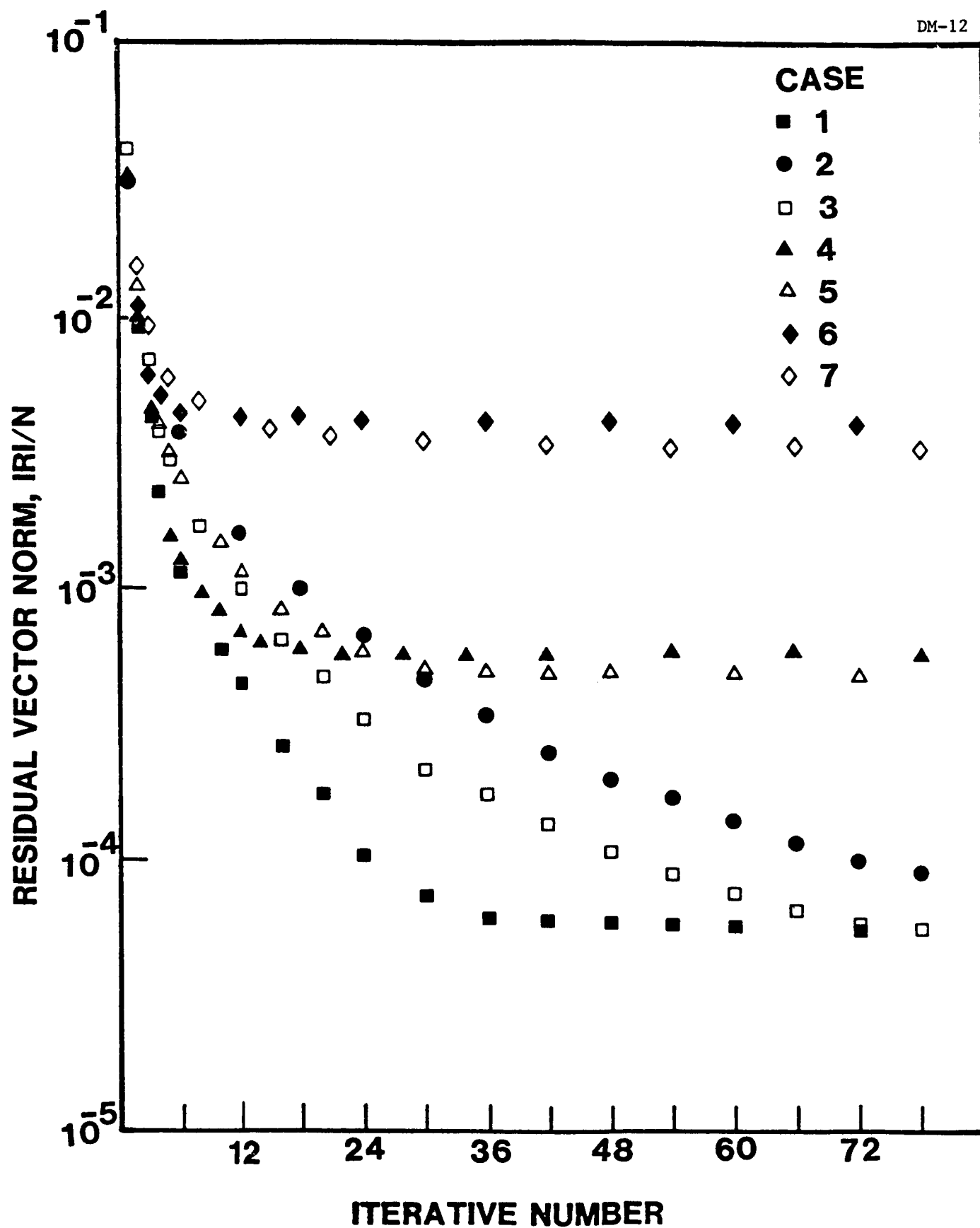
Figure 3. Residual vector norm vs. iterative number for Cases 1-7.
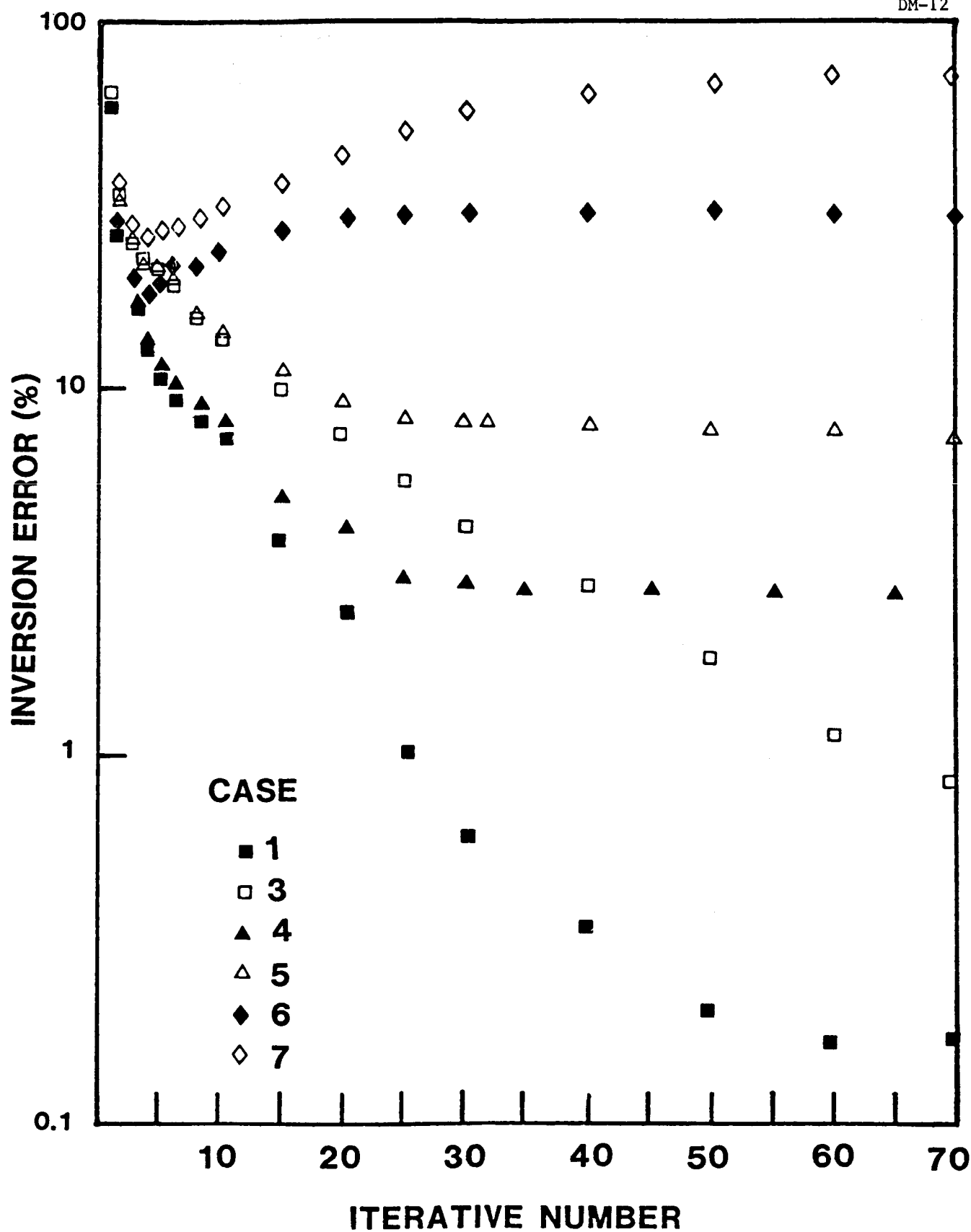
Figure 4. Inversion errors vs. iterative number for Cases 1-7.
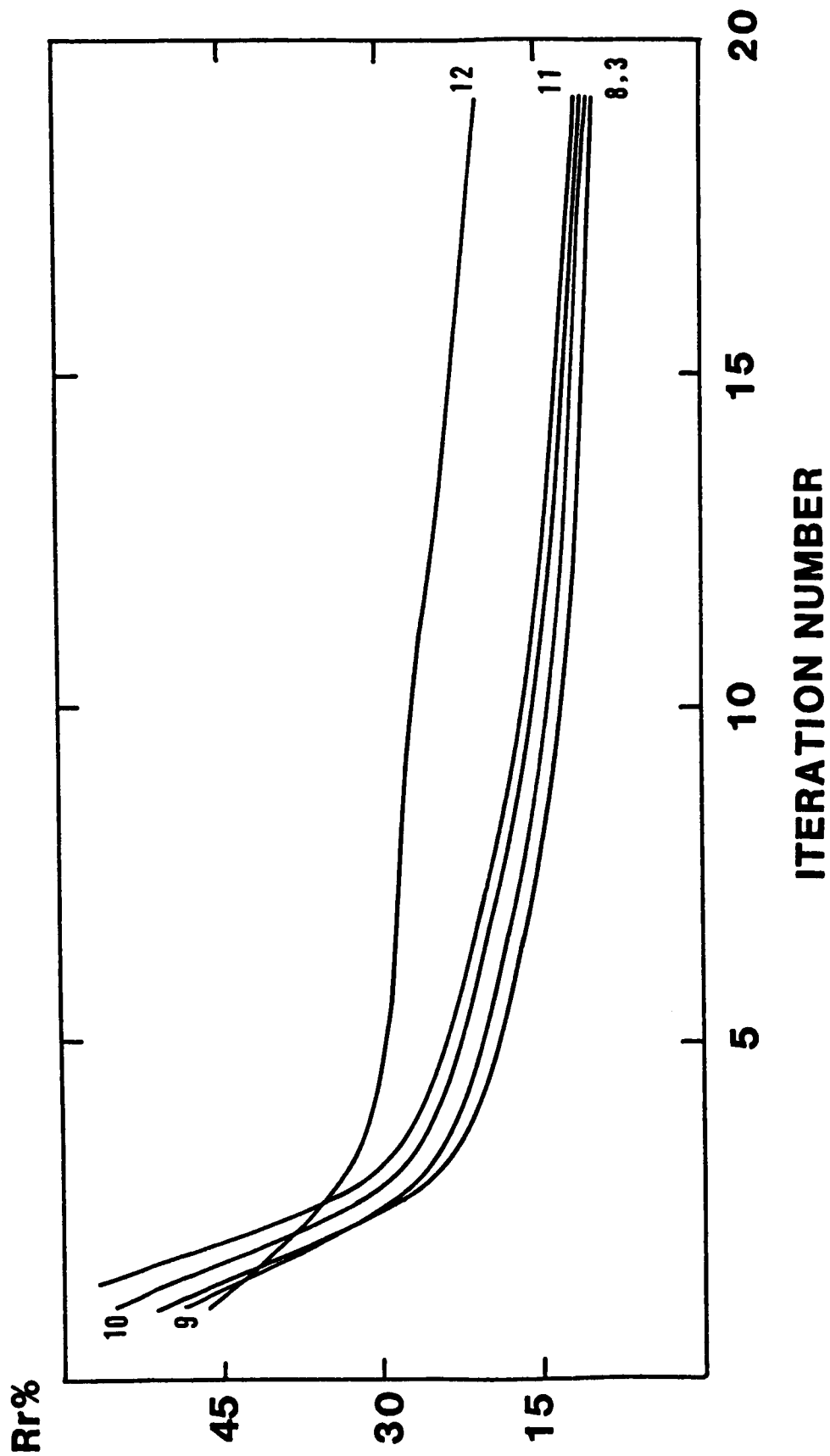
Figure 5. Inversion errors vs. iteration number for different view angles (fringe number round-off error = 0.005 λ).
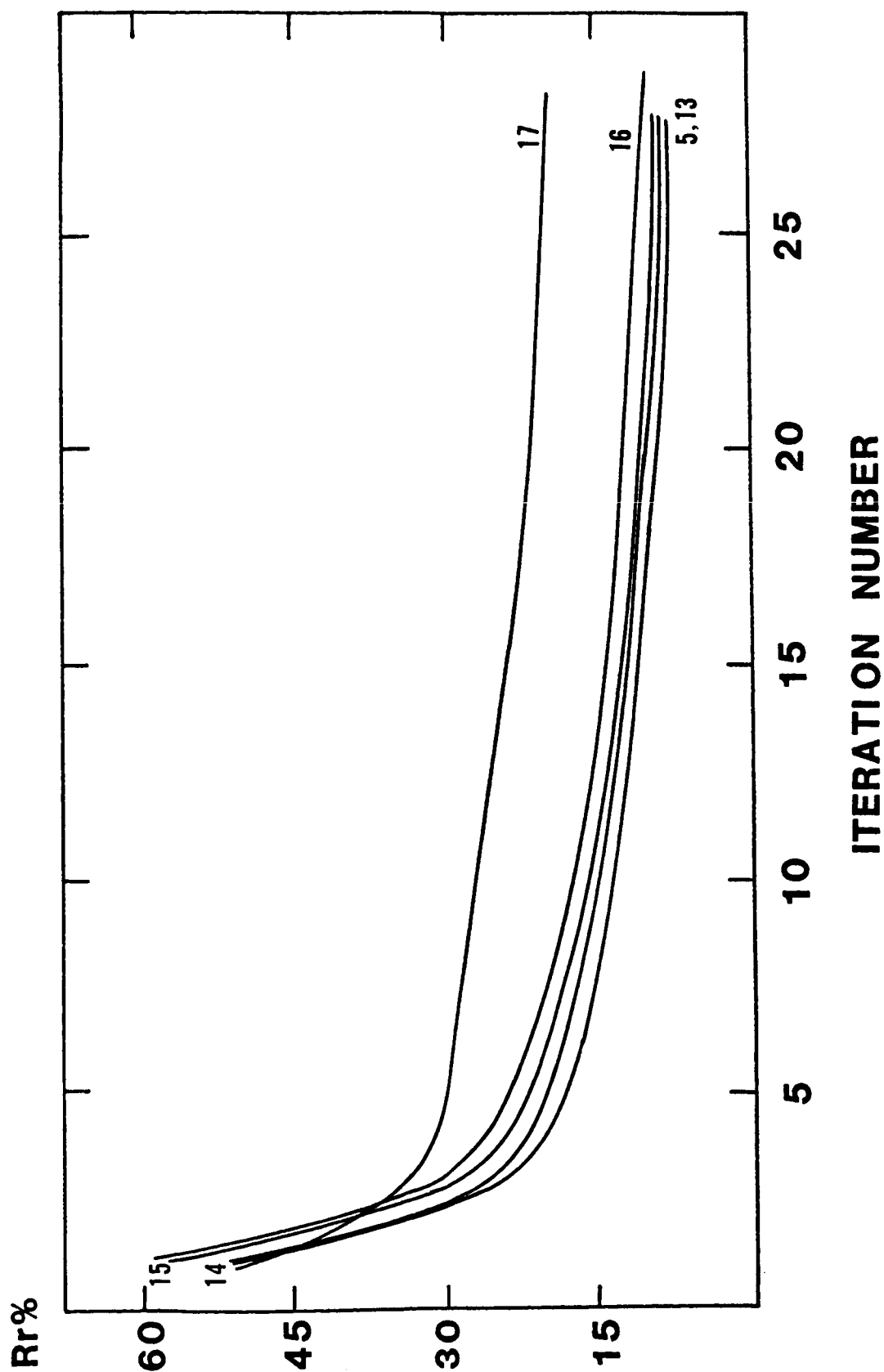
Figure 6. Inversion errors vs. iteration number for different view angles (fringe number round-off error = 0.05 λ).
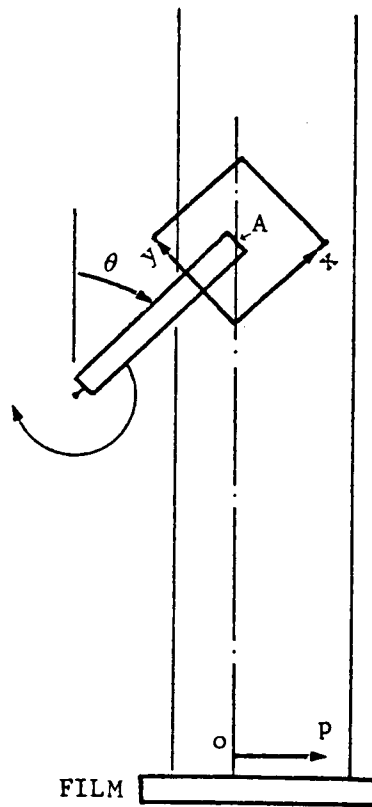
Figure 7.   Rotating blade tip region and the coordinates.
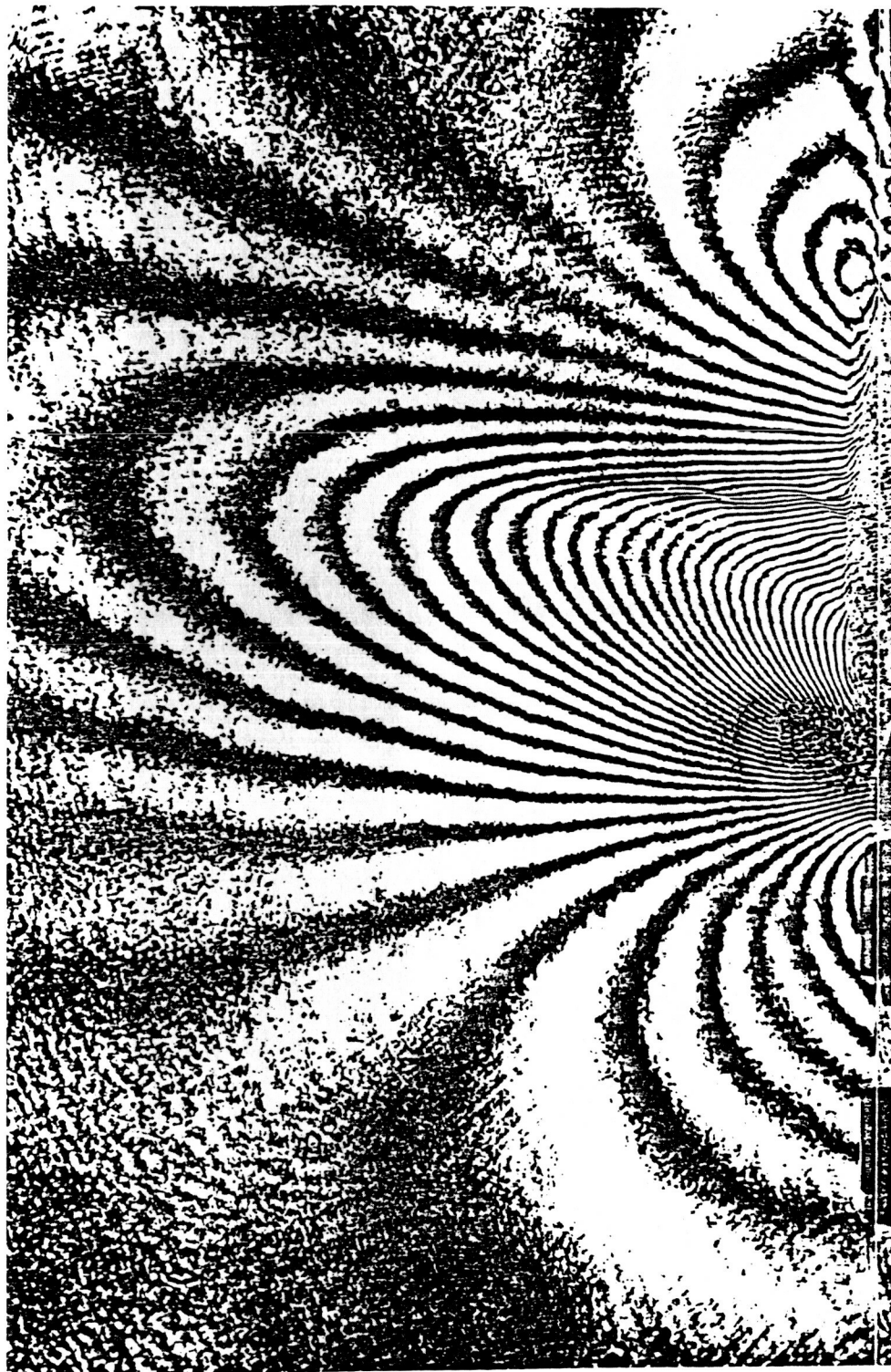
Figure 8. Interferogram of flow over a rotating blade, $\theta = 176.5°$.

z

2"

1.5"

1"

0.5"

T.E

ρ/ρ_o

L.E

y   x
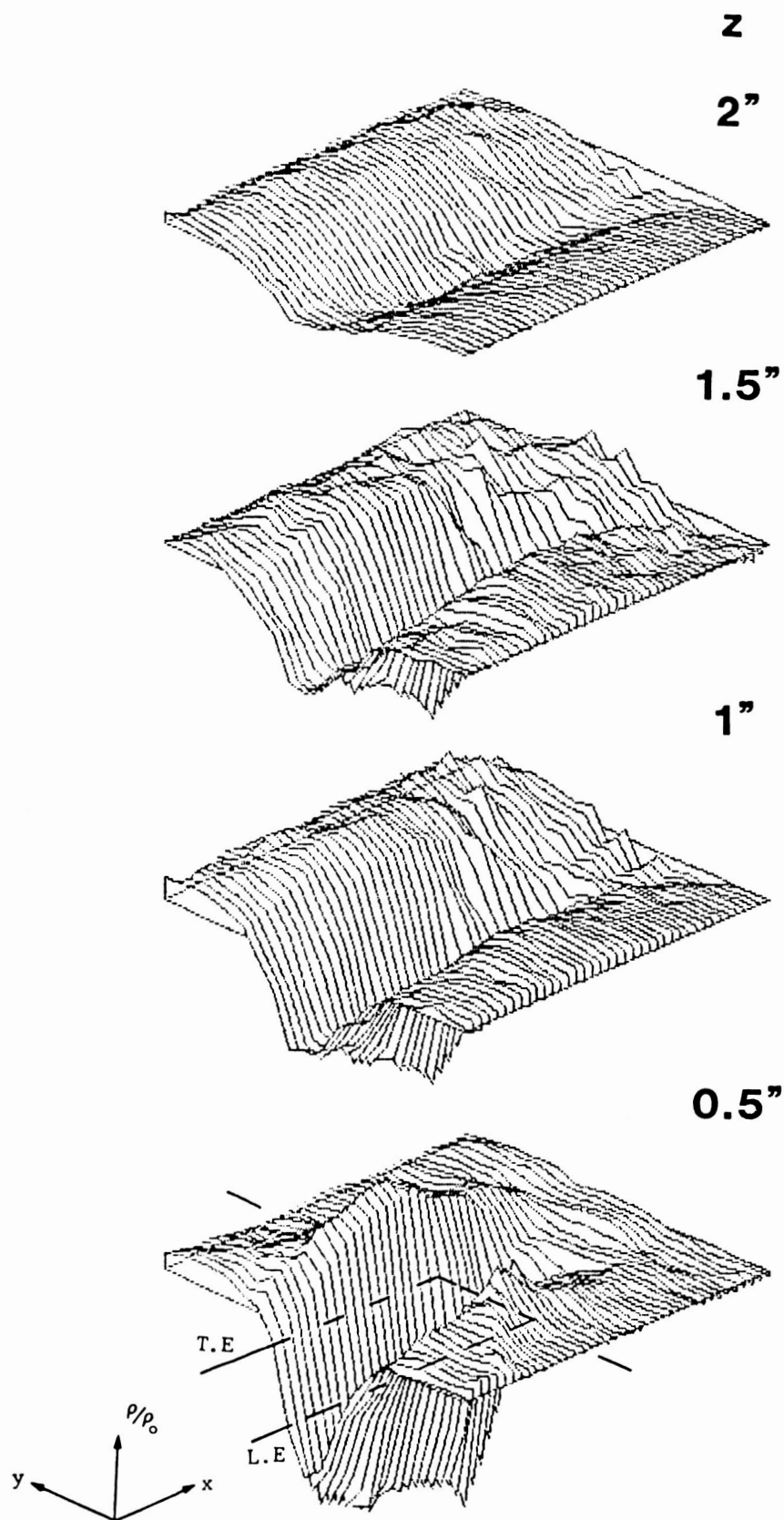
Figure 9.   Reconstructed density fields for different heights above
             blade chord line.
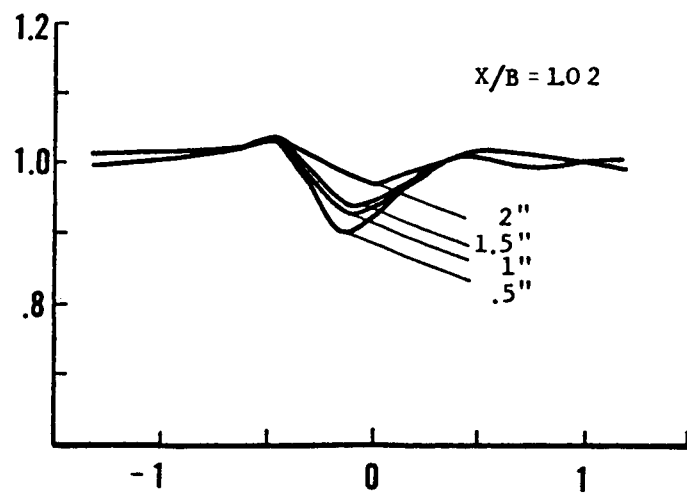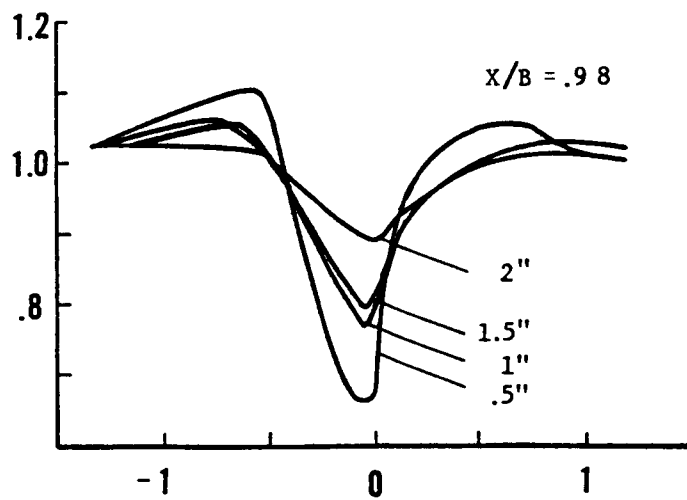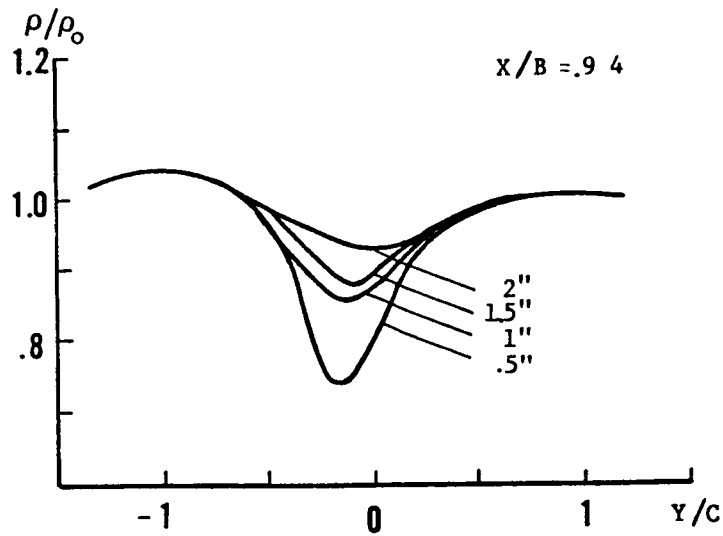
Figure 10. Density ratio profiles (blade length B = 41.1",
            chord length C = 3").

KC-135 AERO-OPTICAL TURBULENT BOUNDARY LAYER/SHEAR LAYER
EXPERIMENT REVISITED

DR. J. CRAIG

SPECTRON DEVELOPMENT LABORATORIES, INC.

3303 HARBOR BLVD., SUITE G-3

COSTA MESA, CALIFORNIA 92626

MAJOR C. ALLEN

ARD

AIR FORCE WEAPONS LABORATORY

KIRTLAND AFB, NEW MEXICO 87106

PRECEDING PAGE BLANK NOT FILMED

PAGE 460 INTENTIONALLY BLANK

ABSTRACT

This paper examines the aero-optical effects associated with propagating a laser beam through both an aircraft turbulent boundary layer and artificially generated shear layers. The data present comparisons from observed optical performance with those inferred from aerodynamic measurements of unsteady density and correlation lengths within the same random flow fields. Using optical instrumentation with tens of microsecond temporal resolution through a finite aperture, optical performance degradation was determined and contrasted with the infinite aperture time averaged aerodynamic measurement. In addition, the optical data were artificially clipped to compare to theoretical scaling calculations. Optical instrumentation consisted of a custom Q switched Nd:Yag double pulsed laser, and a holographic camera which recorded the random flow field in a double pass, double pulse mode. Aerodynamic parameters were measured using hot film anemometer probes and a five hole pressure probe. Each technique is described with its associated theoretical basis for comparison. The effects of finite aperture and spatial and temporal frequencies of the random flow are considered. The results presented represent five flights flown at altitudes from 1.8 km to 10.7 km and at Mach numbers from .32 to .79. Single pass phase deviations for the boundary layer were from .06 to .17 waves (at $\lambda = .53\mu m$) with piston and tilt components removed. Measured phase deviations for the artifically induced shear flows from .10 to .279 waves (at $\lambda = .53\mu m$) with piston and tilt components removed. However, when low order aberrations through coma were removed, the remaining

deviations were only .09 to .18 waves. This resulted in 33% to 250% increase in the Strehl ratio at 14 cm optical aperture. It was further shown that the low order aberrations corresponded to the longer wavelengths in the random flow and these waves propagated with a longer characteristic time than the higher order aberrations (200 to 1000 sec vs 50-100 sec or 1-5 khz vs 10-20 khz). Removing the low order spatial aberrations from the random flowfield up to a temporal frequency of 1 khz significantly improved optical propagation. In addition, the aerodynamic measurements could be correlated to the optical measurements to within 0.2 waves of tilt in the random flow, and aerodynamically measured correlation lengths matched the optical measurements when corrected for tilt and aperture scaling. Thus spatial optical performance parameters can be deduced from aerodynamic measurements.

INTRODUCTION

Previous modelling and experimentation have characterized turbulent wavefronts propagated through aircraft boundary and shear layers. The techniques for the most part employed averaging assumptions that yielded results tending to maximize the distortion of optical wavefronts. All such distortions spread the radiation preventing beam focus to its diffraction limited spot size. The resulting aberrations were assumed to be isotropic and uncorrectable causing severe degradation to airborne astronomical observations, radiation sensing images, and laser beam propagation from aircraft. Better definition in both time and space of the aberrations to the flow was required to ascertain whether the averaged results here-to-fore determined and the resultant pessimistic view for practical applications were the appropriate conclusions. With proper knowledge of the actual flow, corrective techniques, either to the flow or to a propagating beam through the flow, could be applied to partially improve the beam or image to a level where operationally the system application could meet feasibility requirements.

This full scale experiment expanded on previous wind tunnel and airborne experiments described in the first four references. The three purposes of the experiment were (1) to more accurately quantify the boundary layer and artifical shear layer effects on optical propagation; (2) to compare and correlate aerodynamic measurement techniques with an optical diagnostic measurement technique across a turbulent fluid flow; and (3) to compare experimentally collected optical data

with theoretical scaling relationship for varying optical apertures.

The data are similar in nature to data collected in 1978 and reported in reference 1. Specifically the aerodynamic data were repeated using thin films on a five prong rake continuously movable along a radial centered on the laser beam propagation path to collect temperature fluctuations. The rake was replaced with a five hole pressure probe to collect pressure and mean flow velocity completing the aerodynamic measurements.

The optical measurements considered the temporal as well as spatial correlation by collecting 10 nanosecond pulse duration double pulsed holographic images at 5 double pulses per second and varying spacings between pulses (27 µsec to 2 ms). The beam size was analyzed at 1 to 15 cm. Coupling new measurement techniques with improved computerized data reduction and more precise numerical integrations result in aerodynamic and optical measurement self consistency that are uniformly higher than in reference 1.

The experimental setup for the five flight measurement program is shown in figure 1. Altitudes ranged from 1.8 to 10.7 km while Mach numbers varied from .32 to .79. A porous fence was located 7, 76 and 228 cm forward of the centerline of the measurement port, depending on the flight. The struts that hold the return mirror wing in place have curvature for zero lift. Although not observed previously, it was found at the highest mach numbers that weak vertical shocks set up between the struts so as to add some experimentally induced figure to the optical results. Therefore the 5.8 km .57 Mach conditions were con-

FIGURE 1

KC-135 AERO-OPTICS FLIGHT TESTS

AIRCRAFT BOUNDARY LAYER OPTICAL CHARACTERIZATION
WITH DOUBLE PULSE HOLOGRAPHIC INTERFEROMETRY
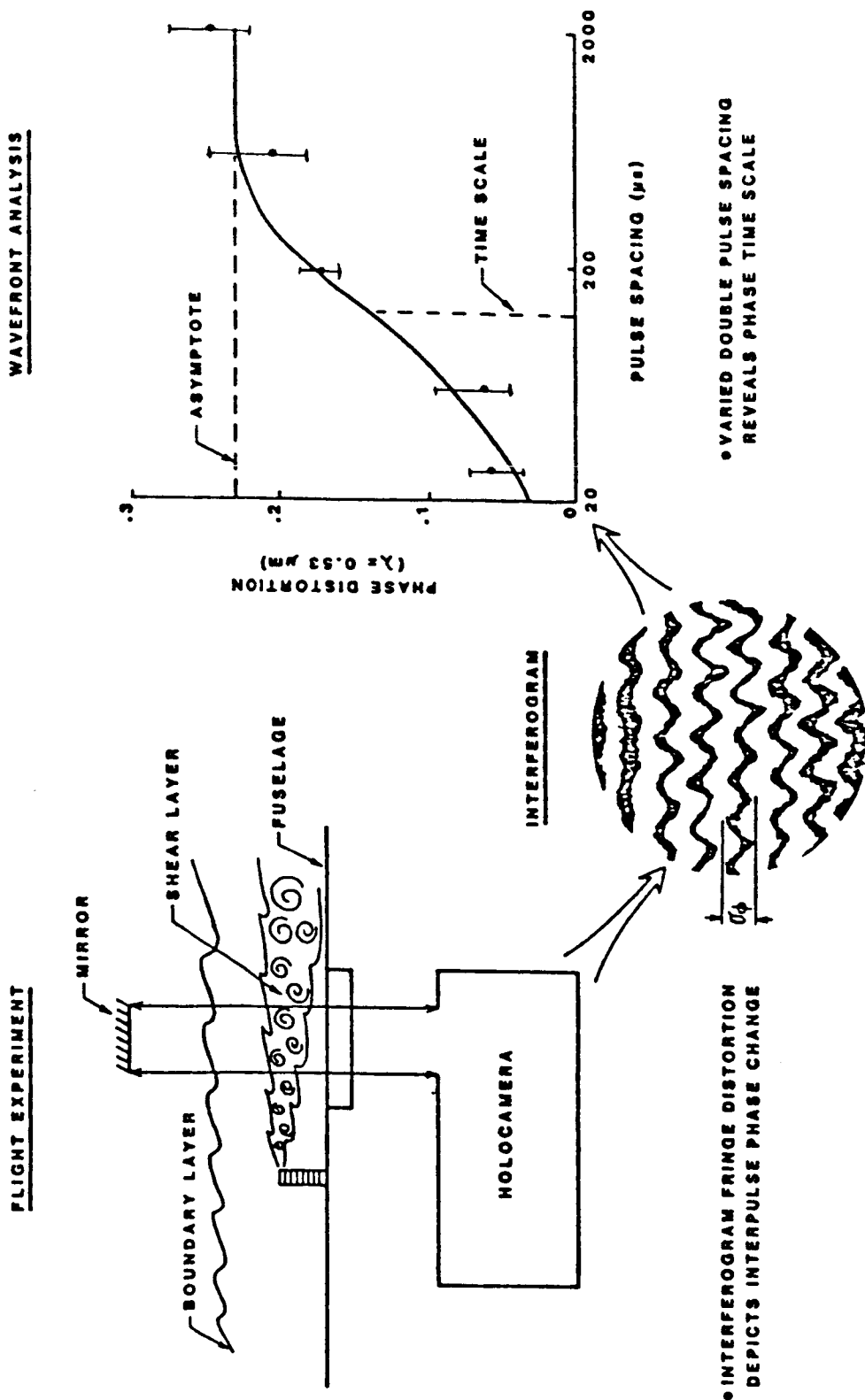
sidered as the baseline cases which excluded the shock perturbation. Although the qualititative average results remain unchanged, more precision and time sensitive data portend a significant decrease in aero-optical contribution to the system error budget with appropriate aeroflow corrective techniques. Further, data reduction improvements will allow significantly more data to be processed more accurately.

CONCLUSIONS

Four major conclusions from these test include the following: Aerodynamic phase variance averaged over time compares with the optical derived phase variance as corrected for infinite aperture to within the tilt compensation which is removed from the optical measurement. Comparing the optical measurement directly with clipped aerodynamic frequencies that relate to tilt, focus, astimatism and coma finds excellent agreement--.12λ versus .13λ . In addition the clipped aerodynamic data yield a correlation length that matches the optically derived length at 2 cm.

The aerodynamic measurements are time averaged along a central volume cylinder in front of the probe and thus time scales determined there cannot be substituted for optically measured timescales which relate the aeroflow as a nearly instantaneous phase screen.

Optical measurements at 15 cm aperture seem to infer that large spatial turbulent wavelengths propagate at slower flow velocities than shorter wavelength turbulence implying significant improvement in optical propagation could be attained with long wavelength relatively slow

compensation.

Finally the theory developed by Dr. Hogge in reference 5 is consistent with different clipped optical data.

Current measurement techniques are precise enough to quantify optical degradation due to aeroflows as a function of time. These data can be used to support (1) research in flow interogation and optical compensation, (2) design to alter the flow characteristics to remove or reduce the non-isotropic portion of the turbulence or (3) design of aeroflow modifiers to transfer isotropic turbulence to large scale turbulence and then couple that turbulence with low order optical corrective techniques. The results are possibly a key to successful use of optical systems on airborne platforms.

APPROACH

The aero-optics program involved several aspects; including instrumentation design and manufacture, development of data analysis procedures, flight test definition and conduct, and data reduction and interpretation. The instrumentation and data analysis procedures are discussed first, and the flight test is described in the remaining portion.

A double-pass holocamera was designed for installation at Station 1050 on an AF NKC-135. A customized frequency-doubled, Nd:YAG laser was used to record the double pulse holograms on 35mm film. The laser was designed and demonstrated to meet USAF airworthiness requirements. A mirror dithering system operating in a phase locked servo control

mode was used in the holocamera reference beam. This subsystem pro-
vided about 20 fringes of tilt on the interferogram either along the
flow or normal to flow direction. An essentially automatic laser/
holocamera control system was designed to provide high confidence and
quality data acquisition. A typical double-pulse, hologram record con-
sisted of about 100 double exposures with finite fringe. The double
pulse measurement removes most system induced errors due to return
mirror vibration and other vibration sources. A residual of one to
three waves tilt above the induced tilt remain therefore the measure-
ments must exclude tilt in the data processing. The double-pulse
holographic interferograms were photographed in a ground laboratory,
and the finite fringe interferograms were digitized on a new system
developed by the Fringe Reduction Facility, FRF, at AFWL. The fringe
detection system provided the ability to obtain quantitative phase sta-
tistics for turbulent flows. A time-differential interferogram analy-
sis was developed to relate the double pulse interferogram data to the
anemometer derived phase data.

The flight tests were designed to provide a comparison of the ane-
mometer and optical diagnostic systems. This comparison was based on
averaged statistically significant data which turned out to be for the
optical data 15 samples per pulse spacing. An essential aspect of the
experiment design was the generation of a flow object or flow field
which could be appropriately sampled through the holocamera optical
aperture. To obtain adequate spatial sampling, a flow field structure
with small length scales was required. The MID FENCE (76 cm) position

was identified as most appropriate. The flow length scales in the ambient boundary layer are quite large at the aircraft measurement station; however, the porous fence disrupts the ambient boundary layer flow along the fuselage. Immediately downstream of the fence (NEAR FENCE at 8 cm), the flow field is composed of a shear layer at the other edge of the fence separating the low speed flow through the fence and the high speed boundary layer flow over the fence. The composite aspects of this flow region make it less desirable for optical comparison. However, further downstream the shear layer has entrained or consumed most of the extraneous turbulence, and this position (MID FENCE) is selected as the primary flow object for data comparison. The optical data here samples up to 75% of the spatial frequencies. In addition, since the flow has not quite reattached at this point, the shear layer turbulence structure is nearly isotropic, particularly in comparison to bounded turbulent flows. At the final fence position (FAR FENCE) (228 cm), the reattaching shear layer has grown considerably in thickness and optical distorting power. A complete double-pulse hologram data set was acquired for three fence positions and through the ambient boundary layer at four flight conditions. The interferograms recorded for increasingly longer pulse spacing revealed stronger fringe distortions as was expected. The ambient boundary layer (NO FENCE) was observed to be the weakest phase distorting object, and with the fence installed, the distortion was observed to increase with distance from the fence. The growth rate of the distortion with distance is increased at higher Mach number.

Double-Pulsed Nd:YAG Laser

A Molectron Corporation Model MY-30 frequency doubled Nd:YAG laser as supplied was intended for laboratory use and consisted of a Nd:YAG oscillator and amplifier and KDP frequency doubler. The unit was designed for operation on 208 volt, 60 cycle AC three phase prime power, and utilized a tap water cooled heat exchanger.

A careful characterization of the laser prior to modification demonstrated that the unit was capable of about 200 mJ/pulse operation at 0.532 μm at 10 Hz, with a coherence length of approximately 1 cm (linewidth of $0.1cm^{-1}$). No double pulse capability existed in the factory unit.

Extensive modifications of the laboratory unit included pulse forming networks, double pulsing electronics, flashlamp simmer circuits, and pockels cell trigger circuits. Airborne power supplies were specified and purchased for operation at 120 VAC 400 cycle three phase aircraft power and 28 VDC.

An environmental housing for the laser optical system was designed and fabricated. Extensive mechanical modifications were incorporated to meet a U. S. Air Force 9g forward load crash requirement. Modifications of the laser output optical path were incorporated to meet aircraft configuration requirements. Vibration testing included an operational demonstration after two cycle of a 2g, 5-500 Hz shake. The laser optical unit was cycled over a ΔT of 40° F and post-test operation was demonstrated.

A freon to water airborne cooler and control system was designed

and incorporated into the NKC-135 aircraft environmental control system.

Double-Pass Holocamera

A custom holographic camera was designed and fabricated for the aero-optics experiment. The optical system consists of an object beam and reference beam. The object beam is expanded to 16 cm diameter and is projected (through an optical port) out of the aircraft through the shear layer to a return mirror mounted on an airfoil wing, thus double passing the flow. The reference beam is pathmatched to the object beam to within .5 cm. A two-axis dither mirror control system is contained in the reference beam to place reference tilt fringes on the resulting holographic interferograms.

The entire optical system is housed in a structure to make the camera light-tight, keep the optical system clean, and meet USAF airworthiness requirements. Access to the holocamera for adjustment in flight is facilitated by twelve hatches which are integral to the top cover.

Features of the camera include:

35mm roll film operation

automatic film writing (frame number) via LED film printer

automatic monitoring of object and reference beam energy and ratio

automatic X and Y dither mirror control via phase locked servo controlled loop

temperature monitoring at three points

vibration monitoring (via accelerometers) at two points

interchangeable 4 x 5 glass plates with 35mm roll film to
obtain single-pulsed holograms

transceiver optical design for object beam utilizing common
path optics

apertures and light baffles to minimize stray radiation and
outside aircraft ambient light

monitoring of aircraft fuselage expansion for various flight
conditions

reference beam remote pathmatch adjustment to compensate
fuselage growth

mechanical design capable of withstanding 9g forward crash
load

airworthy wiring and electronic components

Holographic Reconstruction

After developing, the flight hologram film reels were inserted in
a custom film transport within the reconstruction system. The
reconstruction beam was obtained from a spatially filter HeNe laser.
The holocamera reference beam divergence was reproduced in the

reconstruction system. The reconstructed object beams which constitute the interferogram are spatially filtered to increase fringe contrast. The interferogram aperture is focused on the camera film plane. The aperture is the large lens in the object beam telescope. The interferograms were photographed on Tech Pan film and developed with HCL110F. The film and the developing process were selected to achieve moderate fringe contrast and sufficient exposure dynamic range. Sufficient dynamic range is required to record interferogram intensity variation across the aperture.

Aerodynamic Procedure

Turning now to the aerodynamic procedure. A movable five fingered thin film temperature rake or five-hole pressure probe was inserted into the artificial shear layer along the centerline of the optical measurement. Obtained from this data through the differential form of the equation of state was the density variation of the flow and mean velocity and pressure data. The thin film temperature data was recorded in the FM mode with the films configured to record from 0 to 100 Khz. The pressure probe recorded ambient and total steady state pressure over about 10 second spans. This data, when properly correlated with velocity data, yielded the time averaged density variation and correlation lengths along the centerline and thus a time averaged phase variance. Assuming homogeneity across the flow an infinite aperture Strehl ratio was derived which is a measure of the intensity dispersion caused by the flow. This is the worst case Strehl assuming no temporal or spatial correction and isotropic turbulence.

Fringe Detection and Wavefront Analysis

The interferogram fringe detection and wavefront analysis was performed by the Fringe Reduction Facility at AFWL. The primary data reduction was performed on a set of eighteen interferograms (nine with flow direction fringes and nine with normal to flow direction fringes) for each of 80 test conditions (flight condition [4], model installation [4], and pulse space [5]).

The fringe detection camera was configured with a film transport which could be rotated about the optical axis. The image was detected by scanning a linear photodiode across the image. The film transport was oriented such that the nominal fringe direction was normal to the photodiode array or parallel to the scanned direction. Fringes were numbered from zero to N across the aperture. The maximum fringe number was typically 20, except for the short pulse spacing, 27 μs, for which six or eight fringes were introduced.

The fringe detection system was designed to trace the fringe edges of a few fringes in each scan across the aperture. In the instances where fringe edges were lost in noise, the system would mark the point and continue until the noise dropped and the fringe edge detection was regained. After all identified fringe coordinates had been detected by automatic means, the operator would assist the patching of drop-out regions.

The fringe detection scheme locates fringe center coordinates across the interferogram. After averaging across several ($\sim$10 scan), average fringe centers were connected by the computer into the fringes

along the scan. When the computer could not connect the fringe center, it appealed to human intervention. The phase is constant along fringes and increases by one wave from one fringe to the next fringe. The phase map, as originally detected, is a high frequency random distortion imposed on a highly tilted wavefront (i.e., $\simeq$ 20 waves).

Since the wavefront phase is known only along fringe centers, the nonuniform phase map is interpolated onto a uniformly spaced grid. The grid interval was 128 x 128 or about 0.1 cm spacing in each direction over 15. cm aperture which is ample accuracy to resolve low order Zernike times. Zernike polynomials are orthogonal polynomials that define optical aberration over a phase front (e.g., tilt, focus, coma).

The first step in the wavefront analysis is to determine the Zernike polynomials components of the interferogram and the residual variance using a least square fit of the data for a selected order of fit. This analyses used piston and tilt removed and the residual variance denoted, σ^2_{0-2} and piston tilt focus astimatism and coma removal with residual variance denoted σ^2_{0-8}. So experimental error in tilt was removed first and the low order optical terms were determined to 10% accuracy.

Time Differential Interferogram Analysis

The fringe distortion recorded on the double-pulse holographic interferograms represents a time-differential phase, $\Delta\phi$, or

$$\Delta\phi(x,t) = \phi(x,t) - \phi(x,t-t') \tag{1}$$

where t' is the laser pulse spacing. A correlation analysis is developed in Ref. 2 in which Equation 1 is expanded to provide a relation between the differential, $\Delta\phi$, and absolute, ϕ, phase correlation functions. Specifically, the two point, $\tilde{x}_1$ and $\tilde{x}_2$, spatial correlation function derived from the interferograms is shown to be

$$R\Delta\phi\,(\tilde{x}_1,\tilde{x}_2) = 2\,(R\phi(\tilde{x}_1,\tilde{x}_2) - R\phi(\tilde{x}_1,\tilde{x}_2,\,t')) \tag{2}$$

where $\tilde{x}_1$ and $\tilde{x}_2$ are the cross aperture coordinates at which the phase correlation is being computed. The RHS of Equation 2 is twice the difference of the spatial and space-time phase correlation functions, where the time delay in the space-time correlation is equal to the double-pulse spacing. The major result is obtained from Equation 2 by equating $\tilde{x}_1$ and $\tilde{x}_2$ and letting the pulse spacing become sufficiently long that the space-time correlation function is zero. The differential phase variance, $\sigma^2\Delta\phi$, is twice the conventional variance, or

$$\sigma^2\Delta\phi = 2\sigma^2\phi \tag{3}$$

These temporal phase variances are equivalent to spatial variances for homogeneous phase statistics. Hence, the desired result is that the temporal variance equivalent to that derived from anemometer data is obtained by ensemble averaging the spatially derived differential phase variance, or

$$\sigma^2\phi = \frac{1}{2}\left\langle\sigma^2\Delta\phi\right\rangle\Big|_{t'\,\to\,\infty} \tag{4}$$

The temporal phase statistics are obtained from the double pulse holograms recorded at shorter pulse spacing. Equation 2 is evaluated at zero spatial offset, $\tilde{x}_1 = \tilde{x}_2$, and the temporal phase correlation function, R (t), is obtained from the shorter pulse spacing interferograms, or

$$R\phi(t) = \frac{1}{2}\left(\langle \sigma^2 \Delta\phi \rangle\Big|_{t' = \to \infty} - \langle \sigma^2 \Delta\phi \rangle\Big|_{t' = t}\right) \tag{5}$$

The RHS of Equation 5 is the difference between the ensemble average of the long pulse spacing variance (i.e., Eqn. 4) and a shorter pulse spacing, $t' = t$, variance. The form of the correlation function has been assumed exponential in the data reduction, i.e.,

$$R\phi(t) = \sigma^2 \phi_0 e^{-t/t_0} \tag{6}$$

where the variance, $\sigma^2 \phi_0$, and the time scale, t_0, are the fit parameters obtained by least squares analysis or

$$\sigma^2 = \sigma^2 \phi_0 (1 - e^{-t/t_0}) \tag{7}$$

After examining the statistics of a single data set in great detail, the number of interferograms required for ensemble averaging at each pulse spacing was selected to be 18 or 90 over the 5 time spacings. From optical theory, the phase variance can be decomposed into a series of orthogonal Zernike coefficients.

$$\sigma^2 = \sum_{i=0}^{N} a_i P_i \tag{8}$$

By application of the theory of superposition equation (7) applies to the Zernikes

$$P^2{}_i = P2_{i_{\phi_0}} (1 - e^{-t/t_{oi}}) \tag{9}$$

where each Zernike term has its own time constant. This implies that low order Zernike may respond differently in time than higher order terms.

Flight Test

Six flights were flown from Kirtland AFB and data was taken over White Sands Missile Range, New Mexico, on an Air Force NKC-135 aircraft in the spring of 1984. For each flight, the fence was mounted in a single position and data were acquired at four flight conditions. The fence positions were 8.0, 76., and 38, cm upstream of the measurement station, and for one flight, the fence was not installed. The flight conditions were selected to produce an altitude/Mach number variation at constant Reynolds number (unit Reynolds number = 6.0×10^6/M or running length Reynolds number = $175. \times 10^6$. The fence positions were selected to produce desired flow configuration at the measurement station.

One complete data record was obtained at each flight condition. A data record consisted of a 100 hologram set at each pulse spacing with 45 frames taken in vertical and horizontal fringe orientations, and the remaining ten with infinite fringe spacing. Pulse spacing from 27 μs to 2.0 ms, were obtained.

Data were recorded in eight-minute, steady level flight legs within the controlled airspace.

Data Reduction

The primary optical data reduction approach has been the determination of phase correlation functions. The temporal dependence is obtained by least squares analysis of the time-differential interferograms, and the spatial dependence is obtained by ensemble averaging the products of spatially shifted wavefronts. These analyses result in a phase variance, time scale and length scale.

For large aperture sampling, the resulting phase variance is equivalent to that derived from the anemometer diagnostics. Further, to ascertain the dependence on sampling aperture, the temporal correlation functions are obtained for partial aperture regions. Finally, to obtain the temporal behavior of various low spatial order terms (i.e., focus, astigmatism, and coma), the temporal variance of several low order Zernike coefficients has been obtained for a set of time-differential interferograms. The least squares analysis applied to these Zernike data sets results in, for example, a focus amplitude and time scale.

Time Dependent Phase Correlations

The spatial phase variance samples obtained from time-differential interferograms are obtained by the fringe detection and wavefront analysis techniques described earlier. Actually, the residual variance is

provided after removing piston and tilt components (i.e., $\sigma^2{}_{0-2}$) and after removing Zernike coefficients through a coma aberration (i.e., $\sigma^2{}_{0-8}$). Ninety samples are used in the least squares analysis to obtain the phase variance and time scale (i.e., Equation 6) of the exponential correlation function. The least squares analysis provides the best fit to the following equation:

$$\frac{\sigma^2 \Delta\phi(t')}{8} = \sigma^2 \phi(t') = \sigma^2 \phi_0 (1 - e^{-t'/t_0})$$

where the factor of 8 represents the double pass factor of 4 and the double pulse factor of 2.

The least squares data fit to σ_{0-2} and σ_{0-8} data sets for the 5.8 Km/0.57M MID FENCE position are shown in Figures 2a and 2b. Eighteen data points are plotted at each pulse spacing, and the resultant fit is plotted. For the $\sigma^2{}_{0-2}$, the asymptote is 0.21 waves and the time scale is 192 µs; whereas after removing low order spatial terms (through eighth order Zernike), the asymptote variance is reduced to 0.14 waves with a time scale of 90 µs. The 30 percent reduction in phase variance produces a sizable improvement in Strehl ratio (i.e., from 0.17 to 0.48, respectively, if the exponential relation is assumed valid). For this case, the Strehl ratio improves a factor of three with the removal of correction of low order distortion. The averaged time scale for σ_{0-2} (192 µs) is noted to be significantly larger than the σ_{0-8} value (90 µs). This is because the lower Zernikes propagated slower than the higher order values. Removing the lower Zernike leave

FIGURE 2a   Tilt Removed Least Squares Analysis

5.8 km MID FENCE (0-2) SIG = .210 TAU = 192
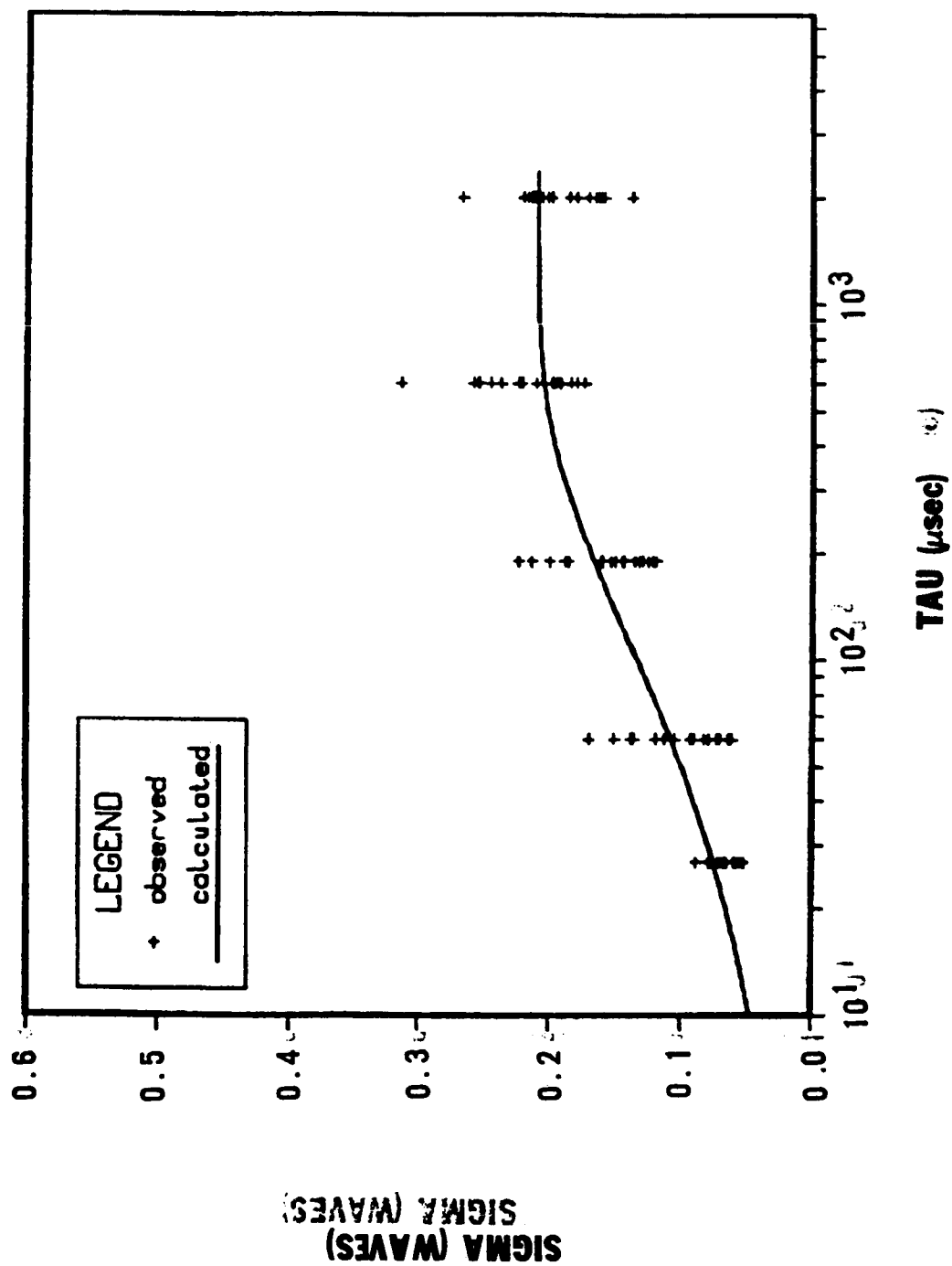
an average time scale that is lower than before. Applying Equation 8 can determine the actual correction frequency for each Zernike term necessary to obtain the average values obtained from the fit.

The entire flight test matrix and the ground calibration data are shown in Table 1. The ground calibration data reveal a noise level of about $\lambda/20$ to $\lambda/30$ for σ_{0-2} and σ_{0-8} data sets. The calibration data reveal no pulse spacing dependence. Strehl improvement of between 30% and 250% at 14 cm aperture was seen, the average time scale is consistently less for the coma removed data indicating short wavelength aberrations appear to move faster than longer wavelengths. The signal-to-noise ratio is poorest at low altitude/Mach number with the boundary layer flow object, and is best for all of the higher altitude/Mach number conditions for the FAR FENCE flow object. As a result of low signal-to-noise for the 1.8 and 5.8 Km boundary layer data, the time scales are judged not applicable.

Space Dependent Phase Correlations

The dependence of the phase correlation on the spatial offset is obtained for a single flight condition, as the computation requires handling of eighteen phase maps each containing 10^4 grid points. The phase spatial resolution is 128 x 128 grid points, or 0.1 cm in the 15 cm aperture. The phase correlation in space is derived from ensemble averages of the product of spatially shifted wavefronts, or

$$R_\phi(x',y') = \frac{\phi(x,y)\ \phi(x-x',y'y')}{<\phi(x,y)^2>}$$

TABLE 1

HOLOGRAPHIC RESULTS

σ, τ, STREHL (WAVES, μSEC, RATIO)

$$\begin{pmatrix} \text{PISTON - TILT REMOVED} \\ \text{PISTON THROUGH COMA REMOVED} \end{pmatrix}$$

ALTITUDE/MACH (km)	BOUNDARY LAYER	NEAR (8 cm)	MID (76 cm)	FAR FENCE (228 cm)
1.8/.32	$\begin{pmatrix} .057, \ 2, \ .880 \\ .042, \ 37, \ .933 \end{pmatrix}$	$\begin{pmatrix} .104, \ 166, \ .652 \\ .093, \ 43, \ .711 \end{pmatrix}$	$\begin{pmatrix} .114, \ 90, \ .599 \\ .084, \ 42, \ .757 \end{pmatrix}$	$\begin{pmatrix} .125, \ 266, \ .540 \\ .087, \ 115, \ .742 \end{pmatrix}$
5.8/.57	$\begin{pmatrix} .113, \ 17, \ .604 \\ .084, \ 8, \ .757 \end{pmatrix}$	$\begin{pmatrix} .181, \ 86, \ .274 \\ .157, \ 83, \ .378 \end{pmatrix}$	$\begin{pmatrix} .210, \ 192, \ .175 \\ .137, \ 90, \ .477 \end{pmatrix}$	$\begin{pmatrix} .279, \ 265, \ .046 \\ .180, \ 122, \ .278 \end{pmatrix}$
8.8/.68	$\begin{pmatrix} .170, \ 166, \ .320 \\ .122, \ 87, \ .556 \end{pmatrix}$	$\begin{pmatrix} .172, \ 91, \ .311 \\ .149, \ 78, \ .416 \end{pmatrix}$	$\begin{pmatrix} .189, \ 129, \ .244 \\ .142, \ 92, \ .451 \end{pmatrix}$	$\begin{pmatrix} .260, \ 152, \ .069 \\ .184, \ 102, \ .263 \end{pmatrix}$
10.7/.79	$\begin{pmatrix} .137, \ 141, \ .477 \\ .104, \ 80, \ .652 \end{pmatrix}$	$\begin{pmatrix} .173, \ 78, \ .307 \\ .150, \ 61, \ .411 \end{pmatrix}$	$\begin{pmatrix} .185, \ 144, \ .259 \\ .127, \ 45, \ .529 \end{pmatrix}$	$\begin{pmatrix} .265, \ 211, \ .063 \\ .175, \ 113, \ .298 \end{pmatrix}$
GND CAL	$\begin{pmatrix} .041, \ \ \ 2, \ .936 \\ .073, \ 1600, \ .810 \end{pmatrix}$			

The ensemble averaging has been performed for the 2.0 ms pulse spacing data broken into vertical and horizontal fringe orientation sets.

The two-dimensional correlation functions obtained from each data set is plotted in slices through the x and y axis in Fig. 3. In general, the correlations decay to zero at about 4 cm shift and reach a lower limit of -0.1 at 6 cm. The spatial length scales are equal in both directions (i.e., about 2 cm), as judged by the shift coordinate at the point where the correlation is e^{-1}. This would indicate that the phase distortion is fairly isotropic.

Partial Aperture Phase Variance

The phase distortion observed through reduced aperture diameters have been determined by cropping the interferogram in the data reduction step. The full aperture data as discussed were actually cropped to 90 percent of the holocamera aperture of 14 cm diameter. The partial aperture diameters were 8.0 cm, 5.0 cm, and 2.5 cm. The wavefront analysis is designed to remove both tilt components before computing the residual phase variance, σ^2_{0-2} or phase deviation σ_{0-2}. New tilt components are computed for successively smaller apertures. The residual phase variance is also computed after removing the first eight Zernike coefficients, and this variance is denoted, σ^2_{0-8}.

The partial aperture phase variances have been obtained for all four model configurations at 5.8 Km/0.57M. The σ_{0-2} data (Table 2) for each model configuration reveal increasing distortion with increasing aperture diameter. This indicates that a larger portion of

486

TABLE 2

5.8 km OPTICAL CLIP ANALYSIS

σ WAVES (.53), τ μSEC, STREHL RATIO

$$\left(\frac{\text{PISTON-TILT REMOVED}}{\text{PISTON-COMA REMOVED}}\right)$$

APERTURE DIAMETER (cm)	BOUNDARY LAYER	NEAR	MID	FAR FENCE
2.5			$\left(\dfrac{.051,\ 66,\ .902}{.025,\quad,\ .976}\right)$	
5	$\left(\dfrac{.055,\ 28,\ .887}{.032,\ 2,\ .960}\right)$	$\left(\dfrac{.118,\ 111,\ .577}{.066,\ 85,\ .842}\right)$	$\left(\dfrac{.097,\ 109,\ .690}{.055,\ 63,\ .887}\right)$	$\left(\dfrac{.120,\ 121,\ .566}{.070,\ 81,\ .824}\right)$
9	$\left(\dfrac{.084,\ 29,\ .757}{.059,\ 37,\ .872}\right)$	$\left(\dfrac{.155,\ 91,\ .387}{.117,\ 78,\ .939}\right)$	$\left(\dfrac{.154,\ 142,\ .392}{.099,\ 93,\ .679}\right)$	$\left(\dfrac{.205,\ 182,\ .190}{.120,\ 92,\ .566}\right)$
14	$\left(\dfrac{.113,\ 17,\ .604}{.084,\ 8,\ .757}\right)$	$\left(\dfrac{.181,\ 86,\ .274}{.157,\ 83,\ .378}\right)$	$\left(\dfrac{.210,\ 192,\ .175}{.137,\ 90,\ .477}\right)$	$\left(\dfrac{.279,\ 265,\ .046}{.180,\ 122,\ .278}\right)$
INFINITE (AERO)		.252/ / .082	.263/ / .065	.904/ / 0

FIGURE 3   Spatial Correlation Function Through X and Y Axes.   5.8 km/0.57M Flight Condition, Mid Fence

488

the spatial frequency phase spectrum is sampled or detected as the aperture diameter is increased. The boundary layer flow object exhibits the best optical quality. The NEAR and MID FENCE flow objects exhibit similar trends; however, the NEAR FENCE data decreases at a slower rate with aperture size, indicating that much of its spectral strength must be at high spatial frequency. This observation is in agreement with the anemometer scale size data.

The ratio of the low order removed deviation to the tilt removed deviation, $\sigma_{0-8}/\sigma_{0-2}$, increases from about 57 percent at 5.0 cm aperture to about 72 percent at 13.5 cm aperture. This trend suggests that for larger apertures the phase distortion moves to higher spatial frequencies relative to the apertures size and, in particular, the low order Zernike terms become less significant for correction. The time scale is observed to increase with aperture size, also suggesting the large scale structures within the flow have lower temporal frequencies.

The temporal sampling variation was sufficient to detect all of the tilt removed spectrum as the phase variance was clearly observed to asymptote at large pulse spacing. In contrast to the temporal sample, the spatial sampling variation was not sufficient to detect the entire spatial frequency spectrum, as a result, the phase variance did not asymptote within the sampled aperture range (i.e., up to 15 cm diameter). Later, the propagation analysis of Hogge will be employed with the anemometer data to estimate the infinite aperture size for all four flow objects at the 5.8 Km/0.57M flight condition.

C-6

Zernike Spatial Decomposition

Turning attention to the low order Zernikes which is corrected can result in a 15 to 40% beam quality improvement. Table 3 shows the peak deviation of each Zernike term. Since the flow is random the mean of each term is very close to zero. Therefore the deviation of each term was used as the measure of merit. For a typical case, a 2σ peak to peak variation is on the order of 1 wave or 4 times the values listed. Correction frequencies are the inverse of the vibration time listed or 2-5 KHz at 14 cm aperture. Large optics would have somewhat lower correction frequencies but may not get the same large percentage improvement because the characteristic size of the turbulence may be near maximum at 15-20 cm. This implies that for large apertures the significant spatial bandwidth may extend to fairly high orders. The data was collected by fitting (as per equation 9) the $1-\sigma$ value of the pertinent Zernike term obtained from statistical analysis of the interferograms for each time spacing and flight condition.

Aerodynamic/Optical Comparisons

A major flight test objective was to provide optical data for validation of hot-wire anemometry based characterizations of turbulent flow optics. The anemometer approach is to derive the optical phase variance by path integration of the refractive index statistics, as determined from the hot-wire anemometer. For spatially homogeneous flows, the temporal phase variance is also indicative of a spatial phase variance as would be subjected to a large aperture wavefront.

TABLE 3

TABULATED LOW ORDER ZERNIKE ANALYSIS

P (WAVES), t(μs) for 14 and 8.9 cm Aperture

ALTITUDE/ MACH (km)		BOUNDARY LAYER	NEAR	MID	FAR FENCE
1.8/.32	P3, t3			.067, 140	
	P4, t4			.147, 458	
	P5, t5			.093, 190	
	P6, t6			.092, 230	
5.8/.57		.074, 44	.102, 147	.153, 293	.266, 1090
		.064, 23	.129, 91	.194, 228	.276, 314
		.241, 4800	.145, 139	.275, 452	.392, 1055
		.081, 70	.161, 89	.278, 404	.154, 69
8.9 Aperture Data for 5.8/ 0.57M	P4	.442, 26	.927, 107	.619, 179	.697, 75
	P5	.160, 100	.043, 87	.345, 140	.516, 222
	P6	.147, 41	.423, 1000	.367, 208	.681, 576
8.8/.68				.101, 85	
				.251, 346	
				.216, 223	
				.159, 151	
10.7/.79				.106, 186	
				.267, 967	
				.231, 320	
				.159, 170	

The propagation characteristics of wavefronts passed through turbulent flows have been described by Hogge. The time average, far-field intensity distributions are obtained for flows resulting in Gaussian phase statistics. In addition, the phase statistics are assumed to be homogeneous and isotropic in space. The phase covariance function, R_ϕ, is simply characterized by a variance, σ^2_ϕ , and a length scale, ℓ_0, in the Gaussian form

$$R_\phi(r) = \sigma^2_\phi e^{(-r/\ell_0)^2} \tag{10}$$

The phase integral scale is

$$L_0 = \frac{\int_0^\infty C_\phi(r) \, dr}{\sigma^2_\phi} = \frac{\pi}{2} \ell_0 \tag{11}$$

or note $L_0 \cong \ell_0$

Expressions are developed for the average far-field irradiance distribution relative to the diffraction limited distribution for strongly phase aberrated wavefront. Specifically σ^2 aero was determined from

$$\sigma^2 = \beta^2 \int_0^L <\rho(r)>^2 \int_{-L}^{L-r} \frac{<\rho(r)\rho(r+\Delta r)>}{<\rho(r)>^2} \, d\Delta r dr \tag{12}$$

where the kernel of the second integral is the correlation coefficient that is fitted with an exponential and when integrated yields the aerodynamic correlation length. β^2 is the Gladstone Dale constant. $<\rho(r)>$ was determined from the differential form of the equation of state $P = \rho RT$. The data was recorded analog from steady-state through 100 hz. Corrections ($\sim 5\%$ effect) to the data are required because the

density variation does not null due to coarse spatial sampling near the aircraft surface. The data thus calculated are the infinite aperture values of the spatial variances and deviation assuming homogeneity across the aperture.

The rationale for the finite aperture correlation follows. The size of the aperture physically describes the largest mode in the flow that can be observed. Any wavelength twice the size of the aperture diameter or larger is seen only as tilt, which is removed. Intuitively it can be seen that as the diameter shrinks the variance in the flow becomes less and thus the Strehl ratio approaches unity or the diffraction limit. At the other limit, as the diameter gets larger, the variance approaches that in the flow where the loss mechanics is that of wide angle scattering. Stated another way, the phase distortion is of high frequency compared to the aperture size. For beam apertures of the same order as the length scale of the phase distortion, the theory predicts an improved Strehl ratio. For such intermediate aperture sizes, the phase aberration results in wide angle scattering, narrow angle scattering, and tilt, where the wide angle scattering is caused by high frequency components in the phase spectrum, the narrow angle scattering is caused by length scales in the phase spectrum of the same order as the Strehl ratio is computed from the optical data using the exponential relation. This is shown in Figure 4. The theory developed by Dr. Hogge (Ref. 5) shows how the Strehl ratio observed in a finite aperture is related to the infinite aperture Strehl. It should be noted that it is not just size of the aperture that varies the Strehl

FIGURE 4

FINITE APERTURE VERSUS STREHL
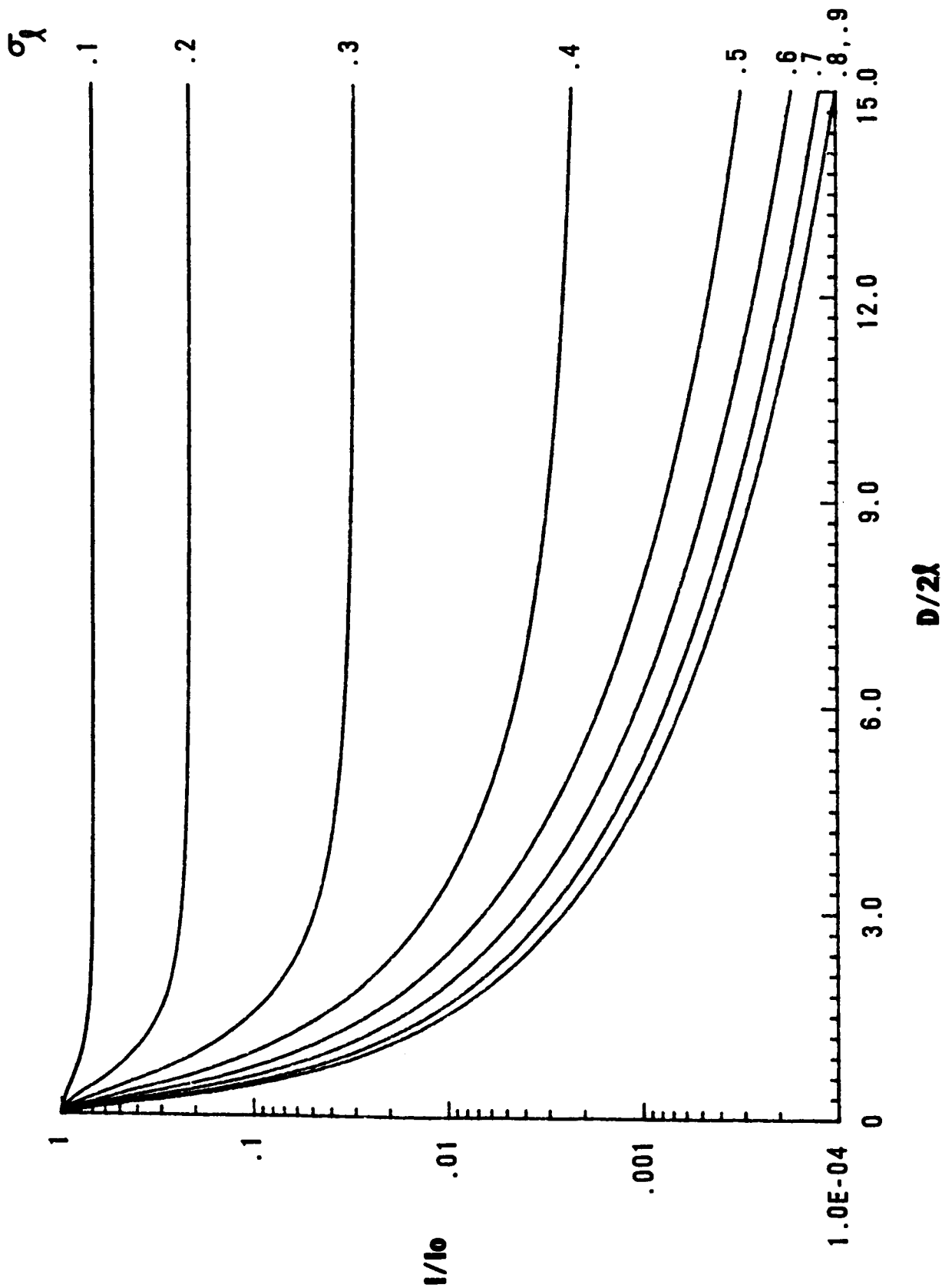
but also the size of the correlation length.

Figure 5 compares the raw finite aperture data with the theory and the aerodynamic data. The plot shows Strehl or intensity ratio as a function of aperture radius times the correlation length of the flow. The three curves are the experimentally determined aerodynamic phase deviation at infinite aperture for the near, mid, and far fence condition (.252, .262, .904 σ respectively). The curves approach a Strehl of one as the aperture is decreased according to Dr. Hogge's theory. The data points show the optical data with piston and tilt removed. Therefore one expects them to be slightly greater than the respective point on the curve. It is of interest to note that for both the near and mid fence, the largest (15 cm aperture) optical data incorporates about 75% of all the flow contribution. (Compare the Strehl at $D/2 \cdot \ell = 2$ with the asymptotic value at 15.) It is for this reason we assert an increase of .15 m optics to 1 m optics will not necessarily degrade the Strehl much more. However, if the measurement point is on the order of 2 m aft of the fence, the degradation can be substantial. (see the far fence data)

Consider now the .16 wave tilt comment on the plot. The infinite aperture deviation for the mid fence calculated from the aerodynamic data is .262. When theoretically clipped the deviation is reduced to .238. The optical deviation is .210 with corresponding Strehl. Remembering that the variance is an infinite sum of Zernike polynomials, the optical measurement is the sum of P4 and up. Using the clipped aero data and the optical measurement and assuming no piston

FIGURE 5

STREHL VERSUS FINITE APERTURE

496
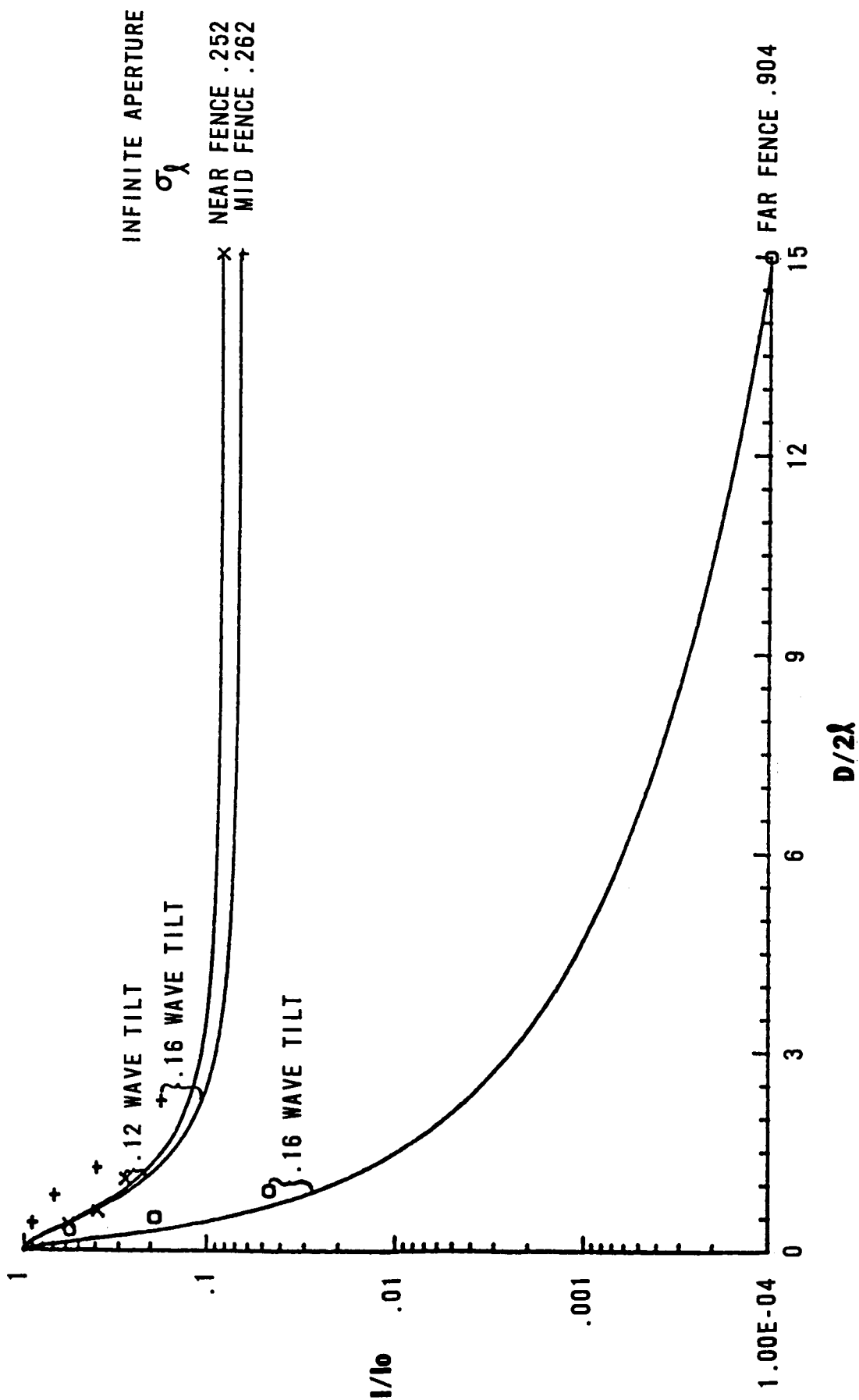
and equal X and Y tilt, a tilt coefficient can be calculated. This calculates to the .16 wave term listed. It is of interest that most data regardless of fence position or altitude yields tilt terms on the order of .2 waves which is the same order as the focus, astigmatism and tilt terms.

Extending the analysis a final step, one may consider the time sensitive aerodynamic temperature data. It is composed of a spectrum of frequency data which is transformed into density fluctuations and ultimately seen as turbules of various sizes. By clipping the frequency spectrum of all frequencies 0 to an f_c, all density fluctuations Vc/fc or greater are removed. V_c is the convection velocity of the flow (assuming $V_c = \lambda f$). This clipping technique removes the effect of the larger turbules on the optical variance and Strehl much like that of the finite aperture optical measurement with tilt removed. What is needed is correlation of the cutoff frequency with the Zernike polynomials tilt, focus, astigmatism or coma.

As a first attempt at correlation the following physical model is proposed. A turbule of size D where D is the optical aperture diameter is modelled as a convex lens of near perfect focus. Focus can be thought of as sinusoidal from 0 to π. Therefore a wavelength must be twice D or for this case 30 cm. To obtain the cutoff frequency of the aerodynamic data requires fixing a convection velocity which is sharply increasing across the shear layer. Time correlated data across the five probe rake requires use of an average convection velocity. That average was taken at .8 velocity halfway between the end probes, thus

f_c was determined. The density data was then clipped of all frequencies 0 to f_c. Then the density variation and correlation lengths were recalculated just as with the complete data set. The correlation length thus determined closely matched the optically calculated value at 2 cm derived above.

The variance also was shown to be consistent with the optical data. To understand this, consider first the form of the Zernike polynomials.

$$\rho \cos\theta; \ \rho \sin\theta \qquad \text{tilt} \quad \rho \text{ terms}$$

$$2\rho^2-1 \qquad \qquad \text{focus}$$

$$\rho^2 \cos 2\theta; \ \rho^2 \sin\theta \qquad \text{astigmatism} \Big\} \ \rho^2 \text{ term}$$

$$(3\rho^2-2)\rho \cos\theta; \ (3\rho^2-2) \ \rho \sin\theta \ \text{coma} \qquad \rho^3 \text{ terms}$$

Tilt translates the image, focus converges (diverges) the image, astigmatism is one-dimensional focus causing nonlinear convergence as the axis is rotated, coma adds third order distortion. It is obvious that the first attempt correlate turbule size has some error. In fact for a turbule of size D has all ρ^2 terms, not just pure focus. Turbules of size 2D centered in the aperture can likewise yield a focus contribution. Only when these turbules are off center do they approximate the tilt or ρ terms. Therefore clipping all λ that are 2D and greater removes some focus and astigmatism components resulting in a variance (deviation) greater than the optical σ_{0-8} and less than σ_{0-2}. By using the aerodynamic data for the middle probe only matching the convection velocity with clipped density profile results

in a $\sigma_{CLIPPEDAERO}$ = .144. By using the aerodynamic data for all five probes with the average velocity it can be shown the effect of the error of using that velocity instead of the actual velocity at the probe point is to clip some turbule data at 75% of D which seems to include ρ^3 Zernike component. This can be visualized comparing figure 6 a and b. The data tends to confirm this theory.

$$\sigma_{\infty aero} = .25\,\lambda$$

$$\sigma_{opt0-2} = .20\,\lambda$$

$$\sigma_{aero}{}^{\lambda>}\,2D = .144\,\lambda$$

$$\sigma_{aero}{}^{\lambda>}\,1.5D = .13\,\lambda$$

$$\sigma_{opt0-8} = .12\,\lambda$$

Thus we conclude for turbules > 4D aperture size, the effect of the aperture is to basically remove tilt; for turbules 3/4 to 2D, the effect is tilt, focus and astigmatism removal; for turbules 1/2 to 3/4D, the effect is tilt through coma removal. This matches the comparison of aerodynamic and optical deviations given. Therefore the spatial correlation between aerodynamic and optical measurement is confirmed.

As a final note in this experiment, 1/2 the data was taken with horizontally induced fringes and 1/2 with vertically induced fringes. It is noted that the deviations obtained from the flow wise interferograms matched those of the normal fringe interferograms. This says for aerodynamic flows, that 20 or so fringes across an interferogram is accurate enough not to perturb the statistical results. Further a study of up to 100 interferograms per condition showed that an ensemble

FIGURE 6a   Zernike Polynomials

ASTIGMATISM
x TILT
COMA
FOCUS
$\theta = 0^o$
FOCUS
COMA
y TILT
ASTIMATISM
$\theta = 90^o$
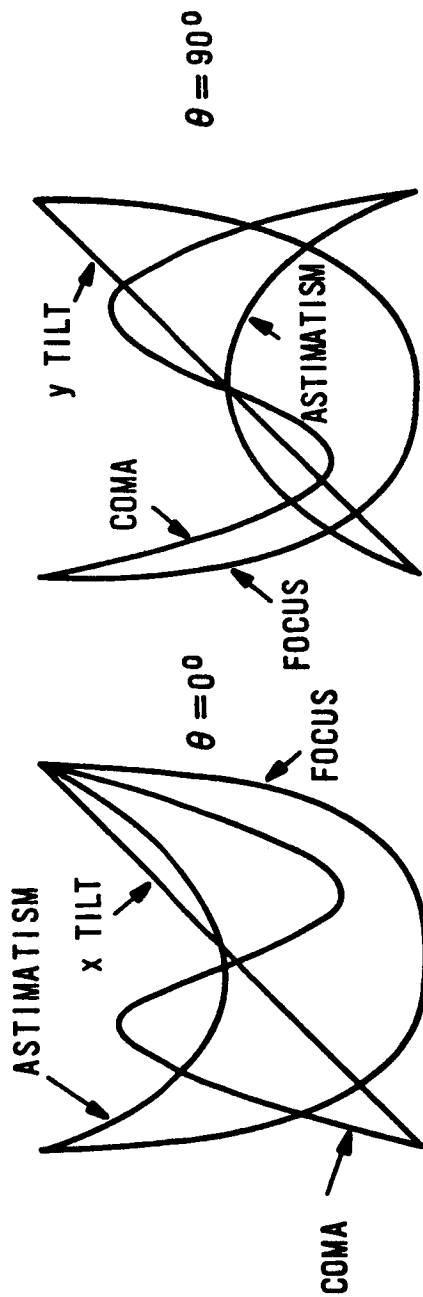
FIGURE 6b   Turbule Size Versus Aperture

2D = TWICE OPTICAL APERTURE
NEAR COMA
NEAR FOCUS AND ASTIGMATISM
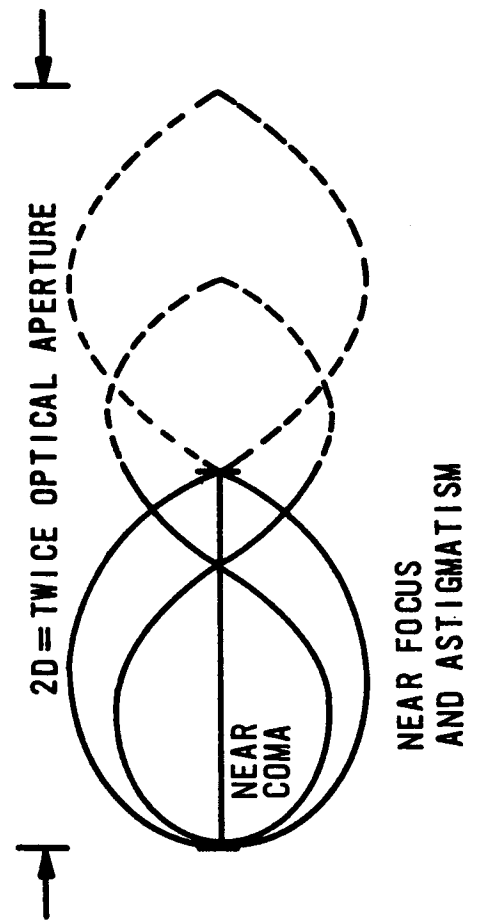
of 15 random holograms yielded statistically equal results. Finally a procedure, for which Rocketdyne Corporation can be truly proud, automated interferogram reduction so that they averaged 40 interferograms reduced per day and peaked at 70 per day. This capability will allow follow-on experiments near next day turnaround of much data.

ACKNOWLEDGEMENTS

REFERENCES

1. Gilbert, K.G., "KC-135 Aero-Optical Turbulent Boundary Layer/Shear Layer Experiments," Proceedings from Joint USAF/NASA Aero-Optics Symposium on Electromagnetic Wave Propagation from Aircraft, NASA CP 2121 National Aeronautics and Space Administration, Moffett Field, CA, April 1980.

2. Craig, J.E., Trolinger, J.D. and Rose, W.C., "Propagation Diagnostic Techniques for Turbulent Transonic Flow," Proceedings from AIAA 22nd Aerospace Science Meeting AIAA-84-0104, American Institute of Aeronautical Astronautics, January 1984.

3. Rose, W.G., Optical Effects of Near-Field Turbulence About a Small-Scale Turret Model, AFWL TR-79-129, Air Force Weapons Laboratory, Kirtland AFB, NM, August 1979.

4. Rose, W.C., Measurements of Aerodynamic Parameters Affecting Optical Performance, AFWL TR-78-191, Air Force Weapons Laboratory, Kirtland AFB, April 1979.

5. Hogge, Charles B., Strongly Phase-Aberrated Nondiffraction Limited Laser Beam, AFWL TR-75-153, Air Force Weapons Laboratory, Kirtland AFB, January 1976.

S23-34

103464

AUTOMATED REDUCTION OF INSTANTANEOUS FLOW FIELD IMAGES

G. A. Reynolds

M. Short

M. C. Whiffen

Lockheed-Georgia Company

Dept. 72-11, Zone 403

Marietta, Georgia 30063

PRECEDING PAGE BLANK NOT FILMED

PAGE 504 INTENTIONALLY BLANK

AUTOMATED REDUCTION OF INSTANTANEOUS FLOW FIELD IMAGES

Abstract. An automated data reduction system for the analysis of interference fringe patterns obtained using the Particle Image Velocimetry technique is described. This system is based on digital image processing techniques which have provided the flexibility and speed needed to obtain more complete automation of the data reduction process. As approached here, this process includes: scanning/searching for data on the photographic record, recognition of fringe patterns of sufficient quality, and finally analysis of these fringes to determine a local measure of the velocity magnitude and direction. The fringe analysis as well as the fringe image recognition are based on full-frame autocorrelation techniques using parallel processing capabilities.

Key words: automated fringe analysis, particle image velocimetry

CONTENTS

1. INTRODUCTION

A number of photographic metrology techniques in solid and fluid mechanics have evolved which rely on multiple exposure recording of particle or speckle images.[1-4] Using these techniques, the translation of a photographed subject is recorded between multiple exposures and used as an instantaneous measure of local in-plane subject motion. For example, in application to fluid flows, an illuminated plane within the flow is the subject and the motion of seeding particles as they follow the flow are recorded from that plane. A typical optical arrangement for such an application is shown in Fig. 1. The resulting photographic recording may then be evaluated to yield an instantaneous velocity field map in the illuminated plane. Due to the quantity and type of data to be evaluated, automation of the data reduction process is instrumental in making these photographic techniques into valuable measurement tools.

Various approaches have been taken for evaluation of the local image displacements from the photographic record. A common approach has been to locally illuminate the film using a small low power laser beam to generate an interference pattern.[5-7] This interference pattern is a parallel set of Young's fringes if the image displacement is uniform within the locality being interrogated. The technique transforms discrete particle or speckle images into a spatial pattern which may be analyzed for its periodic content. Alternately, the local images may be digitized and analyzed directly to obtain their orientation and spacing.[8] The ability to undertake these image processing tasks is enhanced through the use of high speed digital image processing hardware. These capabilities can handle the large quantities of image data involved and provide the flexibility for automation of the various data reduction processes.

The complete automation of the data reduction process consists of a number of stages, including scanning and/or searching of the photograph by the interrogation beam to find data in the form of interference fringes, recognition of good quality fringes, and finally analysis of these fringes to obtain the required information. This process depends on the type of data to be processed, and hence on the manner in which the data was photographically acquired. The data acquisition process is therefore described and can be found in section 2. The subsequent processing of fringe images is discussed in section 3. Finally, the integrated data reduction system is described in section 4 where a reduced set of data is also presented.

2. PHOTOGRAPHIC DATA ACQUISITION

A number of photographic techniques have been utilized to obtain instantaneous velocity field measurements in fluid flows. The Particle Image Velocimetry (PIV) technique has been employed here using a pulsed ruby laser to provide a well collimated light source of sufficient energy density. As was shown in Fig. 1, the laser beam illuminates a thin planar region of the flow field which has been lightly seeded.

This is in contrast to the Laser Speckle Velocimetry (LSV) technique which requires more highly concentrated seeding so that laser speckle is observed instead of actual particle images. The relative merits of the PIV and LSV techniques have been reviewed by Adrian.[9]

The desired application of PIV here is to medium and high speed air flows in wind tunnel studies. The first reported application of this technique in air was due to Meynart[10], who considered a small low Reynolds-number jet. For practical use in most wind tunnel applications a larger probe area is desirable. Therefore a number of difficulties must be addressed in terms of the required laser output energy, the film sensitivity and the provision of adequate flow seeding.

For the application described here a relatively large area was to be probed, covering approximately 130 square centimeters. The probe region was illuminated by a Q-switched ruby laser which was operated in a dual pulse mode. To obtain the required energy density in the illumination sheet the laser was operated in multimode, yielding a total output energy of 2-3 Joules. While this mode of operation provides the needed output energy, a number of problems arise due to the reduced beam collimation in the multimode configuration. These factors are discussed below in particular with regard to selection of an appropriate seeding density.

The illuminated probe plane was imaged from 90 degrees at a magnification close to one using a Schneider 220mm f/5.6 lense. Spherical aberrations, primarily coma, were reduced to an acceptable level by stopping this lense down to between f/8 and f/11. The resulting particle images were recorded on Kodak 2415 cut film which has sufficient resolution (320 lines/mm) and good sensitivity in the red. However due to the required lense settings, it was necessary to preflash the film to a density of 0.3 so that image contrast was optimized.[11] It is apparent that the scattered light levels experienced here were marginal. This is in agreement with the predictions of Adrian[12], which were repeated here for the appropriate seeding material.

As with other laser velocimetry techniques, providing the correct seeding in a wind tunnel application is difficult. This is especially true for PIV where relatively high seeding density must be introduced without affecting the flow quality. In these experiments water droplets generated by an ultrasonic atomizer provided the necessary seeding. While water is less than ideal from an optical standpoint, it was found to be a practical choice for use in the open return wind tunnel facility used here. The resulting particle size was found photographically to be equal to or less than the diffraction limited spot size of the imaging system, that is approximately 20 microns.

In most cases it is desirable to provide a nominal seeding density such that the particles, and hence the resulting data, are continuously distributed. However, using a multimode illumination beam, additional particles are marginally illuminated toward the edges of the sheet. These unwanted particles only contribute to noise in the data reduction

process. This effect was reduced by using relatively sparce seeding so that nominally only one particle image pair would be present in the interrogaton area a time. As a result, the distribution of data on the film could no longer be assumed to be continuous, a fact which the data reduction processes had to accommodate.

Another characteristic of the fringe data which must be recognized by the data reduction system is the presence of cross interference fringes. This is particularly true for dual pulse mode which is most sensitive to the presence of two particle image pairs within the interrogation spot. It is threrefore desirable that the data reduction system be capable of rejecting images having levels of cross interference above some tolerable limit.

3. DATA REDUCTION BY FRINGE ANALYSIS

The question of fringe analysis for the purpose of extracting quantitative information from photographed images is addressed here. With the objective of automation, the approach has been to implement analysis algorithms within the framework of the digital image processing capabilities available. These capabilities include high speed video-rate digitizing, multiple image plane memories, and parallel/pipeline image processing. These processing capabilities allow a series of algebraic and Boolean operations to be performed between image planes in one video frame time. The ability to perform full-frame manipulations is desirable for fringe analysis and is often necessary due to the presence of speckle noise and diffracton halo distortion. Given that parallel analysis of entire fringe images is to be conducted, the speed of the data reduction process is then primarily a function of the relative complexity of a given analysis algorithm.

A general approach to the analysis problem would be the application of a 2-D fast Fourier transform to the fringe image. However this general approach is unnecessarily complex given that a good deal of a priori knowledge is available concerning the fringes being analyzed. That is, the interference pattern should be composed of a parallel array of fringes with the central fringe maximum crossing the center of the diffraction halo. Taking advantage of these properties, a full-frame autocorrelation function similar to that suggested by Meynart[3] has been implemented to extract the fringe spacing in a given direction. This function was obtained by parallel processing the full 512 by 512 fringe image using the relationship:

$$R(d) = \frac{\langle I(-d/2)*I(d/2)\rangle - \langle I\rangle^2}{\langle I^2\rangle - \langle I\rangle^2} \tag{1}$$

509

where $< >$ denotes the mean value. In the above expression, the image mean, $<I>$, and mean square values, $<I^2>$, are assumed to be constants. This condition is closely approximated by filtering the fringe image with a Gaussian neutral density filter. This filtering process has the added advantage of decreasing the image dynamic range due to the diffraction halo. For each value of the shift, d, a single pass through the video processor is required, corresponding to a single video frame time. The resulting 128 point one-sided autocorrelation function shown in Fig. 2 can be obtained in approximately five seconds. The effectiveness of the full-frame analysis in removing uncorrelated speckle noise is evident in the smoothness of the autocorrelation function. Given this function, a FFT may be performed on the host computer to determine the dominant frequency component.[3] Alternately, since the data is of high quality, a common numerical iteration scheme may be used to find the first peak in R(d). This second method has been used such that only the necessary points of R(d) are calculated in the process. Convergence time along a given analysis direction is typically two seconds.

The above operation must be performed in at least two directions to provide the needed fringe wavelength components from which the velocity magnitude and direction can be determined. However, in general a third direction of analysis is required to resolve the angular ambiguity of plus or minus the resultant fringe angle, as demonstrated in Fig. 3. The actual choice of these three analysis directions should depend on the orientation of the fringes in order to obtain the best resolution.

For an arbitrary fringe orientation, three lines of analysis are chosen from four optional directions: 0, +45, -45, and 90 degrees, such that analysis along a direction closely parallel to the fringes is avoided. The least desirable of the four directions is marked by a dominant frequency component which is significantly lower compared to that found in the other three directions. Again this may be reliably found using the autocorrelation function. To accomplish this quickly, the first minimum in R(d) is found using large steps in "d" as shown in Fig. 4(a). The direction exhibiting the longest approximate wavelength is the least desirable and the analysis may then be continued in the remaining three directions, shown in Fig. 4(b).

The accuracy of the data acquisition and data reduction system is of particular interest. Meynart[3] performed a controlled experiment and found the overall system accuracy to be 1%. It was concluded that the accuracy was ultimately limited by the film resolution, although the individual error contributions were not determined directly. The above conclusion was based on the supposition that the uncertainty in the recorded image position is on the order of the effective film grain size. An effective grain size for a film may be expressed as the inverse of the spatial resolving power, that is 320 lines/mm or 3 microns for Kodak 2415. For particle image sizes on the order of the effective grain size, the uncertainty in the image position may be approximated by this grain size. However assuming a diffraction limit of approximately 20 microns, the image sizes can be expected to be at

least an order of magnitude larger than the effective grain size. Under these circumstances the location of the image centroid, as determined by the interrogating laser beam, is known to a precision significantly better than the effective grain size. These considerations suggest that an accuracy of better than 1% may be possible if other system errors can be kept low. In this respect, the relative merits of the data reduction algorithms need to be addressed.

It is clear that the full-frame autocorrelation function provides significant advantages over less comprehensive analysis techniques. For the subsequent determination of fringe spacing from this autocorrelation function, two techniques have been discussed in this section. The approach taken here has been a direct numerical iteration on the autocorrelation function instead of the more robust but slower FFT of the autocorrelation. The resolution of this numerical iteration is significantly better than one pixel, using curve fitting techniques. This resolution is as good or better than the resolution bandwidth expected from a FFT of the full autocorrelation function. For example if the resolution bandwidth for a FFT calculation is, $B = 1/(m + z)$, where m is the number of correlation values and z is the number of added zeroes[13], then a total record length of 2048 is required to obtain one pixel resolution at a nominal fringe spacing of 50 pixels. This 1-D FFT approach is therefore considered desirable only where significant levels of correlated noise, or cross interference, is present. In such a case it is desirable to select the dominant frequency component.

4. APPLICATION TO REDUCTION OF AERODYNAMIC DATA

The above fringe analysis algorithms have been integrated into an automated data reduction system. This system, shown in Fig. 5, operates on fringe images produced by local coherent illumination of dual particle images recorded on a photograghic film which is indexed by an x-y stage. The flexibility of the digital processing system is exploited here to tailor the reduction process to handle the type of data acquired in this application of the PIV technique.

One of the characteristics of the data considered here is due to the inhomogeneous distribution of seeding particles. While an optimum seeding density is desired, nonuniformities in the flow tend to concentrate these particles in some areas, leaving other areas with relatively sparse seeding. This seeding problem is compounded by the problem of poor illumination sheet definition discussed in section 2. For the above reasons, it is not practical to assume data on a regular grid pattern. The photographic record is therefore scanned using a grid pattern which is modified by a local search if data is not present at a prescribed grid point. This searching scheme is demonstrated in Fig. 6.

A searching scheme such as this assumes that fringe images can be recognized when encountered. This recognition is initially contingent upon an image variance threshold which must be met, thus avoiding areas where no particles are present. Before analysis begins, an image of

sufficiently high variance is further classified to avoid the case of multiple interference patterns. The highly unidirectional character of a good fringe image may be discriminated from a cross-hatched image by considering the four autocorrelation functions used to find the optimum analysis directions, discussed in section 3. As was shown in Fig. 4 the wavelength should vary strongly with angle in a good fringe image. If this is the case, optimum analysis directions can be established. However, if the angular dependence is weak as shown in Fig. 7, the optimum analysis directions cannot be determined with reasonable certainty and the image is rejected because of cross-hatching.

The results produced by the automated data reduction system are described below. The PIV technique has been applied to the flow field about a delta wing at a high angle of attack. For this configuration a pair of vortices are generated by separation of the flow at the sharp leading edge of the wing. The acquisition of instantaneous velocity field measurements is particularly desirable in an unsteady vortex flow field of this type.

This test configuration is shown in Fig. 8. The plan view of half the wing, in Fig. 8(a), shows the axis of the leading edge vortex and the field of view of the probe area. In this measurement the probe plane is close to being co-planar with the wing, diverging from the wing apex by an angle of only 1.5 degrees, as shown in the side view of Fig. 8(b). At this location the probe plane is between the wing surface and the plane of the vortex core. The cross section of the expected vortex flow field is shown in Fig. 8(c). The primary features of the flow include the secondary vortex, V_2, generated by the primary one, V_1, and the secondary separation line, s.i., separating the two.

The automated data reduction system has been used to reduce the photographic data within the area which was shown in Fig. 8(a). This reduced data is shown in Fig. 9. Also shown is the secondary separation line which is evident in the original particle image photograph by the collection of seeding particles along that line. Finally, the approximate location of the primary vortex core projected down to the measurement plane has been drawn at an angle of 11 degrees to the leading edge. The data was obtained at a free stream velocity of 10 m/sec and is typical of the data taken in this turbulent vortex flow using the PIV technique. This particular set of data gives an instantaneous quantitative measure of the unsteady vortex flow and its viscous interaction with the wing surface. These velocity measurements demonstrate the feasibility of this type of instantaneous flow field measurement technique in the wind tunnel application. The increased level of automation has also made the technique more desirable as a research tool.

5. SUMMARY AND CONCLUSIONS

An automated fringe analysis system based on digital image processing techniques has been presented which provides a high level of flexibility

without compromising speed. As a result, a more comprehensive automation of the data reduction process has been made possible. This automated data reduction process includes scanning and searching of the photographic record, recognition of good quality fringes, and analysis of these fringes. The fringe analysis itself is based on a full-frame autocorrelation which collapses the the available information into a function of a single variable, minimizing uncorrelated noise in the process. Since noise has been minimized without loss of coherent information, the autocorrelation provides an accurate basis from which the wavelength component in a given direction may be computed.

The actual technique used to obtain the wavelength from the autocorrelation function may be varied depending on the level of noise and cross interference present in the image. For nominal noise levels and low levels of cross interference a numerical iteration to find the wavelength has been advantageous. The accuracy of these measurements should not be limited to 1% by the available film resolution. However, for high levels of cross interference an FFT of the autocorrelation function may be necessary to isolate the desired frequency component.

Simplification of the data reduction process should result from improvements in the quality of the photographic data. Significant improvements may be be attained through use of a monomode laser and improved seeding material. Problems with cross interference will be reduced by multiple pulsing instead of just dual pulse illumination. This will also improve accuracy through the effective thinning of the fringes. Further reductions of cross interference problems may be obtained by adjusting the interrogation spot diameter based on the local flow scales.

6. REFERENCES

1. E. Archbold and A. E. Ennos, Opt. Acta 19, 253 (1972).

2. P. G. Simpkins and T. D. Dudderar, J. Fluid Mech. 89(4) (1978).

3. R. Meynart, Applied Optics 22(4), 535 (1983).

4. L. M. M. Lorenco and M. C. Whiffen, in Proceedings, Second International Symposium on Application of Laser Anemometry to Fluid Mechanics, 6.3 (1984).

5. G. H. Kaufmann, A. E. Ennos, B. Gale, and D. J. Pugh, J. Phys. E: Sci. Instrum. 13, 579 (1980).

6. R. Meynart, Rev. Sci. Instrum. 53(1), 110 (1982).

7. D. W. Robinson, Applied Optics 22(14), 2169 (1983).

8. C. S. Yao and R. J. Adrian, Applied Optics 23(11), 1687 (1984).

9. R. J. Adrian, Applied Optics 23(11) 1690 (1984).

10. R. Meynart, Phys. Fluids 26(8), 2074 (1983).

11. M. J. Eccles, M. E. Sim, and K. P. Tritton, Low Light Level Detectors in Astronomy, Chap 3, Cambridge University Press, New York (1983).

12. R. J. Adrian and C. S. Yao, in Proceedings, Second International Symposium on Application of Laser Anemometry to Fluid Mechanics, 6.4 (1984).

13. J. S. Bendat and A. G. Piersol, Random Data: Analysis and Measurement Procedures, Chap. 9, Wiley-Interscience, New York (1971).

List Of Figure Captions

Fig. 1   Optical configuration for Particle Image Velocimetry.

Fig. 2(a)   Full-frame one-sided autocorrelation function in the
            horizontal direction.

Fig. 2(b)   Digitized fringe image (512 x 512), corresponding to
            Fig. 2(a).

Fig. 3   Fringe angle sign ambiguity for analysis in only two
            directions.

Fig. 4   Determination of optimum analysis directions,
            (a) Autocorrelation along the four optional directions,
            (b) Corresponding fringes and optimum analysis directions.

Fig. 5   Automated data reduction system, F-film plane, L-lense,
            S-beam stop and Gaussian neutral density filter.

Fig. 6   Scanning/searching routine, *-successful data analysis

Fig. 7   Fringe image recognition, (a) Autocorrelation of image with
            low angular dependence, (b) Fringe image rejected because of
            cross-interference.

Fig. 8.   Aerodynamic test configuration, (a) Plan View; L.E.-leading
            edge, Σ-measurement area, σ-reduced data, s.l.-secondary
            separation line, V_1-primary vortex core, (b) Side View;
            W-wing surface, (c) Cross section C; S-secondary separation
            point, V_2-secondary vortex.

Fig. 9.   Reduced data, L.E.-leading edge, s.l.-secondary separation
            line, V_1-primary vortex core.

Pulsed Laser

Cylindrical Lens
Arrangement

Photographic Plate

Seeded Flow

Laser Sheet

Imaged Area

Fig. 1

516
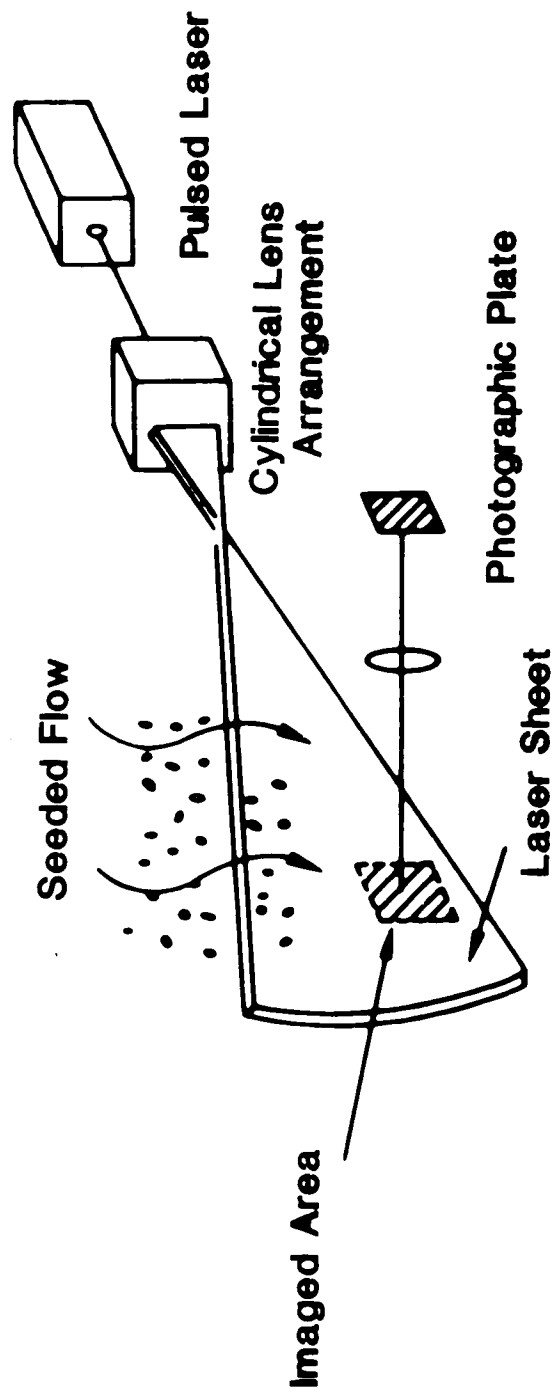
a
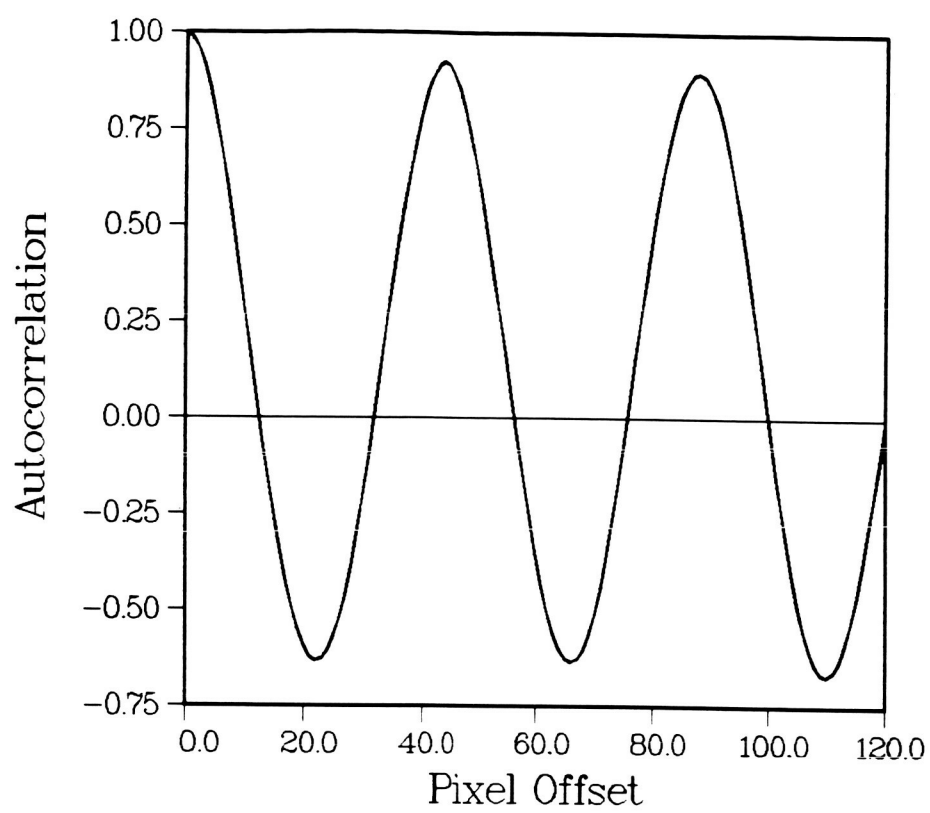
b

Fig. 2
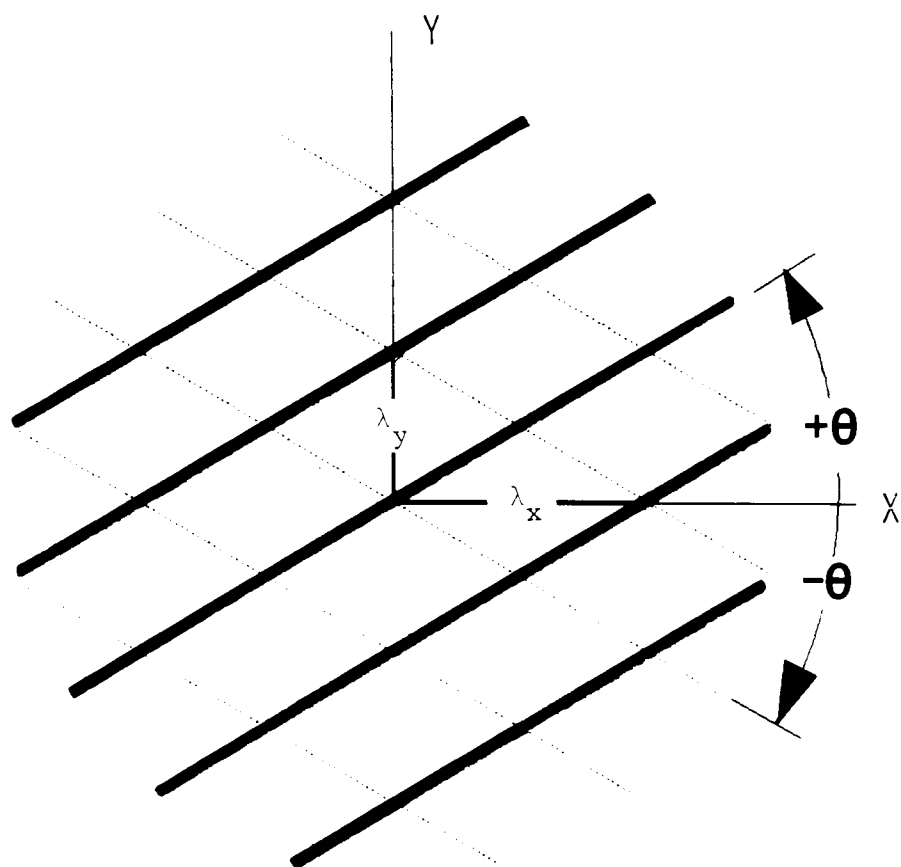
Fig. 3
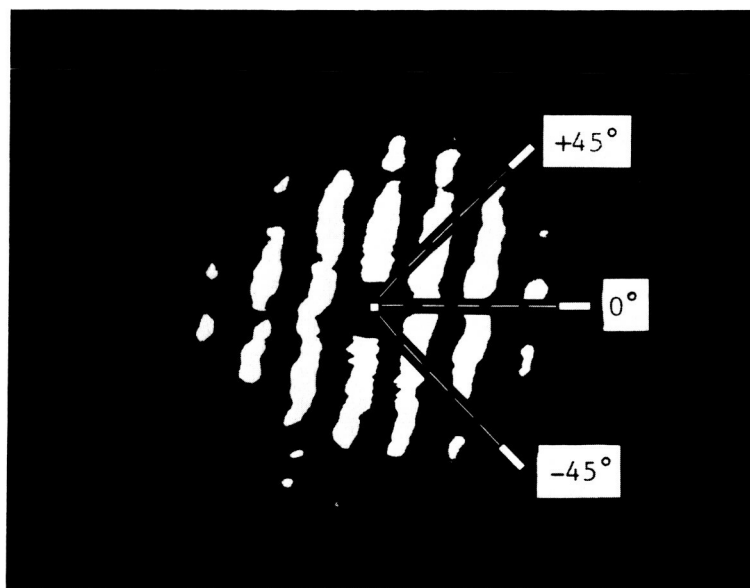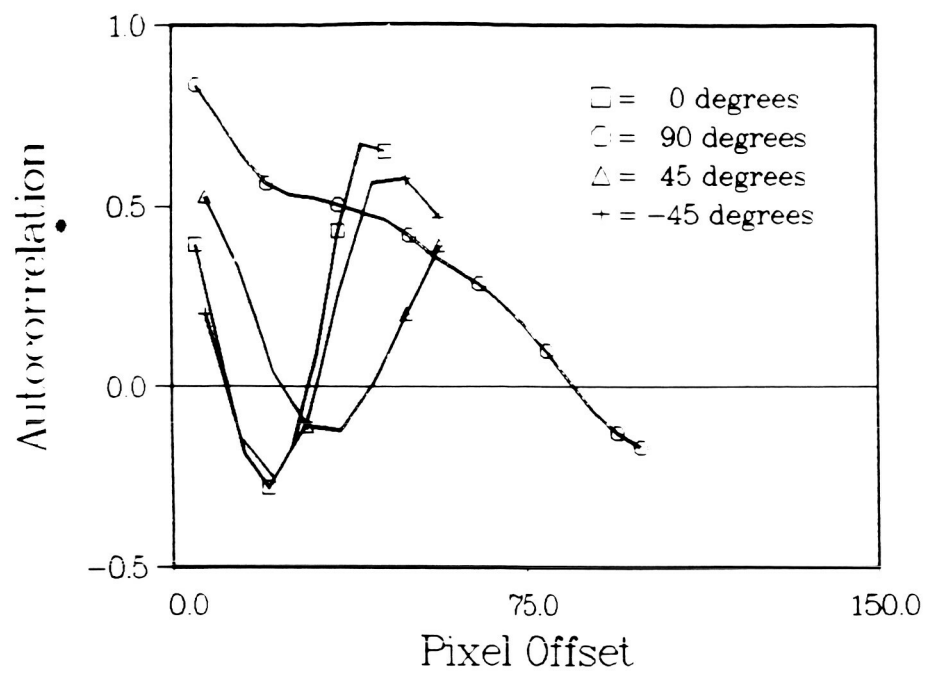
Fig. 4

Fig. 5

Fig. 6

a

b

Fig. 7

a

L.E.

σ

S

Σ

V₁

s.l.

C̶L̶

c

b

V₁

W

Σ

c

V₁

V₂

W

S

Σ
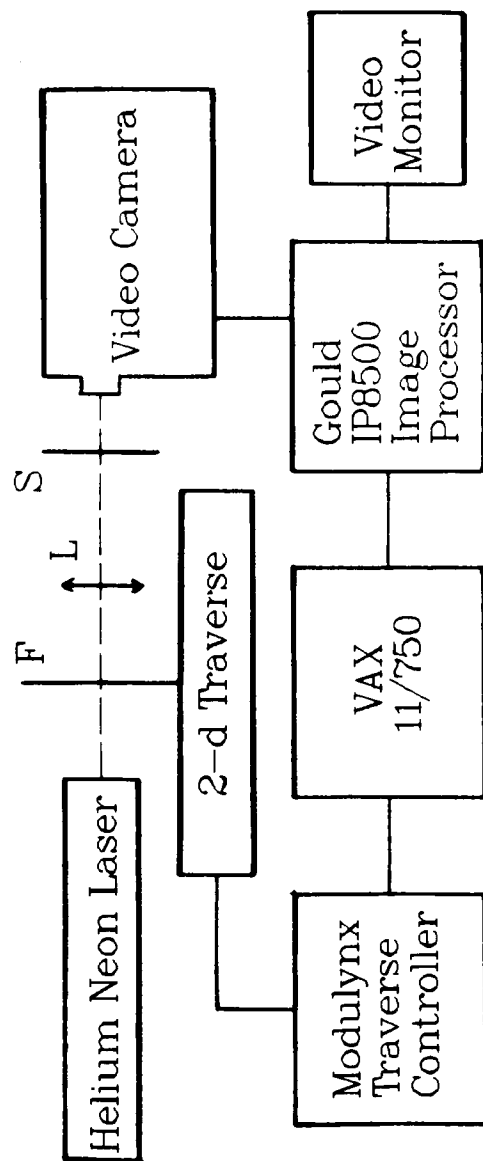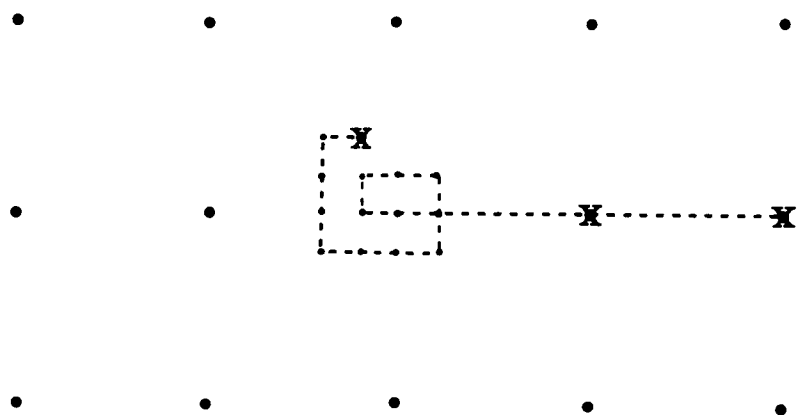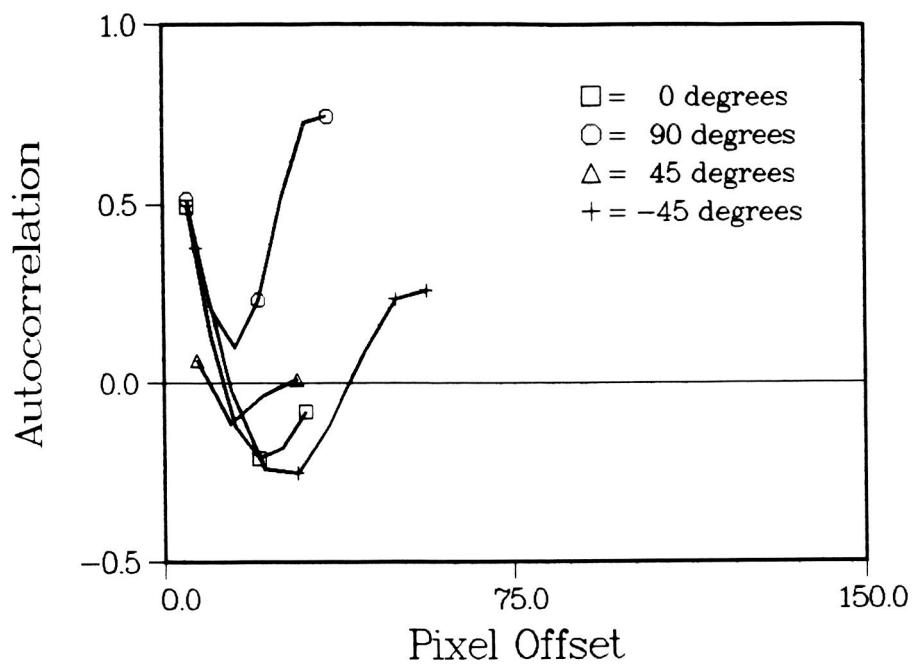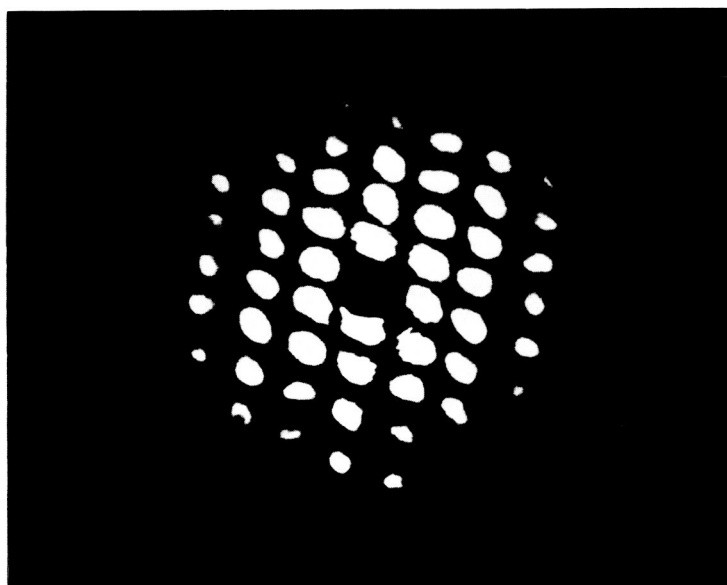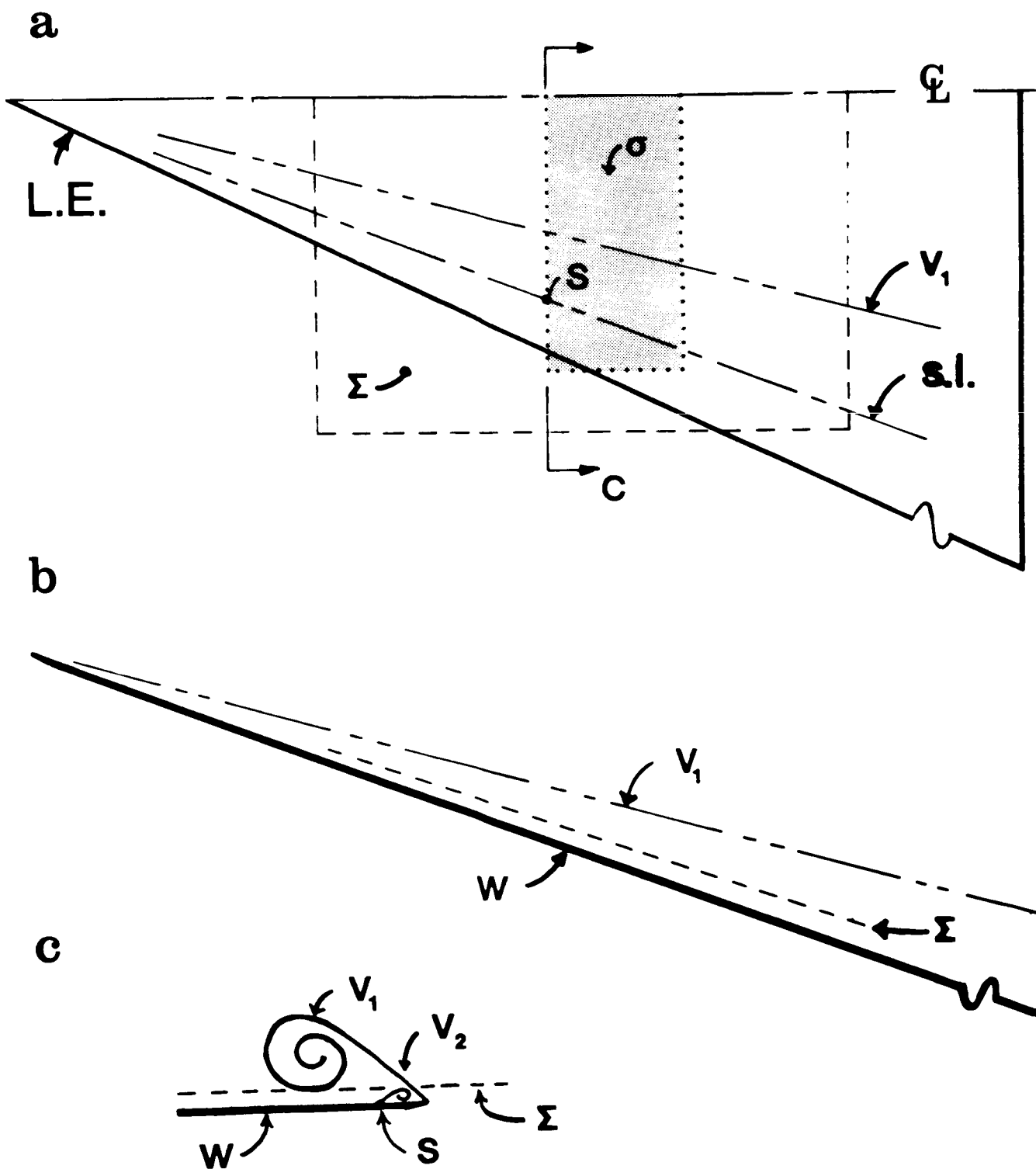
Fig. 8
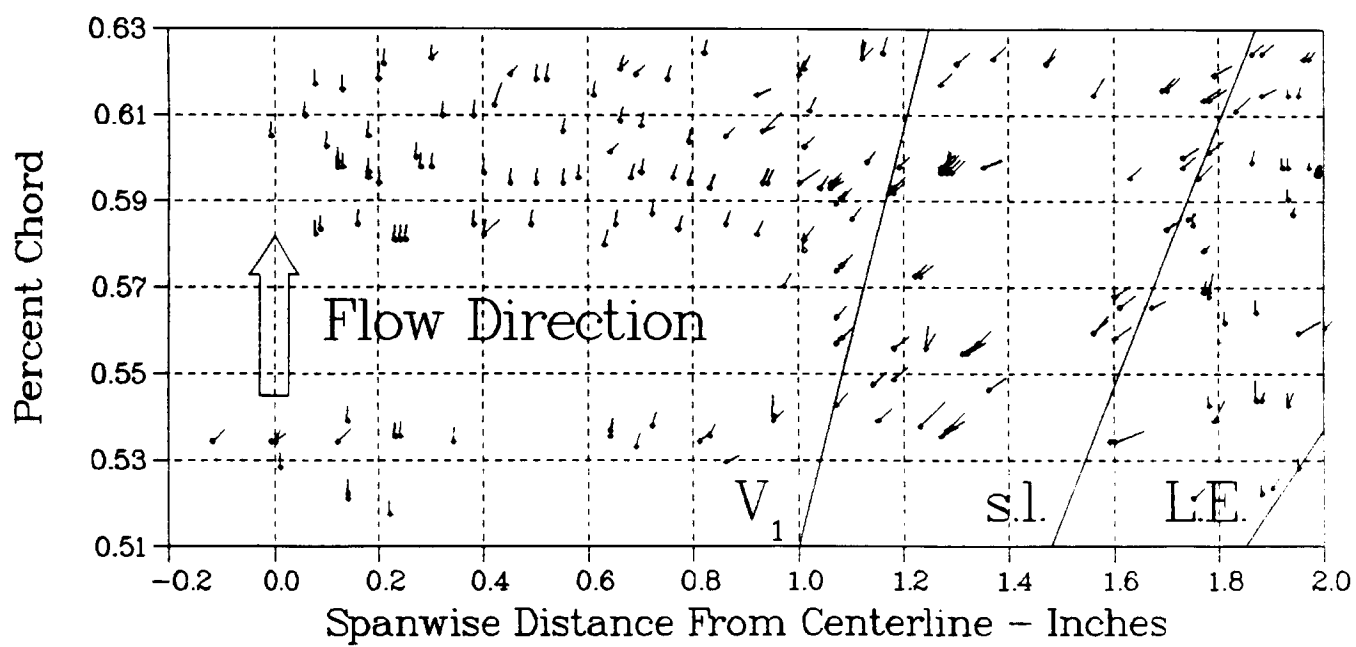
Fig. 9

IMAGE ANALYSIS OF PARTICLE FIELD BY MEANS OF

COMPUTED TOMOGRAPHY

Mitsushige NAKAYAMA

Department of Mechanical Engineering

Gunma University

1-5-1 Tenjin-cho, Kiryu 376 Japan

AABSTRACT

In order to visualize and investigate spray structures, computed tomography technique is applied to analyse droplet information. From the transmitted light intensity through the spray and/or the data of particle size distribution obtained from a Fraunhofer diffraction principle, the quantitative volume of spray droplet or local particle size was calculated and the reconstruction of spray structures was made.

This paper describes the background of computed tomography and some experimental results of the structure of intermittent spray such as diesel spray.

1. INTRODUCTION

In order to visualize and investigate spray structures, non-intrusive measurement technique has been studied. From the

transmitted light intensity through the spray, a qualitative information of droplet size and their number density will be expected. For this purpose a compueted tomography technique was introduced (Ref. 1), and the reconstruction of spray structures was made (Ref. 2).

Visualization technique is wanted for studies in heat transfer and mass transfer, and particularly, for vaporizing process in hot spray (Refs. 3, 4). During recent years, it has come to receive a large amount of attention to these field, but we can not find out any paper on visualization of vaporizing phenomena of spray.

This computed tomography method will be applied to analyse the droplet size distribution of spray such as industrial atomizer, disel nozzle and so on. And it will contribute to analyse on hologram.

This report presents the background of computed tomography and some experimental results of spray structure of intermittent injection such as diesel nozzles.

2. BACK GROUND OF COMPUTED TECHNOLOGY

As shown in Figure 1, let a coordinate system fixed on the subject be (x,y), and a coordinate obtained by rotating the former through degree θ be (X,Y). When a beam parallel to this Y axis and with an intensity of Io is made to impinge on an object with light absorption coefficient distribution of f(x,y), the intensity of light after transmitting through such an object is given by Equation 1.

$$I/I_0 = \exp\left[-\int_{-\infty}^{\infty} f(X\cos\theta - Y\sin\theta,\ X\sin\theta + Y\cos\theta)dY \right] \quad \cdots \cdot (1)$$

The logarithmic transformation g(X,θ) of this attenuation rate is called "Projection Data", which is represented by Equation 2.

$$g(X, \theta) = \int_{-\infty}^{\infty} f(X \cos \theta - Y \sin \theta, \ X \sin \theta + Y \cos \theta) dY \ \cdots \cdots \ (2)$$

By determining this X value from $-\infty$ to $+\infty$, one-dimensional projection data is obtained. Let us then determine this one-dimensional projection data for the range of $0 \leqq \theta < 2\pi$. There are two main methods to reconstruct tomograms from the projection data so obtained, namely the iterative method and the analytical method. In the former method, projection data generated from estimated absorption coefficient distribution is compared with that measured for sucssecive correction. In practice, the analytical method is more widely used because of less calculation time requirement and the higher accuracy it offers. One of the simplest yet strict analytical methods is the Fourier transformation method. Fourier transformation $F(\xi, \eta)$ of f(x,y) when expressed by polar coordinates gives Equation 3.

$$F(\omega \cos \theta, \omega \sin \theta) = \int_{-\infty}^{\infty} g(X, \theta) \exp(-i\omega X) dX \ \cdots \cdots \cdots \cdots \cdots \cdot (3)$$

Therefore, f(x,y) can be determined by Fourier inverse transformation of $F(\xi, \eta)$. A mathematical equivalent method is to perform Fourier inverse transformation of Equation 3 on polar coordinates to obtain Equation 4.

$$f(x, y) = 1/(8\pi^2) \int_0^{2\pi} \left[\int_{-\infty}^{\infty} F(\omega \cos \theta, \omega \sin \theta) |\omega| \exp(i\omega X) d\omega \right] d\theta \ \cdots (4)$$

Namely, by applying a filter function expressed as ω to $F(\xi,\eta)$ and superimposing by inverse projection, the image is reconstructed. This method is called "Filtered back projection method" (Ref. 5). By convolution of Fourier inverse transformation h(X) of this filter function in the original region, Equation 4 can be transformed into Equation 5.

$$f(x,\,y) = 1/(4\pi) \int_{0}^{2\pi} \int_{-\infty}^{\infty} g(X',\,\theta) h(X-X') dX' \, d\theta \quad \cdots\cdots\cdots\cdots (5)$$

This method is called "convolution method" (Ref. 6), which is adopted in the present work.

The filter function ω diverges as $|\omega|$ increases and hence the equation does not lend itself to strict calculation. Therefore, it is necessary to attenuate this function in regions where ω is large. Various filter functions have been proposed.

Let the sampling number in X direction and the number of rotational movements be M and N respectively for each equation. Then, a determinant with MxN matrix $G(X,\theta)$ and MxN matrix H can be obtained as indicated by Equation 6.

$$Q(X,\theta) = H \cdot G(X,\theta) \quad \cdots\cdots\cdots\cdots\cdots\cdots\cdots\cdots\cdots\cdots (6)$$

This equation is to calculate inverse projection and takes as f(x,y) the sum of q(X,θ) for all θ relative to the point (x,y) of interest. However, q corresponding to the point (x,y) is not necessarily on sample point of q(X,θ) and in such case, interporation is made using sample points at both ends.

Figure 2 shows the flow chart of the calculation in computing. The measured projection data then undergo matrix calculation with

precalculated and filed filter function matrix. By back projection of the resultant q(X,θ), f(x,y) is obtained, which is displayed according to the display conditions that can be set s desired.

Generally, it is said that transformation of filter functions for correction of projection data used in Equations 5 and 6 has significant influence on quality of the reconstructed image. In this work, the modified filter function of modified Shepp and Logan (Ref. 7) which is the commonest is used.

Of course, the more samplings there are and the greater number of rotary movements, the higher is the quality of reconstructed image, but a compromise must be found because of limitations, such as measuring instrument accuracy, resolution, computer memory size, CPU time etc. This work deals with liquid spray particles which are macroscopically stable both in time and space, but when a small portion is considered, each particle is constantly moving and hence it is necessary to average them to some extent in time and space for data sampling. Thus, it serves no purpose to attempt to improve the sampling resolution more than necessary. In view of this image quality and time for computation, it was decided to select 61 sample points(reconstruction image pixels 61 x 61) and 30 rotary movements with 6 degree increments, which are also considered industrially applicable. In this work, measurement is done based on these coditions.

3. EXPERIMENTAL APPARATUS AND METHODS.

3.1 Experimental apparatus

In order to visualize and analyse the spray structure and estimate the spray particle size or their spatial density, the

distribution of the transmitted light intensity was measured, and the reco nstruction data of spray was calculated by CT technique, respectively.

The transmitted light intensity is pictured by 35mm photo or detected by TV camera (Type C-1000, Hamamatsu TV) which is controlled by small comuter (LSI 11/23: DEC). The reconstruction of pictures of spray was displayed on CRT (NEXUS 5500: Kashiwagi Lab.) or X-Y plotter.

Fig. 3 shows a block diagram of the hardware utilized in this study. Images are created by dierect imaging of a spray sample area on a high resolution visicon camera. This camera has a resolution of 8 bit and 1024x1024 pixecels.

3.2 Application of Computed Tomography to sprays

Assume a particle group with n particles of diameter D in unit volume. Then, the attenuation of parallel incident light caused by such a group is given by Equation 7.

$$I/I_0 = \exp[-RK_t(\pi D^2/4)nl] \quad \cdots\cdots\cdots\cdots\cdots\cdots (7)$$

where Io is the incident light intensity, I is the light intensity after passing through the particle group, Kt is the total scatter coefficient, l is the optical path length through the particle group and R is a coefficient that depends on the particle size parameter α ($\alpha = \pi D/\lambda$, where λ is incident light wave length) and optical system. The total scatter coefficient Kt is known to be nearly constant at 2 when $\alpha > 30$. In the case visible rays of λ=400 to 700nm, D>10 μm and hence $\alpha > 45$. As a result, Kt may be considered nearly constant. R is less influenced by α when the recieving angle is

narrower. If the receiving angle is small and particle size distribution is limited to a narrow range, R is nearly constant. Therefore, the sum of particle sectional areas $\pi Dn/4$ corresponds to $f(x,y)$ of the Equaton 1. Thus, from the projection data obtained by this light attenuation, the density distribution of particle area on the spray section can be obtained.

4. EXPERIMENTAL RESULTS AND DISCUSSION

In order to confirm the reliability of reconstruction data by CT technique, the relations between the distribution of the transmitted intensity and the measured dispersion rate of spray were verified on the swirl chamber atomizer.

The dispersion rate was measured by one dimentional line type paternator and the reconstructed picture equivalent to dispersion rate was calculated by Computed Tomography technique, in which the data of the transmitted light intensity distribution was used.

The diameters on various point were claculated by means of two kinds of CT. They are the transmitted light energy method as above mentioned and a Fraunhofer diffraction energy distribution method by using the particle sizer (ST-2600HSD).

The reconstruction data of droplet concentration and the measured value of dispersion quantity are shown in Fig. 4. These results were normalized by their maximum amount, respectively. This calculated concentration is called as relative concentration. Judging from the figure, they are coincide with each other, and hence, this evaluation method is effective in the research of spray structures.

Applying an onion model to an axi-symmetric spray, local droplets

diameter and the droplet size distribution will be obtained in near future.

Figs. 5 and 6 show the reconstructed image data of disel spray. Pusudo colour maps corresponding to the concentration of paricles are pictured. As well known, disel spray injection is a kind of intermittent one, so instantaneous data which were taken during the exposure time of 75 nano second.

Fig.5 shows the spacial spray concentration injected from throttle nozzle at 1.1 ms after opening injection and each reconstructed image photo shows the data of cross section at the positions of 10, 20, 30, and 40mm from nozzle. Fig.6 presents the data of spray particle density change with time at 30 mm position from the nozzle tip. Comparison of Figs. 5 and 6 indicates that with diesel spray, later sprayed particles catch up with and overtake preceding particles.

On observing the phenomena of the diesel injection, they are complex and non-steady, so we need to develop new measuring equipment for particle size and its distribution. For example, it is a automatic data reduction system from hologram. We are now undergoing to develop and fabricate prototype of automated data reduction system with auto focus and stage system.

5. SUMMARY

A novel visualization method of spray structure was presented and the pictures of the internal strucures of swirl chamber atomizer and disel injection spray atomizer were reconstructed by Computed Tomography technique.

This method is useful for qualitative estimation of spray structure and particularly, for visualization of evaporation and/or combustion phenomena of particles.

6. AKNOWLEDGEMENT

EOREFERENCES

1. Yule A. J., Seng C. A., Felton P. G., Unggut A. and Chiger N. A., Combustion and Flame 44 (1982) 71.

2. Nakayama M. and Araki T., Preprint of 12th Conf. Liq. Atom. and Spray in Japan (in Japanese) (1984) 105.

3. Nakayama M. and Arai T., 20th Int. Symp. on Combustion, Ann Arbor, Michigan, (1984)

4. Nakayama M. and Araki T., 3rd Intn. Conf. on Liquid Atomization and Spray Systems. London, (1985-7), (will be appeared)

5. Budinger T. F. and Gullberg G. T., IEEE Trans. Nucl. Sci., NS-21 (1974) 2.

6. Ramachandran G. N. and Lakshmimarayanan A. V., Proc. Nat. Acad. Sci. USA 68. No. 9 (1971) 2236.

7. Shepp L. A. and Logan B. F., IEEE Trans. Nucl. Sci., NS-21 (1974) 21.
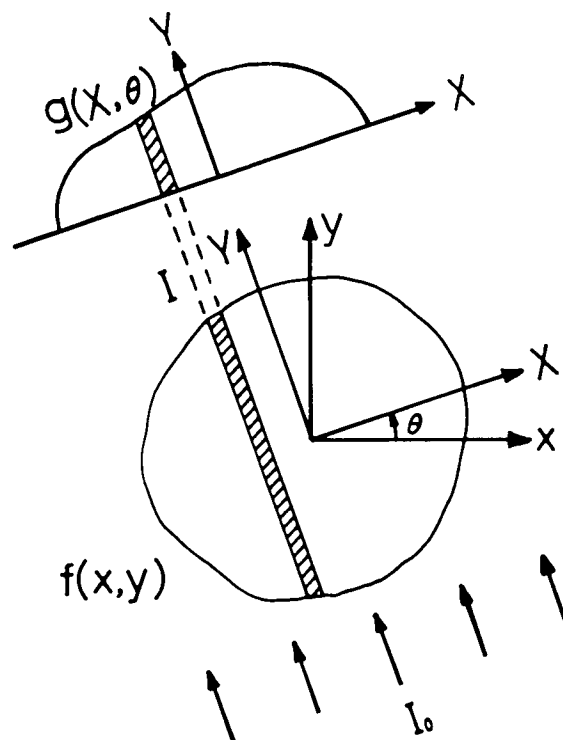
Fig.1   Prjection data g(X, θ)
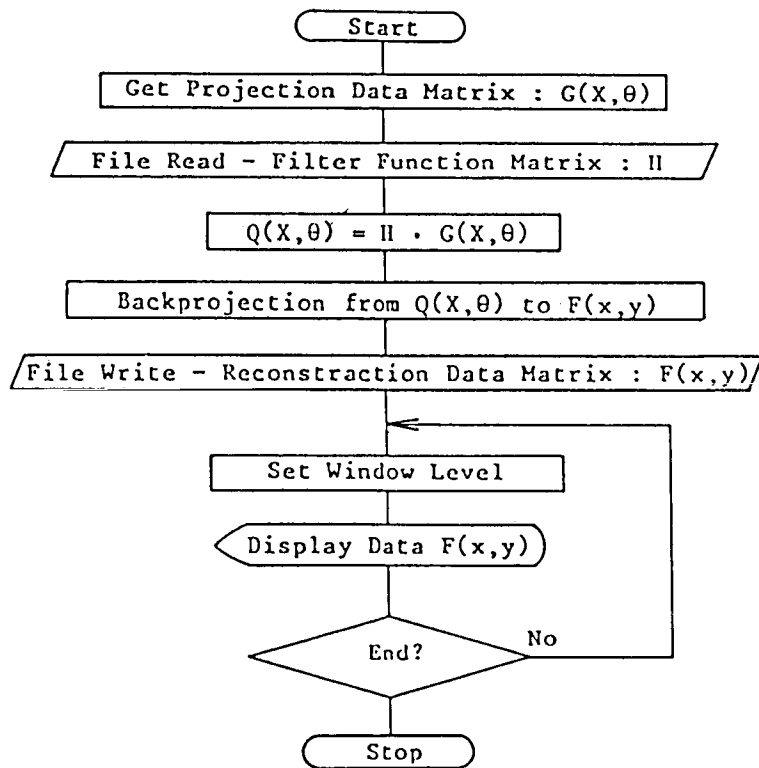
Fig.2 Flow chart of data reduction
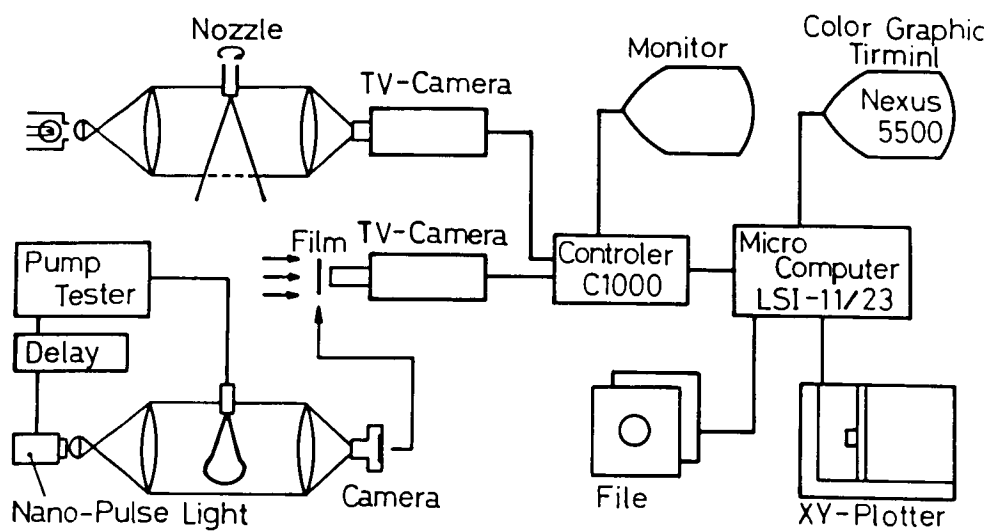
Fig.3 Equipment block diagram
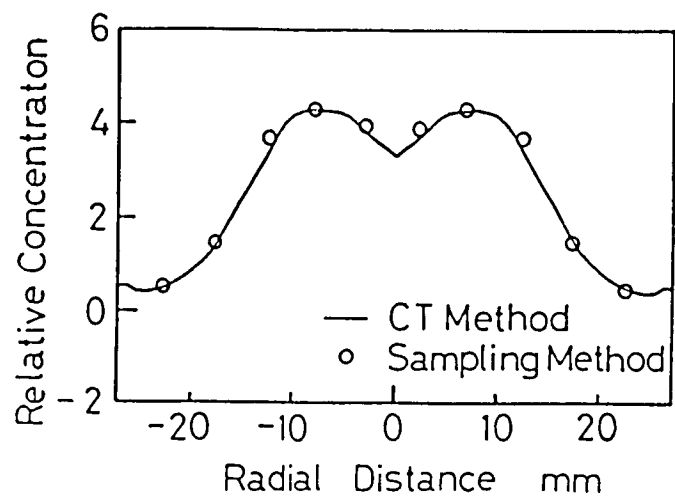
Water: P=1.08MPa Ta=293K
T_1=287K Q=1.76x10^{-6}m^3/s

Fig.4 Comparing between CT and sampling method on relative spacial concentration
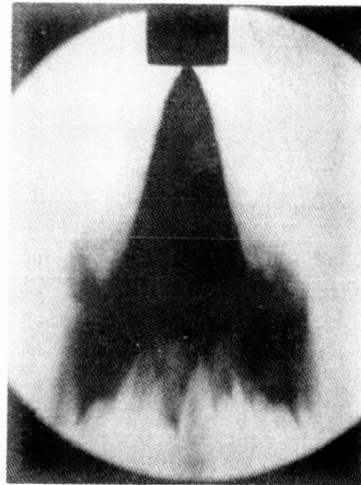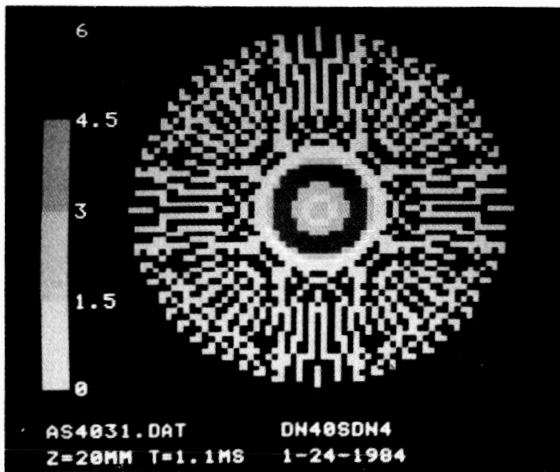
20 mm
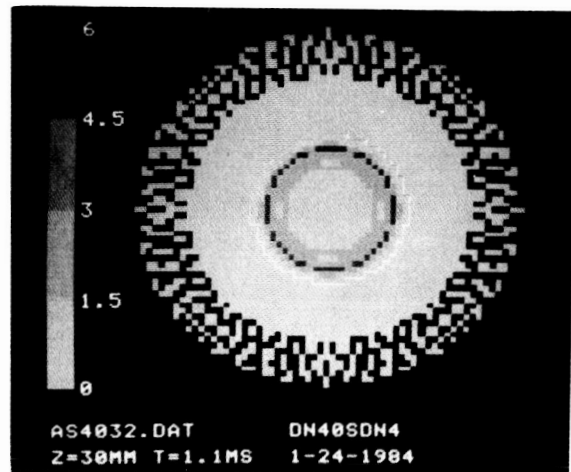
30 mm
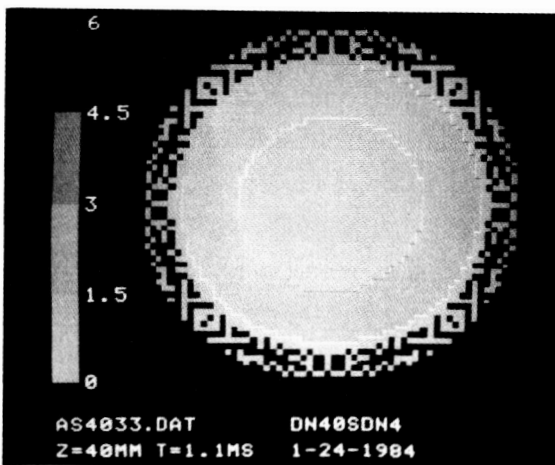
40 mm
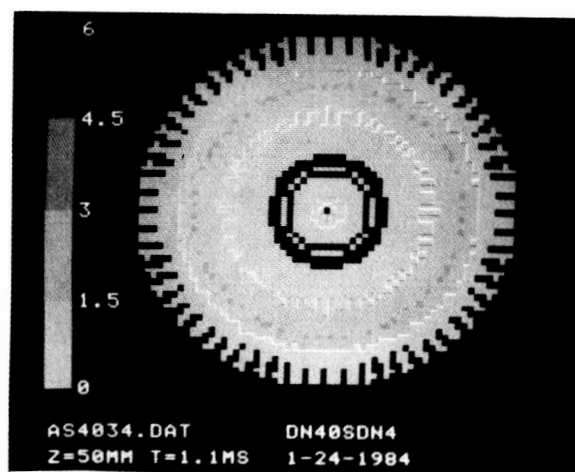
50 mm

Fig.5 Image of diesel spray structure by Computed Tomography
Psudu color corresponding to spray concentration
(Throttle nozzle for Diesel Engine)

0.9 ms

AS4022.DAT   DN40SDN4
Z=30MM T=0.9MS   1-24-1984

1.3 ms

AS4042.DAT   DN40SDN4
Z=30MM T=1.3MS   1-24-1984

1.7 ms

AS4062.DAT   DN40SDN4
Z=30MM T=1.7MS   1-24-1984

2.1 ms

AS4082.DAT   DN40SDN4
Z=30MM T=2.1MS   1-24-1984
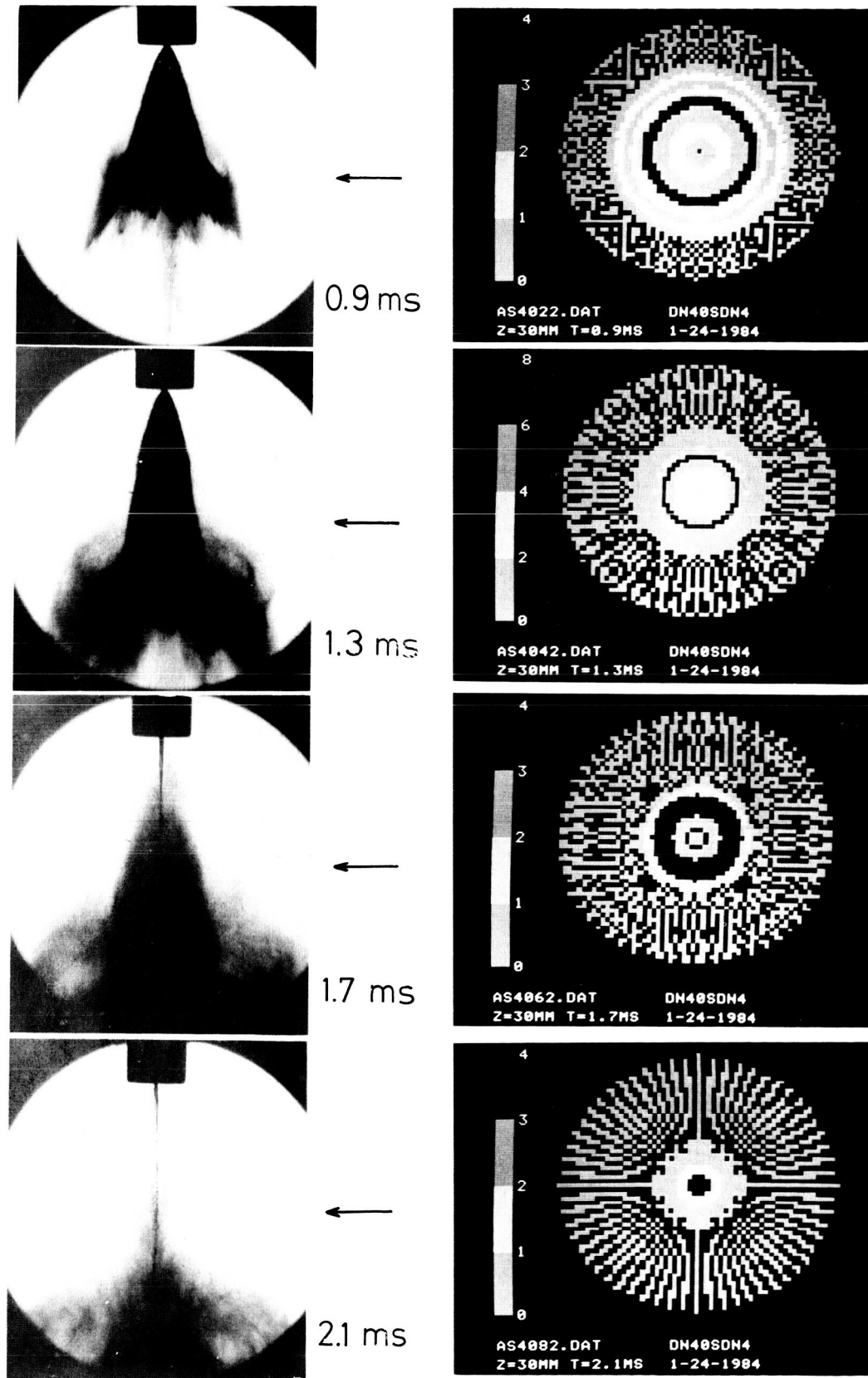
Fig.6 Time dependence of spray density distribution
by CT method
(Throttle nozzle for diesel engine)

Particle field holography data reduction by Fourier transform analysis

Cecil F. Hess
James D. Trolinger

Spectron Development Laboratories, Inc.
3303 Harbor Blvd., Suite G-3, Costa Mesa, California 92626

Abstract

The size distribution of a particle field hologram is obtained with a
Fourier transformation of the Fraunhofer diffraction pattern of the
reconstructed hologram. Off-axis absorption holograms of particle
fields with known characteristics were obtained and analyzed with a
commercially available instrument. The mean particle size of the recon-
structed hologram was measured with an error of ±5%, while the distribu-
tion broadening was estimated within ±15%. Small sections of a pulsed
laser hologram of a synthetic fuel spray were analyzed with this method
thus yielding a spatially resolved size distribution. The method yields
fast and accurate automated analysis of particle field holograms.

Introduction

Pulsed laser holography has been a very powerful technique to charac-
terize particle fields in complex environments. Examples are studies of
pulverized coal combustion[1], fuel sprays[2], and explosions[2]. However,
its use has been restricted because of the tedious effort required to

reconstruct and analyze particle field holograms. The analysis of holograms has been performed by taking photographs at various planes of interest and then analyzing the photographs in computerized image analyzers. This suffers from various shortcomings. The most important are: photographic images have associated depths of field which lead to size errors; the process, even though more automated than the more primitive visual analysis, is still tedious. Recently, a technique using Fraunhofer diffraction analysis was introduced[3]. This technique bases the size measurement in the Fourier transform analysis of the light diffracted by an ensemble of particles illuminated by a laser beam. The direct analysis of a particle field with such method has been used quite extensively[4]. The logic proposed in reference [3] is that since the Fourier transform of the Fraunhofer diffraction pattern of an ensemble yields the size distribution, such transformation will also yield the size distribution if the particles are substituted by a particle field hologram.

This technique was tested[3] in connection with on-line holograms, and its application was illustrated[5] in the measurement of pulsating fuel sprays. There are, however, problems associated with reconstructing on-line holograms such as deterioration of the reference beam and confusion between the real and virtual images.

The approach chosen by the authors and discussed in this paper was to use off-axis holography in conjunction with Fourier transform analysis. Particle fields of known characteristics were measured and compared. The results show that for Rossin Rammler size distributions the mean size was predicted very accurately (±5%), while larger errors were

experienced in the broadening parameter (±15%). Some of these errors and inconsistencies were associated with instrument alignment and extraneous noise which, for the most part, can be eliminated, primarily by increasing the diffraction efficiency of the holograms.

The interface of pulsed laser holography with a Fourier transform analyzer of the diffracted light will greatly extend the capabilities of both. The former will benefit from fast almost-in-line data reduction. The later which is a much slower process when used in conjunction with holography will provide data unattainable until now. Examples are particle sizing in turbulent combustion phenomena, where beam steering is a problem associated with light scattering techniques; explosions, where the events take place in microseconds; and time dependent sprays or other particle laden flows where it is of interest to resolve the time variation of the particle field distribution.

Theoretical Discussion

The amplitude scattered by a particle of radius a through an angle β is given by

$$A = \frac{A_i a J_1(ka\beta)}{\beta} \tag{1}$$

where A_i is the illuminating amplitude

J_1 is the Bessel function of the first kind, and

$k = 2\pi/\lambda$ and it is assumed that

$a \gg \lambda$ the wavelength of light.

If a distribution of particle sizes $f(a)$ exists, then the contribution by those of size between a and $a + da$ is to the amplitude at an angle β is

$$\frac{f(a)da \; aJ_1(ka\beta)}{\beta} \tag{2}$$

and the total amplitude in that direction is

$$A_t = \frac{A_i}{\beta} \int_0^\infty f(a)a \, J_1(ka\beta)da \tag{3}$$

What is sought in particle sizing measurement is $f(a)$ which is given by[6]

$$f(a) = \frac{-2}{ka} \int_0^\infty \beta J_1(ka\beta)Q(\beta)Y_1(ka\beta)d\beta \tag{4}$$

where Y_1 is the Neumann function and

$$Q(\beta) = \frac{d}{d\beta}\left[\pi k^3 \beta^3 \frac{I}{I_o}\right] \tag{5}$$

The above expression has been approximated numerically and is the basis for particle sizing instruments based on a measurement of the angular spectrum of scattered light. There is a one-to-one correspondence between the angular spectrum and the Fourier transform of the scattered light, and the latter is what is usually measured.

If the wavefront scattered by the collection of particles is stored in a hologram as an intermediate step and reconstructed later for analysis, it becomes of concern how the ultimate wavefront may differ from the original one.

The hologram can be represented by a transfer function. The amplitude of light reconstructed from the hologram can be written[7] (using only one of the two dimensions)

$$A_t(\beta/\lambda) = A_i(\beta/\lambda) * T(\beta/\lambda) \tag{6}$$

where

$$T(\beta/\lambda) = \int_{-\infty}^{\infty} t(y) \exp\left[j2\pi\frac{\beta}{\lambda}y\right] dy \tag{7}$$

The convolution has characteristics which can both narrow and broaden the spectrum. If the hologram is too small, then the spectrum will be broadened by its own diffraction. If it is large and perfect, then T is effectively unity. In practice, the transfer function, T, is more likely to decrease gradually with β as the film MTF decreases with

frequency. The effect is to bias the distribution of f(a) to larger particles. These above relations show that with good practice the data derived with holography as an intermediate step can accurately emulate that using the Fourier Transform directly, and they could be used to correct for holograms not having a unity transfer function.

Experimental approach

The approach chosen in this study was that of comparing the size distribution obtained by analyzing a known particle field with that of a hologram of the same particle field. To simplify the experiment, the particle field chosen was stationary thus allowing the use of a cw He-Ne laser for the acquisition of the hologram. The Fourier transformation was performed by a Malvern 2600 particle analyzer. A description of the apparatus and particle fields is now given.

Holographic system

The holographic system was a breadboarded, off-axis, through field system, having separate object and reference beams, as seen in Figure 1. The object beam was disturbed by a particle field, while the reference beam was undisturbed. The two beams interfere when they overlap on a holographic film plate.

A 25 mW Helium Neon Laser (Spectra Physics Model 107) was used as the illumination source. The beam was split with an uncoated glass beam-splitter (Newport Corporation #20B10NC.1). A split ratio of 4:1 (reference to object beam) was chosen to provide good reconstruction

efficiency while remaining in the linear region of the film. The ratio was adjusted by varying the angle of incidence to the beamsplitter, thus changing the reflectivity.

The reference beam was expanded using a 5x microscope objective and spatially filtered with a 40 micron pinhole. It was collimated by a 380 mm focal length achromatic lens and apertured to a 10 mm diameter nearly uniform intensity beam. The collimated reference beam was then directed to the holographic plate, where its peak intensity was measured at 28 $\mu w/mm^2$.

A 10x microscope objective and a 25 micron pinhole were used to expand and filter the object beam. An achromatic collimating lens, with a 125 mm focal length, produced a Gaussian object beam with a diameter of 10 mm ($1/e^2$). The object beam illuminated a particle field which was imaged on the holographic plate by 1:1 magnification lens system. This imaging system consisted of two 50 mm Olympus Lenses positioned back-to-back, connected by bellows. It collected the forward scattered radiation and the unscattered radiation and relayed them to the holographic plate. The object beam peak intensity was measured to be 6.4 $\mu w/mm^2$.

The Fourier Transform Analyzer

The receiver of a Malvern 2600 was used to collect and analyze the Fraunhofer diffraction field. A Fourier transform lens, in the receiver, collects both the forward scattered and unscattered radiation and focuses it onto a concentric photodiode array. The scattered radiation is transformed to a series of diffraction rings at the focal plane of the lens. Thirty concentric half-ring diodes receive these data

which are transferred to a minicomputer for processing. The unscattered radiation is focused on a pinhole at the focal plane of the receiving lens. This radiation illuminates a separate diode, indicating the amount of unscattered radiation.

Figure 2 shows a photograph of the holographic system interfaced to the Malvern receiver which is interfaced to a microprocessor based data reduction system. The holographic recording/reconstruction system was designed to produce holograms capable of simulating the Malvern transmitter beam illuminating a particle field.

Particle fields

Two particle fields were used throughout these experiments. The first was a calibration photomask (Laser Electro-Optics Ltd.[8] #RR 50-3.0-0.08-102.CF) which contains a known size distribution of circular particles. The second was a particle field hologram of a spray of synthetic fuel (SRCII) acquired in a previous program using a pulsed laser holographic system.

The photomask was chosen for two primary reasons:

1. It provided a known and stationary particle field of which holograms could be taken with a cw laser.

2. Both the photomask and holograms of the photomask could be analyzed and compared against an absolute invariable distribution.

JDT-22/14

The calibration standard photomask consisted of a 2-dimensional sample array of 10,000 circular discs of chrome deposited on a glass substrate. The discs are randomly oriented in an 8 mm diameter sample area. The photomask contains a Rossin Rammler size distribution with $\overline{X}$ = 50 μm and a width parameter of 3.0 (Figure 3).

The particle field hologram described here containing a synthetic fuel spray was taken previously using a pulse ruby laser holocamera. The receiving optics provided a premagnification of 3:1. It has previously been determined, through existing reconstruction techniques, that the mean size of the spray droplets in this hologram lies in the range from 50 to 100 μm (depending on location) which will be interpreted as 150 to 300 μm on the magnified image of 3:1.

Procedure to align the Malvern receiver

The reconstructed image of the hologram must be collected by the receiving lens (we used the 300 mm in all the tests) and focused on the diode array. Since the receiving lens of the Malvern has no focus adjustment, it is important that the reconstructed unscattered radiation be collimated and, therefore, produce a sharp focus on the hole in front of the center diode.

The receiver was then steered until its optical axis was parallel to the reconstructed unscattered lighty. It was then translated vertically and horizontally until the light beam entered through the center of the lens.

The final fine adjustments were made with the adjustment screws of the receiver.

JDT-22/14

Signal level requirement

We established that the radiation power of the reconstructed holo-
graphic image was typically between .15 mw and .25 mw. This can be
obviously increased using a more powerful laser or increasing the dif-
fraction efficiency of the hologram (using phase holograms). Since the
Malvern apparatus uses a 2.5 mw laser, we had to establish the perfor-
mance of the photodiode array at low power. The procedure consisted in
illuminating the photomask with different levels of laser power. For
this purpose, a variable neutral density filter was placed in front of
the laser such that the total power of the light incident on the
receiver varied between 50 µw and 2.5 mw. Under each one of these laser
power levels we obtained a size distribution using the Rossin Rammler
and the model independent softwares. Power levels of 100 µw and more
produced the same size distribution of the photomask. Power levels
below 50 µw were not acceptable. It was also necessary, in order to
work with the low power levels, to darken the room to reduce background
radiation. Based on these results, it was expected that the typical
150 µw signal obtained from the reconstructed image would be adequate.
Let us point out again that higher signal levels could be attained by
reconstructing with a more powerful laser or by producing more efficient
holograms. Obviously, increasing the diffraction efficiency without
compromising the linearity would be the preferred choice since part of
the noise comes from scatterers on the emulsion.

Results

Three particle fields were Fourier transform analyzed: (1) a calibration reticle or photomask, (2) a reconstructed image of a hologram of such photomask, (3) reconstructed image of a spray hologram.

The two different softwares provided by Malvern were used where appropriate. The first finds the best fit to a Rossin Rammler distribution, while the second is supposed to be independent of a preconceived model. The values of $\overline{X}$ and N (defined below) were obtained with the Rossin Rammler distribution and are indicated in the figure legends of the model independent data.

The photomask data are summarized on Table 1. This table shows the data obtained by analyzing the scattered light of the reconstructed holographic image of the photomask, and also the light scattered from the direct photomask. The parameters describing the size distribution are $\overline{X}$ and N which are the two parameters of the Rossin Rammler distribution which is given by:

$$V = e^{-(X/\overline{X})^N} \quad , \tag{8}$$

where V is the volume fraction of drop material occurring in drops of diameter greater than X. The volume distribution is given by:

$$\frac{dv}{dx} = \frac{NX^{N-1}}{\overline{X}^N} e^{-(X/\overline{X})^N} \tag{9}$$

TABLE 1

PHOTOMASK DATA

Particle Field	Particle Hologram No.	Background Hologram No.	t_A	η_D	$I_o(mw)$	$\bar{X}$	N	Comments
Hologram of Photomask	12	13		2%	.094/.105	48.2	3.5	Aligned receiver to background only
	12	13		2%		47.4	2.6	Aligned receiver to background only
	12	13		2%		45.2	3.8	Aligned receiver to background and to particle hologram
	21	20	20%	3%	.14/.15	47.4	2.9	Data hologram slightly misplaced
	21	20	20%	3%	.14/.15	50.4	3.8	Data hologram reposi-tioned properly
	21	20	20%	3%	.14/.15	52.1	3.9	First thing in the morning without realigning receiver
	21	20	20%	3%	.14/.15	51.5	3.7	After minor alignment
	21	20	20%	3%	.14/.15	50.5	3.8	
Direct Photomask					1.25	50.6	3.4	3-15-84
					0.14	50.6	3.4	
					0.12	50.8	3.2	3-12-84

8423803Ta/

The SMD is related to $\overline{X}$ and N by the expression:

$$SMD = \frac{\overline{X}}{\Gamma(1 - \frac{1}{N})}$$

(10)

To illustrate the effect of $\overline{X}$ and N on the size distribution, Figure 4 shows two volume distributions corresponding to $\overline{X}$ = 50 and N = 3 and 3.5. Large values of N correspond to narrow distributions.

Light Energy Distribution

The light energy distribution of the photomask and its holographic reconstructed image were also analyzed (Figure 5). One of the difficulties encountered in processing the holographic data stemmed from the inaccuracy in repositioning the hologram. Some of the unscattered radiation would miss the central diode and illuminate the second diode. This will show as a bin in the large size band. Figure 5 illustrates this problem. Notice the large energy level measured on Bin #15 of the holographic data. In general, however, the agreement shown between the light energy distribution produced by scattering from the real photomask and the reconstructed hologram is quite good. This probably justifies the results obtained with the Rossin Rammler software. Namely, $\overline{X}$ = 51.5, N = 3.7 for the reconstructed hologram, and $\overline{X}$ = 50.6, N = 3.4 for the direct photomask. It is not, however, clear why the N value of the hologram is larger (3.7) than the corresponding photomask

(3.4). A large value of N is associated with a narrow distribution and
it is not clear that this should be the case, given that the hologram
has additional noise which should broaden the distribution. This might
be the result of an artifact of the inversion scheme software.

Spray Hologram Data

A hologram of a spray field of synthetic fuel (SRCII) previously
acquired with a pulsed ruby laser was then analyzed. This hologram was
obtained using (almost) uniform object and reference beams and a premag-
nification of 3. To best simulate the conditions normally used by the
Malvern, a Gaussian beam of 6 mm diameter ($1/e^2$) was used for recon-
struction. The reconstructed image had a total power of about 0.25 mw
and a (almost) Gaussian intensity profile. The divergence of the illum-
inating reconstruction wave was controlled to produce a well collimated
reconstructed wave.

Three regions of the hologram were reconstructed and analyzed with
the receiver, and a region without spray was used to obtain the back-
ground information. These data are shown on Figure 6. It is important
to realize that since the hologram was acquired with a 3:1 magnifica-
tion, the actual droplet size is 1/3 of that shown.

Figure 6 shows photograph of a given plane of the 3-D hologram, and
inserts corresponding to the locations where data were acquired. Notice
that the mean value changed from 285 µm (actual size 95 µm) at the edge
of the spray to 165 µm (actual size 55 µm) at the center. This is the
typical trend of sprays formed by simple pressure nozzles in which more
large droplets are found at the edge of the spray.

Acknowledgments

References

1. Trolinger, J. D. and Heap, M. P., Applied Optics, 18, 1757 (1979).

2. Wuerer, J. E., Oeding, R. G., Poon, C. C., and Hess, C. F., AIAA 20th Aerospace Sciences Meeting, AIAA-82-0236 (1982).

3. Ewan, B.C.R., Applied Optics, 19, 1368 (1979).

4. Swithenbank, J., Beer, J. M., Taylor, D. S., Abbot, D., and McCreath, G. C., AIAA 14th Aerospace Sciences Meeting, AIAA-76-69 (1976).

5. Ewan, B.C.R., Swithenbank, J., and Sorusbay, D., Optical Engineering, 23, 620 (1984).

JDT-22/14

6. Abbiss, J. B., "Theoretical Aspects of the Determination of Particle-Size Distributions from Measurements of Scattered Light Intensity." Royal Aircraft Establishment TR70151, August 1970.

7. Goodman, J. W., <u>Introduction to Fourier Optics</u>, p.52, McGraw Hill (1968).

8. Hirleman, E. D., ASME Gas Turbine Meeting, ASME Paper No. 83-GT-232.

JDT-22/14

LASER (25 MW HENE)

1. SHUTTER
2. BEAMSPLITTER
3. 5X OBJECTIVE WITH 40 μM PINHOLE
4. 380 MM ACHROMATIC LENS WITH 10 MM APERTURE
5. 10X OBJECTIVE WITH 25 μM PINHOLE
6. 125 MM ACHROMATIC LENS
7. PARTICLE FIELD PHOTOMASK
8. 2-50 MM OLYMPUS LENSES
9. HOLOGRAPHIC PLATE

SCALE: .13" = 1"
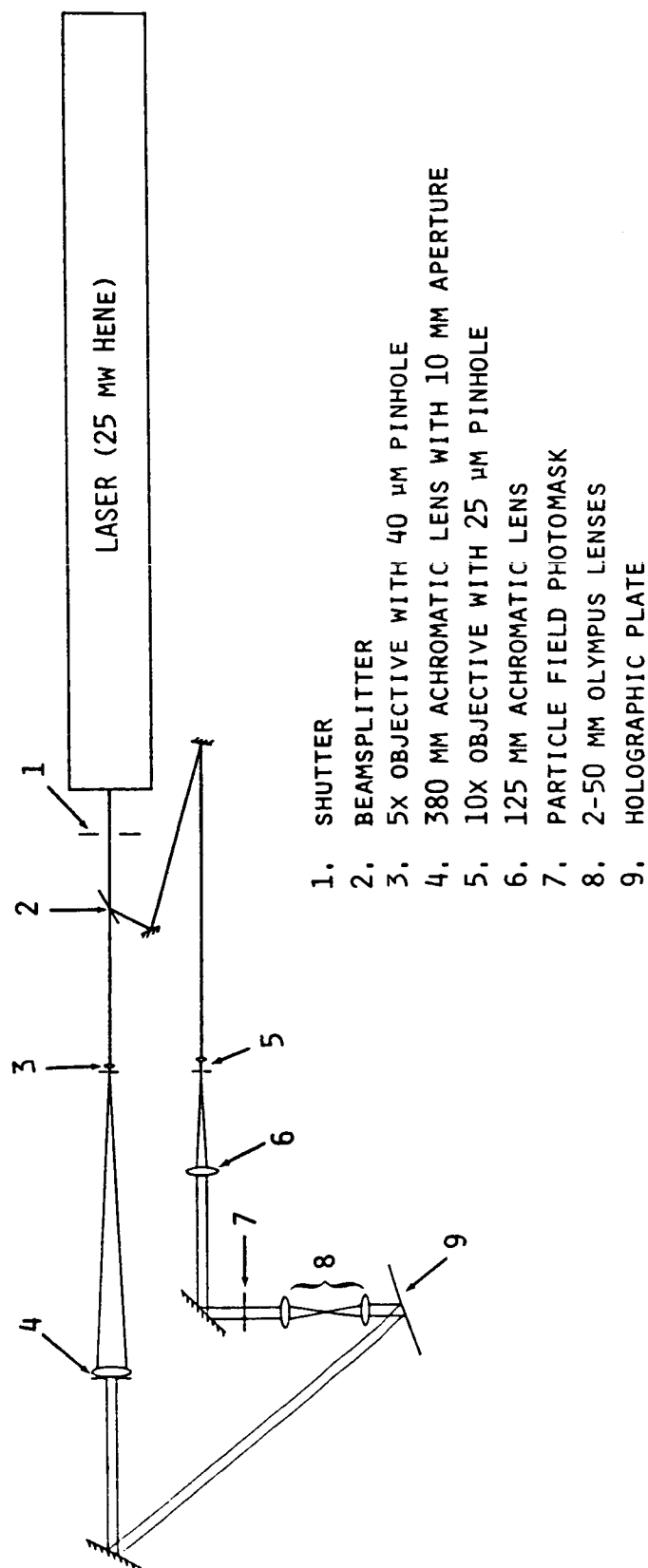
Figure 1. Schematic representation of the holographic system.

557
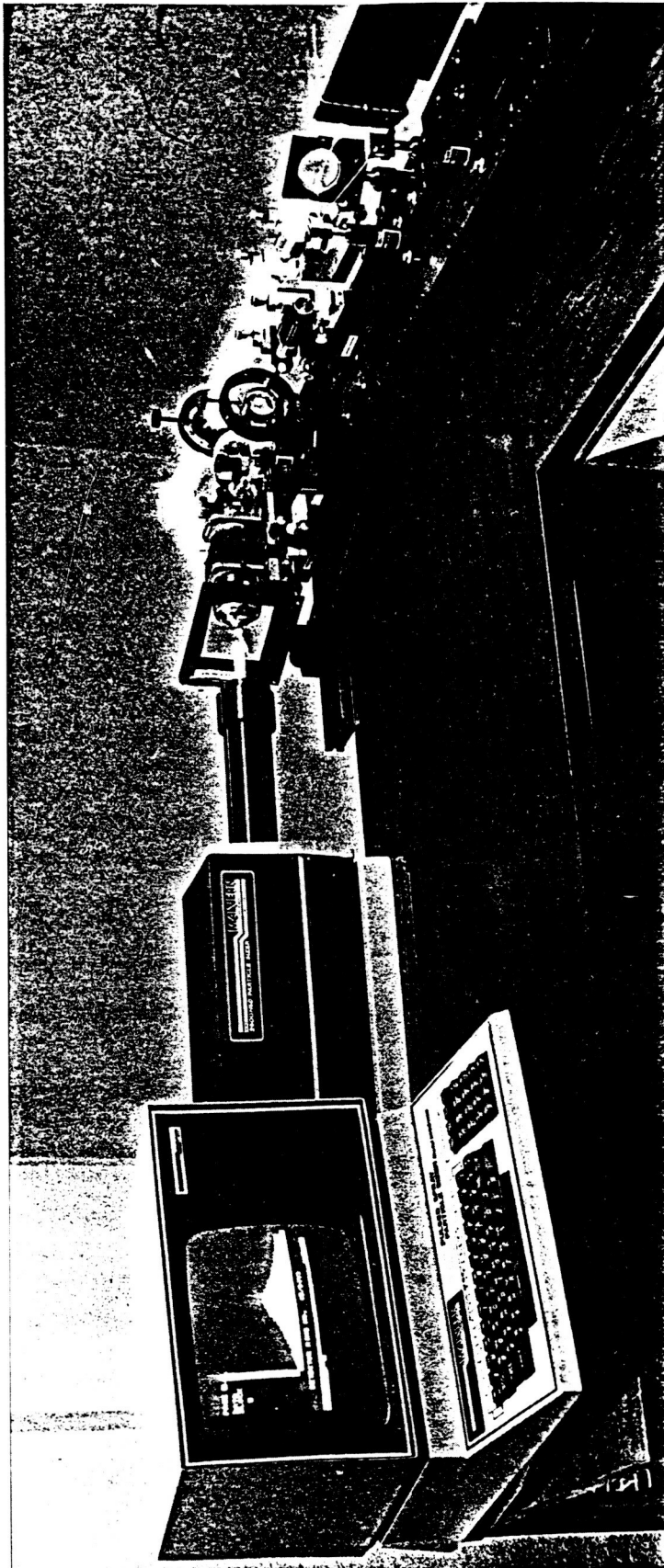
Figure 2. Photograph of holographic system interfaced to the Malvern receiver.
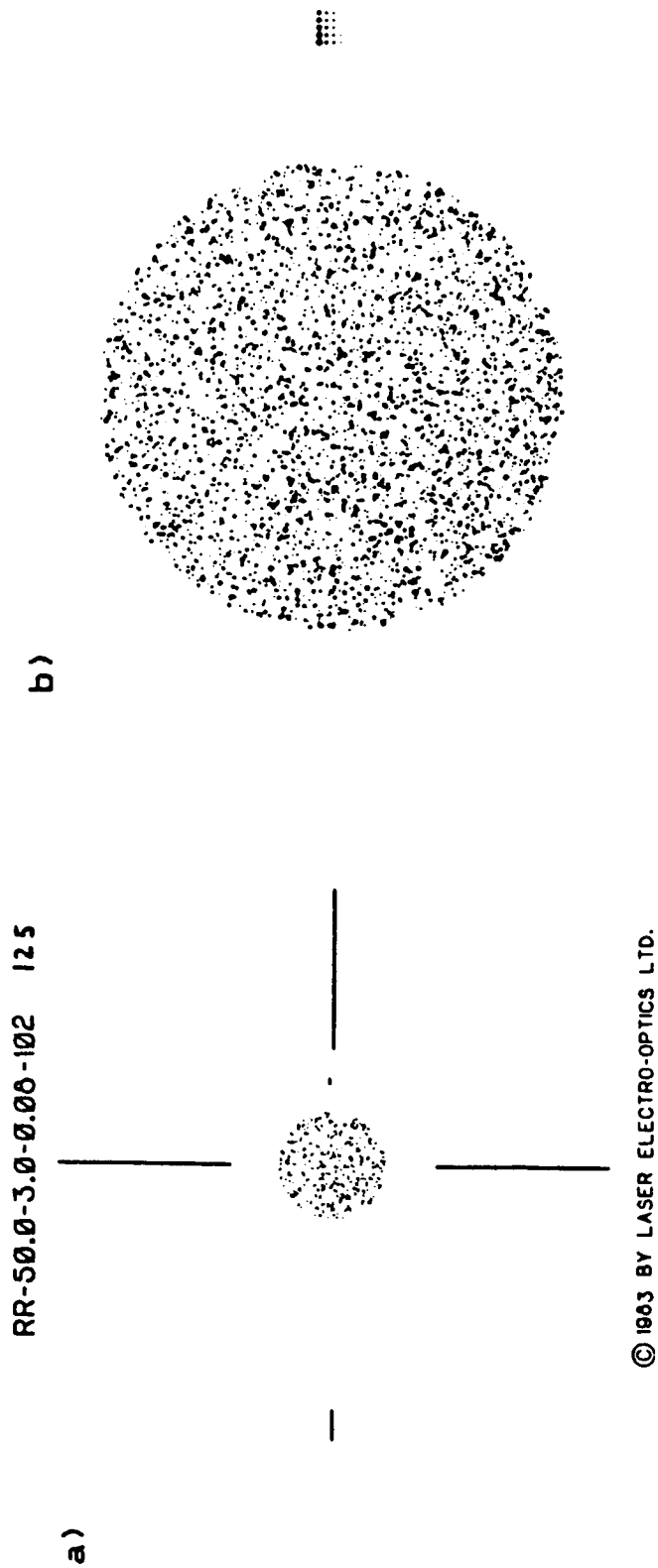
Figure 3. Photograph of calibration reticle RR-50-3.0-0.08-102-CF.
(a) Magnified 1.5X.
(b) Sample area and quality control array magnified 6.37X.

RR-50.0-3.0-0.08-102   125

© 1903 BY LASER ELECTRO-OPTICS LTD.
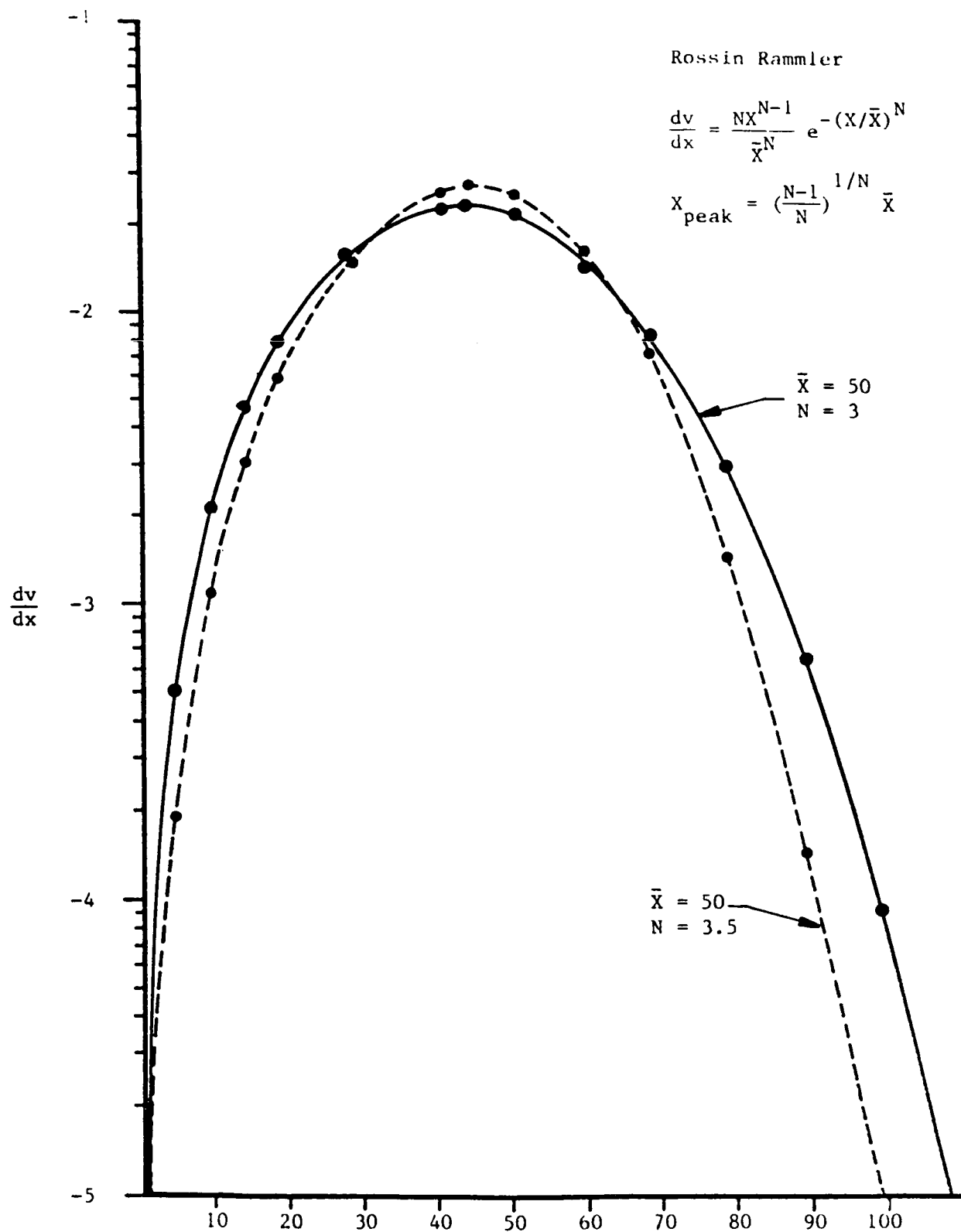
Figure 4. Effect of N on Rossin Rammler volume distribution.
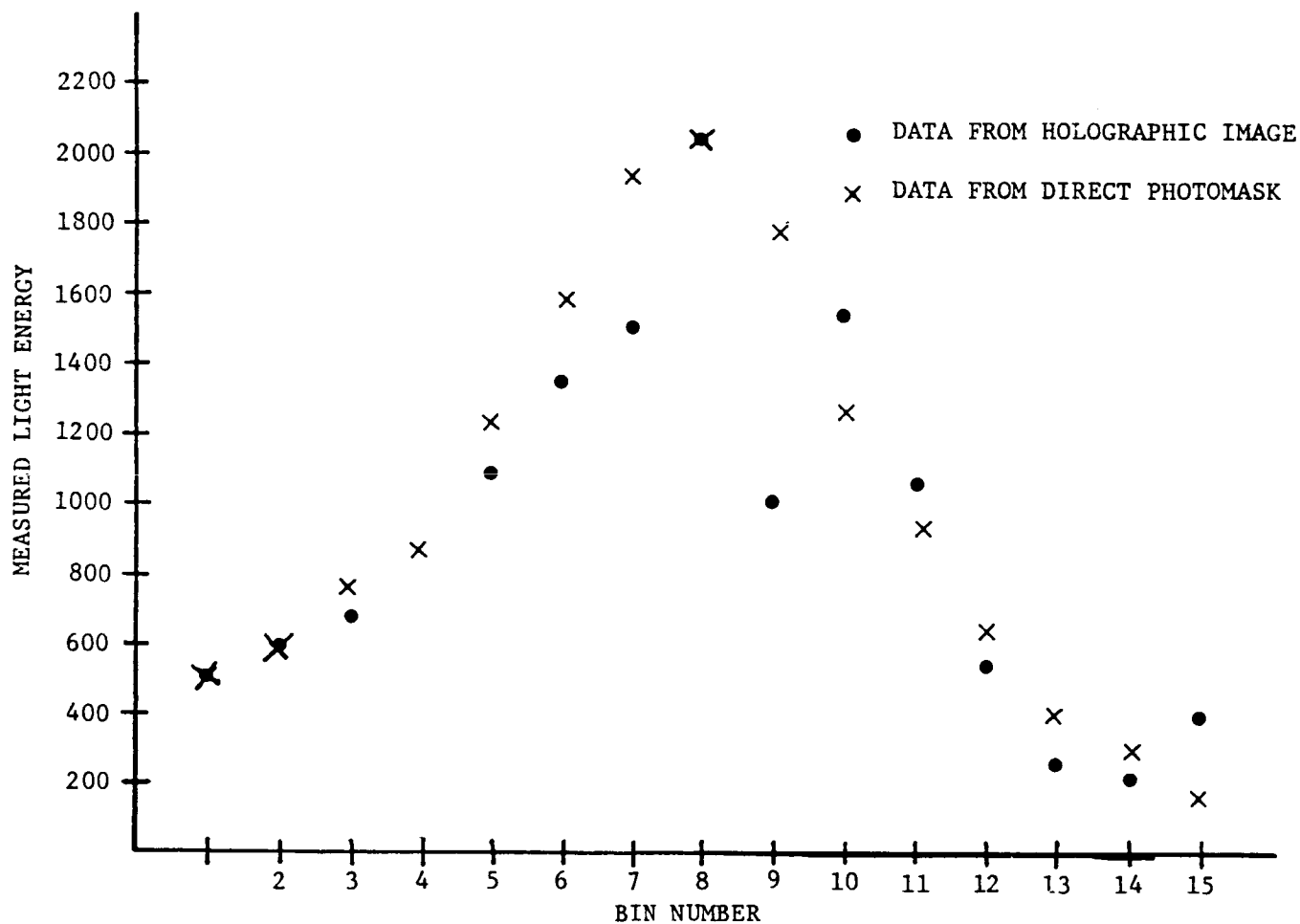
Figure 5. Measured energy levels of the lights scattered by photomask and hologram of photomask on 15 diodes of Malvern receiver. The corresponding Rossin Rammler parameters are $\overline{X}$ = 50.6, N = 3.4 (direct photomask), and $\overline{X}$ = 51.5, N = 3.7 (reconstructed hologram of photomask).

FOURIER DIFFRACTION ANALYSIS

OF A FUEL SPRAY HOLOGRAM

$\bar{X}$ = 165 μm
N = 2.22

$\bar{X}$ = 285 μm
N = 2.03

$\bar{X}$ = 264 μm
N = 2.57

FUEL : SRC 2
NOZZLE : SIMPLEX
CONDITIONS : 100 PSI, 75°F
PRE-MAGNIFICATION OF SPRAY HOLOGRAM : 3X
$\bar{X}$,N : PARAMETERS OF ROSSIN RAMMLER DISTRIBUTION

SCALE FOR DETAIL VIEWS:
500 μm ⊢⊣
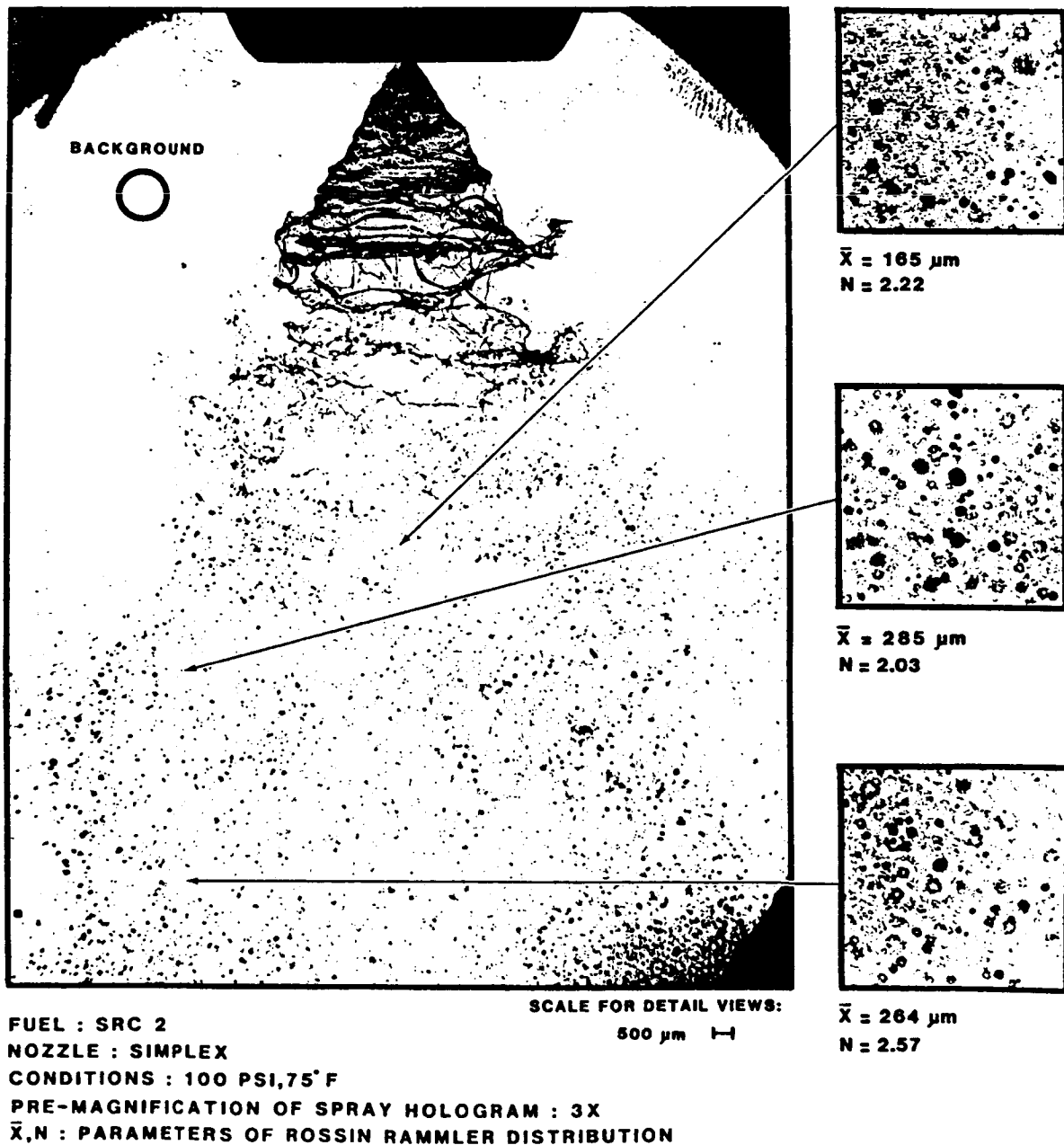
Figure 6.   Fourier transform reduction of a spray hologram
obtained with a pulsed ruby laser.

KEY WORDS

1. Particle field holography

2. Automated data reduction

LIST OF FIGURES

PARTICLE AND FLOW FIELD HOLOGRAPHY
A Critical Survey

J. D. Trolinger
Spectron Development Laboratories, Inc.
3303 Harbor Blvd., Suite G-3
Costa Mesa, California 92626

Abstract

A brief background is provided for the fields of particle and flow visualization holography. A summary of methods currently in use is given, followed by a discussion of more recent and unique applications. The problem of data reduction is discussed. A state of the art summary is then provided with a prognosis of the future of the field. Particle and flow visualization holography are characterized as powerful tools currently in wide use and with significant untapped potential.

Introduction

Strictly speaking, the first application of holography to the study of particles was by Dennis Gabor himself who invented holography in 1947.[1] He produced holograms of a variety of microscopic samples using partially coherent light since lasers were not available for another fifteen years. His application intended to exploit the magnification properties of holograms and not the three dimensional imaging properties. Nearly another twenty years passed before holography left the research laboratory to actually be applied in a field environment. The first such work appears to be that of Thompson and coworkers[2] who used the three dimensional properties of holograms to characterize fog droplets.

The first significant work with flow visualization holography appears to be that of Brooks, Heflinger, and Wuerker who used holographic interferometry to determine the flow field around projectiles in flight.[3] During the past twenty years virtually every test facility in the world with a need for flow diagnostics has incorporated holography to some extent, with some measure of success. Hundreds of publications have reported new innovations, techniques, refinements, and hardware. Many of these amounted to laboratory feasibility demonstrations of a new variation on recording or data extraction and never made it outside the laboratory. One of the first major test facilities to incorporate holography into an operational wind tunnel was the Arnold Engineering Development Center in Tennessee.[4] Research facilities of NASA, Army, Air Force, Navy, and aerospace companies began using or at least exploring the possibility of using the techniques during the early 1970's. European and Asian countries also began incorporating this technology into such facilities.

85-68083/17

Unfortunately, the development of practical data handling techniques lagged far behind what was required to compete with conventional photographic techniques.[5] Holography systems required expert operators and they required more of almost everything when compared with the highly refined science of photographic recording. The result was that the use of holography as a routine tool actually seemed to decline in the major test facilities by the late 1970's. Flow visualization holography has not replaced more conventional methods, but it has become more of a compliment. When a very distinct set of conditions or requirements obtain, flow visualization holography is often the best, or least expensive, or quite often the only way to obtain a desired set of data. It is usually, but not always, the more difficult method since it usually involves less refined, more complicated hardware.

Particle holography has satisfied a need which is so basic to the study of particle fields that its use has continued to grow steadily since the first application.[6] Even though the data handling problem has not been totally solved here either, the number of applications requiring the features of holography has continued to fuel its development and use. With present technology, holography is the only recording method by which one may record an accurate three-dimensional image of a dynamic event. This is particularly useful, for example, in the microscopic examination of combustion and explosive events, droplet breakup and formation mechanisms, and velocity measurement of droplet fields.

Beyond this brief historical survey the intent of this survey is to examine the current status of particle and flow field holography, including a summary of the present state-of-the-art, a summary of the applications and where they are being made, and a prognosis for the future. Particle and flow field holography are commonly treated together since many of the applications involve both technologies. However, the characteristic requirements for holocameras and data reduction for the two techniques are so different that they must be described individually.

A summary of methods

Particle Field Holography

There are two types of recording procedures for recording holograms of particle fields: in-line holography and off-axis holography. With in-line holography a simple wavefront (plane or spherical) is passed through the particle field, which must be about 80 percent transparent for this to be successful. Some of the light is scattered (the object wave) by the particles and some of the light passes through unscattered (the referenced wave). These two waves interfere, creating a diffraction pattern which when recorded is the hologram. With off-axis holography, light which has scattered from the particle field is mixed with a mutually coherent wave which has taken a second path around the particle field (the reference wave).

A second level of classification for both types of holography comes with the use of lenses or mirrors to image the particle field and producing a hologram of this image (appropriately termed image holography). A wide range of imaging systems may be chosen depending on the special needs of a given experiment. Imaging is commonly done to impart a convenient size, location, or magnification to the field of interest, or to relax the required recording capabilities of the hologram.

Off-axis holography is much more versatile with respect to type of object illumination. Off-axis holograms can be categorized according to whether the object illumination is a simple wavefront (plane or spherical), a diffused wavefront, or a structured wavefront. The most common type of structured wavefront in current use is the so-called "sheet of light" produced with a cylindrical lens and a small diameter collimated beam of light. Figure 1 is a categorization of the possible types of recordings that have unique characteristics. Clearly, a large number of combinations are possible. The holocamera itself must be engineered to accomplish the following tasks:

1. Properly illuminate the field of interest.

2. Place the interest field or its image in a suitable place relative to the hologram.

3. Achieve an acceptable F-number for the desired resolution.

4. Deal with environmental factors.

5. Meet coherence requirements.

6. House the film or plate transport, laser, and optics

7. Produce a hologram of acceptable quality.

The reconstruction system must be compatible with the holocamera and must be designed to produce a reconstructed image which is sufficiently bright, noise free, aberration free, the right size, and in the right location for analysis. An extremely important part of this system must cast the data into a useful form. The images may be recorded as photographs, or analyzed directly by an image analyzer.

The question that is often asked is "How many photographs are in a hologram?" This can actually be computed to some degree of accuracy. The resolution limit in an imaging system is given by

$$R \approx \frac{S}{D} \lambda$$

where S is the object distance, D is the diameter of the imaging system, and λ is the wavelength of light. (See Figure 2).

The depth of field in such an image is given by

$$\delta \approx \left(\frac{S}{D}\right)^2 \lambda \approx \frac{R^2}{\lambda}$$

567

Figure 1. Hologram Classification

RESOLUTION ELEMENT, R

$$\ell_s = \frac{RD_h}{2.4\lambda}$$

SAMPLE VOLUME LENGTH IN WHICH HOLOGRAM CAN PROVIDE RESOLUTION, R.

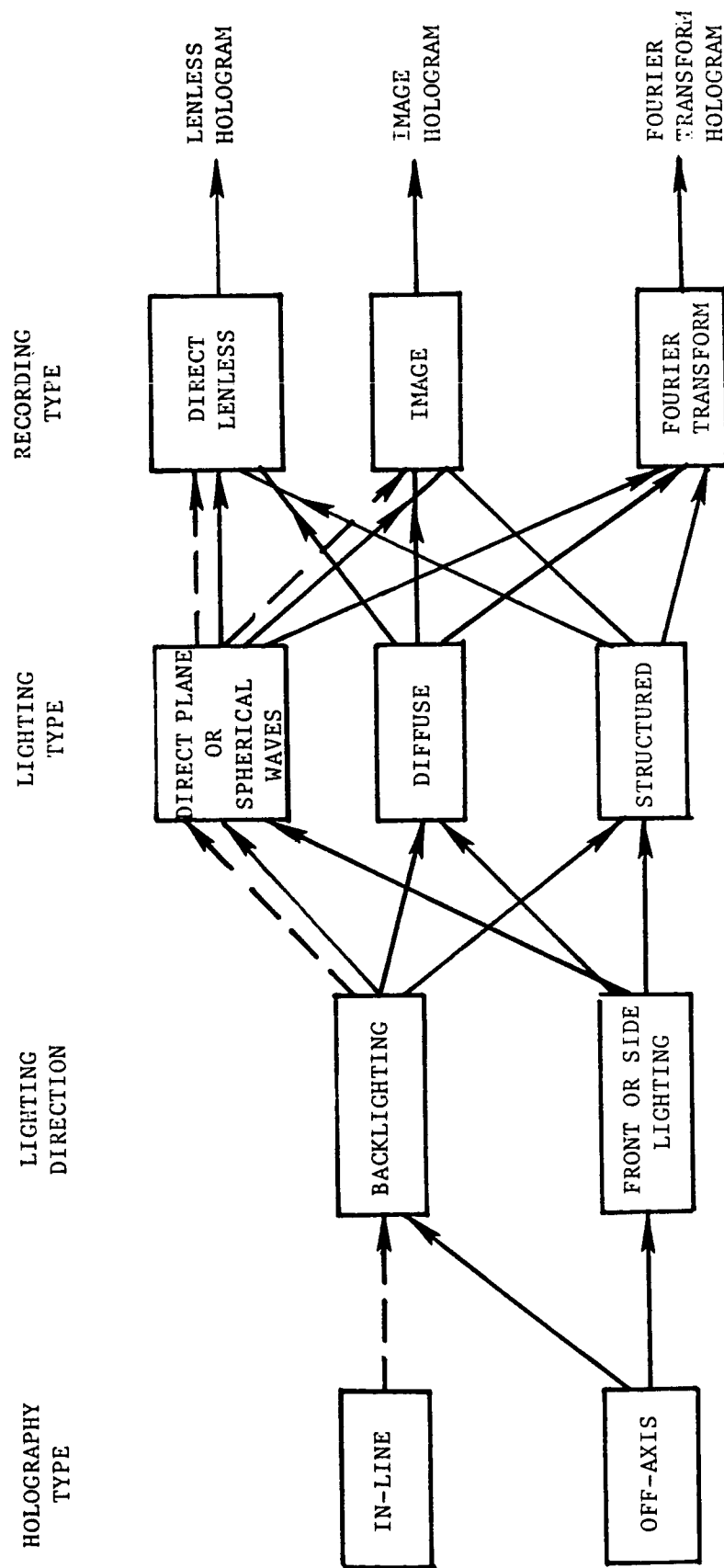ℓ_s

HOLOGRAM

D_h

ℓ_s

DEPTH OF FIELD AT RESOLUTION R is
$\delta = R^2/2\lambda$
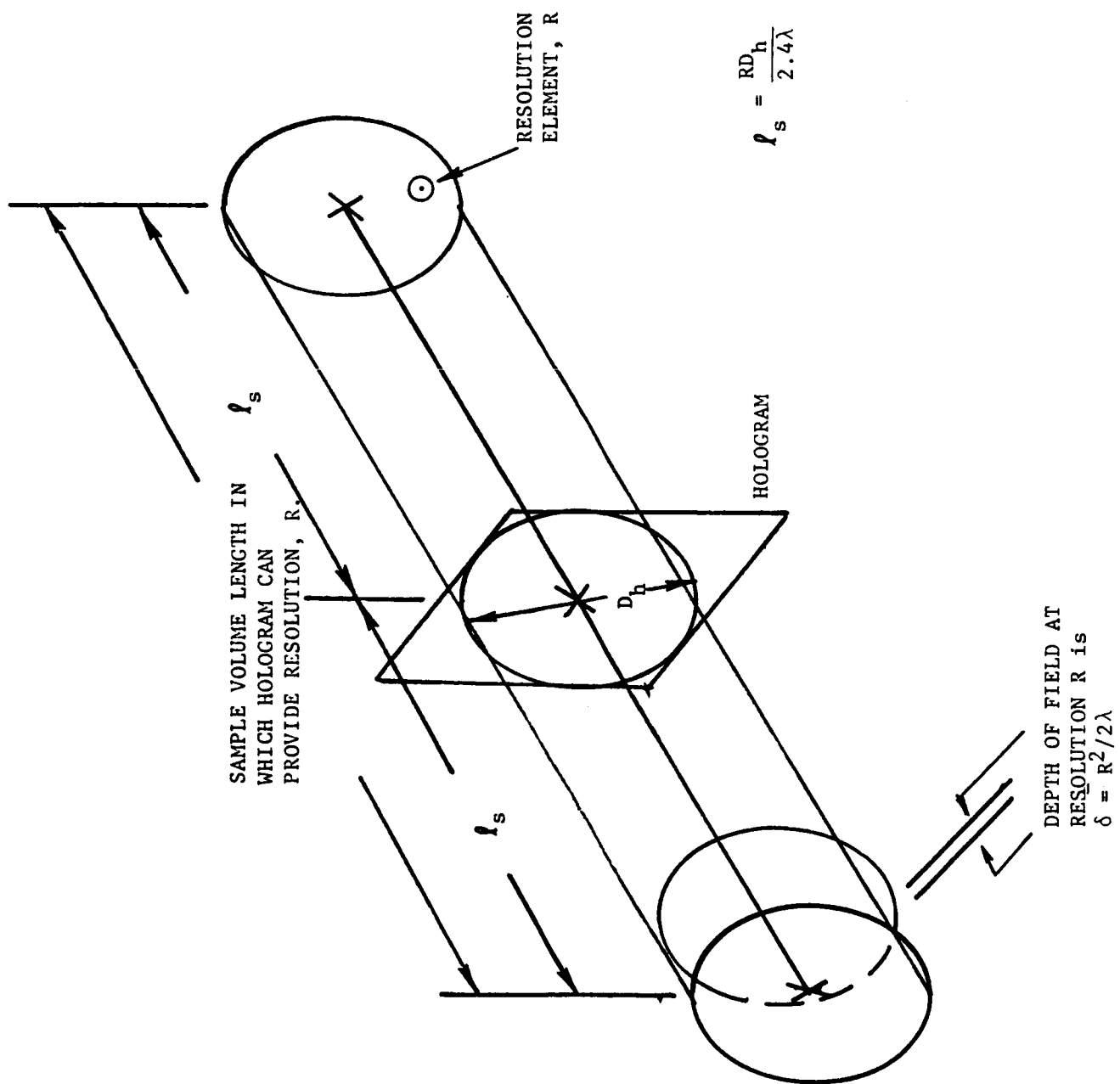
Figure 2. The Sample Volume in a Hologram

A perfect hologram of diameter, D_h, can resolve an image of size, R, if it lies within a distance RD/λ. The ratio of the two sample volumes is therefore equal to the number of distinctively different photographs which can be produced from the hologram and is approximately

$$n \approx \frac{2D_h}{R}$$

When one considers a study of particles of 10 micrometers in diameter in a typical 10 cm. diameter hologram, this number comes to a staggering 20,000 photographs, not counting the photographs which could be taken outside of the sample volume at lower resolution. This provides a clue to the difficulty in data reduction.

Double pulsed holography has been used extensively to study the dynamics of particle fields.[7] Figure 3 illustrates such a hologram of the particle field of a spray nozzle. The central figure is a global view of the entire field while the insets illustrate high resolution focusing at different depths in the field. Two superimposed three-dimensional fields present an extremely complicated image. A variety of ingenious techniques have been devised to overcome the complexity. By giving different exposures to the two recordings one can tell which image belongs to which exposure. Still more elegant methods record the two exposures with two different reference waves or even two different wavelengths. Then during reconstruction the two images can be viewed independently. The so-called "flicker method"[8] shifts back and forth between the two images allowing one to observe the motion. Still another alternative is to reconstruct the two images with reference waves which have been phase- shifted by 180 degrees so that the images will subtract, eliminating the constant noise which would otherwise appear in both recordings and which would otherwise add coherently with the signal, severely reducing the signal-to-noise ratio.[9]

Holocameras can be equipped with any laser which meets coherence requirements; however, except for rather slow moving distributions, pulsed lasers are required. Most commonly, frequency doubled YAG or ruby lasers are used. In recent years, YAG lasers have become more popular because of their ability to operate at higher rep rates. Typical pulse times for YAG lasers are tens of nanoseconds and rep rates are typically tens per second, as compared to ruby lasers with typical rep rates of a few per minute.

Flow Visualization Holography

In flow visualization, the object is usually a phase object and therefore off-axis holography is almost always required. The wavefront which has passed through the flow field and has been modulated by the field can be recorded in its entirety for later analysis. Later analysis may be accomplished by any of the conventional methods of wavefront analysis. Such methods include shadowgraph, Schlieren, deflectometry,

85-68083/17

DOUBLE EXPOSURE HOLOGRAPHY OF A CONICAL SPRAY

10 μs pulse separation

500 μm for detailed views
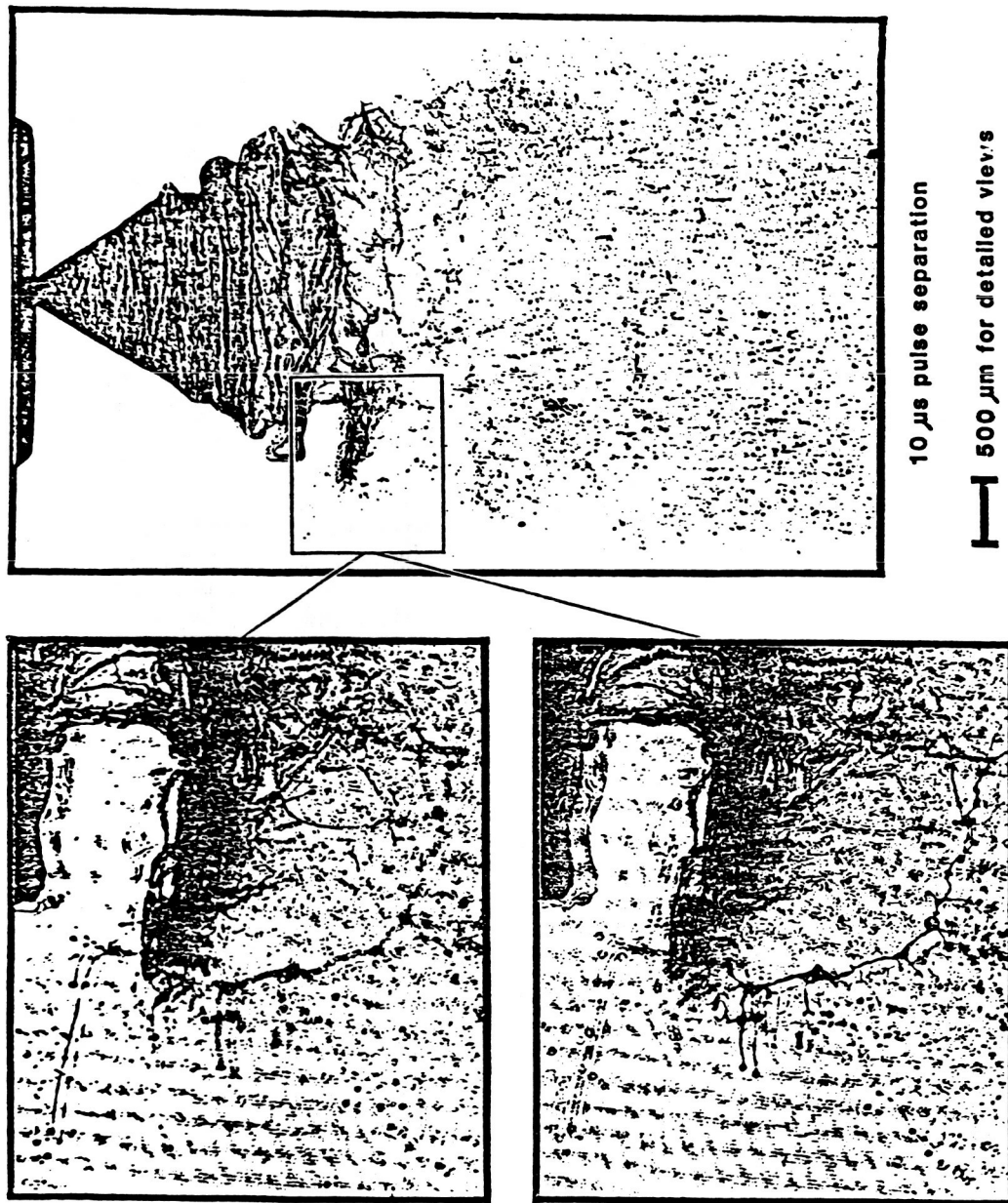
FIGURE 3.

Hartmann, moiré, or interferometry. A significant fact is that one does not have to select which of these will be used until later. Any, or all, of these can be applied to the reconstructed wavefront.

An extremely important technique is to store a wavefront which has been modulated by the optical system only, including the windows in the test facility for later comparison with a wavefront which is also modulated by the flow field. In this way, the effect of the optics can be subtracted from the measured wavefront exactly, allowing the use of low cost optics. Figure 4 briefly summarizes holographic interferometry options for flow diagnostics. Each of these methods has some unique characteristic which makes it ideally suitable for some specialized application.

Figure 5 illustrates the typical flow visualization holocamera, commonly built into a conventional flow visualization system. The system is broken into elements with the possible choices of components listed to illustrate the characteristic state-of-the-art system.

Current applications

This section is intended to provide a summary of current applications and where they are being conducted. At the present time, the use of holography is so wide spread that every application cannot possible be covered here. So this must be considered a highlighting of applications and apologies are offered to those who have been omitted.

Since some applications involve simultaneous particle and flow diagnostics, the discussion here is not exactly divisible into the two areas. Therefore, some intermixing of the discussions seemed inevitable.

Flow Diagnostic Applications

A significant feature of many modern day applications, which has changed from the past, is the number of holograms and recording rate. Early applications of holography commonly amounted to the recording of a few holograms during a day or in extreme cases, a few hundred. In today's experimental applications it is not uncommon to record thousands or even tens of thousands of holograms. This has placed even greater demands on data reduction. Table 1 provides a summary of applications of particle and flow visualization holography, with emphasis primarily on U.S. Government laboratories and universities. Some of these will be discussed in more detail here. An exciting NASA application by Marshall Flight Center is scheduled in the Space Lab 3^{10} space shuttle mission for May, 1985. This will be the first application of holography in space. The system's somewhat unique design was required by the nature and constraints of the space shuttle laboratory. The application is to observe the growth of a crystal in zero gravity and to measure density gradients in the solution surrounding the crystal. Two holocameras and a Schlieren system are combined into a single optical system.

85-68083/17

FIGURE 4A.

HOLOGRAPHIC INTERFEROMETRY WITH
SINGLY EXPOSED HOLOGRAMS
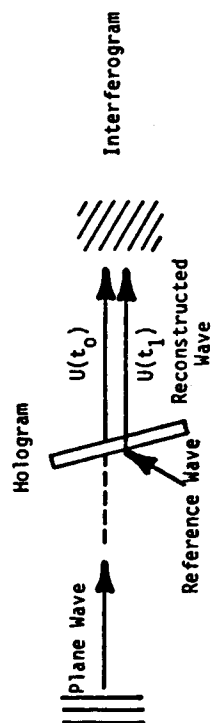
82-68001-5

A. HOLOGRAPHIC INTERFEROMETRY WITH A SINGLE HOLOGRAM
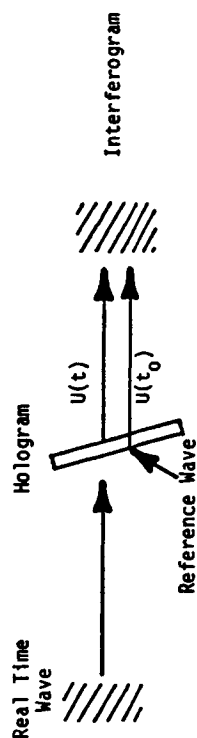
B. REAL TIME HOLOGRAPHIC INTERFEROMETRY
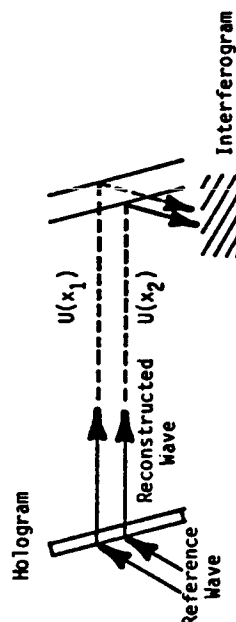
C. HOLOGRAPHIC WAVE SHEARING INTERFEROMETRY
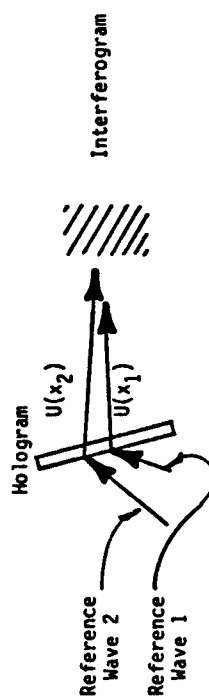
D. TWO REFERENCE WAVE SHEARING

573

FIGURE 4B.

HOLOGRAPHIC INTERFEROMETRY WITH 82-68001-1

MULTIPLE RECORDINGS
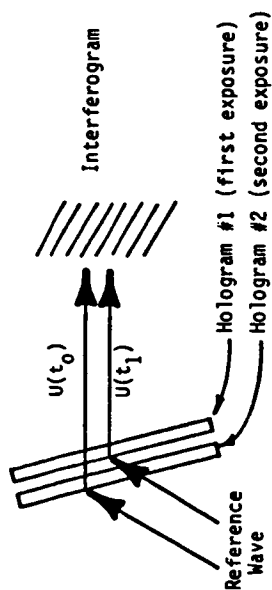
A. DOUBLE PLATE HOLOGRAPHIC INTERFEROMETRY
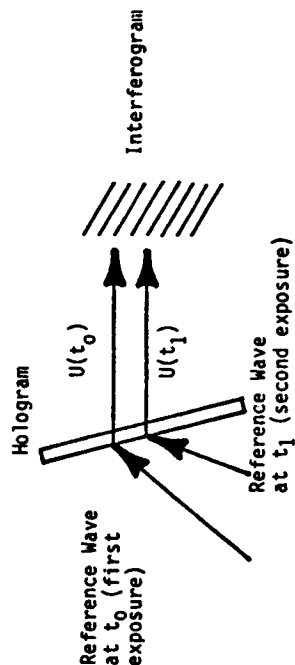
B. DOUBLE REFERENCE WAVE HOLOGRAPHIC INTERFEROMETRY
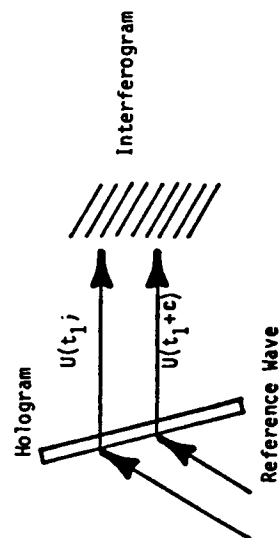
C. DOUBLE PULSED HOLOGRAPHIC INTERFEROMETRY

FIGURE 5.

STATE OF THE ART
HOLOGRAPHIC FLOW DIAGNOSTIC MODULES

85-2421-02

REFERENCE WAVE PATH MATCHING

PULSED LASER SOURCE
YAG 30 PPS & RUBY PPM
EXIMER/DYE - 100 PPS
COPPER VAPOR - 6000 PPS

TOMOGRAPHY
ROTATE FLOW
ROTATE HOLOCAMERA

HOLOGRAM MEDIA
SILVER HALIDE PLATE
ROLL FILM TRANSPORT
THERMO-PLASTICS
PHASE CONJUGATE MATERIALS

M2

M1

REFERENCE WAVE

OPTIONAL
2ND REFERENCE WAVE

FREQUENCY SHIFTING

CW RECONSTRUCTION LASER
ARGON ION
KRYPTON ION
HENE

ON-LINE DATA REDUCTION
FRINGE DETECTION: CCD/IMAGE PROCESSING
PHASE DETECTION: HETERODYNE INTERFEROMETRY

575

TABLE 1 - Application of Particle and Flow Visualization Holography in U.S. Government Laboratories

1. **Particle Sizing**

   A.   Icing Facilities
   B.   Spray Nozzles
   C.   Combustion
   D.   Particle Break-up
   E.   Explosives
   F.   Impact Facilities
   G.   Crystal Growth
   H.   Meteorology
   I.   Pollution
   J.   Multiphase Flow
   K.   Fiberization
   L.   Flow Seeding

2. **Flow Diagnostics**

   A.   Wind Tunnels
   B.   Gun Ranges
   C.   Shock Tubes
   D.   Combustion
   E.   Plasmas
   F.   Tomography
   G.   Movies
   H.   Water Tunnels
   I.   Test Chambers
   J.   Diffusion
   K.   Rocket Exhausts

Users

NASA -	AMES -	2A, F	USA -	ARRADCOM -	1C2B
	Langley -	1K, 2A		AVRADCOM -	2H
	Lewis -	1C, 2A, G		MICOM -	2A
	Marshal -	1B, H, I, ZI, J		CRRL -	1H
	JPL -	1C, D, 2K	NATIONAL LABS -	INEL-	1J2I
USAF-	AEDC-	1ABCDFIJK2ABFGI		SNL -	IE
	AFWAL	1CJ2A		LASL	1E
	CRL -	IH			
	RPL -	1C, 2K			
	WL -	1B2AG			
	BMO -	1EF2B	OTHER	EPA	1I
	OSR -	1BCD			
USN	SWL -	2AC		DOE	1BCDI2D
	WL -	1E		EPRI	1I
	OSC -	2H		DNA	1E
	PGS -	1C			

85-68083/17

For one holocamera, the crystal is side lighted with a choice of direct or diffuse illumination. This will provide a view of the crystaline surface and facets in three dimensions with a resolution of about 30 micrometers.

The second holocamera, which is for flow diagnostics, backlights the crystal and surrounding fluid with direct light. The reconstructed wavefront will be diagnosed for density gradients near the crystal surface. The holocameras operate with a single helium neon laser and holograms are recorded on Kodak SO103 film which is transported by a vacuum back which holds the film flat during recording.

Other significant developments within NASA include holographic movie capability at high framing rates[11] at the Lewis Research Center. This system employs a frequency doubled YAG laser pulsing at framing rates up to twenty per second. Future plans include significant increase in this recording rate. The primary applications to date has been in the study of flow fields over turbine blades and in combustion.

Another unique, but somewhat indirect application of holography at the Lewis Center, involves the use of a holographic optical element in a Laser Doppler Velocimeter to provide the required beam splitting operation while at the same time performing aberration correction for observing flow fields inside of cylindrical chambers.[12]

The NASA Ames Research Center has evolved wind tunnel holography for nearly fifteen years[13,14], and currently has operational flow diagnostic holocameras in several facilities. The current systems employ frequency doubled YAG lasers with various types of holographic interferometry. One of these systems is a permanent installation integrated into a conventional sixty cm. diameter Schlieren system. The Ames applications have been especially significant since they have been complimented with extensive use of other diagnostic instruments such as laser velocimeters and aerodynamic probes.

The NASA Langley Center has likewise applied holographic interferometery for flow diagnostics in a variety of wind tunnel applications.[15]

The U.S. Army applications, almost as extensive as NASA, include a number of extremely important efforts. A highly advanced holography system is operated by the U.S. Army Aeromechanics Laboratory at Moffet Field, California. This system is capable of performing holographic interferometry of a 70 cm. diameter flow field around a helicopter rotor tip. This system is so configured to provide a "look" through the flow field at any angle of view and has been used routinely for tomography of the field of interest, producing three dimensional density distributions. This appears to be the largest operational holographic tomography system in use today. It is producing three dimensional density data of the flow around helicopter blade tips, data which has never been available before.

85-68083/17

Army applications of flow diagnostic holography have also been made at Picatinny Arsenal, Redstone Arsenal, and Aberdeen Proving Ground, and the U.S. Army Research Office has played an important role in supporting research and development of the techniques.

The U.S. Air Force has been instrumental in the development and application of flow diagnostic holography, especially at the major wind tunnel test centers, Arnold Engineering Development Center[17], and Wright Aeronautical Laboratory[18]. The Air Force Office of Scientific Research has been instrumental in advancing the technology[19]. A unique application by the Air Force Weapons laboratory resulted in the development of an airborne holocamera for the diagnostics of flows over cavities and turrets.[20] The ultimate effect under study is the aberration of optical wavefronts by aerodynamic flow fields, a relatively new area of study known as aero-optics. Whereas the usual application is the diagnostics of the flow by studying the phase shifting of an optical beam, aero-optics closes the loop by determining the effect of the flow field on propagation and then examining the ways to achieve some optimum by modifying either the wavefront or the flow field. This particular holocamera system is unique in that it has been employed in an aircraft and is backed up by an automated data reduction system capable of reducing the thousands of holograms produced[21]. The Air Force Wright Aeronautical Laboratory is currently developing a combined flow diagnostic holocamera and laser velocimeter for application in a transonic wind tunnel.

The U.S. Navy has developed and applied flow diagnostic holography at the Surface Weapons Center and the Oceans Systems Center.

The major aerospace aircraft and aircraft engine companies continue to use holographic interferometry for flow diagnostics. A somewhat unique system employed by Rolls Royce Limited produces large area holograms of the flow between fan blades in jet engines[22].

National Laboratories have used holography and continue its use in a variety of instances. For example, the Idaho National Engineering Laboratory has applied holography in two phase flow and in electric arc diagnostics[23], Sandia and Livermore National Laboratories in combustion[24], Los Alamos National Laboratory in nuclear fusion research, Bureau of Standards in combustion.[25]

Other Particle Sizing Applications

Applications in particle sizing are even more widespread than in flow diagnostics, although the areas do overlap somewhat. Almost all of the laboratories mentioned above have also applied particle sizing holography. The basic capability is the high resolution diagnostics of a three-dimensional particle field providing size, shape, number, and velocity of particles.

Areas of application include:

1. Nozzle development and diagnostics

2. Fuel characterization

3. Combustion and explosions

4. Meteorology

5. Pollution and contamination

6. Multiphase flow

7. Fiber generation.

8. Icing facilities

9. Particle Break-up

10. Impact

11. Flow seeding

A few of the more recent or unusual works will be mentioned here. Holography has become more field oriented and airborne applications are becoming more common.[10,26,27] Meteorological applications allow a microscopic look at ice crystals in clouds distributed over a large volume. Particle break-up, a phenomenon which escapes photography, is simple with holography, even at high speeds as observed from aircraft or in test chambers.[19]

Observing detailed particle optical properties with holography is a relatively new technology.[28]

Field holocameras which are rugged, lightweight and portable[29] are not yet in widespread use, but the necessary technology now exists.

Considerable attention has focused on resolution and signal-to-noise improvements in particle holography.[30,31,32] Noise is still a critical factor limiting useful resolution to considerably worse than direct two dimensional microscopy.

Three dimensional velocity fields have been determined through holography from many years. However, new techniques continue to evolve. Murakami, et al, for example, developed a two-color multiple exposure holography system which produces two separate time spaced holograms of the same volume.[33]

In general, the three dimensional, high resolution capability which is made possible by holography, should continue to make this technique unmatched by any other for particle field diagnostics. Automatic data reduction will also provide new impetus to this field.

Automated data reduction technology

One of the most severe obstructions to the widespread use of holography has been data extraction and reduction of the vast amount of data which is stored in a typical hologram. Studies have too often ended

with production of holograms, a few photographs, and little of pains-
taking effort necessary to go further. In recent years great strides
have been made at removing the obstruction. Available computer power,
new codes, and detector arrays have played a key role.

The problem has two major facets, dealing with vast quantities of
data, and dealing with optical noise. Holographic images are character-
ized by speckle, interference, and diffraction noise that too often has
the appearance of signal. Out of focus images also become noise when in
focus images are examined and all optical noise adds coherently, ampli-
fying the problem. The numbers of dimensions in the general problem
includes three for location, two or three for morphology, two for
velocity, four for interferometry, and two more for tomography. For a
volume search at high resolution this quickly adds up to exceed the
storage capacity, even of large computers. Therefore, data compression
and rejection schemes are required. The general problem of automation
is too complex and the most successful schemes require considerable
operator interaction. Figure 6 illustrates the typical data flow and
Table 2 explains the various functions required.

TABLE 2. DATA REDUCTION FUNCTIONS

- Image Analysis —
  - (1) Number of each fringe
  - (2) Locate the center of each fringe
  - (3) Produce XY coordinates for each fringe

- Image Processing —
  - (1) Connect broken fringes
  - (2) Filter out optical noise
  - (3) Subtract off uneven background
  - (4) Allow input to correct ambiguities

- Data Analysis
  - (1) Determines deviation of fringe from a reference line
  - (2) Produces fringe deviation (phase) map ϕ (x,y)

- Data Interpretation —
  - (1) Solves an integral – Radon transform – General
    - Abel integral – axisymmetric
    - Linear equation – two dimensional
  - (2) Derives refractive index N(X,Y,Z)
  - (3) Converts N(X,Y,Z) to desired parameter, e.g. concentration

(4) Determines coefficients of series representations of $\phi(X,Y)$

(5) Provides graphic plots of parameters

A number of laboratories now have operational automated data reduction facilities that have successfully addressed the requirements for holography, and this could be the basis for a new surge in its application.[5]

The current state-of-the-art

The current state-of-the-art frontiers are summarized in Table 3 including some of the associated technology or hardware that is likely to be involved in the advancement of the state-of-the-art. The major advancement in the state-of-the-art in recent years has been associated

TABLE 3. STATE-OF-THE-ART FRONTIERS AND ASSOCIATED TECHNOLOGY

| Parameter	Technology or Hardware
Recording Times	Mode Locking, Pulse Slicing
Recording Rates	YAG, Excimer, Metal Vapor Lasers
Sensitivity	Heterodyne Interferometry
Data Extraction	Thermoplastics, Phase Conjugate Materials
Storage	Nonlinear Materials
Data Reduction	Detector Arrays, Software, Computer Power
Resolution	Recording Technique, New Materials
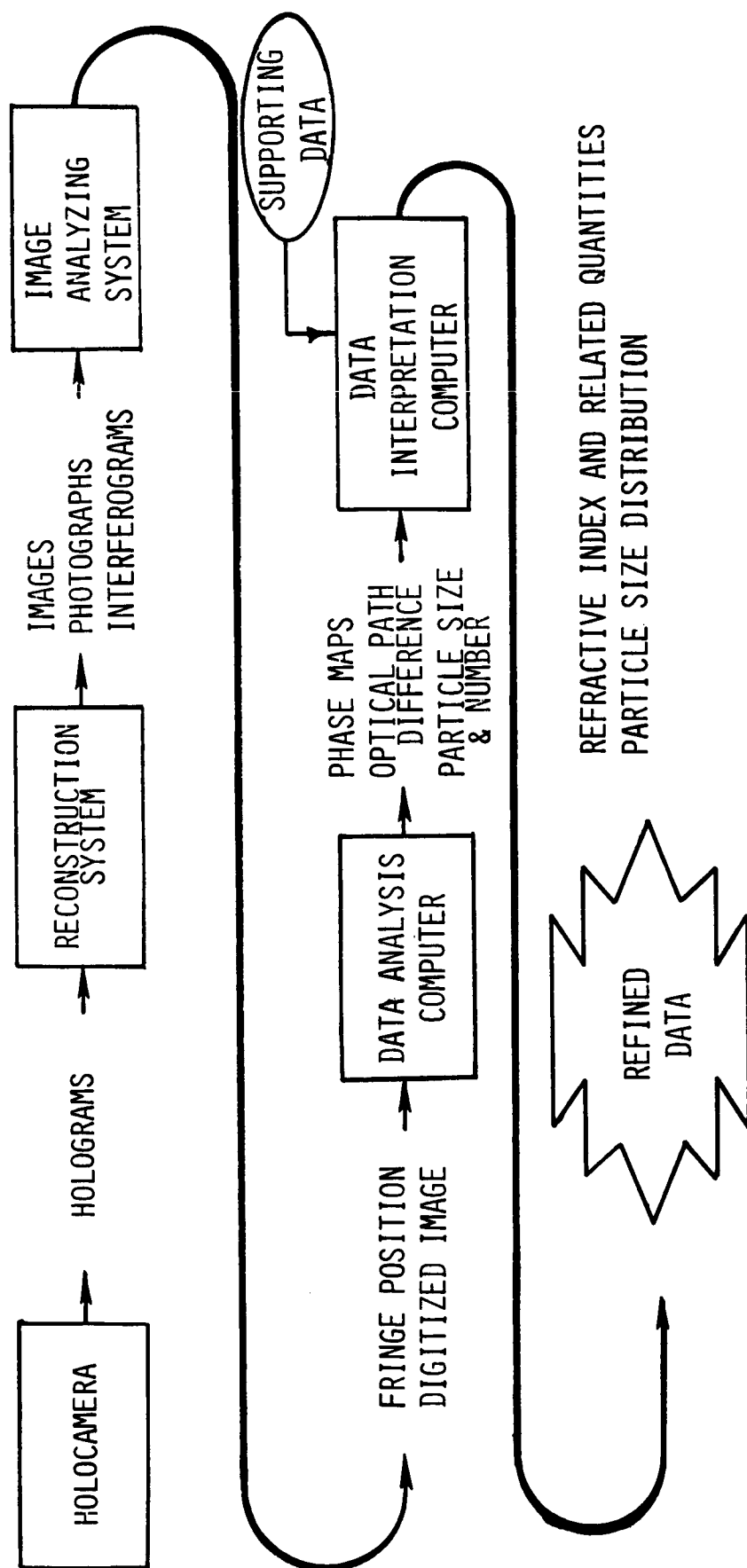
FIGURE 6. DATA FLOW IN HOLOGRAPHY

with automated data reduction. The ability to produce holograms of particle and flow fields which contain useful data has for years exceeded the ability to conveniently extract the data. This condition has been relaxed somewhat by the advent of advanced image analyzers, computers, and software. However, the process, unfortunately is not low in cost and its availability is still extremely limited.

Pulsed laser holography is largely performed using Q-switched ruby, or frequency doubled YAG lasers with pulse times less than 20 nanoseconds. Some work has been done with dye lasers. Recording times can now be reduced by over an order of magnitude by mode locking and/or pulse slicing. This is an area where the state-of-the-art has remained unchanged for many years.

Recording rates in today's holocamera are laser limited. Where YAG lasers are used, power requirements have limited recording rates to about 30 frames per second. This limit applies only to continuous recording. A laser can be multi Q-switched at megahertz rates for a few pulses. Commercially available lasers can deliver three or four pulses with microsecond separation.

Real time or near real time recording media such as thermoplastic and phase conjugate materials have provided opportunities to use holography in some innovative ways. Commercially available thermoplastic recording devices are now in routine use. On-line electronic hologram development makes possible on-line holographic diagnostics. Currently available hardware is nearly adequate to make possible a flow or particle diagnostic holocamera which can produce finished data on line. However, such a system is still yet to be built.

Hologram resolution limits have almost reached diffraction limited in laboratory uses. In field application, this is significantly worse and a typical achievable resolution is greater than 2 micrometers for particles.

A prognosis of the future - ideas beyond the frontier

Flow visualization holography will continue to find application largely where "nothing else works" until automated data reduction technology finds its way into more routine use. This should happen as computers and software continue to become more powerful.

The field of tomography will in the near future experience a new surge in solving flow diagnostic problems which have evaded solution for years and which are sufficiently important to justify the still tedious, though now practical, procedures.

Heterodyne holographic interferometry is an extremely high potential area which still remains virtually untapped. By combining the features of holography with the improved sensitivity made possible by heterodyning, a new, powerful diagnostic method will become available. In addition to sensitivity improvement this method offers a key link

85-68083/17

toward automated data reduction. At present, the problem with sufficient importance has not surfaced to provide someone incentive to develop this technology. It surely will eventuallty.

Four wave mixing has found an application in aero-optics, that of aberration correction of propagating beams. This area is so young there must be other applications in flow diagnostics.

Real time holography materials or fast processing thermoplastics are making on-line holography more practical. Within a few years, holography diagnostics will be done on-line with a system that records, processes electronically, and produces refined data in near real time.

Conclusion

The field of particle and flow visualization holography is alive and well. After an explosive beginning which fizzled, we more realistically accepted less than a miracle panacea and realized that applying holography usually meant more than just showing a reconstructed three-dimensional image. Indeed, the most useful holograms in this field are not optimum for human viewing at all, but are optimized for machine viewing. There have been few major breakthroughs in the past ten years. Growth and improvement have evolved more through refinement and application of improving hardware. These, combined with significant untapped potential, should provide a bright future for serious holographers. The current extent of applications and cost and complexity of hardware are likely to constrain this to be a specialist's technology for some time.

85-68083/17

References

1. Gabor, D., "A New Microscope Principle", Nature 161 777-778 (1948).

2. Thompson, B. J., J. Ward, W. Zinky, "Application of Hologram Techniques for Particle Size Analysis", J. Opt. Soc. Am. 55 1566, (1965).

3. Brooke, R. E., L. O. Heflinger, and R. F. Wuerker, "Interferometry with a Holographically Reconstructed Comparison Beam", Appl. Phys. Letters, 7, 248, (1965).

4. O'Hare, J. E. and J. D. Trolinger, "Holographic Color Schlieren", App. Opt. 8, 204, (1969).

5. May/June issue of "Optical Engineering" will feature Automated Reduction of Image and Hologram Analysis.

6. Trolinger, J. D., M. Azzazy, D. Modarress, and J. E. Craig, "Laser Diagnostic Methods - A Summary in Lasers in Fluid Mechanics and Plasmadynamics edited by C. Wang, AIAA Publication (1983).

7. Trolinger, J. D., and M. Heap, "Coal Particle Combustion Studied by Holography", App. Optics 18, 1757, (1979).

8. Briones, R. and Wuerker R., "Holography of Solid Propellent Combustion", SPIE Volume 125, Advances in Laser Technology for the Atmospheric Sciences, (1977).

9. Trolinger, J. D., "Application of Generalized Phase Reconstruction to Flow Visualiaiton Holography", App. Opt. 18, (1979).

10. Owen, R. B., "Interferometry and Holography in a Low Gravity Environment", App. Opt. 8, 1349, (1982).

11. Decker, A. J., "Measurement of Fluid Properties Using Rapid Double Exposure and Time Average Holographic Interferometry", AIAA 84 - 1461 (1984).

12. Schock, H., S. Case, and L. Konicek, "Window Aberration Correction in Laser Velocimetry Using Multifaceted Holographic Optical Elements", App. Opt. 23, 752, (1984).

13. Craig, J. E., G. Lee, and W. Bachalo, "Nd/YAG Holographic Interferometer for Aerodynamic Research", SPIE Proceedings 353, (1982).

14. Perry, R. L., and G. Lee, "Holographic Interferometry Applied to Symmetrical Aerodynamic Models in a Wind Tunnel", SPIE 523 (1985).

15. Burner, A., "A Holographic Interferometer System for Measuring Density Profiles in High Velocity lows", 73, ICIASF Record, 140, (1973).

16. Kittleson, J., "A Holographic Interferometry Technique for Measuring Transonic Flow Near a Rotor Blade", NASA T.M. 84405, (198).

17. Trolinger, J. D. "Flow Visualization Holography", Optical Engineering 14, 470 (1975).

18. Havener, G., "The Application of Holographic Interferometry to the Measurement of Transaction in Supersonic, Axisymmetric Boundary Layers", AIAA Journal, June (1984).

19. Craig, J. E., "Conventional and Liquid Metal Droplet Breakup in Aerodynamic Nozzle Contractions", AIAA-84-0201, 22nd Aerospace Sciences Meeting (1984).

20. Craig, J. E., J. D. Trolinger, and W. C. Rose, "Propagation Diagnostic Technique for Turbulent Transonic Flow", AIAA-84-0104, 22nd Aerospace Sciences Meeting (1984).

21. Wilkens, M., "Automatic Fringe Reduction Facility", To be published, Optical Engineering, May (1985).

22. Bryanston-Cross, P.J., "Three Dimensional Flow Visualization", in Proceedings of Symposium Measurement Techniques in Transonic Flows and Cascades (1982)

23. Key, J., "Development of Holographic Welding Arc Analysis" Proceedings of the Laser Institute of America 23rd Congress on Laser Applications, Nov. (1983).

24. Sheffield, S., Hess C., Trolinger J., "Holographic Studies of the Vapor Exlosion of Vaporizing Water in Fuel Emulsion Droplets" Proceedings of the Second International Colloquiem on Drops and Bubbles JPL Publication 82-7, Nov. (1981).

25. Kashiwaga, T., "A Study of the Radiative Ignition Mechanisms of a Liquid Fuel Using High Speed Holographic Interferometry", 19th International Symposium on Combustion/Combustion Institute, 1511, (1982).

26. Trolinger, J. D., "Airborne Holography Techniques for Particle Field Analysis", Ann. N.Y. Acad. Sci. 267, 448 (1976).

27. Conway, B., S. Canghey, A. Bentley, J. Turton, "Sound Based and Airborne Holography of Ice and Water Clouds", Atm. Envir. 16, 1193 (1982)

85-68083/17

28. Pikyl, L., C. Vest, "Holographic Imaging of Semi-transparent Droplets", App. Opt. 21, 2541, (1982).

29. Brendon, B., "Miniature Multiple Pluse Q-Switched Ruby Laser Holocamera for Aerosol Analysis", Opt. Engr. 20, (1981).

30. Briones, R., "Particle Holography at Extended distances and Micron Resolutions", Proceedings of SPIE, Recent Advances in Holography, Feb. 1980, 112 (1980).

31. Thompson, B., and P. Dunn, "Advances in Far Field Holography - Theory and Applications", Proceedings Feb. 1980 SPIE Symposium Recent Advances in Holography (198).

32. Trolinger, J. D., "Analysis of Holographic Diagnostics Systems", Opt. Engr. 19, 722 (1980).

33. Murakami, T., "Holographic Observation of Fine Particles by Two Laser Pulses of Different Wave Length", Jap. Soc. Mat. Sci. 27 (1978)

PARTICLE SIZING IN ROCKET MOTOR STUDIES UTILIZING HOLOGRAM IMAGE PROCESSING*

David Netzer and John Powers
Naval Postgraduate School
Monterey, California 93943

ABSTRACT

This paper describes a technique of obtaining particle size information from holograms of combustion products. The holograms are obtained with a pulsed ruby laser through windows in a combustion chamber. The reconstruction is done with a krypton laser with the real image being viewed through a microscope. The particle size information is measured with a Quantimet 720 image processing system which can discriminate various features and perform measurements of the portions of interest in the image. Various problems that arise in the technique are discussed, especially those that are a consequence of the speckle due to the diffuse illumination used in the recording process.

INTRODUCTION

A continuing investigation[1] is being conducted at the Naval Postgraduate School (NPS) to obtain quantitative data that can be used to relate solid rocket propellant composition and operating environment to the behavior of solid particulates (Al, Al_2O_3) within the grain port and exhaust nozzle. These data are needed to improve predictive capabilities of propellant performance, to provide input related to ammonium perchlorate (AP)-aluminum interactions for steady-state combustion models, and to provide in-motor particle size distributions to allow more accurate predictions of damping in stability analyses. The expected range of particle sizes is from 1 µm to 200 µm. While work has been done on a variety of techniques, including high speed motion pictures, analysis of post-fire residue with a scanning electron microscope, and particle sizing by scattered light measurements, this paper will focus on the application of particle sizing using holograms of burning propellant strands and slabs in a cross-flow environment.

HOLOGRAM RECORDING

A diagram of the two-dimensional motor is shown in figure 1. A glass window (18.5 mm diameter) in the motor walls allows recording of the hologram. The window position allows centering

---

of the edge of the largest combustion slab. The smallest combustion slabs are out of view with these window positions. Self-pressurization of the burning slabs was inadequate to achieve desired values (34 atm. and greater), so a nitrogen pressurization technique was incorporated into the top of the motor chamber. A 0-80 screw was mounted outside of the rear window (from the laser) to provide a size and position reference in the reconstructed hologram. Additionally, holograms were recorded of resolution charts and glass beads (both opaque and transparent) of known size for calibration purposes and investigations in changing recording or reconstruction geometries.

The laser system is a pulsed ruby laser[2] consisting of a Q-switched oscillator, a ruby amplifier, beam expanding optics, an alignment autocollimator, a HeNe pointing laser, the capacitor bank, and associated electronic power supplies. The operating wavelength is 694.3 nm with a beam diameter of approximately 3.2 cm. A one joule pulse with a 50 ns pulselength was used for this investigation.

All holograms were recorded with diffuse illumination from the laser in order to minimize the presence of Schlieren interference fringes produced by temperature and density variations of the combustion gas products during the burn. The diffuse illumination was made by introducing a glass diffuser into the scene illumination beam. This diffuse illumination introduces speckle into the reconstructed images as will be discussed in detail later. The primary problem in sizing the particles in the reconstructed image is interference from this speckle which can have a maximum size that is comparable to the particles at the lower end of the expected particle size distribution.

The holocamera[3] (shown in the reconstruction diagram of figure 2) incorporates assisting lenses to increase the effective field of view of the camera with a subsequent increase in resolution. Holographic plates from AGFA-Gevaert (Model 8E75 HD plates) were used for hologram recording.

Holographic recordings have been made successfully using propellant strands burned at operating pressures of 34 and 68 atm. and with various concentrations of alumininum (up to 15% aluminum). Single pulse holography provides a means of effectively stopping motion. It only provides information during the single instant of time, however. Smoke generation (i.e., small Al_2O_3 and binder products, etc.) presents a major obstacle to obtaining good holograms. The smoke reduces illumination levels in portions of the image and also adversely affects the scene-to-reference illumination levels on the hologram recording medium. Minimization of the effects of smoke requires experimental determination of the optimum propellant geometry and the optimum delay time for recording the hologram during the burn.

HOLOGRAM RECONSTRUCTION

During reconstruction, the developed hologram plate is re-attached to the plate holder and placed into the holocamera box (which is mounted on a digitally controlled xyz stage). The plate is illuminated with a krypton-argon laser at an angle of approximately 60° from normal, as shown in figure 2. The krypton laser operates at 647.1 nm, causing slight lateral demagnification of the image equal to the ratio of the reconstructing and recording wavelengths. A longitudinal distortion equal to the square of the wavelength ratio is also expected. The reconstruction laser wavelength was selected close to the ruby laser wavelength to minimize these effects. The real image of the hologram was focused onto a spinning mylar disk that was introduced to reduce speckle effects in the observed image. The spinning disk changes the speckle pattern at a rate faster than the response time of eye or imaging system causing a reduction in the contrast of the speckle pattern. A variable power microscope was used to view the reconstructed image either by eye or with the image scanner of the image processing system. Reconstructed images can be recorded by a 35mm camera from either the screen of the image processing system or from a camera attachment on the microscope. Photographs of typical reconstructed images are shown in figure 3.

IMAGE PROCESSING EQUIPMENT

The Quantiment 720[4] is a general purpose television-type image analyzer that is capable of elementary shape recognition and various physical measurements of objects by distinguishing differences in grey levels in the image and performing various logical tests on measured dimensions. The system is designed in a modular fashion so that additional capabilities can be acquired with extra electronic modules. When used or configured as a 'basic' Quantimet 720, the operator must provide all control and direct all operations. In the 'advanced mode', a computer is used as a controller where all operations are programmed from prior experience. The Quantimet at NPS contains the necessary modules to be operated in the advanced mode but is currently being utilized in the basic mode.

Figure 4 is a block diagram of the image processor in the enhanced basic mode. All switch settings must be made on an interactive basis and data readings are made by the operator from the digital display on the screen.

The Scanner sends a video signal of of the image to the System Control Module where it is digitized and sent to the Variable Frame and Scale module. This module, when activated, enables an operator to select only a portion of the image for analysis, disregarding the rest of the image. The portion of the image of interest to the operator is forwarded to the 1-D Auto Detector module. This 1-D Auto Detector module can differentiate data based on grey level. There are 64 grey levels in an image and differentiation can be made of all levels above a certain

591

level, below a certain level, or between two levels. The threshold levels are under the operator control. Only data that passes the desired grey level test is passed to the other modules for further processing. The Light Pen module is used by the operator to select individual features for further measurements. The Frame Smasher module is of use only for long thin objects and is usually bypassed in our operations. The Standard Analyzer module can measure the selected features of the image. It can measure area, perimeter, largest horizontal dimension, largest vertical dimension, and other quantities. (All measurements are in units of pixels and image calibration is required to reduce the measurements to physical units.) The Standard Analyzer module can also be used to select features for further analysis based on the results of these measurements. For example, the analyzer can be used to select all image features whose horizontal (or vertical) size exceeds a certain value, whose area exceeds a given value, or whose dimensions (either vertical or horizontal) are less than a given value. The logical tests based on measured size can be combined with the logical tests performed by the 1-D Auto Detector module for further feature discrimination. The features that meet the combined specifications are sent to the Function Computer module and the Classifier/Collector module. These modules can perform more measurements on the features of interest or can perform still more logical tests on the dimensions. In the current configuration these units are not brought to bear on the feature measurement or discrimination problem.

In the 'automatic' mode (Fig. 5) a computer controls the setting of the module functions and the various threshold levels of the logical tests, as well as the recording of the data. Individual image frames can be transferred into the computer for data recording or subsequent analysis.

A standard image frame is 688 by 880 pixels. As described above, a subportion of this frame can be analyzed. The Scanner uses a Plumbicon tube selected for its uniformity of response over the complete face of the tube. The usual scan rate is 10 s^{-1}. Scan rates of 1 s^{-1} and 0.4 s^{-1} are switch selectable. The display screen is a long-persistence yellow phosphor that can accommodate the 10 s^{-1} scan rate with a minimum of image loss before refreshing. The screen can present the raw image, the image as processed by the 1-D Auto detector, the image as processed by the Standard Analyzer, or any combination of these images. A digital readout on the top of the screen presents the quantitative data to the operator.

PROBLEM AREAS

In this section we will describe several identified problems in this application of data reduction and potential solutions to them. The problems can be broken up into two parts: those that exist without the speckle being present and those that exist with speckle being present.

The first problem is to compute the number of locations that must be investigated in the hologram (i.e., we must compute the number of planes of interest that exist in the volume of the reconstruction). The technique of particle sizing requires that the system locate the planes of focus of the particles so that the particles can be accurately sized. One of the calculations of interest is to determine how many planes of best focus will exist in the hologram reconstruction. We will assume a nominal depth Δz of 2 mm to the hologram reconstruction. The operating wavelength λ is that of the krypton laser—647.1 nm. A particle of diameter, d, will have a depth of focus, Δp, given by

$$\Delta p \simeq \frac{d^2}{\lambda} \qquad\qquad (1)$$

where the depth of focus is the distance over which the image of the particle will be 'in focus'. (This criterion is that the diameter of the image of the particle be within a factor of $(2)^{1/2}$ of its minimum in-focus value). The minimum number of planes, N, that must be investigated to count and size particles is given by

$$N = \frac{\Delta z}{\Delta p} \qquad\qquad (2)$$

$$= \frac{\Delta z\ \lambda}{d^2} \qquad\qquad (3)$$

Table 1 gives the value N for particles of differing diameters within the range of particle diameters expected in the experiment. As seen from the table the computational burden is not too great for particle sizes larger than 10 μm. As one goes below a size of 10 μm, however, the number of sample planes required increases rapidly. This is the region where speckle size also becomes important, as the size of the speckle is on the same order of magnitude as the diameter of the particle.

Stanton, Caulfield, and Stewart[5] present a technique for reducing the computational burden of finding the in-focus particle and increasing the accuracy of particle location by measuring the Fresnel ring structure of an out-of-focus spherical particle. This technique is not available to us since the Fresnel rings of the particle can not be seen against the speckle background. The particles are not identifiable in the image until the observation plane is close to the particle location.

The Quantimet 720 presents limitations which can lead to inaccurate results. One technique of separating particles from background is to accept for measurement only those pixels that that are darker than a certain threshold. Once the particle have been isolated, the particle size is measured. The 720 locates an

d	Δp	N
1 μm	1.54 μm	1,294
10 μm	154 μm	12.9
50 μm	3.86 mm	1
100 μm	1.54 cm	1
200 μm	6.18 cm	1

Table 1 Depth of focus, Δp, and number of independent
viewing planes, N, in a 2 mm deep hologram volume

edge of a particle by noting regions where there is a sharp change in grey level. The edge location is determined by finding the pixels with greatest and least grey level and locating the edge at the pixel midway between these two locations. This technique is consistent only for particles with the same extremes in grey levels. For frames that include particles of differing grey levels, the edge location is variable. Uneven illumination is the primary cause of differences in particle grey level. The illumination problems can occur in the hologram recording (e.g., laser nonuniform beam pattern, smoke), in the development of the hologram leading to a plate with variable transmissivity (bleaching the plate would help this problem), and in the reconstruction process (e.g., uneven laser illumination, nonuniform spatial response of the image tube). Additionally electronic noise in the various modules and quantization noise can corrupt the image signal leading to measurement errors.

For the case of having speckle present as in our hologram reconstructions (due to the diffuse illumination required to eliminate the Schlieren fringes in the reconstruction as previously described), the initial point is to reduce the maximum size of the expected speckle to the smallest value possible. Speckle is the random interference pattern from a diffuse source interfering with a reference wave. The random pattern of light will contain all grey levels from maximum brightness to total black. The speckle can have two effects on the image. It produces black spots in the background which cannot be readily distinguished from real particles. The second effect is that the speckle can give the perimeter of the particle a 'swiss cheese' appearance where the speckle overlaps the edge. This alters any calculated measurements of the particle, such as area or perimeter. The Quantimet usually ignores any holes within the measured area, but significant error is introduced when the perimeter is altered.

In considering the size of the speckle in the image, we find that the speckle arises from two causes[6] within our images. The first occurs in the recording of the hologram. Objects illuminated with diffuse coherent light will have a speckle pattern superimposed on them with a maximum speckle size $d_{speckle}$ given by[6]

$$d_{speckle} = \frac{\lambda}{\beta \cos \theta} \qquad (4)$$

where λ is the laser wavelength, β is the angle subtended by the illuminating beam as seen from the object (see figure 6), and θ is the angle measured at the object between the axis to the center of the illuminated diffuser and the center of the image plane (i.e., the hologram). For the geometry of the present experiment, λ=676 nm (a nominal wavelength between the recording laser and the reconstruction laser), β is approximately 62.4 milliradians, and θ=180°, giving a speckle diameter on the hologram plane of 10.8 μm. This speckle will be recorded by the hologram and will be present in the reconstructed image. The primary means of reducing the speckle size is to increase the illumination aperture of the diffuser or to reduce the distance from the diffuser to the object.

The second contributor to the speckle in the image is the imaging lenses. In the present system there are two imaging operations in the reconstruction process. The first is the formation of the real image on the spinning mylar disk through the assisting lenses of the holocamera. The second is the imaging of the real image onto the face of the scanner tube through the microscope lenses. The maximum speckle diameter for a diffuse image that is imaged through a lens as depicted in figure 7 is[6]

$$d_{speckle} = \frac{1.22\lambda M}{2 \tan[\sin^{-1}(NA)]} \qquad (5)$$

$$\simeq \frac{1.22\lambda M}{2 \tan[NA]} \qquad (6)$$

where M is the magnification of the imaging system (given by the ratio of the image distance to the object distance) and NA is the numerical aperture of the lens. The numerical aperture of a microscope lens is approximately given by

$$NA \simeq (1/2f_{no}) \qquad (7)$$

$$\simeq \tan^{-1}[d_{lens}/2d_0] \qquad (8)$$

where f_{no} is the f-number of the lens, d_0 is the object distance from the lens, and d_{lens} is the diameter of the lens. Alternate forms of the equation for the maximum speckle diameter are

$$d_{speckle} = \frac{1.22\lambda d_I}{d_{lens}} \qquad (9)$$

$$d_{speckle} = 1.22\lambda(1+M)f_{no} \qquad (10)$$

The first imaging operation is the formation of the real image on the mylar disk from the hologram through the assisting lens set. Although the lens set is involved in the imaging, the primary imaging element is the hologram itself. The hologram can be modeled as a lens with (approximately) unity magnification. the aperture of the lens is the width of the hologram as modified by the assisting lenses. Further work is necessary to complete the modelling of this imaging process.

The second imaging operation is the imaging performed by the microscope objective onto the face of the scanner tube face. The maximum speckle size is given by equation 10 and is plotted vs. the f-number of the lens in figure 8 for a variety of magnifications. Reduction of the speckle diameter to values below 3 or 4 μm will require f-numbers below 0.4 for magnifications of 10x. For magnifications of 1x, f-numbers below 4 are adequate. It is noted that typical f-numbers are in the range of 1.5 to 10 for this range of magnifications, indicating that magnifications of 2x or so are consistent with reducing the speckle to values that are comparable to (or below) the value of the smallest expected particle.

Generally the conclusion is that, to reduce the speckle size, large aperture optics are desirable. Once the speckle is smaller than the typical particle size, the logic test based on the feature size can be implemented in the Quantimet to extract particle information from the background.

If the speckle cannot be made negligible compared to the particle size, other techniques must be used to reduce the contrast level of the speckle relative to the particle. These techniques are based on the fact that the speckle pattern will shift if one or more of many variables are changed while the object position remains fixed. By averaging N images with differing speckle patterns, an reduction in the speckle contrast on the order of $(N)^{-1/2}$ is expected. With reduction of contrast the speckle level can be reduced below the grey level threshold set in the 1-D Auto detector module of the Quantimet. Variables that can be changed to cause a shift in the speckle pattern are:

-Changing the random phase of the diffuse illuminating wave. This is done in our system by rotating the mylar disk that has the real image focussed on it. The speckle pattern changes during the integration time of the scanner tube. The improvement in contrast of the observed image (on the viewing screen) formed with a moving disk over that of a stationary disk is noticeable. The predicted improvement at

higher spin rates or longer integration times is less noticeable to the eye.

—Changing the image aperture. Since the Quantimet requires equal strength images for accurate particle sizing, this technique would require a renormalization of the image amplitudes. This might be possible when the system is in the advanced computer—controlled mode, but the technique holds little promise since one is limited by the limited dynamic range of the sensor to few images.

—Changing the object position or, equivalently, changing the image screen position or changing the imaging lens position). This can be done within the depth of focus of the particle. For small diameter particles few independent images could be expected.

—Computer superposition of images with the different diffuse illumination. This technique is similar to the rotating disk illuminator except that the superposition is done digitally rather than relying on the integration properties of the imaging tube. Limitations here are primarily in the memory capacity of the computer. Using the computer to store and manipulate the images also allows a variety of linear and nonlinear image processing algorithms to be used.

Each of these techniques introduces complexity into the processing of the image. The easiest to implement is the spinning diffuser in the image reconstruction. While the image is dramatically improved when the disk is spinning compared to the image on a motionless disk, the image quality is not dramatically improved with increased rotation rate. The techniques other than computer processing the images appear to present insurmountable problems, leaving the computer processing as the most likely solution. Work has begun on implementing the computer—controlled configuration in an effort to explore this technique.

SUMMARY

The holographic technique has been successfully used to record particles from strand burns and 2-D motor combustion. (Work will soon be done on expanding the hologram recording to a 3-D motor environment) The image particle count and sizing has successfully been done by hand but automatic techniques are preferred. The diffuse illumination required in the recording process to avoid phase fringes due to thermal effects has led to the presence of speckle in the images. Efforts have been made to analyze the size of the speckle to reduce the maximum speckle diameter. The remaining speckle is reduced by using a spinning diffuser in the reconstruction process. The computer—processed images appear to have the most liklihood of further reduction f the speckle contrast. This method is currently under investigation.

REFERENCES

1. R.G. Cramer, R.J. Edington, et al., 'An investigation of experimental techniques for obtaining particulate behavior in metallized solid propellant combustion', , Technical report AFRL TR-84-014, Air Force Rocket Propulsion Laboratory, Edwards AFB, CA 93523

2. R.A. Briones and R.F. Wuerker, 'Instruction manual for the improved ruby holographic illuminator', Technical report AFRL TM-78-11, Air Force Rocket Propulsion Laboratory, Edwards AFB CA 93523

3. R.F. Wuerker and R.A. Briones, 'Operation manual for the lens-assisted muiltipurpose holocamera with reflected light option', Technical report AFRL TM-78-12, Air Force Rocket Propulsion Laboratory, Edwards AFB CA 93523

4. Cambridge Instruments, 'Instruction manual for the Quantimet 720', 40 Pitt Dr., Monsey NY, 1976

5. A.C. Stanton, H.J. Caulfield, and G.W. Stewart, 'An approach for automated analysis of particle holograms', Optical Engineering, 23(5), pp. 577-582, 1984

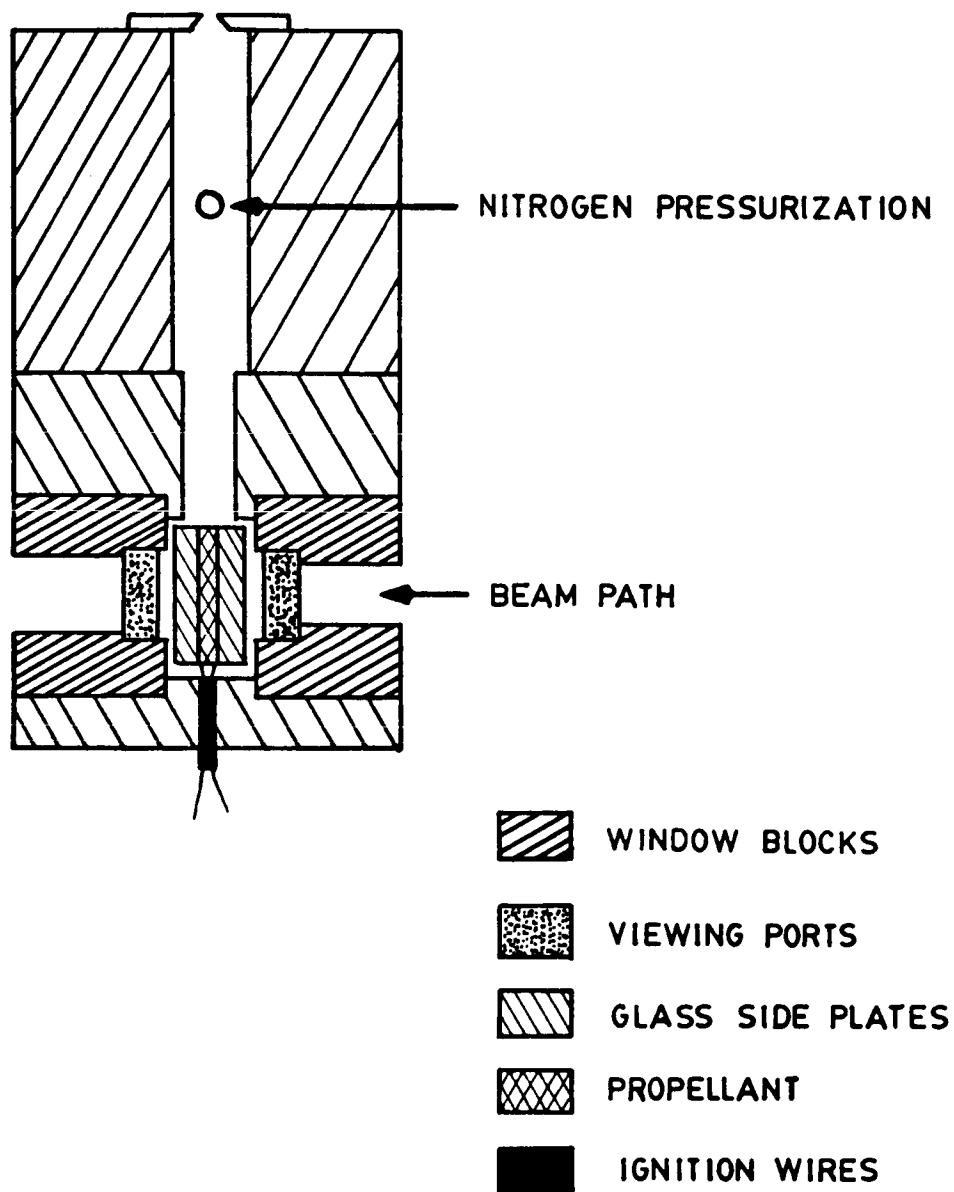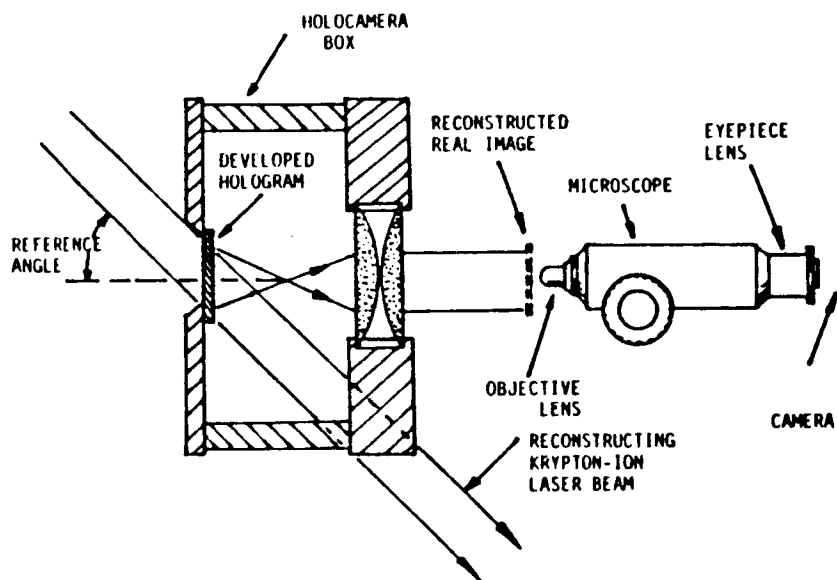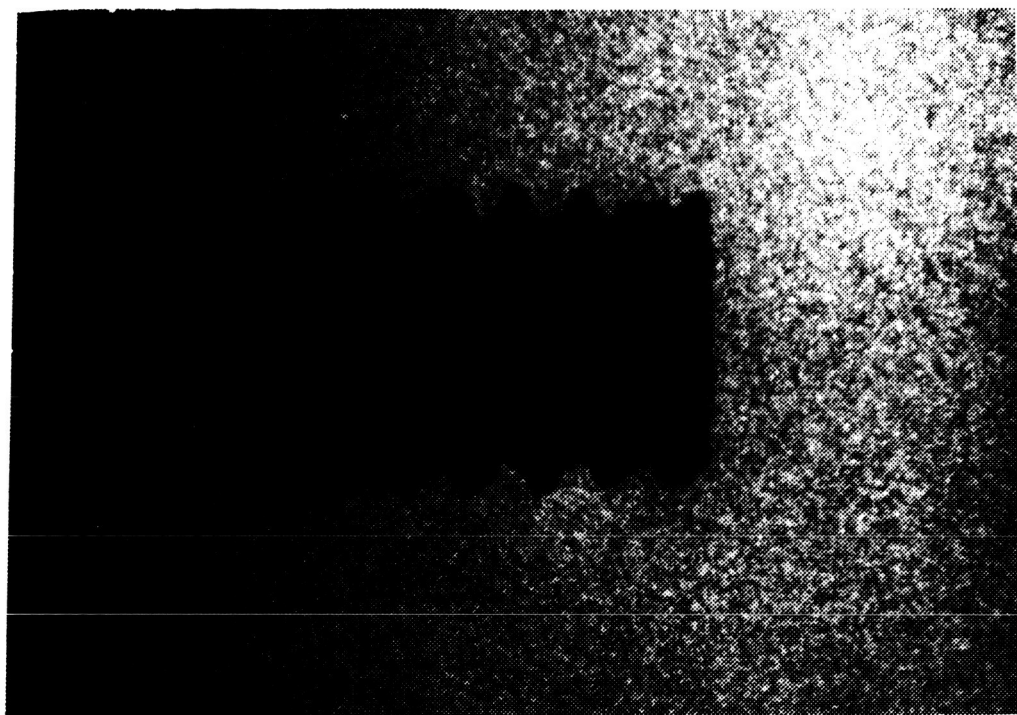6. M. Francon, Laser Speckle and Applications in Optics, pp. 33-34, Academic Press, 1979

NITROGEN PRESSURIZATION

BEAM PATH

▨ WINDOW BLOCKS

▦ VIEWING PORTS

▨ GLASS SIDE PLATES

▩ PROPELLANT

■ IGNITION WIRES

Figure 1. Schematic of 2-D Motor

Figure 2. Schematic of Reconstruction
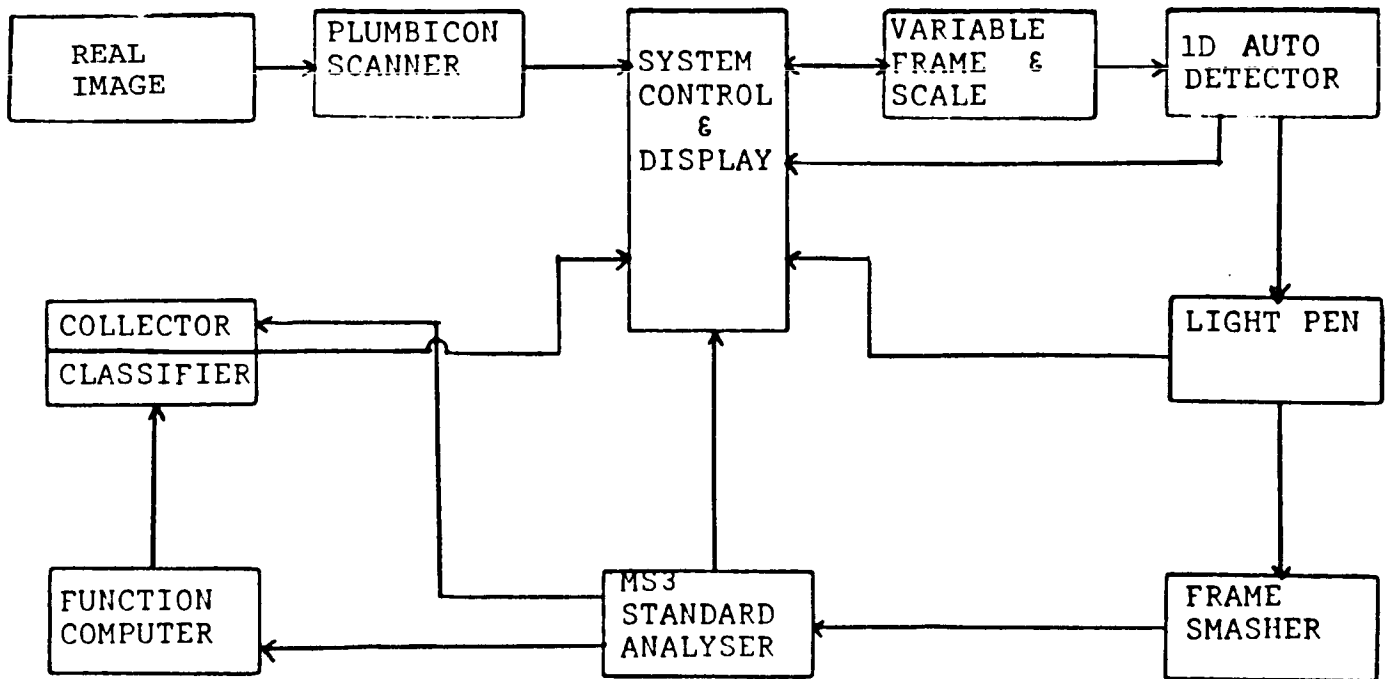Viewing Method (after Ref. 3)
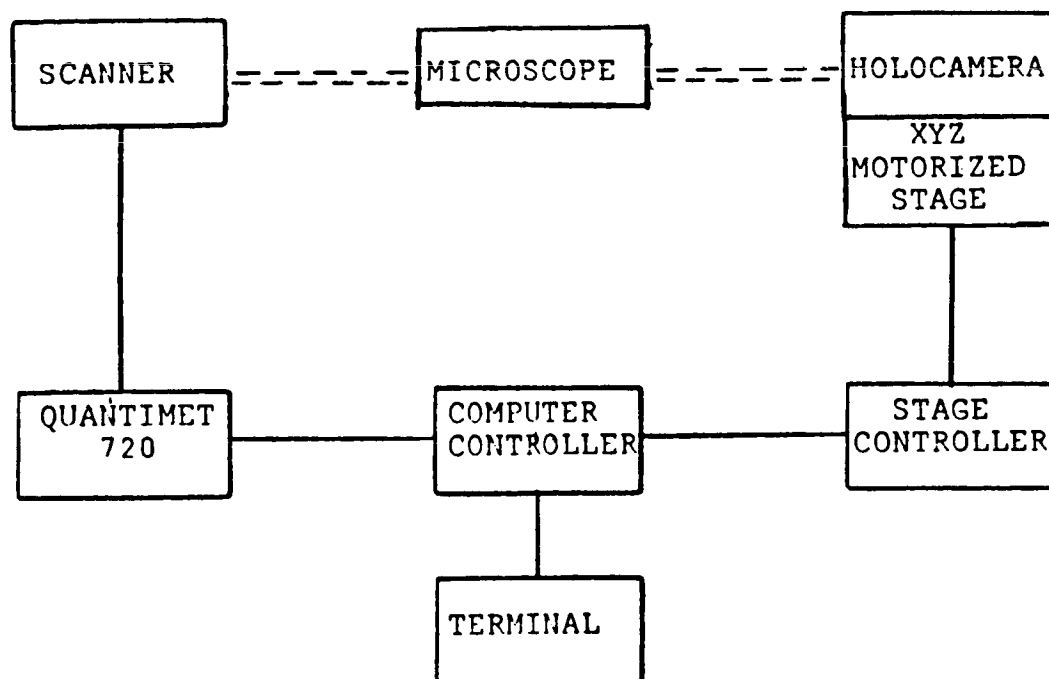
600

(a)   0-80 Screw
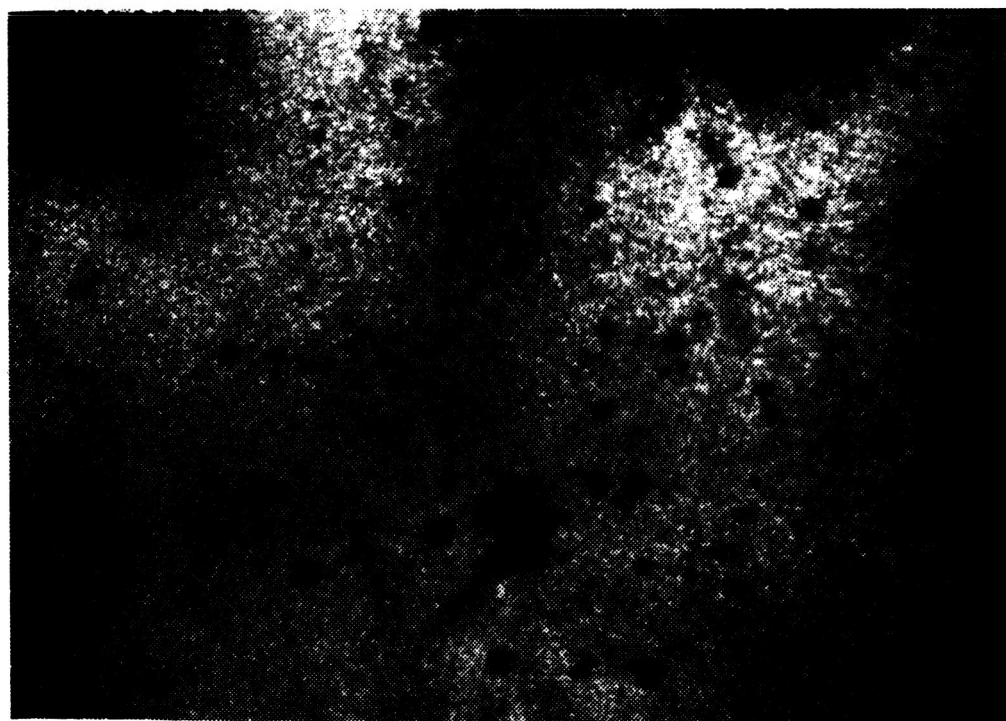
(b)   WGS-ZrC

Figure 3 Photographs of Typical Reconstructed Images

Figure 4 Block Diagram of Quantimet 720
EnhancedBasic Configuration

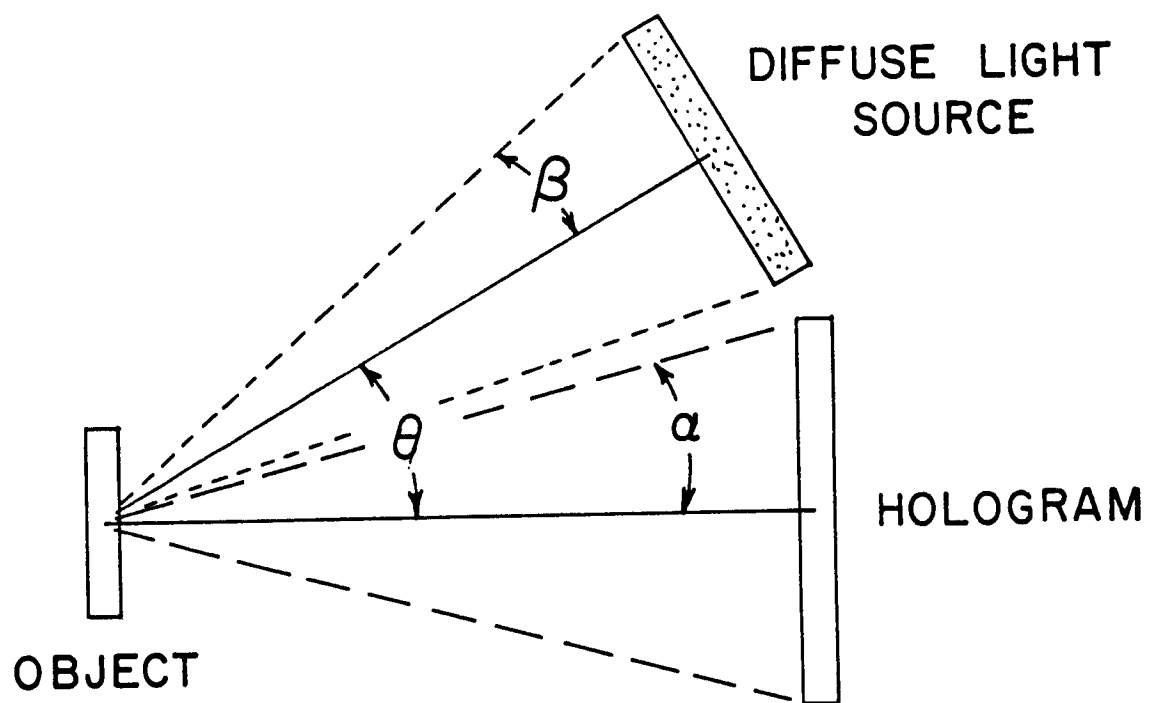**Figure 5 Block Diagram of Semiautomatic Image Reconstruction Setup**

Figure 6. Geometry for Calculating Maximum
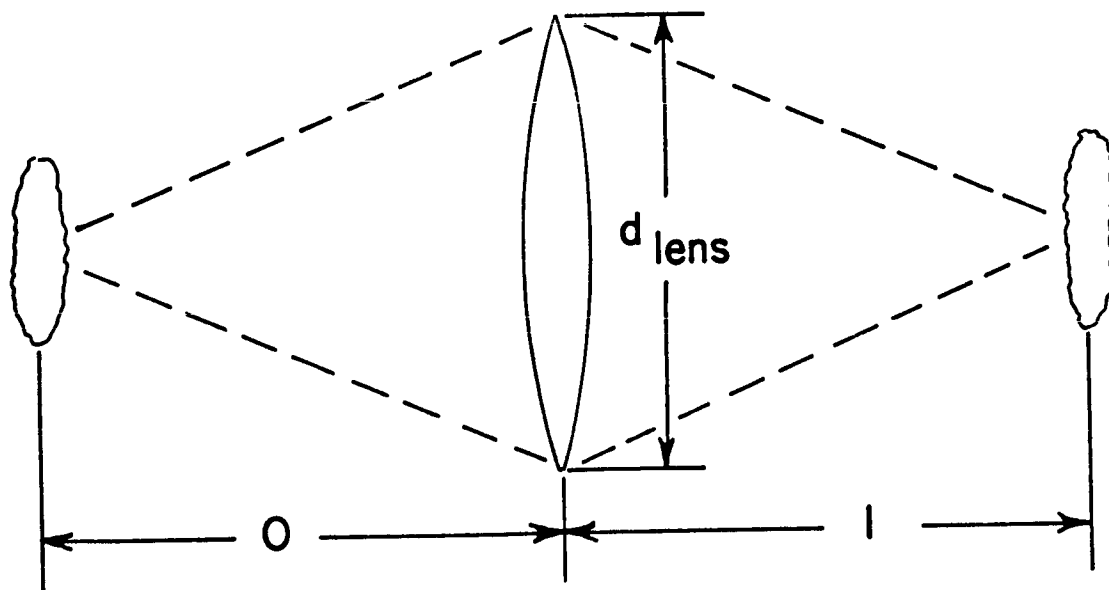Speckle Diameter Due to Diffuse Illuminator

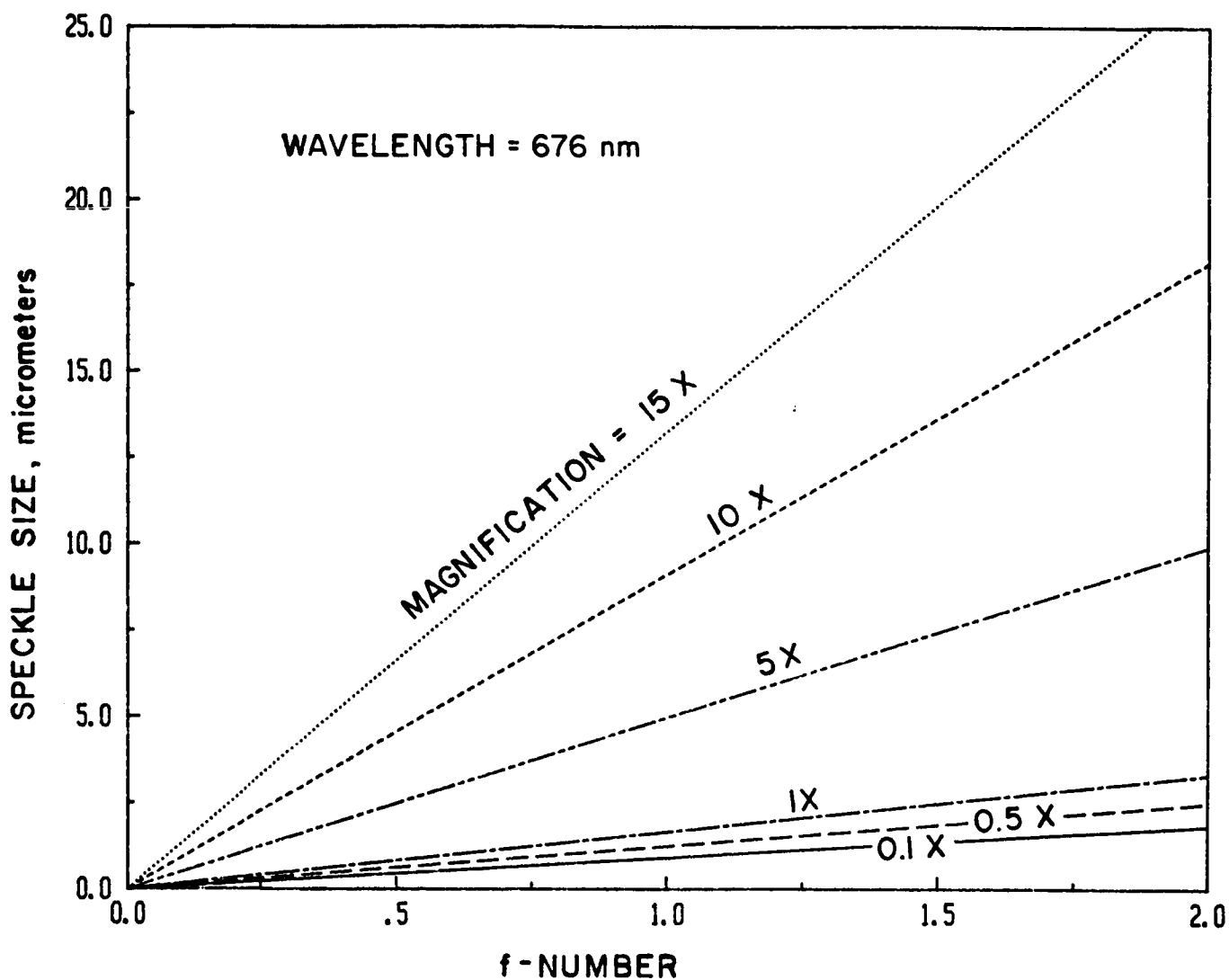Figure 7. Geometry for Calculating Maximum
Speckle Diameter in Imaging

Figure 8. Maximum Speckle Diameter vs.
Lens f-number and Magnification

S28-34
/03469

IMAGE PROCESSING SYSTEM TO ANALYZE

DROPLET DISTRIBUTIONS IN SPRAYS

Gary P. Bertollini

Larry M. Oberdier

Yong H. Lee

Instrumentation Department

General Motors Research Laboratories

Warren, Michigan 48090-9057

December 7, 1984

ABSTRACT

The General Motors Research Laboratories has developed an image processing system which automatically analyzes the size distributions in fuel spray video images. Images are generated by using pulsed laser light to freeze droplet motion in the spray sample volume under study. This coherent illumination source produces images which contain droplet diffraction patterns representing the droplets degree of focus. Thousands of images are recorded per sample volume to get an ensemble average of the distribution at that spray location. After image acquisition the recorded video frames are replayed and analyzed under computer control.

The analysis is performed by extracting feature data describing droplet diffraction patterns in the images. This allows the system to select droplets from image anomalies and measure only those droplets considered in focus. The system was designed to analyze sprays from a variety of environments. Currently these are an ambient spray chamber, a high pressure high temperature spray facility, and sprays in a running engine.

Unique features of the system are the totally automated analysis and droplet feature measurement from the grayscale image. Also it can distinguish non-spherical anomalies from droplets which allows sizing of droplets near the spray nozzle.

This paper describes the feature extraction and image restoration algorithms used in the system. Preliminary performance data is also given for two experiments. One experiment gives a comparison between a synthesized distribution measured manually and automatically. The second experiment compares a real spray distribution measured using current methods against the automatic system.

KEYWORDS

INTRODUCTION

Basic research is being conducted to relate the combustion process and the design and placement of fuel injectors. This is being accomplished by studying fuel spray droplet dynamics. The fuel spray study utilizes a system which records video images of spray droplets directly from a variety of fuel spray environments. These include an ambient spray chamber[1,2], a high temperature, high pressure test chamber, and the combustion chamber of a running engine[3].

Because of the harsh spray environments the analysis of video images at General Motors Research Laboratories is currently done manually by observing the images on a TV and

selecting only "in focus" droplets for velocity and size measurements. Manual data reduction is time consuming, tedious and inconsistent for different operators. These problems led to the development of an automatic system for droplet measurement. This system should access archived image data and extract droplet size information without manual intervention. The system must also analyze poor quality images containing low frequency intensity gradients which exceed droplet contrast levels. The realization of these requirements has pushed the capabilities of this spray analysis system beyond any other direct imaging system[4,5,6,7,8].

HARDWARE

Figure 1 shows a block diagram of the hardware utilized in this study. For further details, refer to Oberdier paper[9]. Images are created by direct imaging of a spray sample area on a high resolution CCD (charge coupled device) array camera . This camera has a sensor resolution of 380 X 480 picture elements (pixels). Illumination of the sample volume is provided by a pulsed 100 μJ nitrogen laser at a wavelength of 337 nm. The 10 ns laser pulses are collimated and passed through the test volume perpendicular to the spray. The imaging lense used has a 117 mm focal length. The recording camera is positioned to give a resolution of 3.3 um per image pixel. This magnification allows a 1.2 X

1.5 mm field of view at the focal plane. Because of the filter operation performed by the software to remove low frequency image degradation, the measurable droplet diameter range is limited at 5 to 50 pixels. This translates an effective droplet diameter range of 16 to 165 um. Thus the imaging lense is switched to accommodate other ranges.

Image acquisition is accomplished by using a microcomputer based controller which synchronizes laser firing, camera scanning and image storage to the experimental process. The controller was developed at General Motors and will synchronize image acquisition at a particular engine crank angle or free run at standard video rates (30 frames per second). Images are stored on a magnetic video disk recorder which allows full frame, random access of the images. After the data is collected the stored images are digitized and analyzed automatically by a Vicom image analysis system. This system digitizes each image to a 512 X 512 pixel array at 8 bits of resolution per pixel. It should be noted that current camera and recorder technologies limit the realization of this specification to 6 bits of of intensity resolution and the horizontal bandwidth to 450 lines.

IMAGE PROCESSING ALGORITHMS

Image processing algorithms were applied to perform the following steps.

1. Image normalization - Remove low frequency degradation in the recorded images.

2. Segmentation - Find places in the image which may be the centroid of droplets.

3. Feature extraction - Extract feature data from the image restored in step one at those centroid locations.

4. Classification - Decide if the object is an in focus droplet by using extracted diffraction feature data.

Image Restoration

The fuel spray images recorded from the high temperature, high presure chamber and the running engine chamber have low frequency intensity degradation. This is caused by droplets which hit the observation window, refracting gradients in the optical path, and sensor scan variations. This degradation has intensity values which can be similar to droplet intensities. This degradation is removed in the following manner.

As discussed in[10,11,12], an image formation model can be represented mathematically as:

(1) $g(x,y) = d(x,y)f(x,y) + n(x,y) + b$

          where

               $g(x,y)$ = detected image

               $f(x,y)$ = original image

               $d(x,y)$ = multiplicative noise

               $n(x,y)$ = additive noise

               b = intensity bias.

We assume that the low frequency degrading function is represented
by $d(x,y)$. The additive noise
$n(x,y)$ represents high frequency (pixel to pixel)
digitization and camera sensor noise. The b term is added
to the model by the authors to account for any intensity bias which
may be added to the image by video circuitry or ambient light.

Solving for the original image, $f(x,y)$, before the degradation
occurred results in:

(2) $f(x,y) = [g(x,y) - n(x,y) - b] / d(x,y)$.

Instead of estimating the additive noise and subtracting it
from the image $g(x,y)$, the image $g(x,y)$ is passed through a
low pass filter. This is accomplished by convolving $g(x,y)$
with a Gaussian impulse response whose coefficients are
given as

0.0	.0004	.002	.0004	0.0
.0004	.032	.113	.032	.0004
.002	.113	.4013	.113	.002
.0004	.032	.113	.032	.0004
0.0	.0004	.002	.0004	0.0

Figure 2 shows a plot of g(x,y) before and after the Gaussian operation. The intensity bias, b is calculated as being the lowest intensity value in the image after the additive noise is removed. This bias is subtracted from every image point in the image.

The last step in this image normalization process is the removal of the low frequency degradation, d(x,y). This is first estimated by using a nonlinear filtering technique called morphological filtering. This was selected over other low pass filters because it preserves edge structure. The effect of this filter operation is to delete image objects smaller than the defined size of the filter. This leaves an image which contains only the background intensity levels. Therefore to estimate d(x,y), the filter size is selected to be larger than the largest object to be measured.

A simple representation of this filter as given in[13] is:

(3) $d(s,t) = \max [\ f(x,y) \cdot \text{circ}\ [\sqrt{(x-s)^2+(y-t)^2}\ /r_0]]$

where $d(s,t)$ = resulting image

$f(x,y)$ = original image

circ $[\sqrt{(x-s)^2+(y-t)^2}\ /r_0]$ describes the circular

structuring element with

radius r_0 and equals:

1 for $\sqrt{(x-s)^2+(y-t)^2}\ /r_0\ <=\ 1$

0 otherwise

The max function propagates local image intensity maxima over the filter size defined by r_0 for every pixel in the image. The original boundaries are preserved by performing a reverse propagation on the transformed image:

(4) $d(s,t) = \min[\ f(x,y) \cdot \text{circ}\ [\sqrt{(x-s)^2+(y-t)^2}\ /r_0]]$

The min function propagates local image intensity minima over the filter size defined by r_0 for every pixel in the image. To normalize the image, the estimated $d(x,y)$ is divided into the intermediate image, ($g(x,y) - n(x,y) - b$) per equation (2).

Figure 3, 4 and 5 show an original image, its background estimate, d(x,y) using this filter, and the normalized image after division.

SEGMENTATION - Locating candidate objects

By utilizing the previous image restoration algorithm, intensity thresholding can be used to segment areas which may or may not be droplets, i.e., candidates[14]. Image threshold levels are selected by analyzing the intensity histogram[15,16]. It is assumed that the largest distribution in the histogram corresponds to the background intensity. The midpoint of this distribution's positive slope is selected as the threshold level if the histogram is unimodal. If there is a peak prior to the background peak the valley between both distributions is selected.

The output of the threshold operation is a binary image in which the dark areas correspond to candidates. Region boundaries are generated by using a 4 adjacency border algorithm[17]. This algorithm allows a fast way to generate all object boundaries at one time by treating the image as a whole. It is defined mathematically as

(5) $B(x,y) = S(x,y) * \left[\bar{S}(x-1,y) + \bar{S}(x+1,y) + \bar{S}(x,y+1) + \bar{S}(x,y-1) \right]$

where

$B(x,y)$ = boundary image

$S(x,y)$ = original threshold image

$\bar{S}(x,y)$ = logical negation of $S(x,y)$

$*$ = logical AND

$+$ = logical OR.

The output of this algorithm is object edge pixels which define the object's boundary. Figures 6 and 7 show a threshold and its associated boundary image.

The image is scanned by a tracking algorithm which follows object boundaries and calculates the centroid, radius (a circle is fit to the points) and number that represents how good the boundary fits the circle. The centroids are points in the normalized image $g(x,y)$ which will be used as feature extraction locations.

Feature Extraction

To extract features from candidate objects two curves are determined. Both curves are calculated by assuming symmetry around the centroids determined in the previous section. One curve is a radial intensity profile, the other a radial standard deviation. To accomplish this, the vector distance from each candidate's centroid to all neighboring points is

618

calculated. Neighboring points are averaged for an area spanning twice the radius value found when calculating the boundary centroid. The distance to neighboring points is modified to compensate for the aspect ratio induced by the camera. This is calculated using 0.8 times the vertical displacement. Intensity values for similar distance vectors are accumulated to get average radial intensity and radial standard deviation. See Figure 8.

Because of the way the centroid was selected two things are possible. First, the calculated intensity and deviation curves may or may not represent a droplet. Many kinds of anomalies are possible. For example the object could represent a multiple droplet cluster, a blob that was created by the selected threshold level or an anomaly created by edge effects after creating an image mosaic. Examples of these are shown in Figure 7. These anomalies are distinguished using the circular fit number generated during boundary tracking along with the intensity and deviation curves during the classification process. Secondly, the centroid may indicate a valid droplet but may not be the real object center. To correct this, the software attempts to reposition all droplet centers by using radial deviation information as an indication of best center position. Repositioning is done by calculating the standard deviation for the four quadrants of a candidate. See Figure 9. The derivative of the quadrant curves 2,3,4 is

cross correlated with the derivative of quadrant 1. The resulting correlation peaks are at index points which weight the direction of center repositioning in the following way:

(6) Delta X = TRUNCATE(0.5 + cosϕ (-Q2 - Q3 + Q4)) (7) Delta Y = TRUNCATE(0.5 + sinϕ (Q2 - Q3 - Q4))

where ϕ = 45 degrees =(.707)

Q1-4 = correlation index values

This procedure iterates up to 5 times per candidate before aborting if the delta valves do not converge to zero. Assuming that the radial intensity profile corresponds to the diffraction pattern of a real droplet, a variety of features describing the pattern are calculated. Some of these features are :

1. Intensity profile slope at the droplet center.

2. Number of rings within the droplet.

3. Slope of intensity profile at droplet edge.

4. Droplet contrast.

5. Intensity profile overshoot height and width.

6. Droplet radius measured at the maximum profile slope at the droplet's edge.

Extracted features and where the feature is measured is shown on the curves in Figure 10. This figure was generated using theoretical radial intensity plots of an ideal opaque

100 micron sphere at 200 and 400 microns from the plane of focus.

A rudimentary classification procedure uses these and other features to select the radial intensity curves which represent droplets that are in the sample volume.

Experimental Procedure

Two preliminary experiments were run to quantify the accuracy of the automatic system vs. manual techniques.   In the first, a slide of polystyrene microspheres was measured using a micrometer attached to a microscope (labeled MICROMETER in Figure 11). 500 measurements were made on the slide to get an ensemble average of the distribution.   In a similar fashion 50 images at random slide positions were analyzed by the automatic system (VIDEO-AUTO).   Images were acquired by illuminating the slide with a 5 mw helium neon laser. A CCD camera inline with the laser detected a sample area using the same 'experimental' optics described in the hardware section. The slide was held in a micropositioning device and images with a high droplet density were recorded. These same images were also measured manually on a video monitor using a scale (VIDEO-MANUAL).

In a second experiment, 400 images were recorded in the high pressure high temperature test facility using a Heptane gasoline spray.   A nitrogen laser and vidicon camera was

used as the illumination source and sensor. The optics used were the same as in experiment 1. The images were manually measured on a video monitor by two different observers (VIDEO-MANUAL #1,#2) and also by the automatic system. Because this experiment measured a real spray the sample counts were corrected for depth of field effects. This procedure compensates for the fact that smaller droplets defocus faster than larger ones for equal distances from the imaging optics plane of focus. Therefor to account for a varying sample volume, the droplet size counts for the sample volume is multiplied by the ratio of depth of fields. The ratio is defined as the maximum measured size's depth of field divided by each size bin's depth of field. This increases count values for smaller droplet size bins exponentially.

A comparison of sizing the droplets manually vs. automatically is given for both experiments in Figures 11 and 12. Both figures compare the percentage of total count vs. droplet size. Also included is the linear, volume, and sauter mean diameters for each method.

Results

The first experiment is more controlled than the second because no decision is necessary on the observer's part as to whether or not a sphere (droplet) is in focus, and thus all objects were counted except for droplet clusters. In

experiment 1, the manual measurement using the video monitor varied from the measurement using the micrometer by a 2-6% range for the distribution's mean diameters. This includes errors induced in the measurement process (selecting the object boundaries in both cases is subjective) and actual distribution differences because of the small sample size (500 for the micrometer, 175 for the monitor) and human error.

The distribution's mean diameters calculated using the automatic system varied over a 3-9% range from the micrometer values. It measured 172 objects, 1 of which was an error.

In experiment 2, the manual #2 measurements varied 2-13% from manual #1 over the various mean diameters. Because this second experiment involved real spray images, a decision as to the selection of droplets by their degree of focus had to be made by the observers. 400 images were analyzed containing approximately 8000 candidate objects. The distribution size totalled 150 and 120 droplets for the #1 and #2 manual measurements respectively. Both manual measurements were averaged to provide mean diameter values to compare against the automatic system. The automatic system varied 5-16% from those average values. It selected 85 focused droplets.

The variation between measurements in both experiments is due to the small sample size and human measurement variations. size[18].

CLOSURE

A system has been developed which automatically measures droplet size distributions from video images. This offers a method to measure areas of spray distributions were conventional devices fail such as at the spray nozzle tip. This method may also be used to verify the calibration of other instruments. The accuracy of this technique has been evaluated by two preliminary experiments and was shown to be in the range of 2-16%. It is felt that this is very satisfactory range. From experience gained in these experiments we feel that a next step is a dual purpose experiment involving larger sample sizes. This would confirm our experimental results and at the same time characterize a spray.

REFERENCES

1. J. M. Tishkoff, Second International Conference on Liquid Atomization and Spray Systems, 10(1), (6),(1982).

2. J. M. Tishkoff, D. C. Hammond and A. R. Chraplyvy, J. Fluids Engineering, 104(9), 313 (1982).

3. B. D. Peters, "Laser-Video Imaging and Measurement of Fuel Droplets in a Spark-Ignition Engine," presented at the Conference on Combustion in Engineering, IME, (4),(1983).

4. C. Ramshaw, J. Inst. of Fuel, (7), 287 (1968).

5. C. S. Ow and R. I. Crane, Int. J. Heat and Flow, 2(1), 47 (1980).

6. M. C. Toner, M. J. Dix and H. Sawistowski, J Phys. E: Sci. Instrum. 11, 960 (1978).

7. C. S. Ow and R. I. Crane, J. Inst of Energy, (9), 119 (1981).

8. R. Fleeter, R. Toaz and V. Sarohia, ASME, reprint 82-WA/HT-23.

9. L. M. Oberdier, ASTM Symposium on Liquid Particle SIze Measurement Techniques, (6),123 (1983).

10. R. C. Dahlberg, Applications of Digital Image Processing III., SPIE, 207(8) ,(1979).

11. H. C. Andrews, Topics in Applied PhysicsPicture Processing and Digital Filtering, 6,1 (1979).

12. T. S. Huang, Topics in Applied physicsPicture Processing and Digital Filtering, 6,32 (1979).

13. E. Reinhardt, R. Erhardt, P. Schwarzmann, W. Bloss and R. Ott, The Intrn. Academy of Cytology Analytical and Quantitative Cytology, 1(2), 143 (1979).

14. K. S. Fu and J. K. Mui, Pattern Recognition, 13,3 (1980).

15. D. H. Ballard and C. M. Brown, "Computer Vision," 152-155 (1982).

16. T. Pavlidis, "Structured Pattern Recognition," 1, 65-69 (1977).

17. A. Rosenfield and A. C. Kak, "Digital Picture Processing," 333-352 (1976).

18. R. W. Tate, Proc. for the 2nd Intrn. Conf. on Liquid Atomization and Spray Systems, 12-4(6), (1982).
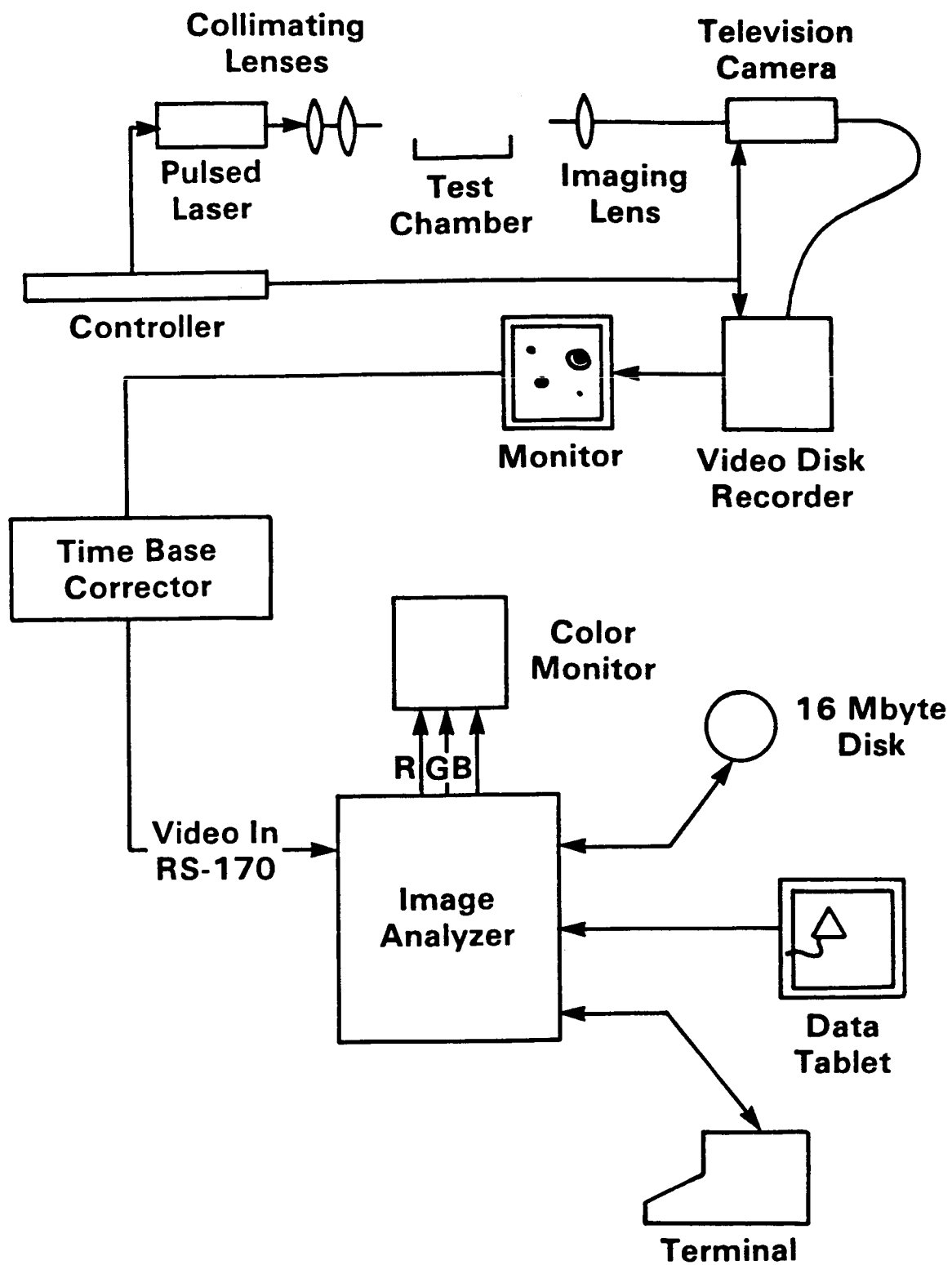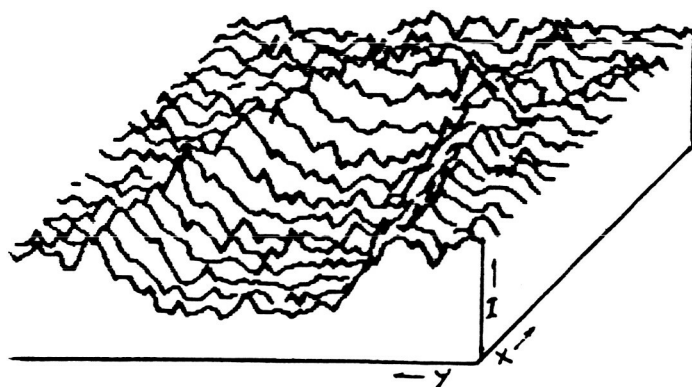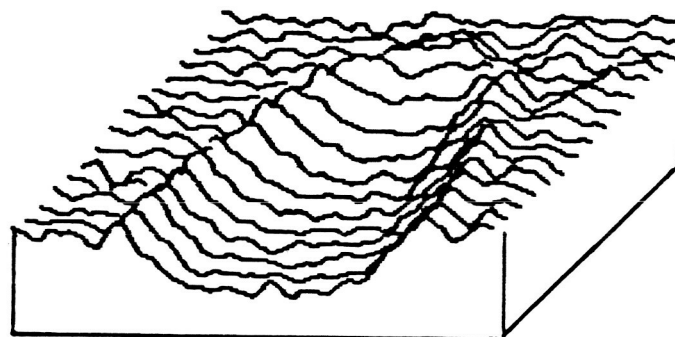
Figure 1. Equipment block diagram

628

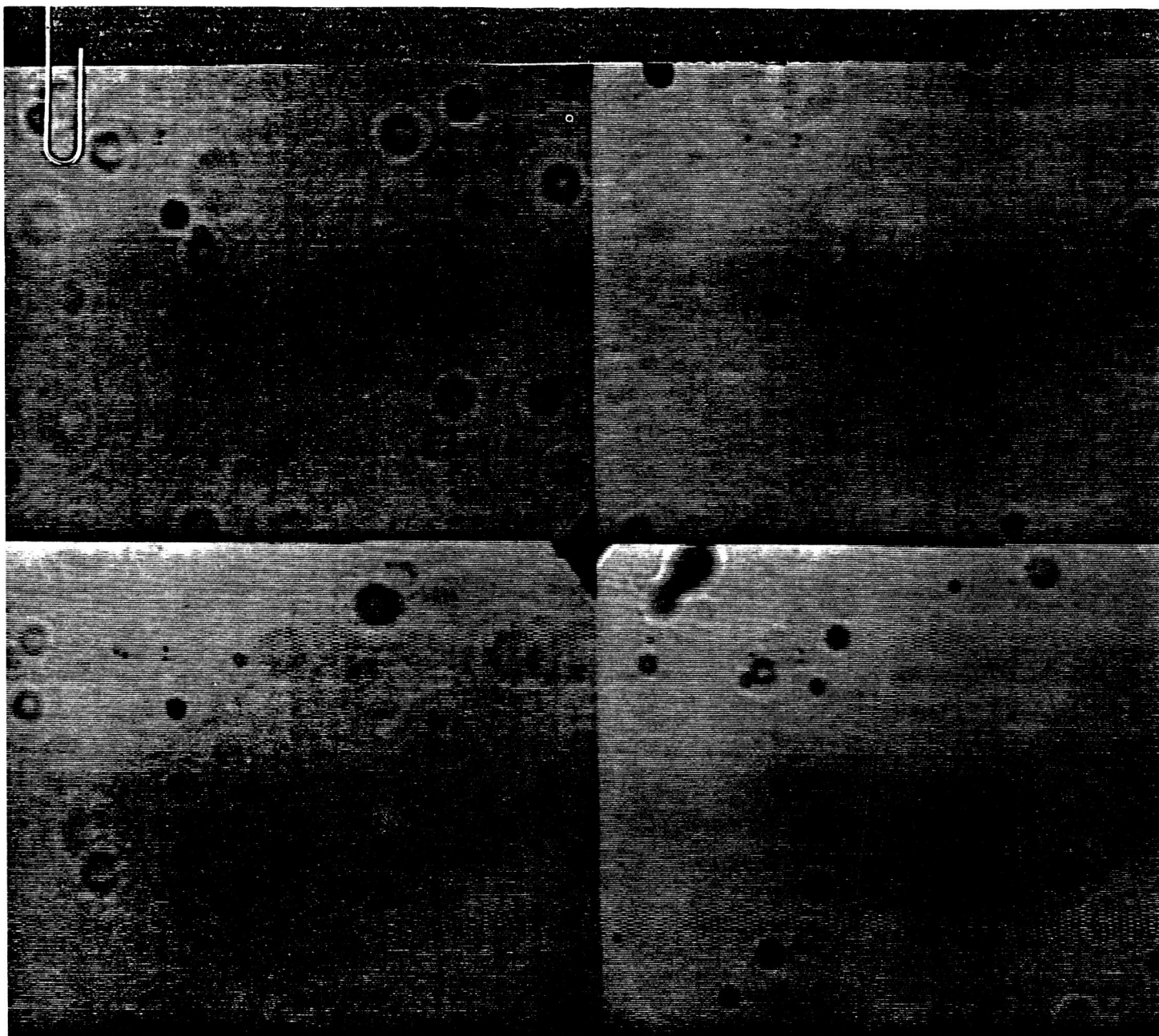Topographic representation of intensity level in area marked above

Original Image

After Gausian Filter

Figure 2. Gaussian filtering operation

Figure 3. Original Image

Figure 4.   Estimation of d(x,y)

631
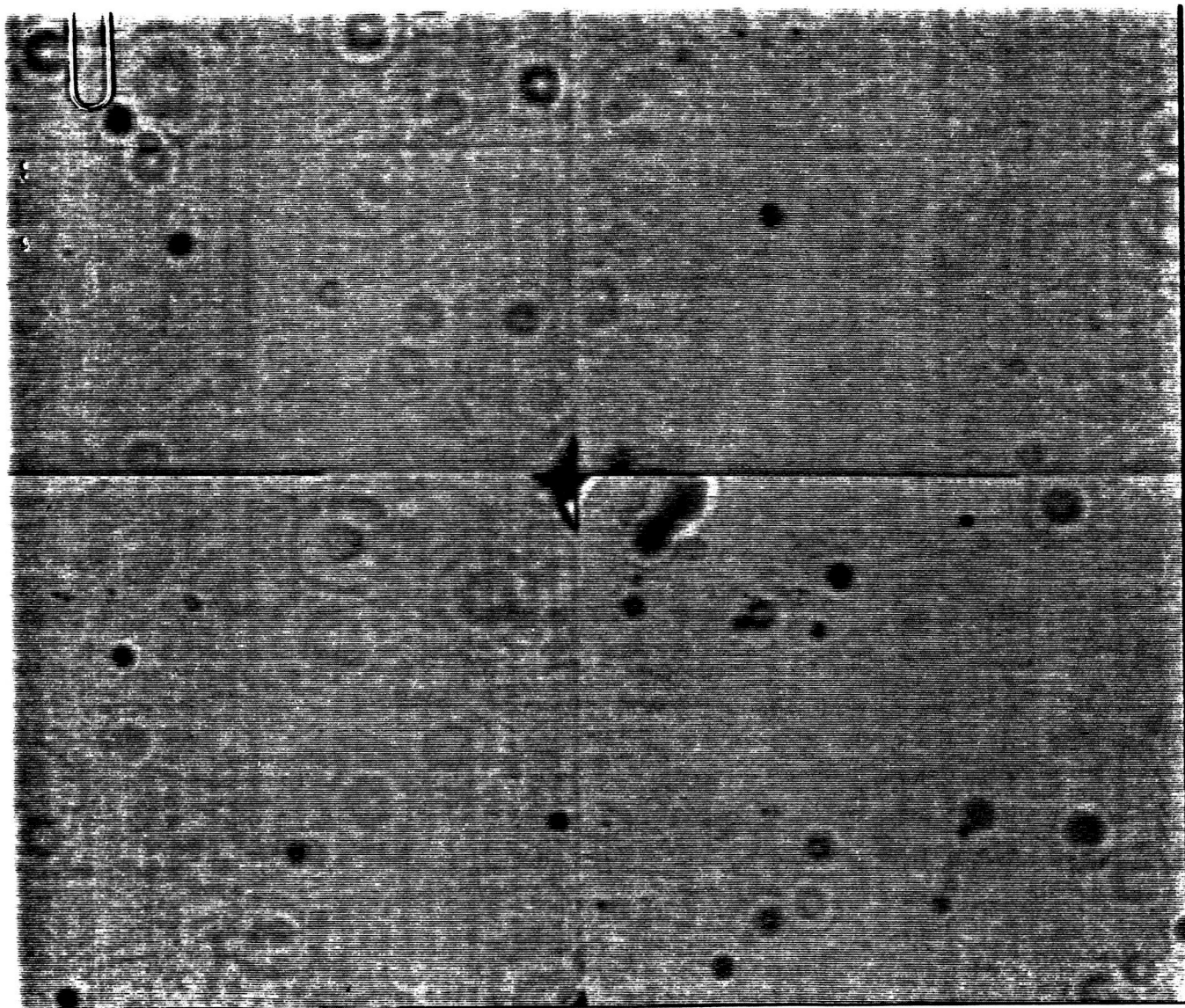
Figure 5. Normalized image

Figure 6. Threshold image

Out of Focus Droplet

Threshold Anomaly

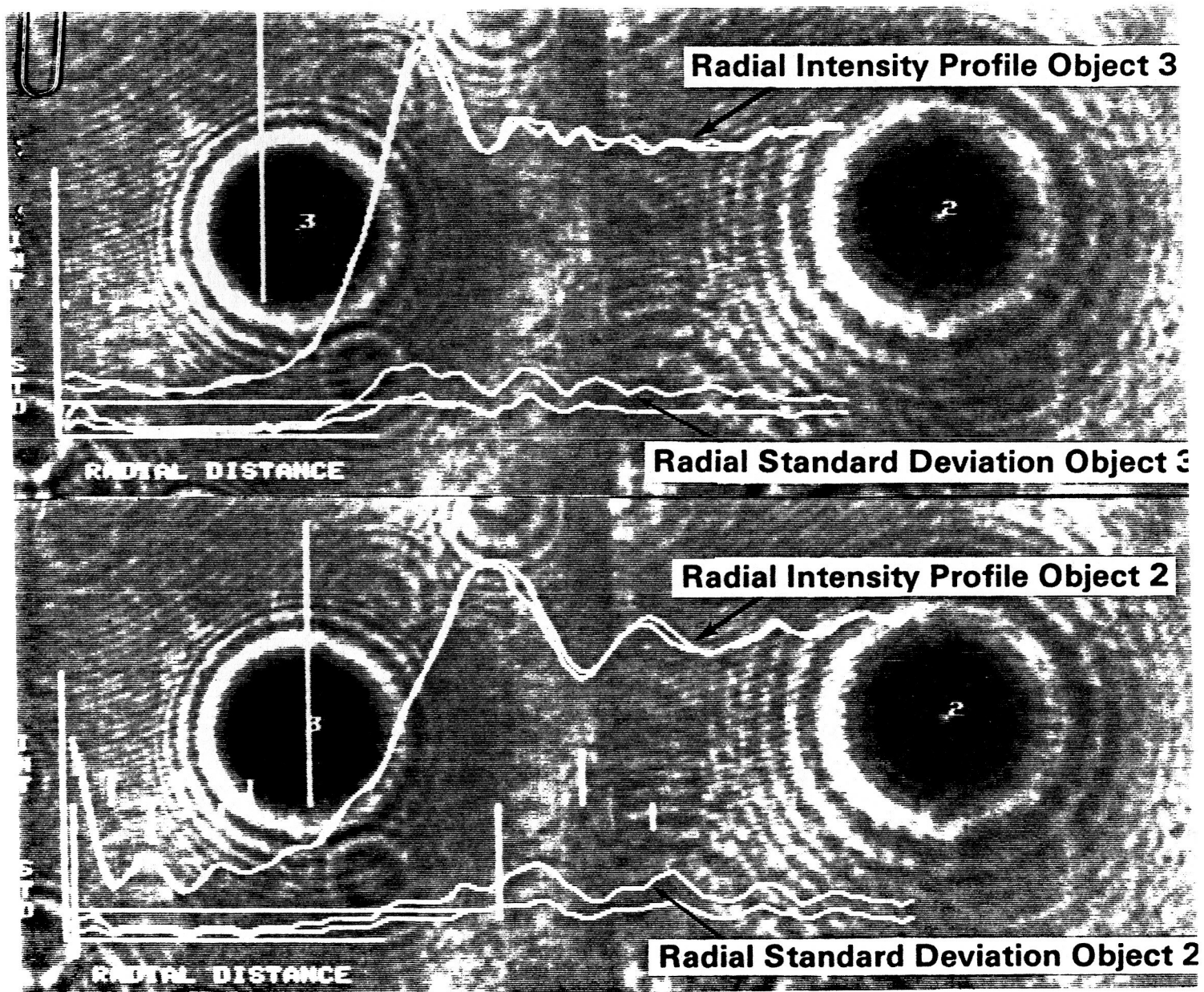**Mosaic Edge Anomaly**

Droplet Cluster
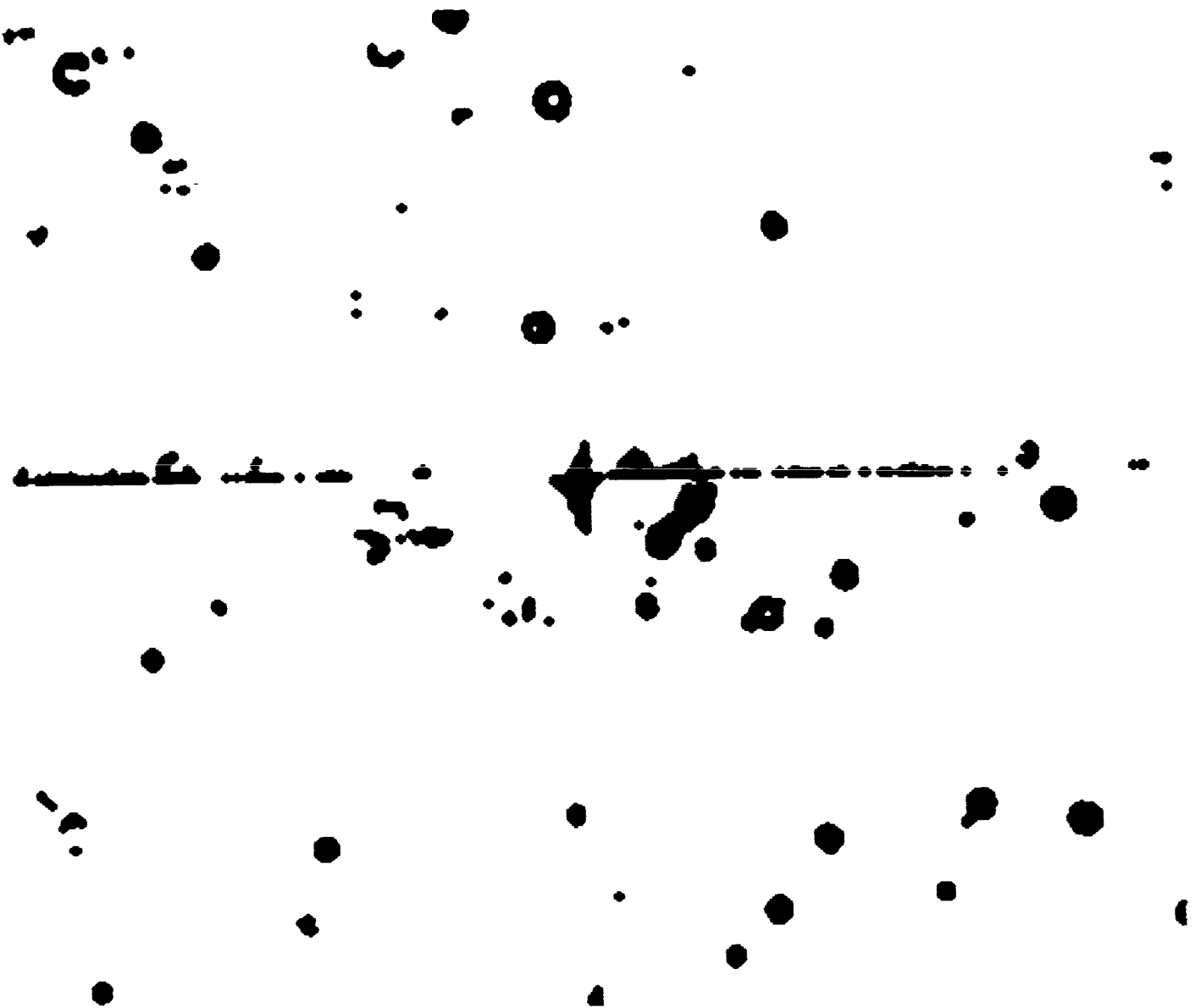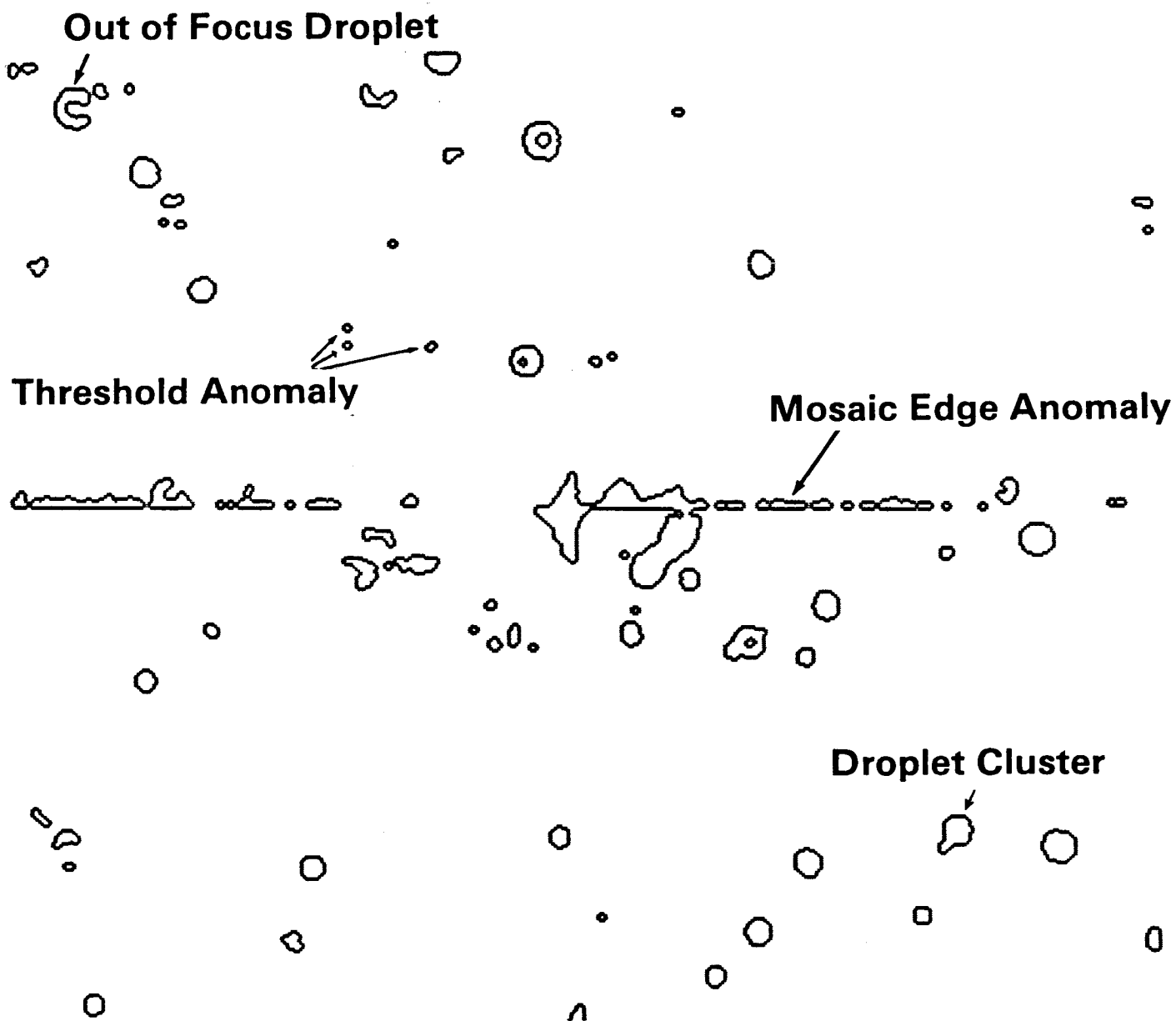
Figure 7. Boundary image

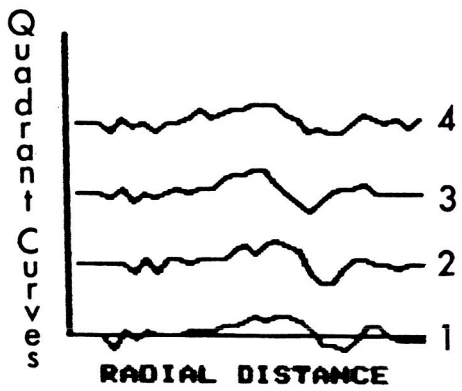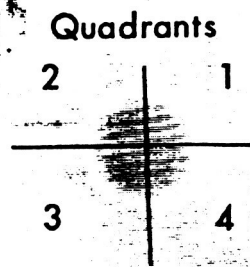Figure 8. Radial and Standard deviation curve for candidate

Before reposition
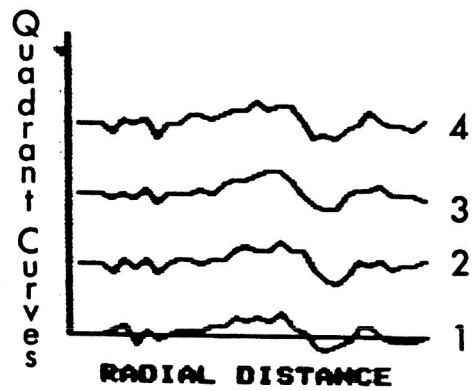
After reposition

Figure 9. Quadrant plots for deviation derivatives

DROPLET DIFFRACTION INTENSITY FUNCTION
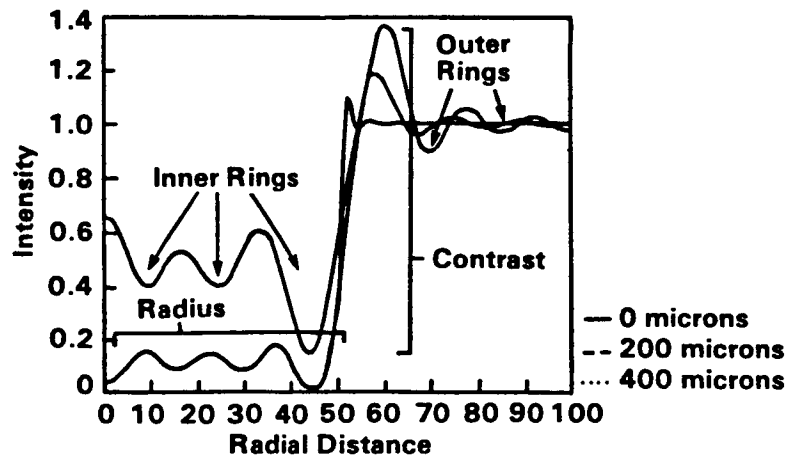
DROPLET DIFFRACTION INTENSITY FUNCTION
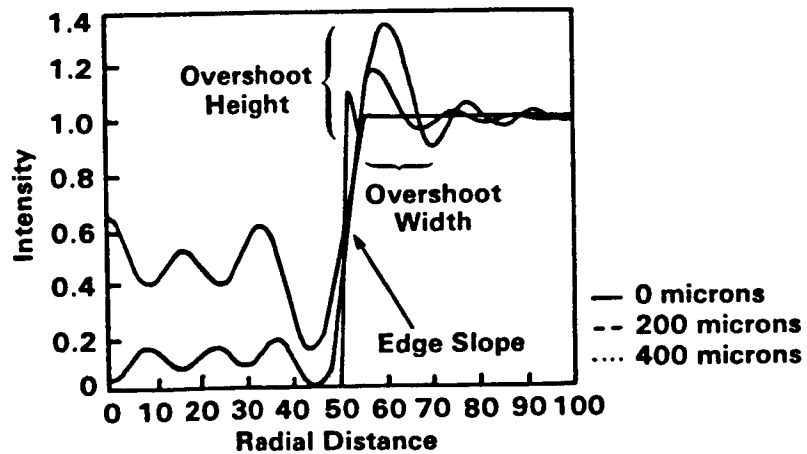
Figure 10. Feature measurement

MEASUREMENT COMPARISON
TV-MANUAL vs. MICROMETER vs. AUTOMATIC
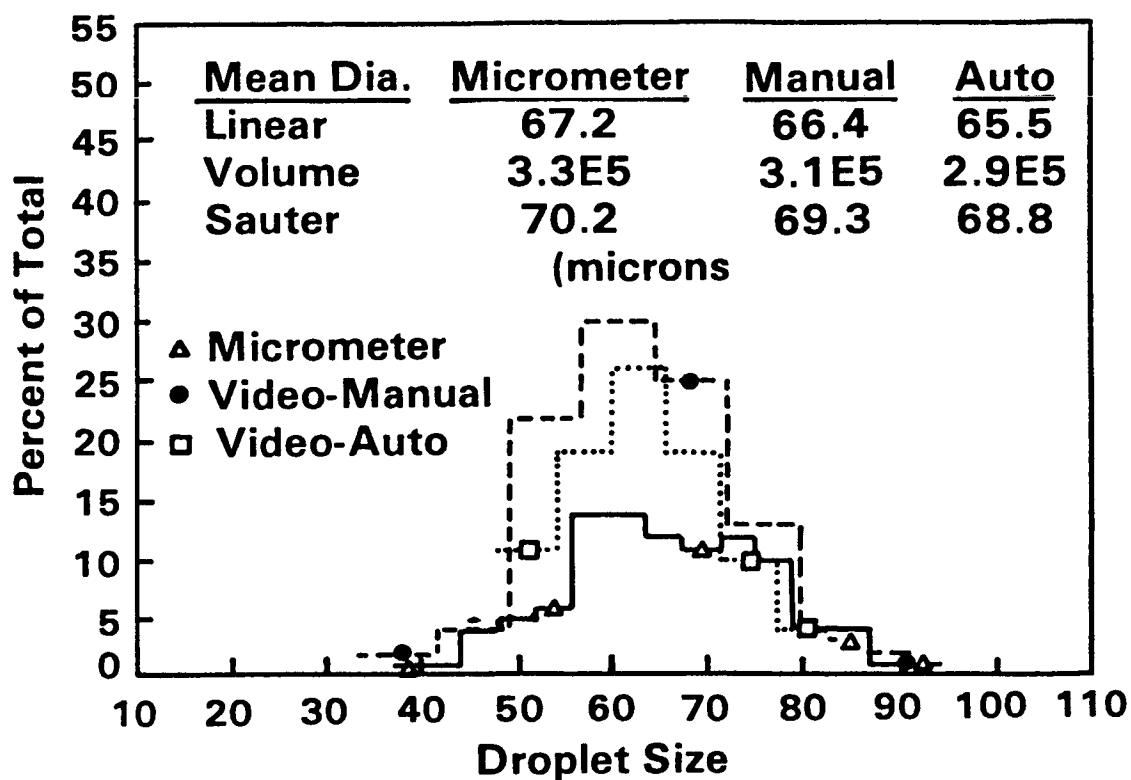
Figure 11. Synthesized distribution on microscope slide

MEASUREMENT COMPARISON
MANUAL vs. AUTOMATIC

Mean Dia.	Manual #1	Manual #2	Auto
Linear	37.4	26.8	28.4
Volume	3.1E4	2.8E4	3.4E4
Sauter	36.4	34.3	37.4
	(microns)		

△ Video-Manual #1
○ Video-Manual #2
□ Video-Auto

Percent of Total

Droplet Size

Figure 12. Heptane spray

Figure Legend

1. Equipment block diagram

2. Gaussian filtering operation

3. Original Image

4. Estimation of d(x,y)

5. Normalized image

6. Threshold image

7. Boundary image

8. Radial and Standard deviation curve for candidate

9. Quadrant plots for deviation derivatives

10. Feature measurement

11. Synthesized distribution on microscope slide

12. Heptane spray

Concluding Remarks

This workshop has brought together many researchers working on many facets of image data reduction. We all feel that this workshop has renewed our optimism for holographic interferometry and that it has great promise based on automated data analysis and reduction advancements. Holography has unique advantages and with correct data handling methods, it could yield ten fold or more information.

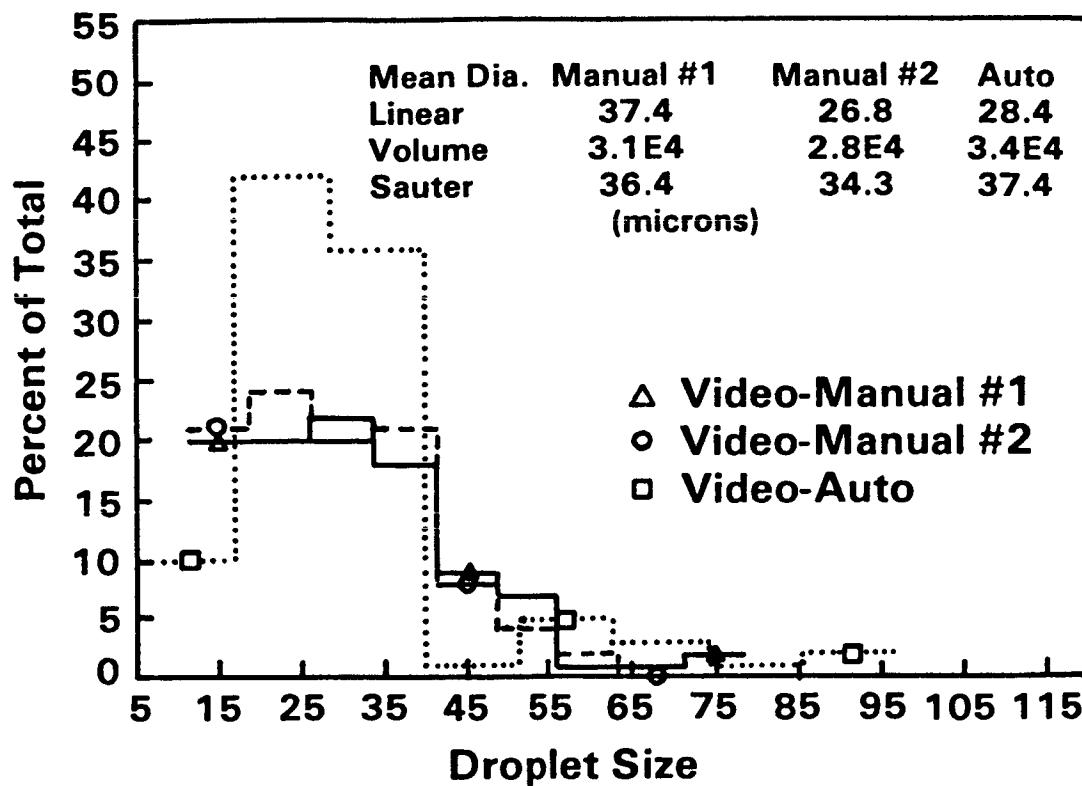It was suggested that a government agency should propose a new imitiative for funding holography and image analysis. Fortunately, the government's "Small Business Inovative Research" program in the past two years has provided funds for this work. Some examples are the development of thermo plastic holographic recording devices, higher power and more stable lasers, and the development of image analysis with artifical intelligence.

It was mentioned that progress on this type of research could be measured in a three or four year period. As such, a second workshop should be held in 1988 or 1989. We are certain that based on the work in progress and in the planning phases that another workshop would be very benefical.

List of Attendees

Chuck Allen	Air Force Weapons Lab, NM
Roland Adrian	University of Illinois
Dennis Alevander	University of Nebraska
Fred Becker	NASA Ames Research Center
Will Bachalo	Aerometrics Inc., CA
Ed Baroth	Jet Propulsion Lab
Gary Bertollini	General Motors
Peter Bryanston-Cross	University of Cambridge
Al Burner	NASA Langley Research Center
John Caufield	Aerodyne Research
Jim Cawthra	Rocketdyne, CA
Walt Christiansen	University of Washington
J. Clark	Catholic University of America
James Craig	Sprectron Development Lab.
Vance Deason	Idaho National Engineering Lab.
Steve Dunagan	NASA Ames Research Center
Richard Field	U.S. Army Armament R and D Ctr.
Arthur Decker	NASA Lewis Research Center
George Havener	Univ. of Dayton Research Inst.
Cecil Hess	Spectron Development Lab.
L. Hesselink	Stanford Univ.
William Horne	NASA Ames Research Center
Takashi Kashiwagi	National Bureau of Standards, MD
Marshall Kingery	Arnold AFB, TN
John Kittleson	NASA Ames Research Center
J. Kompenhans	DFVLR, W. Germany
A. Krothapalli	Florida State Univ.
Munson Kwok	Aerospace Corp.
Donald James	NASA Ames Research Center
Rave Lal	Univ. of Albama A&M
Luiz Lourenco	Florida State University
Gary Lynch	Kirtland AFB, NM
David Mann	U. S. Army Research Office, NC
Bruce Masson	Kirtland AFB, NM
Jonny Martinsson	FMV:Prov, Sweden
John McCrickerd	Newport Corp., CA
Robert Magnsson	University of Texas
Dariush Moddarress	Spectron Development Lab.
M. Nakagama	Gunma University, Japan
David Netzer	Naval Post Graduate School
Robert B. Owen	NASA Marshall Space Flight Ctr.
Kevin Owen	Complere Inc., CA
Dino Ponseggi	NASA Ames Research Center
John Powers	Naval Post Graduate School
Richard Perry	University of the Pacific, CA
W. Roquemore	Wright Patterson AFB, OH
Greg Reynolds	Lockheed Co., GA
Donald Rubin	U. S. Army Missle Command
Ruddy Ruff	NASA Marhsall Space Flight Ctr.
David Reuss	General Motors Research Lab.
Harold Schock	NASA Lewis Research Center
Gary Segal	Aerospace Corp.

George Seibert	Wright-Patterson AFB
Roger Simpson	Virginia Polytechnic Inst. & State Univ.
Ray Snyder	Stanford University
W. Charles Spring	Naval Surface Weapons Center
Don Sweeny	Sandia National Lab., CA
Fredrick Smetana	Army Research Office
Jerry Staton	Teledyne Brown, Inc.
D. Swain	Rockwell International, CA
Marty Taraboccohia	Rocketdyne, CA
Hung Tan	Spectron Development Lab
James Trollinger	Spectron Development Lab
Charles Vest	Univ. of Michigan
Bill Walker	U. S. Army Missile Command
Rupert Wenskus	Max-Planck Institut for Stromungforschung, W. Germany
M. Whiffen	Lockheed Company, GA
William Yanta	Naval Surface Weapons Center

NASA
National Aeronautics and Space Administration

Report Documentation Page

1. Report No. NASA CP 2477	2. Government Accession No.	3. Recipient's Catalog No.
4. Title and Subtitle Automated Reduction of Data from Images and Holograms		5. Report Date May 1987
		6. Performing Organization Code
7. Author(s) G. Lee, J. D. Trolinger and Y. H. Yu		8. Performing Organization Report No. A-87135
		10. Work Unit No. 505-61-01
9. Performing Organization Name and Address Ames Research Center Moffett Field, CA 94035		11. Contract or Grant No.
		13. Type of Report and Period Covered Conference Proceedings
12. Sponsoring Agency Name and Address National Aeronautics and Space Administration Washington, DC 20546		
		14. Sponsoring Agency Code

15. Supplementary Notes

Point of Contact: G. Lee, Ames Research Center, M/S 260-1
Moffett Field, CA 94035 (415) 694-4136 or FTS 464-4136

16. Abstract

Over 60 researchers in the fields of holography, particle sizing and image processing convened at NASA Ames Research Center for a two day workshop to discuss the above topics. The research programs of ten government laboratories, several universities, industry and foreign countries were presented. A number of papers on holographic interferometry with applications to fluid mechanics were given. Several papers on combustion and particle sizing, speckle velocimetry and speckle interferometry were given. Finally, a session on image processing and automated fringe data reduction techniques and the type of facilities for fringe reduction was held.

17. Key Words (Suggested by Author(s)) Interferometry Image analysis Automated digitizing	18. Distribution Statement Unclassified-Unlimited Subject Category - 02		
19. Security Classif. (of this report) Unclassified	20. Security Classif. (of this page) Unclassified	21. No. of pages 677	22. Price A25

NASA FORM 1626 OCT 8   For sale by the National Technical Information Service, Springfield, Virginia 22161